

Edited by  
**Peter Capper**  
**Michael Mauk**

# Liquid Phase Epitaxy

of Electronic, Optical  
and Optoelectronic  
Materials



 **WILEY**

Wiley Series  
in Materials for  
Electronic  
& Optoelectronic  
Applications

# Liquid Phase Epitaxy of Electronic, Optical and Optoelectronic Materials

Edited by

**Peter Capper**

*SELEX Sensors and Airborne Systems Infrared Ltd,  
Southampton, UK*

**Michael Mauk**

*School of Engineering & Applied  
Science, University of Pennsylvania, Philadelphia, USA*



John Wiley & Sons, Ltd



# **Liquid Phase Epitaxy of Electronic, Optical and Optoelectronic Materials**

## **Wiley Series in Materials for Electronic and Optoelectronic Applications**

### **Series Editors**

Dr Peter Capper, *SELEX Sensors and Airborne Systems Infrared Ltd, Southampton, UK*

Professor Safa Kasap, *University of Saskatchewan, Canada*

Professor Arthur Willoughby, *University of Southampton, Southampton, UK*

### **Published Titles**

Bulk Crystal Growth of Electronic, Optical and Optoelectronic Materials,  
Edited by P. Capper

Properties of Group-IV, III-V and II-VI Semiconductors, S. Adachi

Charge Transport in Disordered Solids with Applications in Electronics,  
Edited by S. Baranovski

Optical Properties of Condensed Matter and Applications, Edited by J. Singh

Thin Film Solar Cells: Fabrication, Characterization and Applications,  
Edited by J. Poortmans and V. Arkhipov

Dielectric Films for Advanced Microelectronics,  
Edited by M. R. Baklanov, M. Green and K. Maex

### **Forthcoming Titles**

Molecular Electronics, M. Petty

Luminescent Materials and Applications, Edited by A. Kitai

Photovoltaic Materials: From Crystalline Silicon to Third-Generation Approaches,  
Edited by G. J. Conibeer

CVD Diamond for Electronic Devices and Sensors, Edited by R. Sussmann

Silicon Photonics: Fundamentals and Devices, J. Deen and P. Basu

# Liquid Phase Epitaxy of Electronic, Optical and Optoelectronic Materials

Edited by

**Peter Capper**

*SELEX Sensors and Airborne Systems Infrared Ltd,  
Southampton, UK*

**Michael Mauk**

*School of Engineering & Applied  
Science, University of Pennsylvania, Philadelphia, USA*



John Wiley & Sons, Ltd

Copyright © 2007

John Wiley & Sons Ltd, The Atrium, Southern Gate, Chichester,  
West Sussex PO19 8SQ, England

Telephone (+44) 1243 779777

Email (for orders and customer service enquiries): cs-books@wiley.co.uk

Visit our Home Page on [www.wileyurope.com](http://www.wileyurope.com) or [www.wiley.com](http://www.wiley.com)

All Rights Reserved. No part of this publication may be reproduced, stored in a retrieval system or transmitted in any form or by any means, electronic, mechanical, photocopying, recording, scanning or otherwise, except under the terms of the Copyright, Designs and Patents Act 1988 or under the terms of a licence issued by the Copyright Licensing Agency Ltd, 90 Tottenham Court Road, London W1T 4LP, UK, without the permission in writing of the Publisher. Requests to the Publisher should be addressed to the Permissions Department, John Wiley & Sons Ltd, The Atrium, Southern Gate, Chichester, West Sussex PO19 8SQ, England, or emailed to [permreq@wiley.co.uk](mailto:permreq@wiley.co.uk), or faxed to (+44) 1243 770620.

Designations used by companies to distinguish their products are often claimed as trademarks. All brand names and product names used in this book are trade names, service marks, trademarks or registered trademarks of their respective owners. The Publisher is not associated with any product or vendor mentioned in this book.

This publication is designed to provide accurate and authoritative information in regard to the subject matter covered. It is sold on the understanding that the Publisher is not engaged in rendering professional services. If professional advice or other expert assistance is required, the services of a competent professional should be sought.

The publisher and the author make no representations or warranties with respect to the accuracy or completeness of the contents of this work and specifically disclaim all warranties, including without limitation any implied warranties of fitness for a particular purpose. This work is sold with the understanding that the publisher is not engaged in rendering professional services. The advice and strategies contained herein may not be suitable for every situation. In view of ongoing research, equipment modifications, changes in governmental regulations, and the constant flow of information relating to the use of experimental reagents, equipment, and devices, the reader is urged to review and evaluate the information provided in the package insert or instructions for each chemical, piece of equipment, reagent, or device for, among other things, any changes in the instructions or indication of usage and for added warnings and precautions. The fact that an organization or Website is referred to in this work as a citation and/or a potential source of further information does not mean that the author or the publisher endorses the information the organization or Website may provide or recommendations it may make. Further, readers should be aware that Internet Websites listed in this work may have changed or disappeared between when this work was written and when it is read. No warranty may be created or extended by any promotional statements for this work. Neither the publisher nor the author shall be liable for any damages arising herefrom.

#### ***Other Wiley Editorial Offices***

John Wiley & Sons Inc., 111 River Street, Hoboken, NJ 07030, USA

Jossey-Bass, 989 Market Street, San Francisco, CA 94103-1741, USA

Wiley-VCH Verlag GmbH, Boschstr. 12, D-69469 Weinheim, Germany

John Wiley & Sons Australia Ltd, 42 McDougall Street, Milton, Queensland 4064, Australia

John Wiley & Sons (Asia) Pte Ltd, 2 Clementi Loop #02-01, Jin Xing Distripark, Singapore 129809

John Wiley & Sons Canada Ltd, 6045 Freemont Blvd, Mississauga, Ontario, L5R 4J3, Canada

Wiley also publishes its books in a variety of electronic formats. Some content that appears in print may not be available in electronic books.

Anniversary Logo Design: Richard J. Pacifico

#### ***Library of Congress Cataloging-in-Publication Data***

Liquid phase epitaxy of electronic, optical, and optoelectronic materials / edited by Peter Capper, Michael Mauk.  
p. cm.

Includes bibliographical references.

ISBN 978-0-470-85290-3 (cloth)

1. Electronics—Materials. 2. Optical materials. 3. Optoelectronic devices—Materials. 4. Semiconductors.
5. Liquid phase epitaxy. 6. Crystal growth. I. Capper, Peter. II. Mauk, Michael.

TK7871.L57 2007

621.3815'2—dc22

2007013981

#### ***British Library Cataloguing in Publication Data***

A catalogue record for this book is available from the British Library

ISBN 978-0-470-85290-3

Typeset in 10/12pt Times by Laserwords Private Limited, Chennai, India

Printed and bound in Great Britain by Antony Rowe Ltd, Chippenham, Wiltshire

This book is printed on acid-free paper responsibly manufactured from sustainable forestry in which at least two trees are planted for each one used for paper production.

# Contents

<b>Series Preface</b>	<b>xi</b>
<b>Preface</b>	<b>xiii</b>
<b>Acknowledgements</b>	<b>xix</b>
<b>List of Contributors</b>	<b>xxi</b>
<b>1 Introduction to Liquid Phase Epitaxy</b>	<b>1</b>
<i>Hans J. Scheel</i>	
1.1 General aspects of liquid phase epitaxy	1
1.2 Epitaxial growth modes, growth mechanisms and layer thicknesses	3
1.3 The substrate problem	15
1.4 Conclusions	16
Acknowledgements	17
References	17
<b>2 Liquid Phase Epitaxy in Russia Prior to 1990</b>	<b>21</b>
<i>V.A. Mishurnyi</i>	
2.1 Introduction	21
2.2 Specific features of growth of quantum-well heterostructures by LPE	23
2.2.1 LPE growth from a capillary	23
2.2.2 Low-temperature LPE	25
2.2.3 LPE growth of InGaAsP quantum well heterostructures	29
2.3 Rare-earth elements in LPE technology of some III-V binary compounds and solid solutions	35
2.4 Conclusions	37
Acknowledgements	37
References	38
<b>3 Phase Diagrams and Modeling in Liquid Phase Epitaxy</b>	<b>45</b>
<i>Kazuo Nakajima</i>	
3.1 Introduction	45
3.2 Equilibrium phase diagrams	46
3.2.1 Binary, ternary and quaternary phase diagrams	46



3.2.2	Calculation of binary, ternary and quaternary phase diagrams	49
3.2.3	Calculation of phase diagrams considering the surface, interface and strain energies	54
3.2.4	Experimental determination of phase diagrams	59
3.2.5	Miscibility gap	64
3.3	Technologies of LPE growth	66
3.4	III-V materials for LPE growth	68
3.5	Lattice matching	69
3.6	Growth of misfit-dislocation-free wafers	71
3.7	Phase diagrams of growth mode	73
3.8	Growth kinetics	77
3.8.1	Calculation of III-V layer thickness	77
3.8.2	Compositional variation in III-V ternary layers	78
3.9	Summary	79
	References	79
	Appendix	82
<b>4</b>	<b>Equipment and Instrumentation for Liquid Phase Epitaxy</b>	<b>85</b>
	<i>Michael G. Mauk and James B. McNeely</i>	
4.1	Introduction	85
4.2	Overview, general description and operation of horizontal slideboat LPE system	89
4.3	Crucibles and slideboats	91
4.4	Alternative slideboat designs	92
4.5	Furnaces and heating	96
4.6	LPE ambient	98
4.7	Tubes, sealing and gas handling	99
4.8	Controllers and heating	99
4.9	Temperature measurements and other instrumentation	100
4.10	Safety	101
4.11	Production LPE systems	101
	References	105
<b>5</b>	<b>Silicon, Germanium and Silicon-Germanium Liquid Phase Epitaxy</b>	<b>109</b>
	<i>Michael G. Mauk</i>	
5.1	Introduction and scope of review	110
5.2	Historical perspective	111
5.3	Basis of silicon and germanium LPE	115
5.3.1	Nucleation of silicon from a molten metal solution	119
5.4	Silicon LPE methods	124
5.4.1	Steady-state methods of solution growth and LPE	125
5.5	Solvent selection	135
5.6	Low-temperature silicon LPE	137
5.7	Purification of silicon for solar cells in an LPE process	138
5.8	Electrical properties of LPE-grown silicon	140
5.9	LPE of Si- and Ge-based alloys	141

5.10 Selective LPE and liquid phase ELO	142
5.11 Solar cells	144
5.11.1 Epitaxial silicon solar cells by LPE	145
5.11.2 Si solution growth on nonsilicon substrates for solar cells	149
5.12 Other applications of silicon and germanium LPE	150
5.13 Conclusions and outlook	151
References	151
Appendix 1. Phase equilibria modeling: The silicon-metal liquidus	166
A1.1 The silicon-metal binary liquidus	168
A1.2 Alloy solvents	168
Appendix 2. Impurities and doping in silicon LPE	171
Appendix 3. Effects of oxygen and water vapor in Si LPE	175
A3.1 Thermodynamics of silicon oxidation	176
A3.2 Silicon passivity and melt reducing agents	178
<b>6 Liquid Phase Epitaxy of Silicon Carbide</b>	<b>179</b>
<i>R. Yakimova and M. Syväjärvi</i>	
6.1 Introduction	179
6.2 Fundamental aspects of LPE of SiC	180
6.3 Growth methods for SiC LPE	185
6.3.1 Modified travelling solvent method	186
6.3.2 Dipping method	191
6.3.3 Container free LPE	191
6.3.4 Vapour–liquid–solid mechanism	192
6.4 Characteristic features of SiC LPE	193
6.4.1 Step-bunching	193
6.4.2 Micropipe filling	195
6.5 LPE of SiC under reduced gravity	196
6.6 Applications	198
References	199
<b>7 Liquid Phase Epitaxy of Gallium Nitride</b>	<b>203</b>
<i>Hans J. Scheel and Dennis Elwell</i>	
7.1 Introduction	203
7.2 Control of epitaxial growth modes	207
7.3 Thermodynamics and phase diagrams	209
7.4 Requirements for LPE	211
7.4.1 Solvents	211
7.4.2 Crucibles	213
7.4.3 Growth atmosphere	214
7.4.4 Substrates	215
7.5 LPE results, characterization of LPE(solution)-grown GaN	218
7.6 Cubic GaN	221
7.7 Conclusions and outlook	221
References	222

<b>8 Liquid Phase Epitaxy of Quantum Wells and Quantum Dots</b>	<b>227</b>
<i>A. Krier, X.L. Huang and Z. Labadi</i>	
8.1 Introduction	227
8.2 LPE growth of quantum wells	228
8.3 Thickness of rapid slider LPE layers	231
8.4 Interface abruptness	235
8.5 Compositional homogeneity	236
8.6 Devices incorporating ultrathin LPE layers	237
8.7 LPE growth of InAs quantum wells	239
8.7.1 PL characterisation	241
8.8 LPE growth of quantum dots for mid-infrared optoelectronic devices	243
8.8.1 InSb QDs on GaAs (100) substrates	244
8.8.2 Investigation of InAsSb QDs	247
8.9 Mid-infrared luminescence of encapsulated InAsSb QDs	249
8.10 Electroluminescence of InAsSb QD LEDs	251
8.11 Summary	253
Acknowledgements	253
References	254
<b>9 Liquid Phase Epitaxy of <math>\text{Hg}_{1-x}\text{Cd}_x\text{Te}</math> (MCT)</b>	<b>259</b>
<i>P. Capper</i>	
9.1 Introduction	259
9.2 Growth	261
9.2.1 Introduction	261
9.2.2 Phase diagram and defect chemistry	262
9.2.3 LPE growth techniques	264
9.3 Material characteristics	269
9.3.1 Composition and thickness	271
9.3.2 Crystal quality and surface morphology	272
9.3.3 Impurity doping and electrical properties	273
9.3.4 Multiple-layer heterojunction structures	278
9.4 Device status	278
9.4.1 LPE growth on Si-based substrates	283
9.5 Summary and future developments	283
References	284
<b>10 Liquid Phase Epitaxy of Widegap II-VIs</b>	<b>289</b>
<i>J. F. Wang and M. Isshiki</i>	
10.1 Introduction	289
10.2 Basic properties	289
10.3 LPE technique	291
10.4 Review of some experimental results	292
10.4.1 Growth from Zn, Zn-Ga and halide solvents	293
10.4.2 Growth from Te and Se solvents	296

10.4.3 Growth from Sn solvent	299
10.4.4 Growth from Bi solvent	301
10.5 Conclusion	302
References	302
<b>11 Liquid Phase Epitaxy of Garnets</b>	<b>305</b>
<i>Taketoshi Hibiya and Peter Görnert</i>	
11.1 Introduction	305
11.2 LPE growth	309
11.3 Phase diagram and chemistry	311
11.3.1 Phase diagram	311
11.3.2 Chemical thermodynamics of LPE	314
11.3.3 Effect of oxygen partial pressure on magnetic properties	317
11.4 Growth mechanism and morphology	317
11.4.1 Mass transport and growth rate	317
11.4.2 Control of morphology	321
11.5 Bi-substituted garnet films	323
11.6 Properties of magnetic garnet films	325
11.6.1 Misfit strain	325
11.6.2 Faraday rotation	328
11.6.3 Optical absorption	328
11.6.4 Magnetic anisotropy	333
11.7 Applications of garnet films	334
11.8 Conclusions	337
Acknowledgements	337
References	337
<b>12 Liquid Phase Epitaxy: A Survey of Capabilities, Recent Developments and Specialized Applications</b>	<b>341</b>
<i>Michael G. Mauk</i>	
12.1 Introduction	342
12.2 Comparison of epitaxy techniques and some advantages of LPE	343
12.3 Previous reviews of LPE	355
12.4 Modeling of LPE processes	355
12.5 Survey of new developments and specialized applications of LPE	356
12.5.1 Five- and six-component III-V semiconductor alloys by LPE	357
12.5.2 LPE layers with atomically smooth surfaces	358
12.5.3 Quantum wells, superlattices and nanostructures by LPE	358
12.5.4 Growth of thick ternary and quaternary alloy layers for ‘virtual’ substrates with adjustable lattice parameters	360
12.5.5 Selective epitaxy and ELO	363
12.5.6 Melt epitaxy	366
12.5.7 Rare earth doping and other doping effects in LPE	366
12.5.8 Fundamental studies of crystal growth, melt convection and liquid-metal transport properties	367
12.5.9 Novel melt compositions for LPE	369
12.5.10 Liquid phase electroepitaxy	370

12.5.11 LPE of thallium-, manganese-, and bismuth-containing III-V alloys	373
12.5.12 Control of segregation in LPE-grown alloys	374
12.5.13 LPE heteroepitaxy	376
12.5.14 SiC and III-V nitride LPE	381
12.5.15 Some other materials grown by LPE or solution growth	383
12.5.16 LPE for shaped crystal growth	389
12.6 Conclusions and outlook	391
References	392
<b>13 Liquid Phase Epitaxy for Light Emitting Diodes</b>	<b>415</b>
<i>Michael G. Mauk</i>	
13.1 Introduction	415
13.2 Commercial LEDs	419
13.3 LPE for wide-bandgap (blue and UV) LEDs	420
13.3.1 Silicon carbide LEDs	420
13.3.2 Wide-bandgap II-VI compound LEDs	421
13.3.3 III-V nitride LEDs	422
13.4 LPE for mid-infrared LEDs	422
13.5 LPE for new LED design concepts	424
13.6 Outlook	426
References	430
<b>Index</b>	<b>435</b>

# Series Preface

## WILEY SERIES IN MATERIALS FOR ELECTRONIC AND OPTOELECTRONIC APPLICATIONS

This book series is devoted to the rapidly developing class of materials used for electronic and optoelectronic applications. It is designed to provide much-needed information on the fundamental scientific principles of these materials, together with how these are employed in technological applications. The books are aimed at postgraduate students, researchers and technologists, engaged in research, development and the study of materials in electronics and photonics, and industrial scientists developing new materials, devices and circuits for the electronic, optoelectronic and communications industries.

The development of new electronic and optoelectronic materials depends not only on materials engineering at a practical level, but also on a clear understanding of the properties of materials, and the fundamental science behind these properties. It is the properties of a material that eventually determine its usefulness in an application. The series therefore also includes such titles as electrical conduction in solids, optical properties, thermal properties, and so on, all with applications and examples of materials in electronics and optoelectronics. The characterization of materials is also covered within the series in as much as it is impossible to develop new materials without the proper characterization of their structure and properties. Structure–property relationships have always been fundamentally and intrinsically important to materials science and engineering.

Materials science is well known for being one of the most interdisciplinary sciences. It is the interdisciplinary aspect of materials science that has led to many exciting discoveries, new materials and new applications. It is not unusual to find scientists with a chemical engineering background working on materials projects with applications in electronics. In selecting titles for the series, we have tried to maintain the interdisciplinary aspect of the field, and hence its excitement to researchers in this field.

Peter Capper  
Safa Kasap  
Arthur Willoughby



# Preface

Liquid phase epitaxy (LPE) is a mature technology and has been used in the production of III-V compound semiconductor optoelectronic devices for some 40 years. LPE has also been applied to silicon, germanium, SiC, and II-VI and IV-VI compound semiconductors, as well as magnetic garnets, superconductors, ferroelectrics, and other optical materials. Many semiconductor devices including light-emitting diodes (LEDs), laser diodes, infrared detectors, heterojunction bipolar transistors and heterointerface solar cells were pioneered with LPE. Further, LPE can produce epitaxial semiconductor layers of superior material quality with respect to minority carrier lifetime and luminescence efficiency. Nevertheless, LPE has fallen into disfavor in recent years, especially for device applications requiring large-area uniformity, critical layer thickness and composition control, and smooth and abrupt surfaces and interfaces. For making superlattices, quantum wells, strained layer structures, and heterostructures with large lattice mismatch or heterostructures comprised of materials with substantial chemical dissimilarity (e.g. GaAs-on-silicon), LPE is often dismissed out of hand in favor of other epitaxy technologies such as molecular beam epitaxy (MBE) or metal-organic chemical vapor deposition (MOCVD). One might conclude that despite the long and venerable history of LPE, progress has stagnated with few prospects for new applications. In particular, LPE suffers from widely held perceptions of poor reproducibility, and intrinsic difficulties in scale-up for large-area substrates and high-throughput operation. Nevertheless, and as the chapters in this book describe in detail, on-going efforts and new developments in LPE continue to widen its scope of applications and circumvent its customary limitations. New modes of liquid phase epitaxial growth can provide novel device structures. Some of the traditional shortcomings of LPE as mentioned above are addressed by new techniques and approaches based on novel melt chemistries, alternative methods of inducing growth (e.g. through imposed temperature gradients, electric currents, mixing, Peltier cooling, or solvent evaporation), hybrid processes that combine LPE with other methods of epitaxy, and LPE on structured or masked substrates. Further, unique attributes that distinguish LPE from competing semiconductor epitaxy technologies (MBE and MOCVD) enable it to serve important niches in semiconductor device technology.

To underscore some of the relative or unique advantages of LPE for the growth of semiconductor devices, a few of the more important features of LPE may be listed, and include:

1. High growth rates. Growth rates in the range of  $0.1\text{--}1\ \mu\text{m min}^{-1}$  can be achieved with LPE. This is 10 to 100 times faster than MBE or MOCVD, and thus thick device structures are feasible with LPE.
2. The wide range of dopants available with LPE. Virtually any element added to the melt will be incorporated into the epitaxial layer to some finite degree. Most of the



periodic table can be utilized as dopants in LPE, and thus, LPE is an excellent tool for fundamental doping studies.

3. The preferential segregation of deleterious impurities to the liquid phase that results in low background impurities in the epitaxial layer. LPE can produce semiconductor material of extremely high purity.
4. The low point defect densities due to near-equilibrium growth conditions and/or favorable chemical potentials of crystal components in the liquid phase.
5. The absence of highly toxic precursors or by-products.
6. Low capital equipment and operating costs.
7. The feasibility of selective epitaxy and epitaxial lateral overgrowth (ELO) with high aspect ratios.
8. The ability to produce shaped or faceted crystals for novel device structures.

However, LPE is less forgiving of process variations than other methods and more susceptible to process fluctuations and the effects of uncontrolled variables, both of which can lead to failed growth or poor material quality. In some cases, such as the LPE growth of InGaAsSb quaternary alloys, the growth temperature must be controlled to within 1 °C in order to produce an epitaxial layer. As another example, LPE appears to be much more sensitive to the crystallographic (mis)orientation of the substrate than other epitaxy techniques. On the other hand, and on the positive side, when the LPE process *is* operated within its optimum parameter window, the material quality is often superior to that produced by other epitaxy techniques. Thus, the price for high material quality associated with LPE is more stringent demands on process control and greater susceptibility to process variations. Ultimately, this feature may be attributed in large part to the near-equilibrium nature of LPE that distinguishes it from CVD and LPE. Practitioners of epitaxy may regard this view as overly simplistic, but it offers some explanation to both the historic role of LPE in prototyping new semiconductor materials and device concepts, and to its ultimate disfavor for large-scale, high-throughput production of many commercial semiconductor devices, especially those with tight tolerances for composition, doping, and layer thicknesses.

The simplicity of the LPE process, and its basis on phase equilibria rather than complex precursor chemistry, growth kinetics and mass transfer, provide a good platform for exploring new semiconductor materials and developing and prototyping novel semiconductor devices. Based on chapters in this book, LPE can be advocated for several important applications. The growth of virtual substrates with tunable lattice constants comprised of thick LPE-grown semiconductor alloy layers, possibly incorporating epitaxial lateral overgrowth to reduce defect densities, and possibly enabled with electro-epitaxy, temperature-gradient induced growth, and modifications of a double-crucible apparatus adapted for LPE, would exploit many inherent and unique features of LPE. Such customized virtual substrates would be more costly than current commercial substrate wafers made by CZ, float zone, Bridgman, or vertical gradient freeze techniques. However, in view of the prices obtained for SiC and bulk GaN substrates in the last decade, it is clear that for at least some applications, the semiconductor industry is willing to pay a high premium for substrates that enable improved material quality and/or new devices. LPE

still figures prominently in low-bandgap III-V optoelectronics for mid-infrared applications. In many cases, the best reported results for LEDs and detectors are for devices made by LPE. For these LPE-grown materials (InAsSb, InAsSbP, InGaAsSb, and related alloys), the low defect densities and impurity levels, the latter achieved often with impurity gettering by rare earths, are decisive. Some of the limiting features of LPE may yet be circumvented by novel melt chemistries and new methods of inducing growth, including imposed temperature gradients and/or electric currents, solvent evaporation, solute feeding by mixing or capillary flow, and pre-cooling or pre-heating of the substrate prior to contact with the melt. The ability of LPE to produce a wide range of shaped or faceted crystals is unique among the epitaxy methods and this feature could be exploited in LED designs to increase optical coupling.

While it is unlikely that LPE will continue to compete directly with MBE or MOCVD for production of ‘mainstream’ microelectronics devices, lasers, space solar cells and detector arrays, the foregoing suggests that some of the unique features of LPE can be exploited for specialized semiconductor applications.

In Chapter 1 an introduction to all the aspects of LPE is given and it is noted that for a given crystal or epilayer with a specified application and device performance requirement there can only be one optimum growth technology if one considers all the factors of thermodynamics, growth technology, economics, etc. It is also noted that LPE is the best technique to use for the highest structural perfection, best stoichiometry and atomically flat surfaces/interfaces.

Chapter 2 gives a summary of the work done on LPE in Russia prior to 1990, much of which was not widely known in the West. Many device structures using multilayer III-V heterostructures were grown by LPE. This work culminated in the award of the Nobel Prize in Physics in 2000 to the head of the group, Academician Zh. I. Alferov. Although much of the work is now done using MOCVD and MBE, LPE is still used for some applications because of its near-equilibrium nature, its higher growth rates and its cost advantages.

Phase diagrams and modeling are the topics in Chapter 3, and III-V ternary and quaternary systems are used as examples. These are critical areas in establishing good control over the LPE technologies used. The applications for these systems include optoelectronic devices but also, more recently, TPV cells.

The field of equipment and instrumentation is covered in Chapter 4, where it is noted that an LPE kit is typically a tenth of the price of a commercial MOCVD or MBE apparatus. This makes LPE more suited to development of new systems or niche market applications. The process is also conceptually simpler than other epitaxial techniques, does not use vacuum, does not involve highly toxic substances, in general, and costs of maintenance and operation are also lower. Disadvantages include the lack of *in situ* monitoring during growth, the difficulty of scaleup in many cases, and layer homogeneity and reproducibility.

In Chapter 5 the application of LPE to silicon and germanium is discussed. Ironically, as the interest in LPE of compound semiconductors waned prior to 1990 the interest in this area of LPE growth actually increased. The driving force was the need for an alternative solar cell material to bulk silicon. The work included growth on silicon itself, metals and ceramics. None of these is currently used in a production environment, although the potential of high growth rates and the possibility of using metal solutions to both grow and purify simultaneously are still being assessed.

The wide-bandgap semiconductor SiC is the topic discussed in Chapter 6. This material has properties that make it highly suitable for high-power, high-frequency and high-temperature device types. LPE is the epitaxial technique of choice to grow this material at relatively low temperatures and near to equilibrium. LED device characteristics are improved using LPE-grown buffer layers and reducing micropipe defects leads to other benefits, including better long-term stability.

Another material system used in LEDs and lasers, i.e. GaN-based compounds, is described in Chapter 7. Here again, LPE could be used to produce lower dislocation and pipe defect densities in base-layer materials, the latter by layer overgrowth techniques. High structural perfection and flat surfaces have already been demonstrated in this material grown by LPE.

The growth of ultrathin layers of semiconductors is described in Chapter 8. It is shown to be possible to grow multilayer ternary and quaternary III-V structures that exhibit quantum-size effects. Chemically sharp interfaces are also possible and quantum wells as thin as 20 Å have been prepared. These layers are useful in mid-infrared optoelectronic devices with potential applications as gas sensors.

In Chapter 9 the pre-eminent infrared material, mercury cadmium telluride, is the topic under discussion. The higher structural quality of LPE-grown material makes this the preferred route for current production of second-generation focal plane arrays of photodiodes, particularly in the long-wavelength region. The excellent short- and long-range uniformity of crystal properties in LPE-grown material are additional benefits.

Chapter 10 provides a history of the growth of wide-bandgap II-VI compounds by LPE. Low-resistivity layers of ZnSe have been produced and used to make LEDs that were comparable with MOCVD and MBE material, but the difficulties of high melting points and volatilization make LPE very difficult to perfect in these systems.

The LPE growth of garnet materials has a long history and this is detailed in Chapter 11. These materials are used in microwave devices, bubble domain memories, magnetostatic wave devices, optical isolators and magnetic sensors. Nonmagnetic garnet materials were used as laser hosts, cathodoluminescence devices and substrates for epitaxial growth of magnetic garnets. High-quality layers up to 10 cm in diameter have been grown for commercial applications and research use.

Chapter 12 gives details of the numerous recent developments and specialized applications in the area of LPE. These include growth of five- and six-component II-V alloys, growth of thick (50–500 μm) ‘virtual’ substrates with adjustable lattice constants, II-V antimonide growth, rare-earth doping for impurity gettering, electro-epitaxy, selective epitaxy and epitaxial overgrowth, hybrid heteroepitaxy (with CVD or MBE), novel melt chemistries, and shaped growth for new device applications. A detailed comparison is also given in this chapter of the various current epitaxial growth techniques.

The final chapter, Chapter 13, is concerned with the growth of III-V materials for LEDs. This activity has a long history and it is generally recognized that LPE-grown material produced superior device performance. However, as the field progressed into use of materials containing aluminum, with which LPE has difficulties, CVD and MBE techniques now dominate production. However, the use of LPE continues in niche applications and novel LPE designs are still being researched. It is also possible that LPE could be used to provide improved substrate materials in this area. The economics of LPE for LED production are also discussed.

Finally, the editors would like to sincerely thank all the contributors to the book, as well as Jenny Cossham, Alexandra Carrick and Colleen Goldring of John Wiley & Sons Ltd for all their help and patience throughout the course of the book preparation and production stages. Thanks are also due to SELEX Sensors and Airborne Systems Infrared Ltd. for their support in this project.

Peter Capper  
Southampton, UK  
Mike Mauk  
Pennsylvania, USA



# Acknowledgements

In addition to those contributors who assisted with suggestions for other chapters, the Editors would like to thank the following for their help in various ways during the preparation and production of this book.

**Dr I.M. Baker**

SELEX Sensors and Airborne Systems Infra-Red Limited  
PO Box 217  
Millbrook  
Southampton  
SO15 0EG  
UK

**Mr C.D. Maxey**

SELEX Sensors and Airborne Systems Infra-Red Limited  
PO Box 217  
Millbrook  
Southampton  
SO15 0EG  
UK

**Dr M.B. Reine**

BAE SYSTEMS  
2 Forbes Road  
Lexington  
MA 02421  
USA



# List of Contributors

**Capper, P**

SELEX Sensors and Airborne Systems Infra-Red Limited, PO Box 217, Millbrook, Southampton, SO15 0EG, UK

**Elwell, D**

P.O. Box 1043, Na'alehu, HI 96772, USA

**Goernert, P**

Innovent e.V., Pruessingstr. 27 B, D-07745 Jena, Germany

**Hibiya, T**

Tokyo Metropolitan University, 6-6, Asahigaoka, Hino 191-0065, Japan

**Huang, X. L**

Physics Department, Lancaster University, Lancaster, LA1 4YB, UK

**Isshiki, M**

Institute of Multidisciplinary Research for Advanced Materials, Tohoku University, 2-1-1 Katahira, Aoba-ku, Sendai 980-8577, Japan

**Krier, A**

Physics Department, Lancaster University, Lancaster, LA1 4YB, UK

**Labadi, Z**

Physics Department, Lancaster University, Lancaster, LA1 4YB, UK

**Mauk, M.G**

School of Engineering and Applied Science, University of Pennsylvania, Philadelphia, PA 19101, USA

**McNeely, J. B**

259 Beverly Rd., Newark, Delaware, USA

**Mishurni, V**

Universidad Autonoma de San Luis Potosi, Instituto de Investigacion en Comunicación Optica, Av. Karakorum 1470, Lomas 4 sec., 78210, San Luis Potosi, SLP, Mexico

**Nakajima, Kazuo**

Institute for Materials Research, Tohoku University, 2-1-1, Katahira, Aoba-ku, Sendai 980-8577, Japan



**Scheel, H**

SCHEEL CONSULTING, Groenstrasse Haus Anatas, 3803 Beatenberg, Switzerland

**Syvjärvi, M**

Dept of Physics, Chemistry and Biology, Linköping University, S-581 83  
Linköping, Sweden

**Wang, J**

Institute of Multidisciplinary Research for Advanced Materials, Tohoku University,  
2-1-1 Katahira, Aoba-ku, Sendai 980–8577, Japan

**Yakimova, R**

Dept of Physics, Chemistry and Biology, Linköping University, S-581 83  
Linköping, Sweden

# 1 Introduction to Liquid Phase Epitaxy

HANS J. SCHEEL

SCHEEL CONSULTING, Groenstrasse Haus Anatas, 3803 Beatenberg, Switzerland

---

1.1 General aspects of liquid phase epitaxy	1
1.2 Epitaxial growth modes, growth mechanisms and layer thicknesses	3
1.3 The substrate problem	15
1.4 Conclusions	16
Acknowledgements	17
References	17

---

## 1.1 GENERAL ASPECTS OF LIQUID PHASE EPITAXY

Liquid phase epitaxy (LPE) has been applied to many compounds, but the main applications are compound semiconductors and magnetic rare-earth iron garnets. The electronic, opto-electronic and magneto-optic technologies are based on thin layer- or multilayer structures that are deposited by epitaxial processes onto flat, oriented and single-crystalline substrates. The lifetime and the performance of microelectronic, photonic and magnetic devices are determined by the purity, the structural perfection, the stoichiometry, and the homogeneity of the epitaxial layers (*epilayers*) and by the surface flatness of layers and interfaces. For example, traces of oxygen in GaAs devices reduce their performance, and dislocations have a detrimental effect on threshold voltage of GaAs transistors (Miyazawa *et al.*, 1986) and on the efficiencies of light emitting diodes (LEDs) (Lester *et al.*, 1995).

Liquid phase epitaxy is growth from high-temperature solutions, so that many principles, choice of solvents, and technological experiences from growth of bulk crystals (see Elwell and Scheel, 1975) can be transferred to LPE. The epitaxial deposition can be done from diluted solutions at low temperature, from concentrated solutions at higher temperature and even from melts near the high melting point (Nakajima *et al.*, 2005). In practice, LPE is done mostly from dilute solutions, because this allows firstly to apply lower growth rates for improved thickness control, secondly to apply lower growth temperatures for improved structural perfection and stoichiometry and to reduce the detrimental effects of thermal expansion differences of substrate and epilayer, and thirdly to reduce the risk of unwanted spontaneously nucleated crystallites.

Here we should introduce the *principle of the single optimum growth technology* (Scheel, 2003): *For a given crystal or epilayer with specified application and desirable device performance, there can be only one single optimum growth technology if one considers thermodynamics, features of growth technologies, economics, timeliness, ecology, etc.*

In silicon and GaAs microelectronics, where submicrometer structures are fabricated in integrated circuits, the epitaxial deposition from the vapor phase is generally applied. Due to the high surface tension of the liquid metallic solutions of semiconductors, such small structures of less than 1  $\mu\text{m}$  cannot yet be fabricated directly by LPE growth. However, LPE has numerous advantages and therefore is the major production technique for LEDs (two-thirds of the worldwide LED production) and for magneto-optic bulk layers. In comparison with epitaxy from the vapor phase, the strengths of LPE are:

- due to near-equilibrium conditions during epitaxial layer deposition the structural perfection of the layers is superior and that quasi-atomically flat surfaces and interfaces can be achieved;
- generally excellent stoichiometry of the layers is obtained;
- due to comparably high solute concentrations relatively high growth rates can be applied;
- LPE in most cases is a very economic epitaxial deposition technique, especially when up-scaled to mass production.

There is justified hope that LPE will become essential for production of quasi-perfect layers of SiC, GaN, AlN, and of high-temperature superconductors, and even GaAs and other substrates may provide LPE surface layers of improved perfection in competition with complex substrate preparation and annealing procedures.

However, there are limitations for LPE with respect to miniaturized structure size (which, however, could be achieved by lithography and etching perfect LPE layers), with respect to immiscible compositions that can not be grown by an equilibrium technique, and with respect to stringent substrate requirements (small misfit, similar thermal expansion coefficient of substrate and layer, and very small misorientation) when atomically flat surfaces and interfaces are to be achieved. Purity is not a problem when constituent elements or compounds are utilized as solvents, for example Ga for LPE of GaAs, the BaCuO<sub>2</sub>-CuO eutectic as solvent for the high-temperature superconductor YBa<sub>2</sub>Cu<sub>3</sub>O<sub>7-x</sub> (YBCO). In other cases like LPE of magnetic garnets the solvent can be selected according to the criteria discussed in Chapter 3 of Elwell and Scheel (Elwell and Scheel, 1975), or solvent constituents are chosen that are useful for the application like Bi<sub>2</sub>O<sub>3</sub> for bismuth substitution in magnetic garnets.

In contrast to the widespread opinion that LPE is an easy, simple and old-fashioned technology, it will be shown that the contrary is the case, when large-area extremely flat layers or superlattices are to be grown. LPE has almost disappeared from universities so that the know-how exists practically only in industries, and because the development of a new layer or multilayer structure by LPE requires 1–3 years, in contrast to popular molecular beam epitaxy (MBE) and metal-organic vapor-phase epitaxy (MOVPE). The two latter methods allow, by using expensive computer-controlled machines, preparation of new layers or superlattice structures within typically 3 months, so that the PhD student can spend the majority of his thesis time on device fabrication and physical measurements.

These facts explain why LPE publications have become scarce, so that this important technology is widely forgotten, it is pushed aside by the ‘modern’ technologies.

In the following, the various epitaxial growth modes will be discussed and how they appear as functions of interface thermodynamics, thermodynamic driving force (supersaturation), misfit between substrate and epilayer, and substrate misorientation. From this discussion we shall recognize from a theoretical standpoint why atomically flat and thus extremely homogeneous layers of oxides and of most semiconductor compounds can be achieved only by a near-equilibrium technique, by LPE. This discussion will also clarify the complexity and enormous difficulties when epilayers are grown by *heteroepitaxy*, that is the substrate and layer have different composition. But even in *homoepitaxy*, when substrate and layer have the same composition, except for a small dopant concentration, the growth conditions have to be optimized in order to achieve the flat and perfect layers mentioned above.

The technological realization of the theoretically derived parameters can be quite demanding. LPE is growth from solution where step bunching, growth instability and inclusions occur when misfit, substrate misorientation, supersaturation, and hydrodynamics as the main growth parameters are not carefully optimized. Near-equilibrium growth by LPE does not tolerate any deviation from the optimized conditions, a reason why numerous LPE attempts of researchers have failed, why macrosteps, ripples and meniscus lines are observed: detrimental defects that can be prevented by careful selection and preparation of the substrate surface, by the purity of the gas atmosphere, and by the precise adjustment of the growth conditions. In contrast to LPE, epitaxy from the vapor phase is not so critical regarding all these growth parameters. Besides the high-supersaturation effects discussed below, the main problem in vapor phase epitaxy is stoichiometry control of complex compounds like high-temperature superconductors. In LPE, the control of stoichiometry is in general not a problem, because the growth temperature is well below the melting point and below the coexistence (solid solution) range of the compounds, so that automatically layers of excellent stoichiometry are deposited.

## 1.2 EPITAXIAL GROWTH MODES, GROWTH MECHANISMS AND LAYER THICKNESSES

The layer and surface perfection is determined by the epitaxial growth mode, by the mechanisms of surface nucleation and step propagation. In addition to the three well-known growth modes (Volmer–Weber, Stranski–Krastanov, Frank–Van der Merwe) of Bauer (Bauer, 1958) there are five other distinct growth modes and epitaxial growth mechanisms (Scheel, 1997 and in this chapter) that have been individually described by numerous authors: columnar growth, step flow mode, step bunching, and screw-island or spiral-island growth, and the growth on kinked (rough) surfaces. These eight growth modes are shown in three successive steps of development in Figure 1.1.

The three classical growth modes had been derived thermodynamically from the surface and interfacial free energies with the Frank–Van der Merwe (Frank–Van der Merwe, 1949) mode for dominating the interfacial energy between substrate and epilayer, Volmer–Weber (Volmer–Weber, 1926) for the weakest interfacial energy, and Stranski–Krastanov (Stranski–Krastanov, 1938) as the intermediate case. These three well-known growth modes (Bauer,) are shown in the upper part of Figure 1.1; and they are frequently observed

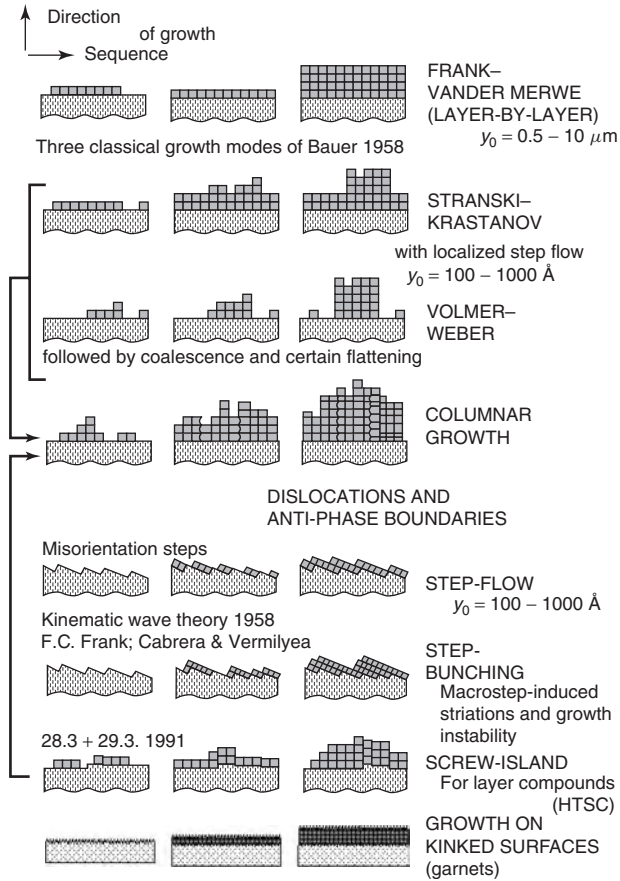


**Figure 1.1** Eight epitaxial growth modes. Reprinted from H.J. Scheel, Chapter 28 *Crystal Growth Technology*, editors H.J. Scheel and T. Fukuda, Copyright (2003), with permission from John Wiley & Sons, Ltd

in epitaxial growth. However, different growth modes have been described for the same substrate–epilayer system, thus indicating that growth methods and growth parameters influence the growth modes. Furthermore, the epitaxial growth experience in the past 40 years has given clear evidence of specific growth features that may be described by five distinct and different epitaxial growth modes that are shown in the lower part of Figure 1.1. In the following, first the main experimental parameters determining the appearance of the growth modes will be briefly described followed by the discussion of the growth modes and their impact on layer properties. Other parameters with some influence on the growth mode such as surface diffusion, stoichiometry of deposited compounds, condensing impurities (surfactants), oxidation stage of surface species and partial pressure of reactive species during growth, and surface liquid or surface melting due to impurities (VLS mechanism) or due to partial decomposition, are not yet well understood and will not be discussed here.

The *concentration* of the epilayer-forming species in the growth fluid is very different for vapor phase epitaxy (VPE) and for LPE. For GaAs the solid density of  $5.3 \text{ g cm}^{-3}$

is reduced to  $0.0065 \text{ g cm}^{-3}$  in the vapor, which corresponds to a concentration of  $10^{-9}$ – $10^{-6}$  in the vapor depending on working pressure and on dilution by the carrier gas, thus depending on the growth method. In comparison the concentration in LPE is much higher, at 10 % solubility  $10^{-1}$ . In growth from the vapor generally the material flux (in number of species  $\text{cm}^{-2} \text{ s}^{-1}$ ) is the rate-determining factor for growth. In LPE it is the mass transport through the diffusion boundary layer  $\delta$  that at a given supersaturation limits the growth rate according to (Nernst, 1904):

$$v = (n - n_e)D/\rho\delta$$

where  $D$  is the diffusion coefficient,  $n$  the effective concentration or vapor pressure,  $n_e$  the equilibrium concentration or vapor pressure, and  $\rho$  the density of the crystal. However, with increasing *supersaturation* and growth rate we observe successively step bunching, wavy macrosteps, formation of inclusions, edge nucleation and surface dendrites, hopper growth and bulk dendrites in the transition from stable growth to growth instability. There is a *maximum stable growth rate*  $v_{\max}$  that is defined as the highest growth rate without growth instability. This was derived from an empirical boundary-layer concept of Carlson (Carlson, 1958) by Scheel and Elwell (Scheel and Elwell, 1972) as a function of the solution flow rate  $u$ , the Schmidt number  $\text{Sc} = \eta/\rho_1 D$  with  $\eta$  the dynamic viscosity and  $\rho_1$  the density of the liquid,  $\sigma$  the relative supersaturation  $(n - n_e)/n_e$ , and  $L$  the crystal size or substrate diameter, as

$$v_{\max} = \{0.214 D u \sigma^2 n_e^2 / \text{Sc}^{1/3} \rho^2 L\}^{1/2}$$

see also Chapter 6 in Elwell and Scheel (Elwell and Scheel, 1975). This approach, in combination with the faceting transition concept described further below, is essential to achieve flat LPE epilayers. In VPE the supersaturation ratio  $\alpha$  of the actual pressure divided by the equilibrium pressure  $p/p_e$  qualitatively describes the decreasing supersaturation with increasing substrate temperature, but can often not be used for quantitative interpretation of growth phenomena. Stringfellow (Stringfellow, 1991) has derived the thermodynamic driving forces of epitaxial processes from the free energy differences between the reactants before growth and the crystalline product. For GaAs and growth temperature 1000 K this comparison of the epitaxial driving forces is shown in Figure 1.2.

One can recognize that the supersaturations in epitaxy from the vapor phase are orders of magnitude higher than in LPE where the supersaturation can be adjusted to a negative value for etching, exactly at zero for thermodynamic equilibrium, and at small positive values suitable for stable and economic growth rates to achieve atomically flat surfaces (Scheel, 1980; Chernov and Scheel, 1995). The free energy differences of Figure 1.2 give only an order of magnitude estimate of the supersaturation. The effective supersaturation during growth can be derived from the surface morphology of as-grown surfaces (Scheel, 1994). The distances  $y_0$  between steps are related to the radius  $r_S^*$  of the critical two-dimensional nucleus as elaborated by Cabrera and Levine (Cabrera and Levine 1956):

$$y_0 = 19 r_S^* = 19 \gamma_m V_m / a^2 RT \sigma$$

with  $\gamma_m$  the energy per growth unit,  $V_m$  the molar volume, and  $a$  the size of the growth unit.

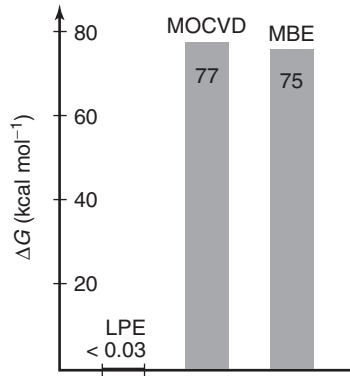


**Figure 1.2** Gibbs free energy differences between reactants and products (layers, crystals). The estimated thermodynamic driving forces for LPE ( $\Delta T < 6$  K), MOCVD (TMGa + arsine) and MBE (Ga + As<sub>4</sub>) of GaAs at 1000 K. (After Stringfellow, 1991) Reprinted from *J. Cryst. Growth*, **115**, Stringfellow, 1, Copyright (1991), with permission from Elsevier

Table 1.1 shows that from typically observed interstep distances for VPE and for LPE for the examples GaAs and the high-temperature superconductor (HTSC) YBCO the supersaturation is about 60 times lower in LPE of GaAs and 200 times lower in LPE of YBCO. This explains the different growth modes for VPE and LPE as shown below.

For HTSCs the measured interstep distances increased with the substrate temperatures as expected (Nishinaga and Scheel, 1996), but due to the thermodynamic stability limits of HTSC compounds the temperature can not be raised sufficiently to achieve interstep distances comparable with LPE.

In heteroepitaxy the *lattice mismatch* between substrate and epilayer at the growth temperature has a significant effect on nucleation behavior and the epitaxial growth mode and thus on the structural perfection of the layer, and the *thermal expansion difference* between the substrate and film may further deteriorate the layer perfection or may cause cracking upon cooling to room temperature. The lattice mismatch or *misfit*  $f$  is defined as the relative difference of the lattice spacings of the substrate  $a_S$  and of the film  $a_F$ :  $f = (a_S - a_F)/a_F$ . During layer deposition the misfit is first accommodated by a homogeneous strain, and after reaching a critical layer thickness, which depends on the degree of misfit, *misfit dislocations* are formed that are characterized by a periodical elastic strain with a period equal to the dislocation spacing (Van der Merwe, 1973). At small misfit, for instance

**Table 1.1** Supersaturation ratios for VPE and LPE derived from interstep distances  $y_0$  of GaAs and of the high-temperature superconductor YBa<sub>2</sub>Cu<sub>3</sub>O<sub>7-x</sub> (YBCO)

	For GaAs		For YBCO	
	MBE, MOVPE	LPE	VPE, MOVPE	LPE
$y_0$	20–100 nm	6 $\mu$ m	14–30 nm	6 $\mu$ m (0.6–17 $\mu$ m)
$r_S^*$	1.1–5.5 nm	300 nm	0.8–1.6 nm	300 nm
	$\sigma_{\text{MBE,MOVPE}} \sim 60 \times \sigma_{\text{LPE}}$		$\sigma_{\text{VPE,MOVPE}} \sim 200 \times \sigma_{\text{LPE}}$	

by epitaxial growth of a doped layer onto an undoped substrate, the formation of misfit dislocations is prevented, but the substrate–layer structure may become bent due to the misfit strain. The curvature can be used, when only one side of the substrate is epitaxially overgrown, to monitor the layer thickness during the growth process by laser reflection.

The *misorientation* of the substrate, i.e. the deviation angle from the ideal crystallographic plane, provides misorientation steps of which the distance is determined by the misorientation angle and by the lattice constants. This interstep distance can be made so small that the formation of nuclei and growth islands can be suppressed resulting in a pure step-flow mode.

The growth on kinked or atomically rough surfaces and on stepped surfaces possible at special crystal orientations, for example in growth of garnet layers, the non-equilibrium surfaces provide kink sites on to which the species can be attached, practically with negligible surface diffusion and without step propagation.

In the following, the seven epitaxial growth modes shown in Figure 1.1 will be described along with features allowing clear distinction that is necessary due to the misuse of layer-by-layer growth for step-flow mode, for example.

In the *layer-by-layer* or *Frank–Van der Merwe* (Frank and van der Merwe, 1949) *growth mode* (F–VM mode) steps with large interstep distances, typically more than  $1\ \mu\text{m}$ , propagate over macroscopic distances. In the case of perfect crystal surfaces, the supersaturation increases until surface nucleation occurs and the steps move to the edge of the crystal until the formation of the monolayer is completed. Then the supersaturation rises again for surface nucleation and the formation of the next monolayer. Normally, however, there are continuous step sources like screw dislocations or other defects, so that the layer-by-layer mechanism works continuously and spreads layers at large interstep distances over macroscopic distances. Screw dislocations may cause the spiral growth mechanism (described by the BCF theory; Burton *et al.*, 1951) that may lead to shallow growth hillocks with very small slopes, depending on supersaturation these can be seconds to minutes of arc. At the hillock boundaries the steps arriving from neighboring hillocks are annihilated and thus may cause screw dislocations or other defects. Thus, the hillock boundaries may cause local strain fields and variation of the incorporation rates of impurities and dopants, or the local strain may getter or reject impurities during annealing processes. This inhomogeneity may be suppressed by providing one single step source or by using substrates of well-defined small misorientation that corresponds to the interstep distance from the applied supersaturation. The F–VM growth mode and such perfect and homogeneous layers can only be achieved by LPE or by VPE at very high growth temperatures (e.g. in silicon epitaxy above  $1100\ ^\circ\text{C}$  interstep distances above  $1\ \mu\text{m}$  can be observed). For compound semiconductors and most oxide compounds with thermodynamic stability limits only LPE at low supersaturation can yield atomically flat surfaces.

The *Volmer–Weber* (Volmer and Weber, 1926) *growth mode* (V–W mode) is typical of VPE where a large number of surface nuclei (typically  $10^6 - 10^{11}\ \text{cm}^{-2}$ ) and growth islands are formed due to the high supersaturation described above. This initial phase is followed by spreading,<sup>1</sup> that is by localized step flow and growth of three-dimensional islands, and finally by coalescence to a compact layer. The supersaturation effect can be dominating so that even in homoepitaxy the V–W mode is observed, for example in HTSC oxide compounds (Konishi *et al.*, 1994). Continued growth of a layer first initiated

<sup>1</sup> Theorists like to call this the birth-and-spread mode.



by the V–W mode often shows *columnar growth* unless there is a healing procedure to enhance surface diffusion, for instance by growth interruption in MBE or by an annealing phase. Columnar growth is a common feature in epitaxy of GaN, diamond, and HTSCs due to their thermodynamic stability limits not allowing a sufficient high growth temperature for reduced supersaturation and effective surface diffusivity and thus healing, see for example the Akasaki–Amano group with columnar growth of GaN on AlN buffer layers (Hiramatsu *et al.*, 1991).

The *Stranski–Krastanov* (Stranski and Krastanov, 1938) *mode* (S–K mode) can be regarded as intermediate between the F–VM and V–W modes. Due to relatively large substrate–epilayer interface energy, first one or two compact monolayers are formed onto which by surface nucleation, analogous to the V–W mode and due to misfit, three-dimensional islands are formed that eventually coalesce to compact layers. As an example, the S–K mode has been demonstrated by MBE growth of InAs onto GaAs substrates (Nabetani *et al.*, 1993).

The detrimental coalescence effects of V–W and S–K films can be suppressed by using substrates of precisely adjusted misorientation (typically  $0.8 - 2.5^\circ$ ), so that from the short interstep distances the formation of islands can be prevented and the pure *step-flow mode* achieved. The advantage of this mode has been more and more recognized and has improved structural perfection of vapor-grown layers and device performance. In LPE the application of misoriented substrates limits the applicable supersaturation in order to prevent step bunching and surface corrugations. *Localized step flow* is frequently observed in films growing by the V–W or S–K mode with interstep distances of less than 50 nm. These steps are frequently misinterpreted as layer-by-layer growth, a term that should be reserved to interstep distances of more than  $1 \mu\text{m}$  and step propagation over macroscopic distances by the F–VM mode.

In LPE, frequently *step bunching* is observed when at high supersaturation a high density of steps moves with large step velocities over the surface. By fluctuations, higher steps catch up with lower steps and then move together as double, triple, or in general as macrosteps. The theory of this traffic flow problem by Lighthill and Whitham (Lighthill and Whitham, 1955) was applied in 1958 by Cabrera and Vermilyea (Cabrera and Vermilyea, 1958) and independently by Frank (Frank, 1958) to step bunching (kinematic wave theory). The macrostep-terrace (or thread-riser) morphology causes different incorporation rates of impurities and dopants due to locally varying growth velocities that lead to *macrostep-induced striations* (Scheel, 2003). These striations were observed in cross-sections of LPE-grown layers by etching or by photoluminescence for example by Kajimura *et al.* (Kajimura *et al.*, 1977), Nishizawa *et al.* (Nishizawa *et al.*, 1986) (Figure 1.3) and by Nishinaga *et al.* (Nishinaga *et al.*, 1989). The upper part of Figure 1.3 shows the topview of a LPE-grown GaP layer with three macrosteps which correspond to the surface steps shown in the cross section in the lower part of the Figure. One can follow the development and broadening of the macrosteps from smaller steps in the etched layer. The opposite, the removal of macrosteps, can be seen with two examples in Figure 1.4. A Nomarski photograph of an angle-lapped and etched 15-layer structure of n- and p- GaAs grown by a slider-free LPE technology (Scheel 1977) is shown in Figure 1.4a. The first 6 layers show macrosteps and their traces in the etched p-GaAs layers until with layer 7 the transition to the facet starts on the left side. With layer 12 and total growth of about  $25 \mu\text{m}$  the faceting transition is complete in this case where the substrate misorientation was  $0.165$  degrees. Figure 1.4b shows an example where the

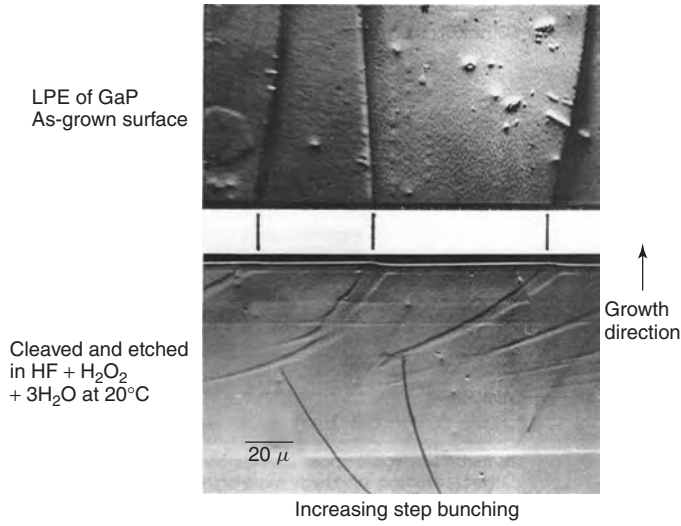


**Figure 1.3** Macrostep-induced striations. Reprinted with permission from *Proc. 2<sup>nd</sup> Int. School on Semiconductor Optoelectronics*, J. Nishizawa and Y. Okuno, Cetniewo, Poland, 1978

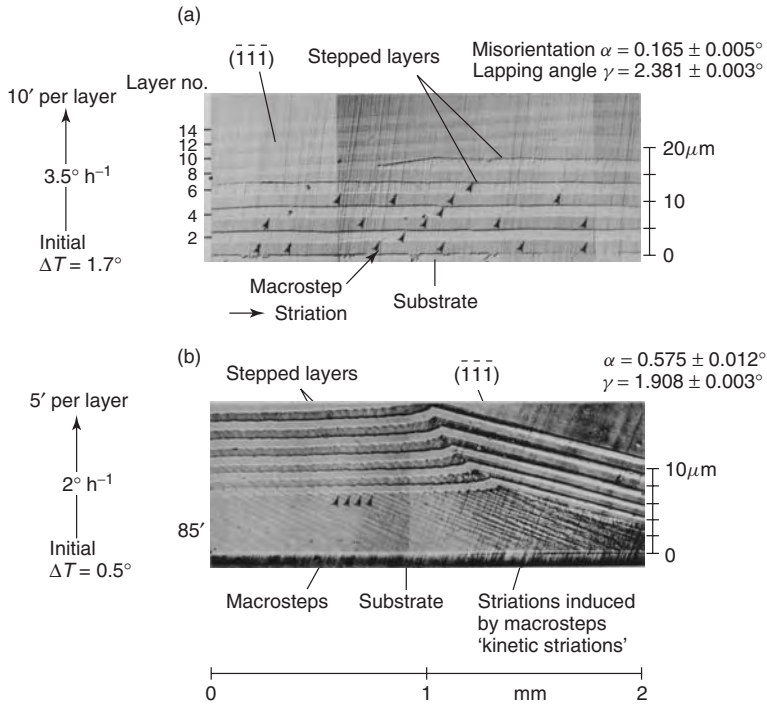


**Figure 1.4** Transition to faceting in LPE. Reprinted from *Appl. Phys. Lett.*, Transition to faceting in multilayer liquid phase epitaxy of GaAs, 37, Scheel, 70–73, Copyright (1980), with permission from American Institute of Physics

transition to the facet was only partially successful due to the large substrate misorientation angle of nearly 0.6 degrees. The facet started on the right side and covers after 15  $\mu\text{m}$  growth nearly half of the photographed surface. The macrosteps and the corresponding striations can be clearly recognized on the left facet-free side. These experimental results (Scheel 1980) were analyzed theoretically by Chernov and Scheel (1995) who showed that by applying a low supersaturation and substrates of small misorientation, step bunching can be suppressed by the transition to faceting, to a growth surface with mono- or double-steps propagating over macroscopic dimensions in the F-VM mode. The resulting quasi-atomically flat surface was proven in the first investigation of an epitaxial surface by scanning-tunneling microscopy by Scheel, Binnig and Rohrer 1982 that showed step heights of 0.65 nm (Figure 1.5), and interstep distances of 6  $\mu\text{m}$  were visible by optical Nomarski interference contrast microscopy (Figure 1.6).

*LPE on the kinked {111} surface* of garnet, a nonequilibrium rough surface, has been developed for the growth of garnet layers for magnetic bubble-domain devices based on

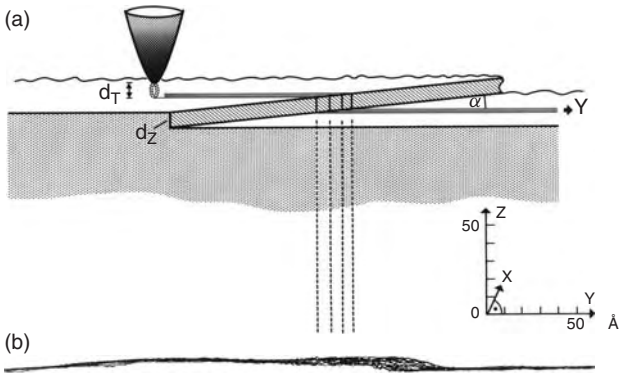


**Figure 1.5** Step height by STM. Reprinted from *J. Cryst. Growth*, **60**, Scheel *et al.*, 199, Copyright (1982), with permission from Elsevier

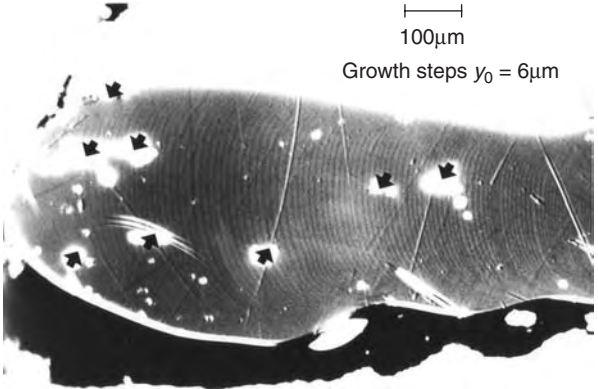


**Figure 1.6** Differential interference contrast microscopy (Nomarski) of facet surface. Nomarski step distances of 6  $\mu\text{m}$  are visible. Reprinted from *J. Cryst. Growth*, **60**, Scheel *et al.*, 199, Copyright (1982), with permission from Elsevier

crystallization studies of garnet spheres by Tolksdorf *et al.* (Tolksdorf *et al.*, 1972) and later for bulk magneto-optical layers of millimeter thickness, whereby special care had to be taken with substrate preparation, supersaturation and solvent composition (Hibiya 1983), and thermal symmetry/hydrodynamic growth conditions for the growth surface to remain flat and to prevent the formation of {211} facets (Iino, 2005).

The *screw-island mode* was discovered in STM investigations of the HTSC YBCO grown by sputter deposition and by MOVPE first by Hawley *et al.* (Hawley *et al.*, 1991) and then by Gerber *et al.* (Gerber *et al.*, 1991), who found a high density of screw islands (or spiral islands). The density of these islands corresponds to the density of initially nucleated islands ( $10^8 - 10^9 \text{ cm}^{-2}$ ) and is dependent on the misorientation of the substrate, so that Scheel (Scheel, 1994) suggested the coalescence of slightly misoriented islands responsible for the formation of screw dislocations with large Burgers vector and thus for the screw-island growth mode. The misorientation angle of the first-formed islands is related to the misfit.

Continuous growth by the screw-island mode leads to coalescence and to columnar growth whereby the number of islands may be reduced at low supersaturation and at high growth temperatures.

For compounds of limited thermodynamic stability or with volatile constituents like GaAs, GaN, SiC, and the HTSC compounds, the appearance of the growth modes is largely predetermined by the choice of the growth method due to the inherent high supersaturations in epitaxy from the vapor phase and the adjustable low supersaturation in LPE. This is demonstrated in Figure 1.7 where the critical radius of the nuclei and the interstep distances are shown as functions of the supersaturation along with typical regions of the epitaxial methods. We can recognize that in LPE the desirable F-VM growth mode can be achieved at low supersaturation and low substrate misfit, whereas a high thermodynamic driving force leads to step bunching. Also misfit, requiring a higher supersaturation for growth, will lead to step bunching and in extreme cases even to V-W or S-K mode that are the typical growth modes for epitaxy from the vapor phase.

For the control of the growth mode, with the goal of achieving the best device performance, the misfit plays an important role, and therefore the use of low-misfit substrates is essential as will be discussed further below. The F-VM growth mode can only be obtained at quasi-zero misfit as can be established from thermodynamic considerations (Van der Merwe, 1979) and as was demonstrated by atomistic simulations using the Lennard-Jones potential (Grabow and Gilmer, 1988). The combined effect of supersaturation and misfit is shown in Figure 1.8, along with the epitaxial methods and the growth modes.

Only in the small corner at low supersaturation and nearly zero misfit can the layer-by-layer growth mode be realized and used to produce low dislocation layers for ultimate device performance, as was early demonstrated with the highest brilliance red LED, and clear green LEDs and many other optoelectronic devices (Nishizawa and Suto, 1994) grown by near-equilibrium LPE. For the example of LEDs the dependence of the efficiency of light output on the structural perfection, i.e. on the dislocation density, was demonstrated in a systematic study of Lester *et al.* (Lester *et al.*, 1995 who collected data of several III-V compound systems. Meanwhile, it has become clear that also for LEDs based on GaN and its alloys, a low dislocation density is important for the brightness.

*Homoeptitaxial LPE* may become important when extremely perfect, quasi-dislocation-free surfaces will be needed for ultimate performance of electronic, optoelectronic, optical

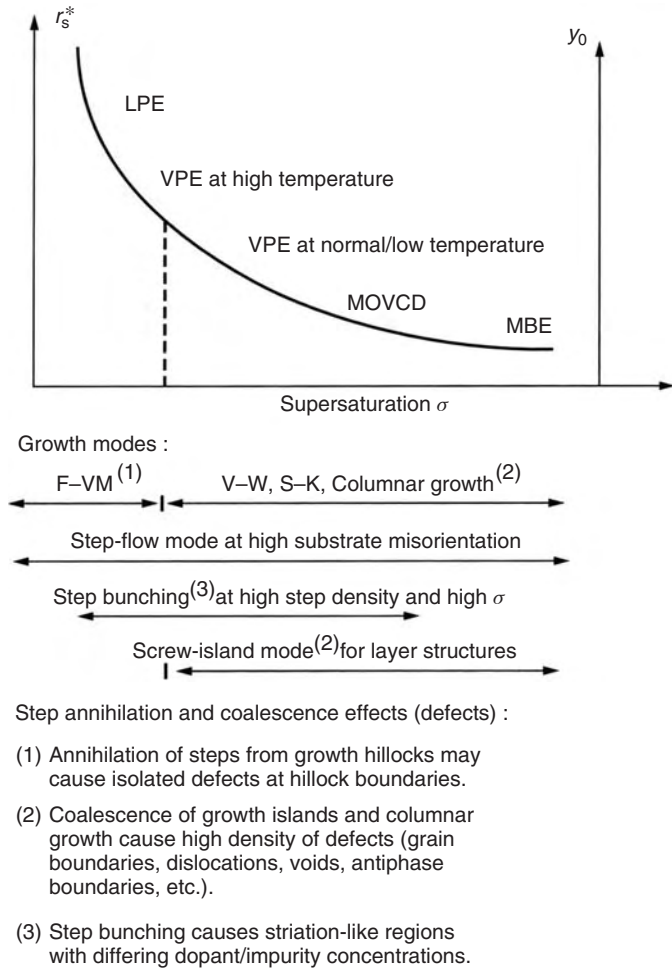


**Figure 1.7** Supersaturation versus step distance and epitaxy method. Reprinted from *Crystal Growth Technology*, editors H.J. Scheel and T. Fukuda, Copyright (2003), with permission from John Wiley & Sons, Ltd

and HTSC devices, and when the preparation of correspondingly perfect substrates can not be achieved, or when the preparation of perfect substrate surfaces is too difficult. Besides GaAs one should mention SiC and GaN substrates that when prepared from the vapor phase contain of the order of 10 pipe defects and  $10^{10}$  dislocations  $\text{cm}^{-2}$ , respectively. By LPE onto GaN (Klemenz and Scheel, 2000) and onto SiC (Ujihara *et al.*, 2005) the defects could be ‘overgrown’ and surfaces of improved perfection achieved.

The *thickness of LPE grown layers* depends on the growth method like dipping, tipping, tilting and the kind of applied supersaturation (step-cooling, cooling rate or supersaturated solution) and hydrodynamics as discussed by Tiller and Kang (Tiller and Kang, 1968), Minden (Minden, 1970), Mitsuata (Mitsuata, 1970), Crossley and Small (Crossley and Small, 1971), Ghez and Lew (Ghez and Lew, 1973), Hsieh (Hsieh, 1974), and Knight

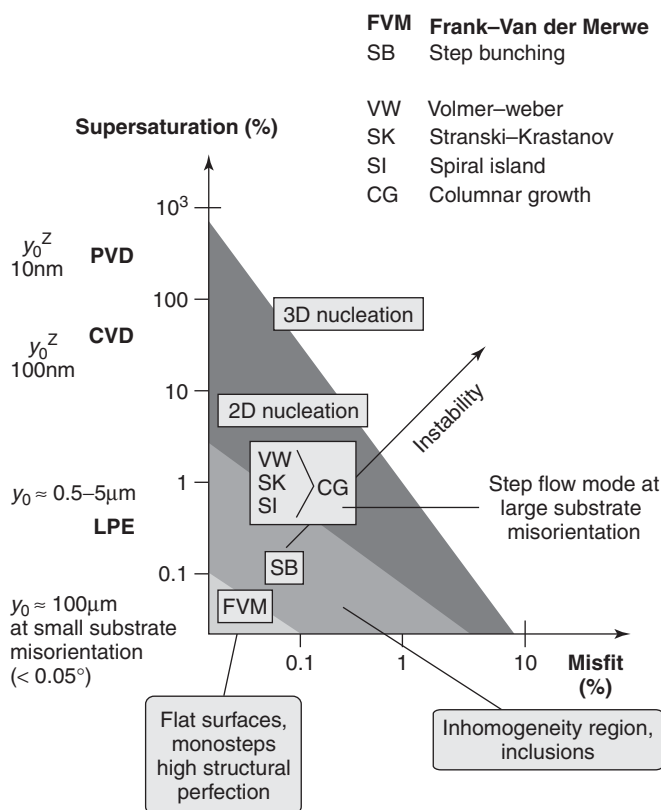


**Figure 1.8** Supersaturation, misfit and growth modes. Reprinted from *Crystal Growth Technology*, editors H.J. Scheel and T. Fukuda, Copyright (2003), with permission from John Wiley & Sons, Ltd

*et al.* (Knight *et al.*, 1974). In LPE of semiconductors the slider technique has been most widely applied, even up to production scale, although it has severe disadvantages as shown in Figure 1.9.

The main disadvantages are scratching of the grown layers and the limitation of total layer or multilayer thickness. A slider-free LPE growth system for semiconductor multilayers and superlattices has been developed ('MultiLPE'; Scheel, 1977) that allowed the transition to faceting and atomically flat surfaces, as discussed above to be achieved, and that in a different topology can be used for *large-scale production of epitaxial multilayers* (Scheel 1975) in a quasi-continuous process (Figure 1.10).

Here a batch of substrates held in an open frame is inserted into the solution that is supersaturated by slow cooling, whereby oscillation about the axis leads to stirring and improves the homogeneity of the melt. By combined rotation and translation of the central axis the batch of substrates is introduced into the next solution, and so on. On both sides of the furnace there are gloveboxes where the substrate batches are mounted and on the other side of the furnace demounted. In the case of GaAs a low oxygen partial pressure, as derived from thermodynamics of oxide formation/Ellingham diagram, is required for the gas atmosphere in order to prevent surface oxidation (scum formation) of the Ga melt

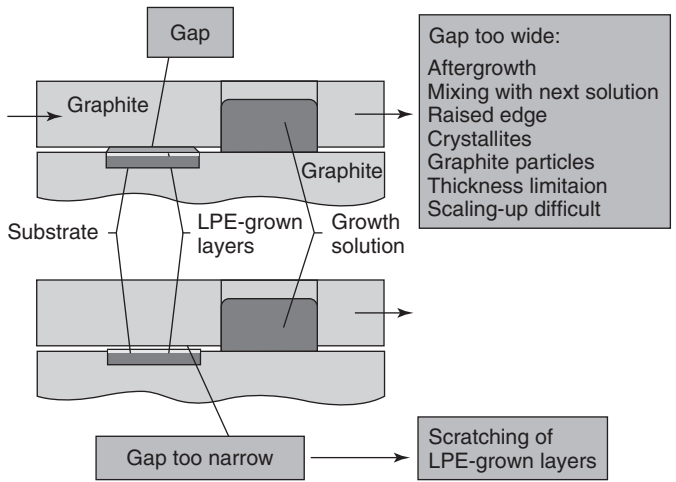


**Figure 1.9** Problems with GaAs slider method in LPE. Reprinted from *Crystal Growth Technology*, editors H.J. Scheel and T. Fukuda, Copyright (2003), with permission from John Wiley & Sons, Ltd

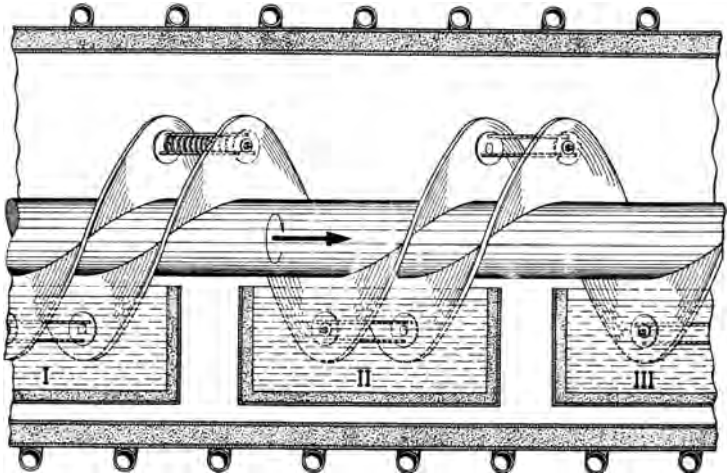


**Figure 1.10** LPE mass production by slider-free technology (Scheel 1975)

that causes wetting of the substrate and thus remaining melt fraction that mixes with the next melt/solution.

For LPE of garnet layers the dipping of rotating substrates (Scheel and Schulz-Dubois, 1972) has become widely used. This has the advantage of an adjustable continuous flow towards the rotating disc that was analyzed by Cochran (Cochran 1934) and then applied to the segregation analysis of Czochralski growth by Burton *et al.* (Burton *et al.*, 1953). The resulting quasi-constant hydrodynamic and diffusion boundary layers facilitate the theoretical analysis (Ghez and Giess, 1974), and the stirring action leads to homogenization of the growth solution and an approach to thermodynamic equilibrium, in contrast

to unstirred solutions where high supersaturations may hamper reproducibility and layer homogeneity.

In LPE growth of bulk garnet layers from stirred solutions, steady state is reached soon after inserting the substrates so that the growth rate is automatically given by the volume of the solution and the total surface area of the substrate(s) that has to accept the material that has to precipitate as a function of the solubility curve and the cooling rate. This should allow high reproducibility to be achieved in bulk oxide layer thickness in the case of rotating substrates, especially for oscillatory rotation.

### 1.3 THE SUBSTRATE PROBLEM

Successful LPE relies on uniform, clean and damage-free substrates with zero or very low dislocation densities. The surfaces should be free from dust, grease, and pits or scratches from the polishing process, and the structural damage from crystal sawing (microcracks, strain) should be removed by a final etching stage. Even commercially available 'epi-ready' substrates should be characterized before use. Normally, the final substrate-preparation stages and the characterization of substrates for LPE are done in clean rooms, depending on the application in class 1000 or class 100 atmosphere. In special cases the meltback of the substrate followed by homoepitaxial regrowth, as proposed by Robertson *et al.* (Robertson *et al.*, 1973), may yield perfect surfaces for following heteroepitaxial LPE growth of the functional layer.

As we have seen above, the orientation, and respectively, the misorientation, of the substrate plays a decisive role in the control of the growth mode and thus in the layer perfection. The required precision of the misorientation angle can be estimated theoretically and taken into account in the crystal sawing, lapping and polishing steps. For the achievement of atomically flat LPE-grown surfaces the misorientation angle should be less than  $0.05^\circ$  (Chernov and Scheel, 1995), which requires a corresponding precision in the crystal-machining steps.

The largest challenge in LPE in the case of heteroepitaxy are the misfit between substrate and epilayer at the growth temperature and the difference of the thermal expansion coefficients.

This problem received much attention during the development of magnetic bubble-domain devices based on garnets during the period 1969–1976, and was approached from both sides, from solid-solution compositions of the layer fitting to the  $\text{Gd}_3\text{Ga}_5\text{O}_{12}$  (GGG) substrates, and to solid solution substrates fitting to layers with optimum device performance. Thereby the lattice parameters of the mixed garnets can be calculated from published values (Geller, 1967; Winkler *et al.*, 1972) of the end-member garnets using Vegard's rule. The different thermal expansion coefficients of GGG substrate ( $\alpha = 9.18 \times 10^{-6} \text{ }^\circ\text{C}^{-1}$ ) and  $\text{Y}_3\text{Fe}_5\text{O}_{12}$  (YIG) magnetic garnet film ( $\alpha = 10.35 \times 10^{-6} \text{ }^\circ\text{C}^{-1}$ ) measured by Geller *et al.* (Geller *et al.*, 1969) leads to tensile stress when films that fit a substrate at growth temperature are cooled to room temperature. The stress in an epitaxial film is given (Besser *et al.*, 1972; Carruthers, 1972) by:

$$\sigma_F = \frac{E}{1 - \mu} (1 - \eta) \left( \frac{a_S - a_F}{a_F} \right) + \eta(\alpha_S - \alpha_F)\Delta T$$



where  $E$  is the Young's modulus,  $\mu$  is the Poisson's ratio of the film,  $a_S$  and  $a_F$  are the room temperature lattice parameters of substrate and film, respectively,  $\alpha_S$  and  $\alpha_F$  their thermal expansion coefficients,  $\Delta T$  the difference between growth and ambient temperatures, and  $\eta$  the fractional stress relief.

The unstrained lattice mismatch  $\Delta a = a_S - a_F$  should be within the limits  $+0.001$  nm (tension) and  $-0.002$  nm (compression) according to Besser *et al.* (Besser *et al.*, 1972), Blank and Nielsen (Blank and Nielsen, 1972) and Tolksdorf *et al.* (Tolksdorf *et al.*, 1972) for VPE- and LPE-grown layers. The tensile stress limit of garnet films can be explained in terms of Griffith's (Griffith, 1920) crack theory that predicts an increasing stress limit with decreasing film thickness (Matthews and Klokholm, 1972). The origin, magnitude and configuration of heteroepitaxial stresses in thin oxide films has been reviewed by Carruthers (Carruthers, 1972). The rapid growth direction of pulled gallium garnet substrate crystals is [111], which is fortunately the preferred orientation of the magnetic garnet layers. In GGG crystal pulling relatively high crystal rotation rates are applied in order to achieve a planar growth interface and to prevent {211} facets. However, a compromise has to be found between the core effect, a central strained region in Czochralski-grown crystals, and the formation of striations.

In epitaxy of compound semiconductors there was for a long time the limitation to simple compound substrates like GaAs, GaP, InP, GaSb, CdTe which narrowed the solid solution ranges of layers and thus the bandgap and wavelength ranges for optoelectronic devices.

Only recently has the commercial production of CdHgTe (Capper *et al.*, 2005) and of GaInSb (Dutta, 2005) been achieved by vertical Bridgman growth with the accelerated crucible rotation technique (ACRT), and promising results have also been obtained for the InGaAs (Nishijima *et al.*, 2005) and SiGe (Nakajima *et al.*, 2002) systems. For the Si-Ge system an optical *in situ* monitoring system of the crystal-melt interface allowed the study and optimization of the solidification of the solid solution crystal (Sazaki *et al.*, 2002).

## 1.4 CONCLUSIONS

LPE is the most powerful epitaxial method to achieve layers and multilayers with the highest structural perfection, best stoichiometry, and with atomically flat surfaces and interfaces. Thus, LPE is most important when ultimate performance of optoelectronic, optical, magnetic, magneto-optic and superconducting devices is envisaged. Future progress is expected when solid-solution substrates become available and then allow the preparation of layers that so far could only be grown by nonequilibrium VPE. However, epitaxy from the vapor phase like MBE and MOVPE is and will remain essential for research when novel layer structures are to be developed in a short time, and for fabrication of devices and integrated structures that can not be made by LPE as the near-equilibrium growth method. On the other hand, there is no fundamental problem to achieve extremely thin layers, even monolayers and superlattices, by LPE, as this is a technological problem that can and will be solved. LPE is the major fabrication method for LEDs and for magneto-optic layers, and it is expected that it will become even more dominant, for instance for the highest efficiency photovoltaic solar cells, when its potential is increasingly recognized. This will be the case when education of epitaxy engineers and epitaxy scientists is established who know thermodynamics and the principles of all epitaxial methods, but

also spread-sheet process analysis, so that they can apply the single optimum economic epitaxial process for their specific epitaxial layer and device requirement. Such multidisciplinary education is urgently needed in order to save resources that are spent when nonoptimal or nonuseful methods are applied for example in HTSCs, where only by LPE the surface flatness required for reliable Josephson/SQUID technology can be expected. Such specialized education is necessary because of the complexity and multidisciplinary nature of crystal and epitaxial growth technology where multiple growth parameters have to be optimized and compromised, and where the substrate problem can be mastered.

## ACKNOWLEDGEMENTS

Part of this chapter was written during a visiting professor stage (October–November 2005) at Nakajima Laboratory, IFCAM, Institute of Materials Research, Tohoku University, Sendai, Japan. The author thanks Prof. Nakajima and his team for hospitality, discussions and support. Furthermore, he expresses his thanks to Profs T. Hibiya and W. Tolksdorf for valuable discussions.

## REFERENCES

- E. Bauer, *Z. Kristallogr.* **110** (1958) 372, 395.  
 P.J. Besser, J.E. Mee, H.L. Glass, D.M. Heinz, S.B. Austerman, P.E. Elkins, T.N. Hamilton and E.C. Whitcomb, *AIP Conf. Proc. No. 5* (1972) 125.  
 S.L. Blank and J.W. Nielsen, *J. Cryst. Growth* **17** (1972) 302.  
 W.K. Burton, N. Cabrera and F.C. Frank, *Phil. Trans.* **A243** (1951) 299.  
 J.A. Burton, R.C. Prim and W.P. Slichter, *J. Chem. Phys.* **21** (1953) 1987.  
 N. Cabrera and M.M. Levine, *Philos. Mag.* **1** (1956) 450.  
 N. Cabrera and D.A. Vermilyea, in *Growth and Perfection of Crystals*, editors R.H. Doremus, B.W. Roberts and D. Turnbull, John Wiley & Sons, Inc., New York, 1958, 393.  
 P. Capper, C. Maxey, C. Butler, M. Grist and J. Price, *J. Cryst. Growth* **275** (2005) 259.  
 A.E. Carlson, PhD Thesis, University of Utah, 1958, in *Growth and Perfection of Crystals*, editors R.H. Doremus, B.W. Roberts and D. Turnbull, John Wiley & Sons, Inc., New York, 1958, 421.  
 J.R. Carruthers, *J. Cryst. Growth* **16** (1972) 45.  
 A.A. Chernov and H.J. Scheel, *J. Cryst. Growth* **149** (1995) 187.  
 W.G. Cochran, *Proc. Cambridge Phil. Soc.* **30** (1934) 365.  
 I. Crossley and M.B. Small, *J. Cryst. Growth* **11** (1971) 157.  
 P.S. Dutta, *J. Cryst. Growth* **275** (2005) 106.  
 D. Elwell and H.J. Scheel, *Crystal Growth from High-temperature Solutions*, Academic Press, London-New York, 1975.  
 F.C. Frank, in *Growth and Perfection of Crystals*, editors R.H. Doremus, B.W. Roberts and D. Turnbull, John Wiley & Sons, Inc., New York, 1958, 411.  
 F.C. Frank and J.H. Van der Merwe, *Proc. R. Soc. London* **A198** (1949) 216.  
 S. Geller, *Z. Kristallogr.* **125** (1967) 1.  
 S. Geller, G.P. Espinosa and P.B. Crandall, *J. Appl. Crystallogr.* **2** (1969) 86.  
 C. Gerber, D. Anselmetti, J.G. Bednorz, J. Mannhart and D.G. Schlom, *Nature* **350** (1991) 279.  
 R. Ghez and E.A. Giess, *J. Cryst. Growth* **27** (1974) 221.  
 R. Ghez and J.S. Lew, *J. Cryst. Growth* **20** (1973) 273.  
 M.H. Grabow and G.H. Gilmer, *Surf. Sci.* **194** (1988) 333.  
 A.A. Griffith, *Phil. Trans. R. Soc.* **A221** (1920) 163.

- M. Hawley, I.D. Raistrick, J.G. Beery and R.J. Houlton, *Science* (1991) 1537.
- T. Hibiya, *J. Cryst. Growth* **64** (1983) 400.
- K. Hiramatsu, S. Itoh, H. Amano, I. Akasaki, N. Kuwano, T. Shiraishi and K. Oki, *J. Cryst. Growth* **115** (1991) 628.
- J.J. Hsieh, *J. Cryst. Growth* **27** (1974) 49.
- T. Ino, Third International Workshop on Crystal Growth Technology, Artworking, Beatenberg, Switzerland, Book of Lecture Notes, editor H.J. Scheel, 2005, 409–420.
- T. Kajimura, K. Aiki and J. Umeda, *Appl. Phys. Lett.* **30** (1977) 526.
- C. Klemenz and H.J. Scheel, *J. Cryst. Growth* **211** (2000) 62.
- S. Knight, B.S. Hewitt, D.L. Rode and S.L. Blank, *Mater. Res. Bull.* **9** (1974) 895.
- M. Konishi, K. Hayashi, A. Odagawa, Y. Enomoto, Y. Yamada, M. Nakamura, K. Ohtsu, Y. Kanamori, M. Tagami, S. Koyama and Y. Shiohara, in *Advances in Superconductivity VI*, editors T. Fujita and Y. Shiohara, Springer, Tokyo, 1994.
- S.D. Lester, F.A. Ponce, M.G. Craford and D.A. Steigerwald, *Appl. Phys. Lett.* **66** (1995) 1249.
- M.J. Lighthill and G.B. Whitham, *Proc. R. Soc.* **A299** (1955) 281, 317.
- J.W. Matthews and E. Klokholm, *Mater. Res. Bull.* **7** (1972) 213.
- H. Minden, *J. Cryst. Growth* **6** (1970) 228.
- T. Mitsuhata, *Jpn. J. Appl. Phys.* **9** (1970) 90.
- S. Miyazawa *et al.*, *IEEE Trans. Electron Devices* **ED-33** (1986) 227.
- Y. Nabetani, T. Ishikawa, S. Noda and A. Sasaki, 12th Rec. Alloy Semiconductor Phys. Electron. Symp. (1993), 223–228.
- K. Nakajima, K. Fujiwara, Y. Nose and N. Usami, *Jpn. J. Appl. Phys.* **44** (2005) 5092.
- K. Nakajima, T. Kusunoki, Y. Azuma, K. Fujiwara, T. Ujihara, G. Sazaki and T. Shishido, *J. Cryst. Growth* **240** (2002) 373.
- W. Nernst, *Z. Phys. Chem.* **47** (1904) 52.
- Y. Nishijima, H. Tezuka and K. Nakajima, *J. Cryst. Growth* **280** (2005) 364.
- T. Nishinaga, C. Sasaoka and K. Pak, *Jpn. J. Appl. Phys.* **28** (1989) 836.
- T. Nishinaga and H.J. Scheel in *Advances in Superconductivity VIII Vol. 1*, editors H. Hayakawa and Y. Enomoto, Springer, Tokyo 1996, 33.
- J. Nishizawa, Y. Okuno and K. Suto, in *JARECT Vol. 19, Semiconductor Technologies*, editor J. Nishizawa, OHMSHA and North-Holland, 1986, 17–80.
- J. Nishizawa and K. Suto, personal communication, 1994.
- J.M. Robertson, M.J.G. Van Hout, M.M. Janssen and W.T. Stacy, *J. Cryst. Growth* **18** (1973) 294.
- G. Sazaki, Y. Azuma, S. Miyashita, N. Usami, T. Ujihara, K. Fujiwara, Y. Murakami and K. Nakajima, *J. Cryst. Growth* **236** (2002) 125.
- H.J. Scheel, U.S. Patent 3,858,553 (Jan. 7, 1975).
- H.J. Scheel, *J. Cryst. Growth* **42** (1977) 301.
- H.J. Scheel, *Appl. Phys. Lett.* **37** (1980) 70.
- H.J. Scheel, in *Advances in Superconductivity VI*, editors T. Fujita and Y. Shiohara, Springer, Tokyo, 1994, 29.
- H.J. Scheel, in *Proceedings of International Symposium on Laser and Nonlinear Optical Materials*, editor T. Sasaki, Data Storage Institute, Singapore, 1997, 10–18.
- H.J. Scheel, in *Crystal Growth Technology*, editors H.J. Scheel and T. Fukuda, John Wiley & Sons, Ltd, Chichester, 2003, Chapter 1, 3–14, Chapter 4, 69–91, and Chapter 28, 623–644.
- H.J. Scheel, G. Binnig and H. Rohrer, *J. Cryst. Growth* **60** (1982) 199.
- H.J. Scheel and D. Ellwell, *J. Cryst. Growth* **12** (1972) 153.
- H.J. Scheel and E.O. Schulz-DuBois, *IBM Techn. Discl. Bull.* **14** (1972) 2850.
- I.N. Stranski and L. Krastanov, *Acad. Wiss. Math.-Naturwiss. Klasse IIb* **146** (1938) 797.
- G.B. Stringfellow, *J. Cryst. Growth* **115** (1991) 1.
- W.A. Tiller and C. Kang, *J. Cryst. Growth* **2** (1968) 345.
- W. Tolksdorf, G. Bartels, G. Espinosa, G.P. Holst, D. Mateika and F. Welz, *J. Cryst. Growth* **17** (1972) 322.

- T. Ujihara, S. Munetoh, K. Kusunoki, K. Kamei, N. Usami, K. Fujiwara, G. Sazaki and K. Nakajima, *Thin Solid Films* **476** (2005) 206.
- J.H. Van der Merwe, in *Treatise on Materials Science and Technology* Vol. 2, editor H. Herman, Academic Press, New York, 1973, 1.
- J.H. Van der Merwe, in *CRC Critical Reviews in Solid State and Materials Science*, editor R. Vanselow, CRC Press, Boca Raton, 1979, 209.
- M. Volmer and A. Weber, *Z. Phys. Chem.* **119** (1926) 277.
- G. Winkler, P. Hansen and P. Holst, *Philips Res. Rep.* **27** (1972) 151.



# 2 Liquid Phase Epitaxy in Russia Prior to 1990

V.A. MISHURNYI

*Universidad Autonoma de San Luis Potosi, Instituto de Investigacion en  
Comunicación Optica, Av. Karakorum 1470, Lomas 4 sec., 78210, San Luis  
Potosi, SLP, Mexico*

---

2.1 Introduction	21
2.2 Specific features of growth of quantum-well heterostructures by LPE	23
2.2.1 LPE growth from a capillary	23
2.2.2 Low-temperature LPE	25
2.2.3 LPE growth of InGaAsP quantum well heterostructures	29
2.3 Rare-earth elements in LPE technology of some III-V binary compounds and solid solutions	35
2.4 Conclusions	37
Acknowledgements	37
References	38

---

## 2.1 INTRODUCTION

It is well known that much progress toward the creation of 'ideal' heterojunctions and devices on their base were achieved by means of liquid phase epitaxy (LPE) at the Ioffe Physicotechnical Institute, Russian Academy of Sciences, in the last quarter of the 20th century. The growth of various multilayer heterostructures by the LPE technique made it possible not only to improve the main parameters of the existing devices but also to develop new ones, such as continuous-wave (cw) heterolasers, which can operate at room temperature. In addition to heterolasers, quite a number of devices with heterojunctions, such as high-efficiency light emitting diodes (LEDs), solar cells, high speed photodetectors, various transistors, switches, etc., were grown by LPE. All these achievements, in their turn, served as a basis for the development of such areas of science and technology as optoelectronics, integral optics, and fiber-optic communication systems.

It is necessary to note that the superiority of Russian scientists and, in particular, the specialists at the Ioffe Institute in the field of development of heterojunction devices was

recognized around the world. Academician Zh.I. Alferov, who has been supervising the heterojunction work since the 1960s, was awarded the Nobel Prize in Physics in 2000. At the same time, the achievements of Russian researchers in the development of the LPE technique, particularly those before 1990, are not known well enough to the global scientific community. The former USSR was a closed country, and very frequently the scientists could not publish their results in the foreign literature. This chapter attempts to eliminate the knowledge gap concerning the Russian work during the later part of the 20th century.

Starting from the 1970s, the LPE technique became the main means of production of various electronic devices. However, LPE is partially replaced nowadays with molecular beam epitaxy (MBE) and gas phase epitaxy, especially metal-organic chemical vapor deposition (MOCVD), and the overwhelming majority of devices based on multilayer structures are now produced using these techniques. This probably happened because it was rather difficult to grow quantum-well (QW) epitaxial layers with controlled thickness by means of LPE. The reproducibility of the main parameters of LPE-grown epitaxial layers, both in a single structure and between different structures, is frequently unsatisfactory. In addition, it is very difficult to grow solid solutions if one of the system's components has a big segregation coefficient. For example, in Al-In systems of III-V solid solutions, such as Al-In-P or Al-Ga-In-P, the segregation coefficient of Al may be as high as  $10^4$ . Naturally, this leads to a very large composition gradient and a gradient of the lattice constant, across the small thickness of an epitaxial layer. Consequently, it is difficult to grow single-crystal epitaxial layers. The LPE growth of such important materials as binary nitrides and various systems of solid solutions on their base is extremely complicated as well.

Despite the advantages of MBE and MOCVD, the LPE technique is still an important technological method for growth of various epitaxial films and multilayer structures. It allows one to produce an excellent quality material. For example, the internal efficiency of radiative recombination for a lightly doped direct-bandgap III-V binary compound and solid solutions grown by LPE is close to 100% [1, 2]. (This probably takes place because the crystallization process in LPE is carried out at conditions not far from equilibrium). The cost of the LPE equipment is considerably lower, in comparison with MBE and MOCVD machines. As opposed to the MBE and MOCVD techniques (in which the speed of crystallization is rather slow and growth of epitaxial structures with high layer thickness is difficult), LPE has a high crystallization speed, and epitaxial layers with a thickness of 50–100  $\mu\text{m}$  can be readily grown from the liquid phase. Therefore, LPE can be used, as before, to grow epitaxial structures for various devices, e.g. high-voltage diodes or avalanche photodetectors.

The most important and interesting, in the author's opinion, results that have been achieved in Russia during the last part of the 20th century in the field of LPE are discussed in the present communication. This review is devoted to the growth technology of AlGaAs and InGaAsP single quantum-well separate confinement (SQW SC) heterostructures and to some peculiarities of use of rare-earth elements in the LPE of III-V compounds and solid solutions. It is clear that the main achievements of the Russian scientists in the research, development, and improvement of the LPE technique are not confined to these areas only, but it is difficult to discuss all these results in a comparatively brief review.

## 2.2 SPECIFIC FEATURES OF GROWTH OF QUANTUM-WELL HETEROSTRUCTURES BY LPE

The thickness of an epitaxial layer primarily depends on the difference of solubilities at the initial and final growth temperatures and, to a certain extent, on the cooling rate, volume of the solvent used, and degree of supercooling. Therefore, QW epitaxial layers with thicknesses of tens or hundreds of angstroms can be grown using the following technological procedures:

1. Growth from a very thin layer of the liquid phase. This method can be used when the liquid phase is located in the capillary between two substrates.
2. Use of lowered growth temperature. For example, the common LPE growth temperature for the AlAs-GaAs system is within 600–800 °C. Originally, these temperatures were used when fabricating cw heterolasers based on AlGaAs/GaAs double heterostructures [3–5]. The thickness of the active regions of these devices was near 0.1–0.2 μm. However, lowering the growth temperature to 350–550 °C made it possible to successfully grow epitaxial layers with thickness of about 10–100 Å.
3. Making shorter the time of contact between the substrate and the liquid phase. This was done by rapidly moving a substrate under the supersaturated liquid phase confined within a narrow slit.

### 2.2.1 LPE growth from a capillary

LPE-grown QW heterostructures can be produced by sharply decreasing the thickness of the liquid phase. The most convenient way to achieve a small thickness of the liquid phase is to create a capillary between two substrates [6,7]. When epitaxial layers are grown from such a capillary formed by different substrates, the processes of crystallization on these materials are different. Let us consider the growth of a GaAs-epitaxial layer from a capillary between GaAs and AlGaAs substrates. The growth on the GaAs substrate occurs in accordance with the homoepitaxial growth model, and that on AlGaAs, with the heteroepitaxial model. The homoepitaxial process is, as a rule, the result of a tangential motion of steps on the substrate surface, i.e. without formation of seeds. There are many steps on the real surface of a crystal, and, therefore, the homoepitaxy takes place at a negligible supercooling. In contrast to the homoepitaxy, the heteroepitaxial process begins with the formation of seeds on the substrate. These seeds, eventually, increase in size and merge to form a continuous epitaxial layer, which can be called the ‘initial’ one. In the case of heteroepitaxy, i.e. in the formation of a continuous epitaxial layer, a strong supercooling is, as a rule, required. Thus, the rate of the homoepitaxial growth is substantially higher than that in the heteroepitaxial process at the same degree of supercooling.

To make the initial AC (GaAs, in the case in question) epitaxial layer grown on an ABC (AlGaAs) substrate as thin as possible, it is necessary, first of all, that the critical radius of AC seeds on the substrate surface should be as small as possible. This can be achieved by creating a high initial supercooling of the A-C liquid phase, because the critical radius of a seed decreases as the supercooling becomes more pronounced. The



heteroepitaxial growth of the AC layer on the ABC substrate occurs until a continuous epitaxial layer is formed. Further growth of the layer is homoepitaxial. At the same time, in order to prevent an increase in the thickness of the initial layer, it is necessary to terminate the homoepitaxial growth of this layer after it is formed as a result of seed merging. In this case, the final thickness of the layer does not differ significantly from the initial thickness, or, to put it differently, from the critical seed radius. This can be achieved by isolating the substrate and the liquid phase or by removing the supercooling, after the initial layer is formed. The supercooling can be removed by raising the temperature to a level at which the formation of the initial layer is complete. In another method [7–9], the supercooling of the A-C liquid phase is removed (relaxation occurs) during the growth of the AC epitaxial layer on the ABC substrate by transfer of C atoms away from the ABC substrate (reverse of mass transport). The reversal of mass transport is enabled by the substantially higher rate of homoepitaxial growth, compared with the rate of the heteroepitaxial process. Therefore, an auxiliary AC (GaAs) substrate (inverting substrate), on which the homoepitaxial growth takes place, is to be parallel to the main ABC substrate to form a capillary with a thickness  $L$ . Before a continuous initial epitaxial layer is formed on the main ABC substrate, relaxation of supercooling will occur, mainly due to the homoepitaxial growth on the AC substrate. Let us assume that  $t_{ho}$  is the time necessary to form a continuous AC epitaxial layer on the ABC substrate. If the supercooling is not removed during this time, further growth occurs on both the substrates by the homoepitaxial mechanism. The time of supercooling relaxation ( $t_r$ ) is determined by the time of diffusion of a C atom in the A-C liquid phase from ABC to AC substrate. Naturally, this time depends on the distance  $L$  between the substrates. In order to obtain an epitaxial layer with a thickness that does not differ substantially from the thickness of the initial layer, i.e. the critical seed radius, it is necessary to satisfy the requirement  $t_{ho} \cong t_r$ . This can be done by selecting the distance  $L$  between substrates or the thickness of the capillary. If  $t_r \gg t_{ho}$ , the flow toward the AC substrate is weak and, therefore, the supercooling of the liquid phase remains strong after the initial AC layer is formed on the ABC substrate. If  $t_{ho} \gg t_r$ , the flow toward the AC substrate is so strong that a solid epitaxial layer cannot be formed because of the fast relaxation of supercooling.

The relaxation LPE technology with reversal of mass transport was analyzed theoretically in [8,9]. The critical radius of GaAs seeds (shown in Figure 2.1), time in which a continuous GaAs epitaxial layer grows, and thickness of layers on the main  $Al_xGa_{1-x}As$  and auxiliary GaAs substrates were calculated as a functions of the initial supercooling. The distance between the substrates ( $L$ ), necessary for crystallization of an epitaxial layer with a thickness close to the critical seed radius, was determined. The dependence of this distance on supercooling is shown in Figure 2.2. The potentialities of relaxation LPE with reversal of mass transfer were demonstrated experimentally with the use of a GaAs- $Al_xGa_{1-x}As$  capillary with  $x = 0.1, 0.2$  and  $0.4$ . The capillary was filled with the liquid phase owing to the surface tension forces. The epitaxial process was carried out at a constant temperature of about  $900^\circ C$ , with the initial supercooling of  $3-5^\circ C$ . The distance  $L$  was 30 and  $50 \mu m$ . Both the theoretical and experimental studies of this method show that the use of the LPE technology with reversal of mass transfer enables successful growth of QW heterostructures with layer thicknesses of tens to hundreds of angstroms [7–9].

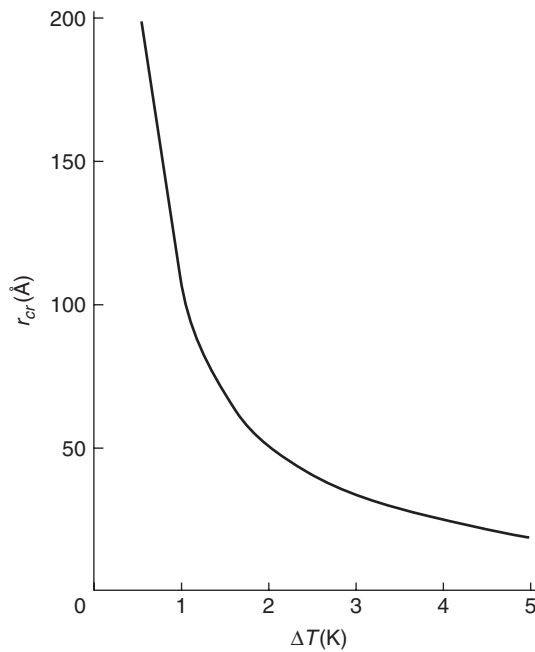


**Figure 2.1** Theoretical dependence of the critical radius of the GaAs spherical seeds ( $r_{cr}$ , Å) on initial supercooling ( $\Delta T$ , K) [7] ( $T = 1000$  K). Reprinted from *Sov. Phys. Tech. Phys.*, 33(8), V. N. Bessolov *et al.*, Relaxation liquid phase epitaxy based on reversal of the mass transport and its potential for making ultrathin layers of III–V materials, 902–905, Copyright (1988) with permission from V. N. Bessolov

## 2.2.2 Low-temperature LPE

One of the most important factors in the LPE growth technology is the design of the boat used to grow epitaxial structures. First multi-layer heterostructures were grown by LPE with the use of a sliding boat. This boat had two parts: a fixed body with openings for the liquid phases and a slider on which one or more substrates are mounted. The multi-layer epitaxial structures were grown by successive displacement of the substrate from one liquid phase to another. The first AlGaAs/GaAs cw-double-heterojunction lasers operating at room temperature were fabricated using this technique.

The boat design described above has some drawbacks. Usually, the weight of the solvent is 3–5 g, and the surface area of the substrate about  $1 \text{ cm}^2$ . Thus, the height of the layer of the liquid phase reaches several millimeters. Analysis of the growth processes from such liquid phases, which can be named semi-limited, shows that a considerable portion of the dissolved material has not enough time to reach the substrate surface and crystallizes in the volume of the liquid phase. For the Al-Ga-As system, experiments conducted with a limited height of growth chamber [10] demonstrated that there is no crystallization in the volume of the liquid phase if its thickness does not exceed 1 mm. In this case, the crystallization efficiency is near 100 %, which means that virtually the whole amount of the dissolved material crystallized on the substrate. If the growth processes are performed from the semi-limited liquid phase, stable seeds appear at a distance of

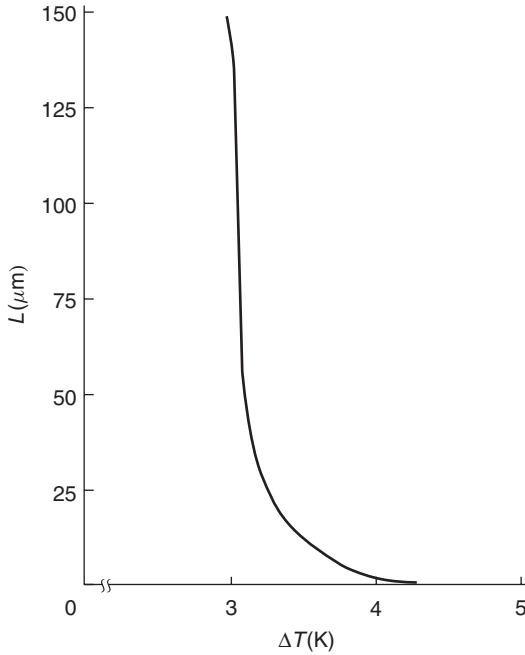


**Figure 2.2** Theoretical dependence of the distance between substrates (capillary thickness  $L$ ,  $\mu\text{m}$ ), necessary for crystallization on the  $\text{Al}_{0.2}\text{Ga}_{0.8}\text{As}$  substrate an epitaxial layer with a thickness close to the GaAs critical seed radius, as a function of initial supercooling ( $\Delta T$ , K) [7] ( $T = 1000$  K). Reprinted from *Sov. Phys. Tech. Phys.*, 33(8), V. N. Bessolov *et al.*, Relaxation liquid phase epitaxy based on reversal of the mass transport and its potential for making ultrathin layers of III–V materials, 902–905, Copyright (1988) with permission from V. N. Bessolov

1 mm or more from the substrate. Therefore, some part of the dissolved material may be washed off by these seeds. This effect may impair the planarity of the epitaxial layer, as it is shown schematically in Figure 2.3. It is advisable to carry out the LPE growth with a limited volume of the liquid phases, with the thickness of the liquid-phase layer not exceeding 1 mm, at least for the Al–Ga–As system.

Another drawback of LPE with a sliding boat is associated with the possible additional defects that appear on the surface of a growing structure during its transfer from one liquid phase to another. These defects can be caused either by ordinary mechanical damage on the substrate or on the surface of epitaxial layers. Moreover, the structure's surface may be oxidized through interaction with trace amounts of oxygen or water vapor in the hydrogen atmosphere, to which this surface is exposed during the transfer from one liquid phase to another. Moreover, oxide films are always present on the surface of the liquid phase, and very frequently it is difficult to remove these films completely, especially  $\text{Al}_2\text{O}_3$ , even by prolonged high-temperature baking. Oxide films of this kind make wetting of the substrate or of a preceding epitaxial layer more difficult, and, naturally, this phenomenon affects the quality of the structure produced.

It is possible to grow heterostructures with layer thicknesses of about  $100 \text{ \AA}$  or less by low-temperature LPE, as mentioned above. For the Al–Ga–As system, ‘low temperatures’ are in the range  $350\text{--}550^\circ\text{C}$ , and it is very difficult to achieve an ideal substrate wetting

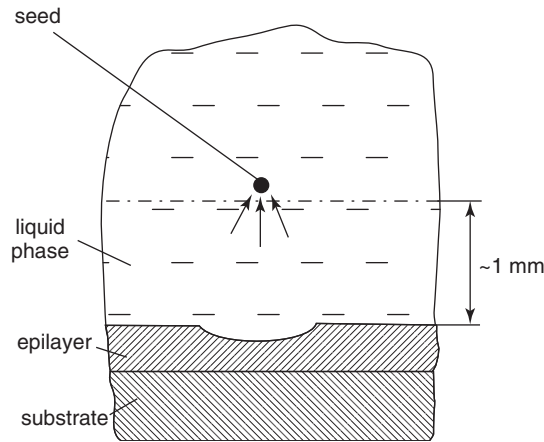


**Figure 2.3** Diagram showing the planarity impairment of the epitaxial layer, when semi-limited liquid phase is used

at these temperatures because of the oxide films present on the surface of the liquid phase (see above). To solve this problem for the case of low-temperature growth of AlGaAs/GaAs heterostructures, a special boat design [11,12], shown in Figure 2.4, was used. In this boat, the liquid phases of different compositions are placed in a container 1, which can move along the body 2. There is a piston chamber 3 with a reciprocating piston 4. The growth chamber 5 is formed by two GaAs substrates 6 with a spacing of 0.5–1.0 mm in between, which are connected with the piston chamber through a narrow slit 7. On the right-hand side, the growth chamber 5 is connected with the container 8 for the liquid phases used by means of a winding slit. This prevents mixing of the liquid phases used with that in the growth chamber.

In the beginning of the process, the piston is in the right-hand position. Then the container 1 is moved to the right in such a way that it provides the exact match between the position of the first liquid phase and the opening 9 in the body of the boat. When the piston is moved to the left, the first liquid phase falls down through this opening into the piston chamber 3. After that, the piston is returned back to the right-hand position, with the result that the liquid phase is squeezed through slit 7 into the growth chamber. This technique provides an effective mechanical cleaning of the melt to remove the oxide films and guarantees an ideal contact of the Al-Ga-As melt with the substrate, even at low temperatures and an Al content in the liquid exceeding 0.5 at. % [11,12]. After the first epitaxial layer is completely grown, container 1 is moved again to the right. Then, as the piston moves back and forth, the second liquid is squeezed into the growth chamber, with the first liquid being forced into container 8. The subsequent replacement of liquid phases is performed in a similar manner. The last liquid phase can be removed from the surface of the lower substrate by shifting the substrate holder (slider 10) outside the growth chamber. However, very frequently, the remaining liquid phase cannot be removed completely from the surface of the structure grown, using this method. Therefore, crystallization from the remainder continues during the cooling of the heater to room temperature. Naturally, this causes a noticeable deterioration of the morphology

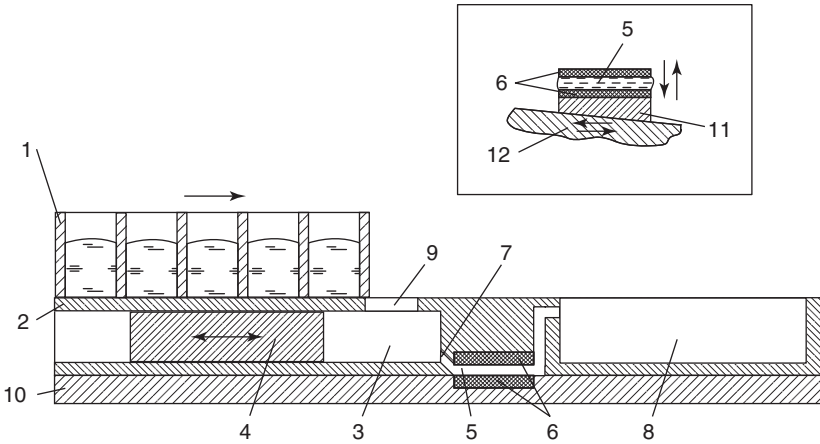


**Figure 2.4** Diagram of the 'piston' boat [11]. The inset shows the 'piston' boat construction with a variable thickness of liquid phase [18]. 1, Container for the liquid phases; 2, body; 3, piston chamber; 4, piston; 5, growth chamber; 6, substrates; 7, narrow slit; 8, container for the used liquid phases; 9, opening; 10, slider; 11, mobile wedge-shaped inset; 12, wedge-shaped slider. Reprinted from *Kristall Technic*, 10(2), Zh. I. Alferov *et al.*, Investigation of a new LPE method of obtaining Al-Ga-As heterostructures, 103–110, Copyright (1975) with permission from V. M. Andreev. Inset: Reprinted from *Sov. Phys. Tech. Phys.*, 23(2), Zh. I. Alferov *et al.*, Fabrication of AlAs-GaAs heterostructures by selective liquid-phase epitaxy, 209–214, Copyright (1978) with permission from V. M. Andreev

or planarity of the last layer, which is extremely undesirable for the subsequent post-growth processing, such as, e.g. photolithography or high-precision etching. However, it is possible to remove the remainder of the liquid phase much more reliably by means of the following procedure [11,12]. The Al-Ga-As liquid phase with composition corresponding to  $\text{Al}_x\text{Ga}_{1-x}\text{As}$  with  $x \geq 0.8$  is squeezed into the growth chamber immediately after the growth of the last layer. After that the furnace is switched off. The  $\text{Al}_x\text{Ga}_{1-x}\text{As}$  solid solution with high content of AlAs crystallizes on the surface of the structure during the cooling of the furnace. As it is known, the  $\text{Al}_x\text{Ga}_{1-x}\text{As}$  solid solutions with  $x \geq 0.8$  are corrosion-unstable and can be easily removed with some selective etchant that is inert toward the working layers of the structure. For example, such etchant as a weak aqueous solution of HCl or  $\text{H}_3\text{PO}_4$  can be used successfully for this purpose. This method guarantees a good planarity and smoothness of the surface of the epitaxial structure. It has been used not only for AlGaAs/GaAs, but also for the AlGaP/GaP system to produce optical modulators and waveguides [13–16]. In the latter case, after the growth of the last epitaxial layer of the AlGaP/GaP heterostructure is completed, the growth chamber is filled with an Al-Ga-P liquid phase, which provides crystallization of an  $\text{Al}_x\text{Ga}_{1-x}\text{P}$  solid solution with  $x \geq 0.8$ . This solution, as in the preceding case of AlGaAs, can be removed from the surface of the structure with any etchant or even warm water.

Therefore, the LPE boat design described above has a number of advantages over the 'sliding' boat type. These advantages are associated with the use of a growth chamber of limited height and squeezing of the liquid phases across a narrow channel, which allows mechanical removal of oxide films from the liquid phases and guarantees a good wetting of the substrate or the preceding epitaxial layer. The planarity and morphology of epitaxial

layers grown with the ‘piston’ boat and the reproducibility of their main parameters are much better in comparison with layers produced using the ‘sliding’ boat.

In the Al-Ga-As system, the solubility of As in the Ga-Al melt varies nonlinearly, and the liquidus lines are convex downwards. Thus, mixing of two Al-Ga-As liquid phases with different compositions causes supersaturation of the liquid obtained. That is why, in the boat with forced exchange of one liquid phase for another, the transition layers between different parts of the structure always occur because of the isothermal mixing of the melts with different compositions. Sometimes, this phenomenon is undesirable in fabrication of various devices, e.g. those with structures with a two-dimensional (2D) electron gas. The thickness of the transition layers can be reduced by lowering the temperature and the Al concentration difference in the melts before their mixing. The results obtained in studies of the relationship between the thickness of the transition layers and the specific features of the technological procedures employed were reported in [12,17].

The boat design described may have different modifications. For example, the growth chamber may have no upper substrate. The thickness of the liquid-phase layer or the height of the growth chamber may also vary during the crystallization process, when a wedge-shaped slider is moving horizontally, as shown in the inset in Figure 2.4. [18]. This modification is very useful in growth of, e.g. heterolasers with QW active layers. In this case, these layers can be grown from a chamber with small height  $h$  ( $\sim 0.1$  mm), but all other layers of the structure, such as wide-gap emitters and the GaAs contact layer, from a chamber with  $h \sim 1$  mm.

Boats of various designs with forced replacement of one liquid phase by another have been used successfully at the Ioffe Institute for many years to fabricate such heterojunction devices as heterolasers [17,19], LEDs [20–23], solar cells [24–29], and transistors [30]. These boats are quite practical if used in growth of various structures by the selective epitaxy method, when the crystallization processes take place in windows within a dielectric film [18,31]. If a ‘slider’ type boat is used, the problem of wetting of a substrate partially covered with an insulator becomes complicated. The squeezing of the liquid phases through a narrow channel by the piston permits an improved wetting of the substrate even when the width of the ‘windows’ is less than  $20 \mu\text{m}$ .

Theoretical and experimental studies of low-temperature LPE have shown [17,32] that at temperatures of  $400\text{--}500^\circ\text{C}$ , the rates of crystallization and layer thickness of GaAs are of the same order of magnitude ( $10^{-1}\text{--}1 \text{ nm s}^{-1}$ ) as in the case of MBE and MOCVD (Figure 2.5) [32]. Therefore, an epitaxial layer grown at low temperatures during  $10\text{--}30$  s can be as thin as several nanometers. More detailed information about the phase diagram, behavior of impurities, and specific features of the low-temperature LPE of GaAs and AlGaAs can be found in [33].

AlGaAs/GaAs heterolaser grown by low-temperature LPE has a typical SQW SC structure. Structures of this kind demonstrated a  $200\text{--}300 \text{ A cm}^{-2}$  threshold current density at room temperature [17,34]. The lowest absolute threshold current of  $1.3 \text{ mA}$  ( $300 \text{ K}$ ) was obtained for buried laser diodes with a stripe width of  $\sim 1 \mu\text{m}$  and cavity length of  $125 \mu\text{m}$  [35].

### 2.2.3 LPE growth of InGaAsP quantum well heterostructures

In all III-V multicomponent systems, except AlGaAs and AlGaP, the lattice constant changes with composition. Therefore, one cannot use boats with forced exchange of the

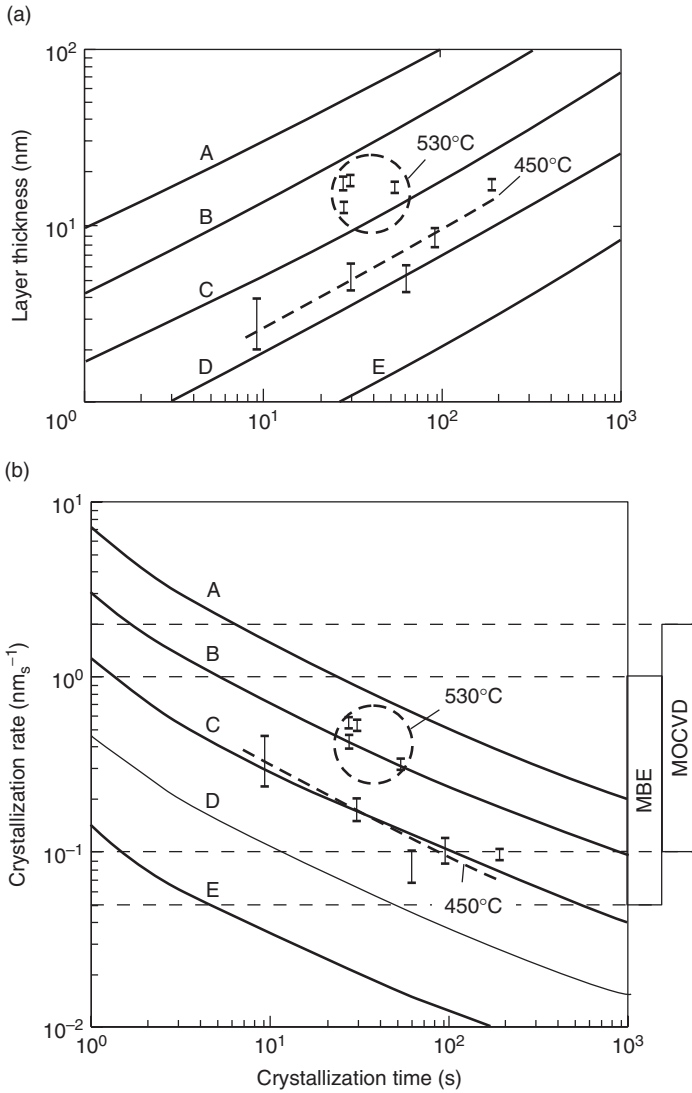


**Figure 2.5** Dependence of the thickness of (a) epitaxial layers and (b) crystallization rates on growth time of GaAs [32]. A, 600°C; B, 550°C; C, 500°C; D, 450°C. Solid lines, theoretical predictions; points  $\bar{I}$  and dashed lines, experiments at 530 and 450°C. Reprinted from *Sov. Tech. Phys. Lett.*, 12(9), Zh. I. Alferov *et al.*, AlGaAs heterostructures with quantum-well layers, fabricated by low-temperature liquid-phase epitaxy, 450–451, Copyright (1986) with permission from V. M. Andreev

one liquid phase for another in the growth technology for these materials. This is due to the formation of transition layers with an uncontrolled variation of the composition and the lattice constant, which would crystallize spontaneously during the mixing of two different liquid phases. Very frequently, these transition layers have a polycrystalline structure because of the lattice mismatch with the substrate or a preceding epitaxial layer and

hinder growth of the succeeding epitaxial layers in the single-crystal state. That is why, in order to grow any heterostructure on the basis of such materials as InGaP, InGaAsP, InGaAsSb, AlGaAsSb, InPAsSb etc., it is necessary to use another technique that would rule out the mixing of liquid phases with different compositions. The most suitable boat design for these cases (which, however, has the disadvantages mentioned above) is the 'sliding' boat, with which the substrates are moved successively from one liquid phase to another.

As already mentioned, one of the most important drawbacks of the LPE technique is its rather poor control over the basic parameters of epitaxial layers and the resulting poor reproducibility of the main properties of various heterostructures. Among the reasons for such a bad reproducibility are different temperature gradients within the reactor and the boat. During the epitaxial growth by the LPE method, it is necessary to measure precisely the real temperature at the interface between the substrate and the liquid phase. In addition, when growing multi-layer structures, e.g. SQW SC heterolasers containing seven, eight, or even more layers, the substrate is moved, if the 'sliding' boat is used, over rather large distances of about 15–20 cm. In this case, it is necessary to measure the temperature distribution over this distance. It is impossible to conduct these measurements with high precision by means of a thermocouple, which is usually placed at some distance from the substrate–liquid interface. Therefore, the data furnished by the thermocouple may differ from the real temperature at this interface, because of the unknown temperature gradients always present in any growth system. Note that this problem is not so important for the 'piston' boat design, in which the substrate is not moved during the entire growth process.

Occasionally, in some solid solutions used to grow heterostructures, it is not very important to know the exact growth temperature of epitaxial layers. For example, changes in the composition of AlGaAs or AlGaP, caused by small temperature gradients, do not actually influence the lattice constant. However, as mentioned above, the lattice constant of the majority of multi-component solid solutions depends directly on the composition determined by their growth temperature. For example, in the case of InGaAsP, AlGaAsSb, InGaAsSb and other multi-component systems, a temperature gradient within the growth reactor can lead to changes in the composition of epitaxial layers and to a lattice mismatch between layers in the structure.

A possible way to determine precisely the temperature at the interface between the liquid phase and the substrate is to measure the solubility [36]. In other words, the temperature at the interface between the liquid phase and the substrate can be determined by the reversal of the procedure used to study the phase diagrams. Usually, this solubility is determined in LPE by the weight loss from the substrate brought in contact with an unsaturated liquid phase. Note that the solubility can be measured with a very high accuracy, which is limited only by the accuracy of the microbalance used. From the thus determined solubility, the sought after temperature can be deduced using the known phase diagram. It is possible to find the temperature distribution in the growth area of the reactor equipped with a boat having several cells for substrates and liquid phases [36]. For this kind of temperature measurements, it is natural to employ the same material as that of the substrate on which device structures are grown. In the case of III-V binary compounds, which are widely used as substrates for various devices, the corresponding phase diagrams are known very well and can be conveniently used to measure the temperature. Obviously, various factors will influence the accuracy with which the solubility is determined from the substrate weight loss. In particular, if the thickness of



the dissolved layer of the substrate exceeds 20–30  $\mu\text{m}$ , which is the case at rather high temperatures, the liquid phase very frequently cannot be removed completely from the substrate. A crystallization process will take place from these liquid phase remainders during the system cool-down. This will raise the error in determining the solubility. To minimize this error, it is advisable to reduce the thickness of the dissolved layer by preliminary sub-saturation of the liquid phase to 60–80 % of the full saturation. In addition, it is possible to take into account the error in determining the substrate weight loss caused by material crystallization when cooling to room temperature. For this purpose, it is necessary to weigh the substrate twice, after the dissolution process and after the removal of the solution remainder by any suitable selective etchant. This makes it possible to find the total amount of liquid phase that remained on the substrate surface and to calculate the thickness or weight of the epitaxial layer grown from these remainders.

A method that successfully removes the remainder of the liquid solution from the substrate surface exists in that, immediately after the dissolution process, a layer with composition strongly different from that of the substrate is grown, as mentioned above. This layer can be removed, along with the undesired remainders of the liquid solution, by a suitable selective etchant. The method has been used successfully for the AlGaP and AlGaAs systems.

There is another simple method to raise the probability of the complete removal of the liquid solution from the substrate surface after the dissolution experiments [37]. In this method, after the substrate is removed to break its contact with the liquid phase; it is passed underneath an ensemble of very closely spaced vertical plates made of the same material as the substrate. The liquid remainders are pulled up into the space between these plates by capillary forces, leaving a clean surface. This method is very useful in growth of multilayer heterostructures because it prevents mixing of any liquid remaining on the substrate with the solution used in the next stage and precludes any uncontrollable changes in the composition of this solution, which, otherwise, could make the lattice match impossible. Another factor that can influence the accuracy of solubility determination and has to be taken into account is the possible evaporation of any volatile component, both from the solid and from the liquid phases [36].

The first lasers based on InGaAsP/InP double heterostructures [38] were grown in Russia using the common ‘sliding’ boat. The typical thickness of the active layers of these structures was 0.7–2  $\mu\text{m}$ , and threshold current densities were in the range from 2.5 to 16  $\text{kA cm}^{-2}$  (300 K) [39]. Later, to grow active layers of SQW SC structures with lower thickness and to reduce the threshold current densities of the lasers fabricated, a special modified ‘sliding’ boat was developed. In this design, the liquid phase used for growth of the active layer is placed in a container or a growth chamber with a closed bottom and a narrow slit in it. As a rule, the slit width in different boat designs was about 1–2 mm. The fast movement of the slider along the body of the boat makes it possible to decrease the time of contact between the liquid phase and the substrate or with the preceding epitaxial layer and, thus, to provide the crystallization of layers with thickness of 100–400  $\text{\AA}$  [40]. To improve the reproducibility of the thicknesses of the growing layers, it is very important to keep the motion speed of the slider invariable. For this purpose, it is convenient to use a linear electric motor, which moves the rod that controls the position of the slider within the body of the boat. This system makes it possible to move the substrate under the liquid phases at a speed of 0.01 to 1.5  $\text{m s}^{-1}$  and

to set the instant of time when the substrate is stopped in the neutral position by means of a computer-controlled linear electric motor [41].

The lattice constant of InGaAsP solid solutions can be adjusted to match InP and GaAs binary compounds, used as a substrate to grow various heterostructures. In addition, it is possible to find for any composition of GaAsP ternary solid solutions the corresponding compositions of InGaAsP for which these two materials have the same lattice constant. Naturally, GaAsP substrates can be used to fabricate various optoelectronic devices intended for shorter wavelengths, in comparison with GaAs substrates. SQW SC heterolasers have been grown successfully using the modified 'sliding' boat, both on binary InP [42–48] and GaAs [49–57] substrates and on GaAsP [58–60] ternary solid solutions. In the latter case, a GaAsP layer was grown preliminarily on the GaAs substrate by means of gas phase epitaxy. The cw laser generation at wavelength 0.65–0.68  $\mu\text{m}$  (300 K) has been obtained on the base of SQW SC GaAsP/InGaAsP structures grown by means of developed LPE growth technology [58–60]. Table 2.1 lists some parameters of InGaAsP/InP and InGaAsP/GaAs SQW SC heterolasers. It can be seen that the main characteristics of these lasers do not differ significantly from those of analogous devices grown by MBE or MOCVD.

The developed LPE growth technology based on a modified 'sliding' boat can be used to grow not only SQW heterolasers, but also multilayer periodic structures. As it was shown in [41], the use of two growth chambers with narrow slits makes it possible to produce such structures by means of repeated reciprocating movements of the slider of the boat, with the substrate situated underneath these slits. A computer-controlled linear electric motor sets the slider in motion and stops this motion when necessary. Some of these structures are shown in Figure 2.6.

Another variant of an LPE boat [61], which is a combination of the 'sliding' and 'piston' designs, is shown in Figure 2.7. In this boat, the liquid phases are in chambers 1 with vertical pistons 2. The pistons can be moved down by a wedge-shaped piston-pusher

**Table 2.1** Some parameters of InGaAsP/InP and InGaAsP/GaAs SQW SC heterolasers

Structure	Threshold current density ( $\text{A cm}^{-2}$ , 300 K)	Active region thickness ( $\text{\AA}$ )	Generation wavelength ( $\mu\text{m}$ )	Resonator	Reference
InGaAsP/InP	280	360	1.31	Four cleaved facet samples (broad-contact, $10^{-3} - 5 \times 10^{-3} \text{ cm}^2$ )	[47]
	450	280	1.30		
	220	410	1.29		
	580	400	1.56		
	600	400	1.56		
InGaAsP/GaAs	90	$\approx 100$	0.86	Four cleaved facet samples (broad-contact, $10^{-3} - 5 \times 10^{-3} \text{ cm}^2$ )	[53, 55, 57]
	250	$\approx 200$	0.79		
	92		0.80		
	165		0.86		

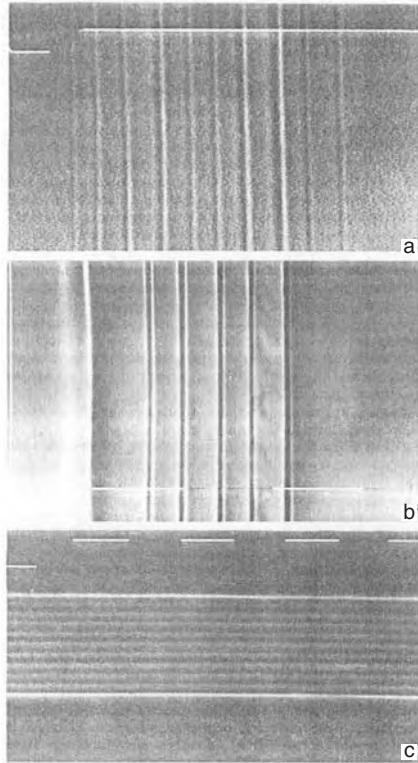


**Figure 2.6** Photographs of some of the InGaAsP multilayer periodical structures grown by LPE [41]. (a)  $\text{In}_{0.7}\text{Ga}_{0.3}\text{As}_{0.66}\text{P}_{0.34}/\text{InP}$  (substrate  $\text{InP} \langle 111 \rangle$ ); (b)  $\text{In}_{0.2}\text{Ga}_{0.8}\text{As}_{0.6}\text{P}_{0.4}/\text{In}_{0.49}\text{Ga}_{0.51}\text{P}$  (substrate  $\text{GaAs} \langle 111 \rangle$ ); (c)  $\text{In}_{0.7}\text{Ga}_{0.3}\text{As}_{0.66}\text{P}_{0.34}/\text{In}_{0.8}\text{Ga}_{0.2}\text{As}_{0.42}\text{P}_{0.58}$  (substrate  $\text{InP} \langle 100 \rangle$ ). The periodical structures (a) and (c) are located between InP substrate and InP epitaxial layer; (b) between two  $\text{In}_{0.49}\text{Ga}_{0.51}\text{P}$  epitaxial layers. The white bar sizes are: (a) and (b)  $0.5 \mu\text{m}$ ; (c)  $0.25 \mu\text{m}$ . Reprinted from *Sov. Tech. Phys. Lett.*, 14 (4), I.N. Arsent'ev *et al.*, Periodic multilayer In-Ga-As-P structures fabricated by liquid-phase epitaxy, 264–266, Copyright (1988) with permission from I. N. Arsent'ev

3 to inject the liquid phase into 1-mm-thick growth chambers through small openings 4 at the bottom of the chamber 1. The excess of liquid phase in the growth chamber can be expelled through a special vertical channel 5 and returned to the upper part of the piston-chamber. As a rule, the liquid phase is to be injected into the growth chamber when the temperature is exactly equal to, or several degrees higher than the liquidus temperature. After the first epitaxial layer is grown, the slider 6 with the substrate 7 are moved to a position under the second growth chamber.

It is known that such solvents, as Sn, In, Bi, Pb, Sb, etc., can be used to grow epitaxial layers on the basis of various solid solution systems. For example, the transition from the Ga- to Sb-rich liquid phases is effective in the growth technology of III-V Sb-based materials [61, 62]. The growth of GaSb and its solid solutions from 'neutral' solvents could be useful to improve the characteristics of these materials. Pb can be used as such 'neutral' solvent [63]. All solvents, mentioned above, have melting points higher than

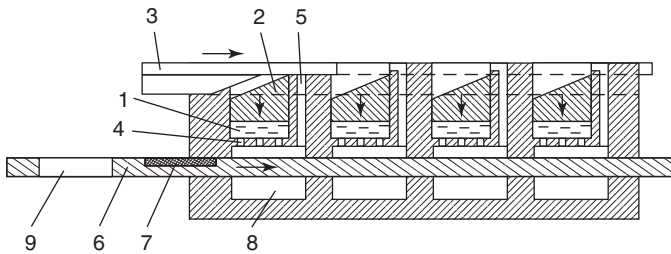


**Figure 2.7** Combination of the ‘sliding’ and ‘piston’ boat designs. 1, Liquid phase; 2, piston; 3, wedge-shaped piston-pusher; 4, small openings; 5, channel for the liquid phase; 6, slider; 7, substrate; 8, container for the used liquid phases; 9, opening

that of Ga and are solid at room temperature. Therefore, the described boat cannot be taken apart after the completion of the LPE-growth process because of the solidification of the liquid phases. That is why it is absolutely necessary to remove the liquid phase from the growth chamber and channel 5, in the case of crystallization processes with the use of a solvent other than Ga. It can be seen in Figure 2.7 that, when the substrate is moving from the first to the second growth chamber, the liquid phase used, and also its remainder in the channel 5, simultaneously fall down into the container 8 through the opening 9. The best composition, lattice matching, reproducibility of layer thickness, and quality of the surface morphology of epitaxial layers, in comparison with those in the case of the ordinary sliding boat, can be achieved with this boat design. It has been used successfully to grow InGaAsSb, AlGaAsAs and various multilayer structures on the basis of these materials. Note, that a similar boat was suggested by Horikoshi [64]. Nevertheless it can be applied only to growth of AlGaAs/GaAs multilayer heterostructures, while the construction described above has been used for different systems of solid solutions.

## 2.3 RARE-EARTH ELEMENTS IN LPE TECHNOLOGY OF SOME III-V BINARY COMPOUNDS AND SOLID SOLUTIONS

Rare-earth elements (REEs) have been used in Russia’s semiconductor technology since the last quarter of the 20th century. In the first articles [65–68], the influence of these elements on various electrical properties of silicon, germanium, and some III-V binary compounds was studied. Later, thorough purification of InP and InGaAsP to remove uncontrolled and undesirable impurities by adding different REEs to the liquid phase was demonstrated [69, 70]. By means of this technological method, the electron concentration was made in these materials as low as  $\sim 10^{13} \text{ cm}^{-3}$ . The carrier mobility at 77 K reached about  $6.5 \times 10^4 \text{ cm}^2 \text{ V}^{-1} \text{ s}^{-1}$  for InP, and about  $10^5 \text{ cm}^2 \text{ V}^{-1} \text{ s}^{-1}$  for InGaAs.

In all LPE experiments, the REE concentration in the liquid phases ( $N_{\text{REE}}^1$ ) was varied in the range 0.001–0.1 at. %. When studying the specific features of the behavior of REE in the liquid phases of the systems In-P and In-Ga-As-P, it was found that the solubility of P increases when these phases are doped with such REEs as Ho, Yb, Gd and Dy. This fact can be accounted for by the formation of high-melting compounds of REEs with P within the liquid, and their subsequent conversion to slag [71, 72]. As to

solid phase, InP epitaxial layers are homogeneous when the  $N_{\text{REE}}^{\text{I}}$  is in the range 0–0.005 at. %. If  $N_{\text{REE}}^{\text{I}} > 0.005$  at. %, inclusions of a second phase can be detected in the epitaxial films. These inclusions consist of compounds of phosphorus (P), oxygen (O) and Group I elements with the REE. The sharp rise in the inclusion density (up to  $10^4 \text{ cm}^{-3}$ ) was observed at  $N_{\text{REE}}^{\text{I}} > 0.01$  at. %. The inclusion sizes amount to 5–200  $\mu\text{m}$  and depend on  $N_{\text{REE}}^{\text{I}}$ . Secondary ion mass spectroscopy [71, 72], X-ray diffraction analysis [71, 72] and Raman spectroscopy [73] show that the concentration of REE atoms in the solid phase is insignificant ( $\sim 10^{13} \text{ cm}^{-3}$ ) when  $N_{\text{REE}}^{\text{I}} = 0\text{--}0.015$  at. %.

Simultaneous doping of the In-P liquid phase with REE and various donors and acceptors was carried out to elucidate the mechanism of interaction between REE and background impurities [71, 72, 74]. It was shown that the material is purified mainly through interaction of REE with Group VI donors. As a result, high-melting REE chalcogenides are formed in the liquid phase and settle to form a slag without being incorporated into the epitaxial layer, which reduces the background donor concentration by several orders of magnitude. Studies of the Hall mobility [74], drift velocity [75, 76], minority-carrier lifetime [77], and low-temperature luminescence (2 K) [71, 72] indicate that a high perfection of the material and its thorough purification are achieved by means of liquid phase doping with REE.

The described technology of epitaxial layer growth from REE-doped liquid phases was used to fabricate various device structures. InGaAs/InP structures with a 2D electron gas were grown by LPE for the first time [78]. For these devices, semi-insulating InP:Fe was used as a substrate. The concentration of electrons in the layers of the structure was reduced to  $< 10^{15} \text{ cm}^{-3}$  by doping the liquid phase with REE. A study of the temperature dependence of the concentration and mobility of electrons and magnetotransport measurements confirmed the existence of a 2D electron gas [79, 80]. The electron mobility in such structures was found to be  $1.23 \times 10^4 \text{ cm}^2 \text{ V}^{-1} \text{ s}^{-1}$  (300 K) and  $7.3 \times 10^4 \text{ cm}^2 \text{ V}^{-1} \text{ s}^{-1}$  (4.2 K), which is, probably, the optimal result for the LPE grown structures.

The creation of devices with ‘purely green luminescence’ was one of the most important tasks in production of LEDs. With its band gap of 2.26 eV at room temperature, GaP is a suitable material for this purpose. Unfortunately, it is difficult to fabricate green GaP LEDs by conventional technology because, in addition to the inter-band emission, there are other lower-energy spectral bands in the luminescence spectra of this material. These spectral bands result from recombination of donor–acceptor pairs associated with Groups II and VI background impurities. It is possible to reduce the concentration of these undesirable impurities by doping of the GaP liquid phase with Y during the growth of LED structures. As it was shown in [72], the use of REE in the LPE makes it possible to fabricate GaP LEDs with purely green luminescence, when the spectrum consists of virtually a single band with  $h\nu_{\text{max}} = 2.234 \text{ eV}$  (300 K).

REE have been successfully used in the LPE growth of various photodetectors, such as:

- InGaAs and InP planar photoresistors for the spectral range 200–1600 nm [80, 81];
- mesa- and planar-types of p-i-n photodiodes with sensitivity of  $0.7 \text{ A W}^{-1}$ , response time  $\sim 50 \text{ ps}$  and dark current of  $5 \times 10^{-8} \text{ A cm}^{-3}$  for the spectral range 1000–1600 nm [82, 83];

- N-p-N phototransistors with a maximum current gain of 1000 at a speed of 100 ns and incident light power of  $10^{-4}$  W [71, 72];
- vertical photo field effect transistors (FETs) with a static gain of  $\sim 100$  [71, 72].

In the technology of microelectronic devices, REEs have been used to fabricate Schottky barriers with a small current leakage, Schottky FETs [85] and metal–insulator–semiconductor structures [71, 72].

All these results confirm the importance and potentialities of application of REEs in the LPE technology of various optoelectronic and microelectronic devices.

## 2.4 CONCLUSIONS

As already mentioned, this paper does not cover all the major achievements of Russian scientists for various aspects of LPE. In particular, a noticeable contribution was made by them to theoretical analysis of phase diagrams, without knowledge of which it is impossible to carry out LPE processes. Models that take into account various mechanisms of atomic interactions in liquid and solid phases and make it possible to calculate phase equilibrium in many III-V solid solutions have been suggested and developed. Fragments of phase diagrams in the composition and temperature ranges commonly used in LPE have been studied experimentally for most of the solid solutions grown by LPE. The following heterostructure devices have been fabricated with the use of LPE: high-voltage diodes, photodetectors and LEDs of various designs, ‘buried’ heterolasers, transistors and switches of various types, a wide variety of active and passive elements for integrated optics, etc. First heterojunction solar cells have also been fabricated in Russia at the Ioffe Institute by means of LPE. The efficiency of solar cells was markedly improved by using low-temperature LPE to grow ultra-thin wide-bandgap windows in these devices. Remarkable results have been obtained in fabrication by LPE of multi-component solid solutions and device structures based on III-V antimonide systems. The practical importance and topicality of the solution of this technological problem is widely known nowadays.

## ACKNOWLEDGEMENTS

I worked for a long time at the Ioffe Institute, Russian Academy of Sciences, in the field of LPE of structures and devices with heterojunctions. The atmosphere at this worldwide-known scientific center is strikingly creative and friendly, which, in my opinion, strongly favored the achievement of the remarkable results in the field of semiconductor science and technology. I believe that I was exceedingly fortunate in having the opportunity to communicate and work with such remarkable scientists as my immediate superiors, Zh.I. Alferov and D.N. Tert'yakov, to whom I will be thankful for the rest of my life. I am deeply grateful to my friends and colleagues at the Ioffe Institute: V.M. Andreev, E.L. Portnoi, V.I. Korol'kov, D.Z. Garbuzov, V.D. Rumyantsev, M.N. Mizerov, V.D. Larionov, V.I. Kuchinskii, and many others.

The review was prepared owing to partial financial support by PROMEP and UASLP (San Luis Potosi, Mexico). I am sincerely grateful to my Mexican colleagues F. De Anda, A. Lastras and H. Navarro for their permanent interest in my work.

## REFERENCES

- [1] Zh.I. Alferov, V.M. Andreev, D.Z. Garbuzov and V.D. Rumiantsev, 100% internal quantum efficiency of radiative recombination in the three-layer AlAs-GaAs heterojunction light-emitting diodes, *Sov. Phys. Semicond.*, 9(3), 305–309 (1975).
- [2] D.Z. Garbuzov and V.B. Khalfin, Single quantum well InGaAsP and AlGaAs lasers: a study of some peculiarities, in *Quantum well lasers*, P. S. Zory Jr (Ed.), Academic Press, Inc., 277–327 (1993).
- [3] Zh.I. Alferov, V.M. Andreev, D.Z. Garbuzov, Yu.V. Zhilyaev, E.P. Morozov, E.L. Portnoi and V.G. Trofim, Investigation of the influence of the AlAs-GaAs heterostructure parameters on the laser threshold current and realization of the continuous emission at room temperature, *Sov. Phys. Semicond.*, 4(9), 1573–1575 (1970).
- [4] Zh.I. Alferov, V.M. Andreev, V.I. Korol'kov, E.L. Portnoi and D.N. Tret'yakov, Coherent radiation of epitaxial heterojunction structures in the AlAs-GaAs system, *Sov. Phys. Semicond.*, 2(10), 1289–1291 (1969).
- [5] Zh.I. Alferov, V.M. Andreev, V.I. Korol'kov, E.L. Portnoi and D.N. Tret'yakov, Current flow mechanism in  $\text{Al}_x\text{Ga}_{1-x}\text{As}$ -GaAs heterojunctions, *Sov. Phys. Semicond.*, 4(1), 132–137 (1970).
- [6] G.T. Aitieva, V.N. Bessolov, A.T. Denisova, S.E. Klimenko, S.A. Kukushkin, M.V. Lebedev and B.N. Tsarenkov, Liquid-phase epitaxial growth of ultra-thin GaAs layers on a GaAlAs substrate, *Sov. Phys. Tech. Phys.*, 31 (5), 552–554 (1986).
- [7] V.N. Bessolov, S.A. Kukushkin, M.V. Lebedev and B.V. Tsarenkov, Relaxation liquid phase epitaxy based on reversal of the mass transport and its potential for making ultrathin layers of III-V materials, *Sov. Phys. Tech. Phys.*, 33 (8), 902–905 (1988).
- [8] V.N. Bessolov, S.G. Konnikov, M.V. Lebedev, K.Yu. Pogrebetskii and B.V. Tsarenkov, Experimental confirmation of model of relaxation liquid epitaxy with reversal of mass transport for making ultrathin III-V films, *Sov. Phys. Tech. Phys.*, 35 (1), 99–101 (1990).
- [9] T.V. Sakalo, V.N. Bessolov, S.A. Kukushkin, M.V. Lebedev and B.V. Tsarenkov, Relaxation liquid phase epitaxy with mass-transport reversal: model and experiment, *Sov. Phys. Tech. Phys.*, 37 (3), 289–292 (1992).
- [10] V.M. Andreev, A.V. Syrbu, Growth of the  $\text{Al}_x\text{Ga}_{1-x}\text{As}$  epitaxial layers from the limited melt volume, *Sov. Phys. Tech. Phys.*, 23(8), 1096–1098 (1978).
- [11] Zh.I. Alferov, V.M. Andreev, S.G. Konnikov, V.R. Larionov and G.N. Shelovanova, Investigation of a new LPE method of obtaining Al-Ga-As heterostructures, *Kristall Technik*, 10(2), 103–110 (1975).
- [12] Zh.I. Alferov, V.M. Andreev, S.G. Konnikov, V.R. Larionov and B.V. Pushny, Liquid phase epitaxy of  $\text{Al}_x\text{Ga}_{1-x}\text{As}$  heterostructures, *Kristall Technik*, 11(10), 1013–1020 (1976).
- [13] P. Dias, V.A. Mishurnyi, E.L. Portnoi, B.S. Ryvkin, and V.B. Smiritskii, Dispersion characteristics of the refractive index of  $\text{Al}_x\text{Ga}_{1-x}\text{P}$  solid solutions, *Sov. Tech. Phys. Lett.*, 3(7), 290–291 (1977).
- [14] E.N. Arutyunov, V.A. Mishurnyi, E.L. Portnoi and V.Z. Pyataev, Tree-layer heteroepitaxial  $\Delta\alpha$  waveguide, *Sov. Tech. Phys. Lett.*, 3(8), 327–328 (1977).
- [15] Zh.I. Alferov, E.N. Arutyunov, V.A. Mishurnyi, E.L. Portnoi and V.Z. Pyataev, GaP- $\text{Al}_x\text{Ga}_{1-x}\text{P}$  double-heterostructure stripe electro-optic modulator, *Sov. Tech. Phys. Lett.*, 3(9), 362–363 (1977).

- [16] M.B. Ivanov, M.N. Mizerov, V.A. Mishurnyi, E.L. Portnoi and V.Z. Pyataev, Characteristics of stripe-geometry electrooptic modulator with a GaP-AlGaP heterostructure, *Sov. Phys. Tech. Phys.*, 24(3), 364–367 (1979).
- [17] V.M. Andreev, O.O. Ivent'eva, S.G. Konnikov, K.Yu. Pogrebetskii, E. Puron, O.V. Sulima and N.N. Faleev, Low-temperature liquid-phase epitaxy of AlGaAs heterostructures with sub-micron ( $10^{-1}$ – $10^{-2}$   $\mu\text{m}$ ) layers, *Sov. Tech. Phys. Lett.*, 12(12), 217–219 (1986).
- [18] Zh.I. Alferov, V.M. Andreev, B.V. Egorov, S.G. Konnikov and V.M. Lantratov, Fabrication of AlAs-GaAs heterostructures by selective liquid-phase epitaxy, *Sov. Phys. Tech. Phys.*, 23(2), 209–214 (1978).
- [19] Zh.I. Alferov, V.M. Andreev, V.Yu. Aksenov, T.N. Nalet, Nguen Tkhan' Fyong, V.D. Romyantsev and V.P. Khvostikov, Milliampere-range ( $I_{\text{thr}} = 2.1$  mA, 300 K) stripe-geometry quantum-well AlGaAs heterostructure lasers fabricated by low-temperature liquid-phase epitaxy, *Sov. Tech. Phys. Lett.*, 14(4), 893–894 (1988).
- [20] Zh.I. Alferov, V.M. Andreev, B.V. Egorov and A.V. Syrбу, High-efficiency heterojunction LED with spherical radiating surface, *Sov. Tech. Phys. Lett.*, 3(8), 293–294 (1977).
- [21] Zh.I. Alferov, V.M. Andreev, B.V. Egorov and A.V. Syrбу, Heterojunction light-emitting Al-Ga-As diodes formed by negative profiling of substrate, *Sov. Phys. Semicond.*, 11(10), 1123–1127 (1977).
- [22] Zh.I. Alferov, V.M. Andreev, D.Z. Garbuzov, N.Yu. Davidyuk, and L.T. Chichya, Efficient 'red' LED with multiple-pass heterostructure, *Sov. Tech. Phys. Lett.*, 4(3), 99–100 (1978).
- [23] Zh.I. Alferov, V.M. Andreev, D.Z. Garbuzov, N.Yu. Davidyuk, V.R. Larionov and L.T. Chichya, High efficiency mesa heterojunction LED ( $\eta_e = 29\%$  at 300 K), *Sov. Tech. Phys. Lett.*, 2(12), 420–421 (1976).
- [24] Zh.I. Alferov, V.M. Andreev, D.Z. Garbuzov, V.R. Larionov and V.D. Rumyantsev, Photocells with intermediate radiation conversion and enhanced concentration of solar radiation ( $K = 2500$ ), *Sov. Tech. Phys. Lett.*, 3(10), 449–450 (1977).
- [25] Zh.I. Alferov, V.M. Andreev, Yu.M. Zadiranov, V.I. Korol'kov and T.S. Tabarov, Al-Ga-As heterostructure photocell with a transition layer, *Sov. Tech. Phys. Lett.*, 4(3), 124–125 (1978).
- [26] Zh.I. Alferov, V.M. Andreev, Yu.M. Zadiranov, V.I. Korol'kov, N. Rakhimov, and T.S. Tabarov, Photo-emf in  $\text{Al}_x\text{Ga}_{1-x}\text{As}$  graded band-gap heterostructures, *Sov. Tech. Phys. Lett.*, 4(4), 149–150 (1978).
- [27] Zh.I. Alferov, V.M. Andreev, M.B. Kagan, V.I. Korol'kov, T.S. Tabarov and F.M. Tadzhibaev, AlGaAs-GaAs graded-heterostructure photocells with expanded sensitivity spectrum, *Sov. Tech. Phys. Lett.*, 3(8), 294–296 (1977).
- [28] Zh.I. Alferov, V.M. Andreev, N.S. Zimogorova and D.N. Tret'iakov, Photoelectric properties of  $\text{Al}_x\text{Ga}_{1-x}\text{As}$ -GaAs heterojunctions, *Sov. Phys. Semicond.*, 3 (11), 1373–1376 (1970).
- [29] Zh.I. Alferov, V.M. Andreev, M.B. Kagan, I.I. Protasov and V.G. Trofim, Solar-energy converters based on p-n  $\text{Al}_x\text{Ga}_{1-x}\text{As}$ -GaAs heterojunctions, *Sov. Phys. Semicond.*, 4 (12), 2047–2048 (1971).
- [30] V.M. Andreev, A.B. Guchmasov, T.V. Decal'chuk, Yu.M. Zadiranov, V.S. Kalinovskii and A.M. Koinova, Heterojunction bipolar transistor made by low-temperature liquid phase epitaxy, *Sov. Tech. Phys. Lett.*, 12 (6), 296–297 (1986).
- [31] V.M. Andreev, A.V. Syrбу, V.G. Trofim and V.P. Iakovlev, Synthesis of GaAs and  $\text{Al}_x\text{Ga}_{1-x}\text{As}$  planar local structures by liquid-phase epitaxy, *Sov. Phys. Tech. Phys.*, 23(8), 1001–1005 (1978).
- [32] Zh.I. Alferov, V.M. Andreev, A.A. Vodnev, S.G. Konnikov, V.R. Larionov, K.Yu. Pogrebetskii, V.D. Rymyantsev and V.P. Khvostikov, AlGaAs heterostructures with quantum-well layers, fabricated by low-temperature liquid-phase epitaxy, *Sov. Tech. Phys. Lett.*, 12(9), 450–451 (1986).
- [33] M. Milanova and V. Khvostikov. Growth and doping of GaAs and AlGaAs layers by low-temperature liquid-phase epitaxy, *J. Crystal Growth*, 219, 193–198 (2000).



- [34] Zh.I. Alferov, V.M. Andreev, A.M. Andriesh, A.Z. Mereutse, A.V. Syrbu and V.P. Yakovlev, Low-threshold ( $I_{th} = 3.0$  mA,  $T = 300$  K) buried-heterostructure AlGaAs quantum-well laser diodes prepared by liquid-phase epitaxy, *Sov. Tech. Phys. Lett.*, 16(3), 192–193 (1990).
- [35] Zh.I. Alferov, V.M. Andreev, A.Z. Mereutse, A.V. Syrbu, G.I. Suruchanu and V.P. Yakovlev, Superlow-threshold ( $I_{th} = 1.3$  mA,  $T = 300$  K) quantum-well AlGaAs lasers with uncoated mirrors prepared by liquid-phase epitaxy, *Sov. Tech. Phys. Lett.*, 16(5), 339–340 (1990).
- [36] V.A. Mishurnyi, F. de Anda, I.C. Hernandez del Castillo and A.Yu. Gorbachev, Temperature determination by solubility measurements and a study of evaporation of volatile components in LPE, *Thin Solid Films*, 340, 24–27 (1999).
- [37] V.A. Mishurnyi, F. de Anda and A.Yu. Gorbachev, Some problems on the phase diagrams research in LPE, *Current Top. Crystal Growth Res.*, 6, 115–125 (2002).
- [38] A.P. Bogatov, L.M. Dolginov, P.G. Eliseev, M.G. Mel'vidskii, B.N. Sverdlov and E.G. Shevchenko, Radiative characteristics of InP-GaInAsP laser heterostructures, *Sov. Phys. Semicond.*, 9(10), 1282–1285 (1975).
- [39] Zh.I. Alferov, A.T. Gorelenok, P.S. Kop'ev, V.N. Mdivani and V.K. Tibilov, Low-threshold laser with In-Ga-As-P heterostructure, *Sov. Tech. Phys. Lett.*, 3(11), 481–482 (1977).
- [40] Zh.I. Alferov, D.Z. Garbuzov, I.N. Arsent'ev, B.Ya. Ber, L.S. Vavilova, V.V. Krasovskii and A.V. Chudinov, Auger profiles of the composition and luminescence studies of liquid-phase-grown InGaAsP heterostructures with  $(1.5-5) \times 10^{-6}$  cm active regions, *Sov. Phys. Semicond.*, 19(6), 679–683 (1985).
- [41] I.N. Arsent'ev, N.A. Bert, A.V. Vasil'ev, D.Z. Garbuzov, E.V. Zhuravkevich, S.G. Konnikov, A.O. Kosogov, A.V. Kochergin, N.N. Faleev and L.I. Flaks, Periodic multilayer In-Ga-As-P structures fabricated by liquid-phase epitaxy, *Sov. Tech. Phys. Lett.*, 14(4), 264–266 (1988).
- [42] L.M. Dolginov, A.E. Drakin, P.G. Eliseev, B.M. Sverdlov, V.A. Skripkin, and E.G. Shevchenko, Injection InGaAsP/InP lasers with threshold current density  $0.5$  kA/cm<sup>2</sup> at 300 K, *Sov. J. Quantum Electronics*, 14(4), 439–441 (1984).
- [43] Zh.I. Alferov, I.N. Arsent'ev, D.Z. Garbuzov, V.P. Evtikhiev, O.V. Sulima, V.P. Chaliy and A.V. Chudinov, Injection separate-confinement InGaAsP/InP double heterostructure lasers with a threshold  $300$  A/cm<sup>2</sup> (samples cleaved along four sides,  $\lambda = 1.25$   $\mu$ m,  $T = 300$  K), *Sov. Phys. Semicond.*, 18(11), 1281–1283 (1984).
- [44] Zh.I. Alferov, D.Z. Garbusov, A.B. Nivin, A.V. Ovchinnikov and I.S. Tarasov, Continuous-wave injection laser with an output power of 60 mW ( $\lambda = 1.35$   $\mu$ m,  $T = 300$  K) based on a separate-confinement InGaAsP double heterostructure formed by liquid epitaxy, *Sov. Phys. Semicond.*, 19(3), 284–286 (1985).
- [45] V.P. Evtikhiev, D.Z. Garbuzov, Z.N. Sokolova, I.S. Tarasov, V.B. Khalfin, V.P. Chaliy and A.V. Chudinov, Spectral features of the threshold characteristics of separately confinement InGaAsP/InP double-heterostructures lasers ( $\lambda = 1.3$   $\mu$ m) with ultra-thin active regions, *Sov. Phys. Semicond.*, 19(8), 873–875 (1985).
- [46] Zh.I. Alferov, D.Z. Garbuzov, A.V. Ovchinnikov, I.S. Tarasov, V.P. Evtikhiev, A.B. Nivin and A.E. Svelokuzov, 17%-efficiency cw separate-confinement InGaAsP/InP double heterostructure laser ( $\lambda = 1.3$   $\mu$ m,  $T = 290$  K), *Sov. Tech. Phys. Lett.*, 11(10), 479–480 (1985).
- [47] Zh.I. Alferov, D.Z. Garbuzov, K.Yu. Kizhaev, A.B. Nivin, S.A. Nikishin, A.V. Ovchinnikov, Z.N. Sokolova, I.S. Tarasov and A.V. Chudinov, Low-threshold separate-confinement InGaAsP/InP lasers with  $\lambda = 1.3$   $\mu$ m and  $\lambda = 1.55$   $\mu$ m ( $I_{th} = 670-700$  A/cm<sup>2</sup>), *Sov. Tech. Phys. Lett.*, 12(2), 87–88 (1986).
- [48] Zh.I. Alferov, D.Z. Garbuzov, N.Yu. Davidyuk, N.D. Il'inskaia, A.B. Nivin, A.V. Ovchinnikov and I.S. Tarasov, High-power InGaAsP/InP separate confinement mesa-stripe lasers for the fiber-optics communication ( $\lambda = 1.3$   $\mu$ m,  $T = 18$  °C,  $I = 300$  mA,  $P = 28$  mW in a 50  $\mu$ m-diameter fiber), *Sov. Tech. Phys. Lett.*, 11(11), 555–556 (1985).
- [49] Zh.I. Alferov, I.N. Arsent'ev, D.Z. Garbuzov, S.G. Konnikov and V.D. Rymiantsev, Generation of coherent radiation in pGa<sub>0.5</sub>In<sub>0.5</sub>P-pGa<sub>x-0.35</sub>In<sub>1-x</sub>As<sub>y-0.10</sub>P<sub>1-y-n</sub>Ga<sub>0.5</sub>In<sub>0.5</sub>P heterostructures, *Sov. Tech. Phys. Lett.*, 1(4), 147–148 (1975).

- [50] Zh.I. Alferov, I.N. Arsent'ev, L.S. Vavilova, D.Z. Garbuzov and V.V. Krasovskii, Low-threshold injection InGaAsP/GaAs double heterolasers with separate confinement, fabricated by liquid phase epitaxy ( $\lambda = 0.78\text{--}0.87\mu\text{m}$ ,  $I_{\text{th}} = 460\text{ A/cm}^2$ ,  $T = 300\text{ K}$ ) *Sov. Phys. Semicond.*, 18(9), 1035–1038 (1984).
- [51] D.Z. Garbuzov, I.N. Arsent'ev, L.S. Vavilova, A.V. Tikunov and E.V. Tulashvili, Continuous-wave separate-confinement InGaAsP/GaAs double-heterostructures laser with power 77 mWt ( $T = 300\text{ K}$ ,  $\lambda = 0.87\mu\text{m}$ ), grown by liquid epitaxy, *Sov. Phys. Semicond.*, 19(1), 83–84 (1985).
- [52] Zh.I. Alferov, I.N. Arsent'ev, L.S. Vavilova, D.Z. Garbuzov and E.V. Tulashvili, Low-threshold pulsed and cw InGaAsP/InGaP/GaAs double-heterojunction lasers emitting visible radiation in the  $0.73\text{--}0.79\mu\text{m}$  range ( $T = 300\text{ K}$ ,  $I_{\text{th}} = 3.5\text{--}1.3\text{ kA/cm}^2$ ), *Sov. Phys. Semicond.*, 18(1), 99–100 (1984).
- [53] N.Yu. Antonishkis, I.N. Arsent'ev, D.Z. Garbuzov, V.I. Kolyshkin, A.B. Komissarov, A.B. Kochergin, T.A. Nalet and N.A. Strugov, High-power cw InGaAsP/GaAs heterostructure lasers with a dielectric mirror ( $I_{\text{th}} = 100\text{ A/cm}^2$ ,  $P = 1.1\text{ W}$ ,  $\text{effic.} = 66\%$ ,  $T = 10^\circ\text{C}$ ), *Sov. Tech. Phys. Lett.*, 14(4), 310–311 (1988).
- [54] Zh.I. Alferov, N.Yu. Antonishkis, I.N. Arsent'ev, D.Z. Garbuzov, V.I. Kolyshkin, T.A. Nalet, N.A. Strugov and A.V. Tikunov, Quantum-well separate-confinement InGaAsP/GaAs  $\lambda = 0.86\text{--}0.78\mu\text{m}$  laser ( $I_{\text{th}} = 100\text{ A/cm}^2$ , efficiency 59%), *Sov. Phys. Semicond.*, 22(6), 650–652 (1988).
- [55] Zh.I. Alferov, N.Yu. Antonishkis, I.N. Arsent'ev, D.Z. Garbuzov, A.V. Tikunov and V.B. Khalfin, Low-threshold quantum-well InGaAsP/GaAs separate-confinement double heterostructure lasers, formed by liquid epitaxy method ( $\lambda = 0.86\mu\text{m}$ ,  $I_{\text{th}} = 90\text{ A/cm}^2$ ,  $L = \infty$ ;  $I_{\text{th}} = 165\text{ A/cm}^2$ ,  $L = 1150\mu\text{m}$ ,  $T = 300\text{ K}$ ), *Sov. Phys. Semicond.*, 21(8), 914–915 (1987).
- [56] Zh.I. Alferov, N.Yu. Antonishkis, I.N. Arsent'ev, D.Z. Garbuzov, V.V. Krasovskii, A.V. Tikunov and V.B. Khalfin, Quantum-well separate-confinement InGaAsP/GaAs double-heterostructure laser prepared by liquid epitaxy ( $\lambda = 0.79\mu\text{m}$ ,  $I_{\text{th}} = 124\text{ A/cm}^2$ ,  $T = 300\text{ K}$ ), *Sov. Phys. Semicond.*, 21(1), 98–100 (1987).
- [57] I.N. Arsent'ev, G.R. Bezhanishvili, P.P. Buinov, L.S. Vavilova, N.A. Strugov, V.P. Chalyi and A.P. Shkurko, Spectral characteristics of the InGaAsP/GaAs  $<111>$  lasers ( $\lambda = 0.8\mu\text{m}$ ) fabricated by liquid-phase epitaxy for pumping YAG: Nd lasers, *Sov. Tech. Phys. Lett.*, 15(8), 598–600 (1989).
- [58] Zh.I. Alferov, I.N. Arsent'ev, L.S. Vavilova, D.Z. Garbuzov and A.V. Tikunov, 10-mW cw short-wavelength ( $\lambda = 0.677\mu\text{m}$ ) injection laser using an InGaAsP/GaAsP separate-confinement double heterostructure, *Sov. Tech. Phys. Lett.*, 11(9), 477–478 (1985).
- [59] Zh.I. Alferov, I.N. Arsent'ev, L.S. Vavilova, D.Z. Garbuzov, V.V. Krasovskii, A.V. Tikunov and V.P. Chalyi, Continuous-wave separate-confinement InGaAsP/GaAsP double-heterostructure injection laser fabricated by liquid epitaxy and emitting at the  $0.677\mu\text{m}$  wavelength, *Sov. Phys. Semicond.*, 19(6), 683–685 (1985).
- [60] Zh.I. Alferov, I.N. Arsent'ev, D.Z. Garbuzov, N.A. Strugov, A.V. Tikunov and E.I. Chudinov, Visible-range InGaAsP/GaAsP separate-confinement double-heterostructure laser fabricated by liquid-phase epitaxy ( $\lambda = 0.65\text{--}0.67\mu\text{m}$ ,  $I_{\text{th}} = 3\text{--}0.8\text{ kA/cm}^2$ ,  $P = 5\text{ mW}$ ,  $T = 300\text{ K}$ ) *Sov. Tech. Phys. Lett.*, 13(3) 153–154 (1987).
- [61] V.A. Mishurnyi, F. de Anda, A.Yu. Gorbachev, V.I. Vasil'ev, N.N. Faleev, InGaAsSb growth from Sb-rich solutions, *J. Crystal Growth*, 180, 34–39 (1997).
- [62] V.A. Mishurnyi, F. de Anda, A.Yu. Gorbachev, V.I. Vasil'ev, V.M. Smirnov and N.N. Faleev, AlGaAsSb and AlGaInAsSb growth from Sb-rich solutions, *Cryst. Res. Technol.*, 33(3), 457–464 (1998).
- [63] R. Hernandez-Zarazua, M. Hernandez-Sustaita, F. de Anda, V.A. Mishurnyi, A.Yu. Gorbachev, R. Asomoza, Yu. Kudriavtsev and J.A. Godines, Investigation of the phase diagram of Pb-Ga-Sb system, *Thin Solid Films*, 461, 233–236 (2004).
- [64] Y. Horikoshi, A new liquid phase epitaxial growth method for the growth of (AlGa)As multilayers, *Jpn. J. Appl. Phys.*, 15 (5), 887–888 (1976).

- [65] S.L. Pyshtkin, S.I. Radautsan and S.V. Slobodchikov, Electrical properties of gallium phosphide activated with elements of lanthanide, *Sov. Phys. Semicond.*, 1(7), 901–904 (1967).
- [66] G.V. Lashkarev, A.I. Dmitriev, G.A. Sukach and V.A. Shershel, Magnetoresistance of germanium doped with neodymium and europium, *Sov. Phys. Semicond.*, 5(11), 1808–1811 (1971).
- [67] V.N. Romanenko and V.S. Kheifets, Distribution ratios and solubility curves of some rare-earth elements in GaAs, *Inorg. Mater.*, 9(2), 172–177 (1973).
- [68] N.T. Bagraev, E.P. Bochkarev, L.S. Vlasenko, V.P. Grishin, R.A. Zhitnikov and Yu.A. Karpov Behavior of Ho, Cd and Yb impurities in silicon, *Inorg. Mater.*, 14(4), 474–477 (1978).
- [69] K.A. Gatsoev, A.T. Gorelenok, S.I. Karpenko, V.V. Mamutin and R.P. Seisyan, Effects of doping with rare-earth elements on the low-temperature edge luminescence of InP, *Sov. Phys. Semicond.*, 17(12), 1373–1375 (1983).
- [70] N.T. Bagraev, L.S. Vlasenko, K.A. Gatsoev, A.T. Gorelenok, A.V. Kamanin, V.V. Mamutin, B.V. Pushnyi, V.K. Tibilov, Yu.P. Tolparov and A.E. Shubin, Influence of the rare-earth elements on the carrier mobility in epitaxial InP and InGaAs films, *Sov. Phys. Semicond.*, 18(1), 49–50 (1984).
- [71] A.T. Gorelenok, A.V. Kamanin and N.M. Shmidt, Rare-earth elements in the technology of InP, InGaAsP and devices based on these semiconductor compounds, *Microelectronics J.*, 26, 705–723 (1995).
- [72] A.T. Gorelenok, A.V. Kamanin and N.M. Shmidt, Rare-earth elements in the technology of III-V compounds and devices based on them, *Sov. Phys. Semicond.*, 37(8), 922–940 (2003).
- [73] B.Kh. Bairamov, L.F. Zakharenkov, G.V. Il'menkov, V.F. Masterov and V.V. Toropov, Influence of rare-earth elements on the properties of bulk InP single crystals, *Sov. Phys. Semicond.*, 23(8), 927–929 (1989).
- [74] A.T. Gorelenok, V.G. Gruzdov, R. Kumar, V.V. Mamutin, T.A. Polianskaya, I.G. Savel'ev and Yu.V. Shmartsev, Density and mobility of the electrons in InP and In<sub>0.53</sub>Ga<sub>0.47</sub>As doped with rare-earth elements, *Sov. Phys. Semicond.*, 22(1), 21–26 (1988).
- [75] A. Galvanuskas, A.T. Gorelenok, Z. Dobrovol'skis, S. Kershulis, Yu. Pozhela, A. Reklaitis and N. Shmidt, Transport phenomena and allowed scattering in In<sub>1-x</sub>Ga<sub>x</sub>As<sub>y</sub>P<sub>1-y</sub>, *Sov. Phys. Semicond.*, 22(9), 1055–1058 (1988).
- [76] V. Balinas, A.T. Gorelenok, A. Krotkus, A. Stalnenis and N.M. Shmidt, Determination of the current–voltage characteristics of InGaAs using picosecond electro-optic sampling apparatus, *Sov. Phys. Semicond.*, 24(5), 534–537 (1990).
- [77] A.T. Gorelenok, V.V. Mamutin, D.V. Pulyaevskii, D.N. Rekhviashvili and N.M. Shmidt, Investigation of minority-carrier lifetime in the narrow-gap region of InGaAsP/InP diode structures, *Sov. Phys. Semicond.*, 21(8), 912–913 (1987).
- [78] Zh.I. Alferov, A.T. Gorelenok, A.V. Kamanin, V.V. Mamutin, T.A. Polyanskaia, I.G. Savel'ev, I.I. Saidashev and Yu.V. Shmartsev, Two-dimensional electron gas in InGaAs/InP heterostructures prepared by liquid phase epitaxy, *Sov. Phys. Semicond.*, 18(7), 768–769 (1984).
- [79] A.T. Gorelenok, D.N. Rekhviashvili, M.Yu. Nadtochii and V.M. Ustinov, Two-dimensional electron gas in In<sub>0.88</sub>Ga<sub>0.12</sub>As<sub>0.23</sub>P<sub>0.77</sub>/InGa<sub>0.47</sub>P<sub>0.53</sub>As heterostructures grown by liquid-phase epitaxy, *Sov. Tech. Phys. Lett.*, 16(4), 302–303 (1990).
- [80] Zh.I. Alferov, A.T. Gorelenok, V.G. Danil'chenko, A.V. Kamanin, V.I. Korol'kov, V.V. Mamutin, T.S. Tabarov and N.M. Shmidt, Highly efficient ultraviolet photodetector, *Sov. Tech. Phys. Lett.*, 9(12), 649–650 (1983).
- [81] A.T. Gorelenok, V.G. Danil'chenko, Z.P. Dobrovol'skis, V.I. Korol'kov, V.V. Mamutin, T.S. Tabarov, N.M. Shmidt and D.V. Pulyaevsky, Study of intrinsic photoconduction in InP and InGaAs epitaxial layer, *Sov. Phys. Semicond.*, 19(8), 1460–1463 (1985).
- [82] V.M. Andreev, M.S. Bogdannovich, A.T. Gorelenok, V.G. Gruzdov, V.G. Danil'chenko, M.Z. Zhingarev, N.D. Il'inskaia, L.B. Karlina, V.I. Korol'kov, V.V. Mamutin, I.A. Mokina,

- N.M. Saradzhishvili, L.M. Fedorov and N.M. Shmidt, Properties of InGaAsP/InP p-i-n photodiodes, *Sov. Phys. Tech. Phys.*, 30(8), 907–909 (1985).
- [83] V.M. Andreev, A.T. Gorelenok, M.Z. Zhingarev, L.E. Kiyachkin, V.V. Mamutin, N.M. Saradzhishvili, V.I. Skopina, O.V. Sulima and N.M. Shmidt, Investigation of leakage current in planar p-n junction in InP and p-i-n InGaAsP/InP structures, *Sov. Phys. Semicond.*, 19(4), 411–414 (1985).
- [84] L.A. Volkov, A.T. Gorelenok, V.N. Luk'yanov, L.A. Rachkov, D.N. Rekhviashvili, N.M. Shmidt and S.D. Yakubovich, Measurement of the amplitude-frequency characteristics of fast photodetectors with a homodyne glass-fiber device for producing amplitude beats in the optical signal, *Sov. Tech. Phys. Lett.*, 13(9), 442–443 (1987).
- [85] Zh.I. Alferov, V.I. Bosyi, A.T. Gorelenok, A.V. Ivashchuk, N.D. Il'inskaia, M.N. Mizerov, I.A. Mokina, D.N. Rekhviashvili and N.M. Shmidt, InGaAsP/InP Schottky barriers and field-effect transistors, *Sov. Tech. Phys. Lett.*, 14(10), 784–785 (1988).



# 3 Phase Diagrams and Modeling in Liquid Phase Epitaxy

KAZUO NAKAJIMA

*Institute for Materials Research, Tohoku University, Katahira 2-1-1, Aoba-ku, Sendai 980-8577, Japan*

---

3.1 Introduction	45
3.2 Equilibrium phase diagrams	46
3.2.1 Binary, ternary and quaternary phase diagrams	46
3.2.2 Calculation of binary, ternary and quaternary phase diagrams	49
3.2.3 Calculation of phase diagrams considering the surface, interface and strain energies	54
3.2.4 Experimental determination of phase diagrams	59
3.2.5 Miscibility gap	64
3.3 Technologies of LPE growth	66
3.4 III-V materials for LPE growth	68
3.5 Lattice matching	69
3.6 Growth of misfit-dislocation-free wafers	71
3.7 Phase diagrams of growth mode	73
3.8 Growth kinetics	77
3.8.1 Calculation of III-V layer thickness	77
3.8.2 Compositional variation in III-V ternary layers	78
3.9 Summary	79
References	79
Appendix	82

---

## 3.1 INTRODUCTION

Liquid phase epitaxy (LPE) has been used mainly for growth of IV semiconductors, and III-V and II-VI binary, ternary and quaternary semiconductor compounds, because high-quality epitaxial layers can be easily grown using simple experimental apparatus, and because complicated structures such as buried-stripe lasers can be easily prepared. The important IV, III-V and II-VI semiconductors grown by LPE are Si, GaP,  $\text{Al}_x\text{Ga}_{1-x}\text{As}$ ,  $\text{In}_{1-x}\text{Ga}_x\text{As}$ ,  $\text{In}_{1-x}\text{Ga}_x\text{As}_{1-y}\text{P}_y$ ,  $\text{In}_{1-x}\text{Ga}_x\text{As}_y\text{Sb}_{1-y}$  and  $\text{Hg}_x\text{Cd}_{1-x}\text{Te}$  which are of potential use for light emitting diodes (LEDs), lasers and photodiode applications. In order

to support thermodynamically the determination of the LPE growth conditions, such as solution composition, solid composition, growth temperature, lattice-matching to substrate, equilibrium phase diagrams have been theoretically and experimentally investigated. Numerous studies about the LPE growth of these compounds have been done to understand fully the growth and characteristics, such as the growth kinetics, purity, misfit dislocations, surface morphology and ease of growth of heterostructure. These results have been sufficiently developed to prepare devices. In this chapter, the LPE growth is described mainly focusing on III-V compound semiconductors such as  $\text{In}_{1-x}\text{Ga}_x\text{As}$  and  $\text{In}_{1-x}\text{Ga}_x\text{As}_{1-y}\text{P}_y$  on InP as model systems. LPE layers grow on the basis of the thermodynamic driving force which consists of deviation from thermodynamic equilibrium, driving diffusion transport across the boundary layer and driving epitaxial growth on the substrate surface. So, LPE growth conditions depend critically on the combination and competition of these driving forces.

## 3.2 EQUILIBRIUM PHASE DIAGRAMS

In order to grow epitaxial layers by the LPE method, accurate binary, ternary and quaternary phase diagrams are required, because LPE growth conditions such as solution composition for the growth, starting growth temperature and degree of supercooling can be effectively known by the phase diagrams which show the relationship between the liquidus, solidus and temperature. These phase diagrams must cover the temperature and composition range permitting LPE growth under reasonable conditions and must supply sufficient information for the growth of lattice-matched layers. The phase diagrams are determined by calculation and experiments near equilibrium conditions.

### 3.2.1 Binary, ternary and quaternary phase diagrams

The binary phase diagrams of the III-V system have accurately been determined, and they can be effectively used to know the LPE growth conditions. As shown in Figure. 3.1, most of the III-V binary phase diagrams involve an AB stoichiometric binary compound such as GaAs, and have a wide region in which the liquid and solid phases coexist. The III-V ternary phase diagram with an  $\text{A}_x\text{B}_{1-x}\text{C}$  ternary compound is expressed as shown in Figure. 3.2. It consists of two A-C and B-C binary phase diagrams with AC and BC compounds, respectively, and a A-B binary phase diagram with complete miscibility in the solid state. The ternary phase diagram is simply expressed using the liquidus and solidus isotherms as shown in Figure. 3.3. Some III-V ternary phase diagrams such as the Al-Ga-As and In-Ga-As systems have been accurately determined, and then accurate effective liquidus and solidus data for the LPE growth are known. Pseudobinary phase diagrams have been reported for most of the III-V ternary systems. Some of them such as the Al-Ga-As and In-Ga-As systems have solid solutions all over the composition and some of them such as the In-P-Sb and In-As-Sb systems have miscibility gaps.

The III-V quaternary phase diagram with an  $\text{A}_x\text{B}_{1-x}\text{C}_y\text{D}_{1-y}$  quaternary compound is expressed as shown in Figure. 3.4. It consists of four A-C-D, A-B-C, A-B-D and B-C-D ternary phase diagrams with  $\text{AC}_y\text{D}_{1-y}$ ,  $\text{A}_x\text{B}_{1-x}\text{C}$ ,  $\text{A}_x\text{B}_{1-x}\text{D}$  and  $\text{BC}_y\text{D}_{1-y}$  ternary compounds, respectively, and a square-type AC-BC-BD-AD pseudoquaternary phase diagram

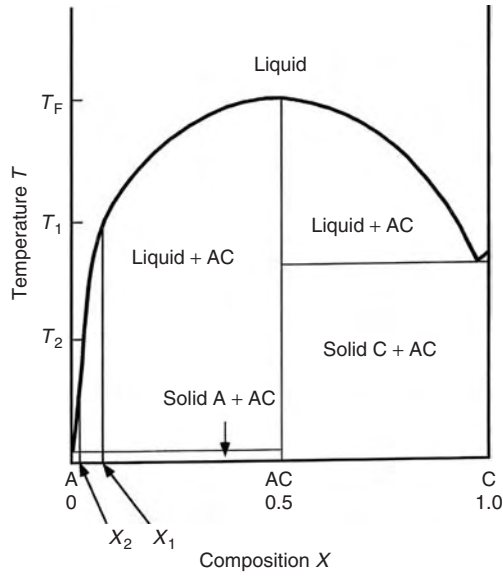


**Figure 3.1** Binary phase diagram of the III-V system with a stoichiometric binary compound. Reprinted from *Ninth Seminar of the Sub-Group of Crystal Technologies. Growth of Alloy Semiconductors—Liquid Phase Epitaxial Growth*, 50–60, figures 1, 2, 3 and 4, Copyright (1982), with permission from Japan Applied Physics

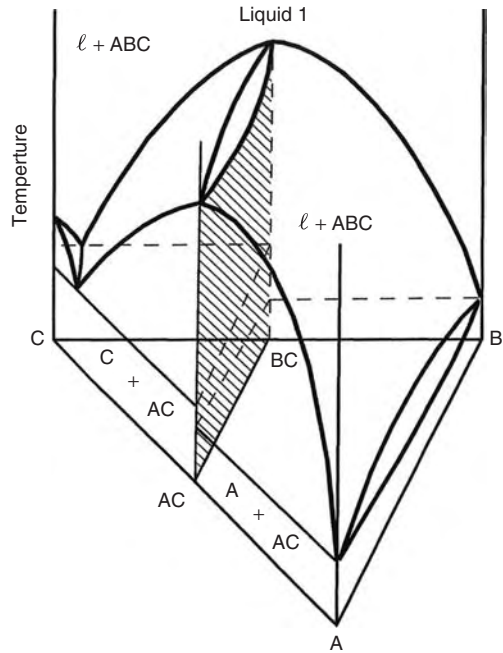


**Figure 3.2** III-V ternary phase diagram with an  $A_xB_{1-x}C$  ternary compound. Reprinted from *Ninth Seminar of the Sub-Group of Crystal Technologies. Growth of Alloy Semiconductors—Liquid Phase Epitaxial Growth*, 50–60, figures 1, 2, 3 and 4, Copyright (1982), with permission from Japan Applied Physics



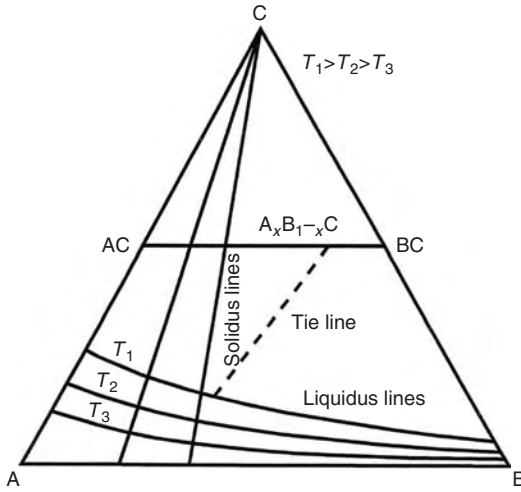


**Figure 3.3** Ternary phase diagram expressed using the liquidus and solidus isotherms. Reprinted from *Ninth Seminar of the Sub-Group of Crystal Technologies. Growth of Alloy Semiconductors—Liquid Phase Epitaxial Growth*, 50–60, figures 1, 2, 3 and 4, Copyright (1982), with permission from Japan Applied Physics

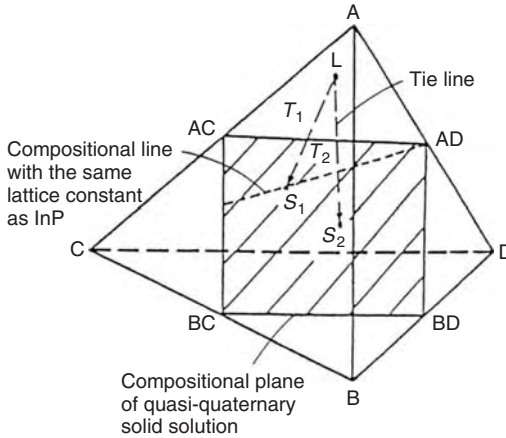


**Figure 3.4** III-V quaternary phase diagram with an  $A_xB_{1-x}C_yD_{1-y}$  quaternary compound. Reprinted from *Ninth Seminar of the Sub-Group of Crystal Technologies. Growth of Alloy Semiconductors—Liquid Phase Epitaxial Growth*, 50–60, figures 1, 2, 3 and 4, Copyright (1982), with permission from Japan Applied Physics

with an  $A_xB_{1-x}C_yD_{1-y}$  quaternary compound. Very few phase diagrams of the III-V quaternary system have been reported. The In-Ga-As-P quaternary phase diagram was accurately determined to facilitate the preparation of closely lattice-matched  $In_xGa_{1-x}As_yP_{1-y}/InP$  heterostructures at 600 and 650 °C by Nakajima *et al.* [1]. Temperatures between 600 °C and 650 °C are commonly used for the growth of  $In_xGa_{1-x}As_yP_{1-y}$  on InP.

The In-Ga-As-Sb and Al-Ga-In-As quaternary phase diagrams were also determined by Nakajima *et al.* [2, 3]. These quaternary phase diagrams are only partly determined, because of the enormous number of experiments that is necessary to determine the whole phase diagram.

### 3.2.2 Calculation of binary, ternary and quaternary phase diagrams

The phase diagrams can be calculated by thermodynamically expressing the properties of the liquid and solid phases under equilibrium condition. For the calculation of phase diagrams, the phase diagrams of III-V compound semiconductors are good targets because of their simplicity. The thermodynamic basis for the calculation of binary III-V and II-VI phase diagrams involving a compound was established by Vieland [4]. He derived the free energy of the compound to calculate the binary phase diagrams. The Gibbs free energy per mole of an A-B binary solution is given by:

$$G^l = \mu_A^l x_A^l + \mu_B^l x_B^l \quad (3.1)$$

where  $\mu_A^l$  and  $\mu_B^l$  are the chemical potentials (in this equation, the partial molar free energies) of the A and B components in the A-B binary solution, respectively, and  $x_A^l$  and  $x_B^l$  are the molar fractions of A and B components in the A-B binary solution, respectively. The chemical potential of A component is given by:

$$\mu_A^l = (\partial G^l / \partial x_A^l)_{T,P,x_B^l} \quad (3.2)$$

$$\mu_B^l = (\partial G^l / \partial x_B^l)_{T,P,x_A^l} \quad (3.3)$$

When the A-B binary solution is in equilibrium with the binary compound AB, we obtain:

$$\begin{aligned} 2G^l - \mu_{AB}^c &= 2(\mu_A^l/2 + \mu_B^l/2) - \mu_{AB}^c \\ &= \mu_A^l + \mu_B^l - \mu_{AB}^c \\ &= 0 \end{aligned} \quad (3.4)$$

where  $\mu_{AB}^c$  is the chemical potential of the AB binary compound (crystal). Then, the liquid–solid equilibrium which is the basis of calculation of the A-B binary equilibrium phase diagram can be expressed as:

$$\mu_A^l + \mu_B^l = \mu_{AB}^c \quad (3.5)$$

The difference of the free energies to generate the compound AB from the stoichiometric binary solution ( $x_A^l = 0.5$ ,  $x_B^l = 0.5$ ) is:

$$\begin{aligned} 2G_{0.5}^l - \mu_{AB}^c &= 2(\mu_A^{s,l}/2 + \mu_B^{s,l}/2) - \mu_{AB}^c \\ &= \mu_A^{s,l} + \mu_B^{s,l} - \mu_{AB}^c \end{aligned} \quad (3.6)$$

where  $\mu_A^{s,1}$  and  $\mu_B^{s,1}$  are the chemical potentials of the A and B components in the solution with the stoichiometric composition ( $x_A^1 = 0.5, x_B^1 = 0.5$ ), respectively. They are

$$\begin{aligned}\mu_A^{s,1} &= \mu_A^{\bullet 1} + RT \ln x_A^{s,1} \gamma_A^{s,1} \\ &= \mu_A^{\bullet 1} + RT \ln 0.5 \gamma_A^{s,1}\end{aligned}\quad (3.7)$$

$$\begin{aligned}\mu_B^{s,1} &= \mu_B^{\bullet 1} + RT \ln x_B^{s,1} \gamma_B^{s,1} \\ &= \mu_B^{\bullet 1} + RT \ln 0.5 \gamma_B^{s,1}\end{aligned}\quad (3.8)$$

where  $x_A^{s,1}$  and  $x_B^{s,1}$  are the composition (fraction) of the A and B components in the solution with the stoichiometric composition, respectively, and they are 0.5.  $\mu_A^{\bullet 1}$  and  $\mu_B^{\bullet 1}$  are the chemical potentials of the pure A and B elements, respectively.  $\gamma_A^{s,1}$  and  $\gamma_B^{s,1}$  are the activity coefficients of the A and B components in the binary solution with the stoichiometric composition, respectively.  $R$  and  $T$  are the gas constant and the absolute temperature, respectively. If the difference between the specific heat of the solution and that of the solid is neglected, Equation (3.6) can be written as:

$$2G_{0.5}^1 - \mu_{AB}^c = \Delta S_{AB}^F (T_{AB}^F - T) \quad (3.9)$$

where  $\Delta S_{AB}^F$  is the entropy of fusion of the compound AB, and  $T_{AB}^F$  is the melting point of the compound AB [1]. From Equations (3.6), (3.7), (3.8) and (3.9), we obtain:

$$\mu_{AB}^c = \mu_A^{\bullet 1} + RT \ln 0.5 \gamma_A^{s,1} + \mu_B^{\bullet 1} + RT \ln 0.5 \gamma_B^{s,1} - \Delta S_{AB}^F (T_{AB}^F - T) \quad (3.10)$$

The equation to calculate the A-B binary phase diagram is given from Equations (3.5) and (3.10) as:

$$RT \ln (\gamma_A^1 \gamma_B^1 / \gamma_A^{s,1} \gamma_B^{s,1}) + RT \ln 4x_A^1 x_B^1 = -\Delta S_{AB}^F (T_{AB}^F - T) \quad (3.11)$$

where  $\gamma_A^1$  and  $\gamma_B^1$  are the activity coefficients of the A and B components in the binary solution, respectively. When we derive Equation (3.11), the following relation is used:

$$\mu_i^1 = \mu_i^{\bullet 1} + RT \ln x_i^1 \gamma_i^1 \quad (3.12)$$

The activity coefficients of the A and B components can be expressed by the regular solution approximation as:

$$\begin{aligned}RT \ln \gamma_A^1 &= (x_B^1)^2 \Omega_{AB}^1 = (1 - x_A^1)^2 \Omega_{AB}^1 \\ RT \ln \gamma_B^1 &= (x_A^1)^2 \Omega_{AB}^1 = (1 - x_B^1)^2 \Omega_{AB}^1 \\ RT \ln \gamma_A^{s,1} &= RT \ln \gamma_B^{s,1} = (1/2)^2 \Omega_{AB}^1\end{aligned}\quad (3.13)$$

where  $\Omega_{AB}^1$  is the interaction parameter of A-B pairs in the binary solution. Equation (3.13) can be obtained as shown in the Appendix. Combining Equations (3.11) and (3.13) gives:

$$(2x_A^1 - 1)^2 \Omega_{AB}^1 + 2RT \ln 4x_A^1 (1 - x_A^1) = -4\Delta S_{AB}^F (T_{AB}^F - T) \quad (3.14)$$

Using Equation (3.14), we can obtain the liquidus line of the A-B binary system.

Ilegems and Pearson [5] extended this to the ternary III-V system and derived a very useful thermodynamic model. In this treatment, the solid solution of composition  $A_xB_{1-x}C$  is treated as a mixture of AC and BC. The liquid–solid equilibrium which is the basis of calculation of the A-B-C ternary equilibrium phase diagram can be expressed as:

$$\begin{aligned}\mu_A^l + \mu_C^l &= \mu_{AC}^c \\ \mu_B^l + \mu_C^l &= \mu_{BC}^c\end{aligned}\quad (3.15)$$

where  $\mu_A^l$ ,  $\mu_B^l$  and  $\mu_C^l$  are the chemical potentials of the A, B and C components in the A-B-C ternary solution, respectively, and  $\mu_{AC}^c$  and  $\mu_{BC}^c$  are the chemical potentials of the AC and BC components (chemical units) in the  $A_xB_{1-x}C$  ternary solid solution, respectively. On the basis of the Vieland expression [1] and the regular solution approximation, the following equations are derived from Equation (15):

$$\begin{aligned}RT \ln \gamma_{AC} + RT \ln x &= RT \ln(\gamma_A^l \gamma_C^l / \gamma^{s,1}_A \gamma^{s,1}_C) + RT \ln 4x^1_A x^1_C \\ &+ \Delta S_{AC}^F (T_{AC}^F - T) \\ RT \ln \gamma_{BC} + RT \ln(1-x) &= RT \ln(\gamma_B^l \gamma_C^l / \gamma^{s,1}_B \gamma^{s,1}_C) + RT \ln 4x^1_B x^1_C \\ &+ \Delta S_{BC}^F (T_{BC}^F - T) \\ x^1_A + x^1_B + x^1_C &= 1\end{aligned}\quad (3.16)$$

where  $\gamma_{AC}$  and  $\gamma_{BC}$  are the activity coefficients of the AC and BC components in the  $A_xB_{1-x}C$  ternary solid solution, respectively.  $\gamma_A^l$ ,  $\gamma_B^l$  and  $\gamma_C^l$  are the activity coefficients of the A, B and C components in the ternary solution, respectively.  $\gamma^{s,1}_A$ ,  $\gamma^{s,1}_B$  and  $\gamma^{s,1}_C$  are the activity coefficients of the A, B and C components in the ternary solution with the stoichiometric composition, respectively.  $x$  is the mole fraction of the AC component in the  $A_xB_{1-x}C$  ternary solid solution.  $x^1_A$ ,  $x^1_B$  and  $x^1_C$  are the molar fractions of A, B and C components in the A-B-C ternary solution, respectively.  $\Delta S_{AC}^F$  and  $\Delta S_{BC}^F$  are the entropy of fusion of the AC and BC pure compounds, respectively.  $T_{AC}^F$  and  $T_{BC}^F$  are the temperatures of fusion (melting points) of the AC and BC pure compounds, respectively. The activity coefficients of the A, B and C components can be expressed by the regular solution approximation as:

$$\begin{aligned}RT \ln \gamma_A^l &= (x^1_B)^2 \Omega_{AB}^1 + (x^1_C)^2 \Omega_{AC}^1 + x^1_B x^1_C (\Omega_{AB}^1 - \Omega_{BC}^1 + \Omega_{AC}^1) \\ RT \ln \gamma_B^l &= (x^1_C)^2 \Omega_{BC}^1 + (x^1_A)^2 \Omega_{AB}^1 + x^1_C x^1_A (\Omega_{BC}^1 - \Omega_{AC}^1 + \Omega_{AB}^1) \\ RT \ln \gamma_C^l &= (x^1_A)^2 \Omega_{AC}^1 + (x^1_B)^2 \Omega_{BC}^1 + x^1_A x^1_B (\Omega_{AC}^1 - \Omega_{AB}^1 + \Omega_{BC}^1)\end{aligned}\quad (3.17)$$

where  $\Omega_{AB}^1$ ,  $\Omega_{AC}^1$  and  $\Omega_{BC}^1$  are the interaction parameters of A-B, A-C and B-C pairs in the ternary solution. The activity coefficients of the A, B and C components in the ternary solution with the stoichiometric composition can be expressed by the regular solution approximation as:

$$\begin{aligned}RT \ln \gamma^{s,1}_A &= RT \ln \gamma^{s,1}_C = \Omega_{AC}^1 / 4 \\ RT \ln \gamma^{s,1}_B &= RT \ln \gamma^{s,1}_C = \Omega_{BC}^1 / 4\end{aligned}\quad (3.18)$$

The activity coefficients of the AC and BC components in the  $A_xB_{1-x}C$  ternary solid solution can be expressed by the regular solution approximation as:

$$\begin{aligned} RT \ln \gamma_{AC} &= \Omega_{AC-BC}^s (1-x)^2 \\ RT \ln \gamma_{BC} &= \Omega_{AC-BC}^s x^2 \end{aligned} \quad (3.19)$$

where  $\Omega_{AC-BC}^s$  is the interaction parameter between AC and BC components. Using Equation (3.16) with Equations (3.17), (3.18) and (3.19), we can obtain the liquidus and solidus lines of the A-B-C ternary system.

The basic equations given by Huber [6] express the chemical equilibrium between the pseudoternary solid of the type  $A_xB_yC_{1-x-y}D$  and the quaternary liquid, and they are useful for the calculation of the Al-Ga-In-As phase diagram [3]. Calculation of this type of quaternary phase diagram is analogous to that of the ternary phase diagram because the mixing of elements is restricted to one sublattice. However, calculation of the  $A_xB_{1-x}C_yD_{1-y}$ -type phase diagram is more complex because the mixing of elements on both sublattices must be considered for thermodynamic treatment of the quaternary solid solution. Jordan and Ilegems [7] considered a more rigorous thermodynamic treatment of solid-liquid equilibrium in this type of quaternary system. They computed the free energy of mixing of the quaternary solid solution by considering the detail of chemical bond energies. The natural components of the quaternary solid solution are considered to be the two kinds of group III atoms mixed on one sublattice and the two kinds of group V atoms mixed on the other sublattice, from an atomistic viewpoint, but not to be binary compounds. In this treatment, the liquid-solid equilibrium which is the basis of calculation of the A-B-C-D quaternary equilibrium phase diagram can be expressed as:

$$\begin{aligned} \mu_A^l + \mu_C^l &= \mu_{AC}^c \\ \mu_A^l + \mu_D^l &= \mu_{AD}^c \\ \mu_B^l + \mu_C^l &= \mu_{BC}^c \\ \mu_B^l + \mu_D^l &= \mu_{BD}^c \end{aligned} \quad (3.20)$$

where  $\mu_A^l$ ,  $\mu_B^l$ ,  $\mu_C^l$  and  $\mu_D^l$  are the chemical potentials of the A, B, C and D components in the A-B-C-D quaternary solution, respectively. The chemical potentials of the AC, AD, BC and BD components in the  $A_xB_{1-x}C_yD_{1-y}$  quaternary solid solution,  $\mu_{AC}^c$ ,  $\mu_{AD}^c$ ,  $\mu_{BC}^c$ ,  $\mu_{BD}^c$ , have the following relation:

$$\mu_{AC}^c + \mu_{AD}^c = \mu_{BC}^c + \mu_{BD}^c \quad (3.21)$$

For the AC, AD, BC and BD pure compound elements:

$$\mu_{AC}^{0c} + \mu_{AD}^{0c} \neq \mu_{BC}^{0c} + \mu_{BD}^{0c} \quad (3.22)$$

where  $\mu_{AC}^{0c}$ ,  $\mu_{AD}^{0c}$ ,  $\mu_{BC}^{0c}$  and  $\mu_{BD}^{0c}$  are the chemical potentials of the AC, AD, BC and BD pure compound elements in the  $A_xB_{1-x}C_yD_{1-y}$  quaternary solid solution, respectively, because they are independent of each other.

On the basis of the Vieland expression [4] and the regular solution approximation, the following equations to express the solid–liquid equilibria for the A-B-C-D quaternary system are derived from Equations (3.20) and (3.21):

$$\begin{aligned}
 \Delta H_{AC}^F - T \Delta S_{AC}^F + RT \ln 4x_A^1 x_C^1 &= M_{AC}^1 + RT \ln a_{AC} \\
 \Delta H_{AD}^F - T \Delta S_{AD}^F + RT \ln 4x_A^1 x_D^1 &= M_{AD}^1 + RT \ln a_{AD} \\
 \Delta H_{BC}^F - T \Delta S_{BC}^F + RT \ln 4x_B^1 x_C^1 &= M_{BC}^1 + RT \ln a_{BC} \\
 \Delta H_{BD}^F - T \Delta S_{BD}^F + RT \ln 4x_B^1 x_D^1 &= M_{BD}^1 + RT \ln a_{BD}
 \end{aligned} \tag{3.23}$$

where

$$\begin{aligned}
 M_{ij}^1 &= \Omega_{ij}^1 [0.5 - x_i^1 (1 - x_j^1) - x_j^1 (1 - x_i^1)] + (\Omega_{ik}^1 x_k^1 + \Omega_{im}^1 x_m^1) (2x_i^1 - 1) \\
 &+ (\Omega_{jk}^1 x_k^1 + \Omega_{jm}^1 x_m^1) (2x_j^1 - 1) + 2\Omega_{km}^1 x_k^1 x_m^1
 \end{aligned} \tag{3.24}$$

where  $i, j, k$  and  $m = A, B, C, D$ ;  $i \neq j \neq k \neq m$ ;  $\Delta H_{ij}^F$  (cal mol<sup>-1</sup>) and  $\Delta S_{ij}^F$  (cal mol<sup>-1</sup> deg<sup>-1</sup>) are the enthalpy and entropy of fusion of the compound  $ij$  at the melting point, respectively, and  $\Omega_{ij}^1$  is the interaction parameter between elements  $i$  and  $j$ , respectively, in the quaternary liquid. In these equations,  $a_{ij}$  represents the activity of the compound component  $ij$  in the quaternary solid solution. Applying the regular solution approach [8, 9] to the quaternary solid solution mixed on both of its sublattices, the activities of the compound components are given by:

$$\begin{aligned}
 RT \ln a_{AC} &= RT \ln(1-x)(1-y) + \Omega_{AB}^s x^2 + \Omega_{CD}^s y^2 - \alpha_c xy \\
 RT \ln a_{AD} &= RT \ln(1-x)y + \Omega_{AB}^s x^2 + \Omega_{CD}^s (1-y)^2 + \alpha_c (1-y)x \\
 RT \ln a_{BC} &= RT \ln x(1-y) + \Omega_{AB}^s (1-x)^2 + \Omega_{CD}^s y^2 + \alpha_c (1-x)y \\
 RT \ln a_{BD} &= RT \ln xy + \Omega_{AB}^s (1-x)^2 + \Omega_{CD}^s (1-y)^2 - \alpha_c (1-x)(1-y)
 \end{aligned} \tag{3.25}$$

where

$$\begin{aligned}
 \Omega_{AB}^s &= (\Omega_{AC-BC}^s + \Omega_{AD-BD}^s) / 2 \\
 \Omega_{CD}^s &= (\Omega_{AC-AD}^s + \Omega_{BC-BD}^s) / 2
 \end{aligned} \tag{3.26}$$

$$\begin{aligned}
 \alpha_c &= \Delta H_{BC}^F - T \Delta S_{BC}^F + \Delta H_{AD}^F - T \Delta S_{AD}^F - (\Delta H_{BD}^F - T \Delta S_{BD}^F) \\
 &- (\Delta H_{AC}^F - T \Delta S_{AC}^F) + (\Omega_{AC}^1 + \Omega_{BD}^1 - \Omega_{AD}^1 - \Omega_{BC}^1) / 2
 \end{aligned} \tag{3.27}$$

and where  $\Omega_{ik-jk}^s$  represents the interaction parameter between  $ik$  and  $jk$  in the quaternary solid solution. The set of equations from (3.23) to (3.27) gives complete expressions for the A-B-C-D quaternary phase diagram. The solid–liquid equilibria [5, 7] were calculated using the regular solution approximation for the solid phase and the simple solution approximation for the liquid phase [8]. In order to calculate precise phase diagrams, it is important to use the precise interaction parameters which represent the thermodynamic properties of the liquid and solid solutions.

### 3.2.3 Calculation of phase diagrams considering the surface, interface and strain energies

The equilibrium phase diagram which is useful as a guide to grow crystals by the LPE method is determined on the basis of the equilibrium between the liquid and solid phases. However, the solid composition of epitaxial layers is not precisely consistent with that determined by the equilibrium phase diagram because the solid composition of the epitaxial layers grown on a substrate is affected by the strain, surface and interfacial energies.

In the growth of InGaP on GaAs, Stringfellow [10] observed that over a certain range of solution compositions, all the LPE layers had the same solid composition rather than a varied composition, consistent with the bulk equilibrium phase diagram. This phenomenon was also reported in the LPE growth of InGaAs on InP (111) substrates and was called the composition-latching phenomenon [11, 12]. In order to understand this phenomenon, it was suggested that the excess strain energy due to lattice mismatch must be added to the chemical free energy of the solid phase [10, 13–15]. de Cremoux [15] studied the elastic strain energy term in the Gibbs free energy of a strained epitaxial layer and showed that III-V ternary compounds could be stabilized by the effect of strain when epitaxially attached to a substrate. Nakajima *et al.* found that the effect of substrate orientation on the solid composition of  $\text{In}_x\text{Ga}_{1-x}\text{As}$  epitaxial layer on InP substrate could not be ignored [16]. Nakajima and Okazaki [17] calculated the In-Ga-As phase diagram by adding the surface energy to the chemical free energy of the InGaAs solid phase to know the substrate orientation dependence of the growth conditions to obtain lattice-matched InGaAs on InP. Therefore, in order to understand the actual relationship between the liquid and solid phases in the LPE growth, the phase diagram must be determined by considering the strain, surface and interfacial energies for the epitaxial layer/substrate structure, and the energy of adhesion of the layer onto the substrate must be added to the chemical free energy of the solid phase which is used for the calculation of the chemical-equilibrium phase diagram.

Nakajima *et al.* [18] calculated the In-Ga-As ternary phase diagram useful for the epitaxial growth of InGaAs on (111) InP by precisely considering the effects of these energies. The calculated phase diagram was compared with the experimental liquidus and solidus data which were obtained by the LPE growth of InGaAs on (111) InP [19], and the effects of the layer thickness and the surface reconstruction ratio of dangling bonds on the phase diagram were determined. These results are put to some use for explanation of the extraordinary behavior of the liquid–solid equilibrium near the lattice-matched composition of InGaAs to InP.

The surface and interface area per mole depends on the layer thickness because the total volume per mole is constant. The maximum surface and interfacial energies per mole are obtained when all atoms per mole cover the entire surface area to make a monolayer and the maximum surface and interface area is generated. So, the surface and interfacial energies per mole must be determined by using the layer thickness as a parameter. The layer thickness is also a parameter of the strain energy per mole. The surface, interfacial and strain energies per mole were obtained using the following parameter  $\alpha$ :

$$\alpha = 1/L \quad (3.28)$$

where  $L$  is the layer thickness which can be expressed by the number of lattice layers. When  $L$  is equal to one and  $\alpha$  is one, the surface area per mole is maximum because the entire surface area is covered by one-lattice-layer-thick bonding pairs such as GaAs or InAs.

On the surface between the liquid and solid phases, the surface free energy  $\gamma_s$  can be given approximately by:

$$\gamma_s = (1 - w/u) \Delta H_d N_0^{2/3} \quad (3.29)$$

where  $u$  is the number of nearest neighbors of an atom in the bulk of the solid and  $w$  is the number of neighbors in the solid of an atom on the face in question,  $\Delta H_d$  is the enthalpy of dissolution of the material, and  $N_0$  is the number of atoms per unit volume [17]. The argument used is that the surface energy is the energy to break all of the nearest neighbor bonds across a given plane. The number of atoms per unit area  $N_s$  can be related to  $N_0$  as follows:

$$N_s = N_0^{2/3} \quad (3.30)$$

For III-V zinc-blende-type compound,  $N_s$  for the (111) face can be given by:

$$N_s = \frac{4}{\sqrt{3}a^2} \quad (3.31)$$

where  $a$  is the lattice constant [20]. For growth from liquid,  $\Delta H_d$  is given by the enthalpy of dissolution  $\Delta H$  per mole as follows:

$$\Delta H_d = \frac{\Delta H}{N_A} \quad (3.32)$$

where  $N_A$  is the Avogadro number ( $N_A = 6.023 \times 10^{23}$ ). For III-V systems, the total number of atoms per mole is equal to the sum of the III and V atoms, not to the sum of the III-V bonding species per mole. Therefore, from Equations (3.28)–(3.32), the surface energy  $G^{su}$  can be written as follows:

$$G^{su} = \alpha A_s (1 - \beta) \gamma_s = \frac{\alpha A_s (1 - \beta) \Delta H}{\sqrt{3} a^2 N_A} \quad (3.33)$$

for the (111) face, where  $A_s$  is the surface area when all atoms per half mole are arranged in a monolayer on the surface,  $\beta$  is the reconstruction ratio of dangling bonds on the surface, which is used as a parameter to vary the effect of the surface energy.  $A_s$  is given by:

$$A_s = \frac{1}{2} \cdot \frac{\sqrt{3} N_A a^2}{4} \quad (3.34)$$

for the (111) face. The  $\frac{1}{2}$  means that half of the total III and V atoms per mole or only III or V atoms per half mole are arranged in a monolayer on the (111) surface.



When the lattice constant of the epitaxial layer  $a$  is larger than that of the substrate  $a_{\text{sub}} (a \geq a_{\text{sub}})$ ,  $a$  is given by:

$$a = ka_{\text{sub}} \quad (3.35)$$

$$\begin{aligned} k &= \Delta a/a + 1 \\ &= (a - a_{\text{sub}})/a_{\text{sub}} + 1 \quad (k \geq 1) \end{aligned} \quad (3.36)$$

where  $\Delta a/a$  means the lattice misfit between the layer and the substrate. It can be assumed that at the interface all dangling bonds on the layer side are bonding with dangling bonds on the substrate side [21, 22]. At the interface, the bonding ratio  $\delta_1$  on the layer side is given by:

$$\delta_1 = 1 \quad (3.37)$$

and the bonding ratio  $\delta_2$  on the substrate side can be expressed by:

$$\delta_2 = 1/k \quad (3.38)$$

where this means that the fraction  $1/k$  of the dangling bonds are satisfied. The interface energy per unit area  $\gamma_i$  can be given by:

$$\begin{aligned} \gamma_i &= (1 - \delta_1)\gamma_s + (1 - \delta_2)\gamma_{\text{sub}} \\ &= \left(1 - \frac{1}{\Delta a/a + 1}\right)\gamma_{\text{sub}} \end{aligned} \quad (3.39)$$

where  $\gamma_{\text{sub}}$  is the surface energy per unit area of the substrate.  $\gamma_{\text{sub}}$  is given by:

$$\gamma_{\text{sub}} = \frac{\Delta H_{\text{sub}}}{\sqrt{3}a_{\text{sub}}^2 N_A} \quad (3.40)$$

for the (111) face, where  $\Delta H_{\text{sub}}$  is the enthalpy of evaporation per mole of the substrate. Therefore, from Equations (3.28), (3.35)–(3.40), the interfacial energy  $G^{\text{if}}$  can be written as follows:

$$G^{\text{if}} = \alpha A_{i(\text{sub})}\gamma_i = \alpha A_{i(\text{sub})} \left(1 - \frac{1}{\Delta a/a + 1}\right) \frac{\Delta H_{\text{sub}}}{\sqrt{3}a_{\text{sub}}^2 N_A} \quad (3.41)$$

for the (111) face, where  $A_{i(\text{sub})}$  is the interface area on the substrate side given by:

$$A_{i(\text{sub})} = \frac{1}{2} \cdot \frac{\sqrt{3}N_A a_{\text{sub}}^2}{4} \quad (3.42)$$

When the lattice constant of the epitaxial layer  $a$  is smaller than that of the substrate  $a_{\text{sub}} (a < a_{\text{sub}})$ ,  $G^{\text{if}}$  can be written as follows:

$$G^{\text{if}} = \alpha A_{i(\text{epi})} \left(-\frac{\Delta a}{a}\right) \frac{\Delta H}{\sqrt{3}a^2 N_A} \quad (3.43)$$

where

$$A_{i(\text{epi})} = \frac{1}{2} \cdot \frac{\sqrt{3}N_A a^2}{4} \quad (3.44)$$

For the calculation of the strain energy, the method on the basis of the elastic model by Nakajima and Furuya [23, 24] was used. In this method, each component layer is divided into many imaginary thin layers [23–26], and the face force and strain balance is considered over all these thin layers with coherent interfaces. The strain energy  $G^{\text{st}}$  is given by:

$$\begin{aligned} G^{\text{st}} &= \sum_{i=1}^m U_i \\ &= \sum_{i=1}^m \frac{\alpha A_i d_i \sigma_i^2}{2E_i} \end{aligned} \quad (3.45)$$

where  $U_i$  is the elastic strain energy in the  $i$ th imaginary thin layer,  $m$  is the total number of imaginary thin layers,  $\sigma_i$ ,  $E_i$ ,  $A_i$  and  $d_i$  are the stress, Young modulus, surface area and thickness of the  $i$ th imaginary thin layer. When the thickness of the imaginary thin layer is one lattice-layer,  $A_i$  and  $d_i$  can be written as follows:

$$A_i = \frac{1}{2} \cdot \frac{\sqrt{3}N_A a_i^2}{4} \quad (3.46)$$

$$d_i = \frac{\sqrt{3}a_i}{4} + \frac{1}{48}a_i^2 \quad (3.47)$$

for the (111) face, where  $a_i$  is the lattice constant of the  $i$ th imaginary thin layer.

For the AC-BC quasi-binary compound ( $A_xB_{1-x}C$ ), the total excess free energy  $\Delta G^{\text{xs}}$  can be given as:

$$\Delta G^{\text{xs}} = \Delta G_m^{\text{xs}} + G^{\text{su}} + G^{\text{if}} + G^{\text{st}} \quad (3.48)$$

where  $\Delta G_m^{\text{xs}}$ ,  $G^{\text{su}}$ ,  $G^{\text{if}}$  and  $G^{\text{st}}$  are the excess free energy of mixing, the surface energy, the interfacial energy and the strain energy, respectively. In the regular solution,  $\Delta G_m^{\text{xs}}$  is equal to the excess enthalpy of mixing of the ternary ABC solid ( $\Delta H_m^{\text{xs}} (= \Delta H_m^{\text{s}}(\text{ABC}))$ ). Equation (16) is used to calculate the phase diagram of the A-B-C ternary system. The In-Ga-As ternary phase diagram which is influenced by the surface, interfacial and strain energies can be calculated by using Equations (3.16) and (3.48).

Figure 3.5 shows the surface, interfacial and strain energies per mole of the (111) InGaAs/InP structure at 650 °C as a function of the Ga fraction  $X_{\text{Ga}}^1$  in the In-Ga-As ternary solution. Around  $X_{\text{Ga}}^1 = 0.03$ , the lattice-matched InGaAs layer on InP can be grown from the solution with this composition. So, the interfacial and strain energies are minimum around  $X_{\text{Ga}}^1 = 0.03$ . The three kinds of energy per mole increases as the parameter  $\alpha$  increases. Figure 3.6 shows the solidus composition of GaAs  $x$  in  $\text{In}_{1-x}\text{Ga}_x\text{As}$  grown on InP as a function of the Ga fraction  $X_{\text{Ga}}^1$  in the In-Ga-As ternary solution at 650 °C. The open circles are experimental data determined from InGaAs epitaxial layers grown on InP by the LPE method [16]. The experimental solidus curve of the GaAs composition almost linearly increases as  $X_{\text{Ga}}^1$  increases, but the slope of the solidus curve becomes smaller

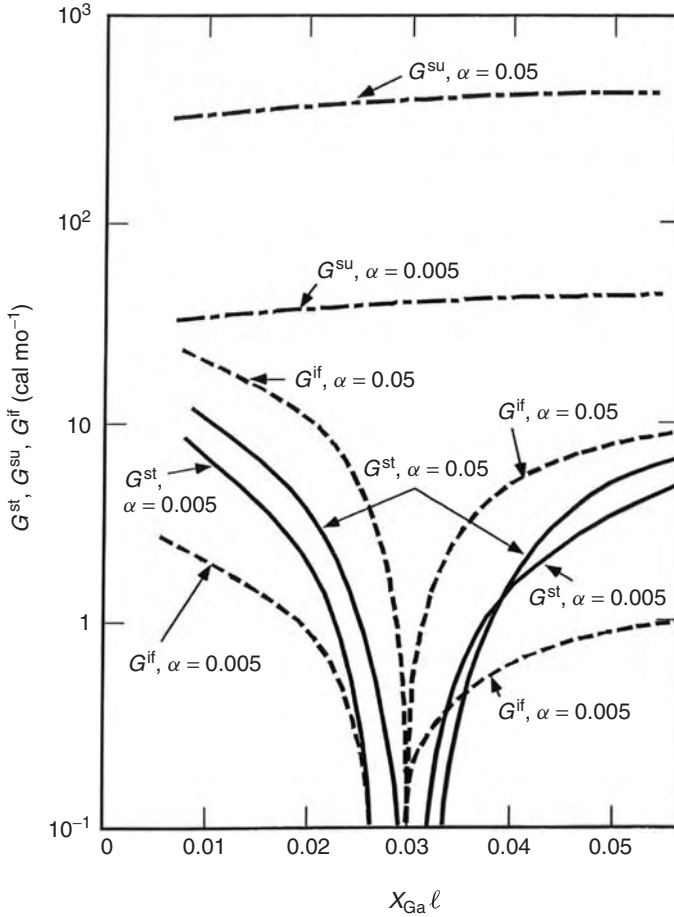


**Figure 3.5** Surface, interfacial and strain energies per mole of the (111) InGaAs/InP structure at 650°C as a function of the Ga fraction  $X_{\text{Ga}}^l$  in the In-Ga-As ternary solution. Reprinted from *J. Cryst. Growth*, **220**, Nakajima *et al.*, 413, Copyright (2000), with permission from Elsevier

near the lattice-matched composition of  $x = 0.47$  because of the latching effect [11, 12]. The dashed line is the solidus composition calculated by the regular solution model. The solid lines are the solidus compositions calculated by considering the surface, interfacial and strain energy effects. When the parameter  $\alpha$  is equal to 0.005, the calculated solidus composition corresponds more to the experimental data.

Strictly speaking, the strain energy and the interfacial energy have a strong relationship between them. Depending on the lattice misfit, there are two regions such as the coherent region in which the epitaxial/substrate interface has no misfit dislocations and the strain-relaxed region in which the hetero-interface has misfit dislocations. In the latter region, the strain energy should be calculated by considering the effect of introduction of misfit dislocations [23, 24, 27]. The interfacial energy should be essentially estimated by considering two effects such as dangling bonds related to the large lattice misfit with misfit dislocations and the abrupt transition of bonding species at the heterointerface [27]. The

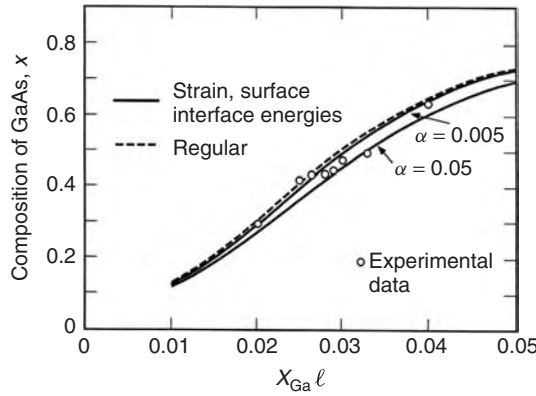


**Figure 3.6** Solidus composition of GaAs  $x$  in  $\text{In}_{1-x}\text{Ga}_x\text{As}$  grown on InP as a function of the Ga fraction  $X_{\text{Ga}}^l$  in the In-Ga-As ternary solution at  $650^\circ\text{C}$ . Reprinted from *J. Cryst. Growth*, **220**, Nakajima *et al.*, 413, Copyright (2000), with permission from Elsevier

interfacial energy related to the abrupt transition of bonding-species  $G_2^{\text{if}}$  can be given as:

$$\begin{aligned} G_2^{\text{if}} &= A_i \gamma_{i(2)} \\ &= A_i (1 - w/u) \Omega_{\text{GaAs-InAs}}^s x_{\text{InAs}}^2 \frac{N_{\text{in}}}{N_A} \end{aligned} \quad (3.49)$$

where  $A_i$  is the interface area,  $\gamma_{i(2)}$  is the interfacial energy per unit area,  $\Omega_{\text{GaAs-InAs}}^s$  is the interaction parameter of the InGaAs compound,  $x_{\text{InAs}}^2$  is the mole fraction of InAs in the InGaAs layer and  $N_{\text{in}}$  is the number of atoms per unit area at the interface. This effect is smaller than the former effect of dangling bonds. Strictly speaking, the interfacial energy related to dangling bonds is effective only in the strain-relaxed region with misfit dislocations.

The compounds consisting of different atoms such as II-VI and III-V compounds show ionicity and these liquids could be assumed to have a partially ionic property. Ionicity gives a possibility of the presence of stable associated complexes in the liquid phase. So, the phase diagram in the II-VI systems such as Zn-Te and Cd-Te, where strong evidence for association exists should be calculated by considering the association in the liquid phase. The liquidus curves of the Cd-Te, Zn-Te [28] and Al-Ga-Sb [29] systems calculated by the associated solution approximation are in excellent agreement with the experimental results.

### 3.2.4 Experimental determination of phase diagrams

Liquidus data are generally determined by the seed dissolution technique [30], the liquid observation method [31] or differential thermal analysis (DTA). The liquidus data determined by DTA are not accurate enough to be used for LPE growth because both liquidus temperatures observed during the cooling and heating processes are very different from each other. The liquidus data determined by the liquid observation method are believed to

be accurate to within  $\pm 2^\circ\text{C}$ . The seed dissolution technique was found to have the same accuracy as the liquid observation method. Therefore, the seed dissolution technique is commonly used in appreciation of its facility for guiding LPE growth.

Figure 3.7 shows schematic representations of LPE growth technologies. Figure 3.7(a) is the Nelson method, which is the most initial LPE method, and Figure 3.7(b) is the dipping method, which has been used for preparation of simple structures such as GaP LEDs. Generally, removing solution or melt on the surface of LPE layers after growth is difficult for the LPE growth by these methods. Figure 3.7(c) shows experimental apparatus for the sliding-boat method, which has been widely used for the LPE growth of many kinds of heterostructures such as lasers, photodiodes and LEDs. The sliding-boat method can be also used for the seed dissolution technique to determine the accurate liquidus. Figure 3.7(d) is the rotating-crucible method, which was used to grow multiple thin-layers.

The experimental determination of phase diagrams is explained by the In-Ga-As-P quaternary system, because it is the most complicated system. To determine the In-Ga-As-P liquidus isotherms, the InP seed dissolution technique can be used [1]. The number of degrees of freedom is three in the quaternary system, according to the phase rule shown the following relation:

$$f = n + 2 - p \tag{3.50}$$

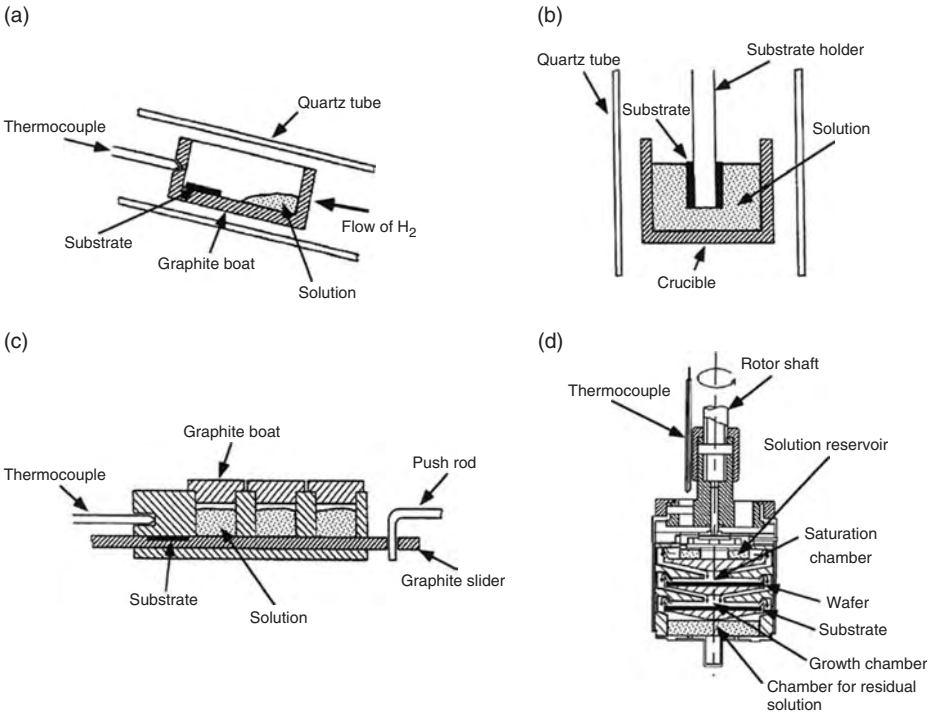


**Figure 3.7** LPE growth technologies: (a) Nelson method; (b) Dipping method; (c) sliding-boat method; and (d) rotating-crucible method. Reprinted from *Encyclopedia of Materials Science and Technology*, Liquid phase epitaxy, 4588–4597, Copyright (2001), with permission from Elsevier

where  $f$  is the degree of freedom or the number of variables which can be freely selected,  $n$  is the number of elements, and  $p$  is the number of phases. The 2 in Equation (3.50) means temperature and pressure. Therefore, if a solution temperature  $T$ , and  $X_{As}^1$  and  $X_{Ga}^1$  are known in an In-Ga-As-P solution,  $X_P^1$  and  $X_{In}^1$  can be uniquely determined. A ternary undersaturated In-Ga-As solution is put into a solution well in a graphite slider. The composition of the solution is known beforehand. An InP crystal as a seed is placed into a slot on a graphite boat. The solution is brought into contact with the InP seed at the liquidus temperature by pushing the push rod. The ternary undersaturated In-Ga-As solution is saturated with P. The P solubility into the ternary solution can be calculated from the weight loss of the seed. The In-Ga-As-P liquidus isotherms can be obtained by  $T$ ,  $X_{As}^1$ ,  $X_{Ga}^1$  and determined  $X_P^1$ . Figure 3.8 shows the 650 °C liquidus isotherms at various  $X_{As}^1$  that were determined by the seed dissolution technique. The liquidus data include values from Nakajima *et al.* [1, 32], Antypas and Moon [33], and Hsieh [34]. The dashed lines are the experimental liquidus isotherms at  $X_{As}^1 = 0.050$  and 0.055. The main effect of the addition of Ga to the quaternary solutions is appreciably to decrease the solubility of P in the solution, whereas the presence of As has a less pronounced effect in this range.

The In-Ga-As ternary liquidus isotherm can be also determined accurately by the InP seed dissolution technique [16]. An InP seed is used as a medium for determining As solubility in the ternary In-Ga-As solution. The apparatus used in the experiments is the same as shown in Figure. 3.7(c). An In-Ga-As ternary solution is brought into contact with an InP seed at 650 °C and kept in contact at this temperature for 30 min. If the As concentration in the ternary solution is below the solubility limit at 650 °C, the initially undersaturated solution becomes saturated with P, and P solubility can be calculated from the weight loss of the seed after removal of the solution. If the As concentration in the solution is just at or above the solubility limit, P cannot be dissolved from the InP seed, and no weight loss can be detected. Therefore, the accurate ternary solution compositions just saturated at 650 °C can be known by measuring P solubility as a function of As concentration. Figure 3.9 shows the P solubility in solutions at 650 °C as a function of

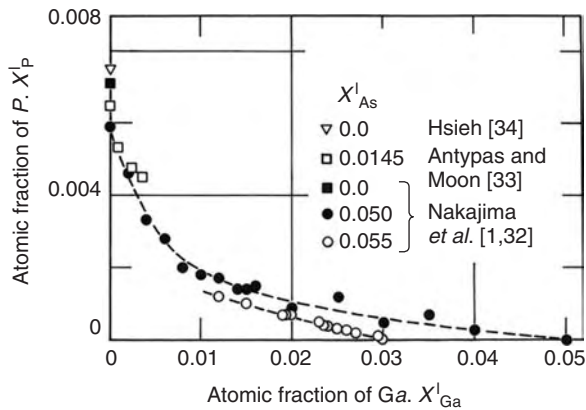


**Figure 3.8** The 650 °C liquidus isotherms at various  $X_{As}^1$  in the In-Ga-As-P system which were determined by the seed dissolution technique. Data included from Antypas and Moon [33] and Hsieh [34]. Reproduced from [32] by permission of the American Institute of Physics

$x_{As}^l$  at several  $x_{Ga}^l$ . At constant  $x_{Ga}^l$ ,  $x_{P}^l$  decreases with increasing  $x_{As}^l$ ;  $x_{P}^l$  becomes zero at a certain value of  $x_{As}^l$ , and  $x_{P}^l$  remains zero when  $x_{As}^l$  is above that value. The value of  $x_{As}^l$  at which  $x_{P}^l$  becomes zero is the As solubility in the ternary In-Ga-As solution just saturated at 650 °C. From the value shown in Figure. 3.9, the In-Ga-As liquidus isotherm at 650 °C is determined as shown by the solid curve in Figure. 3.10. The In-As binary liquidus composition interpolated from the phase diagram reported by Liu and Peretti [35] is also shown in Figure. 3.10.

The solidus isotherm can be determined by electron-probe microanalysis performed on the surface of the epitaxial layer. The apparatus is the same as that used for the seed dissolution technique shown in Figure. 3.7(c). A substrate is placed into the slot

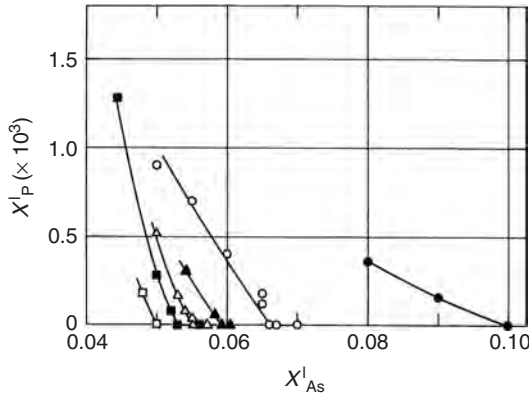


**Figure 3.9** P solubility in In-Ga-As ternary solutions at 650 °C as a function of  $x_{As}^l$  at several  $x_{Ga}^l$ . Reproduced from [16] by permission of the American Institute of Physics

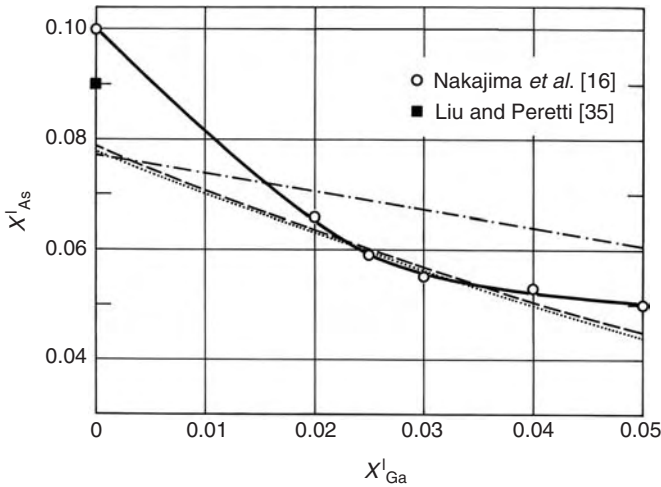


**Figure 3.10** In-Ga-As liquidus isotherm at 650 °C which was determined by the value shown in Figure. 3.9. Data included from Liu and Peretti [35]. Reproduced from [16] by permission of the American Institute of Physics

instead of the seed, and a growth solution is put into a solution well instead of the undersaturated solution. The solution composition used for the growth can be determined from the liquidus data. The solution is just saturated at the starting growth temperature. The solution is brought into contact with the substrate, and the growth is started from the just saturated temperature by cooling. The growth is finished by removing the solution from the substrate.

For the case of the In-Ga-As-P system, InP was used as a substrate, and  $\text{In}_{1-x}\text{Ga}_x\text{As}_{1-y}\text{P}_y$  epitaxial layers with various compositions are grown on it from In-Ga-As-P solutions with various compositions. The starting growth temperature was 600 °C and 650 °C. The relationship between the liquidus and solidus data at various temperatures was determined to generate the solidus isotherms. Figures 3.11 and 3.12 show the solid solubility isotherms for Ga and P into  $\text{In}_{1-x}\text{Ga}_x\text{As}_{1-y}\text{P}_y$  alloys at 650 °C [1], respectively. The quaternary epitaxial layers were grown on InP (111)B substrates under equilibrium conditions. The compositions and temperatures shown in Figures 3.11 and 3.12 were selected to permit LPE growth of InGaAsP lattice-matched layers on InP under reasonable conditions. The distribution coefficient for Ga increases with decreasing  $x_{\text{As}}^I$ , and the P concentration in alloys decreases remarkably with increasing  $x_{\text{Ga}}^I$  at constant  $x_{\text{As}}^I$ .

InGaAs epitaxial layers were grown on InP (100) and (111)B substrates to determine the solidus isotherms. The solution compositions used for the growth can be known from the liquidus isotherm shown in Figure. 3.10. These solutions were just saturated at 650 °C. Figure 3.13 shows the solid isotherms for the (111)B and (100) substrate faces at 650 °C in the In-Ga-As ternary system [16]. The solidus data are strongly dependent on the crystallographic orientation of substrates. There are two experimental solidus isotherms corresponding to the compositions of epitaxial layers grown on the (100) and (111)B substrates. The distribution coefficient of Ga in the growth of  $\text{In}_{1-x}\text{Ga}_x\text{As}$  is greater on the InP (100) face than on the (111)B face by a factor of about 1.2.

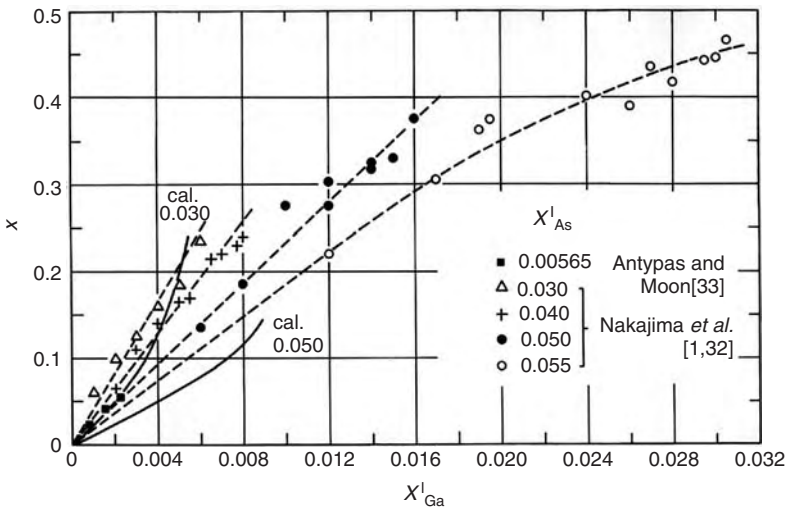


**Figure 3.11** Solid solubility isotherms for Ga into  $\text{In}_{1-x}\text{Ga}_x\text{As}_{1-y}\text{P}_y$  alloys at 650 °C. Data included from Antypas and Moon [33]. Reproduced from [1] by permission of The Electrochemical Society, Inc.



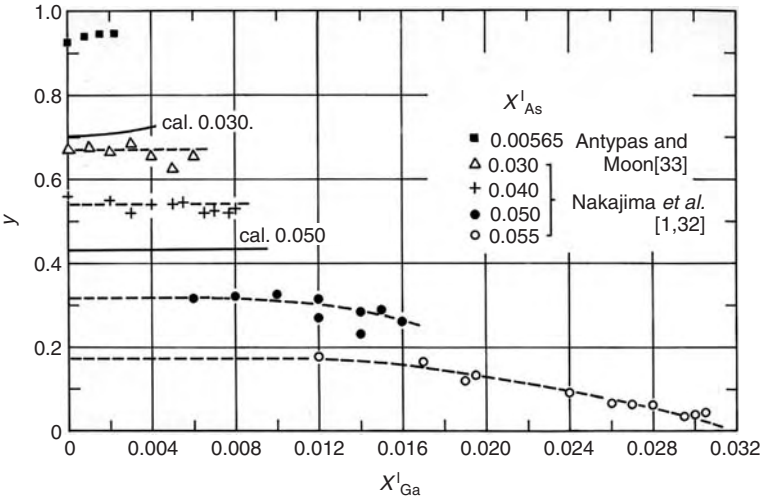


**Figure 3.12** Solid solubility isotherms for P into  $In_{1-x}Ga_xAs_{1-y}P_y$  alloys at  $650\text{ }^\circ\text{C}$ . Data included from Antypas and Moon [33]. Reproduced from [1] by permission of The Electrochemical Society, Inc.

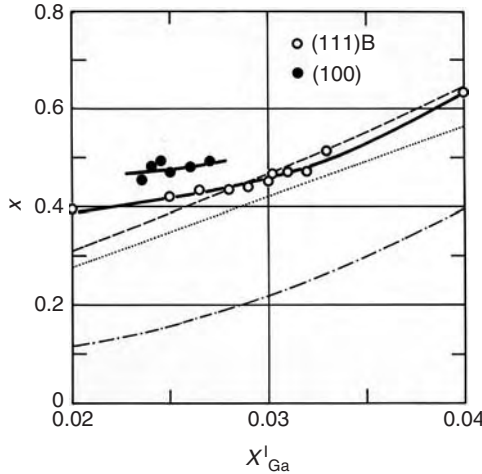


**Figure 3.13** Solid isotherms for the (111)B and (100) substrate faces at  $650\text{ }^\circ\text{C}$  in the In-Ga-As ternary system. Reproduced from [16] by permission of the American Institute of Physics

**3.2.5 Miscibility gap**

Some of the III-V ternary and quaternary phase diagrams have miscibility gaps. In these systems, the interaction parameter between the AC and BC compounds in the solid solution,  $\Omega_{AC-BC}^S$  has a large positive value, such as  $\Omega_{InP-InSb}^S$ ,  $\Omega_{InAs-InSb}^S$  and  $\Omega_{GaP-GaSb}^S$ . The temperature of the top of the miscibility gap of the AC-BC system is given by:

$$T_c = \Omega_{AC-BC}^S / (2R) \tag{3.51}$$

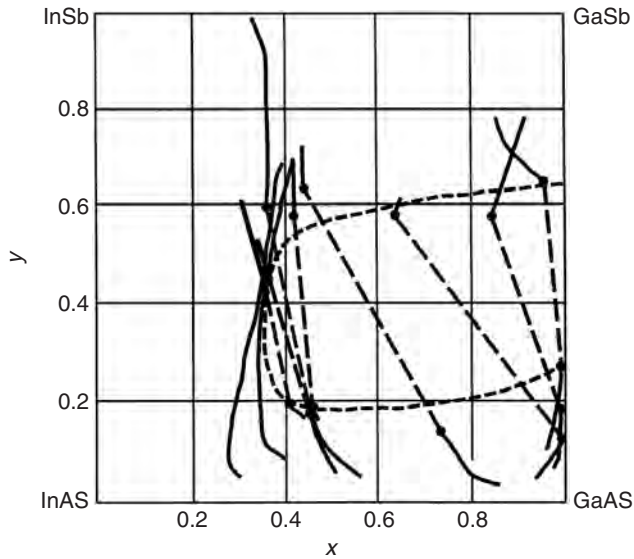


**Figure 3.14** Experimentally determined miscibility gap in the GaInAsSb quaternary system. Reprinted from *J. Cryst. Growth*, **41**, Nakajima *et al.*, 87, Copyright (1977), with permission from Elsevier

where  $R$  is the gas constant. When  $T_c$  is higher than the solidus line, the existence of the miscibility gap affects the LPE growth, and the solid solution or epitaxial layers can not be grown in the composition range where the solidus line and the miscibility gap coexist.

Nakajima *et al.* [2] found experimentally that a miscibility gap existed over a wide region in the  $\text{In}_{1-x}\text{Ga}_x\text{As}_y\text{Sb}_{1-y}$  quaternary system as shown in Figure 3.14. The miscibility gap in the  $\text{Al}_x\text{Ga}_{1-x}\text{As}_y\text{Sb}_{1-y}$  system was also experimentally found by Nahory *et al.* [14]. The strict miscibility gap of the In-Ga-As-P system was calculated by Stringfellow [36] as shown in Figure 3.15, who developed a thermodynamic formalism for the calculation of the region of solid-phase immiscibility for the III-V quaternary system of the type  $\text{A}_{1-x}\text{B}_x\text{C}_y\text{D}_{1-y}$ .

In the In-Ga-As-Sb system, no epitaxial layer can be grown by the LPE method in the region of the miscibility gap [2]. In the In-Ga-As-P system, lattice-matched epitaxial layers can be grown over the entire compositional range of quaternary solid solutions on InP substrates without phase separation, although a miscibility gap exists in the quaternary system [32, 37]. According to Stringfellow [36], the reason a second phase is not formed is that lattice strain stabilizes the one-phase solid, similar to the latching effect observed in  $\text{In}_{1-x}\text{Ga}_x\text{P}$  [10]. Nahory *et al.* [14] have observed that this effect prevents the growth of a highly lattice-mismatched phase in the Al-Ga-As-Sb system. At a relatively low growth temperature of  $590^\circ\text{C}$ , the growth rate of  $\text{In}_{1-x}\text{Ga}_x\text{As}_{1-y}\text{P}_y$  is extremely slow and the surface of the quaternary layer becomes rough [38]. This phenomenon suggests the existence of the miscibility gap below  $600^\circ\text{C}$ . Quillec *et al.* [39] showed that by LPE, it was possible to overcome instability by using the very efficient substrate strain-stabilizing effect though the existence of the miscibility gap was experimentally confirmed over a

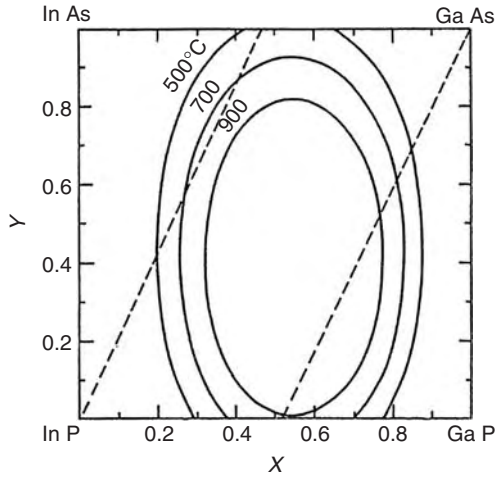


**Figure 3.15** Calculated solidus isotherms and associated tie lines for the In-Ga-As-P miscibility gap region. Reprinted from *J. Cryst. Growth*, **58**, Stringfellow, 194, Copyright (1982), with permission from Elsevier

wide range of composition. Therefore, lattice-matched  $\text{In}_{1-x}\text{Ga}_x\text{As}_{1-y}\text{P}_y$  LPE layers can be grown on InP over an entire composition range. For the crystalline quality of these LPE layers, a quasi-periodic structure was observed in these LPE layers grown on InP by transmission electron microscopy [40]. This structure was observed only inside the instability domain of the miscibility gap. It may correspond to spinodal decomposition of the solid solution.

### 3.3 TECHNOLOGIES OF LPE GROWTH

There are three types of LPE growth technology, as shown in Figure. 3.7. They are the Nelson, dipping, sliding-boat and rotating-crucible methods. The sliding-boat method is the most useful of all, which has several solution wells in the graphite slider to grow a structure with multiple epitaxial layers. Using this method, the precise thickness control can be realized by complete removal of the solution from the substrate after growth of a layer. This permits the fabrication of complicated device structures, such as semiconductor lasers. The LPE method thus has been used as a manufacturing technology to produce semiconductor lasers, LEDs and photo diodes. The rotating-crucible method [41] was used to grow multiple thin-layers and Si layers with large diameter. This rotating-crucible method using centrifuge shows that manufacturing by LPE can be taken to at least 10 cm diameter substrates with acceptable uniformity and total absence of extended defects and solvent inclusions for silicon growth from indium solution.

Accurate control of the alloy composition and layer thickness is a difficult problem in the fabrication of devices by the LPE method. Generally, the alloy composition of LPE layers varies from run to run because of weighing error. Many pieces of ingot of growth solution with the same composition for many growth runs (batch melts) are usually prepared in one process.

LPE quantum-well heterostructures of  $\text{InP}/\text{In}_{1-x}\text{Ga}_x\text{As}_{1-y}\text{P}_y/\text{InP}$  were developed by Rezek *et al.* [42]. They used constant-temperature LPE in a multiple-bin graphite boat having a circular slider geometry. However, the growth of thin layers was performed for the very short time of 26 ms. The controllability of layer thickness and the abruptness of heterointerface remains to be a problem for LPE growth of quantum-wells.

Epitaxial layers with good quality must be lattice-matched to the substrate. If bulk single crystals of ternary compounds were available, epitaxial layers with various lattice constants could be freely grown on the ternary substrate. Bulk single crystals of  $\text{In}_{1-x}\text{Ga}_x\text{As}_{1-y}\text{P}_y$  were prepared by Bachmann *et al.* [43]. The largest problem in preparing homogeneous bulk crystals is compositional variation during growth due to depletion of solute elements. At first, it was attempted to solve this problem by the source-current controlled method in which solute elements were supplied to growth solution by dissolution of source materials due to electric current passed through them [44]. Nakajima and Kusunoki [45] developed the multi-component zone melting method in which source materials are continuously supplied to growth melt during growth by effective use of the temperature gradient.  $\text{In}_{1-x}\text{Ga}_x\text{As}$  ternary and  $\text{Si}_x\text{Ge}_{1-x}$  binary bulk crystals with uniform composition, which have phase diagrams with complete miscibility in the solid state, were prepared by this method [45–49]. Recently, Azuma *et al.* [50, 51] found that the preferential orientation for the growth of  $\text{In}_{1-x}\text{Ga}_x\text{As}$  and  $\text{Si}_x\text{Ge}_{1-x}$  bulk crystals was  $\langle 110 \rangle$ , and using the (110) seed crystals was very effective to prevent polycrystallization during growth. Such a growth of bulk crystals can be viewed as an extension of LPE growth to very thick layers.

The driving force of LPE growth is supersaturation obtained by cooling the growth solution from the equilibrium liquidus temperature. The method to establish supersaturation is categorized into three types namely the ramp- (or equilibrium) cooling, step-cooling and super-cooling techniques as shown in Figure 3.16. Upon ramp-cooling, an epitaxial layer is grown as the temperature is cooled at a constant rate. For the step-cooling technique, the growth temperature is rapidly cooled to obtain a large supersaturation. Melt back, that is, dissolution of substrate in a moment of contact with the growth solution, is suppressed by use of this technique, but the grown thickness is limited by the amount of

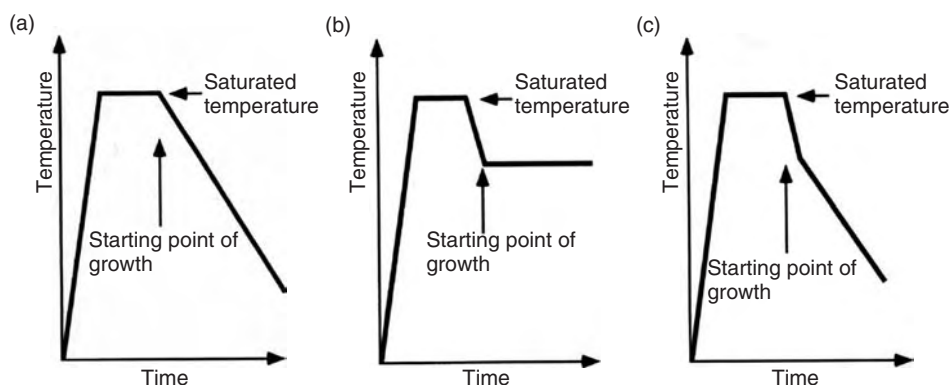


**Figure 3.16** Cooling processes of LPE: (a) ramp-cooling; (b) step-cooling; (c) super-cooling. Reprinted from *Encyclopedia of Materials Science and Technology*, Liquid phase epitaxy, 4588–4597, Copyright (2001), with permission from Elsevier

supersaturation. The supercooling technique has advantages of both the ramp- and step-cooling techniques. At first, an epitaxial layer is grown by large supersaturation, then it is grown at a constant cooling rate. This technique is commonly used for LPE growth.

### 3.4 III-V MATERIALS FOR LPE GROWTH

III-V materials which have been grown by LPE are listed in Table 3.1. The  $\text{Al}_x\text{Ga}_{1-x}\text{As}/\text{GaAs}$  and  $\text{In}_{1-x}\text{Ga}_x\text{As}_{1-y}\text{P}_y/\text{InP}$  alloy systems have been given considerable attention and have been studied extensively as the most promising materials in the III-V alloy systems, because they have many advantages relating to growth and material properties. The greatest advantage of these alloy systems is that they can be lattice-matched to GaAs or InP substrates over wide ranges of band gap. Therefore, these alloy systems are of considerable interest in light sources and detectors for optical fiber communication in the 0.65–0.85  $\mu\text{m}$  and 1.0–1.65  $\mu\text{m}$  wavelength regions, respectively. As substrate for the growth of  $\text{Al}_x\text{Ga}_{1-x}\text{As}$  and  $\text{In}_{1-x}\text{Ga}_x\text{As}_{1-y}\text{P}_y$ , GaAs and InP of good quality and with low dislocation density are available and the temperature of fusion of GaAs (1240 °C) and InP (1070 °C) is sufficiently high to support convenient epitaxial growth on it. The smooth surface of GaAs and InP can be obtained reproducibly by effective chemical etching. Especially, complicated structures of the  $\text{In}_{1-x}\text{Ga}_x\text{As}_{1-y}\text{P}_y/\text{InP}$  alloy system can be easily prepared by using several steps of epitaxial growth and/or selective etching techniques because surface oxidation for these alloy systems is a lesser problem than that

**Table 3.1** III-V materials grown by LPE

Device		Epitaxial layer/substrate (wavelength, $\mu\text{m}$ )	
1970s	LED	$\left( \begin{array}{l} \text{GaP/GaP} \\ \text{Al}_x\text{Ga}_{1-x}\text{As/GaAs} \end{array} \right.$	$\left( \begin{array}{l} (0.565, 0.7) \\ (0.65-0.85) \end{array} \right)$
	Lasers	$\left( \begin{array}{l} \text{Al}_x\text{Ga}_{1-x}\text{As/GaAs} \\ \text{In}_x\text{Ga}_{1-x}\text{As}_y\text{P}_{1-y}/\text{InP} \\ \text{Sn}_x\text{Pb}_{1-x}\text{Te/PbTe} \\ \text{Cd}_x\text{Hg}_{1-x}\text{Te/CdTe} \end{array} \right.$	$\left( \begin{array}{l} (0.65-0.85) \\ (1.0-1.65) \\ (6.6) \\ (> 0.77) \end{array} \right)$
1980s	LED	$\left( \begin{array}{l} \text{In}_x\text{Ga}_{1-x}\text{As}_y\text{P}_{1-y}/\text{InP} \\ \text{In}_{1-x}\text{Ga}_x\text{P/GaP}_y\text{As}_{1-y}/\text{GaAs} \end{array} \right.$	$\left( \begin{array}{l} (1.0-1.65) \\ (0.59) \end{array} \right)$
	Lasers	$\left( \begin{array}{l} \text{In}_x\text{Ga}_{1-x}\text{As}_y\text{P}_{1-y}/\text{InP} \\ \text{Al}_x\text{Ga}_{1-x}\text{As}_y\text{Sb}_{1-y}/\text{GaSb} \end{array} \right.$	$\left( \begin{array}{l} (1.0-1.65) \\ (1.2-1.7) \end{array} \right)$
		$\left( \begin{array}{l} \text{Al}_x\text{Ga}_y\text{In}_{1-x-y}\text{As}/\text{InP} \\ \text{In}_{1-x}\text{Ga}_x\text{As}_y\text{Sb}_{1-y}/\text{GaSb} \end{array} \right.$	$\left( \begin{array}{l} (0.87-1.6) \\ (1.7-4.0) \end{array} \right)$
	Photodiodes	$\left( \begin{array}{l} \text{InP}_x\text{As}_y\text{Sb}_{1-x-y}/\text{GaSb} \\ \text{In}_x\text{Ga}_{1-x}\text{As}_y\text{P}_{1-y}/\text{GaAs} \end{array} \right.$	$\left( \begin{array}{l} (1.5-2.4) \\ (0.67-0.88) \end{array} \right)$
		$\left( \begin{array}{l} \text{In}_{1-x}\text{Ga}_x\text{As}/\text{InP} \end{array} \right.$	$\left( \begin{array}{l} (1.65) \end{array} \right)$
1990s	High efficiency lasers TPV	$\left( \begin{array}{l} \text{In}_{1-x}\text{Ga}_x\text{As thick crystals} \\ \text{In}_{1-x}\text{Ga}_x\text{As}_y\text{Sb}_{1-y}/\text{GaSb} \end{array} \right.$	$\left( \begin{array}{l} \text{---} \\ \text{---} \end{array} \right)$

for crystals containing Al, such as  $\text{Al}_x\text{Ga}_{1-x}\text{As}$ . Such advantages relating to growth have led to effective applications of the  $\text{Al}_x\text{Ga}_{1-x}\text{As}/\text{GaAs}$  and  $\text{In}_{1-x}\text{Ga}_x\text{As}_{1-y}\text{P}_y/\text{InP}$  alloy systems.

Recently, the  $\text{In}_{1-x}\text{Ga}_x\text{As}_y\text{Sb}_{1-y}/\text{GaSb}$  or  $\text{InAs}$  alloy system has been explored by LPE for thermophotovoltaic (TPV) applications. The quaternary system is interesting because it has a large miscibility gap whose region has not been precisely determined yet by experiment. The solution or melt growth of very thick epitaxial layers or bulk crystals of  $\text{In}_{1-x}\text{Ga}_x\text{As}$  [52] and  $\text{In}_{1-x}\text{Ga}_x\text{Sb}$  have provided substrates whose lattice constant can be freely selected. These technologies were developed on the basis of LPE. Quantum-well lasers with the highest gain have been realized by using the  $\text{In}_{1-x}\text{Ga}_x\text{As}$  substrate by Otsubo *et al.* [53]. A high  $T_0$  value of 140 K and lasing up to  $210^\circ\text{C}$  have been attained for  $1.23\ \mu\text{m}$  lasers on  $\text{In}_{0.22}\text{Ga}_{0.78}\text{As}$  substrate. The threshold current density is  $245\ \text{A cm}^{-2}$ , and the temperature sensitivity of the slope efficiency between  $20^\circ\text{C}$  and  $120^\circ\text{C}$  is only  $-0.0051\ \text{dB K}^{-1}$ , showing suppressed carrier overflow owing to deep potential quantum wells. Note,  $1.3\ \mu\text{m}$  lasers are also achieved using  $\text{In}_{0.31}\text{Ga}_{0.69}\text{As}$  substrate.

### 3.5 LATTICE MATCHING

High-quality  $\text{Al}_x\text{Ga}_{1-x}\text{As}$  layers can be easily grown on  $\text{GaAs}$  substrates because  $\text{Al}_x\text{Ga}_{1-x}\text{As}$  remains nearly lattice-matched to  $\text{GaAs}$  regardless of the ternary composition. Therefore, small variations in composition do not significantly affect the perfection of epitaxial growth. On the other hand, the growth of lattice matching is most important to grow high-quality  $\text{In}_{1-x}\text{Ga}_x\text{As}_{1-y}\text{P}_y$  and  $\text{In}_{1-x}\text{Ga}_x\text{As}$  layers on  $\text{InP}$  substrates. It mandates the use of correct solution compositions for lattice matching within tight tolerance. The solution compositions for LPE growth of lattice-matched layers, predicted by the phase diagrams shown in Figures 3.11 and 3.12, are confirmed by lattice-constant measurements of the epitaxial layers grown from these solutions. Using the phase diagram data from Figures 3.11 and 3.12, the solid compositions,  $x$  and  $y$  can be drawn on the square-type  $\text{InAs-GaAs-InP-GaP}$  pseudoquaternary phase diagram with  $\text{In}_{1-x}\text{Ga}_x\text{As}_{1-y}\text{P}_y$  as shown in Figure 3.17. The solid lines mean the solid compositional variation as  $x_{\text{Ga}}^1$  increases at  $650^\circ\text{C}$ . The dashed line shows the solid compositions lattice-matched to  $\text{InP}$ . It is known that the solution compositions to obtain lattice-matched layers can be determined by using  $x_{\text{Ga}}^1$  as a growth parameter whilst keeping  $x_{\text{As}}^1$  and  $650^\circ\text{C}$  constant.

Lattice constants can be measured by the double crystal X-ray diffraction technique. The (400) or (600) and (444)  $\text{CuK}\alpha$  reflections are usually used for the (100) and (111) faces, corresponding to a full width at half maximum of 0.3, 0.17 and 0.2 s, respectively. The precise diffraction angles of the layers were determined by using the substrate reflection as an internal standard. When an epitaxial layer is grown on a substrate, the lattice of the epitaxial layer is deformed due to the lattice misfit. For the  $\text{In}_{1-x}\text{Ga}_x\text{As}_{1-y}\text{P}_y$  and  $\text{In}_{1-x}\text{Ga}_x\text{As}$  layers on  $\text{InP}$  substrates, the lattice misfit perpendicular to the wafer surface is always larger than that parallel to the wafer surface. That is, within the elastic limit the lattice of the  $\text{In}_{1-x}\text{Ga}_x\text{As}_{1-y}\text{P}_y$  and  $\text{In}_{1-x}\text{Ga}_x\text{As}$  epitaxial layers is tetragonally deformed due to the stress at the interface.

The distribution coefficient of the constituent elements in the  $\text{In-Ga-As-P}$  system is strongly affected by the crystallographic orientation of the substrate [54]. Therefore, different solution compositions are required to grow lattice-matched layers on the (100), (111)A

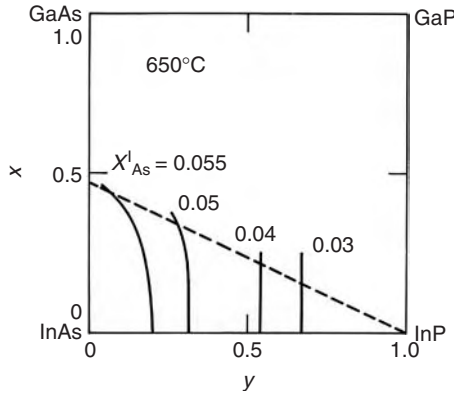


**Figure 3.17** Solid compositions,  $x$  and  $y$  drawn on the square-type InAs-GaAs-InP-GaP pseudoquaternary phase diagram with  $In_{1-x}Ga_xAs_{1-y}P_y$ . Reprinted from *Electric Materials Seminar, Liquid Phase Epitaxial Growth-of-InGaAsP/InP*, EFM-78-11, Copyright (1978), with permission from Japan Electric Society

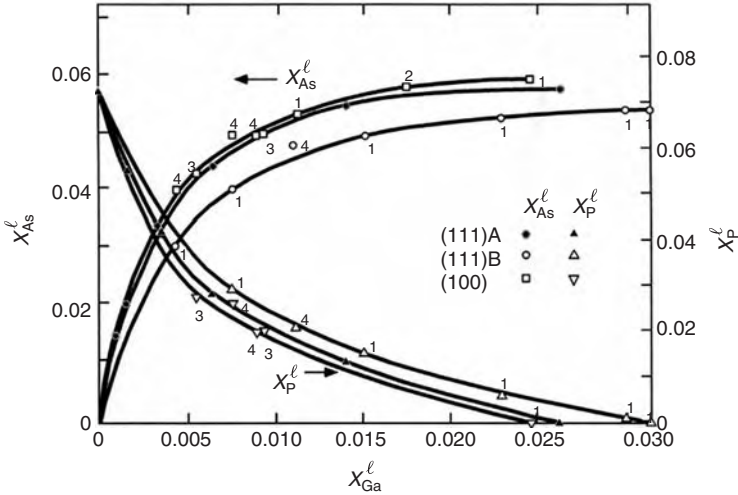


**Figure 3.18** Quaternary solution compositions required for LPE growth of lattice-matched layers on (100), (111)A and (111)B substrates at 650°C. Reprinted from *J. Cryst. Growth*, **71**, 463–469, Copyright (1983), with permission from Elsevier

and (111)B substrates. Nakajima *et al.* [1, 32, 55] systematically determined these solution compositions to grow lattice-matched  $In_{1-x}Ga_xAs_{1-y}P_y$  layers on the (100), (111)A and (111)B at 650 and 700°C over the entire compositional range. Figure 3.18 shows quaternary solution compositions  $X_{As}^l$ ,  $X_P^l$ , and  $X_{Ga}^l$  required for LPE growth of lattice-matched layers on the three types of substrate at 650°C. From the data,  $In_{1-x}Ga_xAs_{1-y}P_y$  layers can be grown on InP substrates over the entire range of  $0 \leq x \leq 0.47$  and  $0 \leq y \leq 1.0$ . The precise solution compositions were determined for the growth of lattice-matched  $In_{0.53}Ga_{0.47}As$  on InP (100) and (111)B substrates [16].

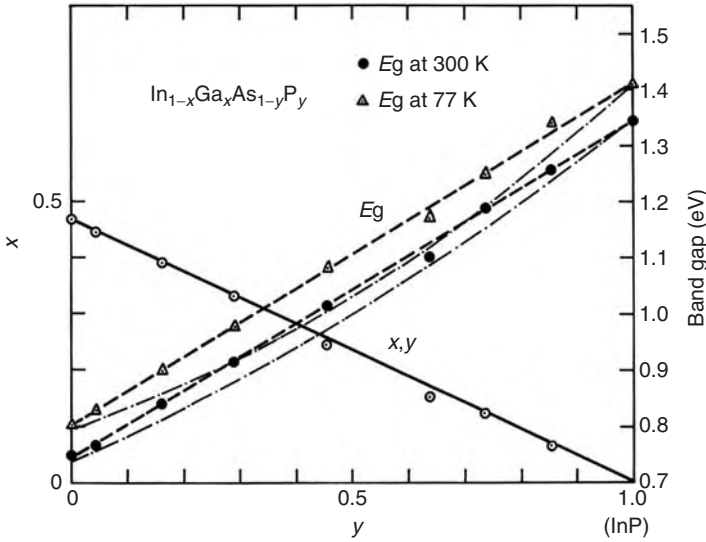


**Figure 3.19** Band gap  $E_g$  of the lattice-matched  $\text{In}_{1-x}\text{Ga}_x\text{As}_{1-y}\text{P}_y$  alloy on InP which was determined over all the lattice-matching compositional range by photoluminescence measurements at 300 and 77 K. Reproduced from [32] by permission of the American Institute of Physics

The band gap of the lattice-matched  $\text{In}_{1-x}\text{Ga}_x\text{As}_{1-y}\text{P}_y$  alloy on InP was determined over all the lattice-matching compositional range by photoluminescence measurements at 300 and 77 K as shown in Figure. 3.19. The band gap as a function of the alloy composition  $y$  can be given as [32]:

$$\begin{aligned} E_g &= 0.74 + 0.61y & \text{at } 300 \text{ K} \\ E_g &= 0.80 + 0.61y & \text{at } 77 \text{ K} \end{aligned} \quad (3.52)$$

Both lines have the same slope, and the energy shift between the band gaps at 300 and 77 K is equal to 0.06 eV. The dot and dash curve is drawn as a quadratic equation given by Nahory *et al.* [56]. The solid line shown in Figure. 3.19 is the calculated result on the basis of Vegard's law. The experimental data points are in good agreement with the calculated line. Thus, Vegard's law may be considered valid for the calculation of lattice constants of  $\text{In}_{1-x}\text{Ga}_x\text{As}_{1-y}\text{P}_y$  over the entire range of composition [32, 56].

### 3.6 GROWTH OF MISFIT-DISLOCATION-FREE WAFERS

Misfit-dislocation-free epitaxial wafers are required for the fabrication of optical devices of good quality. The generation of interfacial misfit dislocations depends on both the lattice misfit  $\Delta a/a$  and the layer thickness under a fixed starting-growth temperature, where  $\Delta a$  is equal to the lattice constant of the epitaxial layer minus the lattice constant of the substrate. The conditions for the growth of thick  $\text{In}_{1-x}\text{Ga}_x\text{As}$  and  $\text{In}_{1-x}\text{Ga}_x\text{As}_{1-y}\text{P}_y$  layers without misfit dislocations were determined by Nakajima *et al.* [19, 57]. X-ray topographs and an etch-pit observation technique were used to determine whether misfit dislocations were



generated or not in a series of  $\text{In}_{1-x}\text{Ga}_x\text{As}/\text{InP}$  and  $\text{In}_{1-x}\text{Ga}_x\text{As}_{1-y}\text{P}_y/\text{InP}$  heterostructure wafers with different  $\Delta a/a$  and layer thicknesses. One-to-one correspondence of etch pit counts and density of dislocations by X-ray topography was established. A series of  $\text{In}_{1-x}\text{Ga}_x\text{As}$  and  $\text{In}_{1-x}\text{Ga}_x\text{As}_{1-y}\text{P}_y$  layers with different  $\Delta a/a$  and final thickness was grown on InP (100) and (111)B substrates at a constant cooling rate of  $0.2^\circ\text{C min}^{-1}$ , starting growth at  $650^\circ\text{C}$  from just-saturated solutions. For ternary layer growth it was found that under conditions leading to the formation of misfit dislocations frequently the defects were introduced into the InP rather than into  $\text{In}_{1-x}\text{Ga}_x\text{As}$ .

Figure 3.20 shows a plot of layer thickness  $d$  ( $\mu\text{m}$ ) of  $\text{In}_{1-x}\text{Ga}_x\text{As}$  as a function of lattice misfit. It reveals boundaries (shown as solid lines) between wafers for which no misfit dislocations were observed after epitaxial growth (represented by open circles), and wafers with misfit dislocations in either InP or  $\text{In}_{1-x}\text{Ga}_x\text{As}$  (represented by crosses). These boundaries thus define thresholds in composition for the formation of misfit dislocations for a given layer thickness. All the results presented in Figure. 3.20 correspond to initiation of growth at  $650^\circ\text{C}$ . They prove that misfit-dislocation-free growth cannot be achieved for wafers with thick ternary layers by exact lattice matching of the epitaxial film to InP at room temperature. Misfit-dislocation-free ternary layers thicker than  $10\mu\text{m}$  can be grown only when  $\Delta a/a$  is between  $-6.5 \times 10^{-4}$  and  $-9 \times 10^{-4}$ . This behavior, resulting in the thickest layer without misfit dislocations for negative lattice misfit at room temperature, is explained by the difference in the thermal expansion coefficients of  $\text{In}_{1-x}\text{Ga}_x\text{As}$  and InP. The thermal expansion coefficient of InP is smaller than that of  $\text{In}_{1-x}\text{Ga}_x\text{As}$ . Therefore,  $\text{In}_{1-x}\text{Ga}_x\text{As}$  lattice-matched to InP at room temperature has a large positive lattice misfit at the growth temperature. On the other hand, a ternary layer with a sufficiently small

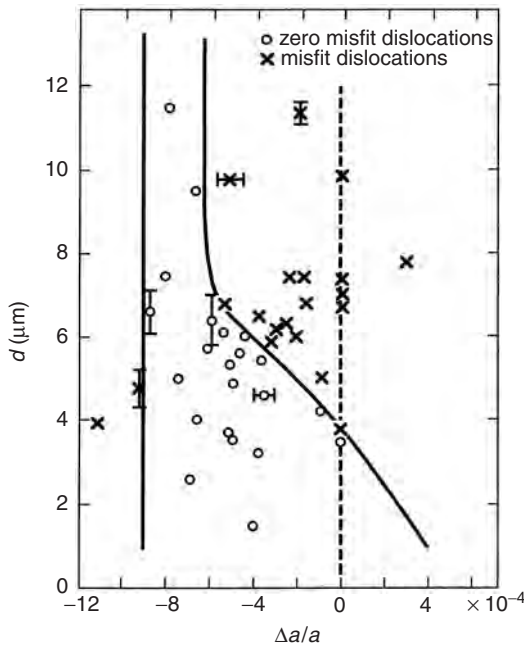


**Figure 3.20** Misfit-dislocation-free region of  $\text{In}_{1-x}\text{Ga}_x\text{As}$  layers on InP. Reproduced from [57] by permission of The Electrochemical Society, Inc.

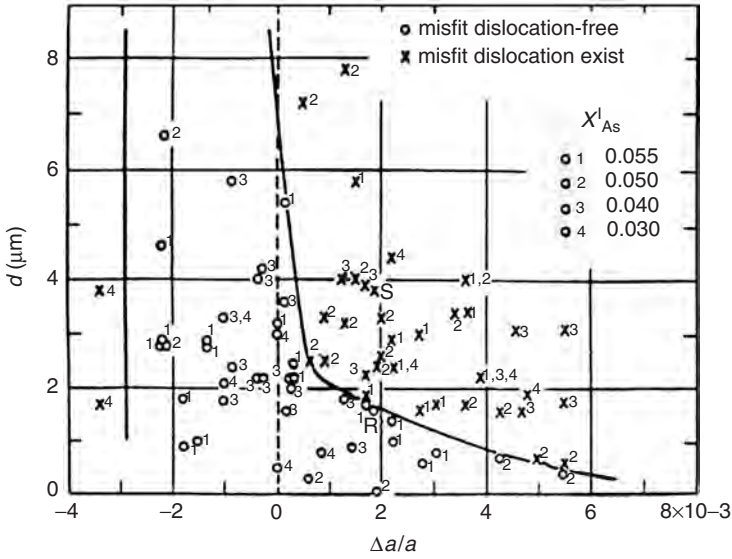


**Figure 3.21** Misfit-dislocation-free region in the plot  $d$  versus  $\Delta a/a$  for  $\text{In}_{1-x}\text{Ga}_x\text{As}_{1-y}\text{P}_y$  layers on InP. It is larger than that of the  $\text{In}_{1-x}\text{Ga}_x\text{As}/\text{InP}$  system shown in Figure 3.20. Reproduced from [19] by permission of the American Institute of Physics

negative lattice misfit at room temperature has diminished lattice mismatch at the growth temperature. In view of the decrease of the yield point with increasing temperature misfit dislocations are more easily formed at high temperature, which explains the observations of Figure 3.20. As an effect of nonuniformity of the temperature distribution across the wafer, misfit dislocations usually were initially introduced near the edges of the wafers and formed unidirectional arrays during later stages of growth.

The misfit-dislocation-free region in the plot  $d$  versus  $\Delta a/a$  for the system  $\text{In}_{1-x}\text{Ga}_x\text{As}_{1-y}\text{P}_y/\text{InP}$  is larger than that of the  $\text{In}_{1-x}\text{Ga}_x\text{As}/\text{InP}$  system as shown in Figure 3.21, which shows the region for the (111)B face [19]. The  $\Delta a/a$  range in which misfit dislocation-free wafers with thick  $\text{In}_{1-x}\text{Ga}_x\text{As}_{1-y}\text{P}_y$  layers can be grown is more than three times wider than that for  $\text{In}_{1-x}\text{Ga}_x\text{As}/\text{InP}$  wafers. This is explained in part as an effect of differences in alloy hardening and in part as an effect of easier accommodation of strain on a local scale due to the larger variability of distributing different size atoms on the two sublattices of the quaternary alloys system than on the cation sublattice only for the ternary alloy system. The dislocation-free region is also larger for growth on the (100) face as compared with growth on the (111)B face in the  $\text{In}_{1-x}\text{Ga}_x\text{As}_{1-y}\text{P}_y/\text{InP}$  system [19]. This is explained as an effect of differences in the number of slip systems available, leading for a given misfit strain and on-axis growth to smaller resolved shear stress for (100) than for (111)B.

### 3.7 PHASE DIAGRAMS OF GROWTH MODE

The growth of thin films has been categorized into three kinds of growth mode, namely Frank–van der Merwe (FM) mode (layer-by-layer growth on a substrate),

Stranski–Krastanov (SK) mode (the first layer or layers remain smooth on a substrate and then clusters form on the top of the layer), and Volmer–Weber (VW) mode (clusters form on a substrate). These growth modes are deduced from equilibrium considerations of the energy balance between the surface energies of the layer, substrate and clusters and the interfacial energy between them. For hetero-epitaxial growth of highly strained structures such as SiGe/Si, however, the elastic strain energy associated with lattice misfit between the epitaxial layer, substrate and epitaxial clusters must be considered. Daruka and Barabási deduced these growth modes by adding consideration of the elastic energy, and phase diagrams of growth mode for the unspecific system were determined as a function of the coverage and misfit [58, 59]. Recently, Nakajima *et al.* have determined the thickness–composition phase diagrams of growth mode for most of the III-V ternary systems, such as InGaAs/GaAs and GaPSb/GaP [21, 22, 60], GaInN/AlN/GaN [27] and SiGe/Si [61], by calculating the strain, surface and interfacial energies for the three kinds of growth mode. These phase diagrams are described as a function of the thickness and composition or lattice misfit. The three kinds of growth mode can clearly appear in the phase diagrams determined only by the calculation of the strain, surface and interfacial energies.

In the calculation, one lattice layer of thickness equal to the lattice constant is taken as unit thickness of a strained layer, and four lattice layers are taken as unit thickness of a cluster [62] as shown in Figure. 3.22, which shows the fundamental structures of the FM and VW modes for the case of one lattice layer. A cluster with four lattice layers on a strained layer with one lattice layer is taken as the fundamental structure of the SK mode for the case of two lattice layers as shown in Figure. 3.23. The total volume of the layer for the FM mode with two lattice layers is equal to the total volume of the cluster and the layer for the SM mode with two lattice layers. For the VW mode, the total volume of the cluster is always equal to that of the layer for the FM mode. The free energy for each structure was derived from the strain, surface and interface energies, and it was determined as a function of composition and thickness of the layer

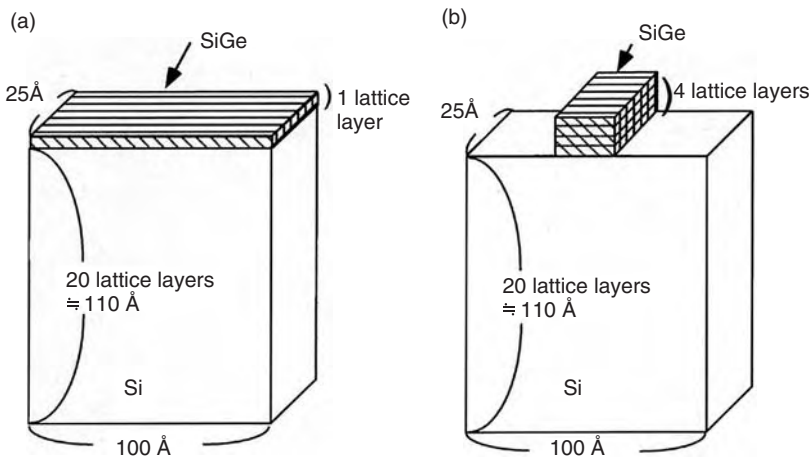


**Figure 3.22** Schematic geometries of (a) SiGe film on Si substrate (FM mode) and (b) SiGe cluster on Si substrate (VW mode) for the case of one lattice layer. Reprinted from *J. Cryst. Growth*, **260**, Nakajima *et al.*, 372, Copyright (2004), with permission from Elsevier

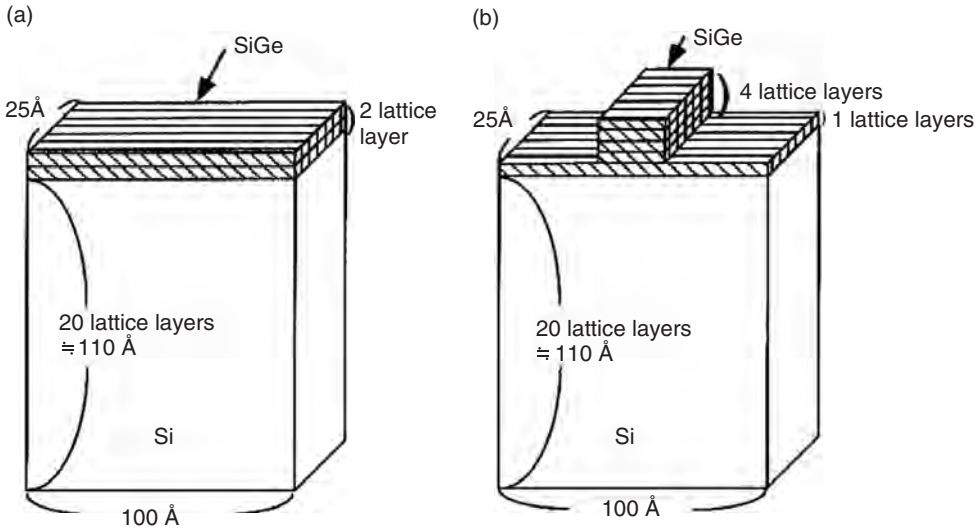


**Figure 3.23** Schematic geometries of (a) SiGe film on Si substrate (FM mode) and (b) SiGe cluster on SiGe film on Si substrate (SK mode) for the case of two lattice layers. Reprinted from *J. Cryst. Growth*, **260**, Nakajima *et al.*, 372, Copyright (2004), with permission from Elsevier

and/or cluster. By comparison of the free energies of the three kinds of growth mode, the phase diagrams of growth mode for several heterostructure systems were determined. These phase diagrams are useful to identify which growth mode can easily appear in heterostructure systems with and without misfit dislocations, and to know in which regions of the thickness and composition, smooth layers by the layer-by-layer growth or self-assembled quantum dots can be obtained. For the calculation of the strain energy, the surface energy and the interface energy Equations (45), (29) and (41) were used.

For the calculation of the SiGe/Si system [61], the strain energy of the FM mode is the largest and that of the VW mode is the smallest. The strain energy of the SK mode is between those of the FM and VW modes. The strain energy increases as the Ge fraction  $x_{\text{Ge}}$  increases or the lattice misfit increases. The surface energy of the FM mode is the smallest and that of the VW mode is the largest. The surface energy slightly decreases as the Ge fraction  $x_{\text{Ge}}$  increases because  $\Delta H$  and  $1/a^2$  decrease as  $x_{\text{Ge}}$  increases. The interface energy of the FM mode is equal to that of the SK mode, and that of the VW mode is the smallest. The interface energy increases as the Ge fraction,  $x_{\text{Ge}}$  increases because  $G^{\text{if}}$  increases as  $\Delta a/a$  increases as  $x_{\text{Ge}}$  increases. The strain energy becomes slightly larger than the surface energy as the Ge fraction increases. The interface energy is the smallest of the three kinds of energy. So, the energy balance between the strain energy and the surface energy is very important in determining the stable mode. The free energy for each structure was derived by summing up these three energies. Figure 3.24 shows the free energy as a function of the Ge fraction  $x_{\text{Ge}}$  for the (111) and (100) SiGe/Si heterostructures. The structures consist of two lattice layers. The free energy of the FM mode is the smallest between  $x_{\text{Ge}} = 0$  and 0.38, that of the SK mode is the smallest between  $x_{\text{Ge}} = 0.38$  and 0.54, and that of the VW mode is the smallest between  $x_{\text{Ge}} = 0.54$  and 1.0 for the (111) surface. That is, each growth mode is stable within the composition range with the smallest free energy.

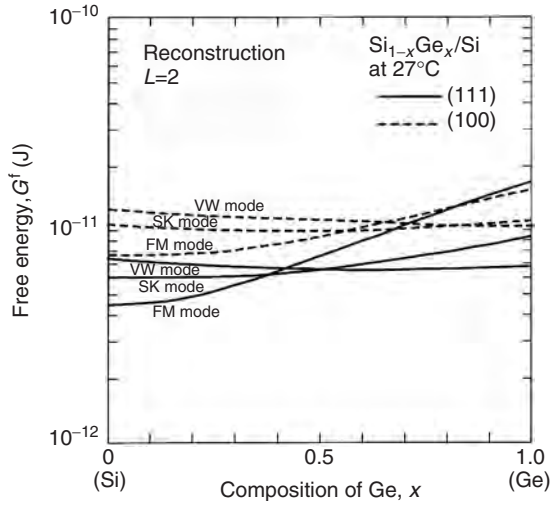


**Figure 3.24** Free energy of the (111) and (100) SiGe/Si heterostructures with two lattice layers for the FM, SK and VW growth modes as a function of Ge composition,  $x$  in  $\text{Si}_{1-x}\text{Ge}_x$ . Reprinted from *J. Cryst. Growth*, **260**, Nakajima *et al.*, 372, Copyright (2004), with permission from Elsevier

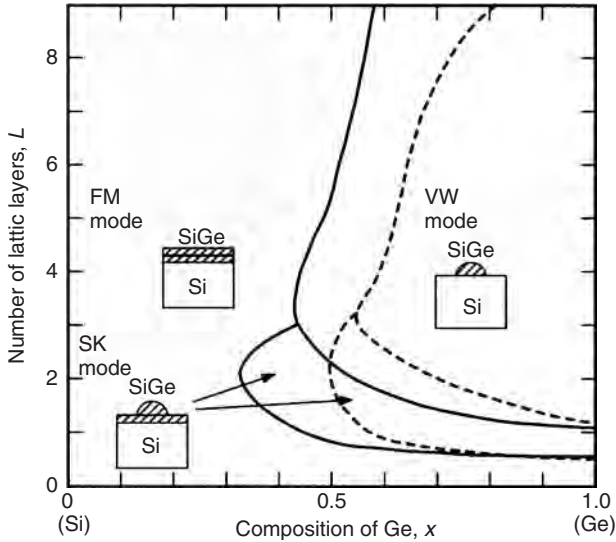


**Figure 3.25** Thickness–composition phase diagram of the FM, SK and VW growth modes for the (111) SiGe/Si heterostructure system without misfit dislocations (shown by the solid curves) and with misfit dislocations (shown by the dashed curves). The region of the SK mode is right below that of the VW mode. The regions of the SK and VW modes for the heterostructure system with misfit dislocations are much narrower than those for the system without misfit dislocations. Reprinted from *J. Cryst. Growth*, **260**, Nakajima *et al.*, 372, Copyright (2004), with permission from Elsevier

By comparing the free energy of each growth mode at various thicknesses, we can determine the thickness–composition phase diagram of growth mode for the SiGe/Si structure. Figure 3.25 is the phase diagram of the FM, SK and VW growth nodes for the SiGe/Si heterostructure system without misfit dislocations for the (111) reconstructed surface at 27 °C (drawn as solid curves). These phase diagrams are expressed as functions of the number of lattice layers,  $L$  and the composition of Ge,  $x_{\text{Ge}}$ . In the phase diagram, when the composition of Ge or the lattice misfit is small, the FM mode is dominant. As the Ge composition increases, the SK and VW modes appear. The region of the SK mode is right below the region of the VW mode. In the actual growth, however, once the wetting layer forms, the SK mode remains even though the VW mode becomes more energetically stable as the thickness increases. So, it is very easy to obtain the SK mode for the SiGe epitaxial growth on Si substrate when the composition of Ge is large.

The most important point for determination of the phase diagram of growth mode is that the phase diagram is important only when it simply shows the relative behavior and average regions of each growth mode, and explains why the three kinds of growth mode and their regions appear in the phase diagram. If we consider these parameters in detail, we must make many phase diagrams of growth mode depending on these growth parameters. The phase diagram of growth mode can not be immutably determined because it depends on the fundamental structure used for the calculation. The phase diagram of growth mode is worthy for the above mentioned qualitative description and for understanding the growth mechanism of heterostructure systems.

## 3.8 GROWTH KINETICS

### 3.8.1 Calculation of III-V layer thickness

In order to understand the growth process and to control the LPE layer thickness, an accurate calculation method of grown-layer thickness is required. The LPE growth process is assumed to be predominantly controlled by diffusion of the V element in the III-element-rich solution, that is, diffusion-limited growth [62]. In order to calculate accurately the ternary and quaternary layer thickness, the concepts of the diffusion process of solute atoms and the liquid and solid compositional variations derived from the phase diagram must be combined. For calculating the variation of liquid and solid compositions during LPE growth, the solution is assumed to have uniform composition throughout its volume except for a very thin layer in the vicinity of the solid–liquid interface during growth. Across this layer one-dimensional diffusive transport occurs, here taken to be parallel to the  $z$ -axis of a Cartesian coordinate system. Therefore, the basic model for obtaining the growth rate is to solve the one-dimensional diffusion equation with initial condition  $c(z, t) = c_{\text{co}}$  for  $t = 0$  and boundary conditions  $c(z, t) = c_{\text{ci}}$  for  $z = 0$ , and  $c(z, t) = c_{\text{co}}$  for  $z = \infty$ , where  $c(z, t)$  is the concentration of solute C in the solution at a distance  $z$  from the substrate, and  $c_{\text{co}}$  and  $c_{\text{ci}}$  are the initial solution concentration and the solution concentration in the vicinity of the growth interface, respectively. The total number of solute atoms C per unit area that leaves the solution and deposits on the substrate in time  $t$  is given by:

$$M_t = \int_0^t D_c \left[ \frac{\partial c(z, t)}{\partial z} \right]_{z=0} dt \quad (3.53)$$

where  $D_c$  is the diffusion coefficient of solute C in the solution. Neglecting the dependence of  $D_c$  on composition and solving Fick's second law with the initial and boundary conditions stated above results:

$$M_t = (4R/3m)(D_c/\pi)^{1/2}t^{3/2} \quad (3.54)$$

where  $R$  is the cooling rate, and the slope  $m$  of the liquidus curve in the vicinity of the interface is given by:

$$m = C_1^{-1} dT/dX_c^l \quad (3.55)$$

$C_1$  is the total number of atoms per unit volume in the solution. The thickness of the grown layer is obtained by converting  $M_t$ .

Note that the above simplified analysis does not include the effects of strain and differences in surface structure for different surface orientations of the substrate, which also affect the growth rate. For example, the growth rate of  $\text{In}_{1-x}\text{Ga}_x\text{As}$  layers on the (100) face of InP is larger than that on the (111)B face [16].

### 3.8.2 Compositional variation in III-V ternary layers

In order to estimate the accurate compositional variation of ternary crystal during growth, a theoretical model must be used under the condition that phase equilibrium between crystal and solution is maintained together with constancy between the transported and incorporated mass at the crystal/solution interface at the same time [63]. For the LPE growth of  $\text{A}_x\text{B}_{1-x}\text{C}$ , the amount of solute  $i$  ( $i = \text{A}, \text{B}$  and  $\text{C}$ ) per unit time which is transported through the crystal/solution interface  $J_i$  is given by:

$$J_i = \left( \frac{\partial M_i^t}{\partial t} \right)_{z=0} \quad (3.56)$$

where  $M_i^t$  is the total number of solute atoms  $i$  per unit area that leave the solution and deposit to the crystal in time  $t$ . The crystal composition determined by the ratio of solute elements, A and C, transported through the interface is given by:

$$x = J_A/(J_A + J_B) = J_A/J_B \quad (3.57)$$

where  $x$  is the composition of A in an  $\text{A}_x\text{B}_{1-x}\text{C}$  crystal. On the other hand, the crystal composition can also be determined by the phase diagram as follows:

$$x = f(x_A^l, x_C^l) \quad \text{at } T \quad (3.58)$$

where  $f$  is the function specifying the solidus–liquidus relation. Conservation of mass and maintenance of phase equilibrium at the interface mandates that the values of  $x$  specified by Equations (3.57) and (3.58) must be equal to each other at any instant, and permits accurate determination of compositional variation in the ternary crystal during LPE growth.

### 3.9 SUMMARY

LPE is an important epitaxial method, because the growth can be performed in comparatively simple and inexpensive apparatus from solutions at relatively low temperature under near-equilibrium conditions, resulting in high purity and low density of defects at low cost of operation. Therefore, LPE has been utilized world-wide in the manufacturing of III-V and II-VI heterostructures, primarily for optoelectronic device applications. In addition to the above discussed III-V systems, it is presently being pursued in the context of TPV cells on the basis of  $\text{In}_{1-x}\text{Ga}_x\text{As}_y\text{Sb}_{1-y}$  and  $\text{Al}_x\text{Ga}_{1-x}\text{As}_y\text{Sb}_{1-y}$ . To obtain quaternary crystals with good quality by LPE, for these systems, their precise miscibility gaps must be experimentally determined. In addition, continuing research and development regarding the growth of the binary and ternary bulk crystals such as SiGe and  $\text{In}_{1-x}\text{Ga}_x\text{As}$  is important, including the development of new substrate technologies. The GaAs-InAs and GaSb-InAs pseudobinary systems are presently being studied to prepare bulk crystals with uniform composition. The most important challenge in this context is the development of methods for *in situ* monitoring and control of the temperature at the growth interface. LPE growth of other semiconductors, such as, Si, SiC, SiGe and GaN is also a new and important area of research and development. Especially, LPE growth of Si from Si melts is very interesting for solar cells with high efficiency, because the nearest equilibrium condition is required for the LPE growth, and the growth has the capability to obtain Si thin crystals with the highest quality. Also, LPE growth of oxide thin films, such as dielectrics, superconductors and semiconductors, is expected to become increasingly attractive in future. There thus exists a broad basis of materials systems and applications for continuing good use of LPE.

### REFERENCES

- [1] K. Nakajima, T. Kusunoki, K. Akita and T. Kotani, Phase diagram of the In-Ga-As-P quaternary system and LPE growth conditions for lattice matching on InP substrates, *J. Electrochem. Soc.*, **125**, 123–127 (1978).
- [2] K. Nakajima, K. Osamura, K. Yasuda and Y. Murakami, The pseudoquaternary phase diagram of the Ga-In-As-Sb system, *J. Cryst. Growth*, **41**, 87–92 (1977).
- [3] K. Nakajima, K. Osamura and Y. Murakami, Phase diagram of Al-Ga-In-As quaternary system, *J. Electrochem. Soc.*, **122**, 1245–1248 (1975).
- [4] L. J. Veland, Phase equilibria of III-V compounds, *Acta Metall.*, **11**, 137–142 (1963).
- [5] M. Ilegems and G. L. Pearson, Derivation of the Ga-Al-As ternary phase diagram with applications to liquid phase epitaxy, *Proc. 1968 Symp. on GaAs (The Inst. Phys., London)*, 3–10 (1969).
- [6] D. Huber, Thermodynamics of III-V solutions with n components, *J. Phys. Chem. Solids*, **34**, 1859–1865 (1973).
- [7] A. S. Jordan and M. Ilegems, Solid-liquid equilibria for quaternary solid solutions involving compound semiconductors in the regular solution approximation, *J. Phys. Chem. Solids*, **36**, 329–342 (1975).
- [8] E. A. Guggenheim, *Thermodynamics*, North-Holland Publishing Co., Amsterdam, 1967.
- [9] A. S. Jordan, Activity coefficient for a regular multicomponent solution, *J. Electrochem. Soc.*, **119**, 123–124 (1972).
- [10] G. B. Stringfellow, The importance of lattice mismatch in the growth of GaInP epitaxial crystals, *J. Appl. Phys.*, **43**, 3455–3460 (1972).



- [11] Y. Takeda and A. Sasaki, Composition latching phenomenon and lattice mismatch effects in LPE-grown  $\text{In}_{1-x}\text{Ga}_x\text{As}$  on InP substrate, *J. Cryst. Growth*, **45**, 257–261 (1978).
- [12] M. Quillec, H. Launois and M. C. Joncour, Liquid phase epitaxy of unstable alloys: substrate-induced stabilization and connected effects, *J. Vac. Sci. Technol.*, **B1**, 238–242 (1983).
- [13] J. P. Hirth and G. B. Stringfellow, A mechanism for liquid-phase epitaxial growth of nonequilibrium compositions producing a coherent interface, *J. Appl. Phys.*, **48**, 1813–1814 (1977).
- [14] R. E. Nahory, M. A. Pollack, E. D. Beebe, and J. C. DeWinter, The liquid phase epitaxy of AlGaAsSb and the importance of strain effects near the miscibility gap, *J. Electrochem. Soc.*, **125**, 1053–1058 (1978).
- [15] B. de Cremoux, instability criteria in ternary and quaternary III-V epitaxial solid solutions, *J. Phys. Colloq. (Orsay, Fr.)*, **43**, C5-19–27 (1982).
- [16] K. Nakajima, T. Tanahashi, K. Akita and T. Yamaoka, Determination of In-Ga-As phase diagram at 650 °C and LPE growth of lattice-matched InGaAs on InP, *J. Appl. Phys.*, **50**, 4975–4981 (1979).
- [17] K. Nakajima and J. Okazaki, Substrate orientation dependence of the In-Ga-As phase diagram for liquid phase epitaxial growth of  $\text{In}_{0.53}\text{Ga}_{0.47}\text{As}$  on InP, *J. Electrochem. Soc.*, **132**, 1424–1432 (1985).
- [18] K. Nakajima, T. Ujihara, G. Sazaki and N. Usami, Phase diagram calculation for epitaxial growth of GaInAs on InP considering the surface, interfacial and strain energies, *J. Cryst. Growth*, **220**, 413–424 (2000).
- [19] K. Nakajima, S. Yamazaki, S. Komiya and K. Akita, Misfit dislocation-free InGaAsP/InP heterostructure wafers grown by liquid phase epitaxy, *J. Appl. Phys.*, **52**, 4575–4582 (1981).
- [20] J. W. Cahn and R. E. Hanneman, (111) surface tensions of III-V compounds and their relationship to spontaneous bending of thin crystals, *Surf. Sci.*, **1**, 387–398 (1964).
- [21] K. Nakajima, Thickness–composition diagrams of Stranski–Krastanov mode in the GaPSb/GaP and InGaAs/GaAs systems, *J. Cryst. Growth*, **203**, 376–386 (1999).
- [22] K. Nakajima, Equilibrium phase diagrams for Stranski–Krastanov structure mode of III-V ternary quantum dots, *Jpn. J. Appl. Phys.*, **38**, 1875–1883 (1999).
- [23] K. Nakajima, Calculation of stresses in GaAs/Si strained heterostructures, *J. Cryst. Growth*, **121**, 278–296 (1992).
- [24] K. Nakajima and K. Furuya, Effect of Si interlayers on stress and curvature radius of GaAs/Si and GaAs/Si/GaAs/Si heterostructures with interfacial misfit dislocations, *Jpn. J. Appl. Phys.*, **33**, 1420–1426 (1994).
- [25] K. Nakajima, T. Kusunoki and C. Takenaka, Growth of ternary  $\text{In}_{1-x}\text{Ga}_x\text{As}$  bulk crystals with a uniform composition through supply of GaAs, *J. Cryst. Growth*, **113**, 485–490 (1991).
- [26] K. Nakajima, K. Kitahara and S. Ochiai, Calculation of stress concentration at the edge of island layer—demonstration for GaAs/Si, *Jpn. J. Appl. Phys.*, **35**, 2605–2613 (1996).
- [27] K. Nakajima, T. Ujihara, S. Miyashita and G. Sazaki, Effects of misfit dislocation and AlN buffer layer on the GaInN/GaN phase diagram of the growth modes, *J. Appl. Phys.*, **89**, 146–153 (2001).
- [28] A. S. Jordan, A theory of regular associated solutions applied to the liquidus curves of the Zn-Te and Cd-Te systems, *Metall. Trans.*, **1**, 239–249 (1970).
- [29] K. Osamura, K. Nakajima and Y. Murakami, Experiments and calculation of the Al-Ga-Sb ternary phase diagram, *J. Electrochem. Soc.*, **126**, 1992–1997 (1979).
- [30] M. Ilegems and M. B. Panish, Phase diagram of the system Al-Ga-P, *J. Cryst. Growth*, **20**, 77–81 (1973).
- [31] M. B. Panish, The Ga+In+P system, *J. Chem. Thermodyn.*, **2**, 319–331 (1970).
- [32] K. Nakajima, A. Yamaguchi, K. Akita and T. Kotani, Composition dependence of the band gaps of InGaAsP quaternary solids lattice matched on InP substrates, *J. Appl. Phys.*, **49**, 5944–5950 (1978).
- [33] G. A. Antypas and R. L. Moon, Growth and characterization of InP-InGaAsP lattice-matched heterojunctions, *J. Electrochem. Soc.*, **120**, 1574–1577 (1973).

- [34] J. J. Hsieh, Thickness of InP layers grown by LPE from supercooling solutions, in *Gallium Arsenide and Related Compounds (St Louis), 1976*, L. F. Eastman (Ed.), Conf. Ser. no. 33b, Institute of Physics, London, 74–80, 1977.
- [35] T. S. Liu and E. A. Peretti, The indium–arsenic system, *Trans. ASM*, **45**, 677–685 (1953).
- [36] G. B. Stringfellow, Miscibility gaps in quaternary III/V alloys, *J. Cryst. Growth*, **58**, 194–202 (1982).
- [37] M. A. Pollack, R. E. Nahory, J. C. DeWinter and A. A. Ballman, Liquid phase epitaxial  $\text{In}_x\text{Ga}_{1-x}\text{As}_y\text{P}_{1-y}$  lattice matched to  $\langle 100 \rangle$  InP over the complete wavelength range  $0.92 \leq \lambda \leq 1.65 \mu\text{m}$ , *Appl. Phys. Lett.*, **33**, 314–316 (1978).
- [38] T. Takahei and H. Nagai, Instability of In-Ga-As-P liquid solution during low temperature LPE of InGaAsP on InP, *Jpn. J. Appl. Phys.*, **20**, L313–L316 (1981).
- [39] M. Quillec, C. Daguet, J. L. Benchimol and H. Launois, InGaAsP alloy stabilization by the InP substrate inside an unstable region in liquid phase epitaxy, *Appl. Phys. Lett.*, **40**, 325–326 (1982).
- [40] P. Henoc, A. Izrael, M. Quillec and H. Launois, Composition modulation in liquid phase epitaxial  $\text{In}_x\text{Ga}_{1-x}\text{As}_y\text{P}_{1-y}$  layers lattice matched to InP substrates, *Appl. Phys. Lett.*, **40**, 963–965 (1982).
- [41] K. Konuma, E. Czech, I. Silier and E. Bauser, Liquid phase epitaxy centrifuge for 100 mm diameter Si substrates, *Appl. Phys. Lett.*, **63**, 205–207 (1993).
- [42] E. Rezek, N. Jr. Holonyak, B. A. Vojak and H. Shichijo, Single and multiple thin-layer ( $L_z < 400 \text{ \AA}$ ) InGaPAs-InP heterostructure light emitters and lasers ( $x = 1.1 \mu\text{m}$ , 77K), *J. Appl. Phys.*, **49**, 69–74 (1978).
- [43] K. J. Bachmann, F. A. Thiel and S. Ferris, The growth of In-rich bulk single crystals of GaInPAs via the gradient freeze method, *J. Cryst. Growth*, **43**, 752–755 (1978).
- [44] K. Nakajima, Liquid-phase epitaxial growth of very thick InGaAs layers with uniform composition by source-current-controlled method, *J. Appl. Phys.*, **61**, 4626–4634 (1987).
- [45] K. Nakajima and T. Kusunoki, Constant temperature LEC growth of InGaAs ternary bulk crystals using the double crucible method, *J. Cryst. Growth*, **169**, 217–222 (1996).
- [46] K. Nakajima, S. Kodama, S. Miyashita, G. Sazaki and S. Hiyamizu, Growth of Ge rich  $\text{Si}_x\text{Ge}_{1-x}$  single crystal with uniform composition ( $x = 0.02$ ) on a compositionally graded crystal for use as GaAs solar cells, *J. Cryst. Growth*, **205**, 270–276 (1999).
- [47] K. Nakajima, T. Kusunoki, Y. Azuma, N. Usami, K. Fujiwara, T. Ujihara, G. Sazaki and T. Shishido, Compositional variation in Si-rich SiGe single crystals grown by multi-component zone melting method using Si seed and source crystals, *J. Cryst. Growth*, **240**, 373–381 (2002).
- [48] Y. Azuma, N. Usami, T. Ujihara, G. Sazaki, Y. Murakami, S. Miyashita, K. Fujiwara and K. Nakajima, Growth of SiGe bulk crystal with uniform composition by directly controlling the growth temperature at the crystal-melt interface using in situ monitoring system, *J. Cryst. Growth*, **224**, 204–211 (2001).
- [49] Y. Azuma, N. Usami, T. Ujihara, K. Fujiwara, Y. Murakami and K. Nakajima, Growth of SiGe bulk crystal with uniform composition by utilizing feedback control system of the crystal-melt interface position for precise control of the growth temperature, *J. Cryst. Growth*, **250**, 298–304 (2003).
- [50] Y. Azuma, N. Usami, K. Fujiwara, T. Ujihara and K. Nakajima, A simple approach to determine preferential growth orientation using multiple seed crystals with random orientations and its utilization for seed optimization to restrain polycrystalline of SiGe bulk crystal, *J. Cryst. Growth*, **276**, 393–400 (2005).
- [51] Y. Azuma, Y. Nishijima, K. Nakajima, N. Usami, K. Fujiwara and T. Ujihara, Successful growth of an  $\text{In}_x\text{Ge}_{1-x}\text{As}$  ( $x > 0.18$ ) single bulk crystal directly on a GaAs seed crystal with preferential orientation, *Jpn. J. Appl. Phys.*, **43**, L907–L909 (2004).
- [52] K. Nakajima, T. Kusunoki and K. Otsubo, Bridgman growth of compositionally graded InGaAs ( $x = 0.05 \sim 0.30$ ) single crystals for use as seeds for InGaAs crystal growth, *J. Cryst. Growth*, **173**, 42–50 (1997).

- [53] K. Otsubo, Y. Nishijima, T. Uchida, H. Shoji, K. Nakajima and H. Ishikawa, 1.3  $\mu\text{m}$  InGaAs/InAlGaAs strained Quantum well lasers on InGaAs ternary substrates, *Jpn. J. Appl. Phys.*, **38**, L312–L314 (1999).
- [54] J. J. Hsieh, M. C. Finn and J. A. Rossi, Conditions for lattice matching in the LPE growth of GaInAsP layers on InP substrates, in *Gallium Arsenide and Related Compounds (St Louis, 1976)*, L. F. Eastman (Ed.), Conf. Ser. no. 33b, Institute of Physics, London 37–44 (1977).
- [55] K. Nakajima and T. Tanahashi, Liquid phase epitaxial growth conditions of lattice-matched InGaAsP layers on (111)A and (111)B InP, *J. Cryst. Growth*, **71**, 463–469 (1985).
- [56] R. E. Nahory, M. A. Pollack, W. D. Johnston Jr and R. L. Barns, Band gap versus composition and demonstration of Vegard's law for  $\text{In}_x\text{Ga}_{1-x}\text{As}_y\text{P}_{1-y}$  lattice matched to InP, *Appl. Phys. Lett.*, **33**, 659–661 (1978).
- [57] K. Nakajima, S. Komiya, K. Akita, T. Yamaoka and O. Ryuzan, LPE growth of misfit dislocation-free thick InGaAs layers on InP, *J. Electrochem. Soc.*, **127**, 1568–1572 (1980).
- [58] I. Daruka and A.-L. Barabási, Dislocation-free island formation in heteroepitaxial growth: a study at equilibrium, *Phys. Rev. Lett.*, **79**, 3708–3711 (1997).
- [59] I. Daruka and A.-L. Barabási, Equilibrium phase diagrams for dislocation free self-assembled quantum dots, *Appl. Phys. Lett.*, **72**, 2102–2104 (1998).
- [60] K. Nakajima, T. Ujihara, S. Miyashita and G. Sazaki, Thickness dependence of stable structure of Stranski–Krastanov mode in the GaPSb/GaP system, *J. Cryst. Growth*, **209**, 637–647 (2000).
- [61] K. Nakajima, T. Ujihara, N. Usami, K. Fujiwara, G. Sazaki and T. Shishido, Phase diagram of growth mode for the SiGe/Si heterostructure system with misfit dislocations, *J. Cryst. Growth*, **260**, 372–383 (2004).
- [62] J. J. Hsieh, Thickness and surface morphology of GaAs LPE layers grown by supercooling, step-cooling, equilibrium-cooling, and two-phase solution techniques, *J. Cryst. Growth*, **27**, 49–61 (1974).
- [63] K. Nakajima, Calculation of composition variation of InGaAs ternary crystals for diffusion and electromigration limited growth from a temperature graded solution with source material, *J. Cryst. Growth*, **110**, 781–794 (1991).

## APPENDIX

The difference between the chemical potential of  $i$  element in the A-B binary solution,  $\check{G}_i (= \mu_i)$  and the free energy of pure  $i$  element,  $G_i$  is expressed as:

$$\begin{aligned}
 \Delta\check{G}_i &= \check{G}_i - G_i \\
 &= RT \ln a_i \\
 &= RT \ln x_i^1 \gamma_i^1 \\
 &= RT \ln x_i^1 + RT \ln \gamma_i^1
 \end{aligned} \tag{A3.1}$$

The mixing free energy of the A-B binary solution,  $\Delta G_m$  is given by:

$$\Delta G_m = \Delta H_m - T \Delta S_m \tag{A3.2}$$

where  $\Delta H_m$  and  $\Delta S_m$  are the mixing enthalpy and mixing entropy of the A-B binary solution, respectively. For the regular solution:

$$\Delta H_m = x_A^1 x_B^1 \Omega_{AB}^1 \tag{A3.3}$$

and

$$\Delta \hat{H}_A = \Delta H_m - x_B^1 (d\Delta H_m/dx_B^1) \quad (\text{A3.4})$$

where the difference between the enthalpy of A element in the A-B binary solution,  $\hat{H}_A$  and the enthalpy of pure A element,  $H_A$  is given as:

$$\Delta \hat{H}_A = \hat{H}_A - H_A = (1 - x_A^1)^2 \Omega_{AB}^1 \quad (\text{A3.5})$$

For the regular solution:

$$\Delta S_m = -R(x_A^1 \ln x_A^1 + x_B^1 \ln x_B^1) \quad (\text{A3.6})$$

using the relation of Equation (A3.4), the difference between the entropy of A element in the A-B binary solution,  $\hat{S}_A$  and the entropy of pure A element,  $S_A$  is given as:

$$\Delta \hat{S}_A = \hat{S}_A - S_A = -R \ln x_A^1 \quad (\text{A3.7})$$

The difference between the free energy of A element in the A-B binary solution,  $\Delta \check{D}_A$  and the free energy of pure A element,  $G_A$  is given as:

$$\Delta \check{G}_A = \Delta \hat{H}_A - T \Delta \hat{S}_A \quad (\text{A3.8})$$

Then, using Equations (A3.5) and (A3.7):

$$\Delta \hat{G}_A = (1 - x_A^1)^2 \Omega_{AB}^1 + RT \ln x_A^1 \quad (\text{A3.9})$$

and using Equation (A3.1):

$$\Delta \check{G}_A = RT \ln \gamma_A^1 + RT \ln x_A^1 \quad (\text{A3.10})$$

We can obtain the following equation by Equations (A3.9) and (A3.10):

$$RT \ln \gamma_A^1 = (1 - x_A^1)^2 \Omega_{AB}^1 \quad (\text{A3.11})$$

and

$$RT \ln \gamma_B^1 = (1 - x_B^1)^2 \Omega_{AB}^1 \quad (\text{A3.12})$$



# 4 Equipment and Instrumentation for Liquid Phase Epitaxy

**MICHAEL G. MAUK**

*School of Engineering and Applied Science, University of PA 19101, USA,  
Philadelphia, Pennsylvania*

**JAMES B. McNEELY**

*259 Beverly Rd., Newark, DE 19711, USA*

---

4.1 Introduction	85
4.2 Overview, general description and operation of horizontal slideboat LPE system	89
4.3 Crucibles and slideboats	91
4.4 Alternative slideboat designs	92
4.5 Furnaces and heating	96
4.6 LPE ambient	98
4.7 Tubes, sealing and gas handling	99
4.8 Controllers and heating	99
4.9 Temperature measurements and other instrumentation	100
4.10 Safety	101
4.11 Production LPE systems	101
References	105

---

## 4.1 INTRODUCTION

This chapter provides an introduction, general description, and survey of liquid phase epitaxy (LPE) systems, and includes a discussion of furnaces, crucibles and slideboats, sealed tube enclosures, gas handling for providing an appropriate ambient, temperature measurement and control, supporting instrumentation, and other peripheral equipment. Emphasis is on horizontal *slideboat* LPE systems used primarily for the research, development and production of semiconductor optoelectronic devices such as detectors, light emitting diodes (LEDs), solar cells, and laser diodes, but brief discussions of *tipping* and vertical *dipping* LPE systems, as well as unconventional, high-throughput LPE systems are also included. Turn-key LPE systems, either standardized or customized, can be procured from a number of equipment vendors. However, this chapter will be directed primarily toward those who wish to construct their own LPE system. Such ‘homemade’

LPE systems prove perfectly adequate for research, prototyping, and small-volume (one to two wafers per day) production.

One of the attractive features of LPE is its low capital equipment and operating costs, especially in comparison to other epitaxy technologies such as molecular beam epitaxy (MBE) and metal organic chemical vapor deposition (MOCVD). A complete LPE system can be assembled for US\$ 20 000–30 000. This is roughly ten times cheaper than the most inexpensive MBE or MOCVD systems. Moreover, as LPE does not utilize a high vacuum, does not consume nor produce highly toxic substances, and does not in general pose any serious safety hazards, the costs of maintenance and operation of an LPE system are also very modest compared with other epitaxy technologies.

LPE is conceptually simple, yet instilled with many subtleties that impact both the quality of the product and the capabilities of the technique. Likewise, LPE systems are at one level straightforward, but certain design features and details of construction, especially with regard to the slideboat apparatus, can be critical to their performance for reproducibly achieving target device structures. In general, LPE suffers from a lack of *in situ*, real-time analysis of the crystal growth process. (Several reports of *in situ*, real-time monitoring of certain aspects of LPE are reviewed below.) The opaque metallic melt obscures the crystal growth interface. This can be contrasted with high-vacuum techniques such as MBE where low energy electron diffraction (LEED) can monitor the surface crystal structure of the growing epilayer, and mass spectrometry can detect the various chemical species that figure in the epitaxy 'reactions.' Even in MOCVD, ellipsometry and residual gas analysis can provide real-time data characterizing the growth process. LPE is in some regards then a 'blackbox' process, and certain operational aspects of the system and details of the growth process must be inferred indirectly from post-growth examination of the epitaxial growth (or lack thereof). Diagnostics of the epitaxy process is thus more subtle in LPE than in competing epitaxy methods. On the other hand, the operator is able to interface with the LPE process in a hands-on fashion to an extent impossible with MBE or MOCVD. In a simple LPE system, the operator weighs out the melts, loads the crucible or slideboat with melt components and substrate(s), inserts the crucible or slideboat into the LPE system, purges the system and establishes an ambient flow of gas, manually positions the substrate(s), initiates and monitors the heating of the melt and the achievement of a steady-state temperature distribution, manipulates the substrate to bring it into and out of contact with the melt(s) for set time periods, decants the melts from the substrates, cools the crucible or slideboat, flushes the system with nitrogen, unseals the system, and retrieves the substrates with epitaxial layers. The LPE technique is an excellent apprenticeship for learning crystal growth. The sophistication of an LPE system represents to what extent these steps are automated, and made more controllable and reproducible.

To a first order, the LPE process can be understood as a straightforward consequence of supersaturation induced by cooling the melt according to a prescribed temperature program. The composition of the resulting epitaxial layer is predicted on the basis of phase equilibria (phase diagram) considerations for the melt composition and temperature range. The growth rate is determined by the liquid phase diffusion of a rate-limiting species, normally the most dilute component of the liquid phase. The melt composition and the process conditions are easy to modify for the growth of a wide selection of materials and incorporation of various dopants.

LPE is often regarded at best as a research tool for prototyping new device concepts or materials systems, but inappropriate for high-volume production. Actually, on the basis of number of wafers processed, high-volume (50–100 wafers per run) production is possible with LPE. Generally, it is true that scale-up of LPE is more difficult than MOCVD. Nevertheless, there are many commercial niche devices such as low-bandgap (<0.5 eV) III-V alloy photodiodes and LEDs with small markets that can be well served by LPE technology.

More serious limitations of LPE are related to layer homogeneity and reproducibility with respect to thickness, alloy composition and doping; surface smoothness; and consistent achievement of thin (<100 nm) layers needed for quantum wells and superlattices. To what extent these are fundamental limitations intrinsic to the LPE technique, or can be overcome by improved equipment and operating procedures, can still be debated. For many applications such as solar cells and laser diodes, LPE has been abandoned as a production technique in favor of MOCVD. The perceived or actual limitations of the LPE technology in its current state are due, in part, to the fact that LPE reached its prime in the late 1970s before being eclipsed by MBE and MOCVD. Efforts to improve LPE waned as its relative importance diminished. Thus, the LPE technique has perhaps not fully benefited from applications of the latest developments in temperature measurement, process monitoring and control, data acquisition, furnace and heating technology, and other instrumentation common in state-of-the-art semiconductor processing equipment. Also, finite element analysis of heat transfer and computational fluid dynamics of melt convection, to the levels of sophistication currently seen with finite element modeling of silicon Czochralski (Cz) growth or MOCVD, can lead to and support improved slideboat/furnace designs and growth protocols (Kimura *et al.*, 1991; Chen *et al.*, 1992; Eck and Emmerich, 2004; Lin *et al.*, 2005).

Other limitations of LPE are more vexing. Some LPE processes are critically dependent on controlling the temperature to within about 1 °C. For example, in the LPE growth of quaternary alloys such as lattice-matched InGaAsSb on GaSb substrates, a temperature deviation of 1 °C can mean the difference between success and failure. In general, near-equilibrium growth processes such as LPE are more sensitive to temperature variations. Such tight temperature control is feasible but challenging with respect to run-to-run reproducibility. Also, convection in molten melts is complex and difficult to suppress or otherwise control. Spatial temperature variations and convection may be the dominant causes of the variability of results observed in LPE. Convection does not necessarily have to be eliminated, so long as it can be reproducibly controlled. In fact, for steady-state and high-growth rate processes, temperature gradients and convective mass transfer can be exploited to enhance growth rates and replenish melts (Sukegawa *et al.*, 1990; Peter *et al.*, 1995).

LPE systems broadly fall into two categories: vertical *dipping* systems (Figure 4.1) and horizontal *slideboat* systems (Figures 4.2 and 4.3). The horizontal slideboat system is the most versatile and is essential for growing multilayered structures such as laser diodes, heteroface solar cells, and double heterostructure LEDs. Vertical dipping systems that can process large batches of wafers are an economic choice for the growth of a single, thick epitaxial layer, such as for solar cells, especially if layer thickness control is not critical.



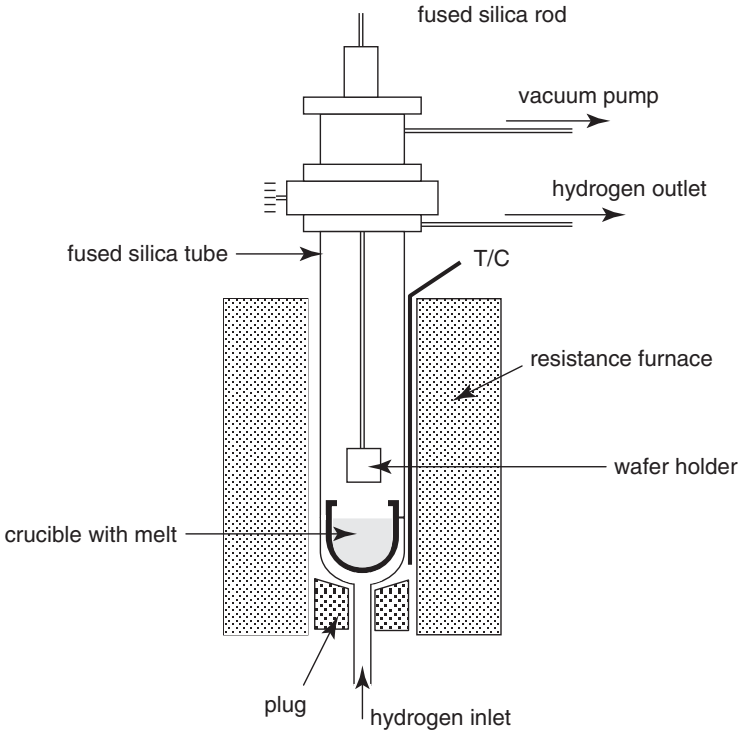


Figure 4.1 Vertical dipping system for LPE (schematic). (After Baliga, 1986)

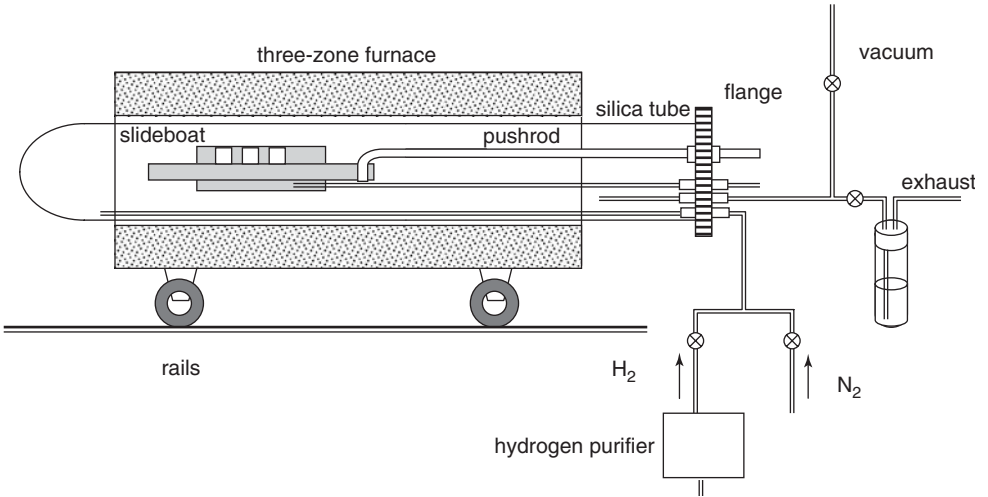
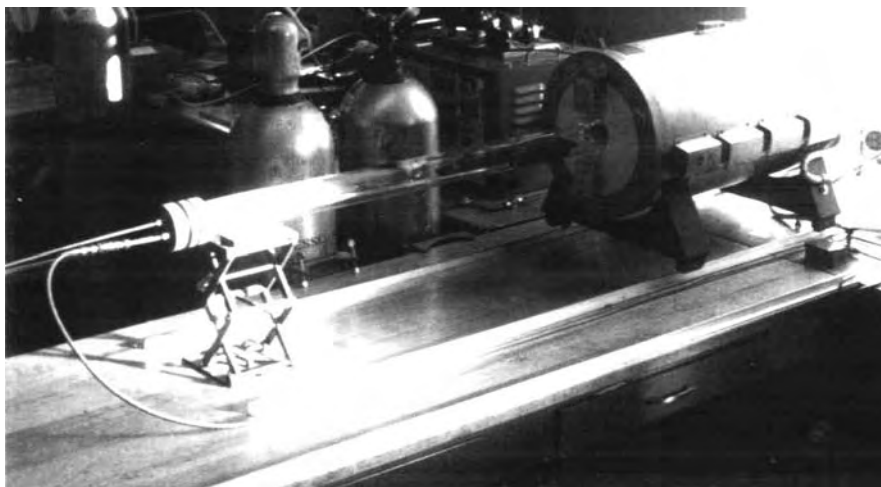
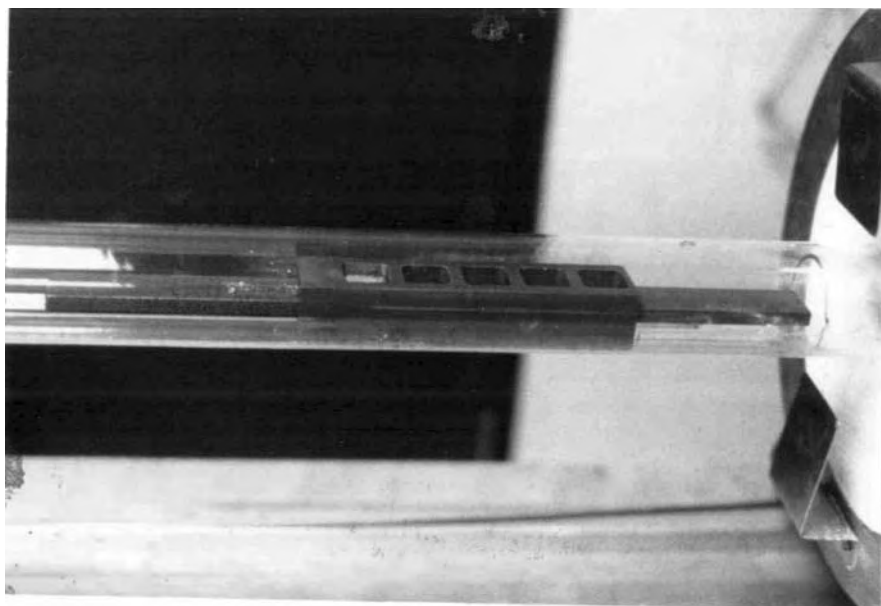


Figure 4.2 Horizontal slideboat LPE system (schematic)

(a)



(b)



**Figure 4.3** Horizontal slideboat LPE system. (a) Horizontal furnace on rollers showing LPE slideboat. (b) Slideboat positioned in silica tube with furnace rolled off slideboat

## 4.2 OVERVIEW, GENERAL DESCRIPTION AND OPERATION OF HORIZONTAL SLIDEBOAT LPE SYSTEM

The horizontal slideboat apparatus contains the melt(s) and provides a sliding mechanism (*slider* or *slidebar*) that supports the substrate and enables the substrate to be brought

into and out of contact with the melts, normally from the underside of the melt(s). The slideboat is situated in a tube sealed at both ends. The tube is almost always made of fused silica. Fused silica is transparent to infrared radiation, thus facilitating heating of the slideboat, and is also thermal shock resistant and available in very high purity. The tube is mounted in a horizontal tube furnace. One end of the silica tube can be fused closed by the supplier, in which case all access is made through the other end of the tube via either: (1) a metal disk that clamps to a collared or flanged end of the silica tube; (2) a compression fitting that slips over and tightens on the tube; or (3) a fused silica ball and socket type ground joint that couples with a metal disk. A double O-ring seal with water cooling is often used to make a vacuum-tight seal between the endcap and the silica tube. Compression fittings are tapped into the metal (stainless steel) end disk through which thermocouple(s), gas inlet and outlet, and a pushrod are inserted into the tube. The push rod, hooked through a hole in the slidebar, slides through a fitting in the endcap sealed with Teflon<sup>®</sup> ferules, and thus the slidebar can be accurately moved at various times during the growth process, either manually or by a stepper motor. The thermocouple is sheathed in a fused silica tube (<6 mm OD) and inserted into the slideboat to monitor its temperature.

Prior to operating the furnace, the slideboat is loaded with substrate(s) and weighed amounts of the melt(s), typically metals in the form of 1- to 3-mm shot. The melts loaded into the slideboat can be first baked-out overnight to remove oxides and residual impurities prior to the LPE step (Scilla *et al.*, 1977). The slideboat is then positioned in the tube. The tube is sealed and the slidebar is aligned using the push rod. The tube is then evacuated with a vacuum pump, and back filled with a gas, normally purified hydrogen. A steady gas flow is established through the tube with a positive pressure slightly above atmospheric pressure. The furnace is then heated to a first set point temperature and the melts equilibrated for about 1 h. Often, the melts are saturated using pieces of semiconductor wafer. The equilibration step assures the melts are homogenous and, if a source wafer is used, saturated to a concentration determined by the equilibration temperature. The furnace temperature is controlled by a programmable microprocessor using a signal from a thermocouple either in the slideboat or contacting the outside of the fused silica tube. After equilibration, a temperature program is initiated to cool the melt at a set rate, and the slidebar is moved in a sequence of steps that brings the substrate into contact with the melt(s) for a prescribed time, and terminates growth by pushing the substrate out of contact with the melt. The wiping action of the slidebar serves to remove any excess molten metal from the surface of the substrate, and is an important advantage of the slideboat method. Further removal of excess melt can be effected by the use of additional 'wash' melts in the slideboat, such that after the epitaxy sequences, the substrate is passed through a melt to dissolve excess portions of the melt carryover from the previous melts. Although this may appear to trade one problem for another, the rationale is that the wash melt material may either adhere less to the substrate or may be relatively easy to remove with post-growth cleaning and etching of the substrate. The furnace is then cooled to room temperature, the tube is flushed with nitrogen and opened to remove the slideboat and retrieve the substrates. The entire process (not including pre-baking of the melts) can be completed in four to eight hours depending on the complexity of epilayers grown. In the foregoing, the components of the LPE system are described in more detail, as well as variations on the basic system described above.

### 4.3 CRUCIBLES AND SLIDEBOATS

Absent a means for (e.g. magnetic) self levitation or other forms of crucibleless confinement, the melt must be contained in some type of vessel. A mechanism to bring the substrate into and out of contact with the melt is also needed. Since the epilayer thickness and uniformity depends on the contact time with the melt, a method of reproducibly and quickly contacting the substrate with the melt is crucial for many applications. Further, a means for wiping or removing excess melt from the surface of the epilayer is desirable. Droplets of melt are difficult to remove and mar the epitaxial surface. Finally, the method should be amenable to growing multilayer structures. The horizontal slideboat apparatus, and its subsequent modifications and variations, is a neat solution to this problem. The slideboat method has established itself as a most common and versatile technique for performing LPE, and the design of the slideboat is the most important aspect of an LPE system.

Figure 4.4 shows an exploded view of a conventional slideboat used to grow LEDs and laser diodes. The two basic components of the slideboat are a slideboat body in which are formed wells to contain the melts and a slider (or slidebar) in which one or more recesses are milled so that the substrate sits flush and can be moved under the melt and out from the melt with the aid of a fused silica pushrod which is bent at the end to form a hook that is inserted into a hole drilled into the end of the slidebar. The clearance between the slidebar and slideboat should be less than 2 mil (100  $\mu\text{m}$ ) to prevent seepage of the melts out of their wells. Prolonged use of the slideboat will result in wear, giving less close tolerance, as evidenced by inadequate wiping action to remove excess melt from the substrate. In this event, a new slidebar can be machined with closer tolerances.

A typical slideboat accommodates a substrate of 1–10  $\text{cm}^2$ , although much larger (100–200  $\text{cm}^2$ ) substrates can also be used. For research purposes, smaller substrates are used and usually scribed or diced into a square shape in order to conserve materials. (Care must be taken not to let kerf from the scribing contaminate the substrate surface.) For production, round wafers (3–10 cm diameter) can be used as substrates.

Most slideboats are milled from high-density (4  $\mu\text{m}$  particle size) pyrolytic graphite (e.g. Grade DFP, Poco Graphite, Decatur, Texas). Machining graphite is messy and is often not a welcomed task in many machine shops, however, graphite suppliers will machine slideboats according to designs submitted on engineering drawings or CAD files, and purify and package the finished product. In addition to graphite, LPE slideboats have also been made from alumina (sapphire) (Tamargo and Reynolds, 1981), boron nitride, fused silica (Minden, 1974), and machinable ceramics. Alumina and silica slideboats may cause unacceptable oxygen doping of the epitaxial layers. In general, these materials prove less satisfactory than graphite but can be useful to reduce carbon contamination of the melt (Gao *et al.*, 2002). Studies of the effect of crucible materials (alumina, graphite, boron nitride and silica) on the impurities and electrical properties of LPE-grown GaAs have been reported (Butcher *et al.*, 1995; Mo *et al.*, 1996). Due to their electrical insulating properties, they are also used in slideboats for electro-epitaxy wherein an electric current is imposed through the melt, and current confinement relies on electrically insulating slideboat parts (Mauk and Curran, 2001). Mixing materials in an epitaxy boat (e.g. fused silica and graphite) is possible but the design must accommodate the considerable differences in thermal expansion between these materials which could lead to inaccuracies in positioning the slidebar or, worse, mechanical failure of the slideboat.

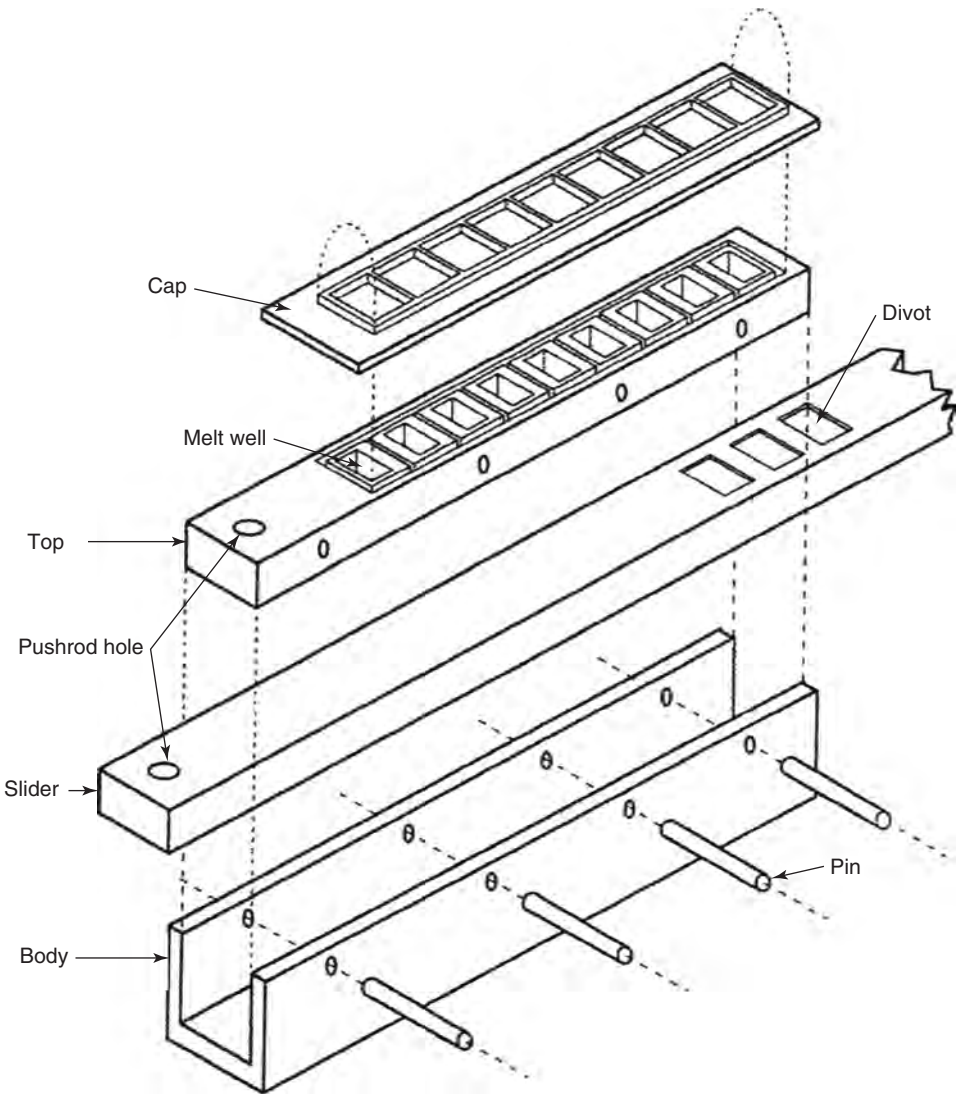
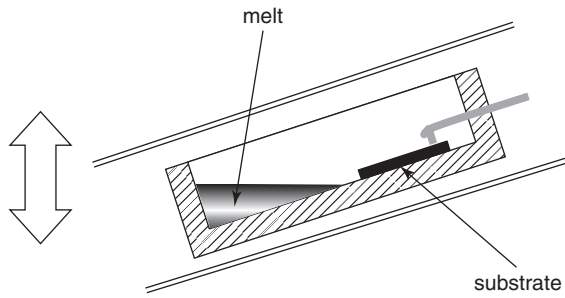


Figure 4.4 LPE horizontal slideboat (exploded view). Courtesy of G. DeSalvo

### 4.4 ALTERNATIVE SLIDEBOAT DESIGNS

Most of the innovation in LPE concerns the slideboat, and thus, the slideboat design differentiates most LPE systems. The overriding objectives are to improve control of epilayer thicknesses and uniformity, and increase throughput of the LPE process by employing larger substrates, operating in a semi-continuous mode, and/or simultaneous epitaxy on multiple substrates. Some of the diverse slideboat designs (and other types of LPE boats) are shown in Figures 4.5–4.14. Prior to the advent of the slideboat, *tipping* type boats that rolled the melt on and off a clamped substrate as the furnace tube was pivoted provided a simple means to grow a single LPE layer (Figure 4.5). A rotating crucible for tipping



**Figure 4.5** LPE tipping boat. (After Nelson, 1963)

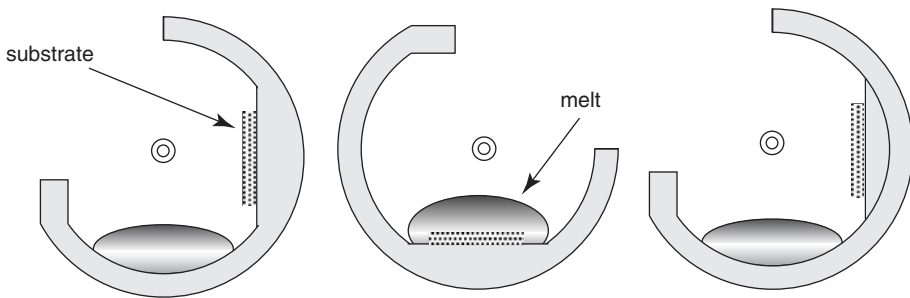


**Figure 4.6** Rotating/tipping LPE apparatus. (After Arch *et al.*, 1992)

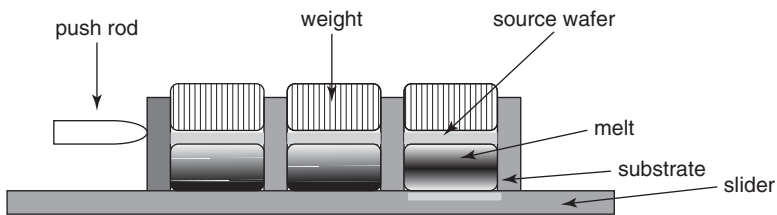


**Figure 4.7** LPE slideboat with weights and source wafers on melt. (After Goodfellow, 1986)

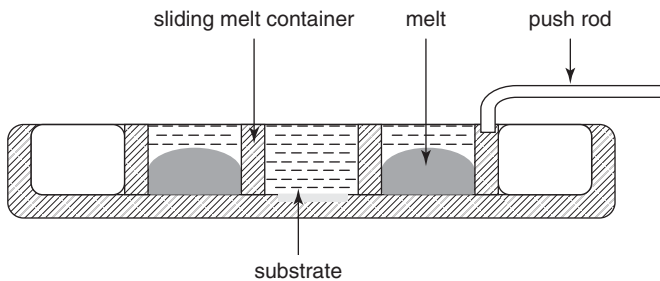


**Figure 4.8** Simple LPE slider apparatus. (After Sankaran *et al.*, 1976)

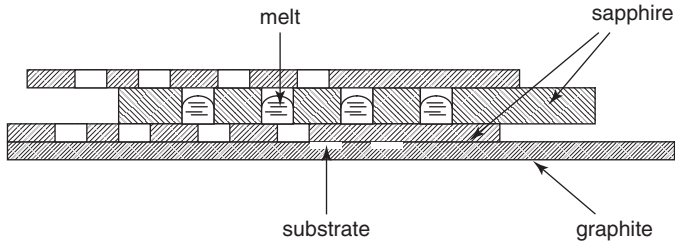


Figure 4.9 LPE slideboat with improved thermal geometry. (After Reynolds and Tamargo, 1984)

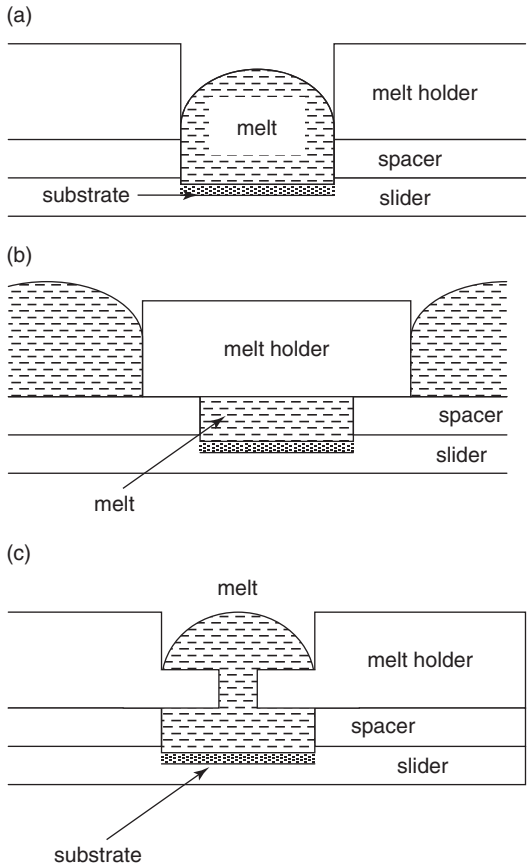
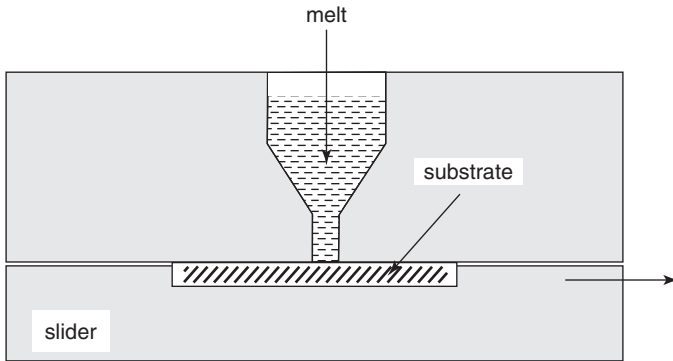
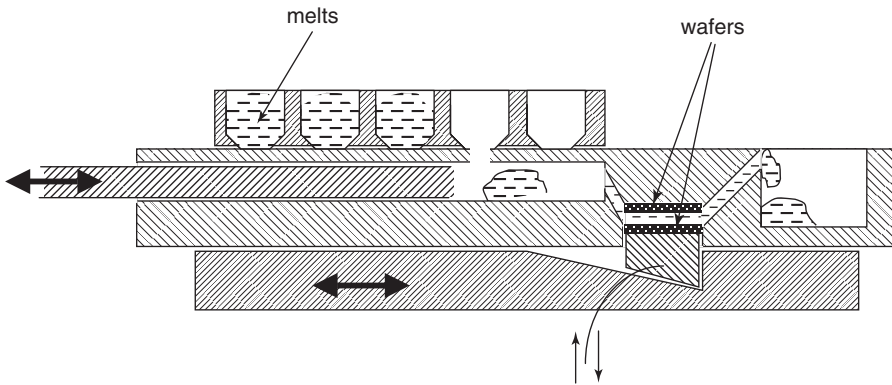


Figure 4.10 Slideboat configurations: (a) conventional; (b) confined; and (c) baffled melt holder. (After Leung and Schumaker, 1982)

is shown in Figure 4.6. In Figure 4.7 a slideboat includes source wafers that float on top of the melt and weights on top of the source wafers. Figure 4.8 is a variation of the slideboat where the substrate holder component remains stationary and the slideboat base is moved to roll the melts over the substrate. Figure 4.9 is an example of a boat made of two different materials. The slideboat body is made of sapphire which has a lower



**Figure 4.11** Slideboat with narrowed melt contact for epitaxy of extremely thin epilayers. From Alverov *et al.* (Alverov *et al.*, 1985) and reproduced in Kuphal (Kuphal, 1991)



**Figure 4.12** LPE piston slideboat. (After Alverov *et al.*, 1978)

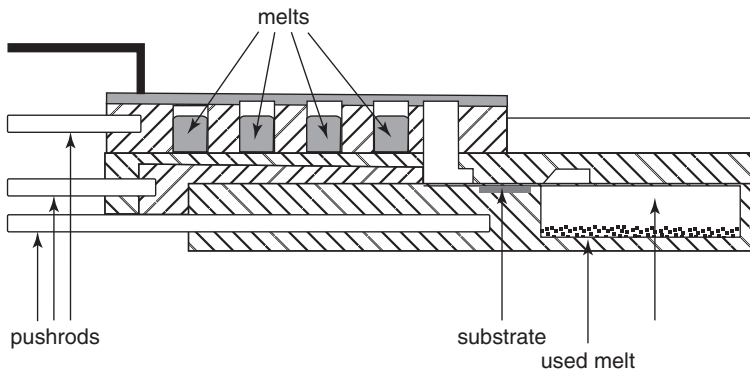


**Figure 4.13** LPE piston slideboat. From Chandvankar *et al.* (Chandvankar *et al.*, 1998)



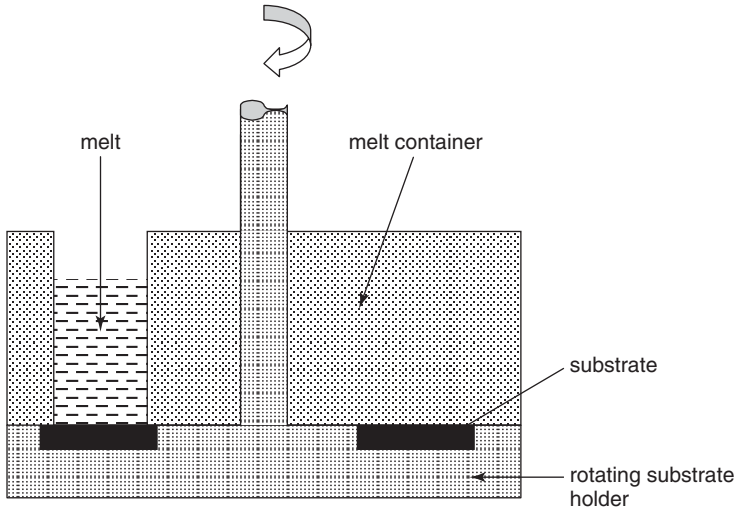


**Figure 4.14** Rotating melt LPE system. (After Almgren and Csigi, 1980)

thermal conductivity than graphite. This design reduces temperature variations around the perimeter of the substrate which contribute to unwanted 'edge' growth effects. Sapphire liners have been used for similar purposes. Figure 4.10 shows various slideboat configurations for aliquoting the melt and controlling slider-induced convection. Figure 4.11 depicts a slideboat design for limiting the contact time of melt with substrate in order to reproducibly grow very thin layers. Figure 4.12 is a piston slideboat for the same purpose of controlling a short contact time between the melt(s) and substrate(s). A somewhat more elaborate version of the piston slideboat is shown in Figure 4.13. Methods of effecting short contact times for thin layer growth have been implemented in various rotating crucible LPE boats, an early version of which is shown in Figure 4.14.

## 4.5 FURNACES AND HEATING

LPE systems normally utilize a tube furnace with a cylindrical bore in which is inserted a long tube in which is situated the crucible or slideboat. There are two approaches to furnace selection. In the more commonly used method, a well-insulated furnace with a large thermal mass is used (Figure 4.15a). A good choice of furnace is a three-zone furnace with a total length on the order of 1 m and a central zone with a very flat temperature profile over about 50 cm. The bore of the furnace depends on the slideboat size, but typically ranges from 25 to 100 mm. The independently controlled end zones compensate for heat loss and are adjusted to give a flat temperature profile over the length of the slideboat. The high thermal mass dampens temperature fluctuations but limits the rate of heating or controlled cooling to less than about  $1\text{ }^{\circ}\text{C min}^{-1}$ , although more rapid cooling to quench melts can be achieved by rolling the wheeled furnace away from the slideboat and directing a cooling fan on the exposed section of the furnace tube containing the slideboat (see below). This type of furnace is usually resistively heated using nichrome heating elements and consumes on the order of 500–3000 W during

(a)



(b)



**Figure 4.15** Horizontal tube furnaces. (a) Typical horizontal LPE furnace (CVD Equipment Corp., Ronkonkoma, NY, USA). (b) Clamshell type furnace (Applied Test Systems, Butler, PA, USA)

heat-up. An additional annular ‘heat pipe’ isothermal furnace linear (Advanced Cooling Technologies, Inc., Lancaster, PA, USA) that shrouds the tube can be used to provide very flat temperature ( $\pm 0.1^\circ\text{C}$ ) profiles along the length of the furnace (and slideboat) and further dampen temperature oscillations, but again this limits the range of controlled heating and cooling rates. A ‘clamshell’-type furnace (Figure 4.15b) can be used to access the heated zones, which if nothing else facilitates repair of faulty heating elements and positioning of the slideboat, slidebar, and thermocouples.. In the second approach, a furnace with low thermal mass is used. This type of furnace is typified by the transparent ‘gold’ furnace shown in Figure 4.16. An outer fused silica tube is coated with a reflective gold film that reflects the infrared radiation generated by heating elements between the outer tube and the inner tube that contains the slideboat. A controller with fast sampling time must be used to regulate temperature. One advantage of a transparent furnace is that the slideboat (and melts) can be viewed during the operation of the furnace, which can be used to check the position of the boat and slidebar, and observe the melting point of the metal charges of the melts.

The furnace is usually outfitted with slotted wheels or linear bearings so that the furnace can travel along rails or shafts, and by which the furnace can be rolled on or off the fused

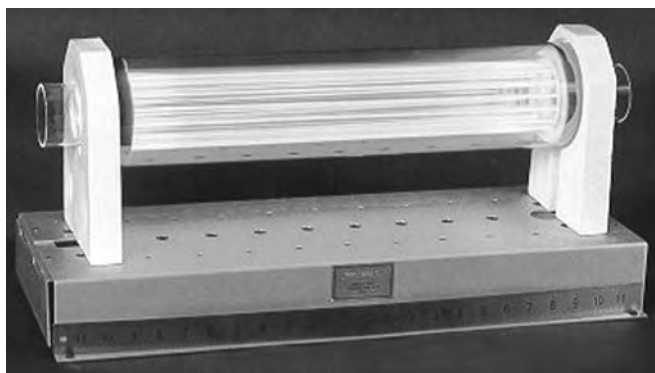


**Figure 4.16** Transparent ‘gold’ furnace (Trans Temp, Thermcraft, Inc., Winston-Salem, NC, USA)

silica tube. The slideboat can be seated on a carriage or crib fashioned from fused silica rods, so that it is centered near the axis of the silica tube and does not directly contact the fused silica tube. Fused silica rods can serve as stops to hold the slideboat. Alternatively, a cantilever anchored to the end flange that seals the tube can be used to suspend the slideboat.

Some specialized LPE systems have used optical or infrared heating or resistive heating elements placed in close proximity to the crucible or slideboat (Peter *et al.*, 1995). These methods usually rely on a temperature-gradient induced mass transport, rather than a programmed transient cooling of the melt, to effect growth. In such cases, a rectangular cross-sectioned fused silica or a steel chamber with fused silica windows is more conducive than the circular cross-sectioned fused silica tubes described above.

## 4.6 LPE AMBIENT

The LPE ambient is most always purified hydrogen at near-atmospheric pressure with flow rates ranging from a few  $\text{cm}^3 \text{min}^{-1}$  to hundreds of  $\text{cm}^3 \text{min}^{-1}$ . Higher hydrogen flow rates may be useful in maintaining low oxygen and water vapor levels in the system, however, the hydrogen flow and its cooling action on the boat may also result in nonuniform slideboat temperatures. Hydrogen prevents oxidation of the graphite slideboat, the melts and substrates. There is little precedence for performing LPE under vacuum, in which evaporation of melts and dopants could be problematic. In this regard, besides the reducing action of hydrogen, its main advantage is that it can be purified by diffusion through a heated palladium membrane to remove oxygen and water. Molecular sieves, catalytic converters, or cold traps can be used to reduce oxygen/water vapor levels, but are not as effective and reliable as purification by Pd diffusion. Another option involves bubbling an inert gas through a molten bath of an indium–gallium–tin liquid metal alloy to remove oxygen and water vapor. As hydrogen presents the biggest safety hazard in LPE (see below), the use of nitrogen, argon, helium or forming gas (hydrogen diluted in nitrogen or argon) can also be considered. The use of forming gas in LPE of GaAs (Czech *et al.*, 1999) and silicon (Bergman and Kurianski, 1993; Shi *et al.*, 1995) has been reported. Oxidation of the silicon substrate is especially problematic in silicon LPE as surface oxides impede wetting of the substrate by the melt (Weber and Blakers, 1995), but the

addition of reducing agents (e.g. aluminum or magnesium) to the melts can help reduce surface oxides and promote better wetting. The amount of oxygen and water vapor in the ambient affects the impurity concentration and electrical properties of the epitaxial layer through a complex set of reactions involving silicon (from the fused silica) (Hicks and Greene, 1971; Weiner, 1972; Greene, 1973; Kan *et al.*, 1977). Reichert *et al.* (Reichert *et al.*, 2004) describe an LPE system for the growth of high-purity GaAs epilayers for application to blocked impurity band (BIB) photodetectors that have extremely stringent purity requirements ( $<10^{12} \text{ cm}^{-3}$ ).

The levels of oxygen and water vapor that can be tolerated impact the design and cost of the LPE system, since a large fraction of the LPE system cost is incurred by means used to seal and evacuate the system, to provide leak-free interconnections and supply the crystal growth ambient with purified gases. At one extreme, an LPE system with a horizontal tube sealed with compression fittings and using dried forming gas as an ambient represents a very inexpensive epitaxy system. For certain applications, such as the growth of nonaluminum-containing III-V compounds and where background impurity levels are not critical, such a system may be adequate. At the other extreme, an LPE system with high-vacuum components including loadlocks, turbomolecular pumps, Pd-diffusion membrane purification to supply ultra-pure hydrogen, a glove box, and a residual gas analyzer can approach in cost that of an MBE system. Thus, the design and total cost of an LPE system will be determined in part by an assessment of the required electrical properties of the epilayers with respect to their susceptibility to oxygen and other impurities (silicon, carbon).

## 4.7 TUBES, SEALING AND GAS HANDLING

As with many semiconductor processing systems such as for diffusion, annealing, chemical vapor deposition, fused silica (often somewhat inaccurately referred to as 'quartz') tubes offer a clean environment for high-temperature processing. For higher temperature ( $>1200^\circ\text{C}$ ) LPE, such as for silicon carbide epitaxy, mullite or alumina tubes can be used. Although the tolerances of specified diameters of fused silica tubes often exceeds that needed to assure leak-free sealing, suppliers can select tubes from their inventory which more closely match the dimensions of a particular system. In some cases, a metal annulus with a bore corresponding to the bore of the endcap fitting can be sent to the supplier to assist in selecting the best diameter fused silica tubes. The tubes can be cleaned in a mixture of HF and  $\text{HNO}_3$ . Over time, with high temperature exposure the tubes will sag. This can partly be ameliorated if the tube is periodically rotated to even out any sag. The deviation of the tube may first be noticed by the furnace scraping as it is rolled along the tube.

The fused silica tube can be sealed at one end, in which case the gas inlet and outlet are made through a flange ported with inlet and outlet tubes, and the inlet is via a long tube that introduces the gas flow at the opposite end.

## 4.8 CONTROLLERS AND HEATING

The furnace power to the heating elements for each zone is provided by silicon controlled rectifies (SCR) circuits.

Commercial microprocessor-based programmable controllers can be used for controlling furnace temperatures. It is especially convenient if the controllers have a

self-tuning proportional integral derivative (PID) control feature. A three-zone furnace can be controlled by three controllers, with the two endzone controllers slaved to the middle zone controller which executes the time–temperature program. Most typical LPE temperature schedules can be simply programmed into the controller using a series of times and temperature setpoints. The controllers should have over-temperature alarms to protect the furnace from overheating in the event of a thermocouple malfunction. Another alternative is to use LabVIEW® or a similar system for personal computer (PC)-based control. This can also add automation, data acquisition and data logging for relevant LPE parameters (time–temperature readings, gas flow rates, slidebar positions, etc.), as well as control algorithms for improved reproducibility (Patel *et al.*, 1998).

#### 4.9 TEMPERATURE MEASUREMENTS AND OTHER INSTRUMENTATION

Thermocouples (e.g. type K, type R or type S) are the preferred method of temperature measurement, providing precision of  $\pm 0.1$  °C in the temperature range of 500–1100 °C. A common configuration uses a thermocouple on the outside tube in the center of the heated zone of the furnace to control the furnace heating, i.e. this thermocouple is used as the input to the controller for the furnace power. A second thermocouple sheathed in a fused silica tube is embedded in the boat. This thermocouple is considered to reflect the melt temperature. Typically, there will be some constant temperature difference between the thermocouple on the outside of the tube and the thermocouple embedded in the slideboat. The thermocouples are sheathed in fused silica tubing. The thermocouple in the slideboat is inserted through a compression fitting and can be moved along the length of the slideboat to provide a temperature profile. Normally, a flat ( $\pm 0.1$  °C) temperature profile is desired, although in principle, a nonuniform temperature profile could also be used to effect growth. The measured temperature profile of the slideboat will depend on the position of the slideboat with respect to the furnace and the tube ends, the position of the slidebar, the amount of melts contained in the slideboat, and the ambient flow which will tend to cool the slideboat. All of these effects should be considered when tailoring a slideboat temperature profile.

Fiber optic temperature sensors and emissivity imagers may provide a less invasive means for measuring temperature distributions in LPE slideboats. The accuracy of fiber optic sensors is slightly less than thermocouples, but precision can be comparable. A slideboat could be probed with ten or twenty multiplexed fiber optic sensors, with little perturbation of the temperature profile. Westphal *et al.* (Westphal *et al.*, 1994) described a precision resistance temperature detector (RTD)-based temperature measurement to control melt temperatures to better than  $\pm 0.005$  °C in an LPE system for MCT (mercury cadmium telluride) materials. Some efforts in providing real-time monitoring of the LPE process are noteworthy. In work that may have some relevance to LPE, Ujihara *et al.* (Ujihara *et al.*, 2002) developed an *in situ* measurement technique for determining solute and temperature distributions in alloy solutions using an infrared camera and an X-ray fluorescence spectrometer. A residual gas analyzer or oxygen/water vapor sensor on the system exhaust for real-time measurement of moisture and oxygen during the LPE process is often useful for material systems that are sensitive to oxygen, or where volatile melt components play an important role. Chang *et al.* (Chang *et al.*, 1983) reported an

*in situ* method for electrochemical monitoring and control of oxygen in GaAs LPE using an yttria-stabilized zirconia electrolyte in contact with the gallium melt. Inatomi *et al.* (Inatomi and Kuribayashi, 1990, 1991; Inatomi *et al.*, 2005) described a method to observe the solid–liquid growth interface in GaP LPE using an infrared imager (with interferometer) and viewing from the backside of the semi-transparent GaP substrate during LPE. Images of the morphology of the LPE layer, and estimations of dissolution and growth rates were feasible.

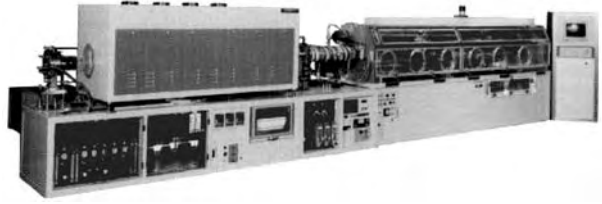
#### 4.10 SAFETY

The LPE method is a comparatively safe technique. The chief potential hazard is a system leak that results in the explosive combination of hydrogen and air. According to the circumstances and the size of the breach in the system sealing, the hydrogen leak may be relatively harmless, or may result in an explosion with the approximate force of a shotgun blast. The actual danger is from flying fragments of the fused silica tube and other furnace parts. Inexpensive hand-held hydrogen leak detectors can be used to check the integrity of the system prior to and during its operation. The hydrogen generator or purification unit also generally includes a hydrogen detection device with automatic shutoff. An attractive recent development is hydrogen generators that generate hydrogen by electrolysis of water contained in a small reservoir and provide low-pressure hydrogen only as needed. These devices eliminate the need for storage and handling of high-pressure cylinders of hydrogen. Flame arrestors should be used with hydrogen cylinders. To mitigate the hazards of an explosion or hydrogen flame, the LPE system can be enclosed in a box made with a steel angle bracket frame and Lexan<sup>®</sup> walls, and with hinged or sliding side members to permit access to the furnace system. A metal grating on top of the enclosure permits natural convective cooling of the furnace. Commercial systems usually feature a metal enclosure for the entire LPE system. A hydrogen leak detector in the laboratory should be used to detect entrainment or buildup of hydrogen in the ceiling or other inadequately vented areas. A relief valve set at two or three times the operating pressure should be included near the inlet gas line. Metal walled enclosures need more active ventilation to dissipate heat. The excess hydrogen is vented through the roof or a fume hood to the outside. Whether the hydrogen should be burned as vented depends on the circumstances of the facilities. Toxic components from the melts (such as arsenic) will normally condense and coat cold portions of the tube and exhaust system. Therefore, proper precautions should be taken when cleaning and replacing tubes and tubing.

#### 4.11 PRODUCTION LPE SYSTEMS

The foregoing discussion pertains to homemade or customized horizontal slideboat systems suitable for research and small-volume production. For large-scale production, commercial LPE systems are available from a number of equipment makers. These systems are generally more instrumented, more automated (solenoid valves, motorized slidebars and furnace positioning), and have high-vacuum hardware (loadlocks, flanges, turbopumps, residual gas analyzers), but the basic design is similar to the systems described above. Figure 4.17 shows several commercial LPE systems. Table 4.1 summarizes ranges of

(a)



(b)



(c)



(d)



Figure 4.17 (continued)

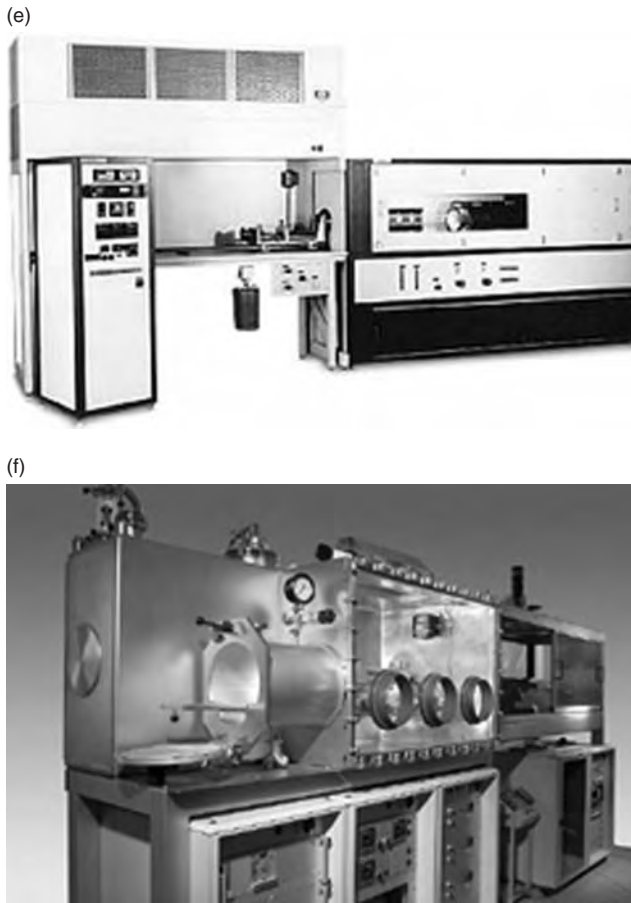


**Figure 4.17** Commercial LPE systems. (a) Koyo Thermosystems Ltd, Nara, Japan; (b) and (c) CVD Corp., Ronkonkomo, NY, USA; (d) Tek-Vac, Brentwood, NY, USA; (e) General Air Corp., Chatsworth, CA, USA; (f) Cyberstar, Echirrolles, France

typical specifications and performance for commercial LPE systems made for production of semiconductor optoelectronic devices.

More substantial departures from the standard horizontal slideboat in a fused silica tube mounted in a tube furnace have also been developed with the aim of a semi-continuous (as opposed to batch) LPE process. Akai *et al.* (Akai *et al.*, 1976) described a production LPE system (Figure 4.18) where a series of substrates are successively positioned under melts supplied with a solid source of material (or replenished from the vapor phase), and steady-state growth is effected by imposition of a temperature gradient across each melt. Mauk *et al.* (Mauk *et al.*, 2000) described a similar LPE system (Figures 4.19–4.21) with a modular design that operates in a semi-continuous mode using steady-state temperature-gradient induced growth on 75-mm diameter substrates. Unlike most LPE systems, the slideboat is enclosed in a stainless steel chamber, rather than a fused silica tube.



**Table 4.1** Typical range of specifications and performance for commercial LPE systems

Specification	Range
Tube diameter (mm)	60–120 mm
Tube length (cm)	30–50 cm
Furnace (zones)	3–5 zones
Central flat zone (mm)	400–600 mm
Hydrogen purity (ppb unpurity)	<50
Max. temperature (°C)	11-50-1300
Power (W)	3000–12 000
Pushrod/slidebar speed (mm s <sup>-1</sup> )	0.06–60
Temperature accuracy (°C)	±0.5
Hydrogen flow rate (lpm)	0–5
Nitrogen flow rate (lpm)	0–5
Leak rate (cm <sup>3</sup> mln <sup>-1</sup> )	<10 <sup>-9</sup>
Cooling	Forced air
Venting	6 in. duct

Compiled from literature provided by CVD Equipment Corp. (Ronkonkoma, NY, USA), Cyberstar (Échirolles, France) and Tek-Vac (Brentwood, NY, USA).

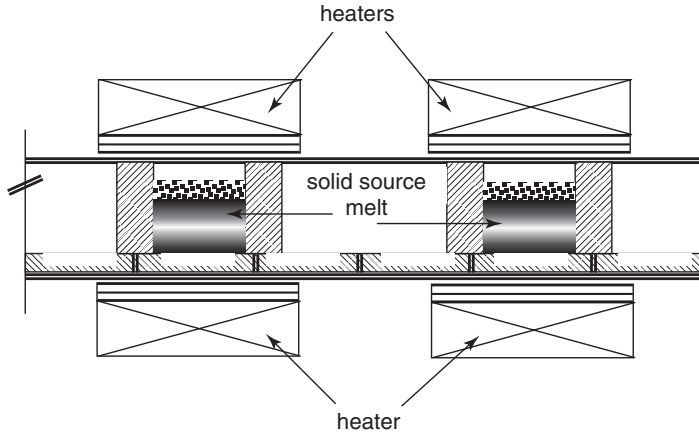


**Figure 4.18** Production LPE system. From Akai *et al.* (Akai *et al.*, 1976)



Figure 4.19 Modular LPE system

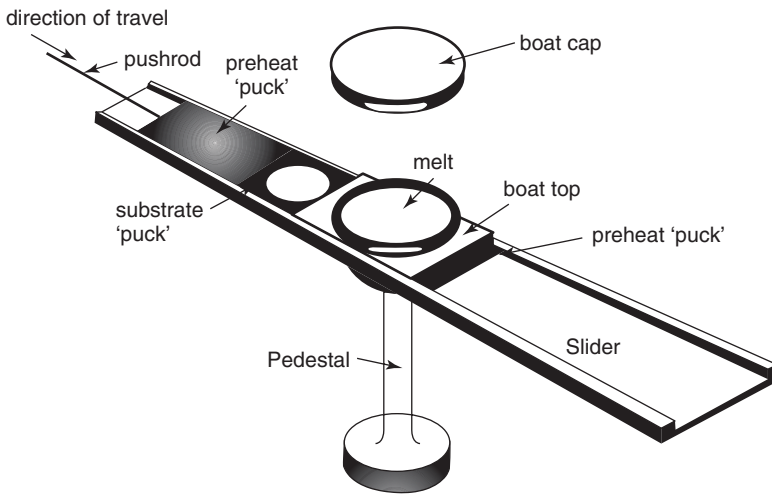
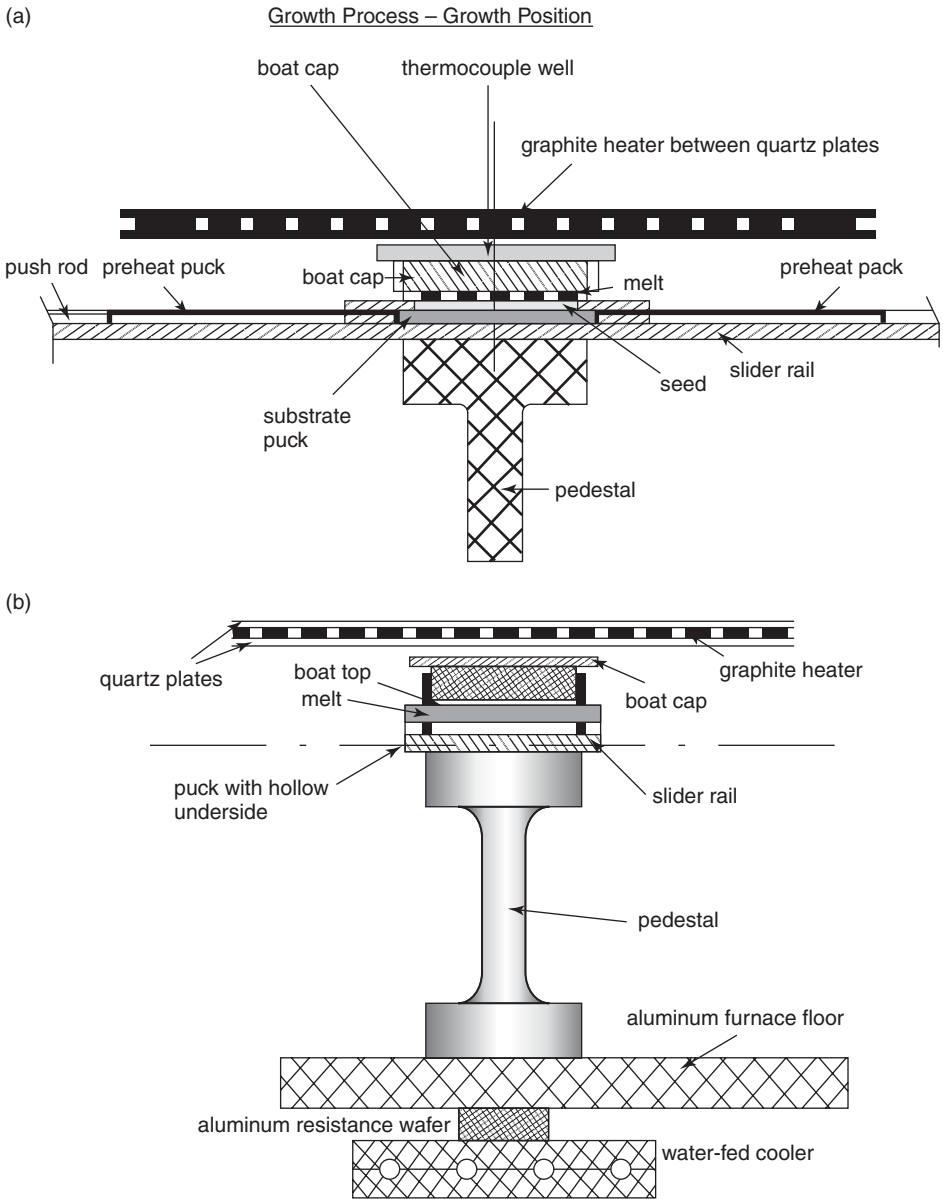


Figure 4.20 Pedestal slideboat in LPE system shown in Figure 4.19 (perspective view)

## REFERENCES

- S.-I. Akai, H. Mori, N. Takahashi and S.-I. Iguchi (1976) Method and apparatus for production of liquid phase epitaxial layers of semiconductors, US Patent 3 933 528.
- D.W. Almgren and K.I. Csigi (1980) GaAlAs/GaAs solar cell process study, NASA-Langley Report CR-3361.
- ZH.I. Alverov, V.M. Andreev, B.V. Egorov, S.G. Konnikov and V.M. Lantratov (1978) Fabrication of AlGaAs-GaAs heterostructures by selective liquid-phase epitaxy, *Sov. Phys. Tech. Phys.* **23**, 209–214.
- ZH.I. Alverov, D.Z. Garbuzov, I.N. Arsent'ev, B.YA. Ber, L.S. Vavilova, V.V. Krasovskil and A.V. Chudinov (1985) Auger profiles of the composition and luminescence studies of liquid phase grown InGaAs heterostructures with  $(1.5-5) \times 10^{-6}$  active regions, *Sov. Phys. Semiconduct.* **19**, 679.



**Figure 4.21** Modular LPE system slideboat/pedestal: (a) side view; (b) end view

J.K. Arch, E. Bauser, S. Kolodinski and J.H. Werner (1992) Characterization of liquid phase epitaxy silicon for thin-film solar cells, 11th *European Community Photovoltaics Solar Energy Conference*, Harwood, Chur, Switzerland, 1993, 1047–1052.

B.J. Baliga (1986) Silicon liquid phase epitaxy: a review, *J. Electrochem. Soc.* **133**, 5C–14C.

R. Bergmann and J. Kurianski (1993) The role of hydrogen in silicon liquid phase epitaxy, *Mater. Lett.* **17**, 137–140.

- K.S.A. Butcher, L. Mo, D. Alexiev and T.L. Tansley (1995) Growth of high purity liquid phase epitaxial GaAs in a silica growth system, *J. Cryst. Growth* **156**, 361–367.
- S.S. Chandvankar, A.P. Shah and B.M. Arora (1998) Doping and surface morphology of  $\text{Al}_x\text{Ga}_{1-x}\text{As}/\text{GaAs}$  grown at low temperature by liquid phase epitaxy, *J. Cryst. Growth* **186**, 329–337.
- S.C. Chang, G.Y. Meng and D.A. Stevenson (1983) In Situ electrochemical monitoring and control of oxygen in liquid phase epitaxial growth of GaAs, *J. Cryst. Growth* **62**, 465–474.
- L.-J. Chen, C.-C. Wan and C. Lin (1992) Simulation of the growth rate and layer thickness for liquid phase epitaxy (LPER) under slider-induced convection, *J. Cryst. Growth* **121**, 322–334.
- E. Czech, G. Götz, G. Cristiani and M. Konuma (1999) Residual impurities in high purity GaAs layers grown by liquid phase epitaxy in  $\text{H}_2$ -Ar atmosphere, *J. Cryst. Growth* **198/199**, 1087–1091.
- C. Eck and H. Emmerich (2004) Models for liquid phase epitaxy preprint 146, spp 1095 *Analysis, Modeling and Simulation of Multiscale Problems*, University of Erlanger (<http://www.am.uni-erlangen.de/~eck/publications.html>).
- Y.Z. Gao, H. Kan, F.S. Gao, X.Y. Gong and T. Yamaguchi (2002) Improved purity of long-wavelength InAsSb epilayers grown by melt epitaxy in fused silica boats, *J. Cryst. Growth* **234**, 85–90.
- R.C. Goodfellow (1986) Semiconductor materials and structures for optical-communication devices in *Crystalline Semiconducting Materials and Devices*, P.N. Butcher, N.H. March and M.P. Tosi, eds. Plenum, New York.
- P.B. Greene (1973) The kinetics of silicon contamination of liquid gallium in silica boats, *J. Phys. D Appl. Phys.* **6**, 1550.
- H.G.B. Hicks and P.D. Greene (1971) Control of silicon contamination, *Proceedings of the 3rd International Symposium on GaAs*, Institute of Physics, London, 92.
- Y. Inatomi and K. Kuribayashi (1990) Direct observation of LPE growth in GaP, *J. Cryst. Growth* **99**, 124–127.
- Y. Inatomi and K. Kuribayashi (1991) Real-time measurement of LPE growth rate in GaP, *J. Cryst. Growth* **114**, 380–388.
- Y. Inatomi, M. Kikuchi, R. Nakamura, K. Kuribayashi and I. Jimbo (2005) In Situ observation for semiconductor solution growth using near-infrared microscope, *J. Cryst. Growth* **275**, 193–200.
- H. Kan, M. Ishii and W. Susaki (1977) Influence of oxygen in ambient gas on LPE GaAs, *Jpn. J. Appl. Phys.* **16**, 461–464.
- M. Kimura, A. Tanaka and T. Sukegawa (1991) Convection phenomenon during dissolution of silicon in an indium solution, *J. Cryst. Growth* **109**, 181–185.
- E. Kuphal (1991) Liquid Phase Epitaxy, *Appl. Phys. A* **52**, 380–409.
- S.Y. Leung and N.E. Schumaker (1982) simulation of slider-induced convection in horizontal LPE slider system, *J. Cryst. Growth* **60**, 421–433.
- K. Lin, P. Dold, H. Figgemeier and K.W. Benz (2005) Numerical modeling and investigation of liquid phase epitaxy of  $\text{Hg}_{1-x}\text{Cd}_x\text{Te}$  infrared detectors, *Crystal Res. Technol.* **40**, 832–838.
- M.G. Mauk, Z.A. Shellenbarger, P.E. Sims, W. Bloothoofd, J.B. McNeely, S.R. Collins, P.I. Rabinowitz, R.B. Hall, L.C. DiNetta and A.M. Barnett (2000) Development of a modular, large-scale, high-throughput semicontinuous-mode liquid-phase epitaxy system, *J. Cryst. Growth*, **211**, 411–415.
- M.G. Mauk and J.P. Curran (2001) Electro-epitaxial lateral overgrowth of silicon from liquid-metal solutions, *J. Cryst. Growth* **225**, 348–353.
- H.T. Minden (1974) A quartz sliding boat for GaAs liquid phase epitaxy, *J. Cryst. Growth* **23**, 79–80.
- L. Mo, K.S.A. Butcher and D. Alexiev (1996) Effect of crucible materials on impurities in LPE GaAs, *J. Cryst. Growth* **158**, 403–408.
- H. Nelson (1930) Epitaxial growth from the liquid state and its application to fabrication of tunnel and laser diodes, *RCA Rev.* **24**, 603–615.

- S.A. Patel, C.B. Chaudhari and D.K. Gautam (1998) In Situ monitoring of crystal growth in LPE using microprocessor, *IETE Tech. Rev.* **15**, 21–26.
- K. Peter, G. Willeke and E. Bucher (1995) Rapid growth of high quality crystalline silicon by a novel temperature gradient liquid phase epitaxy (LPE) technique, 13th European Photovoltaic Solar Energy Conference, Stephens, Bedford, 379–381.
- L.A. Reichert, J.W. Beeman, B.L. Cardoza, N.M. Haegel, E.E. Haller, G. Jacob and R. Katterloher (2004) GaAs BIB photodetector development for far-infrared astronomy, *Proc. SPIE* **5543**, 231–238.
- C.L. Reynolds Jr and M.C. Tamargo (1984) LPE apparatus with improved thermal geometry, US Patent 4 470 368.
- R. Sankaran, R.L. Moon and G.A. Antypas (1976) Liquid phase epitaxial growth of InGaAs on InP, *J. Cryst. Growth* **33**, 271–280.
- G.J. Scilla, L.F. Eastman, R.L. Henry and E.M. Swiggard (1977) The effects of baking time on LPE InP: purity and morphology, *Proceedings of the 6th International Symposium on GaAs and Related Materials*, Institute of Physics, London, 35–40.
- Z. Shi, W. Zhang, G.F. Zheng, J. Kurianski, M.A. Green and R. Bergmann (1995) The growth and properties of liquid phase epitaxial silicon in a forming gas ambient, *J. Cryst. Growth* **151**, 278–284.
- T. Sukegawa, M. Izawa, H. Katsuno, A. Tanaka and M. Kimura (1990) Growth of GeSi thick alloy layers by the yo-yo solute feeding method, *J. Cryst. Growth* **99**, 274–277.
- M.C. Tamargo and C.L. Reynolds (1981) Use of sapphire liners to eliminate edge growth in LPE (Al, Ga) As, *J. Cryst. Growth* **55**, 325–389.
- T. Ujihara, K. Fujiwara, G. Zazaki, N. Usami and K. Nakajima (2002) Simultaneous in situ measurement of solute and temperature distributions in the alloy solutions, *J. Cryst. Growth* **242**, 313–320.
- K.J. Weber and A.J. Blakers (1995) Prevention of oxide formation during liquid phase epitaxy of silicon, *Appl. Phys. Lett.* **66**, 1243–1245.
- M.E. Weiner (1972) Si contamination in open flow quartz systems for the growth of GaAs and GaP. *J. Electrochem. Soc.* **119**, 496–504.
- G. Westphal, L. Colombo and J. Anderson (1994) The application of advanced sensors to the LPE growth of MCT, *Proc. SPIE* **2228**, 342–348.

# 5 Silicon, Germanium and Silicon-Germanium Liquid Phase Epitaxy

**MICHAEL G. MAUK**

*School of Engineering and Applied Science, University of Pennsylvania, Philadelphia, PA 19101, USA*

---

5.1 Introduction and scope of review	110
5.2 Historical perspective	111
5.3 Basis of silicon and germanium LPE	115
5.3.1 Nucleation of silicon from a molten metal solution	119
5.4 Silicon LPE methods	124
5.4.1 Steady-state methods of solution growth and LPE	125
5.5 Solvent selection	135
5.6 Low-temperature silicon LPE	137
5.7 Purification of silicon for solar cells in an LPE process	138
5.8 Electrical properties of LPE-grown silicon	140
5.9 LPE of Si- and Ge-based alloys	141
5.10 Selective LPE and liquid phase ELO	142
5.11 Solar cells	144
5.11.1 Epitaxial silicon solar cells by LPE	145
5.11.2 Si solution growth on nonsilicon substrates for solar cells	149
5.12 Other applications of silicon and germanium LPE	150
5.13 Conclusions and outlook	151
References	151
Appendix 1. Phase equilibria modeling: The silicon-metal liquidus	166
A1.1 The silicon-metal binary liquidus	168
A1.2 Alloy solvents	168
Appendix 2. Impurities and doping in silicon LPE	171
Appendix 3. Effects of oxygen and water vapor in Si LPE	175
A3.1 Thermodynamics of silicon oxidation	176
A3.2 Silicon passivity and melt reducing agents	178

---

## 5.1 INTRODUCTION AND SCOPE OF REVIEW

This chapter reviews the application of liquid phase epitaxy (LPE) to silicon, germanium, and silicon-germanium alloys. *Epitaxy*—as commonly understood—is the seeded, oriented crystallization of a thin film or thick layer on a crystalline substrate. In order to achieve epitaxial growth, there must exist sufficient crystallographic similarity (i.e. the same or related crystal structure; close lattice constant matching) and chemical compatibility between the seeding substrate and the epitaxial film(s). The epitaxial semiconductor film exhibits a definite crystallographic relationship to the substrate, in most cases more or less mimicking the crystal structure and crystallographic orientation of the substrate. In LPE of semiconductors, semiconductor films are grown on single-crystal ‘monocrystalline’ semiconductor wafers from molten metallic solutions, typically in the temperature range of about 400–1200 °C. Accordingly, in silicon LPE, epitaxial films of silicon are crystallized on silicon wafers by cooling molten metallic solutions saturated with silicon. Common metal solvents for silicon LPE include tin, lead, gallium, indium, aluminum, bismuth, antimony, gold, copper, and mixtures of these metals. Solvent metal components of the melt, as well as any impurities (e.g. phosphorus, boron) either intentionally added to or inadvertently contained in the molten solution, are incorporated into the deposited silicon layer to some degree. Controlled doping of the silicon epitaxial layer over a considerable range of impurity concentrations and using a wide selection of dopants is feasible. Repeated epitaxial growth steps, as conveniently enabled by the so-called ‘slideboat’ LPE technique, can be used to make multilayer semiconductor structures with distinct doping profiles for application to a variety of semiconductor devices.

Completely analogous processes can be used for producing germanium epitaxial structures on germanium wafers, but in fact, germanium LPE is much less developed than silicon LPE. As for commercial importance, silicon and germanium LPE find relatively little application to the production of transistors or other common electronic devices. Instead, silicon and germanium LPE has been investigated for application to solar cells, or for niche semiconductor devices such as photodiodes, power transistors, silicon controlled rectifiers, and thermoelectric converters, as well as for customized epitaxial substrate structures. In the last two decades, the main interest in silicon LPE and related metallic solution growth processes has been for application to silicon solar cells, and more particularly, as a low-cost method of depositing 10–50- $\mu\text{m}$ -thick silicon layers on various types of substrates. The relatively fast growth rates ( $\sim 1 \mu\text{m min}^{-1}$ ) compared with other thin-film deposition techniques; the high deposition efficiency with regard to avoiding extraneous deposition of silicon on surfaces other than the substrate; the comparatively low capital equipment and operating costs; the absence of highly toxic precursors or by-products; and the general high quality of LPE-grown semiconductor material with respect to minority carrier mobilities and recombination lifetimes, are important attributes for solar cell applications. Nevertheless, the realization of economic, high-throughput LPE-based processes utilizing large-area, low-cost substrates remains a technically challenging problem.

On account of potential solar cell applications for silicon LPE, the scope of this chapter is expanded to include, in addition to silicon and germanium LPE, metallic solution growth of silicon and germanium layers on dissimilar substrates such as quartz, metals, ceramics, and glasses. In such cases, the deposited silicon or germanium layers are invariably polycrystalline, and there is generally no epitaxial relationship between the silicon film

and substrate, although hopefully there will be a favorable and pronounced texture, i.e. preferred orientation of grains in the deposited polycrystalline silicon layer, as well as a narrow range of grain sizes. This application of LPE or LPE-derived processes to other kinds of substrates represents a considerable departure from the traditional practice of epitaxy wherein homoepitaxial or heteroepitaxial single- or multilayered device structures are formed on polished, meticulously cleaned, low-defect, monocrystalline semiconductor wafers. For the same reasons, it is useful to also review epitaxial growth on polycrystalline (or ‘multicrystalline’) silicon substrates such as those cut from cast silicon ingots or formed as sheets, in which case, the grain structure of the epitaxial layer generally replicates that of the substrate. In this case, a low-cost metallurgical-grade silicon wafer serves as a substrate for deposition of solar cell-quality silicon films. As such, the use of metallic solutions for depositing silicon on a wide variety of substrates offers a potentially commercially important extension of conventional LPE technology, and has motivated much of the recent work in silicon LPE. In addition to silicon and germanium LPE, the liquid phase epitaxial growth of Si-Ge alloys, which generally exhibit complete solid-phase miscibility and which can be grown by straightforward modification of techniques used for silicon and germanium LPE, is also reviewed. The growth of thick layers of Si-Ge alloys can be used to produce surrogate or customized ‘virtual’ substrates with tuned lattice parameters spanning the lattice constants of silicon and germanium. For example, Sembian *et al.* (Sembian *et al.*, 2000) developed LPE methods to grow thick (25–30  $\mu\text{m}$ ), relaxed SiGe alloy (0–16% Ge content) layers on silicon substrates. Good quality epilayers with low defect densities ( $\sim 10^4 \text{ cm}^{-2}$ ) were achieved by LPE with slow cooling rates ( $20^\circ\text{C h}^{-1}$ ). As germanium is closely lattice-matched to GaAs and AlGaAs, compositionally graded  $\text{Ge}_{1-x}\text{Si}_x$  layers could be advantageous as buffer layers to bridge the lattice mismatch between a silicon substrate and III-V device structure. Moreover, LPE has proven especially well-suited for epitaxial lateral overgrowth (ELO) processes on patterned, masked substrates. ELO can provide many novel device structures for defect filtering, dielectric isolation, ‘buried’ electrodes, and ‘buried’ mirrors to exploit light trapping effects and/or enhance optical coupling efficiency.

## 5.2 HISTORICAL PERSPECTIVE

The application of LPE to silicon- and germanium-based semiconductor devices runs counter to the main currents of semiconductor materials technology. An historical perspective of the development of semiconductor epitaxial growth methods serves to underscore some of the motives for and unique features of silicon and germanium LPE. By and large, the main semiconductor epitaxy techniques were developed in the 1960s and 1970s to exploit heterostructure device concepts, to realize device structures that could not be made by dopant diffusion, or to overcome limitations imposed by the poor quality of then-available semiconductor wafers. These issues mostly pertained to compound semiconductor optoelectronic devices, and LPE proved crucial in the development of III-V compound semiconductor light emitting diodes (LEDs), lasers, detectors, and solar cells (Kuphal, 1991). On the other hand, and as the following brief historical sketch recounts, these and similar considerations were not critical issues in silicon semiconductor technology, and the impetus to develop analogous LPE processes for silicon (or germanium) was generally lacking.



Silicon vapor phase epitaxy, or more generally, silicon chemical vapor deposition (CVD), was successfully demonstrated in the 1950s. Silicon CVD is based on pyrolysis reactions of volatile silicon-containing compounds. In silicon CVD, a gaseous stream containing silanes, chlorosilanes, or silicon-halogen compounds decompose on a heated silicon wafer to yield silicon adatoms that nucleate and sustain the formation and growth of a silicon film. Epitaxial silicon layers are particularly useful in forming highly doped 'buried' layers in monolithic planar silicon device technology. Silicon CVD technology is well established and remains a standard processing tool for silicon integrated circuits. Epitaxy technology for compound semiconductors, as represented by GaAs and related alloys such as AlGaAs, followed a somewhat different development path. After the advent of silicon CVD, vapor phase epitaxy processes for III-V compounds were investigated in the early 1960s using halide or hydride precursors for the group III and group V components. However, the hydride or halide vapor phase growth of Al-containing compounds, especially AlGaAs, proved difficult due in part to the high affinity of aluminum for oxygen. Further, such CVD produces nonstoichiometric GaAs with Ga vacancies and/or As antisite defects that reduce luminescence efficiency. This can be attributed to the 'As-rich' conditions of III-V vapor epitaxy as indicated by the high V/III (e.g. AsH<sub>3</sub>/GaCl) precursor ratios necessary for growth from the vapor phase.

Partly to overcome these limitations, the LPE technique was invented in the mid 1960s and extensively developed in the 1970s for the production of LEDs, laser diodes, detectors, and solar cells. In particular, Al<sub>x</sub>Ga<sub>1-x</sub>As layers could be grown on GaAs substrates from Ga-Al melts saturated with As, and LPE could produce high-quality AlGaAs/GaAs heterostructures with high luminescence efficiency due to the reduction in Ga vacancies and antisite defects associated with the Ga-rich conditions inherent in the growth of GaAs from a Ga melt saturated with As. In addition, the quality of then-available III-V wafers was relatively poor, and in this regard it is significant that LPE can yield epitaxial layers with much lower defect levels than the substrate wafers upon which they are grown. LPE shows a tendency to 'anneal out' threading dislocations originating in the substrate (Moon, 1980). This is critical for optoelectronic devices such as lasers and other 'minority carrier' devices. Subsequently, however, the growth of AlGaAs and a host of other III-V compounds was perfected using metal-organic chemical vapor deposition (MOCVD) and molecular beam epitaxy (MBE), and moreover, the quality of III-V wafers improved greatly. As a consequence, the role of LPE in optoelectronics diminished due to its perceived limitations for control of epitaxial layer thicknesses, doping levels, areal uniformity; as well as difficulties in scale-up to large-diameter substrates, all for which MOCVD and MBE were deemed superior to LPE. To summarize, LPE was originally developed to overcome the limitations of early versions of III-V CVD and the poor quality of III-V substrates then available. Such limitations were not crucial to silicon semiconductor technology in general, nor silicon CVD in particular. Stoichiometric defects are not an issue in elemental semiconductors, and historically heterostructures have not figured prominently in silicon device technology. Further, essentially 'defect-free' silicon wafers have been commercially available for over 30 years. Thus, by this account, it would appear that there has never been a great incentive for development of silicon LPE. Consequently, the application of LPE to silicon warrants some explanation. In fact, an application-specific technical and economic rationale for silicon LPE *can* be made, at least for certain optoelectronic and power devices, solar cells, and other specialized semiconductor technologies.

In addition to the technological and potential cost advantages of LPE already mentioned with regard to solar cell production, some more fundamental characteristics of LPE can be exploited for particular applications. LPE occurs under near-equilibrium conditions with relatively low supersaturations and/or supercoolings compared with other methods of epitaxy. Since departures from equilibrium are a driving force for nucleating and sustaining defects such as dislocations, twins, and stacking faults, this suggests LPE should yield reduced defect densities in epilayers. D'Asaro *et al.* (D'Asaro *et al.*, 1969) showed that silicon LPE could produce epitaxial silicon layers with defect densities an order of magnitude lower than that of the silicon substrate. This is in agreement with similar observations cited above for III-V LPE. Baliga (Baliga, 1986) noted that the relatively low growth temperatures of silicon LPE compared with CVD, and the preferential segregation of impurities to the liquid phase should contribute to superior material quality. Comparisons of lowest feasible growth temperatures for different methods of epitaxy involve many stipulations and qualifications especially with regard to the silicon film quality and degree of crystallinity, and therefore, sweeping generalizations should probably be avoided. Nevertheless, there are numerous reports of silicon LPE implemented at growth temperatures in the range of 280–500 °C, depending on the melt composition (see Section 5.6). In view of common silicon epitaxy temperatures in the range of 600–1200 °C, LPE can be rightly considered a low-temperature method of silicon epitaxy.

As is discussed in more detail in Section 5.5, the most basic consideration for any LPE process is the choice and specific formulation of a metal solvent system. High purity silicon and germanium can be grown from molten metal solutions. The purity of LPE-grown material has been amply demonstrated by work on germanium blocked-impurity-band photodetectors made by LPE where residual donor and acceptor levels of  $5 \times 10^{12} \text{ cm}^{-3}$  and  $5 \times 10^{12} \text{ cm}^{-3}$ , respectively, were achieved (Haller and Beeman, 2002). The use of LPE as a method of purification as well as a method of deposition may prove crucial for silicon solar cell applications. Actually, the attainment of high purity and low growth temperatures are interrelated since the incorporation of impurities in the epilayer generally decreases with growth temperature (Trumbore, 1960; Kresse *et al.*, 1990). For silicon crystallized from molten metals at low temperatures (less than 800 to 1000 °C depending on the melt composition), the segregation coefficient  $k_i$  for an impurity  $i$  generally follows a temperature dependence according to:

$$k_i \equiv \frac{C_i^S}{C_i^L} \quad (5.1a)$$

$$= k_{i,0} \cdot \exp \left[ -\frac{b_i}{T} \right] \quad (5.1b)$$

where  $C_i^S$  is the impurity concentration in the solidified silicon,  $C_i^L$  is the concentration of impurity in the liquid phase,  $T$  is the absolute temperature, and  $k_{i,0}$  and  $b_i$  are positive constants specific to the metal. For many of the metallic impurities in silicon and germanium LPE in the temperature range of 500–1200 °C,  $k$  is very small, often ranging from  $10^{-6}$  to  $10^{-3}$ , but boron with a segregation coefficient close to 1 is a notable and sometimes problematic exception. Thus, dramatic purifications are possible by dissolving an impure silicon feedstock in a molten metal, followed by solidification of the dissolved silicon. The impurities will be retained in the metallic phase, which can be discarded or purified for re-use. With regard to doping, it is also useful to note that tin and lead are

isoelectronic with silicon (all are group IV elements) and are electrically neutral in silicon, acting as neither donors nor acceptors. For uniform doping of thick epitaxial layers, it is advantageous that the segregation coefficient is close to 1 in order to avoid dopant depletion from the melt and/or doping gradients in the silicon. As mentioned, boron (acceptor dopant) and to a lesser extent phosphorus (donor) doping approximate this requirement. On the other hand, simple metallic solution growth techniques will not be adequate to purify silicon for solar cell and other applications due to the high levels of boron and phosphorus in most cheap sources of silicon.

The near-equilibrium growth conditions of LPE also permit control of nucleation for selective modes of growth on masked substrates. In selective epitaxy, openings are defined in a masking layer that coats the substrate. The underlying substrate silicon is exposed at the openings which thus provide sites for preferential epitaxy of silicon, while avoiding nucleation on the masked regions of the substrate. The high growth rate anisotropies exhibited by LPE can be exploited in ELO, wherein the epitaxial layer is selectively seeded in openings of a patterned mask coating a silicon substrate. During subsequent stages of growth, the epilayer laterally overgrows the mask (at least partially), thereby simulating a silicon-on-insulator structure. Selective epitaxy and ELO (Section 5.9) can be used for novel device structures, methods of device isolation, and for incorporating buried electrodes or optical features such as buried mirrors.

The wide selection of dopants available with LPE is an important advantage. Almost any element added to the melt will be incorporated into the epitaxially grown silicon layer. Compared with CVD, MBE, diffusion, or ion implantation, LPE provides a relatively simple means of realizing and studying the effects of various dopants on the electrical, optical, mechanical, and magnetic properties of semiconductors. For example, Scott and Hager (Scott and Hager, 1979) studied indium doping of silicon grown from indium melts by LPE. Indium is a *p*-type dopant in silicon that forms a shallow acceptor level, and indium-doped silicon is of some interest for mid-infrared extrinsic (i.e., optical absorption due to impurity states) photodetectors (Schmid *et al.*, 1983). Unfortunately, indium-doped Czochralski-grown bulk silicon crystals were plagued by microprecipitates and other defects, and the range of indium doping was limited. To evaluate the utility of indium-doped silicon, epitaxial silicon layers were readily made by LPE using indium melts. Along similar lines, Schafer (Schafer, 1981) used solution growth to make thallium-doped silicon for 3–5  $\mu\text{m}$  photodetectors. As another example, LPE has been used to investigate rare earth doping of silicon. Binetti *et al.* (Binetti *et al.*, 1998, 1999) described the erbium doping of silicon grown by LPE from silicon-indium-erbium melts at 950 °C. Enhanced photoluminescence was attributed to erbium doping of the silicon. As a final example, Borshchevsky and Fleurial (Borshchevsky and Fleurial, 1993) used metallic solution growth to produce heavily doped silicon-germanium alloys for thermoelectric applications. An interesting discovery resulting from this work was that a substantial enhancement in doping solubility occurs when the melt contains both group III (acceptors) and group V (donors) dopants.

Metallic solution growth of germanium and silicon actually predates epitaxy techniques using CVD. Some early work showed that bulk silicon crystals could be grown from molten metal solutions (Keck and Broder, 1953; Carman *et al.*, 1954). A metallic solution regrowth process, termed *alloying* or *meltback*, was used to make almost all germanium and silicon diodes and bipolar transistors up until about 1960. In the alloying process, a metal bead is placed on the surface of a germanium wafer. The bead is heated

and upon melting dissolves a portion of the germanium wafer. The molten bead is then cooled, and the dissolved germanium precipitates as an epitaxial film. The regrown germanium is doped with the metal solvent. Thus, *p*-type doping can be realized by using aluminum, gallium, or indium beads, and *n*-type doping using antimony beads. A completely analogous process can be used for forming junctions in silicon wafers. In many respects, the alloying method is essentially an LPE process, although the melt/regrowth cycle of the alloying technique does not add any *new* semiconductor material to the substrate. The alloying technique was made obsolete by planar diffusion processing and CVD. However, the technology generated an extensive base of phase equilibria data for material systems containing silicon, germanium and metals, particularly with respect to solid solubilities of metals in germanium and silicon [compiled by Trumbore (Trumbore, 1960)] and solubilities of germanium and silicon in liquid metals [compiled by Thurmond and Kowalchik (Thurmond and Kowalchik, 1960)]. An analysis of the germanium-metal and silicon-metal phase equilibria also demonstrated that *regular* solution models initially developed by chemists for describing organic or aqueous solutions could also be applied to semiconductor-liquid metal systems, as well as the solid solubility of impurities in silicon and germanium. The experimental phase equilibria data and corresponding solution models derived to describe the data serve as the theoretical basis for silicon and germanium LPE.

### 5.3 BASIS OF SILICON AND GERMANIUM LPE

The silicon-metal (or germanium-metal) binary phase diagram serves as the starting point for developing an LPE process. Figure 5.1 shows a typical eutectic type phase diagram that characterizes many silicon-metal and germanium-metal binary systems. A eutectic point E is the lowest temperature that the liquid solution exists and thus represents the lowest possible temperature from which silicon can be grown. For most of the silicon-metal binaries of interest, the eutectic composition occurs at such a small concentration of silicon that the eutectic point may be assumed to be equal to the melting point of the metal constituent. One exception is the silicon-aluminum binary where the eutectic occurs at  $X_{\text{Si}} = 0.12$  and  $82^\circ\text{C}$  below the melting point of aluminum ( $660^\circ\text{C}$ ). Two salient features of the phase diagram are the (hypereutectic) liquidus (see Appendix 1) and the solidus (see Appendix 2). A hypereutectic region (to the right of the eutectic point E) shown shaded is of main interest. It is bound by a liquidus  $L2$  and a solidus  $S2$ . The liquidus (or, more accurately, the *slope* of the liquidus) determines the feasible temperature range for growth, as well as the growth dynamics, e.g. the growth rate and maximum amount of silicon that can be deposited for a given size melt; and also figures in the stability of the growth process. The solidus  $S2$  determines the degree of metal incorporation into the grown silicon or germanium. The subsequent discussion will focus mostly on silicon, but application to germanium-metal binaries will be obvious. The liquidus  $L2$  indicates the solubility of silicon in molten metal solvent as a function of temperature, and most LPE processes are based on the fact that the silicon solubility in liquid metals increases with temperature. (At sufficiently high temperatures, the binary system is generally a single homogeneous liquid phase, but this should not always be assumed. For example, in silicon LPE with tin-rich melts, immiscible liquid phases are evident. Bismuth-containing melts may also show a tendency for such phase separation.

Melts that separate into layers according to their densities should still produce a uniform epilayer, however, if the melt phases disperse, then the resulting epitaxial layer may exhibit thickness and doping variations. Liquid-phase immiscibility is more likely at low growth temperatures.)

As an example of a typical sequence of events when LPE is based on a transient cooling of the melt, reference is again made to Figure 5.1. Starting at an arbitrary temperature and composition denoted by A, and cooling to point B on the liquidus, the solution is then saturated with silicon. This point can be produced by equilibrating a liquid metal in contact with a silicon solid source at a specified temperature corresponding to point B. Next, the silicon source is separated from the silicon-metal liquid solution. The solution is then supercooled by an amount  $\Delta T$  to a point C. Provided no silicon or other seeding surface is in contact with the liquid solution, the system can be maintained in a nonequilibrium metastable condition of supersaturation, denoted by  $\Delta X_{Si}$ . Too great a supercooling will result in spontaneous nucleation, and the supersaturation will be relieved by precipitation of a silicon-rich solid phase, continuing until the concentration of silicon in the liquid phase reaches a point D. In practice, silicon LPE supercoolings typically range from 1 to 30 °C, and the onset of spurious nucleus depends on cooling rates, melt purity, wetting, and the nucleating potential of the walls of the melt containment vessel or free surfaces of the melt. Under equilibrium conditions, the primarily silicon (99+ %) solid phase will contain metal at a concentration given by the solidus S2 curve as denoted by point F. The metal component may be dissolved in the solid silicon matrix as either substitutional or interstitial impurities. The equilibrium solidus curve thus gives the doping level associated with the use of a particular metal solvent and growth temperature. Analysis of solid-phase solubilities in silicon and germanium grown from liquid metals has been carried out by

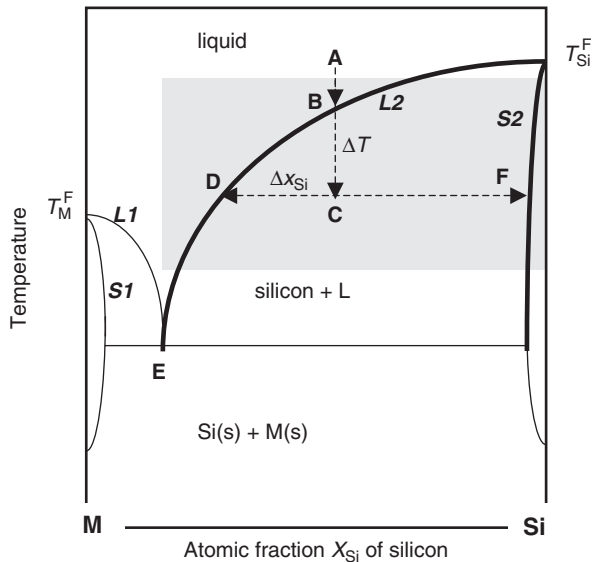


**Figure 5.1** A typical silicon-metal binary phase diagram. A small subsection (shaded) is relevant to silicon LPE.  $T_{Si}^F$  is the melting (fusion) point of pure silicon (1414 °C) and  $T_M^F$  is the melting point of the pure metal. (See text for further explanation)

John (John, 1958), Trumbore *et al.* (Trumbore *et al.* 1959), Trumbore (Trumbore, 1960), Weiser (Weiser, 1960), Lehovec and Slobodskay (Lehovec and Slobodskay, 1964) and Fleurial and Borshchevsky (Fleurial and Borshchevsky, 1990). Actually, as discussed in Appendix 2, somewhat more complex doping behavior is often observed in LPE. Furthermore, as the solid solubility at the growth temperature is higher than that at room temperature, then in principle, as the epitaxial sample is cooled to room temperature, impurities should form precipitates to relieve the supersaturation (Lehovec, 1964). To what extent this occurs depends on many factors such as cooling rates, post-growth annealing, defect densities, and the concentration of other impurities and oxygen. These issues are critical for solar cell applications, especially in cases where a polycrystalline film is deposited and impurities segregate to grain boundaries and dislocations. Nevertheless, a good first approximation is that the epitaxial layer is doped to a level corresponding to the solid solubility at the growth temperature. Figure 5.2 shows a well-known compilation due to Trumbore (Trumbore, 1960), graphically representing the silicon-rich solidus of various silicon-metal binary systems. Most of these data were determined by measuring the metal content of bulk ( $\sim\text{cm}^3$ ) silicon crystals slowly grown ( $\sim\text{days}$ ) from a metal-silicon solution at a specified temperature by an imposed temperature-gradient ( $\sim 10^\circ\text{C cm}^{-1}$ ), and thus should closely approximate equilibrium values of the solubility of a metal in silicon at the specified temperature. These data can be generalized for multi-component liquid phases and nonequilibrium growth conditions using the phase equilibria and doping models presented in Appendix 2.

Phase equilibria models for silicon-metal or germanium metal melts are well established (Thurmond and Kowalchik, 1960; Kozlovskya and Rubinstein, 1962; Stringfellow and Greene, 1970; Petrusheveskii and Gel'd, 1971; Stringfellow, 1971; Girault *et al.*, 1977; Sebkova and Beranek, 1983; Bonnet *et al.*, 1989; Fleurial and Borshchevsky, 1990; Trah, 1990; Bergman *et al.*, 1992; Sudavtsova and Kudin, 2001; Yoshika and Morita, 2005). As derived in Appendix 1, for a silicon-metal binary system, the liquidus (which relates the atomic fraction  $X_{\text{Si}}$  of silicon in the molten metal-silicon binary phase as a function of temperature  $T$ ) is given implicitly by:

$$-L_{\text{Si}} \frac{T_{\text{Si}}^{\text{F}} - T}{T_{\text{Si}}^{\text{F}}} - \int_T^{T_{\text{Si}}^{\text{F}}} \Delta C_{\text{Si}} dT + T \cdot \int_T^{T_{\text{Si}}^{\text{F}}} \frac{\Delta C_{\text{Si}}}{T} dT = RT \ln \gamma_{\text{Si}}^{\text{L}} + RT \ln X_{\text{Si}} \quad (5.2)$$

where  $L_{\text{Si}}$  is the latent heat of fusion for silicon at the melting point of silicon,  $T_{\text{Si}}^{\text{F}}$  is the melting point of pure silicon,  $\Delta C_{\text{Si}}$  is the difference in molar heat capacities between solid and liquid silicon  $\Delta C_{\text{Si}} = C_{\text{Si}}^{\text{L}} - C_{\text{Si}}^{\text{S}}$ , and  $\gamma_{\text{Si}}^{\text{L}}$  is the activity coefficient of silicon in the liquid phase which is a measure of the nonideality of the solution. For ideal solutions  $\gamma_{\text{Si}}^{\text{L}}$  is equal to 1.

For a quasi-regular binary solution:

$$RT \ln \gamma_{\text{Si}}^{\text{L}} = (a_{\text{Si-M}} - b_{\text{Si-M}} \cdot T)(1 - X_{\text{Si}})^2 \quad (5.3)$$

At low temperatures where the solution is dilute in silicon ( $X_{\text{Si}} \rightarrow 0$ ) then:

$$RT \ln \gamma_{\text{Si}}^{\text{L}} \cong (a_{\text{Si-M}} - b_{\text{Si-M}} \cdot T) \quad (5.4)$$

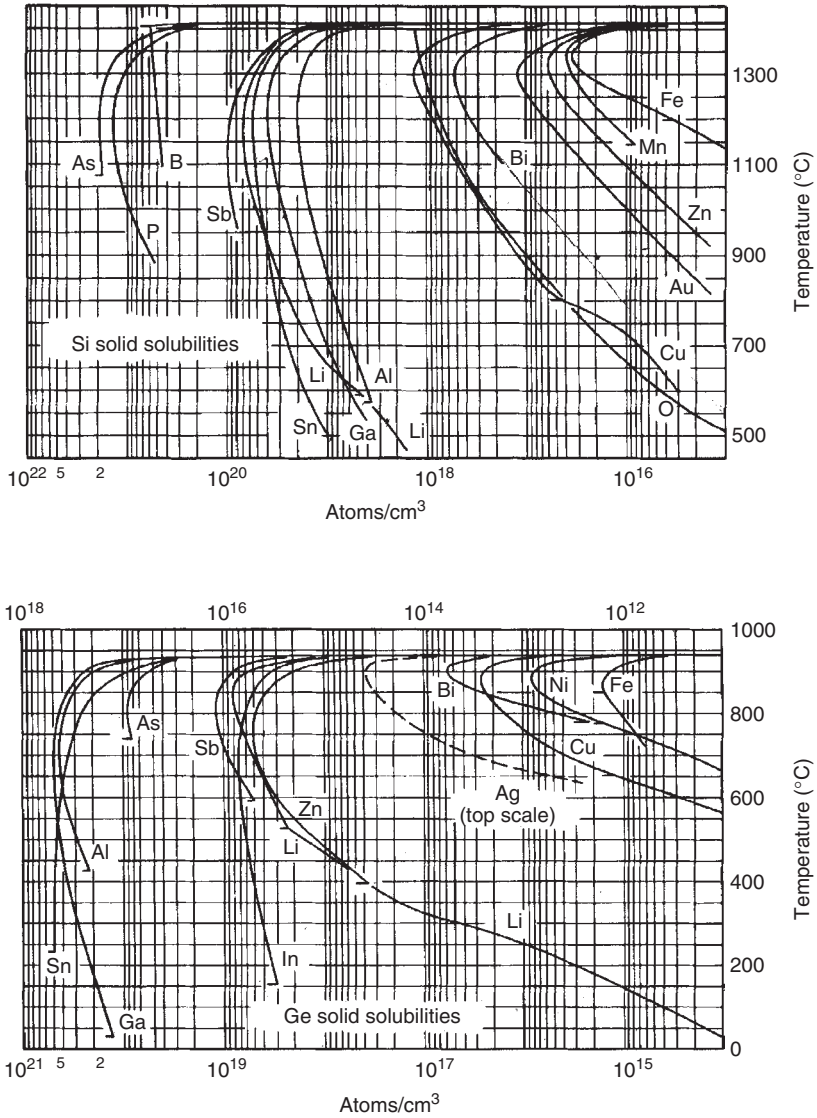


**Figure 5.2** Solid solubilities of metals in silicon as a function of growth temperature. Reprinted from *The Bell System Technical Journal*, Solid solubilities of impurity . . . , XXXIX, Copyright (1960) John Wiley & Sons Inc.

so that (neglecting corrections associated with  $\Delta C_{Si}$ ):

$$X_{Si} = X_0 \cdot \exp\left(-\frac{L_{Si} + a_{Si-M}}{RT}\right) \tag{5.5}$$

with

$$X_0 = \exp\left(\frac{L_{Si} + b \cdot T_{Si}^F}{RT_{Si}^F}\right) \tag{5.6}$$

The quantity  $(L_{\text{Si}} + a_{\text{Si-M}})$  may be interpreted as the molar heat of solution  $\Delta H^{\text{soln}}$  and represents the enthalpy change when silicon is dissolved in the liquid metal, in which case:

$$X_{\text{Si}} = X_0 \cdot \exp\left(-\frac{\Delta H^{\text{soln}}}{RT}\right) \quad (5.7)$$

Under these approximations and assumptions, the slope  $m$  of the liquidus is thus:

$$m \equiv \frac{dT}{dX_{\text{Si}}} = \frac{1}{X_{\text{Si}}} \cdot \frac{RT^2}{(L_{\text{Si}} + a)} = \frac{e^{\Delta H/RT}}{X_0} \cdot \frac{RT^2}{(L_{\text{Si}} + a)} \quad (5.8)$$

Selected values of  $X_{\text{Si}}$  and  $m$ , as well as metallic solvent melting temperatures and binary eutectic points, for several silicon-metal binary systems of interest for silicon LPE are given in Table 5.1.

Returning to the binary phase-diagram analysis of the silicon LPE process effected by a transient cooling of a silicon-metal melt: By a simple mass balance for a dilute solution, the thickness  $h$  ( $\mu\text{m}$ ) of a silicon layer is given by:

$$h = \frac{W_{\text{M}}}{A} \cdot \frac{1}{\rho_{\text{Si}}} \cdot \frac{M_{\text{Si}}}{M_{\text{M}}} \cdot [X_{\text{Si}}(T^{\text{i}}) - X_{\text{Si}}(T^{\text{f}})] \quad (5.9a)$$

$$\cong \frac{W_{\text{M}}}{A} \cdot \frac{1}{\rho_{\text{Si}}} \cdot \frac{M_{\text{Si}}}{M_{\text{M}}} \cdot \left[ \frac{1}{m} \cdot \Delta T \right] \quad (5.9b)$$

where  $A$  is the area ( $\text{cm}^2$ ) of the deposited silicon,  $W_{\text{M}}$  is the mass of metal melt (g),  $M_{\text{M}}$  is the atomic mass of the metal solvent ( $\text{g/mol}^{-1}$ ),  $M_{\text{Si}}$  is the atomic mass of silicon ( $\text{g/mol}^{-1}$ ),  $\rho_{\text{Si}}$  is the density of solid silicon ( $\text{g cm}^{-3}$ ),  $X_{\text{Si}}(T^{\text{i}})$  and  $X_{\text{Si}}(T^{\text{f}})$  are the atomic fractions (dimensionless) of silicon in the liquid phase at temperatures  $T^{\text{i}}$  and  $T^{\text{f}}$ , where  $T^{\text{i}}$  is the temperature (K or  $^{\circ}\text{C}$ ) initiating growth at which point the melt is saturated with silicon, and  $T^{\text{f}}$  is the temperature (K or  $^{\circ}\text{C}$ ) terminating growth. The thickness so calculated corresponds to a sufficiently long growth time ( $\sim$  several hours); crystallization kinetics and heat and mass transfer limitations are neglected.

### 5.3.1 Nucleation of silicon from a molten metal solution

The application of classical nucleation theory to silicon LPE is useful to estimate the degree of supercooling needed for homogeneous nucleation in the bulk melt, and for heterogeneous (seeded) nucleation on silicon and nonsilicon substrates. Controlled nucleation, or prevention thereof, on nonsilicon substrates is crucial for selective epitaxy, ELO, and deposition of silicon on nonsilicon substrates such as ceramics. The silicon nucleation rate is determined by the melt supersaturation, which can be related to the supercooling temperature using relationships derived from phase equilibria considerations (Kozlov *et al.*, 1975). Models of nucleation rates in LPE (specifically for III-V compounds) have been developed by Jothilingham *et al.* (Jothilingham *et al.*, 1995) and Gopalakrishnan *et al.* (Gopalakrishnan *et al.*, 1996).



**Table 5.1** Metal solvent melting points, eutectics, and solid solubilities of and liquidus slopes for Si-metal binaries at selected temperatures

Metal solvent	Solvent melting point ( $^{\circ}\text{C}$ )	Eutectic <sup>a</sup> ( $X_{\text{Si}}^{\text{eut}}$ ) ( $T_{\text{metal}}^{\text{f}} - T^{\text{eut}}$ ) ( $^{\circ}\text{C}$ )	$T$ ( $^{\circ}\text{C}$ )	$X_{\text{Si}}$	$dX_{\text{Si}}/dT _T = m^{-1}$ ( $^{\circ}\text{C}^{-1}$ )	
Aluminum	660	0.12	580	0.125	0.00051	
			82	600	0.135	0.00053
				845	0.295	0.00078
				960	0.395	0.00082
Antimony	630.5	0.003	800	0.014	0.00002	
			1.1	900	0.026	0.00016
				1100	0.081	0.00047
				1200	0.143	0.00091
Bismuth	271.4	$3 \times 10^{-8a}$	1000	0.0026	0.00003	
		$10^{-10a}$	1100	0.0054	0.00016	
Gallium	29.8	$5 \times 10^{-10a}$	495	0.002	0.00003	
			$6 \times 10^{-10a}$	625	0.010	0.00012
				725	0.028	0.00024
				750	0.033	0.00027
Indium	156.2	$2 \times 10^{-10a}$	1000	0.194	0.00120	
			$10^{-7}$	900	0.009	0.00008
				1000	0.002	0.00016
				1100	0.044	0.00034
Lead	327.4	$9 \times 10^{-10a}$	1200	0.097	0.00081	
			$5 \times 10^{-8a}$	1050	0.002	0.00002
				1100	0.003	0.00003
				1150	0.005	0.00004
Tin	231.9	$10^{-7a}$	1200	0.008	0.00006	
			$4 \times 10^{-5a}$	800	0.006	0.00006
				900	0.015	0.00012
				950	0.021	0.00016
			1000	0.035	0.00022	
			1100	0.606	0.00042	

<sup>a</sup>Estimated by quasi-regular solution model (Thurmond and Kowalchik, 1960).

Referring to Figure 5.1, the slope of the liquidus is defined as:

$$m \equiv \left. \frac{dT^{\text{eq}}}{dX_{\text{Si}}} \right|_{T^{\text{i}}} \quad (5.10)$$

where the liquidus temperature denoted as  $T^{\text{eq}}$  emphasizes the equilibrium (silicon-saturated liquid phase) conditions indicated by the liquidus relation; and which is calculated by Equation (5.8) for silicon-metal binaries following quasi-regular solution behavior. For the temperature excursions ( $\Delta T = T^{\text{i}} - T^{\text{f}}$ ) commonly used,  $m$  can usually be taken as a constant at and around a specified growth temperature  $T \cong T^{\text{i}}$ .  $m$  also relates

the supersaturation ( $\Delta X \cong X^i - X^f$ ) to the supercooling ( $\Delta T = T^i - T^f$ ) since

$$m \cong \left. \frac{\Delta T}{\Delta X} \right|_{T^i} \quad (5.11)$$

The supersaturation is the driving force for nucleation and crystal growth, while the supercooling is the most important experimentally controllable parameter. Thus, the slope of the liquidus determines the dynamics, kinetics, and stability of the LPE process. For nucleation and growth to occur, the system must deviate from thermodynamic equilibrium. As discussed in the next section, there are many ways to induce a thermodynamic driving force for crystal growth, but the simplest and most commonly used is a transient cooling of the saturated melt. This process can be analyzed in terms of free energy changes. The molar free energy change  $\Delta \underline{G}^{\text{sup}}$  associated with crystallizing silicon from a melt initially equilibrated at a temperature  $T^{\text{eq}} \cong T^i$  with equilibrium silicon fraction  $X^{\text{eq}}$ , and supercooled by  $\Delta T$  (or equivalently supersaturated by  $\Delta X$ ) is given by (Brice, 1965, 1973, 1986):

$$\Delta \underline{G}^{\text{sup}} \cong RT^{\text{eq}} \ln \left( 1 + \frac{\Delta T}{T^{\text{eq}}} \right) = RT \ln \left( 1 + \frac{\Delta X}{X^{\text{eq}}} \right) \quad (5.12a)$$

$$\cong \Delta H^{\text{sol}} \frac{\Delta T}{T^{\text{eq}}} \quad (5.12b)$$

Nucleation occurs when the supercooling is sufficient that the free energy exceeds the surface energy barrier required to form stable nuclei. To form a spherical nucleus of radius  $r$ , the negative free energy change associated with the supercooling is offset by a positive term associated with the formation of the silicon-metal melt interface, such that the total free energy of an embryonic nucleus is:

$$\Delta G^T = -\frac{4\pi r^3}{3V_m} \Delta H^{\text{sol}} \frac{\Delta T}{T^{\text{eq}}} + 4\pi r^2 \gamma_{\text{Si-M}} \quad (5.13)$$

where  $V_m$  is the molar volume and  $\gamma_{\text{Si-M}}$  is the interface energy between solid silicon and the melt. Due to random clustering of silicon atoms in the melt, embryonic nuclei form that are stable when  $r$  exceeds some critical value  $r^*$  corresponding to the maximum value of  $\Delta G^T$  denoted as  $\Delta G^*$ . Taking the derivative of Equation (5.13) with respect to  $r$  and setting equal to zero, gives the critical radius as:

$$r^* = \frac{2 \cdot \gamma_{\text{Si-M}} V_m T^{\text{eq}}}{\Delta H^{\text{sol}} \Delta T} \quad (5.14)$$

and the critical free energy of nucleation as:

$$\Delta G^* = \frac{16\pi \cdot \gamma_{\text{Si-M}}^3 \cdot (T^{\text{eq}})^2}{3(\Delta H^{\text{sol}})^2 \cdot \Delta T^2} \quad (5.15)$$

For metallic solutions, Brice (Brice, 1973) suggests the following empirical relation as an estimate for  $\gamma_{\text{Si-M}}$ :

$$\gamma_{\text{Si-M}} = \frac{0.25 \cdot \Delta H^{\text{sol}}}{N_0^{1/3} \cdot V_0^{1/3}} \quad (5.16)$$

where  $N_0$  is Avogadro's number. The dependence of silicon surface energies on crystallographic orientation and misorientation is treated by Zdyb *et al.* (Zdyb *et al.*, 2006).

To determine the onset of nucleation, an Arrhenius-type rate equation for the rate of nucleation is assumed:

$$\dot{n} \simeq A \cdot \exp\left(-\frac{\Delta G^*}{RT}\right) \quad (5.17)$$

where  $\dot{n}$  is the rate of nucleation and  $\Delta G^*$  is the critical free energy to form a stable nucleus which is treated as an activation energy barrier for forming stable nuclei, and which depends on the degree of supercooling  $\Delta T$ . The pre-exponential term  $A$  has a complicated form since it involves the frequency of solute atom attachment to the embryonic nuclei, its surface area, and the local density of solute atoms in the liquid phase (Chalmers, 1964). A rough estimate of  $A$  suffices.  $A$  is usually in the range of  $10^{27} - 10^{33} \text{ cm}^{-3} \text{ s}^{-1}$  (Walton, 1969), in which case the nucleation becomes appreciable when:

$$\frac{\Delta G^*}{RT} \simeq \ln 10^{30} \approx 69 \quad (5.18)$$

For homogeneous nucleation in the bulk of the melt, it can be shown that the required supercooling  $\Delta T^{\text{hom}}$  is estimated by (Brice, 1973):

$$\Delta T^{\text{hom}} \approx \left[ \frac{16\pi \cdot \gamma_{\text{S/L}}^3 \cdot T^{\text{eq}}}{210 \cdot \Delta H_{\text{sol}}^2 \cdot V_m \cdot R} \right]^{1/2} \quad (5.19)$$

where  $\gamma_{\text{S/L}}$  is the solid-silicon/liquid metal surface energy and  $\Delta H_{\text{sol}}$  is the enthalpy of solution which is roughly the enthalpy of fusion for silicon. This calculation indicates the amount of supercooling a melt can be subjected to before spontaneous homonucleation occurs, and values so estimated for metal solvents such as aluminum, gallium, and tin are on the order of 100 °C. Garfinkel and Hall (Garfinkel and Hall, 1978) reported supercoolings as high as 70 °C in the silicon-tin system at 1100 °C. Baliga (Baliga 1978b) routinely supercooled tin-silicon melts by 30 °C at 950 °C.

Supercoolings needed for heterogeneous nucleation on, for example, nonsilicon substrates, coatings on a substrate, or walls of the containment vessel can be estimated in terms of a contact angle  $\theta$  the silicon nucleus makes with the surface according to Young's law:

$$\gamma_{\text{sub-M}} = \gamma_{\text{Si-sub}} + \gamma_{\text{Si-M}} \cdot \cos \theta \quad (5.20)$$

where  $\gamma_{\text{sub-M}}$  is the interfacial energy between the substrate (or other nonsilicon seeding surface) and the molten metal,  $\gamma_{\text{Si-sub}}$  is the interfacial energy between the silicon and the substrate or other nonsilicon seeding surface, and  $\gamma_{\text{Si-M}}$  is the interfacial energy between silicon and the molten metal.

The critical energy  $\Delta G^{*,\text{het}}$  for forming a heterogeneous stable nucleus is then:

$$\Delta G^{*,\text{het}} = \Delta G^{*,\text{hom}} \left( \frac{1}{2} - \frac{3}{4} \cdot \cos \theta + \frac{1}{4} \cos^3 \theta \right) \quad (5.21)$$

where  $\Delta G^{*,\text{hom}}$  is the critical free energy for homogeneous nucleation [Equation (5.15)].

Thus, the supercooling  $\Delta T^{\text{het}}$  required to induce heterogeneous nucleation is given by:

$$\Delta T^{*,\text{het}} = \Delta T^{*,\text{hom}} \left( \frac{1}{2} - \frac{3}{4} \cdot \cos \theta + \frac{1}{4} \cos^3 \theta \right)^{1/2} \quad (5.22)$$

where  $\Delta T^{\text{hom}}$  is the supercooling calculated for homogeneous nucleation [Equation (5.19)].

Note that for perfect, lattice-matched, strain-free seeding,  $\theta \rightarrow 0$ ,  $\Delta G^{*,\text{het}} \rightarrow 0$ , and  $\Delta T^{*,\text{het}} \rightarrow 0$ . More complicated geometries, both for the nuclei itself and the surface upon which it forms can be considered (Mutaftschiev, 1993).

While this analysis is somewhat simplistic, it illustrates that nonsilicon surfaces present a more difficult barrier to nucleation than does a clean silicon surface, and that ultimately nucleation on any nonsilicon surfaces will be observed before homogeneous nucleation in the melt. Some qualitative experimental corroboration of these equations is provided by Teubner *et al.* (Teubner *et al.*, 1999), as related to modeling homogeneous nucleation and growth of silicon from small indium droplets. For this reason, it is feasible to restrict nucleation and silicon deposition to silicon surfaces exposed at a substrate, and avoid spurious nucleation and deposition on the crucible walls or free surfaces of the melt. It is also feasible to tailor growth conditions to avoid nucleation on (e.g. oxide-) coated regions of the substrate, thus permitting selective modes of growth on patterned, masked silicon substrates. Considerations with regard to the range of supercoolings are important for determining conditions for depositing silicon on nonsilicon substrates, and control of the nucleation rate and its consequences on film continuity, and grain size and texture, but in practice this proves very difficult.

After stable nuclei are formed, crystal growth is sustained by adatom attachment of silicon or germanium atoms to the nuclei. The kinetics of growth depends on the details of the crystal growth mechanism, which in turn is determined by the nature of the silicon surface, characterized as perfectly singular (atomically flat), imperfect singular containing well-spaced atomic-height steps such as provided by a screw dislocation or misorientation of the silicon or substrate from a low crystallographic index face, or as atomically rough such as may occur at relatively high growth temperatures. The dominant growth mechanism can be deduced from the dependence of growth rate  $v$  on the supercooling  $\Delta T$ :

$$v = B_0 \cdot \Delta T^m \cdot \exp\left(-\frac{B_1}{\Delta T}\right) \cdot [1 - \exp(-B_2 \cdot \Delta T)] \quad (5.23)$$

where exponent  $m$  and values of  $B_i$  are characteristic of the surface-related crystal growth mechanism (Brice, 1973).

LPE of silicon, germanium and silicon-germanium alloys offers an outstanding model system to experimentally study fundamental mechanisms and modes of nucleation and crystal growth. Bauser (Bauser, 1985, 1994, 1997) notes that virtually all of the classical modes of crystal growth can be observed in silicon and SiGe LPE. Experimental studies of the features and mechanisms of liquid phase epitaxial growth, defect-induced growth modes (käss and Strunk, 1981; käss *et al.*, 1985a) including the use of intentional crystallographic misorientation of the substrate to generate atomic steps, substrate masking and patterning to study crystallographic orientation effects, the use of several metal solvents with distinct wetting and surface energetics, and LPE of SiGe alloys to include lattice

mismatch and strain effects, have been presented over the last 20 years (Bergmann, 1991, Bauser *et al.*, 1993; Bauser, 1994, 1996; Hansson *et al.*, 1992a,b; Hanke *et al.*, 2004; Nishinaga, 2005). This work has been reviewed by Konuma (Konuma, 2002).

## 5.4 SILICON LPE METHODS

Compared with other methods of epitaxy, the silicon LPE process is conceptually simple. In its most common embodiments, a liquid-metal solution is equilibrated with silicon at a prescribed temperature  $T_E$ , and then cooled by an amount  $\Delta T$ . The reduced solubility of silicon in the melt at the lower temperature ( $T_E - \Delta T$ ) creates a metastable (non-equilibrium) condition of supersaturation, which is relieved by precipitation of silicon on a substrate that acts as a seed. The substrate should present an energetically-favorable surface for preferential nucleation of silicon, thus restricting silicon deposition to the substrate in the form of a continuous film, and avoiding nucleation of silicon in the bulk of the melt, or on free surfaces of the melt, or on the walls of the containment vessel for the melt. In practice, this is easy to achieve if the substrate is adequately clean silicon (with no surface oxides) and the supercooling is not excessive (see below). For non-silicon substrates the control of nucleation to achieve preferential deposition of a continuous film on the substrate is considerably trickier.

A more detailed description of several implementations of silicon LPE may be useful. In the dipping technique (Figure 5.3), a molten metal saturated with silicon is equilibrated at a temperature  $T_E$ , the melt is then supercooled by an amount  $\Delta T$ , and a substrate (attached to a holder) is immersed into the supersaturated melt for set time  $t$  and then withdrawn from the melt. The substrate is coated with a layer of silicon precipitated from melt. The silicon layer thickness  $h$  is a function of  $t$ :

$$h = \frac{2 \cdot \Delta T \cdot m}{\rho_{Si}} \frac{\rho_{sol}^L}{M_M} \sqrt{\frac{D_{Si}}{\pi}} \cdot t^{1/2} \quad (5.24)$$

here  $\rho_{Si}$  is the density of solid silicon,  $\rho_{sol}^L$  is the density of the solution,  $m$  is the slope of the liquidus,  $M_M$  is the atomic mass of the solvent metal, and  $D_{Si}$  is the diffusivity of silicon in the molten metal.

For applications requiring only a single layer of silicon, such as with many types of solar cells, the simple dipping process is attractive due to its simplicity and compatibility

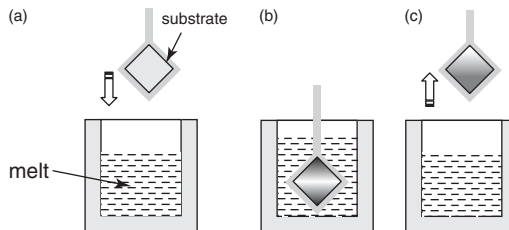


**Figure 5.3** Silicon LPE dipping technique: (a) metallic melt saturated with silicon and supercooled; (b) substrate is immersed in melt resulting in growth of an epitaxial layer; (c) substrate with deposited silicon layer is withdrawn from melt

with large-area substrates. Further, many substrates can be simultaneously dipped into the melt as a large batch process to increase throughput. A *p-n* junction can be formed in the deposited silicon layer by post-growth impurity diffusion. Some means of wiping excess metal droplets from the surface of the deposited silicon film may also be necessary, and in fact, such melt ‘carry over’ is a potential problem in all methods of LPE. Fortunately, and unlike the case with III-V LPE, metal carry-over can be removed from the silicon deposit using post-growth etching with aqua regia (HCl:HNO<sub>3</sub>) which attacks most metals but not silicon.

For the LPE growth of epitaxial junctions and multilayer structures, the horizontal slideboat LPE technique (Casey and Panish, 1987) is a well-established and commonly used method. For research purposes, the typical slideboat accommodates a substrate with dimensions on the order of several centimeters, although larger substrate sizes are feasible. In the slideboat method illustrated in Figure 5.4, one or more melts (~1–10 g each) is contained in the wells of a graphite slideboat situated in a fused silica tube centered in a horizontal tube furnace. The furnace temperature is regulated by a temperature controller to within about 0.5 °C, and can be programmed for various time–temperature schedules. The melts contain appropriate levels of impurities for distinct doping of each layer. A slidebar supporting the substrate ‘seed’ and one or several silicon source wafers can be manipulated by a pushrod. Figure 5.4 shows a typical sequence to grow a two-layer epitaxial structure. The melts are saturated with sacrificial silicon source wafers, separated from the source wafers and supercooled by a prescribed amount, and then successively contacted with the silicon substrate for prescribed times. The wiping action of the slidebar removes excess melt from the surface of the epitaxial layer. The method can be extended for the growth of ~10 or more layers if desired. Typically, layer thicknesses can be controlled down to ~0.1 μm with a thickness control of ±0.05 μm, although more sophisticated boats and techniques can reproducibly achieve much thinner (~0.05 μm) layers. The transient cooling of the melt to effect crystal growth follows a step cooling (typically  $\Delta T \sim 1\text{--}10\text{ }^\circ\text{C}$ ), ramp cooling (typically  $0.1\text{--}1\text{ }^\circ\text{C min}^{-1}$ ), or combination thereof (Hsieh, 1980). Rapid cooling (ranging from  $10\text{ }^\circ\text{C min}^{-1}$  to quenching at  $10^2\text{--}10^3\text{ }^\circ\text{C s}^{-1}$ ) techniques have been introduced to achieve high nonequilibrium conditions—contrary to the normal near-equilibrium nature of conventional LPE—to form metastable epilayer or overcome strain energy barriers due to lattice mismatch (Abramov *et al.*, 1996). Hanke *et al.* (Hanke *et al.*, 2005) used high cooling rates in SiGe LPE from indium melts to attain nonequilibrium conditions for producing ordered islands of SiGe crystals on a silicon substrate. While the slideboat is an excellent tool for LPE research, basic materials studies, and prototyping devices, it is difficult to scale-up for high-throughput production. The transient cooling and depletion of silicon from the melts in both the dipping and slideboat methods makes them inherently batch processes.

### 5.4.1 Steady-state methods of solution growth and LPE

Steady-state continuous- or semi-continuous mode processes for depositing silicon are of interest for high-throughput silicon deposition, particularly for solar cell production. Figure 5.5 shows various methods of adapting LPE for achieving steady-state growth, as well as other nonconventional methods for effecting silicon deposition from a molten (metallic) solution. These configurations are shown in order to indicate alternatives to

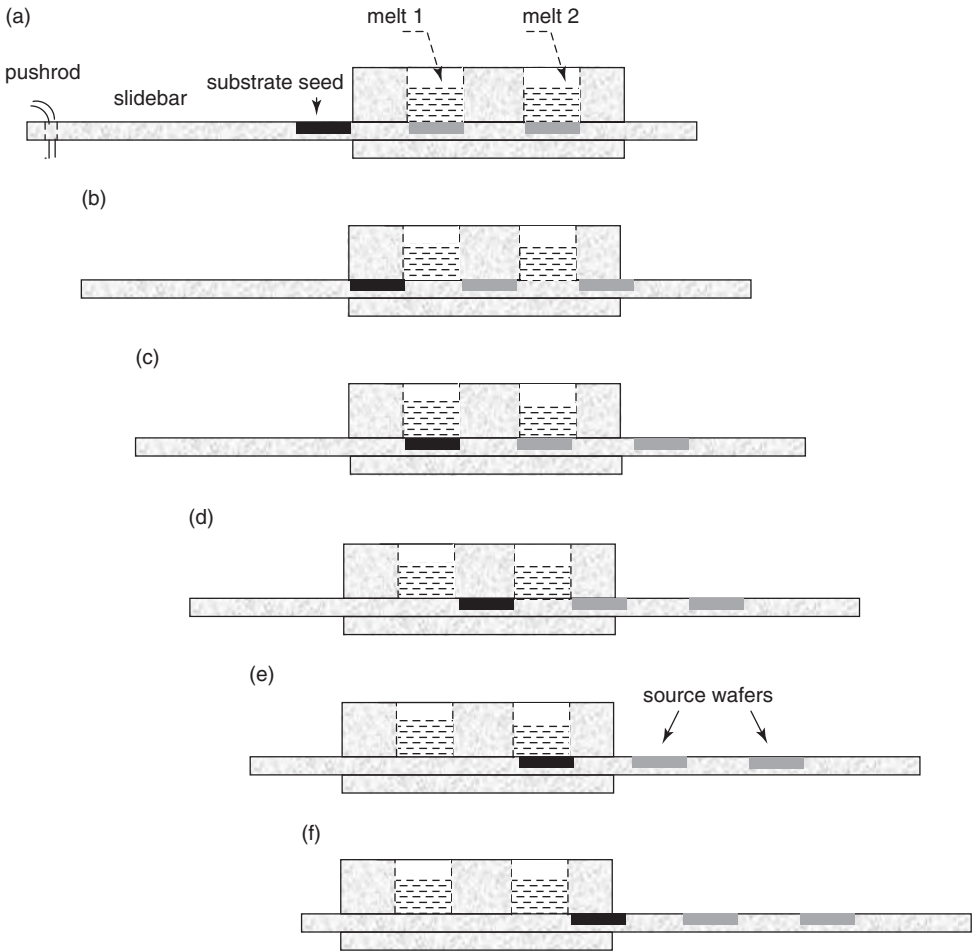


**Figure 5.4** Horizontal slideboat technique to grow a two-layer epitaxial silicon structure. Two silicon source wafers are used to saturate the melts with silicon. Successive stages show: (a) the saturation of melts with 'dummy' source wafers; (b) the separation of source wafers and melts in order to supercool the first melt; (c) contact of the substrate with the supersaturated melt for growth of the first epilayer, and at the same time, re-equilibration of the second melt with a source wafer; (d) separation of wafers from the second melt in order to supercool the second melt; (e) contact of the substrate with the supercooled second melt and growth of the second epilayer; and (f) separation of the substrate from the second melt

growth that relies on transient cooling and consequent depletion of a melt. In many cases, a silicon source is used to continuously replenish the melt with silicon solute, and moreover, the process is either steady-state or cyclic and can therefore operate for long runs. The common basis of these techniques is crystallization of silicon resulting from a difference in silicon chemical potential induced by a variety of means including imposed temperature gradients, convective or forced flow of melt, metastable phases, electric currents, CVD, solvent evaporation, or addition of components that modify the chemical potential of solute silicon in the melt. The basic principles behind many of these

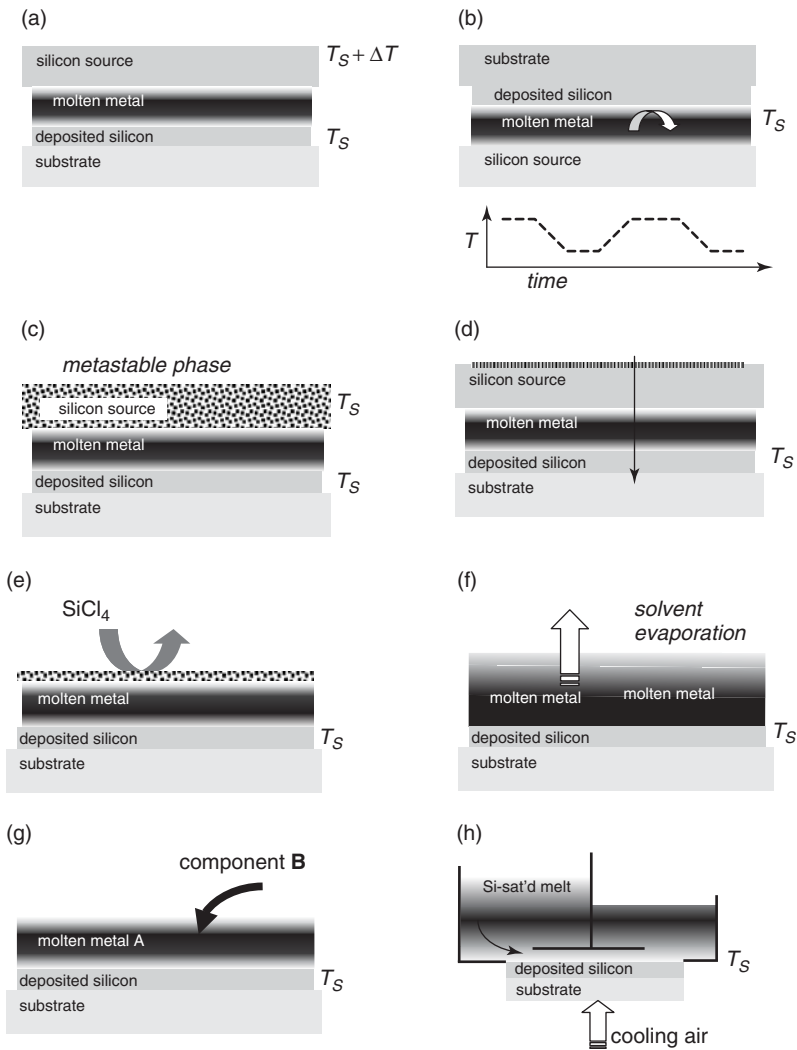


**Figure 5.5** Continuous-mode, steady-state epitaxial growth processes: (a) temperature-gradient growth; (b) convectively-driven growth; (c) growth due to a metastable phase; (d) current-induced growth; (e) vapor–liquid–solid growth; (f) growth by solvent evaporation; (g) growth by isothermal mixing; (h) growth by forced flow (see text for details)

techniques have been analyzed by Hurlle *et al.* (Hurlle *et al.*, 1967) under the guise of thin alloy zone crystallization in which ‘crystallization is achieved via diffusion through a thin alloy (liquid phase) zone from a third phase (solid, liquid, or vapor)’.

#### 5.4.1.1 Temperature-gradient solution growth and LPE

In Figure 5.5(a), a temperature gradient is imposed across the melt such that the silicon source is maintained at a higher temperature than the substrate separated from the source



by a distance  $\delta$ . This creates a concentration gradient of solute silicon and mass transport of silicon from the source to the substrate. Assuming the liquid-phase silicon concentration near the source is in equilibrium with the silicon source at temperature  $T_2$ , and the silicon liquid-phase concentration is close to equilibrium with the growing silicon film at  $T_1$  (the substrate temperature), then a flux  $J_{\text{Si}}$  of silicon ( $\text{g Si cm}^{-2} \text{ s}^{-1}$ ) is given by:

$$J_{\text{Si}} = \frac{D_{\text{Si}}^{\text{L}}}{\delta} [C_{\text{Si}}^{\text{L}}(T_2) - C_{\text{Si}}^{\text{L}}(T_1)] \quad (5.25a)$$

$$\cong \frac{D_{\text{Si}}^{\text{L}}}{\delta} \cdot \rho_{\text{M}}^{\text{L}} \cdot \left( \frac{M_{\text{Si}}}{M_{\text{M}}} \right) \cdot [X_{\text{Si}}(T_2) - X_{\text{Si}}(T_1)] \quad (5.25b)$$

$$\cong \frac{D_{\text{Si}}^{\text{L}}}{m} \cdot \rho_{\text{M}}^{\text{L}} \cdot \left( \frac{M_{\text{Si}}}{M_{\text{M}}} \right) \cdot \frac{\Delta T}{\delta} \quad (5.25c)$$

where  $m$  is the slope of the liquidus and  $\rho_{\text{M}}^{\text{L}}$  is the density of the melt. Further more:

$$v \cdot [C_{\text{Si}}^{\text{S}} - C_{\text{Si}}^{\text{L}}(T_1)] = J_{\text{Si}} \quad (5.26)$$

where  $v$  is the deposition rate of silicon ( $\text{cm s}^{-1}$ ) and  $C_{\text{Si}}^{\text{S}}$  is the concentration (density) of silicon in the solid phase ( $= 2.3 \text{ g cm}^{-3}$ ).

Thus, the rate of silicon deposition  $v$  is proportional to the imposed temperature difference  $\Delta T$ , and inversely proportional to the slope of the liquidus  $m$  and the separation of the source and substrate  $\delta$ . In principle, a constant silicon growth rate can be sustained so long as the silicon source is present. Experimental techniques and analysis of temperature-gradient LPE for compound semiconductors have been reported (Strongfellow and Greene, 1971; Mattes and Route, 1972; Meinders, 1974; Long *et al.*, 1974; Nishizawa and Okuno, 1975; Akai *et al.*, 1976; Ludington and Immorlica, 1979. Lozovskii and Udyanskya (Lozovskii and Udyanskya, 1968) analyzed the mechanism of temperature gradient-driven crystallization from an aluminum-silicon melt, and Meinders (Meinders, 1974) compared predictions with experimental results for silicon grown from tin melts with an imposed temperature gradient. Thomas *et al.* (Thomas *et al.*, 1997) reported temperature gradient ( $10 \text{ K cm}^{-1}$ ) growth of silicon layers on  $10 \text{ cm} \times 10 \text{ cm}$  polycrystalline silicon substrates from In/Ga melts at  $980^\circ\text{C}$ . Growth rates of  $0.3 \mu\text{m min}^{-1}$  were achieved. Epitaxial layers,  $30 \mu\text{m}$  thick, with adjustable dopings (according to In/Ga melt ratio) of  $10^{16} - 2 \times 10^{18} \text{ cm}^{-3}$  had minority carrier lifetimes of  $5 - 10 \mu\text{s}$ . Peter *et al.* (Peter *et al.*, 1995) fashioned a portal in the thermal insulation and heating elements of a cylindrical tube furnace to create a temperature gradient across a tin melt, thus achieving  $2 \mu\text{m min}^{-1}$  silicon growth at a temperature of  $900^\circ\text{C}$ . Nevsky *et al.* (Nevsky *et al.*, 1991) offer a more detailed model of steady-state, temperature-gradient induced silicon LPE. In a process that may entail temperature-gradient driven growth, Mokritskii *et al.* (Mokritskii *et al.*, 1982) stimulated growth of epitaxial Ge layers from an indium-germanium liquid phase by gamma radiation.

#### 5.4.1.2 Solution growth and LPE by temperature-induced melt convection

In Figure 5.5(b), the temperature is cycled as indicated. The temperature cycling causes an inversion of the liquid-phase density and induces free convection which results in

transport of silicon from the (bottom) silicon source to the (top) silicon substrate. Thus, an intermittent but sustained deposition of silicon on the substrate can be achieved. This LPE process employing periodic temperature cycling to induce convectively driven silicon deposition in a substrate–melt–source sandwich configuration has been termed the *yo-yo* solute feeding method by Sukegawa *et al.* (Sukegawa *et al.* 1988, 1989b, 1991a). The technique has also been applied to the growth of thick GeSi alloy layers (Sukegawa *et al.*, 1990, 1991b). Analysis of convectively driven growth in silicon LPE systems has also been described (Kimura *et al.*, 1990, 1996; Dost *et al.*, 1994; Coşkun *et al.*, 2002).

#### 5.4.1.3 Solution growth due to contact with metastable solid phase

In this method [Figure 5.5(c)], the silicon source is a metastable phase comprised of granular, highly defective, small-grained or amorphous forms of silicon. As such, the silicon source has a higher free energy than single-crystal or large-grained polycrystalline silicon due to the interfacial energy associated with grain boundaries, defects and surfaces. Thus, the system can lower its free energy by transporting silicon atoms from the fine-grained silicon source through the liquid phase and depositing them on a larger-grain silicon film. The process is akin to Oswald ripening (Givargizov, 1991) wherein larger-sized phases (e.g. crystals) grow at the expense of smaller-sized phases due to interfacial energy differences. The source can also be stressed to increase its free energy. In this regard, Losovsky and Konstantinova (Losovsky and Konstantinova 1981) showed significant growth rates ( $1\text{--}2\ \mu\text{m min}^{-1}$ ) in a Si–Al system at  $960^\circ\text{C}$  with a source–substrate separation of  $10\text{--}20\ \mu\text{m}$ . The growth rate  $v$  is given by:

$$\frac{v}{(C_{\text{Si}}^{\text{S}} - C_{\text{Si,sub}}^{\text{L}})} = J_{\text{Si}} = u_{\text{Si}}^{\text{L}} \cdot C_{\text{Si}}^{\text{L}} \frac{\Delta\mu}{\delta} \quad (5.27)$$

where  $\Delta\mu$  is the difference in chemical potential between the source and substrate including contributions from grain boundary energy and stress. This flux is in addition to a flux due to a temperature difference between the source and substrate. Losovsky and Konstantinova (Losovsky and Konstantinova 1981) concluded the chemical potential difference was due primarily to stress rather than interfacial (grain boundary) energy.

#### 5.4.1.4 Current-induced solution growth and liquid phase electro-epitaxy

The application of electric fields and currents can be used to induce and control growth from solution. The methods described here are distinct from the electrochemical phenomena that comprise conventional electroplating, such as the silicon electrodeposition from fused salts mentioned in Section 5.5. In metallic solution growth and liquid phase electro-epitaxy (LPEE), also called current-controlled LPE, crystal growth is effected by physical effects such as Peltier cooling or electromigration of solute due to differential momentum transfer from conduction electrons of the molten metal to the solute and solvent atoms of the melt. There is no chemical reduction of species, nor molar equivalence between total current and material deposited (Faraday's law). Nor does the deposition process in LPEE exhibit a threshold voltage, i.e. a characteristic electromotive force as in conventional electroplating.

In Figure 5.5(d), an electric current is imposed across the melt. A dc electric current with appropriate polarity can induce Peltier cooling at the substrate–melt interface, producing a localized supercooling ( $\Delta T \sim 1^\circ\text{C}$ ) of the melt, as well as Peltier heating at the source silicon creating a temperature gradient similar to that of Figure 5.5(a). In either case, the resulting temperature-gradient creates a concentration gradient that drives transport of silicon from the source to substrate. The temperature gradient may also be supplemented or diminished by Joule heating effects at both interfaces. Another mechanism for crystal growth is due to electromigration. An electric current through the melt induces electromigration of silicon solute which contributes to the silicon transport from source to substrate. Less easily explained are reports of LPEE using ac electric fields at frequencies of 50 Hz (Takenaka *et al.*, 1991a, b) where the solute transport involves Lorentz forces due to the magnetic field created by current in the furnace heater coils; and LPEE with applied current frequencies of 1–1000 Hz where net crystallization is the result of asymmetries in growth and dissolution kinetics (Demin *et al.*, 1990).

Such current-induced electro-epitaxy methods are well established with III-V LPE (Bryskiewicz, 1986; Golubev *et al.*, 1995), but there are only two reports of silicon LPEE (Cunningham *et al.*, 1990; Mauk and Curran, 2001) and it is not clear which current-induced growth mechanisms were operative or dominant. Pratt and Sellors (Pratt and Sellors, 1973) provide a comprehensive review of electromigration in liquid metals, but there are few experimental data on electromigration of silicon or germanium in molten metals.

The solute (silicon or germanium) flux  $J_i$  due to electromigration may be expressed as:

$$J_i = C_i \cdot m \cdot Z^{\text{eff}} \cdot \xi \quad (5.28)$$

where  $C_i$  is the concentration of solute,  $m$  is the mobility of the solute,  $Z^{\text{eff}}$  is the effective charge of the solute and  $\xi$  is the applied electric field which can be related to the applied current density  $J$  according to  $\xi = J/\rho$ , where  $\rho$  is the electrical resistivity of the melt. The effective charge can be estimated by a number of simple rules based on valences of the solvent and solute, relative liquid phase resistivities of the pure solvent and solute, or differential change in solution resistivity with solute concentration (Belaschenko, 1965; Pratt and Sellors, 1973; Belaschenko *et al.*, 1974). For instance, the effective charge of silicon in a liquid metal can be estimated based on the valence (periodic table group number)  $Z$  of the silicon and the metal:

$$Z_{\text{Si}}^{\text{eff}} = Z_{\text{Si}} - \frac{Z_{\text{Si}}^2}{Z_{\text{m}}} \quad (5.29)$$

Although the above expression is formulated as if the solute electromigration is due to the effect of an applied electric field on a charged solute species, this is not considered the dominant mechanism of electromigration in liquid metals. This is evidenced by the anomalous behavior of silicon and germanium in liquid metals with respect to their electromigration direction. According to a compilation of Pratt and Sellors (Pratt and Sellors, 1973), solute silicon migrates to the anode when dissolved in molten aluminum, silver, gallium, and indium, and migrates to the cathode when dissolved in molten gold and

**Table 5.2** Some electromigration properties in molten metals

Solute	Solvent	Temperature (°C)	Resistivity (Ω-cm)	Z*
Ge	Bi (0.15 at% Ge)	500	143	0.55
	In (1 at% Ge)	500		-4.2
	Tl	500		-1.3
	Ga (1.7 at% Ge)	500		
As	Ga (0.08 %)	500	36	
Sb	Ga (1.7 at % Sb)	500	38	-6.3

Data from: Belaschenko, 1965; Pratt and Sellors, 1973; Belaschenko *et al.*, 1974.

copper. Solute germanium migrates to the anode in molten silver, aluminum, gallium, indium, and tin, and to the cathode in molten gold. Thus, as silicon and germanium being group IV elements would be expected to have a positive effective charge and migrate to the cathode, in many cases they actually migrate toward the anode rather than the cathode. Instead, the solute migration is due to the electron current resulting from an applied voltage which creates an ‘electron wind’ such that electron momentum is transferred by collisions to both the solute and solvent atoms. As the solvent and solute atoms present distinct scattering cross-section for electrons, the net velocity of solute with respect to solvent depends on the relative electron scattering efficiency of the solute with respect to the solvent. This relative scattering can be correlated with some success to the resistivities of the liquid elements. There are few measured data on the mobility and effective electric charge of silicon and germanium dissolved in molten metals. Some data for effective charges of solute germanium in a few metals (and for As and Sb included for reference) are given in Table 5.2. The mobility can be estimated from diffusivities  $D_{\text{Ge}}^{\text{L}}$  of germanium in the melt according to the Einstein–Nernst equation:

$$\mu_{\text{Ge}} = D_{\text{Ge}}^{\text{L}} \cdot (kT/q)^{-1} \quad (5.30)$$

where  $q$  is the electronic charge.

Diffusivities of silicon in some liquid alloys (including concentration dependence) are investigated in Keita *et al.* (Keita *et al.*, 1976) and Lozovskii *et al.* (Lozovskii *et al.*, 1978), in addition to silicon diffusion coefficients determined by fitting experimental LPE growth kinetics to model equations.

#### 5.4.1.5 LPE and VLS growth, and LPE and solution growth driven by vapor phase saturation of the solution

Silicon can be deposited from a molten metal nourished with silicon provided by a CVD reaction [Figures 5.5(e)]. Wagner and Ellis (Wagner and Ellis, 1964) reported the growth of silicon ‘whiskers’ by disproportionation reactions of  $\text{SiI}_2$  or  $\text{SiCl}_4$  mediated by droplets of molten metals such as Pt, Ag, Pd, Cu or Ni. This process has been termed the VLS

mode of growth to indicate the role of the *vapor* phase reaction to supply silicon, the *liquid* metal solvent phase, the exposed surfaces of which provide a catalyst for the vapor phase reaction that saturates the molten metal with silicon, and from which the *solid* silicon crystals are precipitated. Experimental procedures for controlled VLS growth are described by Wagner and Doherty (Wagner and Doherty, 1966) and Yashina *et al.* (Yashina *et al.*, 2003). Hurle *et al.* (Hurle *et al.*, 1967) review some of the early work on VLS phenomena for growing silicon crystals from liquid films such as gold, copper, tin or indium combined with pyrolysis of a silane derivative. In general, the VLS method encounters difficulty in growing planar silicon films due to the tendency of the liquid metal phase to agglomerate. In an application of interest for solar cells, Graef *et al.* (Graef *et al.*, 1977a, b; Sloem *et al.*, 1979) used a VLS mechanism with silane and a 5- $\mu\text{m}$  thick layer of molten tin to deposit polycrystalline silicon layers on graphite. Wallace *et al.* (Wallace *et al.*, 1994, 1996) deposited silicon layers from a submicrometer thick molten metal (indium or tin, plus a titanium wetting layer) saturated with a silicon sputter source. Hammerling (Hammerling, 1978) demonstrated LPE of GaAs with Ga melts saturated from the vapor phase with  $\text{AsCl}_3$ . Other methods of vapor phase control of solution growth processes are based on controlling the vapor pressure of solute components to induce or maintain supersaturation. Nishizawa and Okuno (Nishizawa and Okuno, 1975) and Suto *et al.* (Suto *et al.*, 1990) perfected GaAs and GaP epilayers grown by a temperature-gradient solution growth process (Ga-rich melt) using an LPE slideboat method and controlling the vapor pressure of the group V species in the growth ambient. The slideboat utilized a tungsten heater to impose a temperature gradient across the melt. Ruda *et al.* (Ruda *et al.*, 1983) described a HgCdTe LPE process that utilized a mercury pressure differential as the sole driving force to initiate and sustain growth. A mercury reservoir generates an excess Hg vapor pressure, adding Hg to the melt and thereby providing an effective supersaturation.

#### 5.4.1.6 LPE and solution growth driven by solvent evaporation

Solvent evaporation techniques are commonly used to grow organic crystals from aqueous solutions, but are seldom applied to semiconductors. The continued evaporation of a metal solvent component will result in an increased concentration of solute (e.g. silicon) eventually leading to a condition of (silicon) supersaturation [Figure 5.5f]. Khukhryanskii and Nikolaeva (Khukhryanskii and Nikolaeva, 1976) obtained single-crystal Ge and Si films on Si(111) substrates by an isothermal LPE process based on evaporation of the solvent metal (Cd or Zn at 650 °C for Ge films and Zn at 700–750 °C for Si films). Shi *et al.* (Shi *et al.*, 1993) reported deposition of silicon from silicon-zinc melts, wherein evaporation of zinc resulted in nucleation of silicon on an oxidized silicon substrate. Mauk *et al.* (Mauk *et al.*, 2001) grew SiC crystals by LPE driven by evaporation of Zn from a Zn/Al solvent. Similar results could be expected for melts with other relatively volatile metals such as bismuth or antimony. This may be a useful method of controlling nucleation density on nonsilicon substrates.

#### 5.4.1.7 LPE and solution growth driven by changing hydrostatic pressure

Mao *et al.* (Mao *et al.*, 2000) have proposed a pressure-variation LPE technique wherein the equilibrium concentration of solute is varied by modulating the total pressure of the

LPE ambient. An analysis made for III-V semiconductors showed that the equilibrium concentration  $X_i$  of components in the melt can be given as:

$$X_i = X_{0,i} \pm b_i \cdot P \quad (0 < P < 1 \text{ atm}) \quad (5.31)$$

Thus, by varying the pressure on the melt, the liquid phase can be supersaturated to induce growth *without* changing the temperature. They contend that this method should provide for a more easily controlled and more flexible LPE process.

#### 5.4.1.8 Solution growth and LPE driven by isothermal mixing and relaxational LPE methods

In principle, the silicon could be precipitated from a melt by addition of a component (another solute or a melt solvent component) that reduces the solubility of silicon [Figure 5.5(g)]. The precipitation of a first solute from solution by addition of a second solute (precipitant) that reduces the solubility of the first solute is sometimes referred to as the 'salting out technique' in reference to the use of salts as precipitants for growing protein crystals. It is not clear whether this technique has ever been exploited for LPE of silicon or germanium, which is contingent upon the identification of ternary or higher-component systems that would suggest a precipitant that did not form a compound with silicon or germanium, nor was a harmful impurity in silicon; although LPE of silicon-germanium alloys using either additional silicon or germanium as a precipitant for epitaxial growth of a silicon-germanium alloy might be feasible. For LPE of compound semiconductors, Woodall (Woodall, 1971) reported an isothermal solution mixing technique where two melts having different compositions on the liquidus of the ternary Al-Ga-As system for a particular temperature are mixed, and the resulting mixture is supersaturated in As, resulting in growth of an AlGaAs layer. Other related methods for isothermally inducing supersaturation and epitaxial growth are possible. For example, Lozovskii *et al.* (Lozovskii *et al.*, 1977) described the isothermal growth of GaAsP layers on GaAs and GaP substrates separated by a 0.5 cm thick layer of molten Ga. According to the authors' explanation, after the substrates are brought into contact with the molten Ga, the dissolution of As and P from the GaAs and GaP substrates, and their diffusion into the melt creates a local supersaturation of As at the GaP substrate and a local supersaturation of P at the GaAs substrate, which results in solidification of a GaAsP alloy. More generally, (isothermal) relaxational LPE methods utilize a second substrate in contact with the melt that induces a reversal in mass transport and self-limiting growth on the first substrate (Bessolov *et al.*, 1988, 1990, 1993).

#### 5.4.1.9 Solution growth and LPE by forced flow of the melt

Figure 5.5(h) indicates still another method of isothermal, quasi-steady-state LPE growth, developed for high-throughput LPE of GaAs (Crisman *et al.*, 1986; Daly *et al.*, 1986), but which could be applied to silicon or germanium LPE as well. A large reservoir of saturated melt supplies a continual stream of melt that flows past a cooled substrate, resulting in deposition on the substrate.

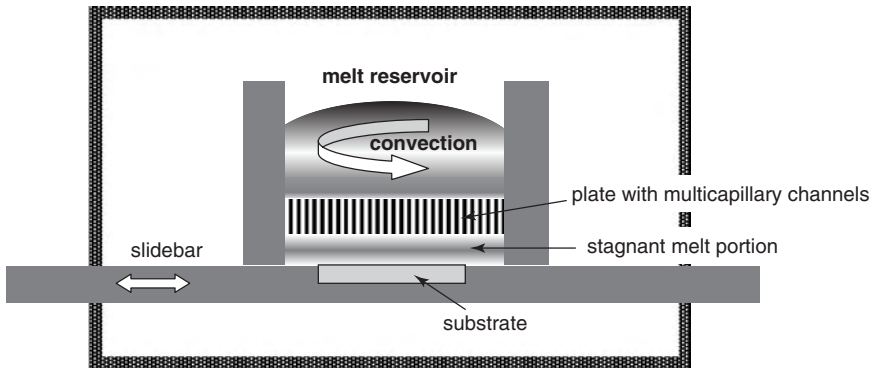


**Figure 5.6** Double crucible method to control dopant segregation. Adapted from Koh and Fukuda (Koh and Fukuda, 1996)

The steady-state growth methods using silicon sources or other means for replenishing the melt with silicon thus enable continuous or semicontinuous processes for sustained deposition of silicon, including deposition on continuously or semicontinuously moving substrates. Dopant depletion is also a potential limitation. In this regard, a doped source can be used to supply dopant to the melt.

#### 5.4.1.10 LPE with microcapillary transport

Some methods to control segregation in melt or solution growth techniques utilize a double-crucible arrangement, an example of which is shown schematically in Figure 5.6. Double crucible methods have been used in Czochralski growth of silicon to provide more uniform doping, and in bulk growth of alloy semiconductors to control the alloy composition (Lin and Benson, 1987; Watanabe *et al.*, 1993; Tanaka *et al.*, 1998; Kozhemyakin, 2000). An inner crucible containing melt and dopant is situated inside a larger outer crucible from which silicon is deposited on the substrate. The inner melt is connected to the melt of the outer crucible through one or more capillary channels. A steady effusion of dopant from the inner melt tends to keep the concentration of dopant near the growth interface constant, and replenishes the dopant depleted from the outer melt due to incorporation into the silicon layer.

#### 5.4.1.11 Solution growth by centrifugal forces

Bauser and Strunk (Bauser and Strunk, 1985), Bauser (Bauser, 1997) and Konuma *et al.* (Konuma *et al.*, 1996) describe the use of centrifugal forces for LPE. In one method, a rotating crucible LPE system uses centrifugal forces for bulk transfer of the melt with respect to the substrate, and thus represents a mechanical means similar to that effected with slideboats and substrate holders in traditional LPE systems. Perhaps more interesting from the point of view of LPE fundamentals are systems that use high-speed (1600–2000 rpm, 80 G force) centrifugation to induce differential migration of components in a melt that is otherwise saturated when quiescent. The centrifugally induced solute concentration gradient creates a supersaturated portion of the melt which is in contact

with a substrate, and an undersaturated melt portion in contact with a source wafer. Thick epilayers of silicon, germanium, and GaAs have been grown by this centrifugal LPE method.

#### 5.4.1.12 Surface-energy driven LPE

Hansson *et al.* (Hansson *et al.*, 1993a, 1994; Albrecht *et al.*, 1996) utilized interfacial energies for germanium-on-silicon liquid phase heteroepitaxy. The driving force for crystal growth from an undersaturated bismuth-rich liquid phase is due to minimization of interfacial energy between the melt and solid. By superheating the growth solution, the driving force for epitaxy can be minimized to produce atomically abrupt Ge/Si interfaces and monolayer control of the growth at temperatures up to 937 °C (Hansson *et al.*, 1993a,b).

### 5.5 SOLVENT SELECTION

The selection of the solvent is probably the most important consideration in formulating a solution growth process. Based on general criteria for solution growth suggested by Elwell and Scheel (Elwell and Scheel, 1975), the properties of an ideal solvent for LPE of silicon include:

- (1) Low melting point so as to form a liquid solution containing an appreciable amount of silicon at temperatures less than 1200 °C.
- (2) Significant silicon solubility at the growth temperature and/or appreciable change in silicon solubility with temperature—minimizing the growth temperature is a common objective.
- (3) Lack of compound formation with silicon (e.g. metal silicides), especially compounds that might be co-precipitated with silicon.
- (4) Available in high purity (probably at least 99.99 %) at low cost (<\$1 g<sup>-1</sup>).
- (5) Able to sufficiently wet the substrate. (In the case of silicon substrates, this is closely related to the ability of the solvent to remove surface oxides.).
- (6) Low volatility at the highest applied temperatures.
- (7) Viscosity in the range of 1–10 cP.
- (8) Low reactivity with the crucible material.
- (9) Low toxicity.
- (10) Low tendency to seep or creep out of the crucible or containment vessel.
- (11) Ease of separation or removal from the grown silicon crystal by physical or chemical means (e.g. selective etching to remove excess solvent from the silicon).
- (12) Low solubility of the solvent in solid silicon, or alternatively incorporation of solvent atoms into the silicon crystal in a controlled manner to effect doping, or else is an electrically inactive impurity in silicon (i.e. does not act as a dopant, recombination center, or carrier trap, nor significantly degrades carrier mobility).



For solution growth of semiconductor silicon and germanium, liquid metals are the best candidate solvents that satisfy all or at least most of these criteria, and solution growth with a number of metallic solvents has yielded silicon and germanium crystals and epitaxial layers suitable for making various semiconductor devices including solar cells, photodiodes, field effect and bipolar transistors, and power devices. Other solutions for liquid phase crystal growth or deposition of silicon have also been investigated. Silicon has been electrodeposited from a number of fused salts such as alkali metal fluorides (KF-LiF,  $K_2SiF_6$ -LiK-KF) at temperatures around 700–800 °C (Rao *et al.*, 1981; Stern and McCollum, 1985; Moore *et al.*, 1997), as well as from organic solutions such as  $SiCl_4$ - $C_2H_4Cl_2$ -ethylene glycol,  $SiCl_4$  in propylene carbonate, and  $SiI_4$  in 1,2-butanediol; as reviewed by Runyan (Runyan, 1976) and Elwell and Feigelson (Elwell and Feigelson, 1982). Zein El Abedin *et al.* (Zein El Abedin *et al.*, 2004) and Endres (Endres, 2004) demonstrated room-temperature electrodeposition of nanoscale silicon and germanium from ionic liquids (defined as a molten salt with melting point below 100 °C) such as 1-butyl-1-methylpyrrolidinium bis(trifluoromethylsulfonyl)imide saturated with  $SiC_4$ . Shimoda *et al.* (Shimoda *et al.*, 2006) reported the deposition of polycrystalline silicon films on silica substrates from silane-based liquid precursors using spin-coating or inkjet printing, followed by annealing (~550 °C) and laser crystallization. The quality of these silicon films deposited from nonmetallic solutions with respect to purity and crystal structure appears to be inadequate for many semiconductor device applications, especially those based on minority carrier phenomena.

Metal solvents successfully used for silicon LPE or solution growth of bulk silicon crystals include aluminum (Lozovskii and Udyanskaya, 1968), antimony (Käss *et al.*, 1986), bismuth (Käss *et al.* 1985b), copper (Ciszek *et al.*, 1993), gallium (Sumner and Foley, 1978), gold (Kresse *et al.*, 1990), indium (Scott and Hager, 1979), lead (Konuma *et al.*, 1999), tin (D'Asaro *et al.*, 1969; Baliga 1977a,b, 1978a,b, 1979a,b, 1980a,b,c, 1981), zinc (Shi, 1993), copper-aluminum (Wang and Ciszek, 1997a,b), gallium-aluminum (Girault *et al.*, 1977), gold-bismuth (Kresse *et al.*, 1990; Lee *et al.*, 1990; Lee and Green, 1991), gallium-indium (Konuma *et al.*, 1995), gold-lead (Lee and Green, 1991), thallium-tin (Schafer, 1981), tin-aluminum (Shi, 1994a,b,c), tin-copper-aluminum (Fatima *et al.*, 2006), tin-lead (D'Asaro *et al.*, 1969), and zinc-tin-aluminum (Shi, 1993). Crystals of germanium have been grown from aluminum, gallium, indium, and tin-antimony (John, 1958). Lehovc and Slobodskay (Lehovc and Slobodskay, 1964) analyzed the crystallization of Ge from Ge-In-Sb melts. Germanium epitaxial layers have been grown on Ge substrates from tin (Donnelly and Milnes, 1966), cadmium and zinc (Khukhryanskii and Nikolaeva, 1976), indium (Maruyama *et al.*, 2005) and lead-tin (Laugier *et al.*, 1970). Zolper and Barnett (Zolper and Barnett, 1989) reported the LPE growth of discrete Ge crystals on silicon from indium, bismuth, and indium-bismuth. SiGe alloy epilayers have been grown from bismuth (Alonso *et al.*, 1988; Trah, 1990; Chen *et al.*, 1992), gallium, indium, tin, and bismuth (Fleurial and Borschevsky, 1990; Fleurial *et al.*, 1991), and gold-bismuth (Healy *et al.*, 1991). The behavior of carbon during silicon LPE from tin melts, and the formation of SiC inclusions is reported by Kozhitov and Burov, (Kozhitov and Burov, 1988).

For semiconductor device applications, the selection of a particular solvent is usually dictated by the degree of solvent incorporation into the solid silicon or germanium (see Appendix 2, Table A2.1) and its effect on semiconductor properties. On this basis, tin and lead are good choices since they are electrically inactive in silicon as expected

for group IV metals that are isoelectronic with silicon and therefore act as neither donor nor acceptor dopants. Indium, a group III element, is a *p*-type dopant but has a low solubility in silicon and may provide for *p*-doped silicon in concentration ranges useful for semiconductor devices. The group III metals aluminum and gallium are also *p*-type dopants (acceptors) in silicon, but they will dope silicon at levels in excess of  $10^{19} \text{ cm}^{-3}$ , rendering the material degenerate and of limited use for semiconductor devices. Antimony, a group V element and donor in silicon will also render silicon heavily *n*-type ( $>10^{19} \text{ cm}^{-3}$ ). Bismuth is a group V element so should act as a donor, but its solubility in solid silicon is in the  $10^{16}$ – $10^{18} \text{ cm}^{-3}$  range, which is tolerable for many semiconductor device applications. Copper, despite its reputation as a life-time killer from the early days of semiconductor technology, actually proves to be a workable solvent for making silicon solar cells (Wang and Ciszek, 1994; Wang *et al.*, 1994). The range of solvent choices can be expanded by using alloys, and the doping of silicon by solvent components can be reduced by diluting the components in other electrically inactive solvents, thus providing a means for controlled doping. In general, the use of multicomponent solvents affords extra freedom in tailoring the properties of the solvent. Even solvents that heavily dope silicon may be useful for the growth of highly doped cladding layers (e.g. back-surface field layers in solar cells), current-spreading layers, regions with built in electric drift fields due to doping gradients (Bergmann *et al.*, 1993; Majumdar *et al.*, 2000, 2003, 2004) and buffer or transition layers between a substrate and low-doped ‘active’ layers of a silicon device (Lee *et al.*, 2003). For example, Sukegawa *et al.* (Sukegawa *et al.*, 1989a) controlled the lattice constant of silicon epilayers, thereby reducing wafer bending and misfit dislocations, by simultaneous doping with tin and phosphorus in LPE in order to compensate doping-induced lattice strains. The deposition of a first heavily doped silicon layer on a substrate may facilitate the subsequent growth of lower doped, low-defect silicon epilayers from other solvents. Moreover, post-growth gettering, taking advantage of the high surface-to-volume ratio of thin film device geometries (Knobloch *et al.*, 1985) or using porous layers as impurity sinks (Bilyalov *et al.*, 2001) may be feasible to reduce any excessive doping resulting from the use of certain solvents. Along similar lines, some solvent components may be useful for improving wetting, nucleation, and overgrowth of silicon.

Some other considerations in the formulation of solvents include possible stratification of the liquid phase due to incomplete miscibility of the solvent components (Novikov *et al.*, 1993), volatility of solvent components at growth temperatures, and wetting ability of the solvent and solid–liquid interface energies between the melt and the substrate and growing crystals (Zettlemoyer, 1968). In this last regard, bismuth is noteworthy in that it has a lower surface tension than most molten metals, and the surface energetics of silicon and germanium from bismuth solvents are markedly different than those from tin or indium solvents, altering the mode of growth (Hansson *et al.*, 1993b; Kawano *et al.*, 1993). High-temperature wetting phenomena relevant to LPE on various substrates are treated by Eustathopoulos *et al.* (Eustathopoulos *et al.*, 1999).

## 5.6 LOW-TEMPERATURE SILICON LPE

There are several incentives for reducing epitaxy temperatures including reduction of background impurities in the epitaxial layer; less thermal degradation of substrate properties,

**Table 5.3** Low-temperature Silicon LPE

Solvent	Growth temperature (°C)	Substrate orientation	Growth rate ( $\mu\text{m min}^{-1}$ )	Reference
Ga	600	(111)	0.05–0.1	Girault <i>et al.</i> , 1977
Ga-Al	450–600	(111)	0.05–0.01	Girault <i>et al.</i> , 1977
Ga	290–400	(111)	0.01	Linnebach and Bauser, 1982
Au	400–800	(100),(111)	0.05–0.1	Kresse <i>et al.</i> , 1990
Au-Bi				
Bi-Au	380–450	(100),(111)		Lee and Green, 1991
Pb-Au				
Al-Sn	350–500	(111)		Shi <i>et al.</i> , 1991
Al-Zn				
Au-Sn				
Ga	440–670	(111)	0.05	Ogawa <i>et al.</i> , 1995
Sn	800	(111)	0.14	Abdou <i>et al.</i> , 2005

especially minority carrier lifetimes; and less smearing of features formed prior to epitaxy such as dopant profiles, metallization, masking layers, etc.

A low-temperature silicon deposition process would also widen the choice of potential substrates for thin-film silicon devices, although in practice, the resulting grain structure or lack of crystallinity for silicon films deposited on nonsilicon substrates, tends to restrict the usefulness of this approach. Growth temperatures are limited by the eutectic temperature of the melt, the ability to achieve or maintain an oxide-free substrate surface (see Appendix 3), the extremely low solubility of silicon in the melt, or small change in solubility with temperature. Low temperature approaches have been based novel melt compositions. Girault *et al.* (Girault *et al.*, 1977) and Lee and Green (Lee and Green, 1991) evaluated a number of binary and ternary silicon-metal melts for low-temperature silicon epitaxy. Table 5.3 lists some results reported for low-temperature silicon LPE. Healy *et al.* (Healy *et al.*, 1991) demonstrated LPE of SiGe alloys from Si-Ge-Au-Bi melt under a  $10^{-4}$  Torr vacuum by cooling the melt from 470 to 395 °C.

## 5.7 PURIFICATION OF SILICON FOR SOLAR CELLS IN AN LPE PROCESS

The purification inherent in solution growth in general, and LPE in particular, is due to the preferential segregation of impurities to the liquid phase. This effect appears to be operative for almost all impurities as the measured distribution coefficients of most elements are very small ( $10^{-2}$  –  $10^{-6}$ ), indicating the deposited silicon will benefit from a substantial reduction in almost every contaminant relative to that of the silicon starting material. There is interest in exploiting such purification phenomena for making silicon for solar cells. Currently, electronic-grade silicon (ppb purity) as used for integrated circuit manufacture, and solar-grade silicon (<ppm purity), as used for photovoltaic devices, costs anywhere

from 20 to 80 times more than metallurgical-grade (MG) silicon (98–99 % pure). The refining of metallurgical silicon to a ‘solar-grade’ suitable for solar cells represents a major cost component for silicon solar cells and its high capital cost is partly responsible for the recurring silicon feedstock shortages that afflict the solar cell industry. Almost all impurities can be effectively removed from silicon by zone-refining, with the exception of boron which is found at unacceptably high levels in metallurgical grade silicon due to its presence in silica ores and the carbonaceous reducing agents used to make MG silicon. Phosphorous is also problematic as its segregation coefficient is close to 1, but the volatility of phosphorus and phosphorus compounds provides for other methods of removal (Suzuki *et al.*, 1990; Miki *et al.*, 1996). As a consequence, most silicon for semiconductor device applications is currently produced by a relatively expensive Siemens process involving the formation, distillation and pyrolysis of silanes or halosilanes.

A silicon LPE process that could utilize a metallurgical-grade silicon or ‘upgraded-metallurgical’ silicon as a source of silicon would yield significant cost reductions in solar cells, as well as enable a virtually unlimited amount of silicon feedstock. Specifically, a relatively impure silicon material could be used to saturate the melt from which silicon of higher purity is deposited, preferably as a large-grain polycrystalline layer on a low-cost substrate. In one scenario, the metallic melt accumulates the impurities due to the silicon starting material, but it would be generally cost-effective to refine the melt for re-use. In another scenario, impurities could be removed or otherwise separated from the melt during the silicon deposition process. For the melts commonly used for silicon LPE, including tin, indium, lead, and bismuth, this does not appear promising since the boron segregation coefficient in these melts is close to 1, and therefore, no significant boron reduction would be expected due to segregation effects. However, McCann *et al.* (McCann *et al.*, 2002) noted that boron segregation in silicon LPE with tin melts was temperature and time dependent, and it appeared that boron levels in both the melt and silicon were gradually reduced over time. They attributed this to precipitation of boron from the tin-rich liquid phase since the boron solubility in molten tin is exceedingly small. This effect is intriguing as it suggests a possible route for removing boron in silicon LPE systems. Some recent work of relevance is the report of boron removal by addition of titanium in solidification refining of silicon from silicon-aluminum melts (Yoshikawa *et al.*, 2005). To account for the behavior of boron, it was surmised that boron forms  $TiB_2$  precipitates. Titanium additions of up to a few thousand parts per million on an atomic basis (ppma) could reduce the boron levels in the melt by about a factor of 10, down to concentrations of 10 ppma. Corresponding reductions of boron levels in the solidified silicon, down to the 1–5 ppma concentration range, were also measured. This particular melt chemistry results in silicon that is heavily doped with titanium and aluminum, but these impurities might be removed by post-growth gettering or zone refining. At any rate, these results suggest melt chemistries could be optimized to effect appreciable boron removal during the LPE, permitting the use of less-pure silicon starting materials. Additionally, purification could be further effected by sparging of the LPE melt with reactive gases such as HCl, water vapor, or ammonia to convert boron to volatile or insoluble boron compounds or boron compounds that could be separated from the melt by precipitation or by separation to an immiscible phase in contact with the melt. Also, fused salt or fused oxide fluxes could be contacted with the melt to absorb boron or boron compounds. Thus, there appears to be many unexplored avenues and promising options to implement some type of purification along with silicon deposition from molten solutions.

## 5.8 ELECTRICAL PROPERTIES OF LPE-GROWN SILICON

Table 5.4 summarizes electrical properties for LPE-grown epitaxial silicon layers using various metal solvents. Bulk minority carrier properties (lifetime and diffusion length) are sensitive to the doping, system purity and defect levels. Also, for thin epitaxial layers it can be difficult to decouple bulk effects from surface and substrate effects. Melts comprised of tin, indium or gallium (at low growth temperatures) can yield diffusion lengths adequate for thin-film silicon solar cells.

**Table 5.4** Semiconductor properties of metallic solution-grown silicon

Melt solvent	Growth temp. (°C)	Doping conc. (cm <sup>-3</sup> )	resistivity (Ω-cm)	Carrier mobility (cm <sup>-2</sup> V <sup>-1</sup> s <sup>-1</sup> )	Minority carrier lifetime (μs)	Diffusion length (μm)	Reference
Al	750	10 <sup>19</sup>		20		≈ 3	Ito and Kojima, 1980
Au-Bi	800–900	10 <sup>14</sup> – 10 <sup>15</sup>			2–10		Ujihara <i>et al.</i> , 2003a
Cu	950	<10 <sup>16</sup>				>100	Ciszek <i>et al.</i> , 1993a, b
Ga	900	1.7 × 10 <sup>19</sup>	0.013	28		<1	Girault <i>et al.</i> , 1977
Ga	600	10 <sup>18</sup>	0.42	70		1	Ito <i>et al.</i> , 1982
Ga <sub>0.7</sub> Al <sub>0.3</sub>	450	1.4 × 10 <sup>18</sup>	0.03	150		<1	Girault <i>et al.</i> , 1977
Ga	500–900				50–175		Satoh <i>et al.</i> , 2005
Ga	300–600	2–200 × 10 <sup>18</sup>		15–70			Käss <i>et al.</i> , 1985
Ga	450–600	8 × 10 <sup>19</sup>	0.005				Ogawa <i>et al.</i> , 1995
In	920	10 <sup>16</sup>		90–260			Kopecek <i>et al.</i> , 2000
In	946	1.8 × 10 <sup>16</sup>	2.17	285			Scott and Hager, 1979
In	1056	1.2 × 10 <sup>17</sup>	1.3	275			Scott and Hager, 1979
In	1150	5 × 10 <sup>17</sup>	0.35	243			Scott and Hager, 1979
In	1250	1.6 × 10 <sup>18</sup>	0.25	206			Scott and Hager, 1979
In	900–1200	10 <sup>17</sup> – 10 <sup>18</sup>				2–12	Ujihara <i>et al.</i> , 2003
In (+ Ga dopant)	600–900	5 × 10 <sup>16</sup> – 10 <sup>17</sup>				50–300+	Kolodinski <i>et al.</i> , 1993
In (+ Ga dopant)	920	5 × 10 <sup>16</sup>		280	120	100–250	Arch <i>et al.</i> , 1993a, b
In (+ Ga dopant)	947	10 <sup>17</sup>			2–3.5	50–65	Wagner <i>et al.</i> , 1997
In (+ Ga dopant)				100–200	25		Shi <i>et al.</i> , 1996
In (+ Ga dopant)	980	10 <sup>16</sup> – 2 × 10 <sup>18</sup>			5–10		Thomas <i>et al.</i> , 1997
In (+ Ga dopant)	920	4–30 × 10 <sup>17</sup>		70–200	~1		Kopecek <i>et al.</i> , 2000
Pb	990		0.2–10				Konuma <i>et al.</i> , 1999
Sn	950	8–22 × 10 <sup>15</sup>	0.2–0.7		0.3–1.0	15–30	Possin, 1984
Sn	900		25–100		5–10		Trumbore <i>et al.</i> , 1959
Sn	950				100		Baliga, 1982
Sn <sub>0.6</sub> Pb <sub>0.4</sub>	1000	≈ 10 <sup>20</sup>	0.2–20				D'Asaro <i>et al.</i> , 1967
Sn <sub>0.14</sub> Tl <sub>0.86</sub>	1100–1370			2000 (77K)			Schafer, 1981
Sn	900	2 × 10 <sup>16</sup>	1–2 (n)	150–300		50–60	Peter <i>et al.</i> , 1995
Sn (+ Al dopant)	930	1.5 × 10 <sup>17</sup>		100–200	8.5		Shi <i>et al.</i> , 1996

### References

- J.K. Arch, E. Bauser, S. Kolodinski and J.H. Werner (1993a) Characterization of liquid phase epitaxy for thin-film silicon solar cells. *Proc. 11th European Photovoltaic Solar Energy Conf.*, Harwood, Chu, Switzerland, 1047–1052.
- J.K. Arch, J.H. Werner and E. Bauser (1993b) Hall effect analysis of liquid phase epitaxy silicon for thin solar cells. *Solar Energy Mater Solar Cells* **29**, 387–396.
- B.J. Baliga (1982) High lifetime silicon liquid phase epitaxy. *J. Electrochem. Soc.* **129**, 665–666.
- T.F. Ciszek, T.H. Wang, R.W. Burrows and X. Xu (1993a) Growth of thin crystalline silicon layers for photovoltaic use. *J. Cryst. Growth* **128**, 314–318.
- T.F. Ciszek, T.H. Wang, X. Wu, R.W. Burrows, J. Alleman, C.R. Schwardtfefer and T. Bekkedahl (1993b) Si thin layer growth from metal solutions on single-crystal and cast metallurgical-grade multicrystalline Si substrates. *Conf. Record of the 23rd IEEE Photovoltaic Specialists Conf.*, IEEE, New York, 65–72.

**Table 5.4** (continued)

- L.A. D'Asaro, R.W. Landorf and R.A. Furanage (1969) Low defect silicon by liquid phase epitaxy in *Semiconductor Silicon, Electrochemical Society Softbound Symposium Series*, R.R. Haberecht and E.L. Kern, eds. Electrochemical Society, New York 233–242.
- B. Girault, F. Chevrier, A. Joullie and G. Bougnot (1977) Liquid phase epitaxy of silicon at very low temperatures. *J. Cryst. Growth* **37**, 169–177.
- K. Ito and K. Kojima (1982) Solution-grown silicon solar cells. *Jpn. J. Appl. Phys., Suppl.* **19-2**, 37–41.
- K. Ito, T. Nakazawa and A. Masamura (1982) Silicon solar cells made by liquid phase epitaxy. *Jpn. J. Appl. Phys., Suppl.* **21**, 125–129.
- D. Käss, M. Warth, W. Appel, H.P. Strunk and E. Bauser (1985) Silicon layers grown by liquid phase epitaxy. *Proc. 1st International Conf. on Silicon Molecular Beam Epitaxy*, Electrochemical Society, Pennington, NJ, 250–258.
- S. Kolodinski, J.H. Werner, U. Rau, J.K. Arch and E. Bauser (1993) Thin silicon solar cells from liquid phase epitaxy. *Proc. 11th European Photovoltaic Solar Energy Conf.*, Harwood, Chur, Switzerland, 53–56.
- M. Konuma, G. Cristiani, E. Czech and I. Silier (1999) Liquid phase epitaxy of Si from Pb solutions. *J. Cryst. Growth* **198/199**, 1045–1048.
- R. Kopecek, K. Peter, J. Hötzel, and E. Bucher (2000) Structural and electrical properties of silicon epitaxial layers grown by LPE on highly resistive monocrystalline substrates. *J. Cryst. Growth* **208**, 289–296.
- H. Ogawa, Q. Guo, and K. Ohta (1995) Low temperature liquid phase epitaxy of silicon from gallium solution. *J. Cryst. Growth* **155**, 193–197.
- K. Peter, G. Willeke, and E. Bucher (1995) Rapid growth of high quality crystalline silicon by a novel temperature gradient liquid phase epitaxy (LPE) technique. *Proc. 13th European Photovoltaic Solar Energy Conf.*, Stephens and Associates, Felpersham, 379–381.
- G.E. Possin (1984) Solution growth of silicon from liquid tin for application to photovoltaic solar cells. *Solid-State Electron.* **27**, 167–176.
- Y. Satoh, N. Usami, W. Pan, K. Fujiwara, K. Nakajima, and T. Ujihara (2005) Influence of growth temperature on minority carrier lifetime of Si layer grown by liquid phase epitaxy using Ga solvent. *J. Appl. Phys.* **98**, 073708-1–073708-4.
- D.E. Schafer (1981) Solution growth of thallium-doped silicon for 3–5 micrometer photoconductive detectors. *Proc. SPIE* **285**, 183–189.
- W. Scott and R.J. Hager (1979) Solution growth of indium-doped silicon. *J. Electron. Mater.* **8**, 581–602.
- Z. Shi, W. Zhang, G.F. Zheng, V.L. Chin, A. Stephens, M.A. Green, and R. Bergmann (1996) The effects of solvents and dopant impurities on the performance of LPE silicon solar cells. *Solar Energy Mater. Solar Cells* **41–42**, 53–60.
- B. Thomas, G. Mueller, P.-M. Wilde, and H. Wawra (1997) Properties of silicon thin films grown by the temperature difference method (TDM). *Conf. Record of the 26th IEEE Photovoltaic Specialists Conf.*, IEEE, New York, 771–774.
- F.A. Trumbore, C.R. Isenberg, and E.M. Porbansky (1959) On the temperature dependence of the distribution coefficient. The solid solubilities of tin in silicon and germanium. *J. Phys. Chem. Solids* **9**, 60–69.
- T. Ujihara, K. Obara, N. Usami, K. Fujiwara, G. Sazaki, T. Shishido and K. Nakajima (2003a) High quality crystalline silicon layer grown by liquid phase epitaxy method at low growth temperatures. *Jpn. J. Appl. Phys.* **42**, L217–L219.
- T. Ujihara, K. Obara, N. Usami, K. Fujiwara, G. Sazaki, T. Shishido, and K. Nakajima (2003b) What is the most important growth parameter on crystal quality of the silicon layer by LPE method? *Proc. 3rd World Conf. on Photovoltaic Solar Energy Conversion*, IEEE, New York, 1241–1244.
- G. Wagner, H. Wawra, W. Dorsch, M. Albrecht, R. Krome, H.P. Strunk, S. Reidel, H.J. Möller and W. Appel (1997) Structural and electrical properties of silicon epitaxial layers by LPE and CVD on identical polycrystalline substrates. *J. Cryst. Growth* **174**, 680–685.

## 5.9 LPE OF Si- AND Ge-BASED ALLOYS

LPE has been employed to grow Si- and Ge-based heterostructures Donnelly and Milnes (Donnelly and Milnes, 1966) reported the epitaxial growth of Ge layers on silicon substrates using tin-rich melts and growth temperatures of 600–650 °C. Kurata and Hirai (Kurata and Hirai, 1968) made Ge-Si heterojunctions by growing Ge layers on silicon substrates from silver and aluminum-based melts at temperatures of 600–800 °C. Laugier *et al.* (Laugier *et al.*, 1970) described the LPE growth of Ge on GaAs from indium and lead-tin melts at growth temperatures of 450–500 °C. *p-n* heterojunctions (*p-Ge/n-GaAs* and *n-Ge/p-GaAs*) were realized at the growth interface. Rosztochy and Stein (Rosztochy and Stein, 1972) grew Ge on GaAs from Ge-Ga-As melts at ~850 °C. Zolper and Barnett (Zolper and Barnett, 1989) developed selective growth of Ge on oxide-masked silicon

using In-Ga-Mg and In-Bi-Mg melts at 600 °C. The germanium-on-silicon structures were used to seed the LPE growth of GaAs from lead melts at 650 °C.

Several alloys of the form  $(IV_2)_{1-x}(III-V)_x$  and related types have been grown by LPE. Saidov and Saidov (Saidov and Saidov, 1991a,b) developed LPE techniques for producing  $(Ge_2)_x(GaSb)_{1-x}$ ,  $(Ge_2)_x(InP)_{1-x}$ ,  $(Ge_2)_x(GaAs)_{1-x}$ , and  $(Si_2)_x(GaP)_{1-x}$  alloys. Saidov *et al.* (Saidov *et al.*, 2001) also reported the LPE growth  $Ge_{1-x}Sn_x$  on Ge substrates from a tin melt in the temperature interval of 450–740 °C. Abramov *et al.* (Abramov *et al.*, 1994) used gallium and tin melts with ultrafast cooling ( $\sim 10^2$ – $10^3$  °C s<sup>-1</sup>) to grow epitaxial layers of metastable  $(Ge_2)_x(GaAs)_{1-x}$  on silicon substrates. Kazikov *et al.* (Kazikov *et al.*, 1990) analyzed the LPE of  $(IV_2)_{1-x}(III-V)_x$  alloys using quasi-regular solution models.

## 5.10 SELECTIVE LPE AND LIQUID PHASE ELO

Selective epitaxy refers to the preferential growth of crystals in openings (also called *vias* or ‘windows’) defined in a masking layer coating a substrate. The openings in the mask expose areas of the substrate that selectively seed the growth of an epitaxial layer; ideally there is no deposition of material on the masked regions of the substrate. Selective epitaxy has been demonstrated for many semiconductors including silicon and most of the III-V compounds using either LPE or CVD. Epitaxial growth methods that operate under near-equilibrium growth conditions, such as LPE and certain types of CVD, are conducive for selective epitaxy due to the ability to control nucleation, thereby limiting growth to the vias and avoiding higher supersaturations that results in extraneous nucleation and deposition on the mask. Masking layers can be made of dielectrics, metals, or metallic compounds, deposited by various thin film deposition methods such as thermal or electron beam evaporation, sputtering, or CVD, and range in thickness from 50 to several hundred nanometers. For selective epitaxy on silicon substrates, thermally grown oxides are commonly used as masking layers.

Kim (Kim, 1972) developed a selective silicon LPE technique for growing silicon pedestals on oxide-masked silicon substrates using Sn-Pb melts and growth temperatures of 700–750 °C. A thin layer of sacrificial nickel was deposited over the masked substrates to prevent oxidation of the window regions; the nickel dissolves in the melt upon contact of the substrate with the melt, thus revealing a clean silicon surface. Baliga (Baliga, 1982b) reported a technique for re-filling silicon grooves in a profiled substrate using liquid phase epitaxy (see Figure 5.7). Zolper and Barnett (Zolper and Barnett, 1989) described selective area solution growth of Ge (and GaAs) on oxide-masked silicon substrates using In-Bi-Mg melts. Wurschum *et al.* (Wurschum *et al.*, 1990) used silicon LPE from a gallium solvent at 560 °C to seal small bore holes (diameter 250–500 μm) in silicon crystals. The laterally overgrown silicon layers were mechanically stable and gas-tight.

Epitaxial lateral overgrowth (ELO) is an extension of selective epitaxy. In ELO on a dielectric-masked substrate, the selectively grown crystals laterally overgrow the insulating masking layer, forming an overgrown region that approximates a silicon-on-insulator structure. Such structures have several unique features and useful applications. First, the oxide mask provides electrical isolation of the epitaxial layer from the substrate. This is useful in high-frequency, high-speed digital, and radiation-hardened device applications since semi-insulating (lattice-matched) substrates compatible with silicon epitaxy

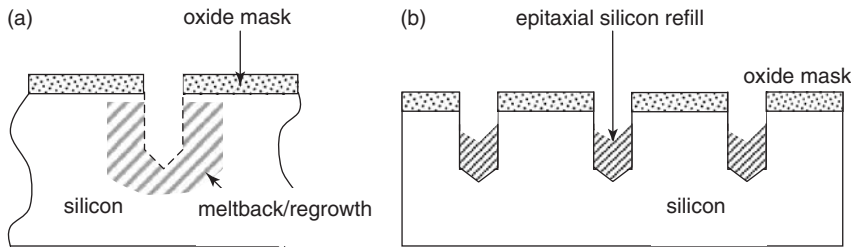


**Figure 5.7** (a) Melt back and regrowth on patterned, masked silicon substrate. (b) Epitaxial refill of vias on oxide-masked silicon substrate. After Baliga (Baliga, 1982b)

are not available. This feature can also be exploited for three-dimensional semiconductor structures (Morrison and Duad, 1985; Bauser and Strunk, 1994). Second, the masking can lower function as a defect filter that blocks the propagation of defects from the substrate or growth interface (Bergmann *et al.* 1990). Although this feature is not so critical in silicon homoepitaxy on silicon substrates since virtually defect-free silicon wafers and low-defect epitaxy methods are available, it nevertheless can be very advantageous for ELO of  $\text{Ge}_{1-x}\text{Si}_x$  layers on masked silicon substrates, especially for providing a low-defect, stress-relieved germanium-on-silicon substrate for near lattice-matched growth of GaAs on germanium-on-silicon in a subsequent epitaxy process using MOCVD, MBE or LPE. Third, the mask can facilitate separation of the epitaxial structure from the substrate to effect its transfer and bonding to another substrate and re-use of the original substrate (Stocks *et al.*, 2003). Fourth, the mask can serve as a 'buried mirror' reflective layer to improve the performance of solar cells and detectors (Mauk and Barnett, 1987). Other types of masking layers may be employed to effect metallic reflectors or buried electrodes (Mauk *et al.*, 1996).

ELO using Si and GaAs vapor phase epitaxy (VPE) was first reported in the 1960s (Tausch and Lapierre, 1965). A figure of merit for ELO is the aspect ratio, defined as the ratio of the width of the epitaxial layer atop the mask to the thickness of the epitaxial layer. VPE typically exhibits aspect ratios of 1–5. The lateral extent of overgrowth atop the mask is typically  $\sim 10\ \mu\text{m}$ . Leamy and Doherty (Leamy and Doherty, 1980) reported nucleation-controlled silicon overgrowth on an oxidized silicon wafer. The silicon crystals were grown from an Al-Si liquid film by nucleation via holes etched in the oxide mask. Appel *et al.* (Appel *et al.*, 1985) and Bauser *et al.* (Bauser *et al.*, 1986) developed ELO using silicon LPE on thermal oxide-masked (111) silicon substrates. The oxide mask was patterned with stripe vias with various widths (1–30  $\mu\text{m}$ ) and LPE was performed using an indium-rich melt. Further refinements and optimization of Si ELO using LPE demonstrated dramatic overgrowth characteristics compared with what had been achieved previously with VPE. Suzuki and Nishinaga (Suzuki and Nishinaga, 1989) investigated the growth kinetics and orientation dependence of the stripe vias for silicon ELO on oxide-masked silicon substrates using LPE with tin melts, and identified the sources of atomic steps that provide for ELO (Suzuki *et al.*, 1990). Suzuki and Nishinaga (Suzuki and Nishinaga, 1990) also described a 'ridge seed' type via, formed as an oxide-capped silicon mesa (with exposed silicon sidewalls for seeding) on an oxide-masked silicon substrate. This allowed ELO layers as thin as  $0.2\ \mu\text{m}$  with aspect ratios over 80. Kinoshita *et al.* (Kinoshita *et al.*, 1991) further developed Si LPE (tin melt,



900 °C growth temperature) ELO on oxide-masked, nonplanar structured (111) silicon substrates with various surface profiles and via sitings. Despite the irregular topology of the substrate, epitaxial layers with flat top surfaces were invariably produced due to the formation of (111) facets in the plane of the epitaxial film. Mauk and Barnett (Mauk and Barnett, 1987) applied silicon LPE ELO from tin melts using a pattern of circular vias formed in an oxide mask on a silicon substrate for application to solar cells with light trapping effected by the intervening oxide mask between the epitaxial solar cell and substrate. Bergmann (Bergmann, 1991) presented a model defect-free ELO of silicon of oxide masking layers by LPE. This work produced the first metal oxide semiconductor (MOS) transistors on insulator by silicon LPE (Zingg *et al.*, 1992). The coalescence of silicon layers in LPE ELO in order to form a continuous film, along with an examination and strains and defect nucleation has been presented by Nagel *et al.* (Nagel *et al.*, 1993) and Banhart *et al.* (Banhart *et al.*, 1991, 1993). Köhler *et al.* (Köhler *et al.*, 1996) studied the vertical stress in silicon LPE ELO layers using X-ray double crystal topography. A model relating stress to adhesive force between the crystal and mask was proposed. The defect-free coalescence of silicon LPE ELO layers and nearly defect-free SiGe LPE ELO layers were achieved by Silier *et al.* (Silier *et al.*, 1996a). Józwik and Olchowik (Józwik and Olchowik, 2006) developed a two-step silicon LPE ELO process to further optimize aspect ratios and defect reduction. Mauk and Curran (Mauk and Curran, 2001) applied silicon electro-epitaxy from bismuth melts on stripe-patterned, tungsten-masked (111) silicon substrates. Continuous (coalesced) lateral overgrowth was achieved and under certain conditions the epitaxial laterally overgrown silicon formed a silicon ‘air bridge’ structure spanning the vias with voids between the silicon epilayer and tungsten. Weber *et al.* (Weber *et al.*, 1998) reported remarkable LPE-grown silicon structures on oxide-masked (100) silicon substrates with line vias arranged in a rectangular pattern. A silicon mesh structure that could be detached from the seeding substrate by selective etching to yield a self-supporting silicon grid was shown. Also reported were hollow pyramid silicon structures using selective LPE on pairs of opposing right-angled vias. Heteroepitaxial lateral overgrowth of  $\text{Ge}_x\text{Si}_{1-x}$  ( $0.8 < x < 1$ ) over patterned, oxide-masked (111) silicon using LPE with Bi-Ge-Si melts at growth temperatures of 800 °C was reported by Hansson *et al.* (Hansson *et al.*, 1991). Significant defect reductions associated with lateral overgrowth were indicated. ELO has also been used in lift-off processes where the epitaxial structure is separated from the substrate, permitting the substrate to be re-used. An interesting variation is the epilift process reported by Weber *et al.* (Weber *et al.*, 1997, 1998, 2003) wherein a silicon frame or mesh structure is epitaxially grown on a grid-patterned, oxide-masked silicon substrate. Aiken and Barnett (Aiken and Barnett, 1999) described an embedded semiconductor grid solar cell made by LPE ELO of silicon on oxide-masked silicon substrates that eliminates front contact shading. Smith *et al.* (Smith *et al.*, 1996, 1997) reported an MOS test structure to measure the minority carrier surface recombination velocity at the interface between the LPE-overgrown silicon layer and oxide mask.

## 5.11 SOLAR CELLS

The adaptation of silicon LPE for solar cells has generated significant interest, both as a means for achieving high-efficiency devices and as a low-cost method of manufacture. Most of this work has been directed at using LPE or LPE-like metallic solution

growth processes for deposition of silicon layers on silicon substrates. Substrates include silicon wafers cut from pulled Czochralski (CZ) single-crystal (monocrystalline) boules or polycrystalline (multicrystalline) cast ingots, silicon sheets and recrystallized CVD-deposited silicon layers on ceramics. LPE and related solution growth processes have several important advantages for solar cell production including high deposition rates; impurity segregation/rejection to the liquid phase (melt), thus avoiding accumulation of electrically active impurities at grain boundaries and yielding silicon layers with low defect densities, especially dislocations. In most cases, LPE has proven to be a workable approach for silicon deposition. More ambitiously, but less successfully, processes analogous to or derived from LPE have been used to deposit silicon layers on foreign (nonsilicon) substrates such as steel or glass.

In one of the earliest considerations of LPE-like processes for producing silicon solar cells, Runyan (Runyan, 1976) assessed the prospects for growing silicon from molten metals including the possibility of depositing large-area thin films of silicon on low-cost substrates such as metal. Runyan correctly concluded that excessive doping of the silicon from the metal solvent (e.g. Al, Au, Ga or Sn), as well as problems related to silicon oxidation and the difficulties in removing surface oxides on silicon would be formidable hurdles. Subsequent work showed that tin, indium, copper, lead and bismuth solvents could be used to grow silicon with doping ranges compatible with good solar cell performance, and that problems associated with silicon oxidation were tractable. The rationale and prospects for thin-film (crystalline and multicrystalline) silicon solar cells, and applications of LPE and metallic solution growth for thin-film silicon solar cells has been reviewed by Slaoui *et al.* (Slaoui *et al.*, 1998), Bergmann (Bergmann, 1999), and Beaucarne *et al.* (Beaucarne *et al.*, 2004). Brendel (Brendel, 2001) has reviewed applications of LPE for layer transfer processes for thin-film silicon solar cells.

### 5.11.1 Epitaxial silicon solar cells by LPE

Since a high-efficiency silicon solar cell can be made on a silicon wafer *without* any epitaxial layers, the use of epitaxy warrants some justification. The rationalization for an epitaxial silicon solar cell is based on the expected savings from substitution of the solar-grade silicon wafer with a relatively low-quality silicon substrate on which an epitaxial layer of high-quality silicon is grown. The photovoltaic effect is due mostly to optical absorption, minority carrier generation, and minority carrier collection in the epitaxial layer; the substrate is merely a mechanical support and back contact or reflector. For example, a large-grain silicon substrate made from metallurgical-grade silicon would be considerably cheaper than the monocrystalline semiconductor-grade silicon wafers used to make high-efficiency silicon solar cells, but would still retain the most important advantages of a silicon substrate used for silicon homoepitaxy including near-perfect lattice and thermal expansion match between the silicon film and substrate. Further, such a substrate could reliably yield an epitaxial layer with large grain size and reduced defects relative to the substrate.

Despite these anticipated advantages of LPE for silicon solar cells, most of the efforts in thin film solar cells focused instead on vapor-phase techniques for depositing amorphous silicon and compound semiconductors. Starting in the early 1980s and continuing for the next 20 years, steady progress was made in both single-crystal and multicrystalline

silicon solar cells that featured at least one silicon layer deposited by LPE or metallic solution growth. Ito and Kojima (Ito and Kojima, 1982) made 10.4% efficient silicon solar cells by forming a *p*-type emitter on an *n*-type silicon wafer using silicon LPE from a gallium melt. Possin (Possin, 1984) proposed a silicon solar cell with a thick (10–50  $\mu\text{m}$ ) LPE-grown epitaxial junction, but this design requires a minority carrier lifetime of  $\sim 10 \mu\text{s}$  in the emitter epilayer, which was considerably higher than the  $\sim 1 \mu\text{s}$  lifetimes achieved for silicon LPE-layers grown from tin at  $900^\circ\text{C}$  in the same work. More interesting for low-cost solar cells are photovoltaic devices where the emitter is formed (e.g. by diffusion or epitaxy) in a base layer deposited by LPE. Gutjahr *et al.* (Gutjahr *et al.*, 1997) used LPE for making SiGe solar cells, achieving an efficiency of 9.1%. Incorporation of  $\text{Si}_x\text{Ge}_{1-x}$  layers into solar cells and other devices may prove useful for tuning the bandgap, controlling defect generation and formation, enhancing luminescence, and altering dominant minority carrier recombination mechanisms (Hansson *et al.*, 1994b; Bremond *et al.*, 1998; Kruger *et al.*, 1998). Efficiencies for LPE homoepitaxial silicon solar cells are as high as 18% (see Table 5.5).

LPE of silicon on multicrystalline and structured silicon wafers has been investigated by a number of workers. Morphology of LPE silicon layers on silicon substrates mis-oriented from a low index plane is described by Kozhitov *et al.* (Kozhitov *et al.*, 1986). The structural features of polycrystalline solution-grown silicon layers were investigated by Lozovskii *et al.* (Lozovskii *et al.*, 1985). Weber and Blakers (Weber and Blakers, 1995a), Steiner *et al.*, (Steiner *et al.*, 1996), Stemmer *et al.* (Stemmer *et al.*, 1996), Voigt *et al.* (Voigt *et al.*, 1996) and Ballhorn *et al.* (Ballhorn *et al.*, 1998) have developed LPE on multicrystalline silicon substrates, and the latter group achieved efficiencies of 15.4%. Wagner *et al.*, (Wagner *et al.* 1997) demonstrated that LPE-grown polycrystalline silicon films have a higher minority carrier lifetime and longer diffusion length compared with silicon films deposited by CVD. This is attributed to the relatively lower density of dislocations at grain boundaries in LPE-grown silicon.

LPE of silicon solar cells on metallurgical-grade silicon has also been investigated (Wang *et al.*, 1996; Peter *et al.*, 2002; Muller *et al.*, 2003), as well as LPE on recrystallized silicon sheets (Tool *et al.*, 2000). Nakagawa *et al.* (Nishida *et al.*, 2001; Nakagawa *et al.*, 2005) patented a silicon LPE dipping method with an optimized time–temperature program to ameliorate the effects of grain boundaries in solar cells. Deguchi *et al.* (Deguchi *et al.*, 1990) investigated the use of recrystallized vapor-deposited silicon seeding layers and ELO for making silicon solar cells by LPE on metallurgical silicon substrates. Berger *et al.* (Berger *et al.*, 2001) and Ould-Abbas *et al.* (Ould-Abbas *et al.*, 2004) reported LPE on porous silicon bilayers with the stated objective of using the porous layer to enable easier removal of the silicon epitaxial layer for transfer to a cheaper substrate and re-use of the seeding substrate. The electrical characteristics were similar for silicon layers formed by either LPE or CVD on porous silicon substrates (Fave *et al.*, 2004). Fave *et al.* (Fave *et al.* 2001) described LPE of silicon on regularly textured silicon substrates, where it is anticipated that the structuring of the silicon substrate could be replicated in ceramics to make low-cost silicon on ceramic solar cells.

McCann *et al.* (McCann *et al.*, 2001) and Catchpole *et al.* (Catchpole *et al.*, 2001) have compiled results for thin crystalline and polycrystalline silicon solar cells made by LPE and CVD techniques on various substrates. Results excerpted for LPE are summarized in Table 5.5, and supplemented with more recent data since these reviews.

**Table 5.5** Results for solar cells made with LPE

Researchers	Substrate	Melt, growth temp.	Results (efficiency; $V_{oc}$ )	Reference
<i>Monocrystalline silicon substrates</i>				
Samsung	<i>p</i> -Si	In	15.8 %; 634 mV	Lee <i>et al.</i> , 2003
MPI	SiGe buffer/Si	In, 950 °C	9.1 %	Gutjahr <i>et al.</i> , 1997a
UNSW	<i>p</i> + sc-Si		16.4 %; 645 mV	Zheng <i>et al.</i> , 1996
UNSW	<i>p</i> +scSi	Sn/Ga	15.4 %; 616 mV	Shi <i>et al.</i> , 1996
		In/Ga	14.7 %; 640 mV	
ANU	<i>p</i> - sc-Si	In, 950 °C	18 %; 666 mV	Blakers <i>et al.</i> , 1995a
ANU	<i>p</i> + sc-Si	In, 950 °C	17 %; 651 mV	Blakers <i>et al.</i> , 1995b
Fraunh ISE	<i>p</i> -silicon		13.3 % (1 × con)	Wagner <i>et al.</i> , 1993
			15.9 % (30 × con)	
MPI	<i>p</i> +sc-Si	In, 950 °C	14.7 %; 659 mV	Werner <i>et al.</i> , 1993
Shinsu U.	<i>n</i> -Si	Al	9.9 %	Ito and Kojima, 1980
<i>Multicrystalline, structured or porous silicon wafer substrate</i>				
Samsung	recrystallized Si	In	13 %; 663 mV	Lee <i>et al.</i> , 2003
Konstanz U.	UMG silicon	In	10 %	Peter <i>et al.</i> , 2002
Canon	porous silicon	In, 950 °C	9.5 %; 520 mV	Nishida <i>et al.</i> , 2001
Konstanz U.	UMG silicon	In	6 %; 551 mV	Hotzel <i>et al.</i> , 2000
ANU	<i>p</i> -mc-Si		15.4 %; 639 mV	Ballhorn <i>et al.</i> , 1997
ANU	<i>p</i> +mc-Si		15.2 %; 639 mV	Ballhorn <i>et al.</i> , 1997
Inst. Krys.	mc-Si	In, 980 °C	$\tau = 5-10 \mu\text{s}$	Thomas <i>et al.</i> , 1997
NREL	MG-Si	Cu, 950 °C	$L = 42 \mu\text{m}$	Wang <i>et al.</i> , 1996
<i>Nonsilicon substrate (may include silicon seeding layer)</i>				
PHASE	alumina + RTCVD Si seed		grain size = 100–300 $\mu\text{m}$	Bourdais <i>et al.</i> , 1998
MPI	glassy carbon + RF-plasma silicon seed	In	grain size = 100–300 $\mu\text{m}$	Gutjahr <i>et al.</i> , 1997b
Daido Hoxon	graphite		grain size = 100–300 $\mu\text{m}$ ; $L = 30 \mu\text{m}$	Mishima <i>et al.</i> , 1998; Ito <i>et al.</i> , 1999
ECN	Si/SiAlON + plasma-spray silicon		grain size = 10–100 $\mu\text{m}$	Schiermeier <i>et al.</i> , 1998
UNSW	high-temp. glass		grain size = 100 $\mu\text{m}$	Shi <i>et al.</i> , 1994
UNSW	high-temp. glass + a-Si seed		grain size = 50 $\mu\text{m}$	Shi <i>et al.</i> , 1993

sc, single crystal; mc, multicrystalline; MG, metallurgical grade; UMG, upgraded metallurgical grade; RTCVD, rapid thermal chemical vapor deposition; a-Si, amorphous silicon;  $V_{oc}$ , open-circuit voltage;  $L$ , minority carrier diffusion length;  $\tau$ , minority carrier lifetime; con, solar light optical concentration. ANU, Australian National University; Daido Hoxon, Daido Hoxon (Japan), ECN, Energy Research Center of the Netherlands (Petten, The Netherlands), Fraunh ISE, Fraunhofer Institute of Solar Energy (Freiburg, Germany); Inst. Krys., Institute of Crystallography (Berlin, Germany); MPI, Max Planck Institute (Germany); NREL, National Renewable Energy Laboratory (Golden, CO, USA); PHASE, PHASE CNRS (Strasbourg, France); UNSW, University of New South Wales (Australia). Adapted from McCann *et al.* (McCann *et al.*, 2001) and Catchpole *et al.* (Catchpole *et al.*, 2001) and supplemented with more recent data.

**Table 5.5** (continued)

---

*References*

- G. Ballhorn, K.J. Weber, S. Armand, M.J. Stocks and A.W. Blakers (1997) High efficiency thin multicrystalline silicon solar cells by liquid phase epitaxy. *Proc. 14th European Photovoltaic Solar Energy Conf.*, Stephens and Associates, Falmersham, 1011–1015.
- A.W. Blakers, K.J. Weber, M.F. Stuckings, S. Armand, G. Matlakowski, M.J. Stocks and A. Cuevas (1995a) 18 % efficient thin silicon solar cell by liquid phase epitaxy. *Proc. 13th European Photovoltaic Solar Energy Conf.*, Stephens and Associates, Falmersham, 33–37.
- A.W. Blakers, K.J. Weber, M.F. Stuckings, S. Armand, G. Matlowski, A.J. Carr, M.J. Stocks, A. Cuevas and T. Brammer (1995b) 17% efficient thin-film silicon solar cell by liquid-phase epitaxy. *Progr. Photovoltaics* **3**, 193–195.
- S. Bourdais, R. Monna, D. Angermeier, A. Slaoui, N. Rauf, A. Laugier, F. Mazel, Y. Jorand and G. Fantozzi (1998) Combination of RT-CVD and LPE for thin silicon-film formation on alumina substrates. *Proc. 2nd World Conf. on Photovoltaic Solar Energy Conversion*, Joint Research Center, European Commission, Luxembourg, 1794–1799.
- A. Gutjahr, I. Silier, N. Rollbuehler, M. Konuma, F. Banhart, K. Said and J. Poortmans (1997a) SiGe layer substrates for solar cell application by liquid phase epitaxy. *Conf. Record 26th IEEE Photovoltaics Specialists Conf.*, IEEE, New York, 759–762.
- A. Gutjahr, I. Silier, G. Cristiani, M. Konuma, F. Banhart, V. Schöllkopf and H. Frey (1997b) Silicon solar cell structure grown by liquid phase epitaxy on glass carbon. *Proc. 14th European Photovoltaic Solar Energy Conf.*, Stephens and Associates, Falmersham, 1460–1464.
- J. Hotzel, K. Peter, R. Kopecek, P. Fath, E. Bucher and C. Zahedi (2000) Characterization of LPE thin silicon on low cost silicon substrates. *Conf. Record 28th IEEE Photovoltaic Specialists Conf.*, IEEE, New York, 225–228.
- K. Ito and K. Kojima (1980) Solution grown silicon solar cells. *Jpn. J. Appl. Phys. Suppl.* **19-2**, 37–41.
- S. Ito, Y. Kitagawa, T. Mishima and T. Yokoyama (1999) Direct grown polycrystalline Si film on carbon substrate by LPE. *Technical Digest International Photovoltaic Science and Engineering Conf.*, 11, Tokyo, Japan, 539–545.
- T. Mishima, Y. Kitagawa, S. Ito and T. Yokoyama (1998) Polycrystalline silicon films for solar cells by liquid phase epitaxy. *Proc. 2nd World Conf. on Photovoltaic Solar Energy Conversion*, Joint Research Center, European Commission, Luxembourg, 1724–1729.
- E. Lee, K. Lee, D. Kim and S. Lee (2003) Optimization of Pt seeding Layer for thin film silicon solar cell by liquid phase epitaxy. *3rd World Conf. on Photovoltaic Solar Energy Conversion*, Arisuni Printing Corp., Japan, 1214–1216.
- S. Nishida, K. Nakagawa, M. Iwane, Y. Iwasaki, N. Ukiyo, M. Mizutani and T. Shoji (2001) Si-film growth using liquid phase epitaxy method and its application to thin-film Si solar cells. *Solar Energy Mater. Solar Cells* **65**, 525–532.
- K. Peter, R. Kopecek, P. Fath, E. Bucher and C. Zahedi (2002) Thin film silicon solar cells on upgraded metallurgical silicon substrates prepared by liquid phase epitaxy. *Solar Energy Mater. Solar Cells* **74**, 219–223.
- S.E. Schiermeier, C.J. Tool, J.A. van Roosmalen, L.J. Laas, A. von Keitz and W.C. Sinke (1998) LPE growth of crystalline silicon layers on ceramic substrates. *Proc. 2nd World Conf. on Photovoltaic Solar Energy Conversion*, Joint Research Center, European Commission, Luxembourg, 1673–1678.
- Z. Shi, T.L. Young, G.F. Zheng and M.A. Green (1993) Investigation of polycrystalline silicon deposition on glass substrates. *Solar Energy Mater. Solar Cells* **31**, 51–60.
- Z. Shi, T.L. Young and M.A. Green (1994) Solution growth of polycrystalline silicon on glass at low temperatures. *Proc. 1st World Conf. on Photovoltaic Solar Energy Conversion*, IEEE, New York, 1579–1584.

**Table 5.5** (continued)

- 
- Z. Shi, W. Zhang, G.F. Zheng, V.L. Chin, A. Stephens, M.A. Green and R. Bergmann (1996) The effects of solvent and dopant impurities on the performance of LPE silicon solar cells. *Solar Energy Mater. Solar Cells* **41–42**, 53–60.
- B. Thomas, G. Müller, P. Heidborn and H. Wawra (1997) Growth of polycrystalline silicon thin films using the temperature difference method. *Proc. 14th European Photovoltaic Solar Energy Conf.*, Stephens and Associates, Felmersham, 1483–1487.
- J. Wagner, Ch. Schletter, O.V. Sulima and A. Bett (1993) 15.9% efficiency for Si thin film solar concentrator solar cell grown by LPE. *Conf. Record of the 23rd IEEE Photovoltaic Specialists Conf.*, IEEE, New York, 356–359.
- T.H. Wang, T.F. Cizek, C.R. Schwerdtfeger, H. Moutinho and R. Matson (1996) Growth of silicon thin layers on cast Mg-Si from metal solutions for solar cells. *Solar Energy Mater. Solar cells* **41/42**, 19–30.
- J.H. Werner, S. Kolodinski, U. Rau, J.K. Arch and E. Bauser (1993) Silicon solar cell of 16.8  $\mu\text{m}$  thickness and 14.7% efficiency. *Appl. Phys. Lett.* **62**, 2998–3000.
- G.F. Zheng, W. Zhang, Z. Shi, M. Gross, A.B. Sproul, S.R. Wenham and M.A. Green (1996) 16.4% efficient, thin active layer silicon solar cell grown by liquid phase epitaxy. *Solar Energy Mater. Solar Cells* **40**, 231–238.

### 5.11.2 Si solution growth on nonsilicon substrates for solar cells

The deposition of silicon films on nonsilicon substrates with properties suitable for solar cell applications is a challenging problem. It is generally difficult to control heterogeneous nucleation to achieve both a sufficiently large (and uniform) grain size and a continuous film. Nevertheless, some promising results have been reported using a variety of approaches. Givargizov (Givargizov, 1991) discusses the general problem of oriented crystallization on amorphous substrates. A common approach is graphoepitaxy whereby the substrate is microstructured in order to induce a preferred orientation of crystals that would otherwise be nucleated with a random orientation (Klykov and Sheftal, 1981). Mori (Mori, 1981) used a two-dimensional grating with 1  $\mu\text{m}$  features formed on a quartz substrate to achieve oriented crystallization of silicon from a gold melt at 380 °C. Filby and Nielsen (Filby and Nielsen, 1966, 1967) demonstrated selective growth of silicon crystals on quartz substrates from gold-silicon alloys. Graef *et al.* (Graef *et al.*, 1977a,b) achieved 5–10- $\mu\text{m}$ -sized grains of silicon on graphite substrates using a vapor–liquid–solid (VLS) technique where the substrate is coated with a 5–10  $\mu\text{m}$  thick layer of molten tin that reacts with gaseous mixture of trichlorosilane and HCl.

One of the first applications of conventional LPE to thin film solar cells on dissimilar substrates is a report by Woodall (Woodall, 1978) describing GaAs LPE on polycrystalline molybdenum substrates demonstrating grain sizes from 10 to 300  $\mu\text{m}$ . Barnett *et al.* (Barnett *et al.*, 1982, 1984), and McNeely *et al.* (McNeely *et al.*, 1984) described LPE of 20- $\mu\text{m}$  thick polycrystalline silicon films on quartz and steel sheet substrates using LPE with tin solvents and growth temperatures of 800–1000 °C. Grain sizes in the range of 25–50  $\mu\text{m}$  were achieved. Lee *et al.* (Lee *et al.*, 1994) investigated solution growth of silicon on quartz from thin layers of molten Al-Si alloy deposited by thermal evaporation and heated to 580–800 °C. Schiermeier *et al.* (Schiermeier *et al.*, 1998) achieved continuous polycrystalline layers of silicon (50  $\mu\text{m}$  thick, grain size 10–70  $\mu\text{m}$ ) on ceramic substrates by deposition from an indium-aluminum (1%) melt saturated with silicon and a deposition

temperature of 960 °C. Gutjahr *et al.* (Gutjahr *et al.*, 2001) achieved continuous silicon films from Ga-Al melts on Si-infiltrated SiAlON tape-cast ceramic substrates. Silier *et al.* (Silier *et al.*, 1996b, c) reported a metallic solution growth method for silicon deposition on glass substrates. The glass substrates were initially coated with a seeding layer of nanocrystalline silicon, deposited deposited with SiH<sub>4</sub>/H<sub>2</sub>. A polycrystalline silicon film was grown on the seeding layer from an In (~900 °C) or Ga (200–350 °C) melt, and exhibited grain sizes up to 100 μm. Shi (Shi, 1994a) described the growth of large-area oriented silicon crystallites grown from Sn-Al melts on patterned SiO<sub>2</sub> layers on silicon substrates. Shi and Green, 1993; Shi (Shi, 1994b,c) also developed a method for depositing large-grain, large-area (10 cm<sup>2</sup>) continuous thin films of silicon on borosilicate glass from Sn-Al-Mg melts saturated with silicon. It is conjectured that aluminum or magnesium in the melt reduces the silica (SiO<sub>2</sub> of the substrate) to form silicon seeding sites for silicon nucleation. Periodic melt-back and regrowth suppressed growth normal to the plane of the substrate and lead to more uniformly sized grains with a (111) preferred orientation and smoother silicon films. Kamada *et al.* (Kamada *et al.*, 2003) report a similar process using Cu-Al-Si melts. Wallace *et al.* (Wallace *et al.* 1993, 1994, 1995, 1996) deposited silicon films on oxide-coated molybdenum substrates from molten indium or tin layers saturated with silicon by a sputtering source. Substrate temperatures during growth ranged from 450–650 °C. When a titanium wetting layer is used, grain sizes up to 25 μm and a (111) texture are observed. Yamada *et al.* (Yamada *et al.*, 2000) used a similar process to form polycrystalline silicon films on glass at temperatures of 650–750 °C. Aluminum nitride was used as a wetting agent. In still another method, Shi (Shi, 1993) utilized growth melts with volatile metal solvents (e.g. Zn), the evaporation of which induces supersaturation in the melt and a resulting nucleation that can be better controlled to determine grain sizes. In related work of possible utility for depositing silicon on nonsilicon substrates, Teubner *et al.* (Teubner *et al.*, 1999) have modeled the solution growth of silicon from small indium droplets. In a metallic solution growth process that is somewhat removed from the usual configurations for LPE or LPE-derived techniques, Kita *et al.* (Kita *et al.*, 2001) have developed a silicon deposition process in which a silicon powder is spread over an aluminum sheet placed on top of an alumina substrate. A scanning lamp heater (moving at 1 μm s<sup>-1</sup>) creates a molten zone of aluminum-silicon liquid from which silicon is crystallized onto the substrate. The remaining aluminum-rich phase solidifies atop the deposited silicon layer and can be removed post-growth by etching or abrasion. Other metal solvents (e.g. in addition to aluminum) are contemplated, as is a silicon seed placed in contact with the melt at the start of the process to control grain size. Lateral growth of silicon sheet from Cu-Si melts was also reported (Kita *et al.*, 2002). The lower growth temperatures afforded by a solution growth process (compared with solidification from a silicon melt) permits easier process control and reduces thermal stress effects. This technology represents an illustrative example of the extent to which the basic silicon metallic solution growth process can be modified to meet the requirements of a particular application such as production of large-area silicon films on a ceramic substrate.

## 5.12 OTHER APPLICATIONS OF SILICON AND GERMANIUM LPE

Several other silicon and germanium device applications have utilized LPE. Si-Ge thermoelectric devices made by LPE provide Si-Ge alloys doped with high concentration of both

donors and acceptors (Fleurial and Borschevsky, 1991). Such highly compensated material is expected to have a favorable combination of electrical conductivity and thermal conductivity needed for high efficiency thermoelectric energy conversion. LPE has also been used to grow isotopically enriched silicon layers which exhibit higher thermal conductivities than silicon with natural isotope abundance (Capinski *et al.*, 1997). Baliga (Baliga, 1980b) described buried grid field-controlled thyristors fabricated using LPE. Sukegawa *et al.* (Sukegawa *et al.*, 1989b) assessed silicon *p-i-n* photodiodes on LPE-grown substrates made by the yo-yo method (see Section 5.4). Bergmann *et al.* (Bergmann *et al.*, 1992) made MOS transistors on silicon epilayers formed over oxide masks using LPE ELO for potential application to three-dimensional integrated circuits. Bandaru *et al.* (Bandaru, 2002) used LPE to make blocked impurity band (BIB) photoconductors for far infrared ( $>200\ \mu\text{m}$ ,  $50\ \text{cm}^{-1}$ ) detection. These devices require extremely low background impurity levels ( $<10^{12}\ \text{cm}^{-3}$ ), which could be achieved in by Ge LPE from highly purified Pb or Sb melts (Goyal *et al.*, 2002; Haller and Beeman, 2002). LPE techniques have been used to form various types of silicon-based nanostructures. Wakayama and Tanaka (Wakayama and Tanaka 1997a,b, 1999a,b; Wakayama *et al.*, 1998) produced self-assembled nanocomposites wherein silicon crystallites grew epitaxially from drops of molten Au deposited on a silicon wafer. Meixner *et al.* (Meixner *et al.*, 2001) and Hanke *et al.* (Hanke *et al.*, 2004) reported the formation of self-assembled nanoscale island chains in SiGe LPE on silicon.

## 5.13 CONCLUSIONS AND OUTLOOK

Prior to the 1990s, the application of LPE to silicon was comparatively infrequent compared with its use for compound semiconductors. Interestingly enough, as LPE declined for compound semiconductor applications, silicon LPE and related solution growth processes were explored and developed quite extensively for solar cell applications. In particular, silicon LPE on monocrystalline and multicrystalline silicon wafers, as well as metallic solution growth processes for depositing silicon layers on nonsilicon substrates such as metals and ceramics, were developed as alternatives to Si CVD. However, it does not appear that any of these processes is currently used for commercial solar cell production. Despite three decades of considerable research efforts in thin film technologies utilizing a wide range of semiconductors, silicon wafer-based solar cells are still the dominant commercial photovoltaic product. Recurring and imminent shortages in silicon wafers and solar-grade silicon feedstock will continue to motivate alternative methods of making silicon solar cells that consume less high-quality silicon including solar cells based on a thin layer of silicon supported on a low-grade silicon or nonsilicon substrate. As discussed herein, there are many phenomena that in principle can be exploited to realize sustained, steady-state deposition of silicon at deposition rates of about  $1\ \mu\text{m}\ \text{min}^{-1}$ . These include temperature-gradient growth, convectively induced growth, and growth driven by a metastable phase. For solar cells, it may be productive to develop metallic solution growth techniques as both a purification process and a deposition process.

## REFERENCES

- F. Abdou, A. Fave, M. Lemiti, A. Laugier, C. Bernard and A. Pisch (2005) Liquid phase epitaxy of silicon from tin alloys at low temperature. *Conf. Record of the 31st IEEE Photovoltaic Specialists Conf.*, IEEE, New York, 1066–1069.



- A.V. Abramov, N.G. Deryagin and D.N. Tret'yakov (1994) Growth of GaAs and  $(\text{Ge}_2)_x(\text{GaAs})_{1-x}$  on Si during ultrafast cooling of the growth solution *Semiconduct. Sci. Technol.* **9**, 1815–1822.
- A.V. Abramov, N.G. Deryagin and D.N. Tret'yakov (1996) Supercritical supersaturations and ultrafast cooling of the growth solution in liquid phase epitaxy of semiconductors. *Semiconduct. Sci. Technol.* **11**, 607–619.
- D.J. Aiken and A.M. Barnett (1999) Alternative contact designs for thin epitaxial silicon solar cells. *Progr. Photovolt. Res. Applicat.* **7**, 275–285.
- S.-I. Akai, H. Mori, N. Takahashi and S.-I. Iguchi (1976) Method and apparatus for production of liquid phase epitaxial layers of semiconductors. US Patent 3933538.
- M. Albrecht, S. Christiansen, J. Michler, H.P. Strunk, P.O. Hansson and E. Bauser (1996) Local varying chemical potential and growth surface profile: a case study on solution grown Si(Ge)/Si. *J. Cryst. Growth* **167**, 24–31.
- M. Alonso, H.-P. Trah, E. Bauser, H. Cerva and H.P. Strunk (1988) Properties of SiGe alloys grown on silicon substrates by liquid phase epitaxy. *Mater. Res. Soc. Symp.* **102**, 419–424.
- W. Appel, E. Bauser, H. Bender, D. Käß, H.P. Strunk, G. Vogel and M. Warth (1985) Monocrystalline silicon layers grown on  $\text{SiO}_2$  by liquid phase epitaxy. *Proc. 15th European Solid State Device Research Conf.*, European Physical Society, Aachen, 172–173.
- J.K. Arch, E. Bauser, S. Kolodinski and J.H. Werner (1993a) Characterization of liquid phase epitaxy silicon for thin-film solar cells. *Proc. 11th European Community Photovoltaic Solar Energy Conf.*, Harwood, Chur, Switzerland, 1047–1052.
- J.K. Arch, J.H. Werner and E. Bauser (1993b) Hall effect analysis of liquid phase epitaxy silicon for thin solar cells. *Solar Energy Mater. Solar Cells* **29**, 387–396.
- B.J. Baliga (1977a) Morphology of silicon layers grown by undercooling of a saturated silicon melt. *J. Cryst. Growth* **41**, 199–204.
- B.J. Baliga (1977b) Kinetics of epitaxial growth from a tin melt. *J. Electrochem. Soc.* **124**, 1627–1631.
- B.J. Baliga (1978a) Liquid phase epitaxial method of covering buried regions for devices. US Patent 4128440.
- B.J. Baliga (1978b) Isothermal liquid phase epitaxy from supersaturated tin. *J. Electrochem. Soc.* **125**, 588–600.
- B.J. Baliga (1979a) Dopant distribution in silicon liquid phase epitaxial layers: meltback effects. *J. Electrochem. Soc.* **126**, 138–143.
- B.J. Baliga (1979b) Buried-grid fabrication by silicon liquid-phase epitaxy. *Appl. Phys. Lett.* **34**, 789–790.
- B.J. Baliga (1980a) Liquid phase epitaxial silicon diodes: n-epitaxial layers on boron-doped substrates. *J. Electrochem. Soc.* **127**, 1168–1172.
- B.J. Baliga (1980b) Buried-grid field-controlled thyristors fabricated using silicon liquid-phase epitaxy. *IEEE Trans. Electron Devices* **ED-27**, 2141–2145.
- B.J. Baliga (1980c) Fabrication of grown-in p-n junction using liquid phase epitaxial growth of silicon. US Patent 4236947.
- B.J. Baliga (1981) Boron autodoping during silicon liquid phase epitaxy. *J. Electrochem. Soc.* **128**, 161–165.
- B.J. Baliga (1982a) High lifetime silicon liquid phase epitaxy. *J. Electrochem. Soc.* **129**, 665–666.
- B.J. Baliga (1982b) Refilling silicon grooves by liquid phase epitaxy. *J. Electrochem. Soc.* **129**, 2819–2823.
- B.J. Baliga (1986) Silicon liquid phase epitaxy—A review. *J. Electrochem. Soc.* **133**, 5C–14C.
- G. Ballhorn, K.J. Weber, S. Armand, M.J. Stocks and A.W. Blakers (1998) High-efficiency multicrystalline silicon solar cells by liquid phase epitaxy. *Solar Energy Mater. and Solar Cells* **52**, 61–68.
- J. Bandaru, J.W. Beeman and E.E. Haller (2002) Growth and performance of Ge:Sb blocked impurity band (BIB) detectors. *Proc. SPIE* **4486**, 193–199.

- F. Banhart, R. Bergmann, F. Phillipp and E. Bauser (1991) Dislocation generation in silicon grown over SiO<sub>2</sub> by liquid phase epitaxy. *Appl. Phys. A* **53**, 317–323.
- F. Banhart, N. Nagel, F. Phillipp, E. Czech, I. Sillier and E. Bauser (1993) The coalescence of silicon layers grown over SiO<sub>2</sub> by liquid-phase epitaxy, Part II: Strains and defect nucleation studied by transmission electron microscopy. *Appl. Phys. A* **57**, 441–448.
- A.M. Barnett, M.G. Mauk, J.C. Zolper and W.A. Tiller (1982) Thin film deposition for high-performance, low-cost photovoltaic solar cells. *Proc. 5th European Community Photovoltaic Solar Energy Conf.*, D. Reidel, Dordrecht, 840–844.
- A.M. Barnett, M.G. Mauk, J.C. Zolper, I.W. Hall, W.A. Tiller, R.B. Hall and J.B. McNeely (1984) Thin-Film Silicon and GaAs Solar Cells. *Conference Record 17th IEEE Photovoltaics Specialists Conf.*, IEEE, New York, 747–754.
- E. Bauser (1985) LPE-grown surfaces and growth mechanisms in *Crystal Growth of Electronic Materials*, E. Kaldis, ed. North-Holland, Amsterdam.
- E. Bauser (1994) Atomic Mechanisms in Semiconductor Liquid Phase Epitaxy in *Handbook of Crystal Growth*, Vol. 3, D.T.J. Hurle, ed. Elsevier Science, Amsterdam, Ch. 20.
- E. Bauser (1997) Liquid-phase epitaxy. *23rd International Conference on the Physics of Semiconductors* (Berlin, July 1996), Vol. 2, M. Scheffler and R. Zimmermann, eds, World Scientific, Singapore, 1043–1050.
- E. Bauser and H.P. Strunk (1985) Multilayer growth of silicon by liquid phase epitaxy. *Mater. Res. Soc. Symp.* **37**, 109–114.
- E. Bauser and H.P. Strunk (1994) Liquid phase epitaxial process for producing three-dimensional semiconductor structures by liquid phase epitaxy. US Patent 5 326 716.
- E. Bauser, D. Käss, M. Warth and H.P. Strunk (1986) Silicon layers grown on patterned substrates by liquid phase epitaxy. *Mater. Res. Soc. Symp.* **54**, 267–272.
- G. Beaucarne, S. Bourdais, A. Slaoui and J. Poortmans (2004) Thin-film polycrystalline Si solar cells on foreign substrates: film formation at intermediate temperatures (700–1300 °C). *Appl. Phys. A* **79**, 469–480.
- D.K. Belashchenko (1965) Electromigration in liquid metals. *Russian Chem. Rev.* **34**, 219–237.
- D.K. Belashchenko, Yu.P. Bychkov, A.P. Ivanenko, F.L. Konopel'ko and I.N. Larionov (1974) Electrotransfer in metallic melts of a group III metal with bismuth. *Inorg. Mater.* **10**, 1487–1489.
- S. Berger, S. Quoisola, A. Fave, A. Ouldabbes, A. Kaminski, S. Perichon, N.-E. Chabane-Sari, D. Barbier and A. Laugier (2001) Liquid phase epitaxial growth of silicon on porous silicon for photovoltaic applications. *Cryst. Res. Technol.* **36** 1005–1010.
- R. Bergmann (1991) model for defect-free epitaxial lateral overgrowth of Si over SiO<sub>2</sub> by liquid phase epitaxy. *J. Cryst. Growth* **110**, 823–834.
- R. Bergmann (1999) Crystalline Si thin solar cells: a review. *Appl. Phys. A* **69**, 187–194.
- R. Bergmann and J. Kurianski (1993) The role of hydrogen in silicon liquid phase epitaxy. *Mater. Lett.* **17**, 137–140.
- R. Bergmann, E. Bauser and J.H. Werner (1990) Defect-free epitaxial lateral overgrowth of oxidized (111)Si by liquid phase epitaxy. *Appl. Phys. Lett.* **57**(4), 351–353.
- R. Bergmann, E. Czech, I. Sillier, N. Nagel, E. Bauser, H.J. Queisser, R.P. Zingg and B. Höfflinger (1992) MOS transistors with epitaxial Si, laterally grown over SiO<sub>2</sub> by liquid phase epitaxy. *Appl. Phys. A* **54**, 103–105.
- R. Bergmann, S. Robinson, Z. Shi and J. Kurianski (1993) Silicon films incorporating a drift-field grown by liquid phase epitaxy for solar cell applications. *Solar Energy Mater. Solar Cells* **31**, 447–451.
- V.N. Bessolov, S.A. Kukushkin, M.V. Lebedev and B.V. Tsarenkov (1988) Relaxation liquid phase epitaxy based on reversal of the mass transport and its potential for making ultrathin layers of III-V materials. *Sov. Phys. Tech. Phys.* **33**, 902–905.
- V.N. Bessolov, S.G. Konnikov, M.V. Lebedev, K. Yu. Pogrebetskii and B.V. Tsarenkov (1990) Experimental confirmation of the model of relaxation liquid phase with reversal of mass transport for making ultrathin III-V films. *Sov. Phys. Tech. Phys.* **35**, 99–101.

- V.S. Bessolov, S.G. Konnikov, S.A. Kukushkin, M.V. Lebedev, E.B. Novikov, K. Yu. Pogrebetskii and B.V. Tsarenkov (1993) Relaxational liquid phase epitaxy with reverse mass transport and its potential for preparing thin films of  $A^3V^5$  semiconductors in *Growth of Crystals*, Vol 19, E.I. Givagizov and S.A. Grinberg, eds. Consultants Bureau, New York.
- R. Bilyalov, L. Stalmans, G. Beaucarne, R. Loo, M. Caymax, J. Poortmans and J. NIJS (2001) Porous silicon as an intermediate layer for thin-film solar cell. *Solar Energy Mater. Solar Cells* **65**, 477–485.
- S. Binetti, A. Cavallini, A. Dellafiore, B. Fraboni, E. Grilli, M. Guzzi, S. Pizzini and S. Sanguinetti (1998) Erbium-doped silicon epilayers grown by liquid phase epitaxy. *J. Lumin.* **80**, 347–351.
- S. Binetti, S. Pizzini, A. Cavallini and B. Fraboni (1999) Erbium-doped silicon epilayers grown by liquid-phase epitaxy. *Semiconductors* **33**, 596–597.
- J. Bloem, G. Gilig, M.W.M. Graef and H.H.C. De Moor (1979) The growth of polycrystalline silicon layers on top of a tin-coated substrate: in-situ observations. *Proc. 2nd European Community Photovoltaic Solar Energy Conf.*, D. Reidel, Dordrecht, 759–767.
- M. Bonnet, J. Rogez and R. Castanet (1989) EMF investigation of Al-Si, Al-Fe-Si and Al-Ni-Si liquid alloys. *Thermochim. Acta* **155**, 39–56.
- A. Borschhevsky and J.-P. Fleurial (1993) Growth of heavily-doped SiGe from metallic solutions. *J. Cryst. Growth* **128**, 331–337.
- G. Bremond, A. Daami, A. Laugier, W. Seifert, M. Kittler, J. Poortmans, M. Caymax, K. Said, M. Konuma, A. Gutjahr and I. Silier (1998) SiGe thin-film structures for solar cells. *Mater. Res. Soc. Symp.* 43–48.
- R. Brendel (2001) Review of layer transfer processes for crystalline thin-film silicon solar cells. *Jpn. J. Appl. Phys., Part 1* **40**, 4431–4439.
- J.C. Brice (1965) *The Growth of Crystals from the Melt*. North-Holland, Amsterdam.
- J.C. Brice (1973) *The Growth of Crystals from Liquids*. North Holland, Amsterdam.
- J.C. Brice (1986) *Crystal Growth Processes*. Blackie/ John Wiley & Sons, Inc., New York.
- T. Bryskiewicz (1986) liquid phase electroepitaxy of semiconductors. *Progr. Cryst. Growth Charact* **12**, 29–43.
- N. Carman, P.E. Stello and C.A. Bittmann (1954) Regrowth of silicon through a low melting zone of a silicon-gold eutectic. *J. Appl. Phys.* **25**, 543.
- W.S. Capinski, H.J. Maris, E. Bauser, I. Silier, M. Asen-Palmer, T. Ruf, M. Cardona and E. Gmelin (1997) Thermal conductivity of isotopically enriched Si. *Appl. Phys. Lett.* **71**, 2109–2111.
- H.C. Casey Jr. and M.B. Panish (1978) *Heterostructure Lasers, Part B, Materials and Operating Characteristics*. Academic Press, New York.
- K.R. Catchpole, M.J. McCann, K.J. Weber and A.W. Blakers (2001) A review of thin-film crystalline silicon for solar cell applications II. Foreign substrates. *Solar Energy Mater. Solar Cells* **68**, 173–215.
- B. Chalmers (1964) *Principles of Solidification*. John Wiley & Sons, Inc., New York.
- J.X. Chen, F. Ernst, P.O. Hansson and E. Bauser (1992) Liquid phase epitaxy of GeSi on {111} Si substrates: lattice defect structure and electronic properties. *J. Cryst. Growth* **118**, 452–460.
- T.F. Ciszek, T.H. Wang, R.W. Burrows and X. Wu (1993a) Growth of thin crystalline silicon layers for photovoltaic use. *J. Cryst. Growth* **128**, 314–318.
- T.F. Ciszek, T.H. Wang, X. Wu, R.W. Burrows, J. Alleman, C.R. Schwertfeger and T. Bekkedahl (1993b) Si thin layer growth from metal solutions on single-crystal and cast metallurgical-grade multicrystalline Si substrates. *Conf. Record of the 23rd IEEE Photovoltaic Specialist Conf.*, IEEE, New York, 65–72.
- A.U. Coşkun, Y. Yener and F. Armc (2002) Simulation of dissolution of silicon in an indium solution by spectral methods. *Model. Simul. Mater. Sci. Eng.* **10**, 539–550.
- E.E. Crisman, J.T. Daly, H.J. Gerritsen and S.K.F. Karlsson (1986) Rapid liquid phase epitaxial growth studies. *Solar Cells Sci. Technol. Applicat. Econom.* **21**, 458.

- D.W. Cunningham, M.G. Mauk, J.P. Curran and A.M. Barnett (1990) Electro-epitaxial growth of thin-film silicon. *Conf. Record of the 21st IEEE Photovoltaic Specialists Conf.*, IEEE, New York, 307–310.
- J.T. Daly, S.K.F. Karlsson, H.J. Gerritsen, E.E. Crisman and S.G. Alexiou (1986) High growth Rate LPE in laminar flow, I. Theory. *J. Cryst. Growth* **78**, 291–302.
- L.A. D'Asaro, R.W. Landorf and R.A. Furnanage (1969) Low defect silicon by liquid phase epitaxy in *Semiconductor Silicon, Electrochemical Society Softbound Series*, R.B. Haberrecht and E.L. Kern, eds. Electrochemical Society, New York, 233–242.
- M. Deguchi, S. Hamamoto, H. Sasaki, T. Ishihara, K. Sato and H. Namizaki (1990) Thin film polycrystalline silicon solar cells on MG-Si substrates. *Tech. Digest Int. Photovoltaics Sci. Eng. Conf. 5*, 927–930.
- V.N. Demin, O.V. Naroahnyaya and F.A. Kuznetsov (1990) Liquid phase electroepitaxy of gallium arsenide in an ac electric field. *Sov. Phys. Tech. Phys.* **35**, 620–622.
- J.P. Donnelly and A.G. Milnes (1966) The epitaxial growth of Ge on Si by solution growth techniques. *J. Electrochem. Soc.* **113**, 297–298.
- S. Dost, N. Djilali, S. Erbay and H.A. Erbay (1994) Effect of solution convection during the growth of silicon in a sandwich system. *Mater. Res. Sec. Symp. Proc.* **299**, 335–340.
- D. Elwell and R.S. Feigelson (1982) Electrodeposition of solar silicon. *Solar Energy Mater.* **6**, 123–145.
- D. Elwell and H.J. Scheel (1975) *Crystal Growth from High-temperature Solution*. Academic Press, New York.
- F. Endres (2004) Electrodeposition of nanoscale germanium and silicon in room temperature ionic liquids. *Meeting Abstracts, 2004 Joint International Meeting, 206th Meeting of the Electrochemical Society*, Electrochemical Society, Pennington, NJ, 1183.
- N. Eustathopoulos, M.G. Nicholas and B. Drevet (1999) *Wettability at High Temperatures*. Pergamon, Amsterdam.
- A. Fatima, A. Fave, M. Lemiti, A. Pisch and C. Bernard (2006) Sn-Cu-Al-Si phase diagrams for the growth of silicon film by liquid phase epitaxy. *Eur. Mater. Res. Soc. Symp.* **1** (abstract).
- A. Fave, S. Berger, A. Beaumont, B. Semmache, P. Kleimann, J. Linnroos and A. Laugier (2001) LPE growth of textured single crystal silicon thin film for PVT applications. *Thin Solid Films* **383**, 209–211.
- A. Fave, S. Quoizola, J. Kraiem, A. Kaminski, M. Lemiti and A. Laugier (2004) Comparative study of LPE and VPE silicon thin film on porous sacrificial layer. *Thin Solid Films* **451–452**, 308–311.
- J.D. Filby and S. Nielsen (1966) Selected area deposition of single crystal silicon on amorphous quartz. *J. Electrochem. Soc.* **113**, 1091–1092.
- J.D. Filby and S. Nielsen (1967) Single crystal films of silicon on insulator. *Br. J. Appl. Phys.* **18**, 1357–1386.
- J.P. Fleurial and A. Borschevsky (1990) Si-Ge-metal ternary phase diagram calculations. *J. Electrochem. Soc.* **137**, 2928–2937.
- J.P. Fleurial, A. Borschevsky and D. Irvine (1991) LPE growth of doped SiGe layers using multicomponent phase diagram calculations. *Modern Perspectives on Thermoelectrics and Related Materials Symposium*. Materials Research Society, Pittsburgh, PA, 123–133.
- M. Garfinkel and R.N. Hall (1978) Floating substrate process: Large-area silicon sheet task low-cost solar array project. Final Report for DOE/JPL Subcontract 954350-78/3 to General Electric Co. (Schenectady, New York), JPL Low-cost Silicon Solar Array Project, US Dept of Energy, Washington, DC.
- B. Girault, F. Chevrier, A. Joullie and G. Bougnot (1977) Liquid phase epitaxy of silicon at very low temperatures. *J. Cryst. Growth* **37**, 169–177.
- E.I. Givargizov (1991) *Oriented Crystallization on Amorphous Substrates*. Plenum Press, New York.
- L.V. Golubev, A.V. Egorov, S.V. Novikov and Yu.V. Shmartsev (1995) Liquid phase electroepitaxy of III-V semiconductors. *J. Cryst. Growth* **146**, 277–282.

- N. Gopalakrishnan, R.S. Qhalid Fareed and R. Dhanasekaran (1996) Epitaxial nucleation and growth mechanism of III-V compound semiconductors. *J. Indian Inst. Sci.* **76**, 223–233.
- S. Goyal, J. Bandrau, J.W. Beeman and E.E. Haller (2002) Germanium blocked impurity band detectors. *Proc. Far-IR, Sub-mm & mm Detector Detector Technology Workshop*, J. Wolf, J. Farhoomand and C.R. McCreight, eds, NASA, Washington, DC, NASA/CP-211408. Manuscript No. 3–16.
- M.W.M. Graef, L.J. Gillig and J. Bloem (1977a) Chemical vapor deposition of silicon on a liquid tin layer. *Proc. European Community Photovoltaic Solar Energy Conf.*, D. Reidel, Dordrecht, 136–142.
- M.W.M. Graef, L.J. Gillig and J. Bloem (1977b) Enhanced crystallinity of silicon films deposited by CVD on liquid layers (CVDOLL process): silicon on tin layers in the presence of hydrogen chloride. *J. Appl. Phys.* **48**, 3937–3940.
- A. Gutjahr, I. Silier, N. Rollbuehler, M. Konuma, F. Barnhart, K. Said and J. Poortmans (1997) SiGe layer structures for solar cell application grown by liquid phase epitaxy. *Conf. Record of the 26th IEEE Photovoltaics Specialists Conf.*, IEEE, New York, 759–762.
- A. Gutjahr, C. Grasso, S.E.A. Schiermeier, P.F. Fung and A. von Keitz (2001) Crystalline silicon growth on silicon nitride and oxynitride substrates for thin film solar cells. *16th European Photovoltaic Solar Energy Conf.*, James and James, London.
- E.E. Haller and J.W. Beeman (2002) Far infrared photoconductors: Recent advances and future prospects. *Proc. Far-IR, Sub-mm & mm Detector Detector Technology Workshop*, J. Wolf, J. Farhoomand and C.R. McCreight, eds, NASA, Washington, DC, NASA/CP-211408. Manuscript No. 2–06.
- H. Hammerling (1978) Liquid phase epitaxy of GaAs with AsCl<sub>3</sub>-saturated gallium/arsenic solutions. *Kristall Technik* **13**, K7–K9.
- M. Hanke, M. Schmidbauer, R. Köhler, F. Syrowatka, A.-K. Gerlitzke and T. Boeck (2004) Equilibrium shape of SiGe Stranski–Krastanow islands on silicon grown by liquid phase epitaxy. *Appl. Phys. Lett.* **84**, 5228–5230.
- M. Hanke, T. Boeck, A.-K Gerlitzke, F. Syrowatka, F. Heyroth and R. Köhler (2005) Size, shape and ordering of SiGe/Si(001) islands grown by means of liquid phase epitaxy under far-equilibrium conditions. *Appl. Phys. Lett.* **86**, 142101-1–142101-3.
- P. Hansson, R. Bergmann and E. Bauser (1991) Heteroepitaxial lateral overgrowth of Ge<sub>x</sub>Si<sub>1-x</sub> over SiO<sub>2</sub>/Si structures by liquid phase epitaxy. *J. Cryst. Growth* **114**, 573–580.
- P.O. Hansson, A. Gustafsson, M. Albrecht, R. bergmann, H.P. Strunk and E. Bauser (1992a) High quality Ge<sub>x</sub>Si<sub>1-x</sub> by heteroepitaxial lateral overgrowth. *J. Cryst. Growth* **121**, 790–794.
- P.O. Hansson, F. Ernst and E. Bauser (1992b) Two-dimensional growth of strained Ge<sub>0.85</sub>Si<sub>0.15</sub> on Si(111) by liquid phase epitaxy. *J. Appl. Phys.* **72**, 2083–2085.
- P.O. Hansson, E. Bauser, M. Albrecht and H.P. Strunk (1993a) Effects of minimizing the driving force for epitaxy in the Ge/Si(001) system. in *Common Themes and Mechanisms of Epitaxial Growth Symposium*. Materials Research Society, Pittsburgh, PA, 53–58.
- P.O. Hansson, E. Bauser, M. Albrecht and H.P. Strunk (1993b) Solvents influencing the morphology of epitaxial solution grown strained Ge/Si layers. *Solid State Phenom.* **32–33**, 403–408.
- P.O. Hansson, M. Albrecht, W. Dorsch, H.P. Strunk and E. Bauser (1994a) Interfacial energies providing a driving force for Ge/Si heteroepitaxy. *Phys. Rev. Lett.* **73**, 444–447.
- P.O. Hansson, M. Konuma, I. Sillier, E. Bauser, M. Albrecht, W. Dorsch, H.P. Strunk (1994b) Growth of high quality c-SiGe p-n double layers for high efficiency solar cells. *First World Conf. Photovoltaic Energy Conversion*. IEEE, New York, 1254–1257.
- S.A. Healy, T.L. Young and M.A. Green (1991) Low-temperature growth of silicon on Si<sub>x</sub>Ge<sub>1-x</sub> by liquid phase epitaxy. *J. Cryst. Growth* **112**, 287–290.
- J.J. Hsieh (1980) Liquid-phase epitaxy. in *Handbook on Semiconductors*, Vol. 3, T.S. Moss and S.P. Keller, eds. North-Holland, Amsterdam, 1980, 415–497.
- R. Hultgren, P.D. Desai, D.T. Hawkins, M. Gleiser and K.K. Kelly (1973) *Selected Values of Thermodynamic Properties of Binary Alloys*. American Society of Metals, Metals Park, OH.

- D.T.J. Hurle (1999) A comprehensive thermodynamic analysis of native point defect and dopant solubilities in gallium arsenide. *J. Appl. Phys.* **85**, 6957–7022.
- D.T.J. Hurle, J.B. Mullin and E.R. Pike (1967) Thin alloy zone crystallization. *J. Mater. Sci.* **2**, 46–62.
- K. Ito and K. Kojima (1982) Solution-grown silicon solar cells. *Jpn. J. Appl. Phys., Suppl.* **19-2**, 37–41.
- S. Ito, Y. Kitagawa, T. Mishima and T. Yokoyama (1999) Direct grown polycrystalline Si film on carbon substrate by LPE. *Technical Digest International photovoltaic Science and Engineering Conf.* 11, Tokyo, Japan, 539–545.
- H.F. John (1958) Properties of some germanium single crystals grown from solutions of molten metals. *J. Electrochem. Soc.* **105**, 741–743.
- R. Jothilingham, R. Dhanasekaran and P. Ramasamy (1995) Studies on nucleation kinetics of  $\text{In}_{1-x}\text{Ga}_x\text{P}/\text{GaAs}$  by liquid phase epitaxy. *Il Nuovo Cimento* **17D**, 117–128.
- I. Jóźwik and J.M. Olchowik (2006) The epitaxial lateral overgrowth of silicon by two step liquid phase epitaxy. *J. Cryst. Growth* **294**, 367–372.
- I. Jóźwik and J.M. Olchowik (2006) Analysis of the processes of silicon epitaxial lateral overgrowth in Ar ambient gas. *Mater. Sci. - Poland* **24**, **4**, 967–973.
- R. Kamada, C.-J. Wen, J. Otomo and H. Takahashi (2003) Solution growth of polycrystalline silicon on quartz glass substrates. *Diffus. Defect Data, Pt. B* **93**, 243–248.
- D. Käss and H. Strunk (1981) Growth-promoting dissociated dislocations in solution-grown silicon. *Thin Solid Films* **81**, L101–L104.
- D. Käss, M. Warth, H.P. Strunk and E. Bauser (1985a) Liquid phase epitaxy of silicon: potentialities and prospects. *Physica* **129B**, 161–165.
- D. Käss, M. Warth, W. Appel, H.P. Strunk and E. Bauser (1985b) Silicon multilayers grown by liquid phase epitaxy. *Proc. 1st International Conf. on Silicon Molecular Beam Epitaxy*, Electrochemistry Society, Pennington, NJ, 250–258.
- A. Kawano, I. Konomi, H. Azuma, T. Hioki and S. Noda (1993) Influence of bismuth as a surfactant on the growth of germanium on silicon. *J. Appl. Phys.* **74**, 4265–4267.
- A.I. Kazikov, V.A. Moritski, V.S. Shobik, V.A. Zavadski and V.N. Brovkin (1990) Peculiarities of eutectic epitaxy in systems CIV-AIIIIV from liquid phase. *Cryst. Res. Technol.* **25**, K114–K117.
- P.H. Keck and J. Broder (1953) The solubility of silicon and germanium in gallium and indium. *Phys. Rev.* **90**, 521–522.
- M. Keita, S. Steinemann and H.U. Kunzi (1976) Measurement of chemical diffusion coefficients in liquid binary alloys. *Ber. Bunsen-Ges. Phys. Chem.* **80**, 722–725.
- Yu.P. Khukhryanskii and E.P. Nikolaeva (1976) Isothermal liquid-phase epitaxy of germanium and silicon. *Sov. Phys. Solid State* **18**, 187–188.
- H.J. Kim (1972) Liquid phase epitaxial growth of silicon in selected areas. *J. Electrochem. Soc.* **119**, 1394–1398.
- M. Kimura, A. Tanaka and T. Sukegawa (1990) Gravity effect on solute transport in dissolution and growth of silicon. *J. Cryst. Growth* **99**, 1295–1299.
- M. Kimura, N. Djilali, S. Dost, H. Kanai, A. Tanaka and T. Sukegawa (1996) Liquid phase epitaxy of silicon: An experimental and numerical parameter study. *J. Cryst. Growth* **167**, 516–524.
- S. Kinoshita, Y. Suzuki and T. Nishinaga (1991) Epitaxial lateral overgrowth of Si on non-planar substrate. *J. Cryst. Growth* **115**, 561–566.
- K. Kita, H. Yamatsuga, C.-J. Wen, H. Komiyama and K. Yamada (2001) Zone-defined growth of multicrystalline silicon film from metal-silicon solution. *Solar Energy Mater. Solar Cells* **65**, 465–470.
- K. Kita, C.-J. Wen, J. Otomo, K. Yamada, H. Komiyama and H. Takahashi (2002) Study of the lateral growth of silicon films from metal solutions with temperature gradient. *J. Cryst. Growth* **234**, 153–158.
- V.I. Klykov and N.N. Sheftal (1981) Diataxial growth of silicon and germanium. *J. Cryst. Growth* **52**, 687–691.

- J. Knobloch, B. Voss and A. Goetzberger (1985) High efficiency crystalline thin film solar cells for optical confinement. *Proc. 6th European Photovoltaic Solar Energy Conf.*, D. Reidel, Dordrecht, 285–289.
- H.J. Koh and T. Fukuda (1996)  $\text{Si}_{1-x}\text{Ge}_x$  mixed crystals grown by pulling-down technique with multi-capillary channels. *Cryst. Res. Technol.* **31**, 151–158.
- R. Kohler, H. Raidt, F. Banhart, B. Jenichen, A. Gutjahr, M. Konuma, L. Silier and E. Bauser (1996) Semiconductor epitaxial and non-epitaxial overgrowth from solutions. *Evolution of Epitaxial Structure and Morphology Symposium*, Materials Research Society Philadelphia, PA, 189–194.
- S. Kolodinski, J.H. Werner, U. Rau, J.K. Arch and E. Bauser (1993) Thin film silicon solar cells from liquid phase epitaxy. *Proc. 11th European Photovoltaic Solar Energy Conf.*, Harwood, Chur, Switzerland, 53–56.
- M. Konuma (2002) Feature and mechanisms of layer growth in liquid phase epitaxy of semiconductors in *Chemical Physics of Thin Film Deposition Processes for Micro- and Nano-technologies*, Y. Pauleau, ed. Kluwer, Dordrecht, 43–68.
- M. Konuma, I. Sillier, A. Gutjahr, E. Bauser, F. Banhart, H. Frey and N. Nagel (1995) Extremely low temperature silicon liquid phase epitaxy. *Mater. Res. Soc. Symp. Proc.* **386**, 339–344.
- M. Konuma, I. Silver, A. Gutjahr, P.O. Hansson, G. Cristiani, E. Czech, E. Bauser and F. Banhart (1996) Centrifugal techniques for solution growth of semiconductor layers. *J. Cryst. Growth* **166**, 234–238.
- M. Konuma, G. Cristiana, E. Czech and I. Silier (1999) Liquid phase epitaxy of Si from Pb solutions. *J. Cryst. Growth* **198/199**, 1045–1048.
- R. Kopecek, K. Peter, J. Hötzel and E. Bucher (2000) Structural and electrical properties of silicon epitaxial layers grown by LPE on highly resistive monocrystalline substrates. *J. Cryst. Growth* **208**, 289–296.
- G.N. Kozhemyak in (2000) Indium inhomogeneity in  $\text{In}_x\text{Ga}_{1-x}\text{Sb}$  ternary crystals grown by floating unable Czochralski method. *J. Cryst. Growth* **220**, 39–45.
- L.V. Kozhitov and S.V. Burov (1988) Behavior of carbon during liquid-phase epitaxy of silicon. *Sov. Phys. Crystallog.* **33**, 415–417.
- L.V. Kozhitov, M.P. Volkov and S.V. Ryazanov (1986) Morphology of epitaxial layers on silicon obtained by liquid phase epitaxy. *Sov. Phys. Crystallogr.* **31**, 700–701.
- Yu.M. Kozlov, L.N. Aleksandrov and A.G. Cherevko (1975) Film growth mechanism in liquid phase epitaxy in *Growth of Crystals*, Vol. 9, N.N. Sheftal' and E.I. Givargizov, eds. Consultants Bureau, New York, 300–304.
- V.M. Kozlovskaya and R.N. Rubinshtein (1962) Calculation solubility and vapor pressure for semiconductor dopant systems. *Sov. Phys. Solid State* **3**, 2434–2440.
- K. Kurata and T. Harai (1968) A study on making abrupt heterojunctions by solution growth. *J. Electrochem. Soc.* **115**, 869–874.
- J.J. Kramer (1960) The oxidation of 3 per cent silicon-iron in various environments. Materials Engineering Report No. 5942-1843-E, Materials Engineering Dept, Westinghouse Corp. (Pittsburgh, PA).
- F. Kresse, G.G. Baumann, O. Jaentsch and K. Habberger 1990 Liquid phase epitaxy of silicon at low temperatures. *J. Cryst. Growth* **104**, 744–747.
- O. Kruger, W. Seiferet, M. Kittler, A. Gutjahr, I. Silier, M. Konuma, K. Said, M. Caymax and J. Poortmans (1998) Electrical properties of SiGe layers grown by LPE and CVD. *Proc. 10th Conf. on Semiconducting and Insulating Materials*, IEEE, Piscataway, NJ, 185–189.
- E. Kuphal (1991) Liquid phase epitaxy. *Appl. Phys. A* **52**, 380–409.
- H.J. Leamy and C.J. Doherty (1980) Nucleation-controlled overgrowth of silicon on silica. *Appl. Phys. Lett.* **37**, 1028–1030.
- A. Laugier, M. Gavano, L. Mayet and L. Castet (1970) Metallurgical aspects of solution-grown Ge-GaAs heterojunctions. *Thin Solid Films* **6**, 217–232.

- E. Lee, K. Lee, D. Kim and S. Lee (2003) Optimization of P<sup>+</sup> seeding layer for thin film silicon solar cell by liquid phase epitaxy. *Proc. 3rd World Conf. Photovoltaic Solar Energy Conversion*, IEEE, New York, 1214–1216.
- S.H. Lee and M.A. Green (1991) Evaluation of binary and ternary melts for the low temperature liquid phase epitaxial growth of silicon. *J. Electron. Mater.* **20**, 635–641.
- S.H. Lee, S.A. Healy, T.L. Young and M.A. Green (1990) Very low temperature liquid phase epitaxial growth of silicon. *Mater. Lett.* **9**, 53–56.
- S.H. Lee, R. Bergmann, E. Bauser and H.J. Queisser (1994) Solution growth of silicon on Al-Si coated quartz glass substrates. *Mater. Lett.* **19**, 1–6.
- K. Lehovec (1962) Thermodynamics of binary semiconductor-metal alloys. *J. Phys. Chem. Solids* **23**, 695–709.
- K. Lehovec (1964) A mechanism causing saturation of impurities during semiconductor crystal growth. *Surf. Sci.* **1**, 165–170.
- K. Lehovec and A. Slobodskay (1964) Impurity content of germanium crystallized from the liquid ternary alloy Ge-In-Sb. *J. Electrochem. Soc.* **111**, 65–73.
- Weh Lin and K.E. Benson (1987) The science and engineering of large-diameter Czochralski silicon crystal growth. *Ann. Rev. Mater. Sci.* **17**, 273–198.
- R. Linnebach and E. Bauser (1982) Low temperature liquid phase epitaxy of silicon. *J. Cryst. Growth* **57**, 43–47.
- S.I. Long, J.M. Ballantyne and L.F. Eastman (1974) Steady-state LPE growth of GaAs. *J. Cryst. Growth* **26**, 13–20.
- V.N. Losovsky and G.S. Konstantinova (1981) Growth from high-temperature solutions effected by chemical potential gradients. *J. Cryst. Growth* **52**, 327–331.
- V.N. Lozovskii and A.I. Udyanskaya (1968) Investigation of the mechanism of crystallization of silicon from aluminum-silicon melts by the zone melting method with a temperature gradient. *Krystallografiya* **13**, 565–566.
- V.N. Lozovskii, V.P. Popov, V.B. Mar'ev and E.G. Kovtun (1977) Isothermal liquid phase epitaxy. *Sov. Phys. Crystallogr.* **21**, 617–618.
- V.N. Lozovskii, N.F. Politova, A.P. Vatulya and N.Ya. Nadtoka (1978) Diffusion of silicon in liquid alloys of Al-Sn, Al-Ag, Al-Cu and Al-Au. *Izv. Akad. Nauk, Metall.* **4**, 79–82.
- V.N. Lozovskii, V.P. Krizhanovskii, É.K. Kov'ev and V.A. Yur'ev (1985) Structural features of polycrystalline layers grown from the liquid phase. *Sov. Phys. Crystallogr.* **30**, 228–229.
- B.W. Ludington and A.A. Immorlica Jr (1979) Temperature-gradient measurement in liquid epitaxial growth systems. *J. Cryst. Growth* **47**, 619–622.
- X.-J. Mao, Y.-C. Chan, Y.-L. Lam, J.-Yi Zhu and Y.-X. Shi (2000) New concept technology-pressure variation liquid phase epitaxy. *Proc. SPIE* **4078**, 191–202.
- D. Majumdar, S. Chatterjee, U. Gangopadhyay and H. Saha (2000) Role of drift field in thin silicon solar cell developed by liquid phase epitaxy. *Proc. SPIE* **3975**, 1262–1265.
- D. Majumdar, S. Chatterjee, U. Gangopadhyay and H. Saha (2003) Modified technique of using conventional slider boat for liquid phase epitaxy of silicon for solar cell applications. *Bull. Mater. Sci.* **26**, 643–654.
- D. Majumdar, S.K. Dutta, S. Chatterjee and H. Saha (2004) Effect of controlled dopant distribution in thin silicon solar cell. *Solar Energy Mater. Solar Cells* **81**, 459–468.
- T. Maruyama, K. Matsuda and S. Naritsuka (2005) Multinuclear layer-by-layer growth Ge(111) by LPE. *J. Cryst. Growth* **275**, e2155–e2160.
- B.L. Mattes and R.K. Route (1972) A temperature gradient cell for liquid phase epitaxial growth of GaAs. *J. Cryst. Growth* **16**, 219–222.
- M.G. Mauk and A.M. Barnett (1985) Thin silicon solar cells with internal reflection and their fabrication by solution growth. *Conf. Record of the 18th IEEE Photovoltaic Specialists Conf.*, IEEE, New York, 192–197.



- M.G. Mauk and A.M. Barnett (1987) Demonstration of optical enhancement in solution-grown thin-film silicon solar cells. *Conf. Record of the 19th IEEE Photovoltaic Specialists Conf.*, IEEE, New York, 392–397.
- M.G. Mauk and J.P. Curran (2001) Electro-epitaxial lateral overgrowth of silicon from liquid metal solutions. *J. Cryst. Growth* **225**, 348–353.
- M.G. Mauk, P.A. Burch, S.W. Johnson, T.A. Goodwin and A.M. Barnett (1996) Buried' metal/dielectric/semiconductor reflectors for light trapping in epitaxial thin-film solar cells. *Proc. 25th IEEE Photovoltaic Specialists Conf.*, IEEE, New York, 147–150.
- M.G. Mauk, and B.W. Feyock, A. Sharma and R.G. Munsperger (2001) Experimental assessment of metal solvents for low-temperature liquid-phase epitaxy of silicon carbide. *J. Cryst. Growth* **225**, 322–329.
- M.J. McCann, K.R. Catchpole, K.J. Weber and A.W. Blakers (2001) A review of thin film crystalline silicon for solar cell applications. *Solar Energy Mater. Solar Cells* **68**, 135–171.
- M.J. McCann, K.J. Weber, M. Petracic and A.W. Blakers (2002) Boron doping of silicon layers grown by liquid phase epitaxy. *J. Cryst. Growth* **241**, 45–50.
- J.B. McNeely, R.B. Hall, A.M. Barnett and W.A. Tiller (1984) Thin-film silicon crystal growth on low cost substrates. *J. Cryst. Growth* **70**, 420–424.
- H. Meinders (1974) An alternative method for liquid phase epitaxy. *J. Cryst. Growth* **26**, 180–182.
- M. Meixner, E. Scholl, M. Schmidbauer, H. Raidt and R. Kohler (2001) Formation of island chains in SiGe/Si heteroepitaxy by elastic anisotropy. *Phys. Rev. B* **64**, 2453071–2453074.
- T. Miki, K. Morita and N. Sano (1996) Thermodynamics of phosphorus in molten silicon. *Metall. Mater. Trans. B* **27**, 937–941.
- V.A. Mokritskii, E.M. Kuritsin, B.A. Danilchenko and V.I. Shakhovtsov (1982) Epitaxial germanium layers grown by liquid phase in  $\gamma$ -radiation field. *Phys. Status Solidi A* **72**, K121–K124.
- R.L. Moon (1980) Liquid phase epitaxy. in *Crystal Growth*, 2nd Edn, B. Pamplin, ed. Pergamon, Oxford, 421–460.
- J.T. Moore, T.H. Wang, M.J. Heben, K. Douglas and T.F. Ciszek (1997) Fused salt electrodeposition of thin layer silicon. *Conf. Record 26th IEEE Photovoltaic Specialists Conf.*, IEEE, New York, 775–778.
- H. Mori (1981) 2-D grating graphoepitaxy of silicon films from silicon-gold supersaturated solution. *Jpn. J. Appl. Phys.* **20**, L905–L908.
- A.D. Morrison and T. Duad (1985) Low defect, high purity crystalline Layers grown by selective deposition. US Patent 4 522 661.
- M. Muller, R. Kopecek, P. Fath, C. Zahedi and K. Peter (2003) Silicon LPE on substrates from metallurgical silicon feedstock for large scale production. *Proc. 3rd World Conf. on Photovoltaic Solar Energy Conversion*, IEEE, New York, 1221–1224.
- B. Mutaftshchiev (1993) Nucleation theory in *Handbook of Crystal Growth*, Vol. 1, D.T.J. Hurle, ed. Elsevier, Amsterdam, 189–247.
- N. Nagel, F. Banhart, E. Czech, I. Silier, F. Phillipp and E. Bauser (1993) The coalescence of silicon layers grown over SiO<sub>2</sub> by liquid phase epitaxy. I. Growth and coalescence of defect-free silicon layers. *Appl. Phys. A* **57**, 249–254.
- K. Nakagawa, S. Ishihara, H. Sato, S. Nishida and Y. Takai (2005) Liquid phase growth method and liquid phase growth apparatus. US Patent 6951585.
- O.B. Nevsky, I.V. Mogunov, L.V. Kozhitov and V.A. Fedorov (1991) The improved model of steady-state LPE growth from solution. *Cryst. Prop. Prep.* **36–38**, 666–677.
- S. Nishida, K. Nakagawa, M. Iwane, Y. Iwasaki, N. Ukiyo, H. Mizutani and T. Shoji (2001) Si-film growth using liquid phase epitaxy method and its application to thin-film crystalline Si solar cells. *Solar Energy Mater. Solar Cells* **65**, 525–532.
- T. Nishinaga (2005) Understanding of crystal growth mechanisms through experimental studies of semiconductor epitaxy. *J. Cryst. Growth* **275**, 19–28.
- J.I. Nishizawa and Y. Okuno (1975) Liquid phase epitaxy of GaP by a temperature difference method under controlled vapor pressure. *Proc. Soc. Information Display* **16**, 135–140.

- S.V. Novikov, I.G. Savel'ev, R. Pashkevich, Yu. V. Shmartsev, M. Panek and M. Tlaczala (1993) Stratification processes in Ga-Bi solutions. *Tech. Phys. Lett.* **19**, 462–463.
- H. Ogawa, Q. Guo and K. Ohta (1995) Low temperature liquid phase epitaxy of silicon from gallium solution. *J. Cryst. Growth* **155**, 193–197.
- A. Ould-Abbas, M. Bouchaour, N.-E. Chabane-Sari, S. Berger, A. Kaminski and A. Fave (2004) Growth of silicon thin film by LPE on porous silicon bilayers. *J. Therm. Anal.* **76**, 685–691.
- K. Peter, G. Willeke and E. Bucher (1995) Rapid growth of high quality crystalline silicon by a novel temperature gradient liquid phase epitaxy (LPE). *Proc. 13th European Photovoltaic Solar Energy Conf.*, Stephens and Associates, Felpersham, 379–381.
- K. Peter, R. Kopecek, P. Fath, E. Bucher and C. Zahedi (2002) Thin film silicon solar cells on upgraded metallurgical silicon substrates prepared by liquid phase epitaxy. *Solar Energy Mater. Solar Cells* **74**, 219–223.
- M.S. Petrushevskii and P.V. Gel'd (1971) Estimation of energy of interaction between unlike atoms in metal-silicon melts. *Russ. J. Phys. Chem.* **45**, 1106–1107.
- G.E. Possin (1984) Solution growth of silicon from liquid tin for application to photovoltaic solar cells. *Solid-State Electron.* **27**, 167–176.
- J.N. Pratt and R.G.R. Sellors (1973) *Electrotransport in Metals and Alloys*. Trans Tech, Riehen, Switzerland.
- G.M. Rao, D. Elwell and R.S. Feigelson (1981) Electrodeposition of silicon onto graphite. *J. Electrochem. Soc.* **128**, 1708–1711.
- H. Reiss (1953) Chemical effects due to the ionization of impurities in semiconductors. *J. Chem. Phys.* **21**, 1209–1217.
- H. Reiss and C.S. Fuller (1956) Influence of holes and electrons on the solubility of lithium in boron-doped silicon. *J. Metals* **8**, 276–282.
- F.E. Rostoczy and W.W. Stein (1972) The growth of Ge-GaAs and GaP-Si heterojunction by liquid phase epitaxy. *J. Electrochem. Soc.* **119**, 1119–1121.
- H. Ruda, P. Becla, J. Lagowski and H.C. Gatos (1983) Mercury pressure-induced LPE growth of HgCdTe. *J. Electrochem. Soc.* **130**, 228–230.
- W.R. Runyan (1976) Melt and solution growth of silicon. *Proc. National Workshop on Low-cost Polycrystalline Silicon Solar Cells at Southern Methodist University*, T.L. Chu and S.S. Chu, eds. Energy Research and Development Administration, Washington, DC, 26–39.
- M.S. Saidov and A.S. Saidov (1991a)  $(IV_2)_x(III-V)_{1-x}, (IV_2)_x(II-VI)_{1-x}, (IV-IV_2)_x(III-V)_{1-x}$  solid solutions—promising semiconductor materials. *Proc. Sixth International Workshop on Physics of Semiconductor Devices*, Tata McGraw-Hill, New Delhi, 227–234.
- A.S. Saidov and M.S. Saidov (1991b) Liquid-phase epitaxy of  $(Ge_2)_{1-x}(GaAs)_x$  and  $(Si_2)_{1-x}(GaP)_x$  solid solutions. *Crystal Prop. Prep.* **36–38**, 515–518.
- A.S. Saidov, S. Dadamukhamedov, B. Sapaev and V. Risava (1991) Liquid-phase epitaxy of  $Si-Si_{1-x}, Si-Si_{1-x}Ge_x-GaAs$  ( $0 < x < 1$ ) structures. *Cryst. Prop. Prep.* **32–34**, 238–242.
- A.S. Saidov, A.S. Razzakov and E.A. Koshchanov (2001) Liquid phase epitaxy of  $Ge_{1-x}Sn_x$  semiconductor films. *Tech. Phys. Lett.* **27**, 698–700.
- Y. Satoh, N. Usami, W. Pan, K. Fujiwara, K. Nakajima and T. Ujihara (2005) Influence of growth temperature on minority carrier lifetime of Si layers grown by liquid phase epitaxy using Ga solvent. *J. Appl. Phys.* **98**, 073708-1–073708-4.
- D.E. Schafer (1981) Solution growth of thallium-doped silicon for 3–5 micrometer photoconductive detectors. *Proc. SPIE* **285**, 183–189.
- S.E.A. Schiermeier, C.J.J. Tool, J.A.M. van Roosmalen, L.J. Laas, A. von Kleitz and W.C. Sinke (1998) LPE-growth of crystalline silicon layers on ceramic substrates. *Proc. 2nd World Conf. on Photovoltaic Solar Energy Conversion*, IEEE, New York, 1673.
- W. Schmid, U. Nieper and J. Weber (1983) Donor–acceptor pair spectra in Si:In LPE layers. *Solid State Commun.* **45**, 1007–1011.
- W. Scott and R.J. Hager (1979) Solution growth of indium-doped silicon. *J. Electron. Mater.* **8**, 581–602.

- J. Sebkova and M. Beranek (1983) Thermodynamic properties of the Al-Mg-Si-Zn liquid alloy. *Koveve Mater.* **21**, 228–240.
- A.M. Sembian, F. Banhart, M. Konuma, J. Weber, S. Babu, S. Moorthy and P. Ramasamy (2000) Defect distribution and morphology development of SiGe layers grown on Si(100) substrates by LPE. *Thin Solid Films* **372**, 1–5
- Z. Shi (1993) Growth of thin film silicon on glass substrates from Zn-based solutions. *Mater. Lett.* **15**, 359–362.
- Z. Shi (1994a) Solution growth of silicon on patterned amorphous SiO<sub>2</sub> substrates. *J. Cryst. Growth* **135**, 273–278.
- Z. Shi (1994b) Growth of polycrystalline-silicon films on glass. *J. Mater. Sci. Electron.* **5**, 305–309.
- Z. Shi and M.A. Green (1993) Improved silicon thin film grown on glass substrates by periodic regrowth. *J. Electrochem. Soc.* **140**, 3290–3293.
- Z. Shi, T.L. Young and M.A. Green (1991) Low-temperature liquid phase epitaxy of silicon. *Mater. Lett.* **12**, 339–343.
- Z. Shi, T.L. Young, G.F. Zheng and M.A. Green (1993) Investigation of polycrystalline silicon deposition on glass substrates. *Solar Energy Mater. Solar Cells* **31**, 51–60.
- Z. Shi, W. Zhang, G.F. Zheng, J. Kurianski, M.A. Green and R. Bergmann (1995) The growth and properties of liquid phase epitaxial silicon in a forming gas ambient. *J. Cryst. Growth* **151**, 278–284.
- Z. Shi, W. Zhang, G.F. Zheng, V.L. Chin, A. Stephens, M.A. Green and R. Bergmann (1996) The effects of solvent and dopant impurities on the performance of LPE silicon solar cells. *Solar Energy Mater. Solar Cells* **41–42**, 53–60.
- T. Shimoda, M. Yasuo, M. Furusawai, T. Aoki, I. Yudasaka, H. Tanaka, R. Wang, M. Miyaska and Y. Takeuchi (2006) Solution-processed silicon films and transistors. *Nature* **440**, 783–786.
- I. Silier, A. Gutjahr, N. Nagel, P.O. Hansson, E. Czech, M. Konuma, E. Bauser, F. Banhart, R. Köhler, H. Raidt and B. Jenichen (1996a) Solution growth of epitaxial semiconductor on insulator layers. *J. Cryst. Growth* **166**, 727–730.
- I. Silier, A. Gutjahr, F. Banhart, M. Konuma, E. Bauser, V. Schöllkopf and H. Frey (1996b) Growth of multi-crystalline silicon on seeded glass from metallic solutions. *Mater. Lett.* **28**, 87–91.
- I. Silier, M. Konuma, A. Gutjahr, E. Bauser, F. Banhart, C. Zizler, V. Schoellkopf and H. Frey (1996c) High quality polycrystalline silicon solar cells grown on dissimilar substrates from metallic solution. *Proc. 25th IEEE Photovoltaics Specialists Conf.*, IEEE, New York, 681–684.
- A. Slaoui, R. Monna, J. Poortmans, T. Vermeulen, O. Evrard, K. Said and J. Nijs (1998) Crystalline silicon thin films: a promising approach for photovoltaics? *J. Mater. Res.* **13**, 2763–2774.
- D.D. Smith, D.J. Aiken and A.M. Barnett (1996) Surface recombination at the Si/SiO<sub>2</sub> overgrowth interface. *Conf. Record of the 25th IEEE Photovoltaics Specialists Conf.*, IEEE, New York, 677–679.
- D.D. Smith and A.M. Barnett (1997) Thin crystalline silicon solar cell with back surface gate electrode. *Conf. Record of the 26th IEEE Photovoltaics Specialists Conf.*, IEEE, New York, 767–770.
- B. Steiner, G. Wagner, A. Voigt, W. Dorsch and H.P. Strunk (1996) Growth and characterization of silicon layers grown by liquid phase epitaxy on cast silicon and silicon sheet material. *Thin Solid Films* **288**, 160–163.
- M. Stemmer, G. Wagner and S. Martinuzzi (1996) LBIC characterization of LPE Si layers deposited on multicrystalline Si substrates. *Mater. Sci. Eng.* **B42**, 153–156.
- K.H. Stern and M.E. McCollum (1985) Electrodeposition of silicon from molten salts. *Thin Solid Films* **124**, 129–134.
- M.J. Stocks, K.J. Weber and A.W. Blakers (2003) Fabrication of solar cells using epilift technique. *Proc. 3rd World Photovoltaic Solar Energy Conf.*, World Conference on Photovoltaic Energy Conversion, Osaka, Japan, 1268–1271.
- B.G. Streetman (1980) *Solid State Electronic Devices*. Prentice-Hall, Englewood Cliffs, NJ.
- G.B. Stringfellow (1971) The calculation of regular solution interaction parameters between elements from Groups III, IV and V of the periodic table. *Mater. Res. Bull.* **6**, 371–380.

- G.B. Stringfellow and P.E. Greene (1970) A quasi-chemical equilibrium calculation of Ge-Si-Sn and Ge-Si-Pb ternary phase diagrams. *J. Electrochem. Soc.* **117**, 1075–1079.
- G.B. Stringfellow and P.E. Greene (1971) Liquid phase epitaxial growth of  $\text{InAs}_{1-x}\text{Sb}_x$ . *J. Electrochem. Soc.* **118**, 805–810.
- V.S. Sudavtsova and V.G. Kudin (2001) Thermodynamic properties of Si-Ge and Si-Sn melts. *Inorg. Mater.* **37**, 319–320.
- T. Sukegawa, M. Kimura and A. Tanaka (1988) Gravity effect on dissolution of silicon in the In-Si system. *J. Cryst. Growth* **92**, 46–52.
- T. Sukegawa, M. Kimura and A. Tanaka (1989a) Compensation effect of lattice constant in silicon n+-n- junctions. *J. Cryst. Growth* **96**, 584–588.
- T. Sukegawa, M. Kimura and A. Tanaka (1989b) Fabrication of p-i-n photodiodes on LPE-grown substrates. *IEEE Electron. Device Lett.* **10**, 20–22.
- T. Sukegawa, M. Izawa, J. Katsuno, A. Tanaka and M. Kimura (1990) Growth of GeSi thick alloy layers by the yo-yo solute feeding method. *J. Cryst. Growth* **99**, 274–277.
- T. Sukegawa, M. Kimura and A. Tanaka (1991a) LPE growth of silicon by yo-yo solute feeding method. *J. Cryst. Growth* **108**, 598–602.
- T. Sukegawa, K. Yamashita, H. Katsuno, M. Kimura and A. Tanaka (1991b) Growth of GeSi thick alloy on a Si substrate by liquid phase epitaxy. *J. Cryst. Growth* **109**, 186–190.
- B.E. Sumner and R.T. Foley (1978) Liquid-phase epitaxial growth of gallium-doped silicon. *J. Electrochem. Soc.* **125**, 1817–1824.
- K. Suzuki, K. Sakaguchi, T. Nakagiri and N. Sano (1990) Gaseous removal of phosphorus and boron from molten silicon. *J. Jpn. Inst. Met.* **54**, 161–167 (in Japanese).
- Y. Suzuki and T. Nishinaga (1989) Epitaxial lateral overgrowth of Si by LPE with Sn solution and its orientation dependence. *Jpn. J. Appl. Phys., Part 1* **28**, 440–445.
- Y. Suzuki and T. Nishinaga (1990) Si LPE lateral overgrowth from a ridge seed. *Jpn. J. Appl. Phys., Part 1* **29**, 2685–2689.
- Y. Suzuki, T. Nishinaga and T. Sanada (1990) Sources of atomic steps in epitaxial lateral overgrowth of Si. *J. Cryst. Growth* **99**, 229–234.
- C. Takenaka, T. Kusunoki and K. Nakajima (1991a) Solute transport mechanism during liquid phase epitaxial (LPE) growth with an applied current. *J. Cryst. Growth* **108**, 519–524.
- C. Takenaka, T. Kusunoki and K. Nakajima (1991b) Effect of an electric current on the LPE growth of InP. *J. Cryst. Growth* **114**, 293–298.
- A. Tanaka, T. Yoneyama, M. Kimura and T. Sukegawa (1998) Control of GaInSb alloy composition grown from ternary solution. *J. Cryst. Growth* **186**, 305–308.
- F.W. Tausch and A.G. Lapierre (1965) A novel crystal growth phenomena: single crystal GaAs overgrowth onto silicon dioxide. *J. Electrochem. Soc.*, **112**, 706–709.
- T. Teubner, T. Boeck and K. Schmidt (1999) Modeling of solution growth from small indium droplets- homogeneous nucleation. *J. Cryst. Growth* **198/199**, 425–429.
- B. Thomas, G. Müller, P.-M. Wilde and H. Wawra (1997) Properties of silicon thin films grown by the temperature difference method. *Conf. Record of the 26th IEEE Photovoltaic Specialists Conf.*, IEEE, New York, 771–774.
- C.D. Thurmond and M. Kowalchik (1960) Germanium and silicon liquidus curves *Bell System Tech.* **39**, 169–204.
- C.J.J. Tool, S.E.A. Schiermeier, A. Gujjahr, L.J. Laas and H.H.C. de Moor (2000) LPE-deposition of crystalline silicon layers on recrystallized silicon-based ceramics. *Proc. 16th European Photovoltaic Solar Energy Conf.*, James and James, London.
- H.-P. Trah (1990) Liquid phase epitaxy in the ternary system Si-Ge-Bi. *J. Cryst. Growth* **102**, 175–182.
- F.A. Trumbore (1960) Solid solubilities of impurity elements in Si and Ge. *Bell System Tech. J.* **39**, 205–233.
- F.A. Trumbore, E.M. Porbansky and A.A. Tartaglia (1959) Solid solubilities of aluminum and gallium in germanium. *Phys. Chem. Solids* **11**, 239–245.

- F.A. Trumbore, H.G. White, M. Kowalchik, C.L. Luke and D.L. Nash (1965) Solubility and electrical behavior of Group IV impurities in solution grown gallium phosphide. *J. Electrochem. Soc.* **112**, 1208–1211.
- T. Ujihara, K. Obara, N. Usami, K. Fujiwara, G. Sazaki, T. Shishido and K. Nakajima (2003) What is the most important growth parameter on crystal quality of the silicon layer by LPE method. *Proc. 3rd World Conf. on Photovoltaic Energy Conversion*, IEEE, New York, 1241–1244.
- A. Voigt, B. Steiner, W. Dorsch, J. Krinke, M. Albrecht, H.P. Strunk and G. Wagner (1996) Solution growth of silicon on multicrystalline Si substrate: growth velocity, defect structure and electrical activity. *J. Cryst. Growth* **166**, 694–699.
- C. Wagner (1958) Passivity during the oxidation of silicon at elevated temperatures. *J. Appl. Physics* **29**, 1295–1297.
- G. Wagner, H. Wawra, W. Dorsch, M. Albrecht, R. Krome, H.P. Strunk, S. Riedel, H.J. Möller and W. Appel (1997) Structural and electrical properties of silicon epitaxial layers grown by LPE and CBVD on identical polycrystalline substrates. *J. Cryst. Growth* **174**, 680–685.
- R.S. Wagner and W.C. Ellis (1964) Vapor-liquid-solid mechanism of single crystal growth. *Appl. Phys. Lett.* **4**, 89–88.
- R.S. Wagner and C.J. Doherty (1966) Controlled vapor-liquid-solid growth of silicon crystals. *J. Electrochem. Soc.* **113**, 1300–1305.
- Y. Wakayama and S.-I. Tanaka (1997a) Nanometer-scale Si/Au bilayer dots fabricated by self-assembly process through liquid phase epitaxy. *Nanostruct. Mater.* **8**, 1033–1039.
- Y. Wakayama and S.-I. Tanaka (1997b) Self-assembled nanocomposite structure of Si-Au system formed by liquid phase epitaxy. *J. Cryst. Growth* **181**, 304–307.
- Y. Wakayama and S.-I. Tanaka (1999a) Fabrication of nanoscale heterojunction of Si/Au and Si/Ag by surface droplet epitaxy. *Nanostruct. Mater.* **12**, 13–18.
- Y. Wakayama and S.-I. Tanaka (1999b) Kinetics of surface droplet epitaxy and its application to fabrication of mushroom-shaped metal/Si heterostructure on nanometer scale. *Surf. Sci.* **420**, 190–199.
- Y. Wakayama, H. Fujinuma and S.-I. Tanaka (1998) Nanoscale liquid phase epitaxy between Si and Au particles. *J. Mater. Res.* **13**, 1492–1496.
- R.L. Wallace, J. Yi and W.A. Anderson (1993) Si film growth by supercooling of a molten silicon alloy. *Microcrystalline Semiconductors: Materials Science and Device Symposium*, Materials Research Society, Pittsburgh, PA, 671–676.
- R.L. Wallace, W.A. Anderson and K.M. Jones (1994) Thin film polycrystalline Si by a novel solution growth technique. *Conf. Record First World Conf. on Photovoltaic Energy Conversion*, IEEE, New York, 1379–1382.
- R.L. Wallace, W.A. Anderson and K.M. Jones (1995) Thin film polycrystalline on silicon by CS solution growth technique. *Microcrystalline and Nanocrystalline Semiconductors Symp.*, Materials Research Society, Pittsburgh, PA, 883–888.
- R.L. Wallace, B. Jagannathan, X. Gu, N. Sridhar, K. Etemadi, D.D.L. Chung and W.A. Anderson (1996) Low-cost, thin-film silicon for terrestrial solar cells. *AIP Conf. Proc.* **353**, 511–518.
- A.G. Walton (1969) Nucleation in liquids and solutions. in *Nucleation* A.C. Zettlemoyer, ed. Marcel Dekker, New York, 205–307.
- T.H. Wang and T.F. Ciszek (1994) Growth kinetics studies of silicon LPE from metal solutions. *Conf. Record of the 1st World Conf. on Photovoltaic Solar Energy Conversion* IEEE, New York, 1250–1253.
- T.H. Wang and T.F. Ciszek (1997a) Incorporation of Cu and Al in thin layer silicon grown from Cu-Al-Si. *AIP Conf. Proc.* **394**, 771–778.
- T.H. Wang and T.F. Ciszek (1997b) Impurity segregation in LPE growth of silicon from Cu-Al solutions. *J. Cryst. Growth* **174**, 176–181.
- T.H. Wang, T.F. Ciszek, Y.S. Tuo, J. Alleman, X. Wu, C.R. Schwerdtfeger and R.W. Burrows (1994) Liquid phase epitaxy for thin-layer silicon PV devices. *AIP Conf. Proc.* **306**, 92–99.

- T.H. Wang, T.F. Ciszek, C.R. Schwerdtfeger, H. Moutinho and R. Matson (1996) Growth of silicon thin layers on cast MG-Si from metal solutions for solar cells. *Solar Energy Mater. Solar Cells* **41/42**, 19–30.
- H. Watanabe, K. Fujita and M. Ichikawa (1993) Thermal decomposition of ultrathin oxide layers on Si(111) surfaces mediated by surface Si transport. *Appl. Phys. Lett.* **70**, 1095–1097.
- K.J. Weber and A.W. Blakers (1995a) Liquid phase epitaxy of silicon on multicrystalline silicon substrates. *J. Cryst. Growth* **154**, 54–59.
- K.J. Weber and A.W. Blakers (1995b) Prevention of oxide formation during liquid phase epitaxy of silicon. *Appl. Phys. Lett.* **66**, 1243–1245.
- K.J. Weber, K. Catchpole, M. Stocks and A.W. Blakers (1997) Lift-off of silicon epitaxial layers for solar cell applications. *Proc. 26th IEEE Photovoltaic Specialists Conf.*, IEEE, New York, 107–110.
- K.J. Weber, K. Catchpole and A.W. Blakers (1998) Epitaxial lateral overgrowth of Si on (100) silicon by liquid phase epitaxy. *J. Cryst. Growth* **186**, 369–374.
- K.J. Weber, A.W. Blakers, M.J. Stocks and A. Thompson (2003) Silicon liquid phase epitaxy for epilift solar cells. *Proc. 3rd World Conf. on Photovoltaic Solar Energy Conversion*, IEEE, New York, 1265–1267.
- K. Weiser (1960) Theory of solubility of interstitial impurities in germanium and silicon. *J. Phys. Chem. Solids* **17**, 149–161.
- J.M. Woodall (1971) Isothermal solution mixing growth of thin Ga<sub>1-x</sub>Al<sub>x</sub>As layers. *J. Electrochem. Soc.* **118**, 492–493.
- J.M. Woodall (1978) Liquid phase epitaxial growth of GaAs on molybdenum. *IBM Tech. Discl. Bull.* **21**, 2584.
- H.F. Wolf (1971) *Semiconductors*. John Wiley & Sons, Inc., New York.
- R. Wurschum, E. Bauser, H.-J. Queisser and H.-E. Schaefer (1990) Sealing of bore-holes in Si crystals by epitaxial overgrowth below 560 °C. *Appl. Phys. A* **50**, 583–585.
- T. Yamada, M. Tachikawa, T. Nishioka and T. Yamada (2000) Poly-crystalline silicon with large grains deposited from Al-Si melt. *J. Cryst. Growth* **209**, 50–54.
- L.V. Yashina, V.I. Shtanov and Z.G. Yanenko (2003) The application of VLS growth technique to bulk semiconductors. *J. Cryst. Growth* **252**, 68–78.
- T. Yoshikawa, K. Arimura and K. Morita (2005) Boron removal by titanium addition in solidification refining of silicon with Si-Al Melt. *Metall. Mater. Trans. B* **36**, 837–842.
- T. Yoshikawa and K. Morita (2005) Thermodynamics of solid silicon equilibrated with Si-Al-Cu alloys. *J. Phys. Chem. Solids* **66**, 261–265.
- A. Zdyb, J.M. Olchowik, and M. Mucha (2006) Dependence of GaAs and Si surface energy on the misorientation angle of the crystal planes. *Mater. Sci. - Poland* **24**, **4**, 1109–1114.
- S. Zein El Abedin, N. Borissenko and F. Endres (2004) Electrodeposition of nanoscale silicon in a room temperature ionic liquid. *Electrochem. Commun.* **6**, 510–514.
- A.C. Zettlemoyer (1968) Chemistry and metallurgy of wetting solid surfaces. in *Ohmic Contacts to Semiconductors*, B. Schwartz, ed. Electrochemical Society, New York, 48–66.
- R.P. Zingg, N. Nagel, R. Bergmann, E. Bauser, B. Höfflinger and H.J. Queisser (1992) First MOS transistors on insulator by silicon saturated liquid solution epitaxy. *IEEE Electron Device Lett.* **13**, 294–296.
- J.C. Zolper and A.M. Barnett (1989) Selective area solution growth of Ge and GaAs on Si. *J. Appl. Phys.* **66**, 210–214.
- K.H. Zschauer and A. Vogel (1971) Dependence of impurity incorporation on growth rate and crystal orientation during GaAs liquid-phase epitaxy. *Proc. 3rd International Symposium*, Institute of Physics, London, 100–107.

## APPENDIX 1. PHASE EQUILIBRIA MODELING: THE SILICON-METAL LIQUIDUS

Although experimental phase diagram data are available for most of the silicon-metal and germanium-metal binary systems of interest for LPE, it is useful to develop a phase equilibria model to assess the thermodynamic consistency of the data, extrapolate the solubility relations into temperature ranges where no experimental data are available, and to extend models to describe multicomponent systems.

In a two-phase system (solid and liquid) phase equilibrium is achieved when for every component  $i$  the chemical potential in the liquid phase equals that of the solid phase  $\mu_i^S = \mu_i^L$ . For multicomponent phases, the chemical potentials can be expressed as:

$$\mu_i^S = \mu_i^{S,\ominus}(T) + RT \ln a_i^S \quad (\text{A1.1a})$$

$$\mu_i^L = \mu_i^{L,\ominus}(T) + RT \ln a_i^L \quad (\text{A1.1b})$$

$\mu_i^{S,\ominus}(T)$  is the standard or reference chemical potential for component  $i$  in the solid phase and  $\mu_i^{L,\ominus}(T)$  is the standard or reference chemical potential for component  $i$  in the liquid phase. The reference chemical potentials are functions only of temperature; not of composition. (Pressure effects are negligible in this analysis of condensed phases.)  $R$  is the ideal gas constant and  $T$  is the absolute temperature.  $a_i$  denotes the activity of component  $i$  in each phase. For the silicon-metal binary system, the equilibria relations then become:

$$\mu_{\text{Si}}^{S,\ominus}(T) + RT \ln a_{\text{Si}}^S = \mu_{\text{Si}}^{L,\ominus}(T) + RT \ln a_{\text{Si}}^L \quad (\text{A1.2a})$$

$$\mu_{\text{M}}^{S,\ominus}(T) + RT \ln a_{\text{M}}^S = \mu_{\text{M}}^{L,\ominus}(T) + RT \ln a_{\text{M}}^L \quad (\text{A1.2b})$$

It is convenient to express the activities  $a_i$  in terms of atomic fractions  $X_i$  and activity coefficients  $\gamma_i$ , such that  $a_i = \gamma_i \cdot X_i$ . Thus, the equilibrium conditions for each component  $i$  are:

$$RT \ln \frac{\gamma_i^L X_i^L}{\gamma_i^S X_i^S} = \mu_i^{S,\ominus}(T) - \mu_i^{L,\ominus}(T) \quad (\text{A1.3})$$

The activity coefficients depend on the choice of reference states for each component in each phase. To determine the (hypereutectic) liquidus in a silicon-metal binary, pure solid silicon and pure liquid silicon are taken as the reference states for the chemical potentials, such that:

$$\mu_{\text{Si}}^{L,\ominus}(T) = \overline{G}_{\text{Si}}^{L,\ominus}(T), \text{ the partial molal Gibbs free energy of } \textit{pure} \text{ liquid silicon} \quad (\text{A1.4a})$$

$$= \underline{G}_{\text{Si}}^{L,\ominus}(T), \text{ the molar Gibbs free energy of } \textit{pure} \text{ liquid silicon} \quad (\text{A1.4b})$$

$$\mu_{\text{Si}}^{S,\ominus}(T) = \underline{G}_{\text{Si}}^{S,\ominus}(T) \equiv \text{the molar Gibbs free energy of } \textit{pure} \text{ solid silicon} \quad (\text{A1.4c})$$

where overbars denote partial molal quantities and underbars denote molar quantities. Since the reference components are pure phases, the partial molal and molar quantities

are the same. Thus:

$$RT \ln \frac{\gamma_{\text{Si}}^{\text{L}} X_{\text{Si}}^{\text{L}}}{\gamma_{\text{Si}}^{\text{S}} X_{\text{Si}}^{\text{S}}} = \mu_{\text{Si}}^{\text{S},\Theta}(T) - \mu_{\text{Si}}^{\text{L},\Theta}(T) \quad (\text{A1.5a})$$

$$= \overline{G}_{\text{Si}}^{\text{S}}(T) - \overline{G}_{\text{Si}}^{\text{L}}(T) \quad (\text{A1.5b})$$

$$= \underline{G}_{\text{Si}}^{\text{S}}(T) - \underline{G}_{\text{Si}}^{\text{L}}(T) \quad (\text{A1.5c})$$

$$\equiv -\Delta \underline{G}_{\text{Si}}^{\text{FUS}}(T) \quad (\text{A1.5d})$$

The utility of this formulation is that all terms on the right-hand side of Equation [A1.5(a–d)] are properties of pure silicon, and therefore functions only of temperature. All of the distinctive features of the liquidus are implied by the activity coefficients. Further, the quantity  $\Delta \underline{G}_{\text{Si}}^{\text{FUS}}(T)$  denotes the free energy of fusion of pure silicon and may be determined as:

$$\Delta \underline{G}_{\text{Si}}^{\text{FUS}}(T) = L_{\text{Si}} \left( 1 - \frac{T}{T_{\text{Si}}^{\text{M}}} \right) + \int_{T_{\text{Si}}^{\text{M}}}^T \Delta C_{\text{Si}} dT - T \int_{T_{\text{Si}}^{\text{M}}}^T \frac{\Delta C_{\text{Si}}}{T} dT \quad (\text{A1.6})$$

where  $L_{\text{Si}}$  (46.4 kJ mole<sup>-1</sup>) is the molar heat of fusion of silicon at the melting point  $T_{\text{Si}}^{\text{M}}$  (1683 K) of silicon, and  $\Delta C_{\text{Si}}$  is the difference in molar heat capacities of pure liquid silicon and pure solid silicon:

$$\Delta C_{\text{Si}} \equiv C_{\text{Si}}^{\text{L}} - C_{\text{Si}}^{\text{S}} \quad (\text{A1.7})$$

which for silicon may be calculated as:

$$\Delta C_{\text{Si}} = 7.11 - 4.28 \times 10^{-3} \cdot T + \frac{4.44 \times 10^{-3}}{T^2} \quad (\text{A1.8})$$

with temperature in K and  $\Delta C_{\text{Si}}$  in J K<sup>-1</sup> mol<sup>-1</sup>.

For ideal solutions, the activity coefficients  $\gamma_i$  can be set equal to 1. For nonideal solutions, the activity coefficient for each species in each phase is given by:

$$RT \ln \gamma_i = \Delta \overline{H}_i^{\text{mix}} - T \cdot \Delta \overline{S}_i^{\text{ex-mix}} \quad (\text{A1.9})$$

where  $\Delta \overline{H}^{\text{mix}}$  is the partial molar enthalpy of mixing, and  $\Delta \overline{S}^{\text{ex,mix}}$  is the excess (over and above ideal) entropy of mixing.

In the *quasi-regular* binary solution model, the activity coefficient can be determined according to:

$$\Delta H_i^{\text{mix}} = a(1 - X_i)^2 \quad (\text{A1.10a})$$

$$\Delta S_i^{\text{mix}} = b(1 - X_i)^2 \quad (\text{A1.10b})$$

Other solution models may be regarded as special cases of the quasi-regular model. As mentioned, if  $a = b = 0$  the solution is *ideal*. If  $a \neq 0, b = 0$  the solution is termed *regular*. If  $a = 0; b \neq 0$  the solution is termed *athermal*.



More generally, the activity coefficients for components  $i$  and  $j$  of a binary are:

$$RT \ln \gamma_i = \alpha_{ij}(T) \cdot (1 - X_i)^2 \quad (\text{A1.11a})$$

$$RT \ln \gamma_j = \alpha_{ij}(T) \cdot (1 - X_j)^2 \quad (\text{A1.11b})$$

where  $\alpha_{ij}(T) = a_{ij} - b_{ij}T$  is the temperature-dependent, concentration-independent binary interaction parameter. More complex solution models utilize interaction parameters that are higher-order functions of temperature and composition,

### A1.1 The silicon-metal binary liquidus

The hypereutectic liquidus in a silicon-metal binary is given by:

$$RT \ln \frac{\gamma_{\text{Si}}^{\text{L}} X_{\text{Si}}^{\text{L}}}{\gamma_{\text{Si}}^{\text{L}} X_{\text{Si}}^{\text{L}}} = -\Delta \underline{G}_{\text{Si}}^{\text{FUS}}(T) \quad (\text{A1.12})$$

As the solid phase is nearly pure silicon.

For the quasi-regular solution model (Table A1.1):

$$a - bT = \frac{-\Delta \underline{G}_{\text{Si}}^{\text{FUS}}(T) - RT \ln X_{\text{Si}}^{\text{L}} + RT \ln X_{\text{Si}}^{\text{S}}}{(1 - X_{\text{Si}}^{\text{L}})^2} \quad (\text{A1.13})$$

$$X_{\text{Si}}^{\text{L}} \cong \exp \left[ \frac{-L_{\text{Si}}}{RT} \left( 1 - \frac{T}{T_{\text{Si}}^{\text{M}}} \right) - \frac{(a - bT)}{RT} \right] \quad (\text{A1.14})$$

$$m \cong \frac{X_{\text{Si}}^{\text{L}}}{RT} \left( \frac{L_{\text{Si}}}{T_{\text{Si}}^{\text{FUS}}} + b - R \ln X_{\text{Si}}^{\text{L}} \right) \quad (\text{A1.15})$$

### A1.2 Alloy solvents

The binary model can be generalized to melts with two or more solvent components:

$$RT \ln \gamma_i = \sum_{\substack{j=1 \\ i \neq j}}^m \alpha_{ij} X_j^2 + \sum_{\substack{k=1 \\ k < j, j \neq 1}}^m \sum_{\substack{j=1 \\ i \neq k}}^m (\alpha_{ij} + \alpha_{ik} - \alpha_{kj}) X_k X_j \quad (\text{A1.16})$$

For a ternary system (silicon plus two metals 1 and 2) the activity coefficient of silicon is given more explicitly by:

$$RT \ln \gamma_{\text{Si}}^{\text{L}} = \alpha_{\text{Si-M1}} X_{\text{M1}}^2 + \alpha_{\text{Si-M2}} X_{\text{M2}}^2 + (\alpha_{\text{Si-M1}} + \alpha_{\text{Si-M2}} - \alpha_{\text{M1-M2}}) X_{\text{M1}} X_{\text{M2}} \quad (\text{A1.17})$$

Since the melt composition is not significantly altered by the depletion of silicon during growth, it is convenient to define a ratio of metal components in the melt as:

$$r \equiv \frac{X_{\text{M1}}}{X_{\text{M2}}} \quad (\text{A1.18})$$

**Table A1.1** Liquid phase (quasi-regular solution) binary interaction parameters

Binary pair	Interaction parameter <sup>a</sup> (J mol <sup>-1</sup> )	Reference
Al-As	-26 736-23.0 · T	Casey and Panish, 1978
Al-Bi	14 054	Hultgren <i>et al.</i> , 1973
Al-Cu	-1004	Wang and Ciszek, 1997
Al-Ga	435	Casey and Panish, 1978
Al-Ge	-22 426-13.2 · T 2-11 422	Thurmond and Kowalchik, 1960; Stringfellow and Greene, 1970; Stringfellow, 1971
Al-In	18 405	Hultgren <i>et al.</i> , 1973
Al-In	18 405	Hultgren <i>et al.</i> , 1973
Al-P	7322-8.4 · T	Illegems and Panish, 1973; Casey and Panish, 1978
Al-Pb	30 865	Hultgren <i>et al.</i> , 1973
Al-Sb	51 020-41.8 · T	Panish and Illegems, 1972
Al-Sn	8050	Hultgren <i>et al.</i> , 1973
Al-Si	-11 966	Stringfellow and Greene, 1970; Stringfellow, 1971
	23 698	Wang and Ciszek, 1999
Al-Sn	8368	Panish, 1973
Al-Si	-11 966	Stringfellow and Greene, 1970; Stringfellow, 1971
	23 698	Wang and Ciszek, 1999
Al-Sn	8368	Panish, 1973
As-Ga	21 589-38.3 · T	Panish, 1974; Casey and Panish, 1978
As-In	16 150-41.8 · T	Lichter and Sommelet, 1969
Au-Ge	-15 293	Stringfellow and Greene, 1970; Stringfellow, 1971
Au-Si	-21 004	Stringfellow and Greene, 1970; Stringfellow, 1971
Bi-Ge	23 034-6.3 · T	Thurmond and Kowalchik, 1960
Bi-Si	49 597 +0.75 · T	Trah, 1990
Cu-Si	24 078	Wang and Ciszek, 1997
Ga-Ge	-879	Stringfellow and Greene, 1970; Stringfellow, 1971
	-628	Thurmond and Kowalchik, 1960
Ga-In	9414	De Cremoux, 1981
	8870	Pearsall <i>et al.</i> , 1979
Ga-P	8870-18.6 · T	Panish, 1973
Ga-Sb	19 665-25.1 · T	Panish, 1974
Ga-Si	8201	Stringfellow and Greene, 1970; Stringfellow, 1971
	13 598-3.5 · T	Thurmond and Kowalchik, 1960
Ga-Sn	0	Shunk, 1969; Panish, 1973
Ge-In	4247	Stringfellow and Greene, 1970; Stringfellow, 1971
	4151-2.1 · T	Alonso and Bauser, 1987
Ge-Pb	19 560	Stringfellow and Greene, 1970; Stringfellow, 1971
	36 700-17.1 · T	Thurmond and Kowalchik, 1970
Ge-Sb	11 045-8.4 · T	Thurmond and Kowalchik, 1960
Ge-Si	6757	Stringfellow and Greene, 1970; Stringfellow, 1971
Ge-Sn	3075	Stringfellow and Greene, 1970; Stringfellow, 1971
	7029-4.5 · T	Thurmond and Kowalchik, 1960
In-P	14 970-14.8 · T	Panish, 1974
In-Sb	14 226-50.2 · T	Panish and Illegems, 1972

(continued overleaf)

**Table A1.1** (continued)

Binary pair	Interaction parameter <sup>a</sup> (J mol <sup>-1</sup> )	Reference
In-Si	36 213 (calc.) 39 221 - 7.1 · T	Stringfellow and Greene, 1970; Stringfellow, 1971 Alonso and Bauser, 1987
Pb-Si	55 312 82 968 - 20.1 · T	Stringfellow and Greene, 1970; Stringfellow, 1971 Thurmond and Kowalchik, 1960
Si-Sn	26 819 34 079 - 6.3 · T	Stringfellow and Greene, 1970; Stringfellow, 1971 Thurmond and Kowalchik, 1960
Sb-Si	13 765 - 6.7 · T	Thurmond and Kowalchik, 1960

<sup>a</sup>Interaction parameter  $a - b \cdot T$ .

#### References

- M.I. Alonso and E. Bauser (1987) Growth of Si<sub>1-x</sub>Ge<sub>x</sub> on silicon by liquid-phase epitaxy. *J. Appl. Phys.* **62**, 4445-4449.
- H.B. Casey Jr and M.B. Panish (1978) *Heterostructure Lasers, Part B; Materials and Operating Characteristics*. Academic Press, New York.
- B. de Cremoux (1981) The crystallization path: A way to the Ga<sub>x</sub>In<sub>1-x</sub>As<sub>y</sub>P<sub>1-y</sub> phase diagram. *IEEE J. Quantum Electron.* **QE-17**, 123-127.
- R. Hultgren, P.D. Desai, D.T. Hawkins, M. Gleiser and K.K. Kelley (1973) *Selected Values of the Thermodynamic Properties of Binary Alloys*. American Society of Metals, Metals Park, OH.
- M. Illegems and M.B. Panish (1973) Phase diagram of the system Al-Ga-P. *J. Cryst. Growth* **20**, 77-81.
- B.D. Lichter and P. Sommelet (1969) Thermal properties of A<sup>III</sup> B<sup>V</sup> compounds-1. *Trans. AIME* **245**, 99-105.
- M.B. Panish (1973) Phase equilibria in the system Al-Ga-As-Sn and electrical properties of Sn-doped liquid phase epitaxial Al<sub>x</sub>Ga<sub>1-x</sub>As. *J. Appl. Phys.* **44**, 2667-2675.
- M.B. Panish (1974) A thermodynamic evaluation of the simple solution treatment of the Ga-P, In-P and Ga-As systems. *J. Cryst. Growth* **27**, 6-20.
- M.B. Panish and M. Illegems (1972) Phase equilibria in ternary III-V systems in *Progress in Solid State Chemistry*, H. Reiss and J.O. McCaldin, eds. Pergamon, New York, 39-83.
- T.P. Pearsall, M. Quillec and M.A. Pollack (1979) The effect of substrate orientation on the liquid-solid distribution coefficients for Ga<sub>x</sub>In<sub>1-x</sub>As in the temperature range 600-700 °C. *Appl. Phys. Lett.* **35**, 342-344.
- F.A. Shunk (1969) *Constitution of Binary Alloys*. McGraw-Hill, New York.
- G.B. Stringfellow (1971) The calculation of regular solution interaction parameters between elements from Groups III, IV, and V of the periodic table. *Mater. Res. Bull.* **6**, 371-380.
- G.B. Stringfellow and P.E. Greene (1970) A quasi-chemical equilibrium calculation of the Ge-Si-Sn and Ge-Si-Pb ternary phase diagrams. *J. Electrochem. Soc.* **117**, 1075-1079.
- C.D. Thurmond and M. Kowalchik (1960) Germanium and silicon liquidus curves. *Bell System Tech. J.* **39**, 169-204.
- H.-P. Trah (1990) Liquid phase epitaxy in the ternary system Si-Ge-Bi. *J. Cryst. Growth* **102**, 175-182.
- T.H. Wang and T.F. Ciszek (1997) Impurity segregation in LPE growth of silicon from Cu-Al solutions. *J. Cryst. Growth* **174**, 176-181.

For melts relatively dilute in silicon the silicon liquid phase atomic fraction is:

$$X_{\text{Si}}^{\text{L}} = \exp \left[ \frac{-\Delta G_{\text{Si}}^{\text{FUS}}(T) - \alpha_{\text{Si-M1}} \cdot r - \alpha_{\text{Si-M2}} \cdot r^{-1} + (\alpha_{\text{Si-M1}} + \alpha_{\text{Si-M2}} - \alpha_{\text{M1-M2}})}{RT} \right] \quad (\text{A1.19})$$

## APPENDIX 2. IMPURITIES AND DOPING IN SILICON LPE

The doping and purity of silicon grown from metallic melts in LPE or LPE-related processes is a critical issue. The performance of semiconductor devices depends on the concentrations of electrically active impurities that act as dopants (acceptors or donors), recombination centers, or scattering centers. Further, in some cases it may be possible to exploit inherent purification of solution growth wherein impurities preferentially segregate to the liquid phase, resulting in reduced contamination of the deposited silicon. For these reasons, a detailed exposition of doping effects relevant to the growth of silicon from molten metal solutions is presented here.

The analysis for the liquidus may be used to determine the solidus and thus the equilibrium concentration of metal dissolved in the silicon crystallized from the melt. The concentration and nature of the impurities are critical for determining the semiconductor properties of the LPE-grown silicon. The sources of impurities in silicon are due to the metallic solvent itself, minor constituents added to the melt to effect doping, and unwanted contaminants in the melt. An estimation of impurity segregation is needed in order to controllably dope the silicon epilayer as well as establish criteria for melt purity needed to attain an epilayer of specified purity.

The *segregation coefficient*, also sometimes called the *distribution coefficient*, for an impurity or melt component  $i$  is defined as:

$$K_i \equiv \frac{X_i^{\text{S}}}{X_i^{\text{L}}} \quad (\text{A2.1})$$

Following a thermodynamic dynamic analysis similar to that used to derive the liquidus curve, the segregation coefficient can be calculated as

$$K_i \equiv \frac{X_i^{\text{S}}}{X_i^{\text{L}}} = \frac{\gamma_i^{\text{L}}}{\gamma_i^{\text{S}}} \exp \left( \frac{\Delta G_i^{\text{FUS}}}{RT} \right) \quad (\text{A2.2})$$

The activity coefficient for the impurity can be determined using quasi-regular solution models.

As impurity concentrations in semiconductors are customarily expressed in terms of atoms per  $\text{cm}^3$  ( $C_i$ ) such that:

$$C_i \cong \frac{\rho_{\text{Si}}}{M_{\text{Si}}} \cdot N_0 \cdot X_{\text{Si}}^{\text{S}} \quad (\text{A2.3})$$

where  $\rho_{\text{Si}}$  is the density of solid silicon,  $M_{\text{Si}}$  is the atomic mass of silicon, and  $N_0$  is Avogadro's number, a more useful segregation coefficient is defined as:

$$k_{0,i} \equiv \frac{C_i}{X_i^L} = K_i \left( \frac{L\rho_{\text{Si}}}{M_{\text{Si}}} \right) \quad (\text{A2.4})$$

For silicon-metal binary systems and at temperatures sufficiently below the melting point of silicon wherein the liquid phase is dilute in silicon, then  $X_i^L \rightarrow 1$ . In this case, the doping due to the metal solvent depends only on the growth temperature. Of more general interest is the incorporation of melt components over a wide range of concentrations. For instance, small amounts of dopants (e.g. boron or indium) added to tin or lead, can effect  $p$ -type doping over several orders of magnitude according to the amount of dopant added to the melt.

The above analysis assumes the impurities are electrically neutral in silicon. For impurities which ionize in silicon, i.e. function as dopants, a distinction can be made between ionized and un-ionized (neutral) impurities (Reiss, 1953; Trumbore *et al.*, 1959, 1965; Lehovc, 1962). If the concentration of neutral donor impurities in silicon is  $C_D^0$  and that of ionized donors is  $C_D^+$  then:

$$C_D = C_D^+ + C_D^0 \quad (\text{A2.5})$$

where  $C_D$  is the total concentration of impurities, both ionized and neutral. Similarly, for acceptor impurities:

$$C_A = C_A^+ + C_A^0 \quad (\text{A2.6})$$

Using Fermi-Dirac statistics, the fraction of total impurities that are ionized is:

$$\frac{C_D^+}{C_D} = \left[ 1 - \frac{1}{1 + \frac{1}{g_D} \exp\left(\frac{E_D - E_F}{kT}\right)} \right] \quad (\text{A2.7})$$

where  $E_D$  is the donor energy level,  $E_F$  is the Fermi level, and  $g_D$  is a degeneracy factor equal to 2 in this case. Similarly, for acceptors:

$$\frac{C_A^+}{C_A} = \left[ \frac{1}{1 + g_A \exp\left(\frac{E_A - E_F}{kT}\right)} \right] \quad (\text{A2.8})$$

where  $E_A$  is the acceptor energy level and the degeneracy factor  $g_A$  in this case is 4.

Thus, for donors or acceptors, the distribution of dopant is according to:

$$k_i \equiv \frac{C_D}{X_i^L} = k_{0,i} \left[ 1 + \frac{1}{2} \exp\left(\frac{E_D - E_F}{kT}\right) \right] \quad (\text{A2.9a})$$

$$k_i \equiv \frac{C_A}{X_i^L} = k_{0,i} \left[ 1 + \frac{1}{4} \exp\left(\frac{E_F - E_A}{kT}\right) \right] \quad (\text{A2.9b})$$

These equations imply that the incorporation of electrically active impurities in silicon depends on the position of the Fermi level during the growth process, a phenomenon which was demonstrated implicitly by Reiss and Fuller (Reiss and Fuller 1956). For impurities with a high mobility in silicon at the growth temperature, it is the position of the Fermi level in the bulk silicon which determines the impurity segregation. On the other hand, for impurities which diffuse slowly from the growth interface into the bulk of the growing silicon crystal, it is the position of the Fermi level at the surface (melt/silicon interface) which determines the impurity segregation. Zschauer and Vogel (Zschauer and Vogel, 1971) suggest the following criteria to distinguish between these two limiting cases. If:

$$\frac{D_i^S}{L_{\text{Debye}}} > 10 \cdot v \quad (\text{A2.10})$$

where  $D_i^S$  is the diffusivity of impurity  $i$  in the solid silicon at the growth temperature,  $v$  is the growth rate of silicon, and  $L_{\text{Debye}}$  is the Debye length, then dopant segregation is determined by the position of the Fermi level in the bulk of the grown silicon. On the other hand, if:

$$\frac{10 \cdot D_i^S}{L_{\text{Debye}}} < v \quad (\text{A2.11})$$

then it is the position of the Fermi level at the surface of the growing silicon that determines dopant segregation. Between these two limits, the doping is growth-rate dependent.

The Debye length  $L_{\text{Debye}}$  is a function of temperature and carrier concentration (Wolf, 1971):

$$L_{\text{debye}} = \sqrt{\frac{\epsilon_{\text{Si}} k T}{2q^2 N_{\text{dop}}}} \cong 150 \sqrt{\frac{T}{N_{\text{dop}}}} \text{ cm} \quad (\text{A2.12})$$

where  $\epsilon_{\text{Si}}$  is the dielectric constant of silicon,  $k$  is Boltzman's constant,  $T$  is the absolute temperature,  $q$  is the electronic charge, and  $N_{\text{dop}}$  is the carrier concentration.

If the semiconductor is relatively lowly doped, then  $N$  is given by the intrinsic carrier concentration  $n_i$ , otherwise  $N$  is the extrinsic doping concentration  $C_{\text{D}}$  or  $C_{\text{A}}$ . The distinction between the intrinsic and extrinsic regimes is made by determining the intrinsic carrier concentration at the growth temperature:

$$n_i = \sqrt{N_{\text{C}} N_{\text{V}}} \left( \frac{T}{300} \right)^{3/2} \exp \left( \frac{-E_{\text{g}}}{kT} \right) \quad (\text{A2.13})$$

or more explicitly for silicon:

$$n_i = 3.7 \times 10^{19} \left( \frac{T}{300} \right)^{3/2} \exp \left[ \frac{E_{\text{g}}(T)}{2kT} \right] \text{ cm}^{-3} \quad (\text{A2.14a})$$

$$E_{\text{g}}(T) = \frac{1.17 - 4.73 \times 10^{-4} T^2}{(T + 636)} \text{ eV} \quad (\text{A2.14b})$$

which takes into account the temperature dependence of the density of states and the bandgap.

If  $n_i$  exceeds the doping concentration, the material is effectively intrinsic. Growth temperatures in silicon LPE are typically in the range of 500–1200 °C, and even at moderately high doping levels, as adjudged by room temperature electrical properties, the silicon material may be effectively intrinsic at the growth temperature. Impurity diffusion coefficients in solid silicon range from  $10^{-16}$  to  $10^{-10}$  cm<sup>2</sup> s<sup>-1</sup>, depending on the impurity and growth temperature. Growth rates will typically vary from 0.1 to 2 μm min<sup>-1</sup>. Thus, application of the criteria of Zschauer and Vogel [Equations (2.10) and (2.11)] indicates that either regime of dopant segregation, i.e. surface-determined or bulk-determined, may be encountered in silicon LPE, depending on the impurity (melt component), growth temperature, and growth rate. As an aside, it is noted that Hurle (Hurle, 1999) contends that although the Schottky barrier model for dopant segregation described above has held sway for many years, a strong case can be made that doping phenomena for GaAs LPE are not compatible with the Schottky barrier model and that it should be rejected in favor of an equilibrium thermodynamic native point defect model to explain dopant incorporation. As an analogous native point defect model is not relevant to silicon or germanium, the Schottky barrier model of doping can be tentatively retained.

In cases where the doping is determined by the Fermi level in the bulk silicon and the silicon is effectively intrinsic, then:

$$E_F = E_i \cong E_g/2 \quad (\text{A2.15})$$

On the other hand, if conditions are such that the silicon is extrinsic, then the position of the Fermi level depends on the concentration of impurity. For donors:

$$E_F - E_i = kT \ln \left( \frac{\gamma_n C_D}{n_i} \right) \quad (\text{A2.16a})$$

and for acceptors:

$$E_i - E_F = kT \ln \left( \frac{\gamma_p C_A}{n_i} \right) \quad (\text{A2.16b})$$

$\gamma_n$  and  $\gamma_p$  can be regarded as correction factors derived from Fermi–Dirac statistics and which are used when the doping level is high ( $>10^{20}$  cm<sup>-3</sup>) (Reiss, 1953; Lehovec, 1962; Casey and Panish, 1978). A graphical or numerical method should be used to determine the position of the Fermi level when more than one electrically active impurity is being incorporated into silicon. The donor concentration is related to the impurity atomic fraction in the melt as

$$\frac{C_D}{X_i^L} = k_{0,i} \left[ 1 + \frac{1}{2} \frac{n_i}{C_D} \exp \left( \frac{E_D - E_i}{kT} \right) \right] \quad (\text{A2.17})$$

where  $X_i^L$  is the mole fraction of impurity in the liquid phase. To a good approximation, the above equation becomes:

$$C_D = \left[ \frac{k_0 \cdot n_i}{2} \exp \left( \frac{E_D - E_i}{kT} \right) \right]^{1/2} \sqrt{X_i^L} \quad (\text{A2.18})$$

**Table A2.1** Dependence of silicon doping on impurity concentration in melt

Growth rate	Donors	Acceptors
Slow	$C_D = \left[ \frac{k_{0,i} \cdot n_i}{2} \exp\left(\frac{E_D - E_i}{kT}\right) \right]^{1/2} \sqrt{X_i^L}$	$C_A = \left[ \frac{k_{0,i} n_i}{4} \exp\left(\frac{E_i - E_A}{kT}\right) \right]^{1/2} \cdot \sqrt{X_{Si}^L}$
Fast	$C_D = k_{0,i} \cdot \left[ 1 + \frac{1}{2} \cdot \exp\left(\frac{-2E_g}{kT}\right) \right] \cdot X_i^L$	$C_A = k_{0,i} \cdot \left[ 1 + \frac{1}{4} \cdot \exp\left(\frac{-E_g}{3kT}\right) \right] \cdot X_i^L$

with

$$k_{0,i} = \left( \frac{L\rho_{Si}}{M_{Si}} \right) \frac{\gamma_i^L}{\gamma_i^S} \exp\left[ \frac{\Delta G_i^{FUS}(T)}{RT} \right]$$

indicating that under the conditions for which it was derived the concentration of impurities in the solid silicon goes as the square root of the atomic fraction of impurity in the liquid phase. Similarly, for acceptor-type impurities:

$$C_A = \left[ \frac{k_{0,i} n_i}{4} \exp\left(\frac{E_i - E_A}{kT}\right) \right]^{1/2} \cdot \sqrt{X_{Si}^L} \quad (A2.19)$$

For conditions where the Zschauer and Vogel criterion [Equation (A2.11)] suggests that the position of the Fermi level at the surface determines the impurity segregation, the following analysis is used. Because the liquid metal melt has a high concentration of electrons, the growth interface may be treated as a surface-state dominated Schottky barrier. For *n*-type silicon, the band bending at the surface is such that:

$$E_D - E_F = \phi_{BN} \approx \frac{2}{3} E_g \quad (A2.20)$$

with a barrier height of  $\phi_{BN}$ . The results of this analysis are summarized in Table A2.1.

### APPENDIX 3. EFFECTS OF OXYGEN AND WATER VAPOR IN Si LPE

Silicon has a very high affinity for oxygen, and the silicon substrate surface is highly susceptible to oxidation. Oxide films impede epitaxial growth by reducing the wetting of the substrate by the molten metal solution and by creating a barrier to nucleation. The effects of oxygen and water vapor in the growth ambient are critical in silicon LPE, more so than with LPE of III-V materials. Oxidation problems in LPE can be prevented by a combination of HF etching of the silicon substrate wafer prior to growth, a leak-tight LPE system that can sustain vacuum pressures of  $10^{-5}$  Torr or less, the use of Pd-diffused purified hydrogen (at 1 atm pressure) as the growth ambient, and 6- to 12-h degassing of the melts to remove residual oxygen.



Nevertheless, in solar cell production there may be incentive to implement LPE systems where reduced oxygen and water vapor levels are not as easily achieved as in conventional LPE systems used for research and production of optoelectronic components, and where protocols can tolerate higher levels of oxygen and water vapor. Pure hydrogen can combine explosively with air in the event of a leak. The hazards of hydrogen can be reduced by diluting the hydrogen in nitrogen or argon, e.g. using a forming gas mixture of 5–15 % H<sub>2</sub>: 85–95 % N<sub>2</sub> or argon. Several workers have reported Si LPE using forming gas (Mauk and Barnett, 1985; Zhi *et al.*, 1995) or argon (Józwik and Olchowik, 2006). Forming gas and argon cannot be purified by Pd diffusion however. Water vapor can be removed from forming gas using molecular sieves, metal catalysts, cold traps, or bubbling the forming gas through molten Ga/Al, but these expedients are generally not as effective as using hydrogen purified by Pd-diffusion. Healy *et al.* (Healy *et al.*, 1991) reported low-temperature Si LPE under a vacuum ( $\sim 10^{-4}$  Torr). Presumably the vacuum conditions help avoid oxidation of the silicon substrate. More elaborate procedures for preventing oxide formation during LPE have been described by Weber and Blakers (Weber and Blakers, 1995b). If surface oxides cannot be avoided, it may be possible to add small amounts (<1 %) of reducing agents, e.g. Al, Ga, Mg or rare earths to the melt to reduce surface oxides (Bergmann and Kurianski, 1993; Shi, 1994b; Wang *et al.*, 1994; Shi *et al.*, 1996). When gallium is added to the melt to reduce SiO<sub>2</sub>, any Ga<sub>2</sub>O<sub>3</sub> formed tends to float on top of the melt, away from the growth interface, while any Ga<sub>2</sub>O is volatile. Aluminum oxide Al<sub>2</sub>O<sub>3</sub>, on the other hand, *may* form on the silicon substrate in place of the SiO<sub>2</sub>, obviating its intended purpose of producing an oxide-free silicon surface. Many reducing agents may act as undesirable dopants however. It would therefore be best to avoid the formation of silicon and melt oxides altogether. For these reasons, it is useful to review the thermodynamics and kinetics of silicon oxidation under conditions typical of LPE processes.

### A3.1 Thermodynamics of silicon oxidation

Whether a silicon surface remains clean (oxide free) or oxidizes can be estimated by determining the concentration of oxidizing species in equilibrium with solid silicon.

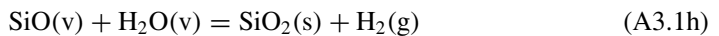
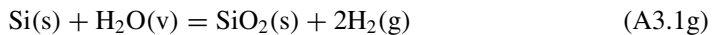
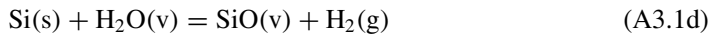


**Table A3.1** Partial pressures (in atm) of volatile species in equilibrium with silicon

Species	Temperature (°C)				
	800	900	1000	1100	1200
H <sub>2</sub>	1	1	1	1	1
H <sub>2</sub> O	6 × 10 <sup>-9</sup>	3 × 10 <sup>-8</sup>	2 × 10 <sup>-7</sup>	7 × 10 <sup>-7</sup>	3 × 10 <sup>-6</sup>
O <sub>2</sub>	10 <sup>-35</sup>	10 <sup>-31</sup>	10 <sup>-28</sup>	10 <sup>-25</sup>	10 <sup>-23</sup>
SiO	10 <sup>-8</sup>	3 × 10 <sup>-7</sup>	4 × 10 <sup>-6</sup>	4 × 10 <sup>-5</sup>	3 × 10 <sup>-4</sup>

Only three of these reactions are independent and the equilibrium concentrations may be determined through:

$$\frac{a_{\text{SiO}_2}}{a_{\text{Si}} \cdot p_{\text{O}_2}} = \exp \left[ \frac{-\Delta G_1(T)}{RT} \right] \quad (\text{A3.2a})$$

$$\frac{p_{\text{SiO}}^2}{a_{\text{Si}} \cdot a_{\text{SiO}_2}} = \exp \left[ \frac{-\Delta G_2(T)}{RT} \right] \quad (\text{A3.2b})$$

$$\frac{p_{\text{H}_2\text{O}}}{p_{\text{H}_2} \cdot p_{\text{O}_2}^{1/2}} = \exp \left[ \frac{-\Delta G_3(T)}{RT} \right] \quad (\text{A3.2c})$$

which represents the equilibrium law of mass action applied to Reactions (A3.1a), (A3.1b) and (A3.1c). The activities of the solid species,  $a_{\text{Si}}$  and  $a_{\text{SiO}_2}$  are set equal to 1, although as thin films their activities may be different from their bulk activities due to strain energy at the silicon/silica interface and other surface effects.  $\Delta G_1(T)$ ,  $\Delta G_2(T)$ , and  $\Delta G_3(T)$  are the Gibbs free energies for their respective reactions, and may be estimated (in J mol<sup>-1</sup>) from (Kubaschewski *et al.*, 1967):

$$\Delta G_1(T) = 40540 + 3.08 \cdot \log T - 29.71 \cdot T \quad (\text{A3.3a})$$

$$\Delta G_2(T) = 51530 - 9.92 \cdot T \quad (\text{A3.3b})$$

$$\Delta G_3(T) = 13683 + 1.07 \cdot T \cdot \log T - 0.53 \cdot T \quad (\text{A3.3c})$$

Using these relations, the partial pressures of the volatile species in equilibrium with silicon are shown in Table A3.1.

For a given temperature, the partial pressure of oxygen and water vapor must be kept below their equilibrium values to prevent oxidation of a pristine silicon surface. In practice, this can be achieved in a leak-tight system if a hydrogen ambient is used that is purified by palladium diffusion, in which case the ambient is essentially free of oxygen and water vapor.

According to Le Chatellier's principle, silicon oxidation can be prevented, or surface silicon dioxide can be reduced, by maintaining partial pressures of the volatile species below these equilibrium values. For 1000°C, the dew point corresponding to

the equilibrium water vapor pressure is about  $-70^{\circ}\text{C}$ . Therefore, in principle at least, a liquid nitrogen cold trap should be sufficient to reduce the water vapor content of the ambient gas in order to avoid silicon oxidation.

### A3.2 Silicon passivity and melt reducing agents

Wagner (Wagner, 1958) has shown that under certain circumstances, the conditions necessary to prevent surface oxidation are not as stringent as a thermodynamic analysis might suggest. At low oxygen concentrations in the gas phase, the oxidation of the surface is determined by the formation and transport of silicon monoxide through the surface boundary layer. In Wagner's analysis, a silicon surface will remain free of silica provided the oxygen partial pressure does not exceed a maximum given by:

$$p_{\text{O}_2}(\text{max}) \approx \frac{1}{2} \left( \frac{D_{\text{SiO}}}{D_{\text{O}_2}} \right) \cdot p_{\text{SiO}}(\text{equilibrium}) \quad (\text{A3.4})$$

where  $D_{\text{SiO}}$  and  $D_{\text{O}_2}$  are the diffusivities of silicon monoxide and molecular oxygen through the boundary layer. Wagner (Wagner, 1958) and Kramer (Kramer, 1960) have found experimental evidence of surface passivity in silicon-oxygen systems. For  $1000^{\circ}\text{C}$ , the maximum oxygen partial pressure is about  $10^{-5}$  atm.

# 6 Liquid Phase Epitaxy of Silicon Carbide

R. YAKIMOVA AND M. SYVÄJÄRVI

*Dept of Physics, Chemistry and Biology, Linköping University, S-581 83 Linköping, Sweden*

---

6.1 Introduction	179
6.2 Fundamental aspects of LPE of SiC	180
6.3 Growth methods for SiC LPE	185
6.3.1 Modified travelling solvent method	186
6.3.2 Dipping method	191
6.3.3 Container free LPE	191
6.3.4 Vapour–liquid–solid mechanism	192
6.4 Characteristic features of SiC LPE	193
6.4.1 Step-bunching	193
6.4.2 Micropipe filling	195
6.5 LPE of SiC under reduced gravity	196
6.6 Applications	198
References	199

---

## 6.1 INTRODUCTION

Silicon Carbide (SiC) belongs to the class of wide band gap semiconductors ( $E_g \sim 3$  eV) with a large number of polymorphs (more than 200), which makes it unique among the other materials of this class. Another exceptional feature of SiC is the potential to grow homoepitaxially due to the existence of its own substrates. It is also extremely hard (second after diamond in the Mohs scale), chemically stable (no acid can attack it) and radiation resistant. Therefore, SiC is excellently suited for the fabrication of a range of high power, high frequency and high temperature devices, as well as sensors for harsh environments.

Crystallographic modifications of SiC occur due to different stacking ability of the elementary building blocks—tetrahedrons formed of Si and C atoms. Two basic configurations arise from the stacking of the tetrahedrons: either cubic or hexagonal. The stacking direction is the c-axis of the crystal and this one-dimensional polymorphism is called polytypism. The main polytypes of SiC are 3C, 4H and 6H where the number refers to the

periodicity of the stacking sequence along the *c*-axis while the letter denotes the crystal symmetry (C, cubic; H, hexagonal).

Although being the most developed among the wide band gap semiconductors, SiC crystalline material still supports a high density of structural defects. While the variety of SiC polytypes may offer an exclusive combination of physical and electronic properties suited for many applications, polytypism may cause difficulties in fabrication of high-quality bulk crystals and epitaxial layers. Owing to the low stacking fault energy it is difficult to restrict parasitic polytype formation (foreign polytype inclusions) during growth, and particularly because two polytypes thermodynamically may occur at the same temperature. Other persistent extended defects are different types of dislocations. They originate from several sources, such as seed/substrate crystal, nucleus misalignment, thermal stress, etc. Besides, screw dislocations are growth-supporting defects, since the basic growth mechanism occurs via spiral evolution. The presence of a large number of dislocations causes their interaction and formation of a merged dislocation centre with a giant Burgers vector, which in turn is a prerequisite of micropipe generation. Micropipes are unique defects but frequently observed in SiC crystals. According to the Frank model [1] micropipes are considered as empty-core screw dislocations with large strain energy (large Burgers vector). The strain field around a dislocation with a large Burgers vector contains a high energy that can be minimized by removing the crystalline material around the dislocation line and creating a new surface in the form of a hollow tube. Micropipes usually penetrate the entire crystal, and they tend to be replicated from the substrates into the epitaxial layers. They are found to have a detrimental effect on device performance. It is very promising for the commercialization of SiC that the number of micropipes in industrially produced substrates has been dramatically decreased during recent years by better controlling the kinetics during growth [2].

Liquid phase epitaxy (LPE) is a simple and elegant technique with several advantages such as low process temperature, relatively high growth rate, easy for technical implementations in various geometries, doped layers and multiplayer structures. The main advantage, however, is that the process is carried out at relatively low temperature and close to thermodynamic equilibrium conditions, which presumes a low concentration of point defects in the epitaxial layers. Hence, the quality of the grown material is mainly limited by morphological features. LPE is particularly interesting for SiC because the first finding of micropipe closing was reported for this technique [3]. For a detailed description of LPE of semiconductor materials see [4–6].

## 6.2 FUNDAMENTAL ASPECTS OF LPE OF SiC

LPE of SiC is a technique, which for the practical use of the grown layers takes place by growth from solutions on a crystalline substrate. The advantage of using a solution is given by growth close to thermodynamic equilibrium and low growth temperatures, which are issues important for the structural perfection of the material. Another advantage of LPE is that the SiC substrate can be given any desired crystal orientation and still the thermodynamics support homoepitaxial growth conditions to a higher extent than in vapour phase growth. Polytype inclusions were observed to appear in SiC vapour phase epitaxy and these were substantially reduced by applying substrates off-oriented towards  $[11\bar{2}0]$  and step-flow growth mode.

In solution growth, the components of the crystal to be grown are dissolved in a solvent, which may be of similar or different nature. The concentration of crystallizing species is low and depends on the solubility in the solvent at the growth temperature. The solute diffuses from the bulk of the solution to the growth front. Close to the growth front, there is a gradient in the solute concentration due to depletion of the solute substance near the interface. In the case of SiC epitaxy, due to more complicated solvent–solute systems, complexes with the constituents may often form in the solution and diffuse through the solution. The growth steps at which nucleation occurs are reached by surface diffusion and breaking of the complexes.

SiC does not form a stoichiometric liquid phase at normal conditions and therefore growth from solutions has been naturally of interest for decades. The Si-C phase diagram is shown in Figure 6.1(a). SiC starts to decompose at about 1800 °C and melts incongruently at 2830 °C. Consequently, SiC can be grown from a nonstoichiometric liquid phase, i.e. by LPE. The natural choice of the solvent is silicon since this is a constituent of SiC and high-purity silicon is readily available. Techniques for SiC LPE from silicon solutions saturated with carbon were studied more than 30 years ago [7] and reproducible growth of 100  $\mu\text{m}$  thick layers was shown already at that time. The studies were performed having the substrates in the initial silicon melt during the whole process which easily caused cracking of the crystals during solidification. The growth rates using silicon as a solvent are not high since the solubility of carbon in silicon is very low at temperatures less than 2000 °C [8]. The temperature dependence of the carbon solubility in silicon is shown in Figure 6.1(b). For practical purposes, the low carbon solubility in silicon creates the need to increase the saturated value by increased growth temperatures and utilizing other solvents, e.g. some metals. The availability of the phase diagrams of a SiC–solvent system is important in order to determine the growth conditions prior to experiments. However, the phase diagrams for high-temperature solutions are difficult to acquire. This makes the availability scarce and growth studies using complex multi-component systems require more experimental work than for those systems in which information from the phase diagrams is available.

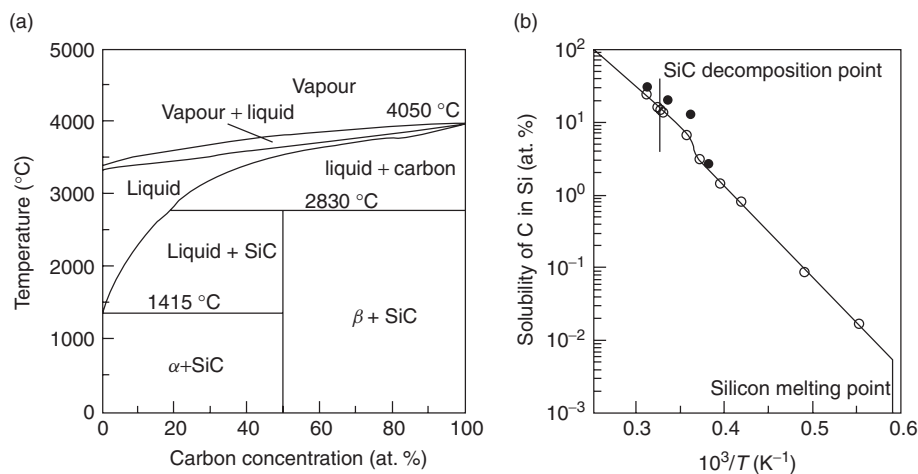


**Figure 6.1** (a) The phase diagram of the Si-C system; (b) the temperature dependence of the C solubility in Si. After Tairov and Tsvetkov [9]. Reproduced by permission of Professor Yu. Tairov

The solubility of carbon may be increased by introducing a certain metal to the silicon melt. Typically transition metals are used for this purpose. For example, chromium and some rare earth metals were applied in the 1960s. Later, Yakimova and Kalnin [10] re-examined the idea by proposing to explore the Si-Sc-C system for liquid phase growth of SiC. The solvent composition mainly used in this work was Si:Sc=72:28 at. % (Si:Sc=60:40 wt %) and the temperature was 1750 °C. They were chosen empirically because at that time no phase diagram of this system existed, but later on it was found that this composition corresponds to an eutectic point in the Si-Sc phase diagram [11]. Growth using this solvent and composition in LPE of SiC has demonstrated beneficial influence on the structure (crystallinity and surface morphology) of the SiC epitaxial layers. The use of the Si-Sc solvent, however, creates complications that have to be considered, owing to the formation of scandium carbides ( $Sc_xC_{1-x}$ ) and possibly scandium silicides. Six scandium carbides are known to exist [12] but no details are reported. Some information exists only on ScC, which has a high melting point. The values of the melting points are scattered in the literature (1800 °C [12], 1722 °C [13]) but they are in a similar range to the growth temperature, which indicates their possible presence during LPE of SiC. Additionally, the preparation procedure of the solvent has to be done with special attention to avoid formation of oxides, e.g.  $Sc_2O_3$  reacts with C at 1900 °C or aluminium oxide in the case of using Al-Si solution. The utilization of a multi-component solvent in LPE of SiC requires special attention since complexes of silicon, metal atoms and carbon may be formed. Their transport may be dominating in the solution rather than the individual components. Use of Al-Si as a solvent for SiC LPE creates possibilities to reduce the growth temperature substantially. Temperatures below 1200 °C have been reported [14, 15], however, the reactivity of this solution with the crucible has to be considered. The use of aluminium addition to silicon to yield p-n junctions has been studied with the dipping method and container-free LPE.

The choice of solvent composition is very important since this influences the growth rate, morphology and quality of the grown material. The requirements on the solvent are that it should be able to dissolve carbon from the source (e.g. a graphite crucible or SiC) efficiently, transport the constituents in the solution and provide conditions for efficient nucleation of the growing crystal. Most solute and solvent compounds have mixed bonding character and interaction between the solvent and solute may be strong. As an example of the influence of solvent composition on the growth, the growth rate from various Si-Sc solvent compositions [16] is shown in Figure 6.2. The growth rate increases with increasing scandium content due to increasing carbon solubility in the solution.

The wetting property of the solvent is crucial to consider since, when the substrate is brought into contact with the solvent, a low wetting angle is one of the prerequisites for uniform growth. A solvent placed in contact with a substrate will not float out, but remains as a drop with an angle of contact (the wetting angle) between the liquid and the solid. The total energy of the system is minimized if the drop has the shape of a spherical cap. The surface free energy of the substrate and the surface tension of the solvent yield a substrate/solvent interfacial energy. The three energies are related via a certain wetting angle. The relation is described by Young's equation as further discussed below and schematically illustrated in Figure 6.3. Besides the direct implication of the wetting and dissolution properties of the solvent, the interfacial and surface free energies have a pronounced effect on the growth since they are closely related to the nucleation rate.

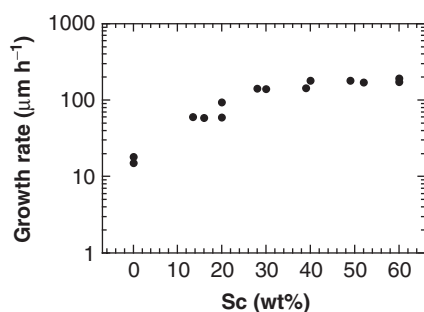


**Figure 6.2** Growth rate in SiC LPE by travelling solvent method depending on  $\text{Si}_x\text{Sc}_y$  solvent composition, data taken from [16]; growth temperature  $1750^\circ\text{C}$

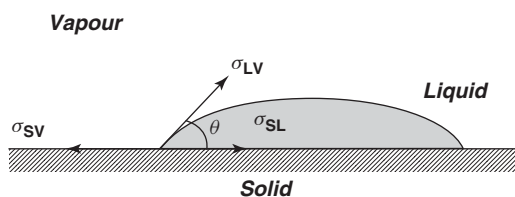


**Figure 6.3** Wetting between a liquid and a solid with surface/interfacial energies

The solvent will dissolve the substrate surface when brought into contact with it and until reaching saturation of the solution. The impact of the solvent composition on the dissolution morphology, and consequently on the starting growth conditions, in the Si-Sc-C system is shown in Figure 6.4 for the silicon face of 6H-SiC substrates [17]. Since the melting temperature of pure scandium is  $1541^\circ\text{C}$ , a slightly higher temperature was used for the scandium solvent compared with the solvents containing silicon. These temperatures are closer to the melting one of the solvent than actual growth temperatures, i.e. the conditions may be considered as the initial stage of dissolution. The dissolution morphology obtained with pure silicon exhibits small circular and hexagonal features [Figure 6.4(a)]. The features appear when the dissolution rate is low. The origin of the circular features is subtle, however, this type of feature has been observed on dissolved surfaces of other materials [18]. The dissolution morphology changes as scandium is introduced into the silicon melt. For small amounts of scandium the dissolved surface shows triangular shaped features [Figure 6.4(b)]. With increasing scandium content in the solvent these triangular features develop into larger triangular pits. Figure 6.4(c) illustrates the composition typically used for growth in the Si-Sc-C system at which a high growth rate is achieved. The morphology is roughening severely when the content of scandium is above 40 wt% and no clear dissolution patterns are observed. For pure scandium the dissolution morphology is rough with some areas following the hexagonal symmetry of the SiC crystal [Figure 6.4(d)]. These observations can be explained by an increased dissolution rate and with a dissolution mechanism having more intense (reactive) character at higher scandium compositions.

The studies were performed by melting the solvents on SiC substrates and after the solidification of the solutions the wetting angles of the solidified liquid droplet were



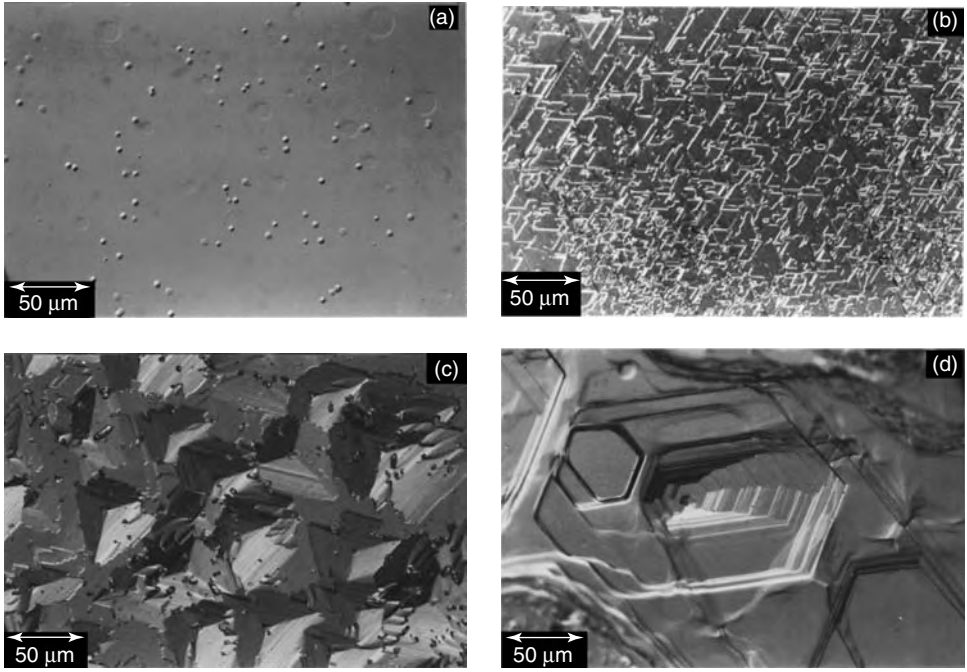


**Figure 6.4** Dissolution morphology of 6H-SiC Si-face with different solvent compositions (wt%): (a) Si:Sc=100:0; (b) Si:Sc=85:15; (c) Si:Sc=60:40; (d) Si:Sc=0:100. Temperatures: (a)–(c) 1540 °C; (d) 1560 °C. Reproduced from [17] by permission of The Electrochemical Society, Inc.

measured both for 6H-SiC and 4H-SiC [17]. From the experimental value of the wetting angle, the interfacial energy  $\sigma_{\text{int}}$  of the melt/SiC system can be estimated by using Young's equation:

$$\sigma_{\text{int}} = \sigma_{\text{SiC}} - \sigma_{\text{melt}} \cdot \cos \theta \quad (6.1)$$

where  $\sigma_{\text{SiC}}$  is the surface free energy of SiC,  $\sigma_{\text{melt}}$  is the surface tension of the melt and  $\theta$  is the wetting angle. There are no reliable data on the surface free energy of  $\alpha$ -SiC. However, the (0001) faces of 6H-SiC have the same atomic configuration as (111) faces of 3C-SiC and the stacking sequence of 6H and 3C-SiC are the same down to at least four layers from the surface [19]. Additionally, the low energy electron diffraction patterns for the (111) surface of 3C-SiC and the (0001) surface of 6H-SiC were found to be essentially identical [20]. These observations suggest that the calculated data on the surface free energy for 3C-SiC(111) [21] may be used for 6H-SiC(0001). The difference in the calculated surface free energy for the silicon and the carbon terminated face, 1767 erg cm<sup>-2</sup> and 718 erg cm<sup>-2</sup>, respectively, is quite large. Taking Si-Sc as an example for the calculations, there exist published data of the surface tension of molten silicon [22], molten scandium [12] and their temperature coefficients. The surface tension of the alloy  $\sigma_{\text{Si-Sc}}$  is estimated by the relation [23]:

$$\sigma_{\text{Si-Sc}} = \frac{\sigma_{\text{Si}} \cdot \sigma_{\text{Sc}}}{x_{\text{Sc}} \cdot \sigma_{\text{Si}} + x_{\text{Si}} \cdot \sigma_{\text{Sc}}} \quad (6.2)$$

**Table 6.1** Surface tension of different SiC solvents at 1750 °C

Object	Surface tension (erg cm <sup>-2</sup> )
Si	715 <sup>a</sup>
Sc	1130 <sup>b</sup>
Si-Sc (alloy)	800 <sup>c</sup>
Si-Sc-C (solution)	740 <sup>c</sup>

<sup>a</sup>Chung *et al.* [22].<sup>b</sup>Horowitz [12].<sup>c</sup>Syväjärvi [17].**Table 6.2** Estimated interfacial energies at 1750 °C of Si and Si-Sc alloy solvent

Object	Interfacial energy (erg cm <sup>-2</sup> )
6H(0001)/Si	1160
6H(000 $\bar{1}$ )/Si	180
6H(0001)/alloy	1010

<sup>a</sup>Reproduced from [17] by permission of The Electrochemical Society, Inc.

where  $x$  are the atomic fractions of the constituents in the alloy. The surface tension for different SiC solvents at the temperature of epitaxial growth (1750 °C) is given in Table 6.1. From this the interfacial energies between the melts (solvents) and 6H-SiC are obtained (Table 6.2). Since the temperature dependence of the surface free energy of 6H-SiC is not known, a constant value is assumed. The lower interfacial energy with the alloy suggests that it is energetically more favourable to grow with the Si-Sc solvent than using a pure silicon solution. Further, assuming the interfacial energy between silicon melt and 4H-SiC to be close to that between Si-melt and 6H-SiC, the experimental values of the wetting angle on 4H-SiC [17] are used to estimate the surface free energy of 4H-SiC (Table 6.3).

### 6.3 GROWTH METHODS FOR SiC LPE

The growth of SiC by LPE may be based on either deposition by slow cooling (top seeded solution growth method) or with an applied temperature gradient (e.g. the travelling solvent method). In the slow-cooling technique the supersaturation is provided by slowly decreasing the temperature. If the cooling rate is slow enough, this will result in inclusion free crystals. In this technique it is important to control the ratio of the crystallizing area to the volume of the solution since it affects the cooling programme and temperature

**Table 6.3** Calculated surface free energies of 6H-SiC [21] and estimated surface free energies of 4H-SiC [17]

Object	Surface free energy (erg cm <sup>-2</sup> )
6H(0001)	1767
6H(000 $\bar{1}$ )	718
4H(0001)	1800
4H(000 $\bar{1}$ )	750

Reproduced from [17] by permission of  
The Electrochemical Society, Inc.

control [24]. The top seeded solution growth method has been applied to SiC for growth of bulk crystals from silicon solvent [25]. In this work, the high vapour pressure of silicon, which may limit the maximum growth temperature due to excessive losses, is reduced by the use of a high-pressure inert atmosphere. The travelling solvent method, which has been initially proposed for fabrication of bulk crystals with a stationary heater [26] has been exploited in a modified version for LPE of SiC by applying a temperature gradient across a sandwich-like structure [10].

### 6.3.1 Modified travelling solvent method

One principle advantage here is that the solvent is not in contact with crucible walls and the supersaturated solution is continuously maintained at similar conditions. The supersaturation in the travelling solvent method is given by a solute concentration gradient in the solution from a source to a substrate. A temperature difference is established between the SiC source crystal and the substrate at a certain distance from the source and at a lower temperature. The solute concentration decreases from the source to the substrate since the solubility of the components changes with temperature. Ideally, when a steady state of solute transport is reached, the source will dissolve with the same rate as the epilayer grows (Figure 6.5).

In the travelling solvent process applied to the Si-Sc-C system, the solution is prepared by melting and alloying pieces from high purity silicon and scandium on the SiC source crystal. A pre-melting is necessary owing to the exothermic reaction of the Si-Sc alloy [11] and to form the Si-Sc solvent in order to avoid transitions in the subsequent growth.

At a given solvent composition and temperature, the growth rate depends mainly on the temperature gradient and growth rates exceeding 300  $\mu\text{m h}^{-1}$  have been obtained [27]. However, a time dependence of the growth rate was observed (Figure 6.6). Two growth series for 4H and 6H-SiC using a temperature gradient of  $\sim 30^\circ\text{C cm}^{-1}$  are illustrated. There is no obvious difference in the growth rates for the two polytypes indicating that the rate limiting mechanism is not related to kinetics at the substrate surface. The result implies that stable conditions are reached during the first hour of growth; this is a similar observation as presented by other groups [28], i.e. quasi-stationary conditions (dissolution, transport and growth) occur within the first hour of epitaxial growth. The reduction

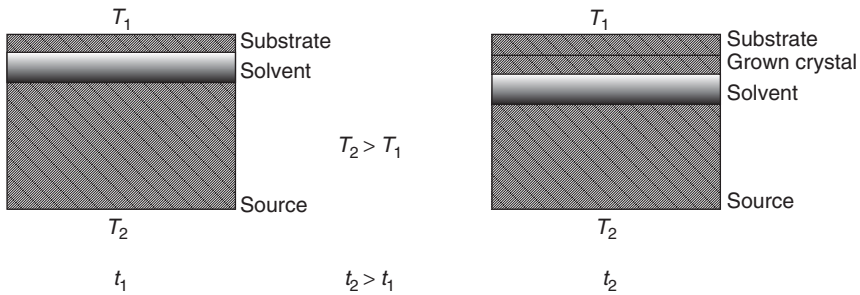


**Figure 6.5** Principle of travelling solvent method. At a time  $t_1$  the solvent is brought in contact with both the substrate and the source, the latter being at higher temperature. Dissolution occurs continuously at the source while the dissolved material travels through the solution and nucleates on the substrate ( $t_2$ ). As time goes by the solvent position moves since the growth rate and dissolution rate are ideally equal

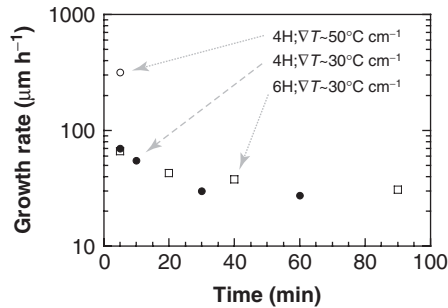


**Figure 6.6** The time dependence of the growth rate for 4H and 6H-SiC in the travelling solvent growth process [27]. The growth rate for 4H-SiC with higher temperature gradient ( $\nabla T$ ) is also shown. Growth temperature is  $1750^\circ\text{C}$ . Reprinted from *J. Crystal Growth*, Vol. 197, M. Syväjärvi *et al.*, 147–154, Copyright (1999), with permission from Elsevier

in the growth rate is believed to be due to formation of structural complexes in the solvent during growth. This is supported by the different activation energies obtained after different growth times (Figure 6.7). From the Arrhenius plot of the growth rate apparent activation energies of the growth processes are calculated to be 24 and  $75\text{ kcal mol}^{-1}$  after 5 and 60 min of growth, respectively.

Among the main processes (dissolution, diffusion and nucleation) diffusion is typically the slowest one and is therefore growth rate controlling. Actually, it has been observed that a convection transport mechanism may be present as well [29]. Nevertheless, the activation energy value for 5 min growth ( $24\text{ kcal mol}^{-1}$ ) is higher than typically reported for liquid diffusion [30]. However, a difference may be expected owing to the complicity of the Si-Sc-C system. The activation energy for 60 min growth is rather high ( $75\text{ kcal mol}^{-1}$ ) and supports the hypothesis of formation of large structural complexes in the liquid zone at longer process duration. The phase diagram of the Sc-C system [13] shows that for small amounts of C, solid  $\text{Sc}_x\text{C}_{1-x}$  is likely to form at the growth temperatures used. A formation of  $\text{Sc}_y\text{Si}_{1-y}$  complexes is also possible when using the Si-Sc-C system [11].

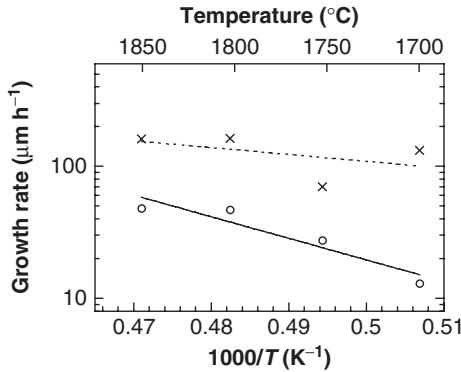


**Figure 6.7** Temperature dependence of 4H-SiC growth rate after 5 (x) and 60 min (o) growth [27]. Temperature gradient  $\sim 30^\circ \text{ cm}^{-1}$ . Reprinted from *J. Crystal Growth*, Vol. 197, M. Syväjärvi *et al.*, 147–154, Copyright (1999), with permission from Elsevier

A raise in temperature leads to breakdown of the complexes and subsequent stronger temperature dependence of the growth process.

The growth rate is also dependent on the solvent zone thickness (Figure 6.8). In the case of small zone thickness (below  $\sim 40 \mu\text{m}$ ), the growth process is kinetically limited [16] and the growth rate depends on the zone thickness. With thick liquid zones the growth rate is controlled by diffusion. In practice, the solvent zone must be thick enough to provide a stable growth front at the solid–liquid interface. If the zone is too thin the morphology of the grown layers will be disturbed (Figure 6.9) whereas if the zone thickness is sufficient to provide a stable growth interface the morphology is improved. The convective flows in the solution serve also to improve the mixing of the components in the solution. In the case of reduced convection by a decreased solvent zone thickness, an inhomogeneous solution could be formed which provides conditions for unstable growth behaviour. Additionally, when a low surface tension component (in this case silicon) is mixed with another component with a higher surface tension (scandium), the component with the lower surface tension may concentrate on the surface and the surface tension is decreased from the ideal mixture of the components [31].

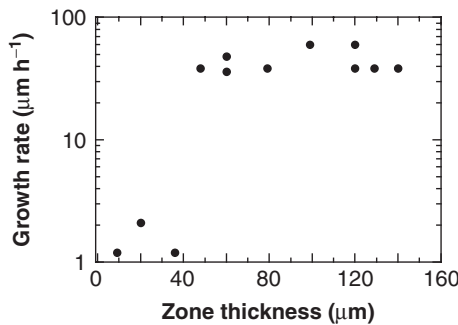


**Figure 6.8** Growth rate in the sandwich configuration for SiC LPE depending on solvent zone thickness, data taken from [16]; growth temperature  $1750^\circ \text{ C}$

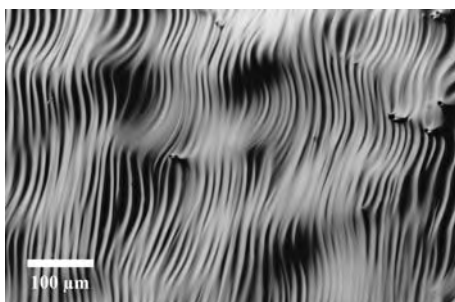


**Figure 6.9** Disturbed step-flow growth front due to a thin melt zone thickness

The layer morphology of 4H-SiC after 5 min of growth with a temperature gradient of  $\sim 50\text{ }^{\circ}\text{C cm}^{-1}$  is shown in Figure 6.10. For the off-oriented substrates both spiral and dendrite-like growth occur on the same layer while widespread step-flow growth is expected. As seen in Figure 6.10(a) growth steps are present as well but perturbed to a large extent. Close to the spiral [Figure 6.10(b)] two circular depressions are seen which are believed to be caused by silicon inclusions and are probably formed during the rapid cooling process when growth is terminated. The spiral mechanism is favoured when the supersaturation is below a certain ‘critical’ supersaturation [32]. Above this transition point the growth is two-dimensional. At even higher supersaturations there exists a second transitional supersaturation above which unstable growth occurs. This corresponds to dendrite-like growth showing that large deviations from equilibrium have existed and indicating constitutional super-cooling. Since spiral and dendrite-like growth occur at the same time, it can be presumed that the solute distribution is not uniform at the initial growth stage using a temperature gradient as high as  $\sim 50\text{ }^{\circ}\text{C cm}^{-1}$ . Additionally, in this case the temperature ramp to the growth temperature was very steep which may create a very high supersaturation at the initial growth stage, i.e. providing conditions for unstable growth. It has also been reported that dendrite-like growth may occur at high growth temperatures at which intense evaporation of the solvent occurs [28,33]. Using the same temperature gradient but with a larger misorientation of the substrate surface, step-flow growth is present from the initial stage [Figure 6.10(c)]. When the temperature gradient is smaller ( $\sim 30\text{ }^{\circ}\text{C cm}^{-1}$ ), steps are present after 5 min of growth from the initial growth stage independently of substrate misorientation. This shows that, since the solute is not rejected at the growth front (no appearance of growth disturbances), it is possible to use a higher supersaturation by increasing the off-orientation of the substrate or decrease the temperature gradient to achieve a stable growth front.

The sandwich geometry with a temperature gradient provides not only high epitaxial growth rates, but also conditions to study growth kinetics and some physical characteristics of the material system employed. For example, the diffusion coefficient,  $D$  of the crystallizing species being transported through the liquid zone, can be determined by using the formula:

$$V_c = \frac{D}{C_c^S - C_c} \frac{dC}{dT} G \quad (6.3)$$

where  $V_c$  is the experimentally determined growth rate,  $dC/dT$  is the slope of the liquidus curve,  $C_c^S$  is the concentration of the crystallizing substance in the solid phase,  $C_c$  is the

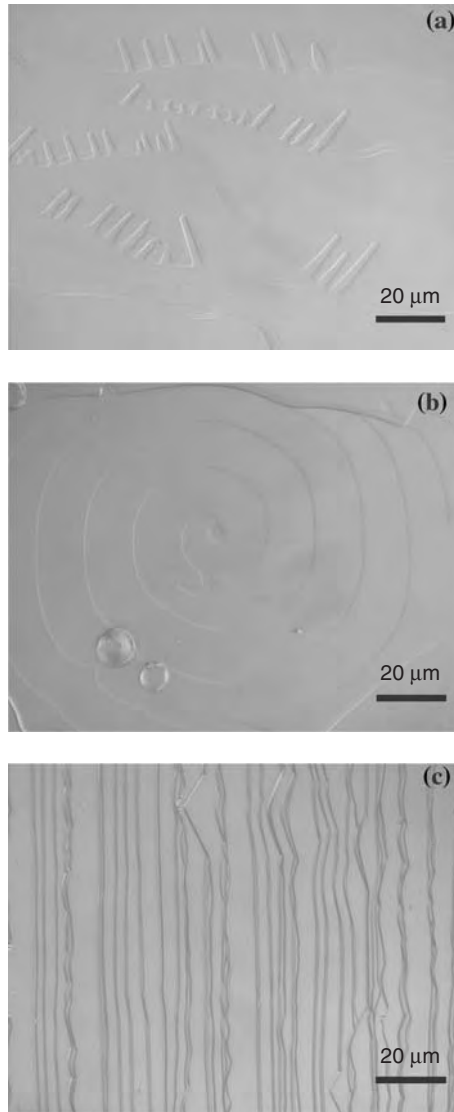


**Figure 6.10** Morphology of 4H-SiC grown at 1750 °C and a temperature gradient of  $\sim 50$  °C  $\text{cm}^{-1}$  for 5 min on Si-face substrates: (a) dendritic and perturbed steps on 3.5° off-oriented substrate; (b) spirals on same substrate as in (a); (c) steps on 8° off-oriented substrate. Reprinted from *J. Crystal Growth*, Vol. 197, M. Syväjärvi *et al.*, 147–154, Copyright (1999), with permission from Elsevier

same but in the liquid phase, and  $G$  is the temperature gradient in the liquid zone. All listed characteristics are either available from the experiment or can be calculated. An example is presented by Yakimova and Yanchev [34] for the Si-Sc-C system, yielding  $D = 6 \times 10^{-4} \text{ cm}^2 \text{ s}^{-1}$ . This value falls well within the range of diffusion coefficients in molten metals.

### 6.3.2 Dipping method

In many early studies of SiC LPE, the solvent was put in contact with the crucible material. This causes difficulties by the interaction of the silicon based solution and the crucible material, especially at the cooling stage as the solidification of the solution may easily cause an increased surface roughness and cracking of the material. This was avoided by a dipping technique through attachment of a substrate to a graphite holder, which then could be introduced to the melt and removed prior to cooling of the liquid [35]. The schematic arrangement is shown in Figure 6.11. The graphite crucible was heated inductively, and sealed with a graphite lid to reduce evaporation of silicon. This way the silicon as well as crucible could be used several times. Light emitting diodes using the technique have been produced [36, 37] and it was shown that the light efficiency was improved in LPE grown layers compared with those grown using vapour phase epitaxy [37].

### 6.3.3 Container free LPE

A version of a container free LPE method to avoid solidification of the solution in contact with the substrate using a liquid metal suspended in a high-frequency electromagnetic field has been developed by Dmitriev and co-workers [38, 39] (see Figure 6.12). In the liquid state, silicon is a metal and radiation heating is applied to heat solid silicon to  $\sim 1000$  °C to yield metallic conductivity. In the container free LPE technique the surface of the liquid is only in contact with SiC and the reaction chamber, which is filled with an inert gas. The melting temperature is determined by the composition and the volume of

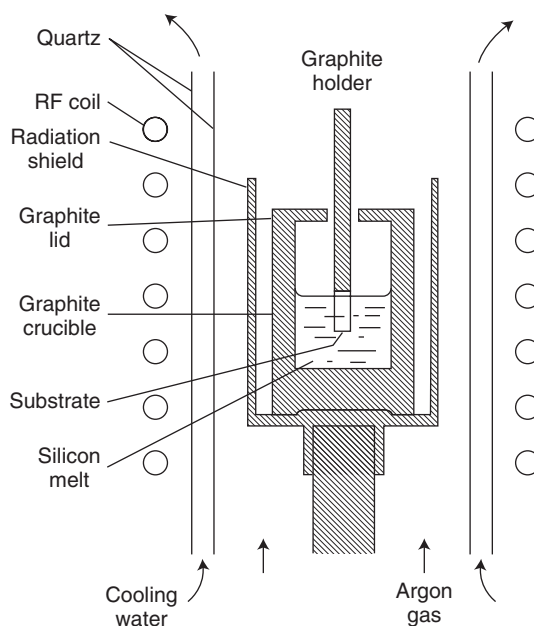


**Figure 6.11** Schematic illustration of the growth arrangement for the dipping technique. After Suzuki *et al.* [35]. Reproduced from [35] by permission of the American Institute of Physics



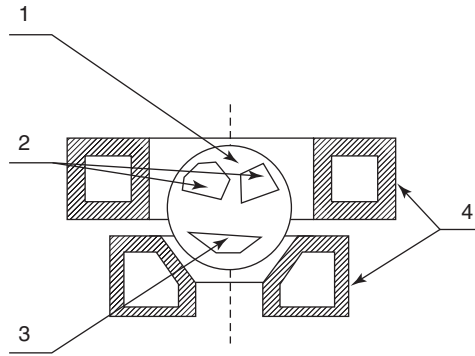


**Figure 6.12** Schematic of the container free LPE. 1, Silicon; 2, 3, SiC crystals; 4, inductor to produce electromagnetic field [39]. Reprinted from *J. Crystal Growth*, Vol. 343, Dmitriev and Cherenkov, 343, Copyright (1993), with permission from Elsevier

the solvent, as well as the gas pressure. The mixing of the solvent is obtained through the electromagnetic field. Growth may be applied under isothermal conditions, a cooling process or under an applied temperature gradient. In these cases, silicon is initially melted by radiation heating to reach a metallic state and further temperature control is given by the electromagnetic field. After reaching the molten state of silicon, the SiC substrate is brought into contact with the liquid phase. A SiC source crystal placed below the silicon acts as the carbon source in the case when the substrate is brought into contact with the top of the silicon liquid or the silicon can be placed on the SiC substrate, i.e. with the substrate being below the silicon. In the nonisothermal conditions, the silicon melt may be saturated by dissolution of the SiC substrate (and SiC source if used) and the SiC epitaxial layers are grown by cooling the solution. The temperature of the liquid silicon is lower at the top of the liquid than in the bottom part where the source is placed. In this case there will be a temperature gradient under which epitaxial growth takes place when the substrate is brought into contact with the carbon saturated silicon by the SiC source. The growth rate may be controlled by varying the surface area of the source with respect to that of the substrate. The growth rate may be varied two orders of magnitude up to  $120 \mu\text{m h}^{-1}$ . Doping is achieved by introducing aluminium to the melt for p-type doping or by filling the reaction chamber with nitrogen gas for n-type conductivity of the epitaxial layers.

### 6.3.4 Vapour–liquid–solid mechanism

The vapour–liquid–solid (VLS) method [40] has recently been re-examined to produce one-dimensional structures (whiskers) for nanophysics technology or other applications. The VLS mechanism has been also developed for growth of SiC epitaxial layers. Some of the basic mechanisms involved in the VLS method are similar to LPE. In the case of LPE, carbon is supplied by the graphite container, a solid SiC source in direct contact with the solution or initial dissolution of the substrate while in the VLS method the carbon is provided through the reaction of a carbon containing gas phase with a free silicon surface. The use of a liquid wetting layer on a substrate with crucibles which are not made of

graphite while applying the carbon containing gas, demonstrates the occurrence of VLS growth of SiC. The difference to 'conventional' LPE growth conditions is that VLS growth may be performed even at a negative temperature gradient, i.e. the temperature is higher at the substrate than in the liquid or the top of the solution, and the requirements on the temperature gradient are not as strict. The carbon containing gas is cracked above the free liquid surface (vapour–liquid interface). (Figure 6.3 illustrates the technique assuming a carbon gas support in the vapour phase.) Then the dissolved carbon will migrate to the substrate driven by the carbon activity gradient between the top of the liquid and the bottom of the liquid (at the liquid–solid interface). Studies using propane as carbon supply for SiC VLS growth with Al-Si liquid demonstrates that the growth rate has a linear dependence on the propane flux [41]. In contrast, linearity is not observed in silicon enriched chemical vapour deposition (CVD), which shows the possibility of VLS growth at lower temperatures than in normal SiC CVD growth conditions [42]. At high propane flux a SiC crust on the droplet is formed and blocks further growth [43]. Depending on the technological implementation [44], the liquid may be removed by suction and the appearance of macroscopical steps on the surfaces becomes less pronounced. One of the main issues in this method is to have a uniform silicon based layer on the SiC seed. The use of too thin layers, e.g. to decrease the diffusion length within the silicon solvent to increase the growth rate, may result in the substrate partially lacking coverage of the solution and thus nonuniform growth occurs. This wetting layer is a parameter in relation to either growth of whiskers [45, 46] or epitaxial layers [16, 43]. The VLS mechanism is more pronounced at the edge of the silicon wetting layer and may increase the growth rate at the edge while the polytype of the substrate may not be replicated [47]. Similar to LPE, the growth rate becomes low using pure silicon due to the low solubility of carbon in silicon. To promote the carbon solubility and reduce the growth temperature, various alloys based on silicon may be used. The silicon based alloys extensively studied for SiC VLS growth are Al, Fe, Ni and Co [48]. The composition of the solution is a crucial parameter utilizing metallic elements, which dissolve a high concentration of carbon. A solvent with an excess of metal atoms in comparison with the silicon content provides a pronounced dissolution of the substrate. Conditions favourable for growth are reached by increasing the silicon content. SiC whiskers easily form at the cooling stage and suction of the liquid prior to cooling is crucial to avoid formation of the SiC whiskers when epitaxial layers are targeted.

## 6.4 CHARACTERISTIC FEATURES OF SiC LPE

### 6.4.1 Step-bunching

Both in LPE and the VLS method the surfaces may contain macroscopic step-bunching using off-oriented SiC substrates [47, 49]. Causes of macroscopic step-bunching are misoriented surfaces at high supersaturation, impurities, or local fluctuations of the supersaturation. Step-bunching in SiC epitaxy has been studied earlier for vapour phase epitaxy [50]. However, in LPE and VLS growth of SiC on off-oriented substrates the step-bunching is more pronounced and it has been frequently observed that macrosteps have surfaces with a deviation from the off-orientation (Figure 6.13).

Similar splicing features have been observed in vapour phase growth of SiC, however, those features are not as pronounced as in LPE of SiC. Lateral growth in  $\langle 1100 \rangle$  and

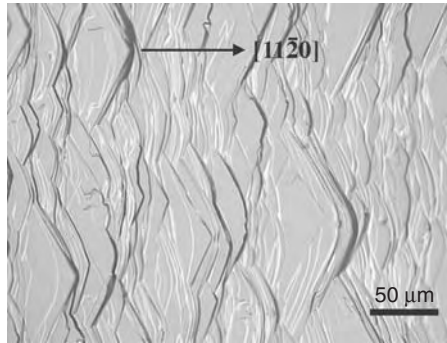


**Figure 6.13** Illustration of step-bunching in SiC LPE with facets deviating from the step-direction. Reprinted from *J. Crystal Growth*, Vol. 236, M. Syväjärvi *et al.*, 297, Copyright (2002), with permission from Elsevier

$\langle 1120 \rangle$  directions may be denoted as *step growth* and *kink growth* [51], respectively. It was shown that the lateral velocity of steps ( $v_{\text{step}}$ ) and kinks ( $v_{\text{kink}}$ ) are different both in the case of CVD [51] and LPE [52]. The anisotropy of the lateral growth rate depends on the incorporation probabilities at the step  $\{1100\}$  and the kink  $\{1120\}$  site [51]. Disregarding the influence of the surface by temperature, the kink site has a higher density of sites where arriving atoms on the surface preferably attach. However, by increasing the temperature the density of atomic steps (kinks) at the step site will increase. Thus the probability of attachment of arriving atoms will increase, and as a consequence the lateral growth rate in this direction will increase, i.e. the  $v_{\text{step}}/v_{\text{kink}}$  ratio will increase. There is experimental evidence that at temperatures below 1600 °C the lateral growth rate is higher in a  $\langle 1120 \rangle$  direction than in a  $\langle 1100 \rangle$  direction [51, 52]. However, extrapolation of the data to higher temperatures [53] as applied for LPE gives that the lateral growth rate should be higher in a  $\langle 1100 \rangle$  direction than in a  $\langle 1120 \rangle$  direction (assuming a linear dependence) above a certain temperature. The anisotropic step-bunching effect becomes pronounced in LPE layers when the thickness reaches a few micrometres. For these layers, step heights up to  $\sim 1 \mu\text{m}$  are commonly observed. The apex of the step caused by anisotropic step-bunching points in the  $\langle 1120 \rangle$  direction and  $\langle 1100 \rangle$  facets are well resolved (Figure 6.13).

One question which arises is why the surfaces are rougher and the steps are more irregular on layers grown by LPE than in those grown by vapour phase epitaxy through sublimation at equal growth temperatures [53]. The surfaces are far smoother on the sublimation grown layers even though the layers are thicker. The interface roughness, its anisotropy and dependence on growth parameters are crucial issues in crystal growth. A description of the interface roughness depending on growth parameters and in different growth systems is not very straightforward. The interface roughness is sometimes evaluated using the generalized  $\alpha$ -factor, which can be viewed as a material constant [54]. One important difference is that in the solution growth there is a strong solid–fluid interaction whereas the interaction is absent in the pure vapour phase growth. The general expectation for the same material is that  $\alpha_{\text{solution}} < \alpha_{\text{vapour}}$ , which is interpreted as the interface will be rougher in liquid phase growth and smoother in vapour phase growth as discussed in more detail in Sunagawa [54]. Due to this, larger steps with more irregular shape and pronounced anisotropic behaviour would be allowed to occur in liquid phase growth compared with vapour phase growth of SiC. The surface of a growing crystal is

bounded by interfaces with different roughness and the smoothest interface will eventually remain as the morphologically stable face [54]. For SiC, the morphologically stable surfaces of a macrostep will be  $\{0001\}$  and  $\{1\bar{1}0x\}$ . It was reported that for 6H-SiC  $\{1\bar{1}04\}$  is a low-index surface [55] and such facets have also been observed in 6H- and 4H-SiC epitaxial layers grown under reduced gravity conditions [56].

The occurrence of anisotropic step-bunching seems to be dependent on the difference between the temperature dependent lateral growth rates in the  $\langle 1100 \rangle$  and  $\langle 1120 \rangle$  directions in connection with the preferred formation of low-index  $\{1\bar{1}0x\}$  facets for minimization of the total surface free energy of the macrostep [53]. In the mechanism for preferred low-index surfaces, the interface roughness will be important for developing the facets. Either this appears as a splicing as observed in vapour phase epitaxy or well developed facets in LPE [53].

### 6.4.2 Micropipe filling

A common defect in SiC substrates is the micropipe, generally viewed as a microchannel, which runs through the SiC crystal along the *c*-axis. Micropipes penetrate into device structures and cause device failure [57]. It was first observed in LPE that micropipes from the substrate are possible to close in the epitaxial layer [49]. In Figure 6.14 two micropipes emerging from the substrate are not observed on the surface of the epilayer grown by LPE [49] whereas they are observed using transmission microscopy with focus inside the substrate. Instead a spiral has appeared on the as-grown epilayer. This observation inspired other research groups studying LPE of SiC to focus on the phenomenon [28, 58]. The results of micropipes filling during LPE have been unambiguously confirmed [3].

LPE is a technique which provides growth conditions close to thermodynamic equilibrium and the driving force needed to achieve growth is small, i.e. the epitaxial layers grow at a low supersaturation. In sublimation growth to produce SiC substrates the supersaturation is much higher and temperature fluctuations may easily result in a local deviation from optimal growth conditions and micropipe formation. This is not expected in the LPE growth. From the experimental observations it follows that during LPE favourable conditions exist to break micropipes, which are commonly believed to be hollow dislocation cores [1]. One possible model for micropipe closing is based on the following findings: (i) the interfacial energy between the crystal (micropipe wall) and the liquid feeding phase is low, so that growth can occur even if the driving force for crystallization is low; (ii) micropipes contain screw dislocations and the wall surface is stepped [59]. Finally, growth hillocks and spirals are observed at the locations of former micropipes. Thus it appears to be energetically easy to start growth inside a micropipe during LPE and this results in a stable micropipe healing. The growth mechanism resembles nucleation in a confined space. Due to the capillary effect the solvent penetrates into micropipe channels and depending on the surface tension stops up to a certain level [3]. The solution in contact with the crystal becomes supersaturated and the growth starts at the most favourable nucleation sites, e.g. steps provided by dislocations. What makes micropipe walls unstable so that a new surface can grow is probably meltback due to contact with solvent, which changes the surface activity. The model is illustrated in Figure 6.15.

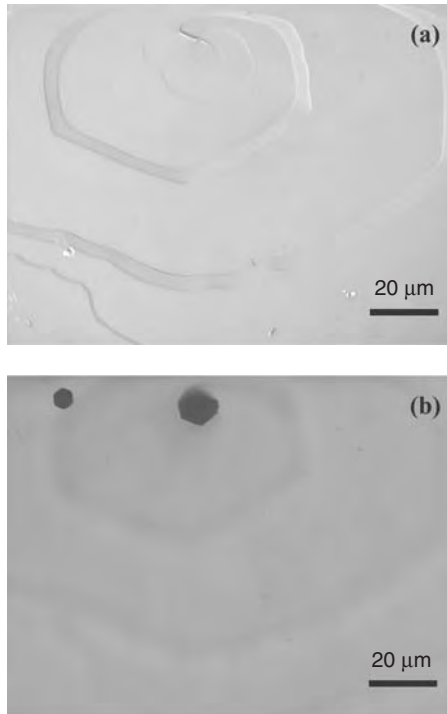


**Figure 6.14** Optical micrographs taken from a 6H-SiC LPE layer with filled micropipes: (a) in reflected light and focused on the surface; (b) transmission light focused below the layer surface. Reproduced from [3] by permission of Trans Tech

## 6.5 LPE OF SiC UNDER REDUCED GRAVITY

The layers grown by the travelling solvent method often have nonuniform thickness while an advantage is that the impurity distribution in the grown material is very homogenous. Buoyancy-driven convection is attributed as the cause for the nonuniform thickness. This convection is made up of unintentional flows in the liquid solution due to the forces (e.g. gravity) acting on the particles in the solution when the temperature gradient is applied. The convection is characterized by the Rayleigh number:

$$\text{Ra} = \frac{\alpha g \nabla T d^4}{\nu \kappa} \quad (6.4)$$

where  $\alpha$  is the solvent thermal expansion coefficient,  $g$  is acceleration due to gravity,  $d$  is a characteristic dimension of the fluid,  $\nabla T$  is the temperature gradient,  $\nu$  is kinematic viscosity and  $\kappa$  is thermal diffusivity. As the Rayleigh number increases the convective flows within the solution increase. The effect of buoyancy-driven convection is expected in a vertical geometry with an applied temperature gradient, but is commonly neglected if the distance between the source and the substrate is small, as in the travelling solvent method. This, however, is not always the case as demonstrated by the results published

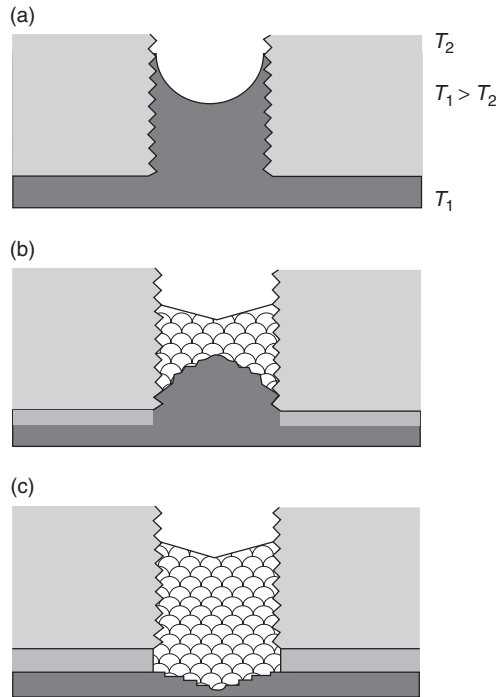


**Figure 6.15** Illustration of the model for micropipe closing in SiC LPE. The structure is a schematic of the travelling solvent method with the substrate on top and the solvent below: (a) initial conditions for LPE with the solvent penetrating into the microchannel; (b) nucleation on the substrate and inside the channel at the stepped surface of the micropipe; (c) continuous nucleation and formation of a spiral on the epilayer

by Yakimova and co-workers [29]. The presence of convective flows serves to reduce the stagnant boundary layer at the solid surface through which the solute has to diffuse.

Growth from a solution may give rise to impurity micro-segregation and growth instabilities due to the gravitation-induced convection, resulting in an alteration of the point defect density. In this respect, LPE growth under microgravity enables the elimination of one growth parameter, which is not possible to control under normal conditions. An LPE experiment of SiC was launched with the European microgravity rocket MASER 7 at Esrange in May 1996. The total time of microgravity was about 6–7 min and the residual acceleration after burnout stage was less than  $10^{-4}g$ . The SiC growth furnace was developed by the Swedish Space Corporation and was capable of processing samples at high temperature ( $1800\text{ }^{\circ}\text{C}$ ) in a high-purity growth ambient ( $10^{-6}$  mbar). This together with the fast heating/cooling rates makes the furnace construction unique [60]. The use of Si-Sc solvent allowed high growth rate ( $>150\text{ }\mu\text{m h}^{-1}$ ) and thus made possible a successful experiment with a short duration of microgravity time. Two identical sets of samples were prepared for growth in microgravity and on-ground, respectively. Four samples were processed simultaneously in microgravity and immediately after the flight the four reference samples were grown.

All samples have a single polytype structure identical to the substrate polytype [29]. The results from the samples grown under microgravity indicate a lower defect density

in comparison with samples grown on-ground. The thickness of the layers grown in microgravity and on-ground differs considerably. The average growth rates therefore are  $150 \mu\text{m h}^{-1}$  for the microgravity samples and  $225 \mu\text{m h}^{-1}$  for the on-ground samples. The explanation for the different growth rates may be found in the influence of the gravitation-induced convection, e.g. described by the Rayleigh number, and the effect is rather pronounced when growth is performed in a solution with an applied vertical temperature gradient [61]. In this case the convective mass transfer can prevail over the diffusive one and thus increase the growth rate. Under microgravity the growth process is predominantly diffusion limited and the growth rate becomes smaller. To date, because the liquid zone thickness is quite small, probably approximately 0.3 mm, the convection effect has been neglected in this type of growth configuration. It seems, however, that in the travelling solvent system the difference in the specific gravity of the solute, C, and the other species in the solution (Si, Sc and complexes) play an essential role [62].

The impurity incorporation in the layers showed an impact in relation to scandium, which was a component of the solvent. It was found that scandium reaches its solubility limit in on-ground grown material ( $2 \times 10^{17} \text{ cm}^{-3}$ ) and falls down to  $5 \times 10^{15} \text{ cm}^{-3}$  in the microgravity grown material [29]. The difference in the scandium doping can be understood as a consequence of the convection effect. In particular, at the growth temperature the diffusion rate ( $V_d$ ) of the main components (Si and C), as well as of Sc, in the epitaxial layers is low compared with the growth rate ( $V_g$ ). This implies that the composition of the growing layer will depend on surface growth kinetics and growth rate, which are a function of the solvent (Si-Sc) convection flow delivering solute species to the growing surface. Since scandium has a distribution coefficient less than unity it will be rejected from the growing surface and the liquid will become scandium rich with time. If the growth rate is high compared with  $V_d$ , scandium atoms adsorbed at the crystal surface will easily be captured by the growing surface, thus resulting in a higher real distribution coefficient [63]. This real distribution coefficient,  $K$ , obeys the following dependence:

$$K = K_0 + (K_s - K_0) \exp(-V_d/V_g) \quad (6.5)$$

where  $K_0$  is the equilibrium distribution coefficient of scandium and  $K_s$  is the concentration ratio of adsorbed scandium atoms on the layer surface and scandium atoms in the adjacent liquid. Thus, convection during LPE may change the surface growth kinetics and the growth rate and by this cause micro-inhomogeneities in the epitaxial layer composition.

## 6.6 APPLICATIONS

Some examples of SiC based device applications by LPE are given briefly. More than 30 years ago it was demonstrated that high doping may be obtained through LPE of SiC and blue-emitting light emitting diodes may be produced [35–37, 64]. Contact resistivity of ohmic contacts to p-type SiC is currently a limitation for SiC based power and microwave power bipolar devices. A substantial decrease of the specific contact resistance with Al-Ti contacts was obtained with high aluminium  $p^+$  doping through LPE using a Al-Si solution for p-type contact layers on SiC pn structures [65]. The specific contact resistance of the ohmic contact structures was  $10^{-4} \text{ ohm cm}^2$  while with an additional  $p^+$  contact layer grown by LPE it was one order of magnitude less.

The efficient micropipe healing in SiC substrates by LPE has the advantage that device characteristics may be significantly improved using buffer layers grown by LPE prior to epitaxy of the device structure. This is of particular importance in Schottky diodes where micropipes in the substrate have been shown to cause premature breakdown [57]. In a study particularly aimed at other defects than micropipes in device structures using reduced micropipe density by LPE, there was no significant difference in breakdown voltage [66]. The problem of surface roughening with the layer thickness may be resolved by growing a thin LPE layer to close micropipes and then an active layer grown by vapour phase epitaxy. As the surface roughness of LPE layers increases with increasing layer thickness, it was shown that when the LPE layer thickness is less than 1  $\mu\text{m}$ , the stress and strain in the subsequently grown device layer is low [67]. Thus the structural quality and morphology may be improved with subsequent vapour phase epitaxy on LPE buffer layers [68].

The long-term stability in pn-diodes is greater in structures grown by LPE in comparison with CVD grown material regarding the degradation in forward voltage drop [69]. An increased forward voltage drop with time has been interpreted as formation of recombination-enhancing stacking faults.

## REFERENCES

1. F.C. Frank, *Acta Crystallogr.* **4**, 497 (1951).
2. D. Hobgood, M Brady, W Brixius, G. Fechko, R. Glass, D. Henshall, J Jenny, R. Leonard, D. Malta, S.G. Muller, V. Tsvetkov and C. Carter, *Mater. Sci. Forum* **338–342**, 2 (2000).
3. R. Yakimova, M. Syväjärvi, S. Rendakova, V.A. Dmitriev, A. Henry and E. Janzén, *Mater. Sci. Forum*, **338–342**, 237 (2000).
4. J.J. Hsieh, Liquid phase epitaxy, in *Handbook of Semiconductors*, Vol. 3, Ch. 6, T.S. Moss (Ed.), North-Holland, Amsterdam (1980).
5. E. Bauser, Atomic mechanisms in semiconductor LPE, in *Handbook of Crystal Growth*, Vol. 3, Ch. 20, D.T.J. Hurle (Ed.), Elsevier Science BV, Amsterdam (1994).
6. E.A. Giess and R. Ghez, Liquid phase epitaxy, in *Epitaxial Growth Part A*, Ch. 2.6, J.W. Matthews (Ed.), Academic Press, New York (1975).
7. R.W. Brander and R.P. Sutton, *Br. J. Appl. Phys.* **2**, 309 (1969).
8. R.I. Scace and G.A. Slack, *J. Chem. Phys.* **30**, 1551 (1959).
9. Yu.M. Tairov and V.F. Tsvetkov, Handbook on electrotechnical materials, in *Semiconductor Compounds A<sup>IV</sup>B<sup>IV</sup>*, Vol. 3, Ch. 19, Yu.V. Koritskii, V.V. Pasyukov and B.M. Tareev (Eds), Energomashizdat, Leningrad (1988).
10. R.T. Yakimova and A.A. Kalnin, *Phys. Status Solidi A* **32**, 297 (1975).
11. V. Kotroczó and I. J. McColm, *J. Alloys Comp.* **203**, 259 (1994).
12. C.T. Horowitz, *Scandium*, Academic Press, London (1975).
13. V.R. Sidorko, L.V. Goncharuk, O.V. Gordiyuchij and R.V. Antonchenko, *J. Alloy Comp.* **228**, 159 (1995).
14. D. Chaussende, C. Jaquier, G. Ferro, J.C. Viala, F. Cauwet, and Y. Monteil, *Mater. Sci. Forum* **353–356**, 85 (2001).
15. D. Chaussende, C. Jaquier, G. Ferro, J.C. Viala, F. Cauwet and Y. Monteil, *J. Mater. Sci.* **37**, 3299 (2002).
16. R.T. Yakimova PhD Thesis, LETI, Leningrad (1974) (in Russian).
17. M. Syväjärvi, R. Yakimova, and E. Janzén, *J. Electrochem. Soc.* **146**, 1565 (1999).
18. I. Sunagawa, Investigations of crystal growth in earth and planetary sciences, in *Handbook of Crystal Growth*, Vol. 2, Ch. 1, D.T.J. Hurle (Ed.), North-Holland, Amsterdam (1994).
19. J.E. Northrup and J. Neugebauer, *Phys. Rev. B* **52**, 17001 (1995).



20. R. Kaplan, Surf. Sci. **215**, 111 (1989).
21. T. Takai, T. Halicioğlu and W.A. Tiller, Surf. Sci. **164**, 341 (1985).
22. S.I. Chung, K. Izunome, A. Yokotani and S. Kimura, Jpn. J. Appl. Phys. **34**, L631 (1995).
23. V.K. Semenchenko, *Surface Phenomena in Metals and Alloys*, Pergamon Press, London (1961).
24. C. Klemenz and H.J. Scheel, Mater. Sci. Forum **276–277**, 175 (1998).
25. D.H. Hofmann and M.H. Müller, Mater. Sci. Eng. **B61–62**, 29 (1999).
26. G.A. Wolff and A.I. Mlavsky, Travelling solvent techniques, in *Crystal Growth: Theory and Techniques*, Vol. 1, Ch. 3, C.H.L. Goodman (Ed.), Plenum Press, London (1974).
27. M. Syväjärvi, R. Yakimova, H.H. Radamson, N.T. Son, Q. Wahab, I.G. Ivanov and E. Janzén, J. Cryst. Growth **197**, 147 (1999).
28. M. Müller, M. Bickermann, D. Hofmann, A.-D. Weber and A. Winnacker, Mater. Sci. Forum **264–268**, 69 (1998).
29. R. Yakimova, M. Syväjärvi, C. Lockowandt, M. Linnarsson, H.H. Radamson and E. Janzén, J. Mater. Res. **13**, 1738 (1998).
30. M.A. Wright, J. Electrochem. Soc. **112**, 1114 (1965).
31. T. Utigard, ISIJ Int. **34**, 951 (1994).
32. A.A. Chernov, Equilibrium, in *Modern Crystallography III: Crystal Growth*, Ch. 5, A.A. Chernov (Ed.), Springer Verlag, Berlin-Heidelberg (1984).
33. V. Ivantsov and V. Dmitriev, Mater. Sci. Forum **264–268**, 73 (1998).
34. R.T. Yakimova and I.Y. Yanchev, J. Cryst. Growth **51**, 223 (1981).
35. A. Suzuki, M. Ikeda, N. Nagao, H. Matsunami and T. Tanaka, J. Appl. Phys. **47**, 4546 (1976).
36. M. Ikeda, T. Hayakawa, S. Yamagiwi, H. Matsunami and T. Tanaka, J. Appl. Phys. **50**, 8215 (1979).
37. W.v. Munch, W. Kurzinger and I. Pfaffeneder, Solid State Electron. **19**, 871 (1976).
38. V.A. Dmitriev, P.A. Ivanov, I.V. Korokin, Ya.V. Morozenko, I.V. Popov, T.A. Sidorova, F.V. Strelchuk and V.E. Chelnokov, Soviet Tech. Phys. Lett. **11**, 98 (1985).
39. V. Dmitriev and A. Cherenkov, J. Cryst. Growth **343**, 343 (1993).
40. R.S. Wagner, *Whisker Technology*, A.P. Levittl (Ed.), John Wiley & Sons, Inc., New York, 1970.
41. C. Jacquier, G. Ferro, C. Balloud, M. Zielinski, J. Camassel, E. Polychroniadis, J. Stoemenos, F. Cauwet and Y. Monteil, Mater. Sci. Forum **457–460**, 735 (2004).
42. D. Chaussende, G. Ferro and Y. Monteil, J. Cryst. Growth **234**, 63 (2002).
43. G. Ferro, D. Chaussende, F. Cauwet and Y. Monteil, Mater. Sci. Forum **389–393**, 287 (2002).
44. C. Jacquier, G. Ferro, F. Cauwet, D. Chaussende and Y. Monteil, Crystal Growth Design **3**, 285 (2003).
45. S. Motojima, M. Hasegawa and T. Hattori, J. Crystal Growth **87**, 311 (1988).
46. I.-C. Leu, Y.-M. Lu and M.-H. Hon, Mater. Chem. Phys. **56**, 256 (1998).
47. P. Ferret, A. Leray, G. Feuillet, P. Lyan, C. Pudda and T. Billion, Mater. Sci. Forum **433–436**, 201 (2003).
48. F. Abdou, C. Jacquier, G. Ferro, F. Cauwet and Y. Monteil, Mater. Sci. Forum **457–460**, 249 (2004).
49. R. Yakimova, M. Tuominen, A.S. Bakin, J.-O. Fornell, A. Vehanen and E. Janzén, Inst. Phys. Conf. Ser. **142**, 101 (1996).
50. T. Kimoto, A. Itoh, H. Matsunami and T. Okano, J. Appl. Phys. **81**, 3494 (1997).
51. T. Kimoto and H. Matsunami, J. Appl. Phys. **76**, 7322 (1994).
52. A.E. Nikolaev, V.A. Ivantsov, S.V. Rendakova, M.N. Mlashenkov and V.A. Dmitriev, J. Cryst. Growth **166**, 607 (1996).
53. M. Syväjärvi, R. Yakimova and E. Janzén, J. Crystal Growth **236**, 297 (2002).
54. I. Sunagawa, Morphology of minerals in *Morphology of Crystals*, Ch. 7, I. Sunagawa (Ed.), Terra Scientific, Tokyo (1987).
55. J. Yang, S. Nishino, M. Mehragany and P. Pirouz, Inst. Phys. Conf. Ser. **137**, 17 (1994).
56. B. Pécz, R. Yakimova, M. Syväjärvi, C. Lockowandt, H. Radamson, G. Radnóczy and E. Janzén, Thin Solid Films **357**, 137 (1999).

57. P.G. Neudeck, IEEE Electron Device Lett. **15**, 63 (1994).
58. S.V. Rendakova, I.P. Nikitina, A.S. Tregubova and V. A. Dmitriev, J. Electron Mater. **27**, 292 (1998).
59. J. Heindl, H.P. Strunk, V.D. Heydemann and G. Pensl, Phys. Status Solidi A **162**, 251 (1997).
60. C. Lockowandt, R. Yakimova, M. Syväjärvi and E. Janzén, Acta Astronautica **44**, 23 (1999).
61. T. H.U. Walter, *Fluid Sciences and Material Sciences in Space—A European Perspective*, Springer-Verlag, Berlin (1987), p. 327.
62. T. Sukegawa, M. Kimura and A. Tanaka, J. Crystal Growth **108**, 598 (1991).
63. Yu.M. Tairov and V.F. Tsvetkov, *Technologiya Poluprovodnikovyh I Dielectrheskih Materialov*, Vysshaya Shkola, Moscow (1983), p. 189 (in Russian).
64. W.v. Munch and W. Kurzinger, Solid State Electron. **21**, 1129 (1978).
65. S. Syrkin, V. Dmitriev, O. Kovalenkov, D. Bauman and J. Crofton, Mater. Sci. Forum **389–393**, 291 (2002).
66. T.E. Schatner, J.B. Casady, M.C.D. Smith, M.S. Mazzola, V.A. Dmitriev, S.V. Rendakova and S.E. Sadow, Mater. Sci. Forum **338–342**, 1203 (2000).
67. H. Jacobson, R. Yakimova, M. Syväjärvi, A. Kakanakova-Georgieva, T. Tuomi and E. Janzén, J. Cryst. Growth **256**, 276 (2003).
68. M. Syväjärvi, R. Yakimova, H. Jacobsson and E. Janzén, J. Appl. Phys. **88**, 1407 (2000).
69. G. Sarov, R. Kakanakov, T. Cholakova, L. Kassamakova, N. Hristeva, G. Lepoeva, P. Philipova, N. Kuznetsov and K. Zekentes, Mater. Sci. Forum **433–436**, 929 (2003).



# 7 Liquid Phase Epitaxy of Gallium Nitride

**HANS J. SCHEEL**

*SCHEEL CONSULTING, Groenstrasse Hans Anatas, 3803 Beatenberg, Switzerland*

**DENNIS ELWELL**

*PO Box 1043, Na'alehu, HI 96772, USA*

---

7.1 Introduction	203
7.2 Control of epitaxial growth modes	207
7.3 Thermodynamics and phase diagrams	209
7.4 Requirements for LPE	211
7.4.1 Solvents	211
7.4.2 Crucibles	213
7.4.3 Growth atmosphere	214
7.4.4 Substrates	215
7.5 LPE results, characterization of LPE(solution)-grown GaN	218
7.6 Cubic GaN	221
7.7 Conclusions and outlook	221
References	222

---

## 7.1 INTRODUCTION

Gallium nitride (GaN) and its solid solutions with aluminum nitride (AlN) and indium nitride (InN) have a large bandgap, strong inter-atomic bonds, and very high thermal conductivities. Therefore these nitrides are of great interest for numerous applications, for example for the development of high-brightness light emitting diodes (LEDs) and laser diodes (LDs) for the wavelength range between 200 nm and 640 nm corresponding to the direct energy gaps between 6.2 eV for (AlN) and 1.9 eV for InN. The blue-, green- and UV-emitting diodes in combination with phosphors for white LEDs have become commercially available. The latter eventually are expected to replace conventional illumination of incandescent and fluorescent lamps (Craford, 1992) and thus will allow enormous energy savings. Backlights for liquid crystal displays and for flashlamps for cellular phone cameras are developed. Extremely bright LEDs and LDs with the wavelength range of

400–410 nm are expected to be applied for next-generation high-density digital versatile discs (DVDs) and for high-resolution printing. Another application of UV-emitting LEDs based on GaAlN is the replacement of mercury lamps to disinfect water by portable systems, and for several other applications like curing materials such as adhesives, and for medical skin treatments. Besides optoelectronic applications of GaN and its alloys there are also microelectronic and high-temperature power-electronic applications where the nitrides will become important. Reviews on nitride-based semiconductors for blue and green LEDs including their historical development have been given by Davis (Davis, 1991), Morkoc *et al.* (Morkoc *et al.* 1994), and Ponce and Bour (Ponce and Bour, 1997).

GaN was first synthesized in 1932 by Johnson *et al.* (Johnson *et al.*, 1932) by the direct reaction between gallium and ammonia. The photoluminescence in the UV region reported by Lorenz and Binkowski (Lorenz and Binkowski, 1962) and the direct bandgap of 3.39 eV measured by Maruska and Tietjen (Maruska and Tietjen, 1969) on single-crystalline films, grown by hydrogen vapor phase epitaxy (HVPE), attracted many laboratories interested in LEDs in the short wavelength range. Pankove *et al.* reported GaN electroluminescent diodes (Pankove *et al.*, 1971), GaN layers grown by metal-organic chemical vapor deposition (MOCVD) were reported by Manasevit *et al.* (Manasevit *et al.*, 1971) and stimulated UV emission at 2 K by Dingle *et al.* (Dingle *et al.*, 1971). These studies initiated a broad interest in nitrides in the early 1970s. However, the structural perfection of the GaN layers for applications had to await the AlN buffer layers first developed by Yoshida *et al.* (Yoshida *et al.*, 1983) and the p-type doping by Amano *et al.* (Amano *et al.*, 1989) and Nakamura *et al.* (Nakamura *et al.*, 1992). These achievements allowed the p-n junction GaN LED to be developed in the laboratory of Amano *et al.* (Amano *et al.*, 1989) and the development of commercial blue, blue-green and UV GaN-based LEDs by Nakamura *et al.* (Nakamura *et al.*, 1994a, b, 1995).

In all GaN layers grown by metal-organic vapor phase epitaxy (MOVPE) and molecular beam epitaxy (MBE) the observed dislocation densities have been  $10^8$ – $10^{11}$  cm<sup>-2</sup>, and a reduction by up to four orders of magnitude could be achieved by epitaxial lateral overgrowth (ELO). Here the grown layers are covered by amorphous layers into which windows are etched through which successive epitaxial growth can be achieved and a large fraction of dislocations blocked. However, successive growth by vapor phase epitaxy (VPE) will again lead to a high density of growth islands which by coalescence cause new dislocations in addition to the dislocations which have propagated through the ELO window.

Despite the very high dislocation densities of  $10^9$ – $10^{10}$  cm<sup>-2</sup> of the VPE- and MOCVD-grown layers grown mostly on AlN or GaN buffer layers on sapphire substrates (Lester *et al.*, 1995), very high brightnesses of up to 10 cd and long lifetimes exceeding 50 000 h could be achieved for the blue and green LEDs.

The role of dislocations in GaAs and its solid solutions for microelectronic and for optoelectronic devices has been clearly established. For example, Booyens *et al.* (Booyens *et al.*, 1978) and Miyazawa *et al.* (Miyazawa *et al.*, 1986) have shown the variation of electrical conductivity and of threshold voltage of transistors, respectively, as a function of the distance from the dislocation core, and Lester *et al.* (Lester *et al.*, 1995) reviewed the efficiency of GaAs- and GaP-based LEDs as a function of the dislocation density as measured by etch-pit density, (Figure 7.1).

The dislocations originate from the substrate, and further dislocations are formed by the coalescence of nucleated islands due to the very high supersaturation in VPE. In addition,

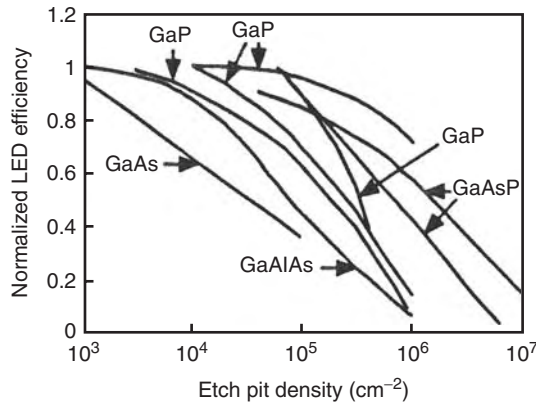


**Figure 7.1** Efficiency of GaAs and GaP LEDs as a function of dislocation density. Reprinted from *Appl. Phys. Lett.*, **66**, S.D. Lester, F.A. Ponce, M.G. Craford and D.A. Steigerwald, High dislocation densities in high efficiency GaN-based light-emitting diodes, 1249, Copyright (1995), with permission from American Institute of Physics

misfit dislocations are formed as a function of misfit at the growth temperature and of the thermal expansion difference between substrate and layer in heteroepitaxy (Jesser and Matthews, 1967; Basson and Ball, 1978; Matthews, 1979). Owing to the spatial variation of the electrical conductivity in the vicinity of the dislocation, a corresponding variation of the temperature will arise there due to Joule heating when an electrical field is applied (Basson and Ball, 1978). Since the diffusion constant is an exponential function of temperature, the temperature variation (and the stress field) in the vicinity of the dislocation results in enhanced diffusion of point defects towards the dislocation provided that there is a concentration gradient of point defects near the dislocation line.

It is increasingly accepted that dislocations also play a role in performance and lifetimes of III-nitride-based devices although their detrimental effect is not as pronounced as in the GaAlInAsP systems. Especially the crucial role of dislocations and other structural defects was recognized when GaN-based injection lasers were developed, in addition to the other factors like cleavage problems required for the cavities, the so far too resistive contacts, and to the required flatness of the interfaces and p-n junctions. It is hoped that with improved layer and interface perfection the threshold current density for nitride lasers can be reduced along with a reduction of the related device heating, so that lifetime and beam performance can be improved. Also, here liquid phase epitaxy (LPE) will become important to prepare low-dislocation density substrates and low-pipe defect base nitride layers as discussed in the following sections.

Other expected important applications of GaN, AlN, InN and their alloys are high-frequency devices and high-power devices operating at high temperatures as can be recognized from Table 7.1.

In the lower part of the table are shown the ratios of the figures of merit of high-temperature materials to silicon for computer logic applications of Keyes (Keyes, 1972) and for discrete devices for high-frequency high-power applications of Johnson (Johnson, 1965; after Davis, 1992). These aspects explain the great interest in III-nitrides for devices for gigahertz logic, microwave communications, high-temperature microprocessors and radiation-hard applications. It is expected that in nitride technology there will

**Table 7.1** High-temperature semiconductor materials

	Si/SOI	GaAs	SiC	III-N	Diamond
Bandgap (eV)	1.1	1.3	2.9	1.9–6.4	5.5
$T_{\max}$ signal devices ( $^{\circ}\text{C}$ )	300	300	>600	>550	?
$T_{\max}$ power devices ( $^{\circ}\text{C}$ )	250	250	>600	>550	?
Processing maturity	Medium	Medium	Low	Low	None
Key issues	Electromigration	Ohmics, electromigration	Substrates, ohmics	Substrates, ohmics	Substrates, dopants
Development costs	Low	Medium	High	High	Very high
Commercially available	Yes	Yes	Yes	2007	?
Johnson (Power Devices)	1.0	7	694	282	8206
Keys (Computer Logic)	1.0	0.5	5	2	32

be less development hurdles (substrates, layer growth, doping, contacts, etc.) than with SiC and with diamond although the SiC technology is presently more advanced. Also, for the above-mentioned electronic applications of nitrides, the high structural perfection of nitride substrates and base layers, and thus LPE, will be essential.

The main emphasis so far has been on the hexagonal wurtzite  $\alpha$ -modification of GaN (and AlN, InN) whereas the metastable cubic  $\beta$ -GaN phase with zinc blende structure has not received much attention. In analogy with the III-V arsenide and phosphide compounds one would expect a number of advantages of cubic GaN, AlN and InN (Nagahara *et al.*, 1994): reduced doping problems (Lei *et al.*, 1992), cleavage for laser cavities, integrated structures of nitride devices with Si and GaAs technology (Lei *et al.*, 1992; As *et al.*, 1996), piezoelectricity and a larger bandgap compared with the wurtzite-type GaN extending light emission to shorter wavelengths. Therefore, in addition to improvement of the light emission (Godlewski *et al.*, 1998; Yang *et al.*, 2000) and electronic applications mentioned above for  $\alpha$ -GaN, one would expect micro-electromechanical system (MEMS) technology, with many types of microfabricated devices like pressure sensors and microsensors, accelerometers with applications at high temperature and extreme conditions, to profit from the unique properties of GaN and the other III-nitrides.

From this discussion one could list the crystal growth problems as:

- development of large-diameter high-quality substrates with minimum differences of lattice constants and thermal expansion coefficients, of cubic and hexagonal GaN, AlN and InN;
- overgrowth of vapor-grown substrates by LPE to minimize the defect density;
- development of LPE to prepare the quasi defect-free base layers of cubic and hexagonal III-nitrides with excellent surface flatness;
- development of nitride multilayer structures by LPE with flat interfaces and p-n junctions;
- development of solid-solution substrates of GaAlN and of the allowed range of GaInN compositions followed by LPE overgrowth to improve perfection and surface flatness.

In the following the theoretical and technological requirements for LPE of nitrides will be described with emphasis on GaN.

## 7.2 CONTROL OF EPITAXIAL GROWTH MODES

The majority of GaN layers and multilayer structures have been prepared by VPE, by MOCVD or MOVPE, by MBE using metal-organic precursors and reactive nitrogen sources (ammonia or hydrazine compounds) or nitrogen with plasma or electron cyclotron resonance (ECR) to activate the relatively stable nitrogen molecules to form activated nitrogen species, or by reactive magnetron sputtering (Ross and Rubin, 1991). The thermodynamic and kinetic processes involved in these VPE-prepared GaN layers and especially the role of activated nitrogen have been described by Newman (Newman, 1996). Investigation of the surface morphology of MBE-grown GaN layers by Fujii *et al.* (Fujii *et al.*, 1997) reveals island formation by Volmer–Weber growth mode and oriented grains (columnar growth) at low growth temperatures (500–730 °C). At the higher growth temperature of 1030 °C the MOVPE-grown GaN layers show the Stranski–Krastanov growth mode and step flow growth mode in the flat areas in agreement with the concepts discussed in Chapter 1. Fujii *et al.* (Fujii *et al.*, 1997) also investigated the effect of strain and of substrate misorientation on the surface morphology. In general, the distances  $y_0$  between successive growth steps are below 100 nm unless very high growth temperatures above 1000 °C are employed. Rohrer *et al.* (Rohrer *et al.*, 1996) reported interstep distances between 50 nm and 150 nm for GaN MOVPE-grown at 1040 °C, and on the surfaces grown by Ilegems (Ilegems, 1972) by hydride/chloride VPE the steps could be recognized by interference contrast microscopy and thus are about 1  $\mu\text{m}$  apart. These large interstep distances can be explained by the supersaturation ratio  $\alpha = P/P_e$ , which is lowered by high growth temperatures and thus increases the interstep distance, as discussed in Chapter 1. (Here  $P$  is the actual pressure and  $P_e$  the equilibrium pressure at the growth temperature.)

The comparison of supersaturation in VPE and in LPE can be achieved according to Stringfellow (Stringfellow, 1991) by the difference of the thermodynamic driving force by means of the Gibbs free energy differences between the precursors/reactants (or the mobile phases) before growth and the crystalline product after growth. For GaN this comparison between MOVPE/MBE and LPE is shown in Figure 7.2. In LPE the effective supersaturation can be adjusted by the undercooling to very small values (a few  $\text{cal mol}^{-1}$ ), to exact equilibrium, or to a negative value leading to etching.

The driving force for VPE of course depends on the kind of process and precursors, and also on the growth temperature as shown above.

The adjustable low supersaturation in LPE allows control of the growth mode under the condition that homoepitaxy is used, or that in heteroepitaxy the substrate has at the growth temperature a very small misfit with the layer to be grown (Scheel, 2003). This misfit should typically be smaller than 0.5%, otherwise a higher supersaturation is required to initiate epitaxial growth. This increased supersaturation then may lead to step bunching, growth instability, and even to spontaneous formation of three-dimensional nuclei. The substrate requirements will be discussed further below.

By the near-equilibrium growth in LPE the layer-by-layer growth mode named after Frank and Van der Merwe can be achieved, i.e. layers (steps) propagate over macroscopic distances, and typically observed interstep distances in LPE of GaAs are of the order of several micrometers. This was shown by Scheel (Scheel, 1980) and Scheel *et al.* (Scheel *et al.*, 1982) in the first scanning tunnel microscopy (STM) investigation of GaAs epitaxial layers. The essential difference between LPE and VPE is that island formation by the



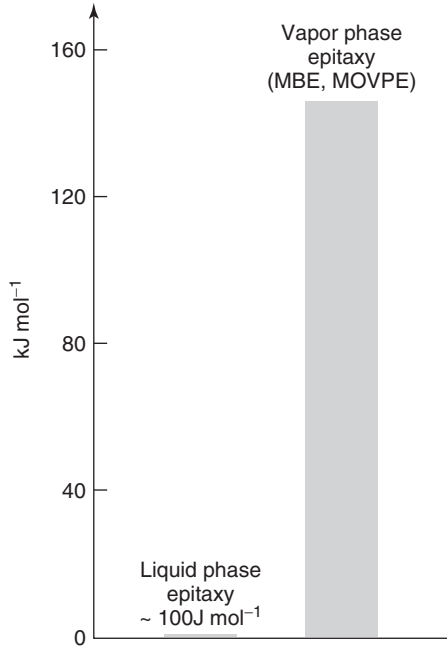


**Figure 7.2** Thermodynamic force comparison for MOVPE/MBE versus LPE

Volmer–Weber or the Stranski–Krastanov mode can be suppressed in LPE with the consequence that the dislocations and other defects originating from the coalescence of the islands in VPE can be prevented. Also by misorientation of the substrate the island formation can be reduced when the interstep distance from the misorientation is sufficiently small (see Chapter 1). However, this multi-stepped surface is quite rough, as defined by the roughness parameter (Scheel 2003), and does not give flat interfaces and p-n junctions.

Another feature of LPE is that vapor-grown substrates or epilayers of, for example, SiC or GaN, with high defect density can be overgrown by near-equilibrium deposition from the liquid solution so that the defect density can be drastically reduced, depending on the LPE layer thickness, by several orders of magnitude. For example, the micropipe defects in SiC, which are penetrating into the device structures and causing their failure (Neudeck, 1995), are originated by inclusions (Dudley *et al.*, 1999) or by coalescence of misoriented islands (Scheel, unpublished). These micropipe defects can be filled and overgrown by LPE (Yakimova *et al.*, 1996, 2000; Mueller *et al.*, 1998, Rendakova *et al.*, 1998; Ujihara *et al.*, 2004, 2005). In the case of GaN layers grown by MBE or MOCVD the micropipe defects were investigated by scanning force microscopy and by high-resolution transmission electron microscopy (Qian *et al.*, 1995) and in addition by energy-dispersive X-ray spectrometry (Kang and Ogawa, 1999): the micropipes contained impurities whereas threading dislocations are formed by coalescence of islands of 50–500 nm with in-plane misorientations of less than 3°. As in the case of SiC the defects of GaN layers are expected to be reduced or eliminated by LPE.

The growth rate in LPE of GaN from the low-concentration solutions is limited by mass transport, by diffusion of the growth species through the diffusion boundary layer (Scheel and Klemenzt, 1996). The maximum stable growth rate  $v_{\max}$  where neither inclusions are

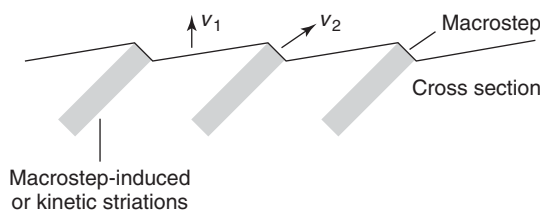


**Figure 7.3** Diffusion and growth stages for the stable and unstable growth regimes. If the macrostep speed  $v_2$  exceeds the microstep speed  $v_1$ , striations can result. Reprinted from *J. Cryst. Growth*, **287**, H.J. Scheel, 24, Copyright (2006), with permission from Elsevier

trapped nor other forms of growth instability like dendrites occur, is given by (Elwell and Scheel, 1975):

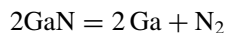
$$v_{\max} = \left( \frac{0.214Du\sigma^2 n_e^2}{Sc^{1/3} \rho^2 L} \right)^{1/2}$$

Here  $D$  is the diffusion coefficient,  $u$  the solution flow rate,  $\sigma$  the relative supersaturation,  $n_e$  the solubility at temperature  $T$ ,  $Sc$  the Schmidt number ( $Sc = \eta/\rho D$ ),  $\rho$  the density of the solution,  $\eta$  the viscosity, and  $L$  the length of the substrate. Figure 7.3 illustrates the diffusion and growth stages for the stable and unstable growth regimes. The difference of the propagation rate of the macrostep  $v_2$  and the faster monostep velocity  $v_1$  leads to inhomogeneity of dopants and impurities, to macrostep-induced striations (Scheel, 2006).

Extremely flat surfaces by LPE can be achieved by the transition of the slightly mis-oriented surface to faceting, to extremely flat surfaces as shown experimentally by Scheel (Scheel, 1980) and theoretically by Chernov and Scheel (Chernov and Scheel, 1995). Nearly dislocation-free GaAs surfaces could be achieved by this faceting transition. It follows from this discussion that also for GaN one would expect such improvements in layer and surface perfection by LPE as long as conditions for the stable growth regime are established.

## 7.3 THERMODYNAMICS AND PHASE DIAGRAMS

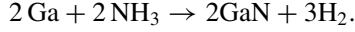
GaN is relatively stable in comparison with other III-V semiconductors. Van Vechten (Van Vechten, 1973) has estimated the melting point of GaN as 2790 K. The reaction:



has been mostly studied by monitoring the decomposition kinetics under various nitrogen pressures. Sime and Margrave (Sime and Margrave, 1956) measured the activation energy of sublimation as  $130 \text{ kcal mol}^{-1}$  at 1300 K, and considered that dissociative evaporation was more likely than sublimation of GaN molecules.

The reverse reaction, namely formation of GaN by direct reaction between gallium and molecular nitrogen, is influenced by the high stability of the nitrogen molecule. Group III metals catalyze the decomposition of nitrogen but the GaN formation reaction does not proceed at significant rates under normal furnace conditions. Ammonia is typically a

thousand or more times more effective as a source of active nitrogen since the N–H bond is weaker than N–N, so the reaction to synthesize GaN is normally:



The reaction typically proceeds at 600–1000 °C.

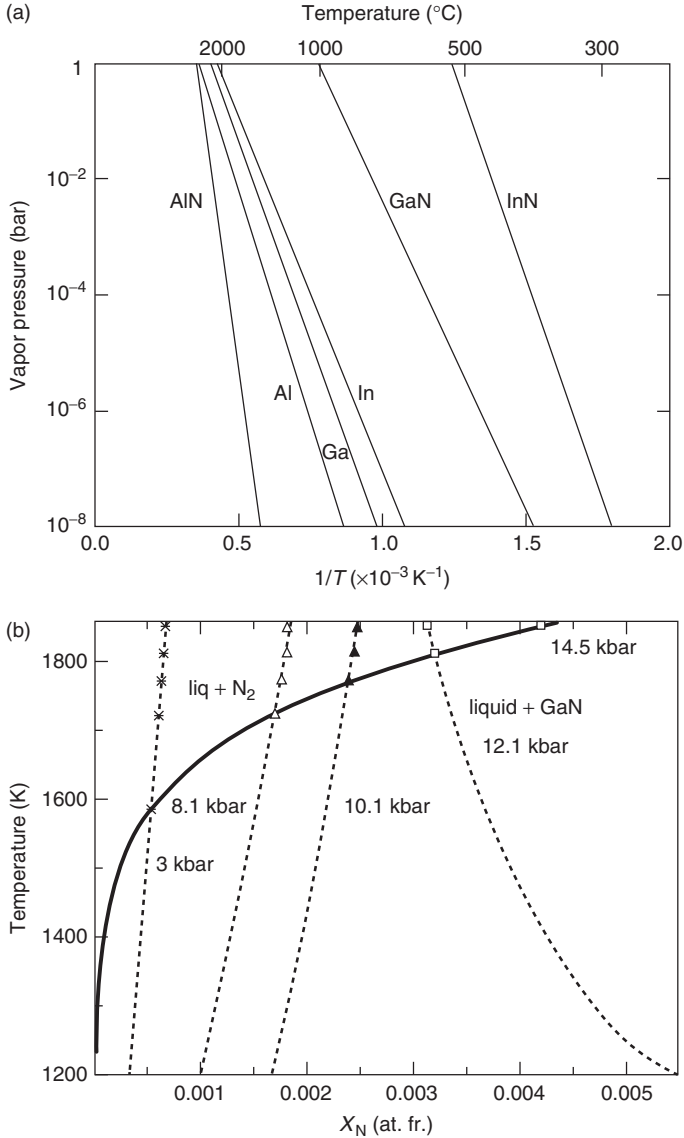


**Figure 7.4** (a) Pressure–temperature diagram for GaN coexisting with Ga and molecular  $\text{N}_2$ ; (b) approximate solubility curve for GaN in gallium. Reprinted from *J. Cryst. Growth*, **246**, I. Grzegory *et al.*, 177, Copyright (2002), with permission from Elsevier

Karpinski *et al.* (Karpinski *et al.*, 1984) measured the equilibrium activity of  $N_2$  over GaN up to around 1900 K using high pressure apparatus, and measured the standard Gibbs free energy change for the decomposition of GaN in equilibrium with molecular nitrogen. The pressure–temperature diagram for the coexistence of GaN with gallium and molecular nitrogen is shown in Figure 7.4(a) (Grzegory *et al.*, 2002), along with data for AlN and InN.

These authors estimate that the nitrogen molecule has to overcome a potential barrier of 3 eV to reach the gallium surface and so high temperatures and pressures have to be used in order to grow crystals or epilayers of GaN at acceptable rates. Note that the data of Figure 7.4(a) extend to temperatures above 2000 K.

Grzegory *et al.* (Grzegory *et al.*, 2002) used the data of Figure 7.4(a) to plot a solubility curve at the equilibrium pressure and these data are shown in Figure 7.4(b).

The maximum of the scale, 0.5 mol%, is rather low for crystal growth, and this value requires temperatures of over 1800 K and pressures above 15 kbar. The heat of solution/crystallization was estimated by these authors as  $44.7 \text{ kcal mol}^{-1}$  or 0.49 eV per bond and represents the bonding energy in the crystal relative to the solution phase.

The growth process for GaN formation may be described as a VLS (vapor–liquid–solid) process first described by Wagner and Ellis (Wagner and Ellis, 1964) for growth of silicon whiskers on top of which liquid gold droplets dissolved silicon arriving as silane from the gas phase. In GaN it is nitrogen gas for growth from high-pressure solutions at high temperatures, whereas ammonia is the nitrogen source for growing GaN at low or ambient pressure.

## 7.4 REQUIREMENTS FOR LPE

### 7.4.1 Solvents

In the case of GaN and the other III-nitrides the optimum solvent has not yet been found. In the following the general discussion of solvents follows that of Elwell and Scheel (Elwell and Scheel, 1975). An ideal solvent should show a high solubility of the solute of at least a few percent at a practical high temperature, and an appreciable temperature dependence of the solubility which allows precise adjustment of the supersaturation. The desired crystal phase should be the only stable solid phase. Further advantages are a low viscosity, low melting point, low vapor pressure at the highest applied temperature, low toxicity, and a low reactivity with the container/crucible material. For the growth of semiconductors the solvent should not contain harmful constituents which are incorporated into the crystallized phase, and thus it should be available in very high purity.

In order to arrive at high solubility the chemical bonding of crystal (epilayer) and solvent should be similar ('*similia similibus solventur*' meaning 'similar solute is soluble in similar solvent'), whereas large crystal chemical differences with respect to ionic or covalent radii and/or with respect to the magnitude of ionic or covalent valency would minimize incorporation of unwanted species in the epilayer. In other words, the species of the solvent should have a very low distribution coefficient unless they are useful as dopants or they are neutral for the device application.

The optimum is a solvent which is a constituent of the epilayer compound like Ga for GaN. Quite often good solvents form compounds with the composition to be crystallized, with a compound melting point or eutectic temperature below the growth temperature for

LPE. Thus nitrides like  $\text{Li}_3\text{N}$  [melting point (mp)  $895^\circ\text{C}$ ],  $\text{Ba}_3\text{N}_2$  and  $\text{Ca}_3\text{N}_2$  (mp  $1195^\circ\text{C}$ ) have been suggested. The frequently applied sodium (Yamane *et al.*, 1997; Kawamura *et al.*, 2005) has the disadvantage of extreme reactivity when coming into contact with water (formation of explosive hydrogen) or with other oxygen-containing compounds, and thus requires special handling and precautions. The solubility of nitrogen or of GaN in sodium can be increased by pressure and by addition of Li or Ca. The rate of dissolution of nitrogen is significantly increased by plasma activation or by using nitrogen compounds which decompose at the growth temperature (ammonia, hydrazines).

Because of the low solubility of nitrogen in gallium, a few alternative solvents have been explored. The addition of bismuth to gallium by Thurmond and Logan (Thurmond and Logan, 1972) reduced the spontaneous nucleation of GaN, which was not confirmed by Elwell *et al.* (Elwell *et al.*, 1984). The latter authors also used Ga/Sn alloys in place of gallium in their crystal synthesis experiments but found no improvement versus gallium alone. A more promising approach to the choice of a solvent may be the use of alkali metals or alkali or alkaline earth metal nitrides. Lithium is the only alkali metal that forms a stable nitride ( $\text{Li}_3\text{N}$ ). This has a melting point of  $813^\circ\text{C}$ , high for a typical high-temperature solvent but the nitrogen-rich solvent may be favorable for GaN deposition. Magnesium and barium form nitrides that decompose on melting so perhaps the most promising solvent among the group II nitrides is  $\text{Ca}_3\text{N}_2$ , which has a melting point of  $1195^\circ\text{C}$ . Either Li or Ca added to gallium may increase the solubility of GaN so there is scope for the choice of a solvent.

The use of sodium as a flux together with gallium was suggested by Yamane *et al.* (Yamane *et al.*, 1997) but the solubility and growth rate were low when molecular nitrogen under pressure was used as the source of nitrogen. More recently Iwahashi *et al.* (Iwahashi *et al.*, 2003) used ammonia as the source of nitrogen with a Ga/Na solvent at  $800^\circ\text{C}$ . The solvent had a composition of 79 at. % Na/21 at. % Ga contained in a sealed BN crucible. Under a high total pressure, the concentration of ammonia in a nitrogen/ammonia gas mixture was determined. Formation of GaN was observed with 5 atm  $\text{NH}_3$  but required 20 atm total pressure when the ammonia concentration was reduced to 4%. Growth on small GaN seeds was also studied but polycrystalline growth was observed on the seeds under all conditions of the experiments.

Morishita *et al.* (Morishita *et al.*, 2005) also used sodium/gallium at medium high nitrogen pressure. The solubility of GaN in the 27 at. % Ga/73 at. % Na solvent was determined to be 0.11 % at  $800^\circ\text{C}$  and 0.23 % at  $850^\circ\text{C}$ . Experiments were conducted to deposit GaN layers in three regions of supersaturation: 36–65 %, 65–85 % and 85–148 %. (Results discussed in the next section.) The same group (Morishita *et al.*, 2005) increased nitrogen dissolution by adding Li or Ca to the Ga-Na melt, improved the accuracy of the solubility measurements, and established the conditions for the growth of transparent crystals.

Song *et al.* (Song *et al.*, 2004) proposed that lithium is preferable to sodium as a solvent for GaN since its nitride is much more stable. They investigated crystal growth in a binary system  $\text{Li}_3\text{N} + \text{Ga}$  reacted in a tungsten crucible at  $800^\circ\text{C}$  with an overpressure of 1–2 atm of nitrogen. The relatively low nitrogen overpressure was considered a major potential advantage in relation to the high temperature/high pressure methods. After reacting the starting materials, the resulting solution was cooled at  $2\text{--}3^\circ\text{C day}^{-1}$  and clear hexagonal platelets (of millimeter size) were obtained. Similarly Ohta *et al.* (Ohta *et al.*, 2006) reported the synthesis of GaN crystals from  $\text{Li}_3\text{N}$ -added Ga melt in Na vapor.

Feigelson and Henry (Feigelson and Henry, 2005) used a gallium free solvent composed of  $\text{Li}_3\text{N}$  together with  $\text{BaF}_2$  and  $\text{LiF}$  to reduce the melting point. The solution was held in a tungsten crucible at  $800^\circ\text{C}$  under 25 bar of nitrogen to prevent evaporation. A sintered tablet of GaN was used as source material and gradient transport used to deposit crystals by spontaneous nucleation in the cooler region. The crystallites grown in these experiments were up to  $0.5 \times 0.1$  mm in size and optically clear. These experiments were preliminary studies to evaluate the viability of top-seeded crystal growth.

As noted above, calcium nitride ( $\text{Ca}_3\text{N}_2$ ) with a melting point of  $1195^\circ\text{C}$  also could be considered if mixed with other nitrides to reduce the melting point. However, purity is a problem since these compounds are not yet available in ultra-high purity as required for preparation of device-quality nitride layers.

An alternative approach is ammonothermal growth (analogous to hydrothermal growth) which had been introduced by Juza *et al.* (Juza *et al.*, 1966) and applied to GaN by Raghothamachar *et al.* (Raghothamachar *et al.*, 2006) to epitaxial growth of thick plates of GaN and AlN.

In summary, solution growth has not yet established the viability of any method for development as a scaled-up technological process for growth of bulk GaN crystals and for LPE of GaN. GaN substrates grown by halide VPE are available commercially up to 5 cm in diameter, but these have dislocation densities of  $10^6 \text{ cm}^{-2}$  and above. Small solution-grown platelets with dislocation densities as low as  $10^2 \text{ cm}^{-2}$  are available for evaluation.

The gallium solvent requires high pressure for showing appreciable solubility of GaN, and the important question is whether a growth method can be developed to use gallium solvent at ambient pressure despite the extremely low solubility.

Preliminary results of LPE of GaN from Ga solvent at ambient pressure (Klemenz and Scheel, 2000) will be discussed in Section 7.5.

## 7.4.2 Crucibles

At the high growth temperatures (above  $850^\circ\text{C}$ ) oxide crucibles like alumina and silica glass are wetted and corroded by the solvents discussed in the previous section, and are nitrated by ammonia and by plasma-activated nitrogen leading to successive dissolution of the nitride. Wetting angles of Ga reported for  $1000^\circ\text{C}$  are  $100^\circ$  on silica glass,  $112^\circ$  on  $\text{Al}_2\text{O}_3$ ,  $120^\circ$  on graphite and  $132^\circ$  on BN (Scheel, 1977; Lucas, 1984). Thus boron nitride crucibles have been mostly applied, and pyrolytic graphite in earlier work (Logan and Thurmond, 1972). An important question is whether the crucibles are available in the high purity required for fabrication of semiconductor devices. Highest-purity graphite may be further purified by heating to  $> 1400^\circ\text{C}$  for 10 h (in vacuum of  $< 5 \times 10^{-3}$  torr, slow He inlet) before use (Scheel, 1977). In certain cases paintable ultra-high temperature coatings of BN and of other materials may be applied (ZYP Coatings, Oak Ridge, TN, USA).

Also the surface roughness (Zhou and De Hosson, 1995) and the dynamic wetting angles of moving liquids should be considered in the optimum choice of crucible material and growth method. With moving liquids the deviation from the equilibrium wetting angles are:

$$\Theta_{\text{advancing}} > \Theta_{\text{equilibrium}} > \Theta_{\text{receding}}$$

The polarity of substrate and of the grown faces have an effect on wetting: the Ga-face will be wetted more by Ga than the N-face of GaN {111}. Furthermore the wetting behavior can be modified by additives to the solvent.

Surface contamination by an oxide scum or crystallization at the surface reduces the wetting angle so that liquid creeps up the crucible walls and may form a polycrystalline GaN layer in the upper region of the container (Logan and Thurmond, 1972; Elwell *et al.*, 1984; Dyck *et al.*, 1999). The oxide scum problem is very pronounced when Al-containing melts are used to fabricate GaAlN solid-solution layers. The required low oxygen partial pressure in the atmosphere will be discussed in the next section.

### 7.4.3 Growth atmosphere

One of the challenges in the growth of high-quality GaN is the presence of traces of oxygen or humidity in the growth atmosphere. In the case of AlGaAs-based LEDs and lasers oxygen is detrimental to photoluminescence and performance of the devices by the introduction of deep-level states which may act as nonradiative recombination centers (Chen *et al.*, 1997). Earlier works have shown that dark-spot defects and the carrier concentration are reduced and the mobility increased when the oxygen level in the ambient gas in LPE of GaAs is reduced below 0.03 ppm (Kan *et al.*, 1977), and the temperature dependence of the distribution coefficient of oxygen was established by Otsubo *et al.* (Otsubo *et al.*, 1973). For GaN and its solid solutions similar detrimental effects of oxygen incorporation can be expected, and the occurrence of yellow luminescence seems to be related to oxygen. Also the formation of an oxide scum surface should be prevented, and the required extremely low oxygen partial pressure can be derived for the given system (Ga, Ga + Al, etc.) and the growth temperature from thermodynamic data or more easily from the Ellingham diagram (Elwell and Scheel, 1975).

The gas atmosphere consists of nitrogen, ammonia, hydrogen and possibly a noble gas in a ratio determined by the process and the growth temperature. Logan and Thurmond (Logan and Thurmond, 1972) applied an ammonia partial pressure greater than the equilibrium pressure at 1000 °C of  $10^{-3}$  atm and checked the exit gas from the furnace by titration with a dilute solution of HCl of known volume and normality using methyl red as indicator. Elwell *et al.* (Elwell *et al.*, 1984) found that no GaN was formed when the partial pressure of ammonia in hydrogen was less than  $0.34 \times 10^{-3}$  atm. Klemenz and Scheel (Klemenz and Scheel, 2000) applied 20 vol % ammonia in nitrogen in their LPE experiments, and the synthesis of GaN with undiluted NH<sub>3</sub> at temperatures above 1000 °C mostly yielded needle-like crystals and whiskers of small size (Johnson *et al.*, 1932; Pichugin and Yaskov, 1970; Zetterstrom, 1970; Aoki and Ogino, 1979). The addition of hydrogen is helpful to reduce the oxygen partial pressure but has to be consistent with doping requirements.

In order to prevent surface oxidation of the melts and to minimize the incorporation of oxygen into the LPE-grown layers the oxygen level of the gas atmosphere should typically be less than  $10^{-8}$  or 0.01 ppm or 10 ppb. Gases with this level of purity are not readily available, and further contamination is expected from the gas tubing, from the growth apparatus and any leaks, and from the inserted chemicals, crucibles and substrates. Experiment preparation is best done in a glovebox with attached furnace system, but commercial gloveboxes have oxygen and humidity levels in the 1–10 ppm range.

A super-glovebox with oxygen and humidity below 0.03 ppm, the detection limits at that time, has been reported by Scheel (Scheel, 1985). The steel glovebox chamber with balance and attached furnace could be outgassed at  $10^{-6}$  torr at  $70^{\circ}\text{C}$ , the lowest permeability rubber gloves could be evacuated separately, and all materials introduced to the glovebox were outgassed in the airlock. A helium-hydrogen mixture with 2–3 vol %  $\text{H}_2$  was circulated and regenerated by means of a membrane pump, a palladium catalyst and by chemisorption on reduced chromium oxide on silicagel as carrier (OXISORB $\equiv$ ). The hydrogen concentration is below the 4–5 % flammability limit in air and below the 26 %  $\text{H}_2$  limit in helium (Satterly and Burton, 1919; Coward and Jones, 1952), but is sufficient for achieving the low oxygen partial pressure and for the regeneration process. The detrimental effects of small leaks may be avoided by applying a small overpressure in the reaction chamber (and in the glovebox) as was estimated by Battat *et al.* (Battat *et al.*, 1974), or alternatively by using high flow rates of the gas mixture.

#### 7.4.4 Substrates

The substrate requirements are much more stringent in near-equilibrium LPE compared with VPE. Desirable would be a small misfit at growth temperature of less than 0.1 %, and the difference of the thermal expansion coefficient between substrate and epilayer should be smaller than 5 % in order to prevent cracking upon cooling from growth temperature to room temperature. In case of larger misfit the advantage of LPE to achieve the layer-by-layer growth mode of Frank–van der Merwe and atomically flat surfaces is lost because a higher supersaturation is required to initiate epitaxial growth. Jesser and Kuhlmann-Wilsdorf (Jesser and Kuhlmann-Wilsdorf, 1967) and Blakeslee and Mathews (Mathews, 1975) have shown that there is a maximum thickness for coherent overgrowth in which the lattice of the layer was stretched or compressed to fit the substrate but that, for layer thicknesses greater than this critical value, misfit dislocations are formed in order to partially release the strain in the layer. Another effect of strain in the layer is bending which depends on the thicknesses of substrate and layer and on their elastic moduli (Sugita *et al.*, 1973). It follows from this discussion that homoepitaxy is preferred in order to exploit the advantages of LPE: highest structural perfection and extreme flatness of layers and p-n junctions. Otherwise substrates with small misfit and small difference of thermal expansion have to be found. A certain flexibility with respect to substrate adaptation exists with the variation of the GaN lattice parameters with the growth conditions (Seifert *et al.*, 1980) and with the composition pulling effect observed in InGaN and AlGaN MOCVD-grown on GaN (Hiramatsu *et al.*, 1997).

A further requirement for substrates are a high chemical stability so that they are not corroded or dissolved during initial LPE growth leading to contamination of the solution and of the layer. A special condition for achieving extremely flat surfaces is a small misorientation of the substrate surface, of less than  $0.1^{\circ}$ , as was discussed by Chernov and Scheel (Chernov and Scheel, 1995) and briefly in Chapter 1 of this book.

The choice of a proper substrate has been a troublesome issue in the development of GaN technology so that a Substrates Discussion Forum had been established (Hellman, 1996). The growth of bulk GaN of sufficient size or perfection has not yet been achieved as in the growth from high-pressure solutions there is an inherent size limit of a few millimeters of high-quality GaN crystals unless a huge effort is spent so that economic



substrates cannot be expected by this approach. The growth of GaN at ambient pressure or low overpressure of say 10 bar could become viable but still is not much advanced. The best chance at present seems to be the fabrication of large-diameter GaN substrates of low structural perfection by hydride vapor phase epitaxy (HVPE) (Naniwae *et al.*, 1990; Feng, 2006; commercially now for instance by Sumitomo, see Table 7.2) followed by LPE overgrowth to improve the structural perfection. Alternative large GaN surfaces have become available and are called templates: GaN epitaxially grown by HVPE on large sapphire substrates, however with low structural perfection which can be improved somewhat by ELO.

The most popular substrate is still sapphire with a lattice mismatch of 8.3 % but great progress has been made in understanding how to accommodate this huge mismatch by control of the deposition process (Matsuoka, 2004; Napierala *et al.*, 2006) and through the use of buffer layers first introduced by Yoshida *et al.* (Yoshida *et al.*, 1983). The crystallographic relations between sapphire substrates and wurtzite-type GaN films have been elaborated by Kung *et al.* (Kung *et al.*, 1994), and the cracking behavior of GaN-sapphire structures were studied by Itoh *et al.* (Itoh *et al.*, 1985).

SiC is a substrate of increasing interest due to its high thermal conductivity, its hardness, its lower mismatch of 2.5 % with GaN, and due to its commercial availability up to large diameters (~10 cm). Sasaki and Matsuoka (Sasaki and Matsuoka, 1988) and Sasaki *et al.* (Sasaki *et al.*, 1989) have shown that the polarity of 6H-SiC strongly influences the surface morphology and the photoluminescence properties of the GaN layers, and that the GaN layers adapt the polarity of the substrates. Recently it has been shown by the GaN groups at the University of California at Santa Barbara that nonpolar GaN surfaces, although of lower structural perfection, might increase the output power of LEDs and improve the doping control in high energy mobility transistor (HEMT) devices (Chakraborty *et al.*, 2006; Metzger, 2006). Further work is required to establish the optimum MOCVD growth conditions for controlling the threading dislocations and basal-plane stacking faults.

Zinc oxide has a mismatch of only 0.2 % but is attacked by halides and other materials used in crystal growth and has not been reported as a candidate for GaN LPE; however, it could have a chance if a first base layer were deposited from the gas phase.

Lithium tantalate ( $\text{LiTaO}_3$ ) is hexagonal with a lattice constant of 0.5154 nm, so the lattice mismatch with  $\langle 0001 \rangle$  GaN is 7.2 %. Large diameter substrates are available, but it has not been reported for LPE of GaN. Lithium aluminate ( $\text{LiAlO}_2$ ) and lithium gallate ( $\text{LiGaO}_2$ ) (Ishii *et al.*, 1997) have been proposed as substrates for GaN, but reactions limit their application temperatures to 900 and 800 °C, respectively. Klemenz and Scheel (Klemenz and Scheel, 2000) have reported cracking of these substrates upon cooling from LPE growth temperature. Alternative substrates like  $\text{NdGaO}_3$  and yttrium-stabilized zirconia (YSZ) have been tested by Paszkiewicz *et al.* (Paszkiewicz *et al.*, 2001). Silicon and GaAs have been used as substrates in VPE of GaN after being surface-nitrided at high temperature, but have not been used in LPE of GaN. The commercial sources of substrates (except for sapphire) are listed in Table 7.2.

Perhaps bulk GaN substrates or GaN template surfaces will be preferably used in LPE of GaN in order to develop layers of high structural perfection and excellent surface flatness. Also the development of solid solution substrates of GaN-AlN and of GaN-InN in the possible miscibility range should be considered.

**Table 7.2** Suppliers of AlN, GaN, SiC, ZnO and LiAlO<sub>2</sub>, LiGaO<sub>2</sub>, substrates and templates. (The numerous suppliers of sapphire substrates are not included)

AlN	Crystal-is, USA	<a href="http://www.crystal-is.com">www.crystal-is.com</a>
	Marubeni, Japan/USA	<a href="http://www.marubeni-sunnyvale.com">www.marubeni-sunnyvale.com</a>
GaN	TDI, USA	<a href="http://www.tdii.com">www.tdii.com</a>
	ATMI, USA	<a href="http://www.atmi.com">www.atmi.com</a>
	AXT, USA	<a href="http://www.axt.com">www.axt.com</a>
	Lumilog, USA	<a href="http://www.lumilog.com">www.lumilog.com</a>
	Marubeni, Japan/USA	<a href="http://www.marubeni-sunnyvale.com">www.marubeni-sunnyvale.com</a>
	Nitride Semiconductors, Japan	<a href="http://www.nitride.co.jp/english">www.nitride.co.jp/english</a>
	Nitronex Corp., USA	<a href="http://www.nitronex.com">www.nitronex.com</a>
	Phys Tech-WBG, Russia	<a href="http://www.ru.com/PhysTech_WBG/index.htm">www.ru.com/PhysTech_WBG/index.htm</a>
	Picogiga/SOITEC, France	<a href="http://www.picogiga.com">www.picogiga.com</a>
	Reade, USA	<a href="http://www.reade.com">www.reade.com</a>
	Sumitomo Electric Industries, Japan	<a href="http://www.sei.co.jp/sc/English/index_e.html">www.sei.co.jp/sc/English/index_e.html</a>
	TDI, USA	<a href="http://www.tdii.com">www.tdii.com</a>
	TopGaN Ltd, Poland	<a href="http://www.topgan.fr.pl">www.topgan.fr.pl</a>
WaferWorld Inc., USA	<a href="mailto:sales@waferworld.com">sales@waferworld.com</a>	
SiC	ATMI, USA	<a href="http://www.atmi.com">www.atmi.com</a>
	CREE, USA	<a href="http://www.cree.com">www.cree.com</a>
	Epigress, Sweden	<a href="http://www.epigress.se">www.epigress.se</a>
	Intrinsic Semiconductor Corp., USA	<a href="http://www.intrinsicsemi.com">www.intrinsicsemi.com</a>
	Marubeni, Japan/USA	<a href="http://www.marubeni-sunnyvale.com">www.marubeni-sunnyvale.com</a>
	Nippon Steel Corp., Japan	<a href="http://www.nsc.co.jp">www.nsc.co.jp</a>
	SiCrystal AG, Germany	<a href="http://www.sicrystal.de">www.sicrystal.de</a>
	Sterling Semiconductor Inc., USA	<a href="http://www.sterling-semiconductor.com">www.sterling-semiconductor.com</a>
	Wafer Technology, UK	<a href="http://www.wafertech.co.uk">www.wafertech.co.uk</a>
	II-VI Inc., USA	<a href="http://www.iivivbg.com">www.iivivbg.com</a>
ZnO	Cermet Inc., USA	<a href="http://www.cermetinc.com">www.cermetinc.com</a>
	Cradley-Crystals, Russia	<a href="http://www.cradley-crystals.com">www.cradley-crystals.com</a>
	Eagle Picher Technologies, USA	<a href="http://www.soxxess.uv.es">www.soxxess.uv.es</a>
	EU Project on ZnO	<a href="http://www.kmtcrystal.com">www.kmtcrystal.com</a>
	Hefei Kejing Materials, China	<a href="http://www.mticrystal.com">www.mticrystal.com</a> ; <a href="http://www.mtixtl.com">www.mtixtl.com</a>
	MTI Corp., China/USA	<a href="http://www.mticrystal.com">www.mticrystal.com</a> ; <a href="http://www.mtixtl.com">www.mtixtl.com</a>
	Nimswave Inc., Japan	<a href="mailto:info@nimswave.com">info@nimswave.com</a>
	WaferWorld Inc., USA	<a href="mailto:sales@waferworld.com">sales@waferworld.com</a>
LiAlO <sub>2</sub> , LiGaO <sub>2</sub>	CrysTec GmbH, Germany	<a href="http://www.crystec.de">www.crystec.de</a>
	Hefei Kejing Materials, China	<a href="http://www.kmtcrystal.com">www.kmtcrystal.com</a>
	MTI Corp., China/USA	<a href="http://www.mtixtl.com">www.mtixtl.com</a>
	Toplent Photonics, Australia	<a href="http://www.toplent.com">www.toplent.com</a>

## 7.5 LPE RESULTS, CHARACTERIZATION OF LPE(SOLUTION)-GROWN GaN

The first reproducible growth of GaN layers on sapphire (0001) substrates at ambient pressure has been achieved by Logan and Thurmond (Logan and Thurmond, 1972). Pure gallium and Ga-Bi alloys have been used as solvents. The pyrolytic graphite boats in a horizontal furnace did not cause dissociation of  $\text{NH}_3$ , but devitrified quartz glass had to be replaced by new silica glass in order to prevent  $\text{NH}_3$  decomposition. At a growth temperature of  $1000^\circ\text{C}$ ,  $P(\text{NH}_3)$  around  $2 \times 10^{-3}$  atm and growth times between 16 and 64 h epitaxial layers up to  $40\ \mu\text{m}$  could be achieved. The surfaces were faceted and consisted of hexagonal hillocks and macrosteps with interstep distances of a few micrometers. At layer thicknesses over  $30\ \mu\text{m}$  cracks were observed due to lattice mismatch and thermal expansion difference between substrate and layer.

LPE of GaN layers up to  $10\ \mu\text{m}$  thickness on sapphire (0001) substrates has been achieved by Madar *et al.* (Madar *et al.*, 1975) in the temperature range  $1000\text{--}1200^\circ\text{C}$  and pressure range  $1500\text{--}5000$  bar. The estimated growth rate was  $1\ \mu\text{m day}^{-1}$ , and the surfaces showed a terrace/macrostep structure with interstep distances up to a few micrometers. Hall and Seebeck coefficient measurements at  $300\ \text{K}$  gave for n-type  $\sigma = 5 \times 10^{-3}\ \Omega\text{cm}$ ,  $\mu = 70\ \text{cm}^2\text{V}^{-1}\text{s}^{-1}$  and  $n = 10^{19}$ , and for p-type (polycrystalline)  $\sigma = 50\ \Omega\text{cm}$ ,  $\mu = 3\ \text{cm}^2\text{V}^{-1}\text{s}^{-1}$  and  $N_A - N_D = 10^{17}$ .

Growth of oriented thick GaN films from thin Ga films using plasma-activated nitrogen was reported by Dyck *et al.* (Dyck *et al.*, 1999). The layers grown at  $700\text{--}800^\circ\text{C}$  in a nitrogen plasma at 5 torr and 400 W of microwave power had a columnar structure with a high density of stacking faults and a dislocation density of approximately  $10^{10}\ \text{cm}^{-2}$ .

Rotating substrates of sapphire (0001),  $\text{LiGaO}_2$  (001) (“LGO”),  $\text{LiAlO}_2$  (100) (“LAO”) and of HVPPE-grown GaN films on  $\text{Al}_2\text{O}_3$  have been used by Klemenz and Scheel (Klemenz and Scheel, 2000) in order to reduce the diffusion barrier in growth from low-concentration GaN solutions in Ga and Ga-Bi melts at ambient pressure. The experimental set-up is shown in Figure 7.5.

LGO and LAO have limited stability allowing maximum growth temperatures of  $900^\circ\text{C}$  thus leading to very low concentrations of the solutions and corresponding low growth rates. Furthermore these substrates cracked into pieces after growth and cooling to room temperature. Best results were achieved on the HVPE seed layers with growth islands and macrosteps visible in Nomarski microphotographs.

Grzegory *et al.* (Grzegory *et al.*, 2002) discuss the growth of GaN crystals in a temperature gradient, with nitrogen dissolved from the gas phase at the surface of a vertical crucible (Figure 7.6). Typical temperatures for growth by this method were in the range  $1700\text{--}1900\ \text{K}$  and the temperature difference between the hotter surface of the liquid and the lower region where growth occurred was typically  $20\text{--}50\ \text{K}$ . The pressure up to  $1\ \text{GPa}$  was maintained above the measured equilibrium so that nitrogen continually dissolved at the surface and flowed by convection and diffusion to the cooler region near the base. Crystals grew in the form of hexagonal platelets with dominant  $\{0001\}$  basal planes. Over a growth period of  $100\text{--}150\ \text{h}$ , the maximum lateral size of the crystals grown was  $10\text{--}14\ \text{mm}$  with a thickness of  $80\text{--}120\ \mu\text{m}$ . The crystals were optically clear.

Bockowski *et al.* (Bockowski *et al.*, 2004) used a similar arrangement to study growth on SiC, sapphire, and on MOCVD-grown GaN on sapphire. Because of the constraint on the equipment imposed by the requirement of high pressure, the working diameter is

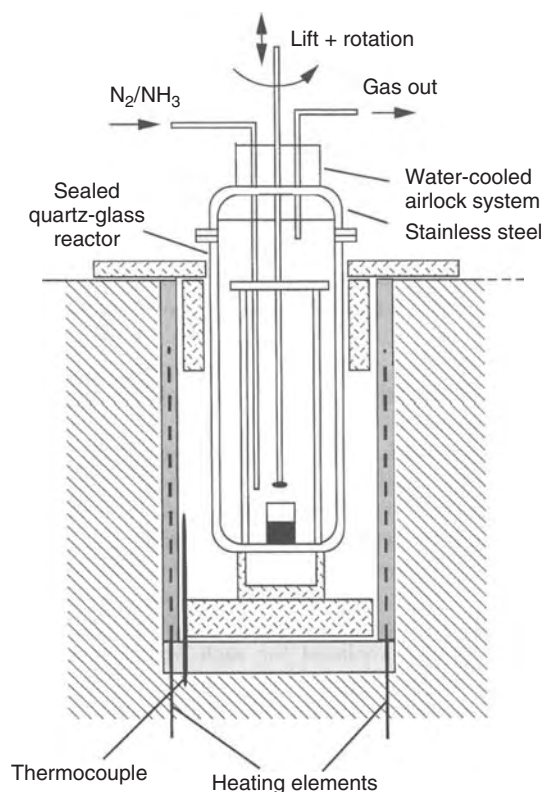


**Figure 7.5** Arrangement for LPE growth of GaN on a rotating substrate. Reprinted from *J. Cryst. Growth*, **211**, C. Klemenz and H.J. Scheel, 62, Copyright (2000), with permission from Elsevier

limited to 1 cm. It was found necessary to increase the overpressure of nitrogen in order to achieve growth by heteroepitaxy. The authors describe their experiments as deposition of bulk GaN but they could be considered as preliminary studies of the conditions for LPE. In either case, significant scale-up would be necessary for either bulk crystal growth or of epitaxial films for usable devices. As in the experiments described in the previous paragraph, gradient transport of dissolved nitrogen was used to produce supersaturation. A comparison was made between growth at the bottom and top of the melt, by reversing the temperature gradient in the latter series so that the substrate was always in the cooler region. The temperature gradient across the vertical crucible was in the range 20–70 K cm<sup>-1</sup> and the authors reported a large horizontal temperature gradient. Growth on sapphire was observed to be polycrystalline near the center of the substrate. Similar results were seen when the sapphire was first coated with a thin layer of GaN using MOCVD. The conductivity of the material grown under pressure contained native donors at around  $5 \times 10^{19}$  cm<sup>-3</sup>. The etch pit density was around  $10^{19}$  cm<sup>-2</sup> in the MOCVD layer and an order of magnitude lower in the pressure-grown material. The growth rate was higher using the reverse gradient, with the substrate at the top of the melt. On SiC the deposit cracked and was in the form of small grains about 0.1 mm across and misoriented by a few minutes. In every case, the growth rate could not exceed about 1 μm h<sup>-1</sup> otherwise there

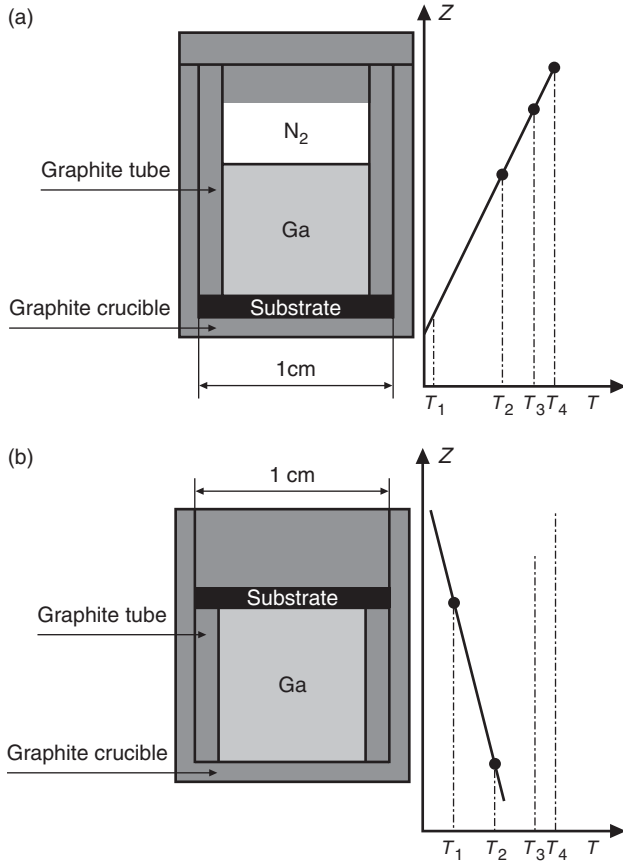


**Figure 7.6** Schematic arrangement for growth of GaN in a positive (a) or negative (b) vertical temperature gradient. The nitrogen can be supplied from a solid source such as polycrystalline GaN or supplied continuously from the vapor phase. Reprinted from *J. Cryst. Growth*, **270**, M. Bockowski *et al.*, 409, Copyright (2004), with permission from Elsevier

was a major increase in defects. Similarly, the morphology deteriorated if the thickness of the deposit exceeded about 100 μm. In general, much work is still needed before high pressure growth can be considered a viable challenger for large scale development. The most promising observation in this study was regions of dislocation density  $5 \times 10^7 \text{ cm}^{-2}$  on SiC, but lower values are needed for technical applications.

Morishita *et al.* (Morishita *et al.*, 2005) and Kawahara *et al.* (Kawahara *et al.*, 2005) used a sodium/gallium solvent to study deposition on a sapphire substrate with a GaN coating deposited by MOCVD. The use of a medium–high nitrogen pressure of 50 atm necessitated the use of a small crucible, in this case an alumina crucible 9 mm in diameter and 50 mm tall. The addition of 4% ammonia to the nitrogen allowed the pressure to be reduced to 2.5–3 MPa, and the addition of 10 mol % Ca to the flux allowed the threshold pressure for synthesizing GaN to be reduced further to about 1 MPa. Deposition occurred at 850 °C for 96 h. A significant advance over previous experiments was that these authors were able to estimate the supersaturation. The solubility of GaN in the 27 at. % Ga/73 at.

% Na solvent was determined to be 0.11 % at 800 °C and 0.23 % at 850 °C. Experiments were conducted to deposit GaN layers in three regions of supersaturation: 36–65 %, 65–85 % and 85–148 %. The variation of growth rate with supersaturation could not be established quantitatively because of spontaneous nucleation around the surface of the solution. However it was found that no deposition occurred below 30 % supersaturation, a high value for most epilayer deposition. As expected, the highest quality films grew in the lowest supersaturation range. The dislocation density in the 850 °C crystals was in the range  $5 - 11 \times 10^4 \text{ cm}^{-2}$ , significantly lower than the value of  $8 \times 10^6 \text{ cm}^{-2}$  in the substrates. The detailed growth mechanism leading to the reduction in dislocation density was not established. Growth at intermediate and high supersaturation exhibited hopper growth characteristic of a high supersaturation gradient across the face of the substrate. The layers deposited were transparent, in contrast to deposits at 800 °C that were always black. The coloration was ascribed to native donors. Photoluminescence and reflection spectra (Omae *et al.*, 2004) showed about 100 times higher integrated intensities of LPE-grown GaN than MOCVD-grown GaN. The relatively low dislocation density under the best conditions and the optical data are promising for further development of LPE for GaN.

## 7.6 CUBIC GaN

The zinc blende  $\beta$ -GaN is reported to be the thermodynamically metastable phase of GaN which, in analogy with other cubic III-V semiconductors, is hoped to be more amenable to doping (Lei *et al.*, 1991) and to be more suitable for fabrication of laser cavities than  $\alpha$ -GaN. Furthermore, the epitaxial growth by MBE on Si (Lei *et al.*, 1991), GaAs (Mizuta *et al.*, 1986) and  $\beta$ -SiC (Paisley *et al.*, 1989) opens the possibilities of integrated device structures of nitride with conventional semiconductors. Also MgO has been used as substrate for MBE growth of cubic GaN (Powell *et al.*, 1993). The dependence of optical properties on sample morphology was studied by Godlewski *et al.* (Godlewski *et al.*, 1998), whereas blue LEDs from cubic GaN were reported by Yang *et al.* (Yang *et al.*, 2000). Here the question is whether cubic GaN is really a metastable phase in which case it would be difficult to grow by LPE as a near-equilibrium growth process, or whether  $\beta$ -GaN is a low-temperature phase which could be grown by LPE at low temperatures.

## 7.7 CONCLUSIONS AND OUTLOOK

LPE of GaN has been demonstrated in several laboratories to achieve layers of high structural perfection and best surface flatness, i.e. with large distance between growth steps indicating the Frank–van der Merwe layer-by-layer growth mechanism which one would not expect in VPE due to the large thermodynamic driving force in MOCVD and MBE. However, significant developments are required to develop LPE as a mass fabrication process for nitride-based optoelectronic and microelectronic devices which one would expect because LPE eventually will become the most economic and ecologic production method for all nitride structures since thermodynamics allows growth by a near-equilibrium process. However, LPE cannot be used for growing compositions in the

GaN-InN-AlN system which show immiscibility. Also, it will not be possible to grow by LPE small lateral structures of less than 1  $\mu\text{m}$  dimension, whereas by LPE extremely thin layers, even monolayers and superlattices, can be grown by proper technological development.

Progress in LPE of nitrides has been slow due to the challenging problems which can be solved only by data and experience in crystal growth from high-temperature solutions and the ability to optimize complex processes. In contrast, epitaxy from the vapor phase by MOCVD and MBE is quite advanced due to the availability of commercial equipment and the comparatively simple processes, even for mass production of nitride-based LEDs and lasers.

The greatest challenges in LPE of nitrides are the low solubility at ambient pressure and the substrate problem. Optimum solvents have to be found and the solubilities determined, and economic substrates for homoepitaxy must be developed. The latter problem can be reduced if nitride solid-solutions suitable for applications and fitting commercial substrates like SiC with respect to misfit and thermal expansion difference can be developed. Eventually, solid-solution substrates will be needed for LPE of nitrides.

The first large-scale application of LPE is expected for the overgrowth of HVPE-grown GaN substrates to cover micropipe defects and to reduce dislocations and stacking faults by several orders of magnitude, in order to achieve highest-quality GaN surfaces for fabrication of highest-performance devices. A modification of a slider-free LPE process (Scheel, 1977) adapted for VLS growth may be developed for mass production. Another expected application of LPE of nitrides will prevent the formation and multiplication of dislocations after an ELO step in device fabrication, thus leading to a combination of epitaxy from the vapor phase and from the liquid phase.

## REFERENCES

- H. Amano, M. Kito, K. Hiramatsu and I. Akasaki, *Jpn. J. Appl. Phys.* **28** (1989) L2112.  
M. Aoki and T. Ogino, *Oyo Butsuri* **48** (1979) 269.  
D.J. As, D. Schikora, A. Greiner, M. Luebbbers, J. Mimkes and K. Lischka, *Phys. Rev.* **B54** (1996) R11118.  
J.H. Basson and C.A.B. Ball, *Phys. Status Solidi A* **46** (1978) 707.  
D. Battat, M.M. Faktor and M.A. Savva, *Chem. Ind.* (16 March 1974) 263.  
M. Bockowski, I. Grzegory, S. Krukowski, B. Lucznik, M. Wroblewski, G. Kamler, J. Borysiuk, P. Kwatiakowski, K. Jasik and S. Porowski, *J. Cryst. Growth* **270** (2004) 409.  
H. Booyens, J.S. Vermaak and G.R. Porto, *J. Appl. Phys.* **49** (1978) 1149, 3272.  
A. Chakroborty *et al.*, *Jpn. J. Appl. Phys.* **45** (2006) 739.  
C.H. Chen, S.A. Stockman, M.J. Peanasky and C.P. Kuo, in *Semiconductors and Semimetals*, editors G.B. Stringfellow and M.G. Craford, Academic Press, San (1997) Diego 97.  
A.A. Chernov and H.J. Scheel, *J. Cryst. Growth* **149** (1995) 187.  
H.F. Coward and G.W. Jones, *Limits of Flammability of Gases and Vapors*, Bulletin 503, Bureau of Mines, US Government Printing Office, Washington (1952).  
M.G. Craford, *IEEE Circuit Devices* **8** (1992) 25.  
M.G. Craford, *MRS Bull.* (2000) 27.  
R.F. Davis, *IEEE Proc.* **79** (1991) 702.  
R.F. Davis, *Overview of Growth, Characterization and Device Development in Large Bandgap Semiconductor Thin Films*, Lecture Notes from Troisieme Cycle, M.D. Reymond, Universite de Lausanne (1992) 2–3, 86–87.

- R. Dingle, K.L. Shaklee, R.F. Leheny and R.B. Zetterstrom, *Appl. Phys. Lett.* **19** (1971) 5.
- M. Dudley, X.R. Huang, W. Huang, A. Powell, S. Wang, P. Neudeck and M. Skowronski, *Appl. Phys. Lett.* **75** (1999) 784.
- J.S. Dyck, K. Kash, M.T. Grossner, C.C. Hayman, A. Argoitia, N. Yang, M.-H. Hong, M.E. Kordesch and J.C. Angus, *MRS Internet J. Nitride Semicond. Res.* **4S1** (1999) G3.23.
- D. Elwell and H.J. Scheel, *Crystal Growth from High-temperature Solutions*, Academic Press, London (1975) Ch. 6.
- D. Elwell, R.S. Feigelson, M.M. Sunkins and W.A. Tiller, *J. Cryst. Growth* **66** (1984) 45.
- B.N. Feigelson and R.L. Henry, *J. Cryst. Growth* **281** (2005) 5.
- Z.C. Feng (ed.) *III-Nitride Semiconductor Materials*, Imperial College Press, Cambridge (2006) 1–40.
- H. Fujii, C. Kisielowski, J. Krueger, M.S.H. Leung, R. Klockenbrink, M. Rubin and E.R. Weber, *Mater. Res. Soc. Symp. Proc.* **449** (1997) 227.
- M. Godlewski, E.M. Goldys, M.R. Philips, J.P. Bergman, B. Monemar, R. Langer and A. Barski, *MRS Internet J. Nitride Semicond. Res.* **3** (1998) 1.
- I. Grzegory, M. Bockowski, B. Lucznik, S. Krukowski, Z. Romanowski, M. Wroblewski and S. Porowski, *J. Cryst. Growth* **246** (2002) 177.
- E.S. Hellman (1996) <http://nsr.mij.mrs.org/discussions/substrates/>
- K. Hiramatsu, Y. Kawaguchi, M. Shimizu, N. Sawaki, T. Zheleva, R.F. Davis, H. Tsuda, W. Taki, N. Kuwano and K. Oki, *MRS Internet J. Nitride Semicond. Res.* **2** (1997) 6.
- M. Ilegems, *J. Cryst. Growth* **13/14** (1972) 360.
- T. Ishii, Y. Tazoh and S. Miyazawa, *Jpn. J. Appl. Phys.* **36** (1997) L139.
- N. Itoh, J.C. Rhee, T. Kawabata and S. Koike, *J. Appl. Phys.* **58** (1985) 1828.
- T. Iwahashi, F. Kawamura, M. Morishita, Y. Kai, M. Yoshimura, Y. Mori and T. Sasaki, *J. Cryst. Growth* **253** (2003) 1.
- W.A. Jesser and D. Kuhlmann-Wilsdorf, *Phys. Status Solidi* **19** (1967) 95.
- W.A. Jesser and J.W. Matthews, *Philos. Mag.* **15** (1967) 1097.
- E.O. Johnson, *RCA Rev.* **26** (1965) 163.
- W.C. Johnson, J.B. Parsons and M.C. Crew, *J. Phys. Chem.* **36** (1932) 2651.
- R. Juza, H. Jacobs and H. Gerke, *Ber. Bunsen-Ges. Phys. Chem.* **70** (1966) 1103.
- H. Kan, M. Ishii and W. Susaki, *Jpn. J. Appl. Phys.* **16** (1977) Suppl. 16-1, 461.
- J. Kang and T. Ogawa, *J. Mater. Res.* **14** (1999) 1.
- J. Karpinski, J. Jun and S. Porowski, *J. Cryst. Growth* **66** (1984) 1.
- M. Kawahara *et al.* *J. Caram. Process. Res.* **6** (2005) 146.
- F. Kawamura, M. Morishita, K. Omae, M. Yoshimura, Y. Mori and T. Sasaki, *J. Mater. Sci. Mater. in Electron.* **16** (2005) 29.
- R.W. Keyes, *Proc. IEEE* **60** (1972) 225.
- C. Klemenz and H.J. Scheel, *J. Cryst. Growth* **211** (2000) 62.
- P. Kung, C.J. Sun, A. Saxler, H. Ohsato and M. Razeghi, *J. Appl. Phys.* **75** (1994) 4515.
- T. Lei, M. Fanciuli, R.J. Molnar, T.D. Moustakas, R.J. Graham and J. Scanlon, *Appl. Phys. Lett.* **59** (1991) 944.
- T. Lei, T.D. Moustakas, R.J. Graham, Y. He and S.J. Berkowitz, *J. Appl. Phys.* **71** (1992) 4933.
- S.D. Lester, F.A. Ponce, M.G. Craford and D.A. Steigerwald, *Appl. Phys. Lett.* **66** (1995) 1249.
- R.A. Logan and C.D. Thurmond, *J. Electrochem. Soc.* **119** (1972) 1727.
- M.R. Lorenz and B.B. Binkowski *J. Electrochem. Soc.* **109** (1962) 24.
- L.D. Lucas, *Tech. Ing. Paris* **67** (1984) M65.
- R. Madar, G. Jacob, J. Hallais and R. Fruchart, *J. Cryst. Growth* **31** (1975) 197.
- H.M. Manasevit, F.M. Erdmann and W.I. Simpson, *J. Electrochem. Soc.* **118** (1971) 1864.
- H.P. Maruska and J.J. Tietjen, *Appl. Phys. Lett.* **15** (1969) 327.
- J.W. Matthews (ed.) in *Epitaxial Growth*, Parts A and B, Academic Press, New York (1975).
- J.W. Matthews, in *Dislocations in Solids*, Vol. 7, editor F.R.N. Nabarro, North-Holland, Amsterdam (1979) 461.



- T. Matsuoka, in *Advanced Materials in Electronics*, editor Quixin Guo, Research Signpost, Trivandrum, Kerala, India (2004) 45.
- R. Metzger, *Compound Semicond.* **12** (August 2006) 20.
- S. Miyazawa *et al.*, *IEEE Trans. Electron Devices* **ED-33** (1986) 227.
- M. Mizuta, S. Fujieda, Y. Matsumoto and T. Kawamura, *Jpn. J. Appl. Phys.* **25** (1986) L945.
- M. Morishita, F. Kawamura, M. Kawahara, M. Yoshimura, Y. Mori and T. Sasaki, *J. Cryst. Growth* **284** (2005) 91.
- H. Morkoc, S. Strite, G.B. Gao, M.E. Lin, B. Sverdlov and M.J. Burns, *J. Appl. Phys.* **76** (1994) 1363.
- M. Mueller, M. Bickermann, D. Hofmann, A.-D. Weber and A. Winnacker, *Mater. Sci. Forum* **264–268** (1998) 69.
- M. Nagahara, S. Miyoshi, H. Yagushi, K. Onabe, Y. Shiraki and R. Ito, *J. Cryst. Growth* **145** (1994) 197.
- S. Nakamura, T. Mukai, M. Senoh and N. Iwasa, *Jpn. J. Appl. Phys.* **31** (1992) L139.
- S. Nakamura, T. Mukai and M. Senoh, *Appl. Phys. Lett.* **64** (1994a) 1687.
- S. Nakamura, T. Mukai and M. Senoh, *J. Appl. Phys.* **76** (1994b) 8189.
- S. Nakamura, M. Senoh, N. Iwasa and S. Nagahama, *Jpn. J. Appl. Phys.* **34** (1995) L797.
- K. Naniwae, S. Itoh, H. Amano, K. Itoh, K. Hiramatsu and I. Akasaki, *J. Cryst. Growth* **99** (1990) 381.
- J. Napierala, D. Martin, N. Grandjean and M. Ilegems, *J. Cryst. Growth* **289** (2006) 445.
- P.G. Naudeck, *J. Electron. Mater.* **24** (1995) 283.
- N. Newman, *Electrochem. Soc. Proc.* **96–11** (1996) 1.
- T. Ohta, T. Yamada, H. Yamane, H. Iwata and S. Sarayama, 15th International Conference on Ternary and Multinary Compounds, March 6–10, 2006, Kyoto, Japan.
- K. Omae, T. Iwahashi, F. Kawamura, M. Yoshimura, Y. Mori and T. Sasaki, *Jpn. J. Appl. Phys.* **43** (2004) L173.
- M. Otsubo, K. Segawa and H. Miki, *Jpn. J. Appl. Phys.* **12** (1973) 797.
- M.J. Paisley, Z. Sitar, J.B. Posthill and R.F. Davis, *J. Vacuum Sci. Technol.* **A7** (1989) 701.
- J.I. Pankove, E.A. Miller and J.E. Berkeyheiser, *RCA Rev.* **32** (1971) 383.
- R. Paszkiewicz, B. Paszkiewicz, R. Korbutowicz, J. Kozlowski, M. Tlaczala, L. Bryja, R. Kudrawiec and J. Misiewicz, *Cryst. Res. Technol.* **36** (2001) 971.
- I.G. Pichugin and D.A. Yaskov, *Izv. Akad. Nauk SSSR, Neorg. Mater.* **6** (1970) 1973.
- F.A. Ponce and D.P. Bour, *Nature* **386** (1997) 351.
- R.C. Powell, N.-E. Lee, Y.-W. Kim and J.E. Greene, *J. Appl. Phys.* **73** (1993) 189.
- A. Purdy, *J. Crystal Growth* **281** (2005) 355.
- W. Qian, M. Skowronski, M. De Graef, K. Doverspike, L.B. Rowland and D.K. Gaskill, *Appl. Phys. Lett.* **66** (1995) 1252; **67** (1995) 2284.
- B. Raghathamachar, J. Bai, M. Dudley, R. Dalmau, D. Zhuang, Z. Herro, R. Schlessler, Z. Sitar, B. Wang, M. Callahan, K. Rakes, P. Konkapaka and M. Spencer, *J. Cryst. Growth* **287** (2006) 349.
- S.V. Rendakova, I.P. Nikitina, A.S. Tregubova and V.A. Dmitriev, *J. Electron. Mater.* **27** (1998) 292.
- G.S. Rohrer, J. Payne, W. Qian, M. Skowronski, K. Doverspike, L.B. Rowland and D.K. Gaskill, *Mater. Res. Soc. Symp. Proc.* **395** (1996) 381.
- J. Ross and M. Rubin, *Mater. Lett.* **12** (1991) 215.
- T. Sasaki and T. Matsuoka, *J. Appl. Phys.* **64** (1988) 4531.
- T. Sasaki, T. Matsuoka and A. Katsui, *Appl. Surf. Sci.* **41/42** (1989) 504.
- J. Satterly and E.F. Burton, *Trans. Royal Soc. Canada* **13** (1919) 211.
- H.J. Scheel, *J. Cryst. Growth* **42** (1977) 301.
- H.J. Scheel, *Appl. Phys. Lett.* **37** (1980) 70.
- H.J. Scheel, *Inert Working Atmospheres*, American Association for Crystal Growth Workshop, May 14–17, 1985, Pajaro Dunes/Watsonville, CA, USA.

- H.J. Scheel, in *Crystal Growth Technology*, editors H.J. Scheel and T. Fukuda, John Wiley & Sons, Ltd, Chichester (2003) Ch. 28.
- H.J. Scheel, *J. Cryst. Growth* **287** (2006) 214.
- H.J. Scheel and C. Klemen, *Electrochem. Soc. Proc.* **96-11** (1996) 20.
- H.J. Scheel, G. Binnig and H. Rohrer, *J. Cryst. Growth* **60** (1982) 199.
- W. Seifert, H.-G. Bruehl and G. Fitzl, *Phys. Status Solidi A* **61** (1980) 493.
- R.J. Sime and J.L. Margrave, *J. Phys. Chem.* **60** (1956) 810.
- Y.T. Song, X.L. Chen, W.J. Wang, W.X. Yuan, Y.G. Cao X. and Wu, *J. Cryst. Growth* **260** (2004) 327.
- G.B. Stringfellow, *J. Cryst. Growth* **115** (1991) 1.
- Y. Sugita, M. Tamura and K. Sugawara, *J. Appl. Phys.* **14** (1973) 3442.
- C.D. Thurmond and R.A. Logan, *J. Electrochem. Soc.* **119** (1972) 622.
- T. Ujihara, S. Munetoh, K. Kusunoki, K. Kamei, N. Usami, K. Fujiwara, G. Sazaki and K. Nakajima, *Mater. Sci. Forum* **457-460** (2004) 633
- T. Ujihara, S. Munetoh, K. Kusunoki, K. Kamei, N. Usami, K. Fujiwara, G. Sazaki and K. Nakajima, *Thin Solid Films* **476** (2005) 206.
- J.A. Van Vechten, *Phys. Rev.* **B 7** (1973) 1479.
- R.S. Wagner and W.C. Ellis, *Appl. Phys. Lett.* **4** (1964) 89.
- R. Yakimova, M. Tuominen, A.S. Bakin, J.-O. Fornell, A. Vehanen and E. Janzen, *Inst. Phys. Conf. Ser.* **142** (1996) 101.
- R. Yakimova, M. Syvaejaervi, S. Rendakova, V.A. Dmitriev, A. Henry and E. Janzen, *Mater. Sci. Forum* **338-342** (2000) 237.
- H. Yamane, M. Shimada, S.J. Clarke and F.J. DiSalvo, *Chem. Mater.* **9** (1997) 413.
- H. Yang, S.M. Zhang, L.M. Zheng, D.P. Xu, D.G. Zhao and S.F. Li, *First Joint Symposium on Opto- and Microelectronic Devices and Circuits*, April 10-15, 2000, Nanjing, China.
- S. Yoshida, S. Misawa and S. Gonda, *Appl. Phys. Lett.* **42** (1983) 427.
- R.B. Zetterstrom, *J. Mater. Sci.* **5** (1970) 1102.
- X.B. Zhou and J.Th.M. De Hosson, *J. Mater. Res.* **10** (1995) 1984.



# 8 Liquid Phase Epitaxy of Quantum Wells and Quantum Dots

A. KRIER, X.L. HUANG AND Z. LABADI

*Physics Department, Lancaster University, Lancaster LA1 4YB, UK*

---

8.1 Introduction	227
8.2 LPE growth of quantum wells	228
8.3 Thickness of rapid slider LPE layers	231
8.4 Interface abruptness	235
8.5 Compositional homogeneity	236
8.6 Devices incorporating ultrathin LPE layers	237
8.7 LPE growth of InAs quantum wells	239
8.7.1 PL characterisation	241
8.8 LPE growth of quantum dots for mid-infrared optoelectronic devices	243
8.8.1 InSb QDs on GaAs (100) substrates	244
8.8.2 Investigation of InAsSb QDs	247
8.9 Mid-infrared luminescence of encapsulated InAsSb QDs	249
8.10 Electroluminescence of InAsSb QD LEDs	251
8.11 Summary	253
Acknowledgements	253
References	254

---

## 8.1 INTRODUCTION

It is generally accepted that liquid phase epitaxy (LPE), which is an equilibrium growth technique, produces epitaxial material of the highest crystalline perfection containing few point defects and impurities and is therefore well suited to the fabrication of optoelectronic devices. The main arguments against conventional LPE are: nonuniformity in layer thickness, inability to grow abrupt junctions or interfaces because of intermixing or cross-diffusion effects, and the fast initial growth rate which results in poor reproducibility for thin layer epitaxy. Growth techniques such as molecular beam epitaxy (MBE) and metal-organic vapour phase epitaxy (MOVPE) which have superior thickness control are now extensively used for the growth of quantum well lasers and a variety of other optoelectronic devices. However, it is also possible to use LPE to grow multilayer III-V structures

which exhibit quantum size effects [1–17] and with appropriate modifications LPE can be successfully employed to grow quantum well heterostructure lasers containing quaternary III-V layers [3–7]. We also note that it is possible to grow chemically abrupt interfaces by LPE [11–14] and that quantum wells as thin as 20 Å have been successfully prepared [12, 17]. In this chapter the growth of ultrathin layers from the liquid phase will be considered and in particular with respect to their potential use in mid-infrared optoelectronic devices.

## 8.2 LPE GROWTH OF QUANTUM WELLS

The combination of high quality epitaxial layers and the advantages afforded by quantum well structures is surely very attractive for optoelectronic device applications. However, for the growth of quantum well structures, precise thickness control is of paramount importance, and a high growth rate is not advantageous. Nevertheless, by careful control of the supersaturation it is certainly possible to grow ultra-thin or quantum well layers using conventional LPE. For example, Becher *et al.* [18] demonstrated the growth of  $\text{In}_{0.88}\text{Ga}_{0.12}\text{As}_{0.26}\text{P}_{0.74}$  ( $\lambda_g = 1.05 \mu\text{m}$ ) single quantum wells lattice-matched to InP with thicknesses in the range 30–200 Å. Low temperature photoluminescence and transmission electron microscopy (TEM) measurements are effective characterisation tools for such structures and have been effectively used to confirm the thickness and quality of the resulting quantum wells [18]. Another approach is to exploit the difference in growth rates between homo- and heteroepitaxy. Homoepitaxy usually proceeds through tangential movement of growth steps across the surface and does not rely on the formation of nuclei to produce the first layer. However, because heteroepitaxy does require the formation of small nuclei, a high initial supersaturation is needed until the first continuous layer is formed. So, for a given melt supersaturation, homoepitaxy will proceed at a much greater rate than heteroepitaxy. This leads to the technique of ‘reversed mass transport’, where two substrates are arranged together, an auxiliary (reversing) GaAs substrate being placed in parallel with the AlGaAs substrate onto which the ultrathin layer of GaAs is to be grown. A thin (30–50  $\mu\text{m}$ ) capillary layer of melt is introduced and growth ensues such that the supersaturation becomes zero just as the growth of the thin layer ends. The technique has not been widely adopted but has been successfully used to grow thin layers of GaAs on AlGaAs [19].

Although careful control of the supersaturation can yield ultrathin LPE layers this can be difficult to achieve in practice. Consequently alternative techniques have been devised, primarily by using very short growth periods, of the order of milliseconds. Instead of allowing the substrate and melt solution to remain in contact for several seconds (or minutes) the melt solution is quickly passed over the substrate, (giving rise to the term ‘rapid slider’ LPE). In order to achieve this the conventional graphite boat geometry needs to be modified accordingly and various designs have been employed. Using a cylindrical revolving boat as shown in Figure 8.1, it is possible to achieve short growth times (9–100 ms) and grow InGaAsP multilayers [4–7] with a layer thickness of typically 100 Å for use in InP based lasers (see below). This geometry has also been very successfully used for the growth of AlGaAs/GaAs quantum wells [14, 20]. Similarly, a centrifugal LPE technique for the growth of AlGaAs/GaAs and modulation doped GaAs semiconductor structures with precisely defined unperturbed surface morphology has been developed for fundamental investigation of interface abruptness and transition layer thickness [21].

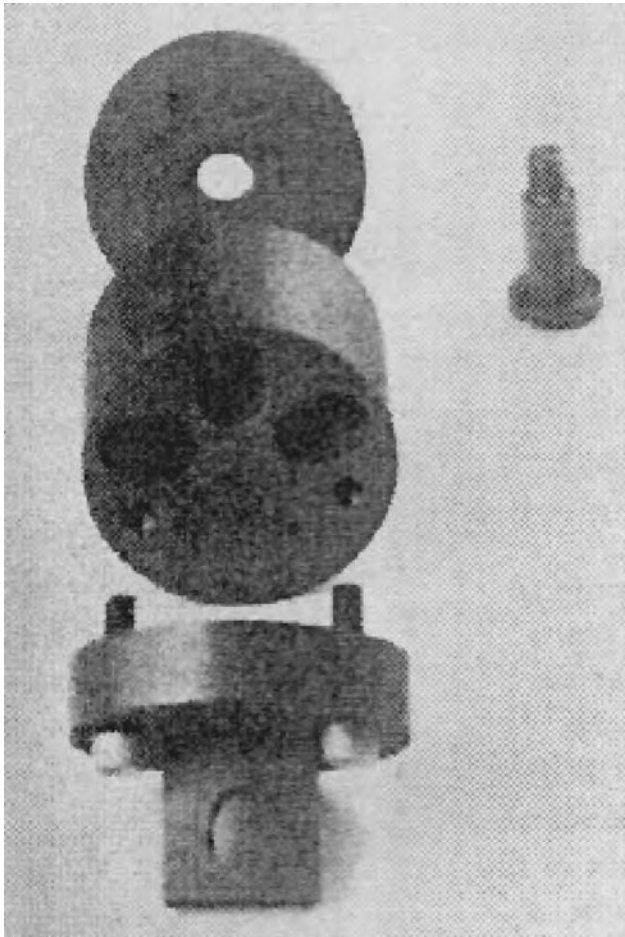


**Figure 8.1** The cylindrical-slider graphite boat (2.5 cm in diameter) used for multilayer LPE growth of ultrathin  $\text{In}_{1-x}\text{Ga}_x\text{As}_y\text{P}_{1-y}$  epitaxial layers. After Holonyak *et al.* [6]. Reproduced from [6] by permission of the American Institute of Physics

Linear sliding boats have also been successfully employed for the growth of InGaAsP/InP [16,22], AlGaAs/GaAs [11] and more recently for InAsSb/InAs [23]. These types of rapid slider graphite boat are of the ‘moving substrate’ type, since rapid movements of the solutions (as in a ‘moving melt’ boat) would result in melt splashing into the worktube, or nonuniform melt contact with the substrate. Low friction is essential since any sticking or judder can cause ripples in the resulting epilayers. During operation the graphite slider is essentially pushed along such that the substrate makes contact with each of the growth melts in turn until the desired number of epitaxial layers is deposited on the substrate wafer. The rapid movement of the substrate is normally achieved by using a computer-controlled motor. The contact time for growth is made very short by the combination of a narrow slit ( $\sim 1$  mm) in the graphite chamber containing the melt and a high slider speed ( $\sim 1$  m s $^{-1}$ ) provided by the (linear) motor. This essentially results in a wiping action of the melt across the substrate surface. Figure 8.2 shows a schematic

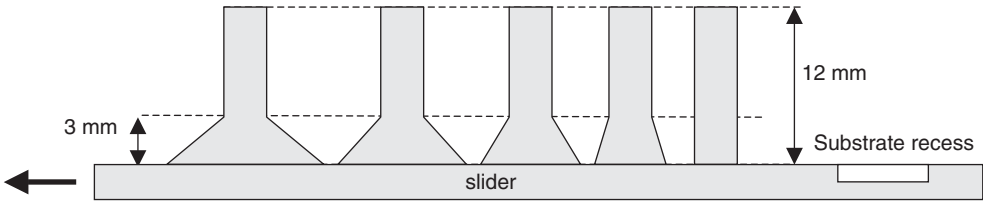


**Figure 8.2** Cross-section of a linear rapid slider boat, showing the sidewalls with knife-edges, which together can form an adjustable slit of dimensions 1–6 mm when pressed into the graphite carriage. Straight sidewalls were used to create wide melt chambers for epitaxy of thicker layers in the usual manner

cross-section of the linear rapid slider boat used in our laboratory. The complete boat is shown in Figure 8.3 together with the removable sidewalls, which were employed to form the slit in the melt chamber. The sidewalls have carefully machined knife-edges and were engineered to be a tight resistance fit into the main body of the boat so that they remained held in place during the growth run. Appropriate pairs of sidewalls are selected to obtain the required slit dimensions corresponding to the desired structure to be grown. Straight sidewalls (without knife edges) were used to form chambers for growth of conventional bulk, cladding or buffer layers in devices. One advantage of this arrangement is that both quantum wells and thick layers can be grown together in a single growth run within a short time interval. Owing to the high growth rate of LPE ( $\sim 1 \mu\text{m min}^{-1}$ ) compared with MBE ( $1 \mu\text{m h}^{-1}$ ) a complete quantum well laser with thick cladding layers could be grown in a few minutes rather than several hours. The knife-edges were used to reduce the melt carry-over, which is particularly important when producing multi-layer structures requiring abrupt interfaces [24]. The boat was capable of producing both high quality bulk and ultrathin layers.

More sophisticated boat geometries, such as the meander type developed by Nohavica and Teminova have also been used to grow multi-quantum well (MQW) devices [22,

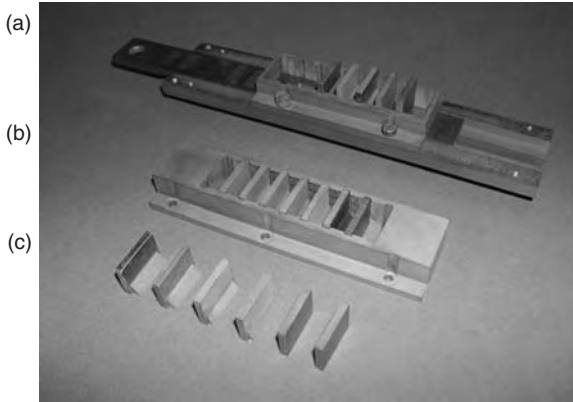


**Figure 8.3** Rapid slider linear graphite boat: (a) fully assembled with sidewalls fitted; (b) showing alternative melt container with sidewalls fitted; and (c) sidewalls removed showing different knife-edges for adjustable 1–6 mm slit widths

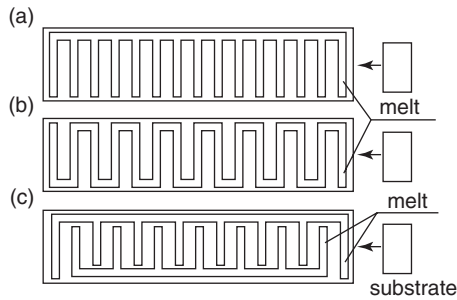


**Figure 8.4** Plan views of meander type boats: (a) and (b) are for the growth of single composition structures; and (c) is for the growth of alternate layers of two different compositions. After Nohavica and Oswald [24, 25]. Reprinted from *J. Cryst. Growth*, **146**, Nohavica and Oswald, Preparation of periodic structures by meander type LPE, 287, Copyright (1995), with permission from Elsevier

24–26]. This type of boat uses a single melt chamber for the growth of a number of layers of the same composition, and has the advantage that the relative motion of the melt/substrate is in one direction only (no push–pull motion is necessary) and also that multiple layers can be grown from a single melt. Results using this arrangement have shown that a thick layer of InP composed from 31 successive thin layers grown in this manner did not show any degradation of electrical or optical properties [22]. Examples of the meander type boats are shown in Figure 8.4 for the growth of single and two composition structures. Further modifications [24, 25] enabled the homogenisation of melts *in situ* prior to the growth of a device structure containing conventional bulk epilayers around a MQW structure with three quantum wells and four barrier layers.

### 8.3 THICKNESS OF RAPID SLIDER LPE LAYERS

Due to quantum confinement the effective transition energy in a quantum well heterostructure is strongly dependent on the width of the well. For this reason it is essential to be able to accurately and reproducibly control the layer thickness during epitaxy to produce the required quantum well energy levels. In LPE the thickness of the epilayer is determined by a number of parameters, such as contact time and supersaturation, depending on the growth technique used. Although the step cooling technique has found favour in the growth of multiple thin layers of InGaAsP, because compositional uniformity from one layer to the next was desirable, the near equilibrium growth technique employing very low supercooling ( $\sim 0.1^\circ\text{C}$ ) has been employed to grow single layers of InGaAsP [27] and (Al,Ga)As [28].

Early work on InGaAsP layers revealed that the thickness dependence on growth time differed from that predicted using diffusion limited theory. However, growth occurring during the first few milliseconds may be considered as transient growth and does not take place in a steady state. Therefore, it is not surprising that the thickness does not depend on time as expected, i.e.  $t^{1/2}$  for step-cooled growth (supercooling) or  $t^{3/2}$  for equilibrium (diffusion-limited) growth using the static model [29]. To investigate this, Rezek *et al.* grew a ‘composite’ sample comprised of nine thin layers of InGaAsP grown sequentially from the same melt solution at constant temperature [7]. A scanning electron microscope



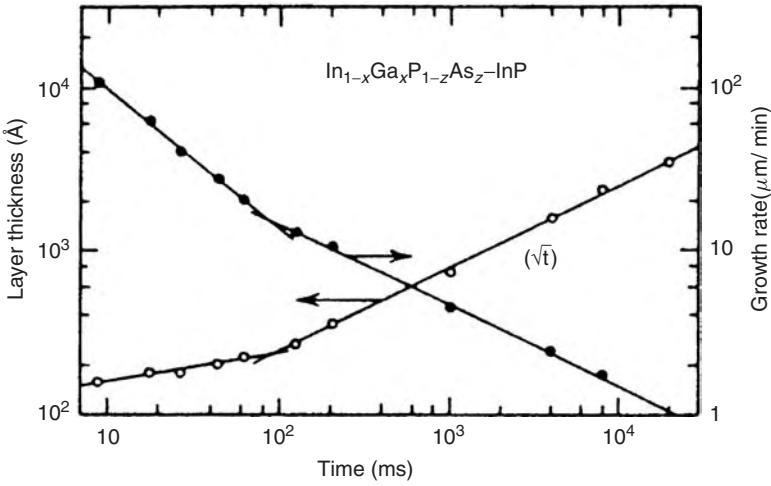


**Figure 8.5** Variation in epilayer thickness and growth rate with contact time for InGaAsP. After Rezek *et al.* [36]. Reproduced from [36] by permission of TMS and IEEE

was used to measure the thickness of the total number of layers in the composite sample and hence the thickness of a single layer was determined. The measured dependence of layer thickness on growth time,  $t$ , is shown in Figure 8.5 and was found to depart significantly from the predicted  $t^{1/2}$  dependence for step-cooled growth for growth times shorter than 200 ms. The growth rate was higher than that predicted by the  $t^{1/2}$  dependence, but became less with increasing contact time. This enhanced initial growth rate has also been observed in the AlGaAs system for near equilibrium growth [28]. Rezek *et al.* proposed that the transient growth rate was either limited by the attachment kinetics of the solutes on the surface, or by the melt flow (convection) arising from the relative motion of the substrate with respect to the solution. There is some evidence for the attachment kinetics argument, since the incorporation of Ga, As and Zn into LPE grown InGaAsP layers on InP was found to be sensitive to the substrate orientation by Antypas and Shen [30]. The fact that the different nucleation sites that are presented by the different crystal orientations influence the solute incorporation may also lend weight to the importance of surface attachment kinetics during the growth process. Rezek *et al.* suggested that the actual time taken to grow the transient layer was much shorter than the shortest measured contact time, so that varying the contact time above some critical value would have little effect.

Inserts of graphite or molybdenum have been used in the melt bin to reduce the contact area between the melt solution and the substrate [16]. However, it was found that melt bins with slit widths of less than 2 mm resulted in discontinuous layer growth if graphite inserts were used, due to the inability of the indium melt to wet the graphite, although slits of 0.4 mm could be tolerated when molybdenum inserts were used instead. To investigate the effect of different melt bin geometries on the growth rate and layer thickness in more detail, Garbuzov *et al.* [1, 2] used straight-sided melt bins of length 1, 3 and 10 mm and a funnel shaped bin, as shown in Figure 8.6. Figure 8.7 shows that for contact times above 10 ms, the growth rate followed the expected diffusion-limited growth model with the usual  $t^{1/2}$  dependence. However, in the short growth time regime ( $<10$  ms), the layer thickness became independent of the contact time. This peculiarity was attributed to a

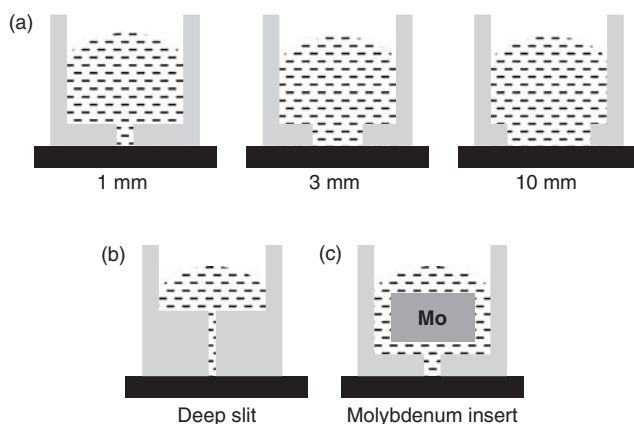


**Figure 8.6** Showing the various melt bin geometries employed by Garbuzov *et al.*: (a) three bins with a slot width of 1, 3 and 10 mm, respectively; (b) a funnel shaped bin; and (c) a bin with a molybdenum insert. After Garbuzov *et al.* [1, 2]. Reprinted from *J. Cryst. Growth*, **110**, Garbuzov *et al.*, On the peculiarities of short time ( $T_g < 10$  ms) solid solution LPE growth onto the moving substrate, 955, Copyright (1991), with permission from Elsevier

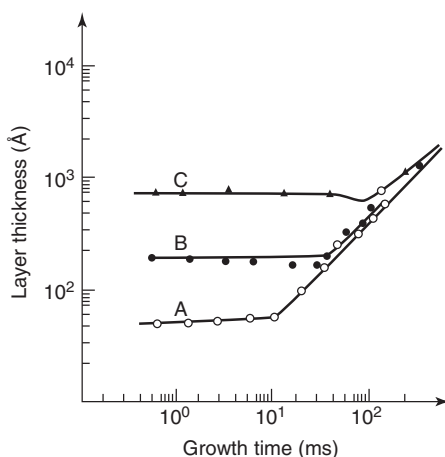


**Figure 8.7** The variation in layer thickness with growth time for samples grown under the same conditions but with melt chambers of different widths (A, 1; B, 3; C, 10 mm). The contact time was maintained constant by compensating with the sliding speed through the melt. After Garbuzov *et al.* [1, 2]. Reprinted from *J. Cryst. Growth*, **110**, Garbuzov *et al.*, On the peculiarities of short time ( $T_g < 10$  ms) solid solution LPE growth onto the moving substrate, 955, Copyright (1991), with permission from Elsevier

melt flow or rolling effect, due to the rapid slider substrate motion, which removes the depleted melt from the growth interface and replaces it with ‘fresh melt’ which has higher supersaturation. The layer thickness was found to increase as the width of the melt bin increased for the rectangular shaped bins. (The contact time was maintained constant by varying the sliding speed accordingly.) Therefore, the dominant factor in determining

the thickness of the epilayer should be the melt flow or rolling caused by movement of the substrate slider, for if surface attachment kinetics were the dominant factor, no difference in thickness would be expected on changing the boat dimensions. By using the melt bin geometries shown in Figure 8.6(b) and (c), with either a funnel shaped bin or a molybdenum insert, the rolling effect of the melt can be suppressed and the layer thickness decreases with the sliding velocity. Thin epitaxial layers down to 3 nm in thickness have been obtained, once again consistent with the diffusion-limited mechanism.

The rolling motion of the melt results not only in replacement of the depleted solution by fresh melt but also in a significant increase of the concentration gradient at the growing surface (compared with the diffusion-limited case) due to the high normal velocity of the melt flowing into the slit. The concentration gradient varies more rapidly along the substrate than at low sliding velocity and as a result the greater part of the layer is deposited in a rather small fraction of the slit width adjacent to the rear wall of the slit. The increase of the concentration gradient with sliding velocity may be sufficient to compensate for the decrease of the growth time, so that the layer thickness should be independent of the sliding speed. In any case it is evident that the increase of the layer thickness with slit width cannot be explained by kinetic growth arguments and is connected with the change of the melt flow structure, namely with the increase of the effective growth area. Assuming that the initial rapid growth may be attributed to a flow mechanism in the melt produced by the movement of the slider, the relation between layer thickness and growth time may be written as:

$$d(t) = d_F(t') + \frac{2T_s}{C_s m} \left(\frac{D}{\pi}\right)^{\frac{1}{2}} (t - t')^{\frac{1}{2}} + \frac{4}{3} \frac{R}{C_s m} \left(\frac{D}{\pi}\right)^{\frac{1}{2}} (t - t')^{\frac{3}{2}} \quad (8.1)$$

where the first term  $d_F$  represents the constant thickness obtained during the time,  $t'$  for which the melt is in motion. The second and third terms represent the usual terms associated with supersaturation and diffusion limited growth in the static case. ( $T_s$  is the supercooling,  $C_s$  is the solute concentration,  $m$  is the slope of the liquidus,  $D$  is the diffusion coefficient and  $R$  is the cooling rate.) Reynolds *et al.* obtained good agreement with experiment for this formula applied to the growth of  $\text{Al}_x\text{Ga}_{1-x}\text{As}$  over a wide range of contact times [28].

The effect of the slider motion on the growth melt has been simulated using a dye in an aqueous solution and a transparent plexiglass boat [31, 32]. Using this method the effect of the crystallisation kinetics is eliminated. It was observed that:

- (1) Slider-induced convection played a major role in the mixing of the melt solution.
- (2) The motion of the melt causes convective mass transfer and the growth rate is enhanced.
- (3) The dynamic behaviour of the convection depends on the speed and the duration of the slider motion.
- (4) The geometry of the melt reservoir affects the pattern of the convection and the time for which it is in operation.
- (5) The convection can persist for several minutes.

- (6) The mass transfer rate is almost independent of the depth of the solution and therefore the mass transfer boundary layer is much smaller than the solution depth.

Lueng and Schumaker [31] used the Péclet number,  $P_e$ , to ascertain the relative importance of convective transport in a gallium melt, with a slider velocity of  $1 \text{ cm s}^{-1}$  moved over a distance of 1 cm. The Péclet number is the ratio of the convective to diffusion mass transport, and is given by  $P_e = UL/D$  (where  $U$  is the characteristic velocity,  $L$  is the characteristic length and  $D$  is the diffusion coefficient), and for the situation described above has a value of 25 400, implying that convective transport is indeed dominant. The convection in the melt was thought to enhance the mixing of the melt solution, bringing the supersaturated solution from the top of the melt to the interface, providing a possible mechanism for the initial rapid growth of thin layers. Furthermore, it was also thought that convection improved the mixing of any carried over melt into the melt solution, so that sharper interfaces were attainable. Brunemeier *et al.* attributed the difference in layer thickness uniformity between samples to the dominance of either laminar or turbulent melt motion [33]. It was suggested that the poor uniformity observed by Reynolds *et al.* [28] in the growth of AlGaAs thin layers using slider velocities of  $\sim 1 \text{ cm s}^{-1}$  was due to laminar melt flow, which may also give rise to compositional inhomogeneity along the layer. The superior thickness uniformity of their InGaAsP layers was attributed to the turbulent nature of the melt solution motion, produced using a slider velocity of  $70 \text{ cm s}^{-1}$ . Lueng and Schumaker used a Reynolds number of  $\sim 3 \times 10^5$  for a rectangular plate moving in a semi-infinite liquid and a kinematic viscosity of  $1.2 \times 10^{-3} \text{ cm}^2 \text{ s}^{-1}$  for gallium at  $800^\circ\text{C}$  to conclude that the flow is laminar, rather than turbulent, for a velocity of  $1 \text{ cm s}^{-1}$ . (The Reynolds number indicates the nature of fluid motion and is the ratio of inertial force to viscous force. It is given by  $Re = UL/v$ , where  $v$  is the kinematic viscosity.) However, some velocities used in the growth of thin layers are up to 500 times higher than that modelled by Lueng and Schumaker and the probability of achieving turbulent flow cannot be discounted.

## 8.4 INTERFACE ABRUPTNESS

One of the reservations about the suitability of the LPE technique for growing very thin layers, is that of poor interface quality. Whilst this is important for all LPE growth, it is of particular interest in the growth of thin layers when the thickness of the epilayers may become comparable with that of the transition region. The extent of the transition region between one epilayer and the next has been investigated by a number of researchers. Feng *et al.* [34] and Cook *et al.* [35] used a combination of Auger spectroscopy and ion beam milling to profile the elemental species through InGaAsP/InP and InGaAsP/GaAs heterojunctions. They estimated the interface widths to be of the order of  $90 \text{ \AA}$  from these measurements but noted that this figure was perhaps more representative of the resolution of the equipment rather than of the actual interface width. Rezek *et al.* suggested that this technique led to an overestimation of the transition layer and used transmission electron microscopy to investigate interface quality, concluding that the transition region may in some cases be of the same order as the lattice constant [36]. This has been substantiated in several material systems: InGaAsP/InP, AlGaAs/GaAs [11] and InGaAsSb/GaSb [37]. Arsent'ev *et al.* [15] reported the growth of InGaAsP wells as thin as  $40 \text{ \AA}$  and deduced that the transition layers were

very thin in comparison with the well width, since the PL emission energies observed were close to those predicted using a rectangular, rather than a parabolic well. Using TEM, Keltling *et al.* [17] observed a transition region of 10 Å in a 70 Å AlGaAs well and Moiseev *et al.* observed a 10–12 Å transition region in an InGaAsSb/GaSb heterojunction [37]. Morlock *et al.* grew narrow GaAs/AlGaAs quantum wells and used photoluminescence lineshape analysis to quantify the thickness as being two to six monolayers with an upper limit of interface roughness of 0.2–0.4 monolayers [12].

There have, however, been some reports of a discrepancy between the transition widths of the two interfaces of a double heterostructure. Auger spectroscopy profiling revealed that in InGaAsP-InP-InGaAsP double heterostructures the width of the transition region was dependent on the lattice mismatch [34] and is related to the speed of nucleation for lattice-matched and mismatched epilayers. For the growth of a mismatched epilayer, the surface energy is increased and nucleation is slow, permitting greater dissolution of the underlying material. The dissolved material contaminates the melt solution resulting in a graded epilayer. However, the grading was not found to be solely dependent on lattice mismatch: reasonably sharp interfaces can be obtained for the growth of a range of InGaAsP quaternaries on InP, but this is not necessarily true for InP on the quaternaries. Further work revealed that the grading also occurs in lattice-matched systems under certain circumstances: a lattice-matched InGaAsP-InGaAs-InGaAsP heterostructure exhibited greater grading at the InGaAsP on InGaAs interface than for that of InGaAs on InGaAsP. The general conclusion from the work of Feng *et al.* [34] and Cook *et al.* [35] was that there was significant dissolution of a layer if it had a higher arsenic concentration than the subsequent layer to be deposited. Later work by Arsent'ev *et al.* supported this conclusion to some extent, but proposed that a refinement was necessary to explain the complete absence of etch back in the growth of  $\text{In}_{0.2}\text{Ga}_{0.8}\text{As}_{0.6}\text{P}_{0.4}/\text{In}_{0.49}\text{Ga}_{0.51}\text{P}$  double heterostructures on  $\langle 111 \rangle$  GaAs substrates [15]. Meanwhile, Becher *et al.* were successful in growing InGaAsP wells as thin as 50 Å on InP, but the samples exhibited low photoluminescence intensities and large FWHM values [18]. It was thought these features were produced as a result of wide transition regions between the InGaAsP and InP layers [38]. Significant improvements in both the intensity and FWHM were observed after substituting the InP cladding layers for those of a high bandgap InGaAsP quaternary, grown with a high supercooling in order to enhance nucleation. Double heterostructures in the AlGaAs system have also exhibited some asymmetry in their transition widths [39]. A transition width of less than 10 Å was observed at one  $\text{Al}_{0.35}\text{Ga}_{0.65}\text{As}/\text{Al}_{0.05}\text{Ga}_{0.95}\text{As}$  interface compared with a width of 30–50 Å at the inverted interface. The increased width in this case was thought to arise from the 'wavy' interface caused by a nonuniform arrival of Al and As atoms at the interface in the high Al content melt.

## 8.5 COMPOSITIONAL HOMOGENEITY

Rezek *et al.* used Auger spectroscopy to study the homogeneity of a thin InGaAsP epilayer and found that away from the interface regions the In, Ga, As and P counts were unchanged throughout the layer, indicating that the layer was homogeneous [36]. However, the photoluminescence from a thick sample and a stack of thin layers grown from an identical melt exhibited different peak wavelengths. The thick sample exhibited a peak at 1.06 μm at low excitation, whereas the composite sample exhibited a peak at 1.075 μm

and at high excitation the bulk sample exhibited both peaks. The difference in peak wavelengths was attributed to the layers being of different composition. i.e. the compositions resulting from transient growth and from diffusion limited growth were different. The effects of transient growth are not normally observed because this region is very thin compared with the remainder of the epitaxial layer, but the composite sample used by Rezek *et al.* consisted of a stack of 18 such transient growth layers. Brunemeier *et al.* also observed and analysed the transient growth and consequent gradient in the InGaAsP composition [33]. They interpreted this as a fundamental result of the highly nonequilibrium nature of the first few milliseconds of the LPE growth which leads to layers of significantly different lattice constant and energy gap than expected from diffusion-limited growth. The change in PL peak wavelength alone cannot be used to determine the composition of the thin layer of quaternary. Brunemeier *et al.* [33] used a combination of the PL peak wavelength and the lattice constant determined from X-ray analysis to calculate the composition of the active layer. They studied different compositions of GaInAsP lattice matched to InP, and concluded that transient growth favoured the incorporation of the larger size, band gap lowering species, i.e. indium was incorporated preferentially over gallium and arsenic over phosphorus. This effect has also been observed in the GaInAsSb/InAs system where the interface region is heavily In- and Sb-rich [37].

Despite the transient growth taking place under nonequilibrium conditions, the layer homogeneity and crystalline quality can be as good as, if not better than, that of diffusion-limited conventionally grown samples. Rezek *et al.* [36] reported a full width at half-maximum (FWHM) of 25 meV in low temperature photoluminescence (PL) for a 'composite' sample of InGaAsP thin layers compared with a value of 33 meV obtained for a single thick layer grown from an identical melt. Brunemeier *et al.* suggested that the improvement in layer quality over a thick sample was due to the elimination of unwanted thermal convection currents, arising from temperature gradients within the melt [33]. Such convection currents cannot become established during the very short growth times.

## 8.6 DEVICES INCORPORATING ULTRATHIN LPE LAYERS

Rapid slider LPE grown quantum wells were first incorporated into LED and laser structures operating in the 1–1.55  $\mu\text{m}$  spectral range [7, 9, 40] and more recently into quantum well lasers operating at 880 nm [41]. For example, Rezek *et al.* [7] reported the threshold current dependence on temperature of InGaAsP quantum well lasers emitting near 1.1  $\mu\text{m}$ . The characteristic temperature,  $T_0$  was 160 °C below 20 °C and 62 °C above 20 °C. In the low temperature range, the  $T_0$  was higher than that observed in InGaAsP double heterostructure lasers due to the two-dimensional nature of the active region. Above 20 °C the characteristic temperature was rather similar to that of a conventional double heterostructure laser and was attributed to a common materials problem (possibly a deep level in the quaternary alloy), which is often observed in heterostructures in this materials system. Dutta *et al.* reported a threshold current of 45–50 mA for double channel planar buried heterostructure (DCPBH) InP-InGaAsP-InP lasers emitting at 1.3  $\mu\text{m}$  as shown in Figure 8.8 [9]. They were able to measure the temperature dependence of the carrier lifetime at threshold for their quantum well laser compared with a conventional double heterostructure laser. The weaker temperature dependence of the quantum well device confirmed that a temperature dependent loss mechanism had been suppressed.

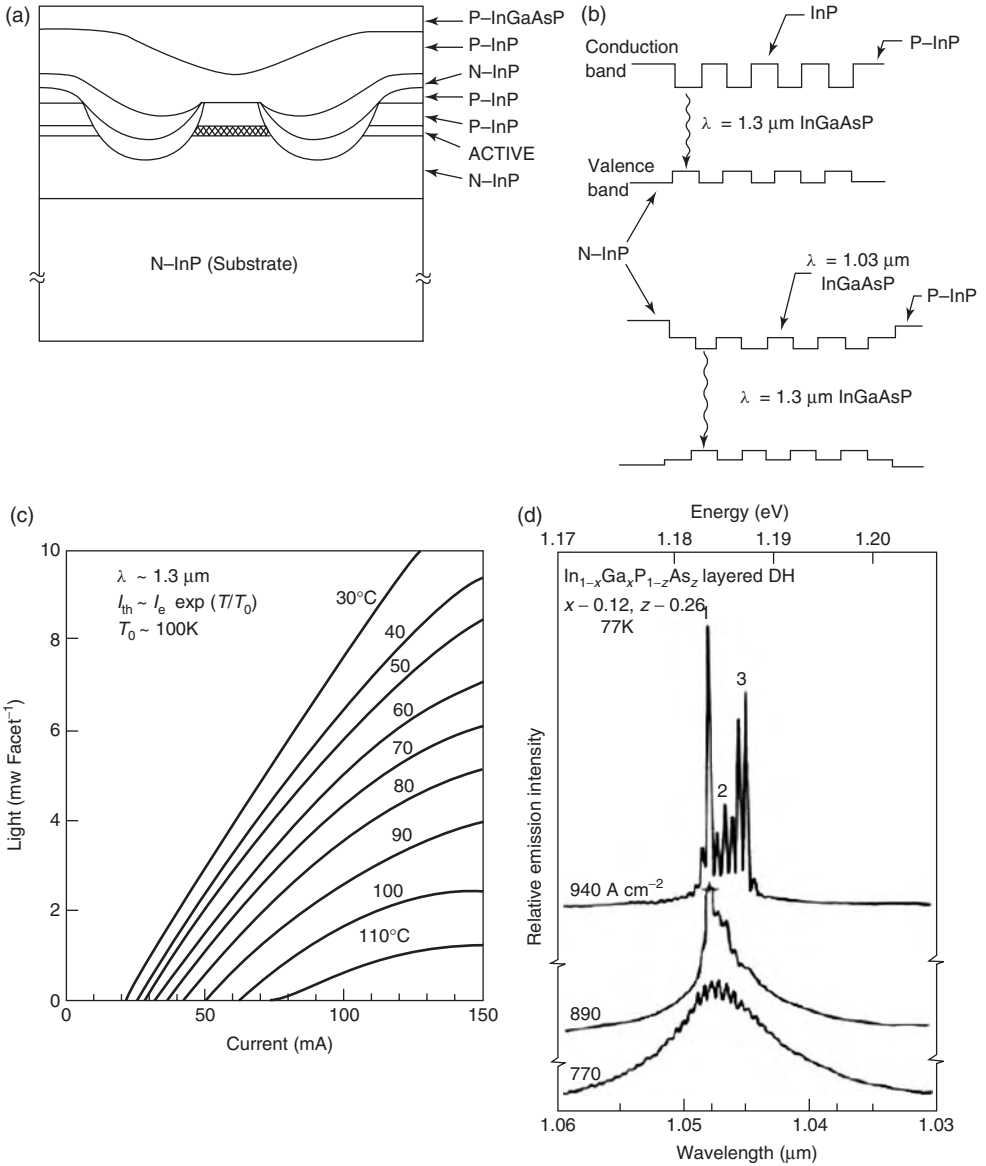


**Figure 8.8** Details of the MQW laser structure grown by Dutta *et al.* [8] using rapid slider LPE: (a) DCPBH in cross-section; (b) active layer schematic showing quantum wells; (c) light–current characteristics from the DCPBH laser; (d) the onset of laser emission from a MQW double heterostructure laser containing 10 quantum wells. After Rezek *et al.* [5]. (a, b, d) Reproduced from [8] by permission of the American Institute of Physics. (c) Reproduced from [5] by permission of the American Institute of Physics

Nohavica *et al.* also obtained DCPBH lasers in this system using their meander type boat design [42], the lowest threshold current recorded being about 46 mA. But, yield was reduced due to the strain concentration at the boundary of the active region after double channel etching and the nonideal planarity of the layers. Sasai *et al.* were able to improve on the threshold current, by using InGaAsP barriers instead of InP [40]. The reduction in threshold current down to 19 mA at room temperature was attributed to improved interface quality due to reduced etch-back and a lower growth temperature. Carrier leakage was responsible for the relatively low value of  $T_0 \sim 60^\circ\text{C}$  observed at high temperatures (above  $20^\circ\text{C}$ ). Dutta *et al.* also adopted InGaAsP barriers and were able to increase the maximum operating temperature to  $110^\circ\text{C}$  with a  $T_0$  of  $60^\circ\text{C}$  between  $10^\circ\text{C}$  and  $60^\circ\text{C}$  [8]. The improvement in performance was attributed to more efficient injection into the MQW active region. Using four InGaAsP quantum wells and three InGaAsP barriers and a distributed feedback geometry, a characteristic temperature of  $95\text{--}100^\circ\text{C}$  was achieved with a threshold current of  $25\text{--}30\text{ mA}$  for a  $1.3\text{ }\mu\text{m}$  laser [43]. MQW lasers for  $1.55\text{ }\mu\text{m}$  emission have also been fabricated using this technique and the improved threshold current density compared with double heterostructure devices was attributed to reduced absorption losses in the MQW structures [8, 44]. More recently, ‘Al-free’ InGaAsP quantum well lasers grown by LPE have been shown to compare very favourably with those produced by MOVPE and MBE [41]. Although the threshold current was somewhat higher at  $500\text{ A cm}^{-2}$  compared with  $100\text{--}200\text{ A cm}^{-2}$  (attributed to thickness variations in the well), the reliability was found to be better than in AlGaAs/GaAs high power laser diodes. Considering that LPE is capable of producing quantum well lasers comparable with those using the more expensive thin layer epitaxy methods, and given that the superior material quality could lead to increased reliability one could speculate that the technique still holds some promise especially where production costs must be kept to a minimum.

## 8.7 LPE GROWTH OF InAs QUANTUM WELLS

Although the growth of quantum wells has been successfully demonstrated in the InGaAsP and GaAs systems, there have been few reports of the growth of thin layers of narrow gap materials such as InAs and InAsSb by a liquid phase technique. This has arisen due to the successful advent of MBE and MOVPE but also partly due to the requirement for suitable lattice-matched barrier materials. The InAsSbP quaternary system contains a miscibility gap but is highly suitable since it is capable of providing alloys with energy gaps up to  $\sim 0.5\text{ eV}$  which are lattice-matched to InAs. The details of the procedures used for the LPE growth of this quaternary alloy have been described in detail elsewhere [45]. Recently, the InAs/InAsSbP system has been used to investigate the growth of InAs quantum wells for use in mid-infrared optoelectronic devices. A linear rapid slider boat of the type shown in Figure 8.3 was used and the growth was initiated at  $568^\circ\text{C}$  using a slow ramp rate of  $0.2^\circ\text{C min}^{-1}$ . Typically four to six thin layers were grown in one growth cycle. The InAs quantum well layers were sandwiched between  $\text{InAs}_{0.36}\text{Sb}_{0.20}\text{P}_{0.44}$  confinement layers a few hundred nanometres in thickness and closely lattice matched to the InAs. The compositions of the corresponding liquid phases were calculated using phase diagram data obtained from the literature [46, 47]. The quaternary melts were always saturated to  $573^\circ\text{C}$ , but the InAs melt saturation point (and therefore the supersaturation) was set differently in the different growth runs to investigate the effects of melt supercooling on



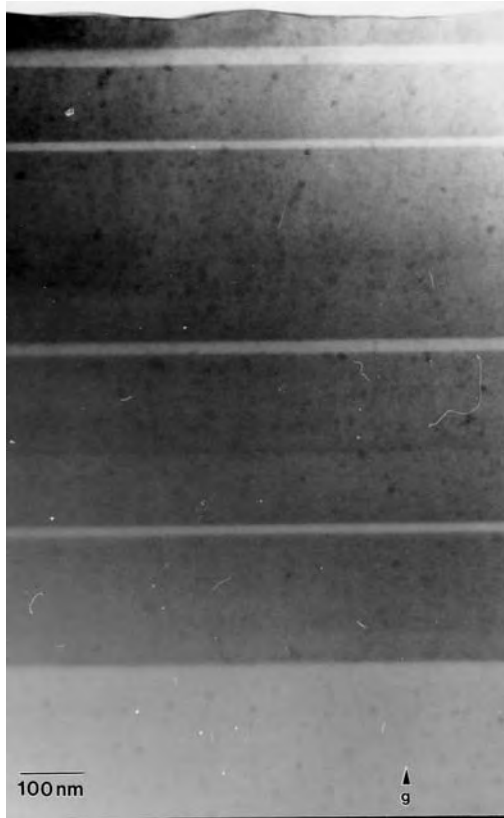


**Figure 8.9** Cross-sectional TEM photographs of a series of InAs quantum wells grown by LPE. Light regions are InAs quantum wells; the dark regions are lattice matched  $\text{InAs}_{0.36}\text{Sb}_{0.20}\text{P}_{0.44}$  barriers. Measured InAs quantum well thicknesses are (from top to bottom) 25, 11, 19 and 16 nm, respectively, g indicates crystal growth direction. Reprinted from *Appl. Phys. A*, Photoluminescence from InAs quantum wells grown by liquid-phase epitaxy, Krier *et al.*, **71** (3), 249, Copyright (2000), with permission from Springer-Verlag GmbH

the resulting epitaxy. Figure 8.9 shows a cross-sectional TEM photograph obtained from a sample containing a typical stack of layers. The bright regions are the InAs quantum wells which have thickness in the range 10 nm to 30 nm. In a similar manner to the other alloys, by using careful boat design and by selecting appropriate contact times and supercooling, InAs quantum wells as thin as 25 Å were readily obtained. From the high contrast between the layers it is apparent that the rapid slider LPE technique has the capability of growing uniform, ultrathin InAs epitaxial layers with abrupt interfaces and that solid phase interdiffusion was negligible. It is important to note that these are valid observations either in the case of InAs on InAsSbP or InAsSbP on InAs heteroepitaxy.

The kinetics of the ultrathin layer growth obtained for InAs is rather similar to that obtained for InGaAsP described above. Figure 8.10 shows the measured InAs layer thickness plotted against the effective contact time, calculated from the slit width and the sliding speed. (Different symbols indicate different growth conditions, i.e. different slit widths and slider speeds.) Once again the expected square root dependence becomes evident only

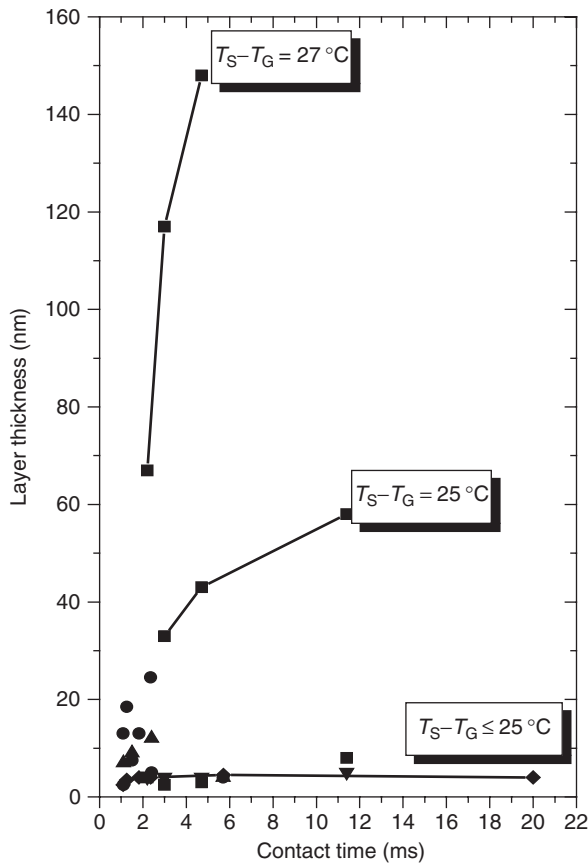


**Figure 8.10** Experimentally measured InAs layer thickness dependence on melt-substrate contact time at different supercooling

for sufficiently high values of supercooling. The layer thickness becomes independent of contact time as the supercooling is reduced. Below a critical value of approximately  $25^\circ\text{C}$  the layer thickness becomes independent of the contact time, while above that the layer thickness steeply increases. Again the results can be explained by assuming that a small amount of melt inside the slit rolls over the wafer such that the initial growth is determined by the formation of a localised depleted region at the melt-substrate interface. This results in a supercooling dependent delay time after which diffusion controlled growth begins. A mathematical description of this process using a least squares error function to fit the measured layer thicknesses has been used to arrive at an empirical expression for the layer thickness [48].

### 8.7.1 PL characterisation

The PL emission spectrum obtained at 4 K from a sample containing a 33 nm InAs quantum well is shown in Figure 8.11. The lower curve shows two emission peaks at

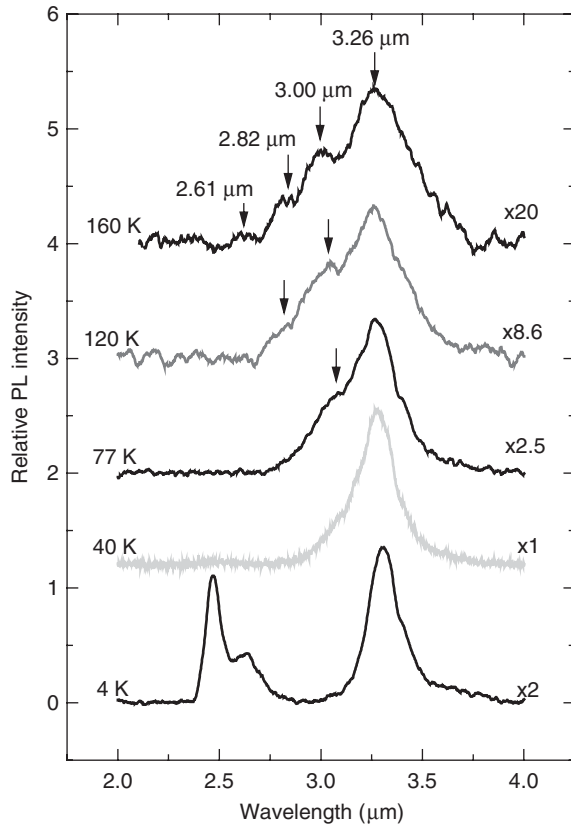


**Figure 8.11** Temperature dependence of the PL emission from the 33 nm InAs quantum well sample. Reprinted from *Appl. Phys. A*, Photoluminescence from InAs quantum wells grown by liquid-phase epitaxy, Krier *et al.*, **71** (3), 249, Copyright (2000), with permission from Springer-Verlag GmbH

2.5  $\mu\text{m}$  and at 2.65  $\mu\text{m}$  that originate from the  $\text{InAs}_{0.36}\text{Sb}_{0.20}\text{P}_{0.44}$  quaternary barriers. A more intense PL peak from the InAs quantum well is observed at 3.3  $\mu\text{m}$  [49]. Note that PL emission from bulk InAs is normally obtained at a shorter wavelength of around 3.0  $\mu\text{m}$ . We therefore conclude that the 3.3  $\mu\text{m}$  PL arises from the InAs quantum well, which is consistent with emission from the type II InAsSbP/InAs system and comprising a deep conduction band well with good electron confinement. This is consistent with conduction band and valence band offsets of 278 and 39 meV, respectively, obtained using a linear interpolation of the parameters of Adachi [50] within the framework of the model solid theory of Van der Walle and Martin [51].

The relative intensity of the InAs quantum well emission is almost four times higher than that of the InAs bulk. From the temperature dependence of the PL emission it is evident that as the temperature increases the barrier emission quenches rapidly compared with the emission from the InAs quantum well and has vanished altogether at 40 K. This indicates a competition between photo-generated carrier diffusion, capture and recombination mechanisms at different temperatures. As the temperature increases further additional

peaks appear in the InAs quantum well spectrum. At 160 K four peaks (3.26, 3.00, 2.82 and 2.61  $\mu\text{m}$ ) become evident. These peaks are attributed to recombination from the four confined states in the 33 nm InAs conduction band quantum well, which become populated at higher temperatures. There is also a small but noticeable blue shift in these peaks with increasing temperature which is further evidence for the quantum confined origin of the emission. Assuming that the  $E_1$  ground state wavefunction is a maximum at the centre of the InAs quantum well and in a type II system the holes are confined in the InAsSbP barrier regions adjacent to the quantum well interface, the electron–hole wavefunction overlap would be substantial for a thin well but could be much less for a well as thick as 33 nm. This indicates that in this case it is perhaps more likely that there is significant band bending within the 33 nm InAs layer so that the conduction band essentially occupies two different regions near the two interfaces. The quantised levels should then be strictly regarded as two-dimensional states confined near each interface rather than states spread over the entire quantum well. These results are encouraging for the development of sources and detectors for the mid-infrared spectral range.

## 8.8 LPE GROWTH OF QUANTUM DOTS FOR MID-INFRARED OPTOELECTRONIC DEVICES

There is currently much interest in strain induced islands or ‘quantum dots’ (QDs), which form during the early stages of heteroepitaxy in many materials systems via Stranski–Krastanov (S–K) growth [52]. These nanoscale structures can be used for basic studies of quantum confinement, but also have considerable potential for the fabrication of novel electronic and optoelectronic devices [53, 54]. The narrow gap III–V semiconductor materials InAs, GaSb, InSb, their alloys and nanostructures are particularly interesting and useful materials in this respect since they offer the promise of being able to access the 2–10  $\mu\text{m}$  wavelength region and should provide the next generation of light emitting diodes (LEDs), lasers and photodetectors for applications such as infrared gas sensors, molecular spectroscopy and thermal imaging [55]. Self-assembled InAs and GaSb based QDs have attracted particular interest and investigation in the past few years [56–58]. In this section the growth of InSb and InAsSb QDs by LPE on InAs and GaAs substrates is briefly considered.

If the lattice mismatch between QD layer and substrate were chosen to be large enough for S–K growth then it would appear that the rapid slider technique should be capable of QD growth. In our laboratory, both InAs (100) and GaAs (100) substrates were used to study the possibility of growth of InSb QDs [54]. In either case, the substrate was cleaned *in situ* with a wash melt, of either undersaturated As in Ga solution for GaAs substrates, or undersaturated As in In solution for InAs substrates, immediately before the InSb QD melt was wiped across it. The melts were baked at 50 °C above the liquidus point for 1 h to produce a homogeneous melt and to purify the material. Initially, the temperature was lowered quickly towards the growth temperature at a ramp rate of 2 °C  $\text{min}^{-1}$ , followed by a second slower ramp at 0.2 °C  $\text{min}^{-1}$  for about 30 min to avoid overshoot and to induce a well defined amount of supercooling before the growth was initiated.

### 8.8.1 InSb QDs on GaAs (100) substrates

Figure 8.12(a) shows a high magnification atomic force microscopy (AFM) image of InSb QDs grown on a GaAs(100) substrate at 330 °C with 16 °C supercooling and 60 s contact time [59]. The InSb QDs are 5 nm in height and 50 nm in diameter with an area density of  $1 \times 10^{10} \text{ cm}^{-2}$  which is generally similar to the results obtained for InSb QDs grown

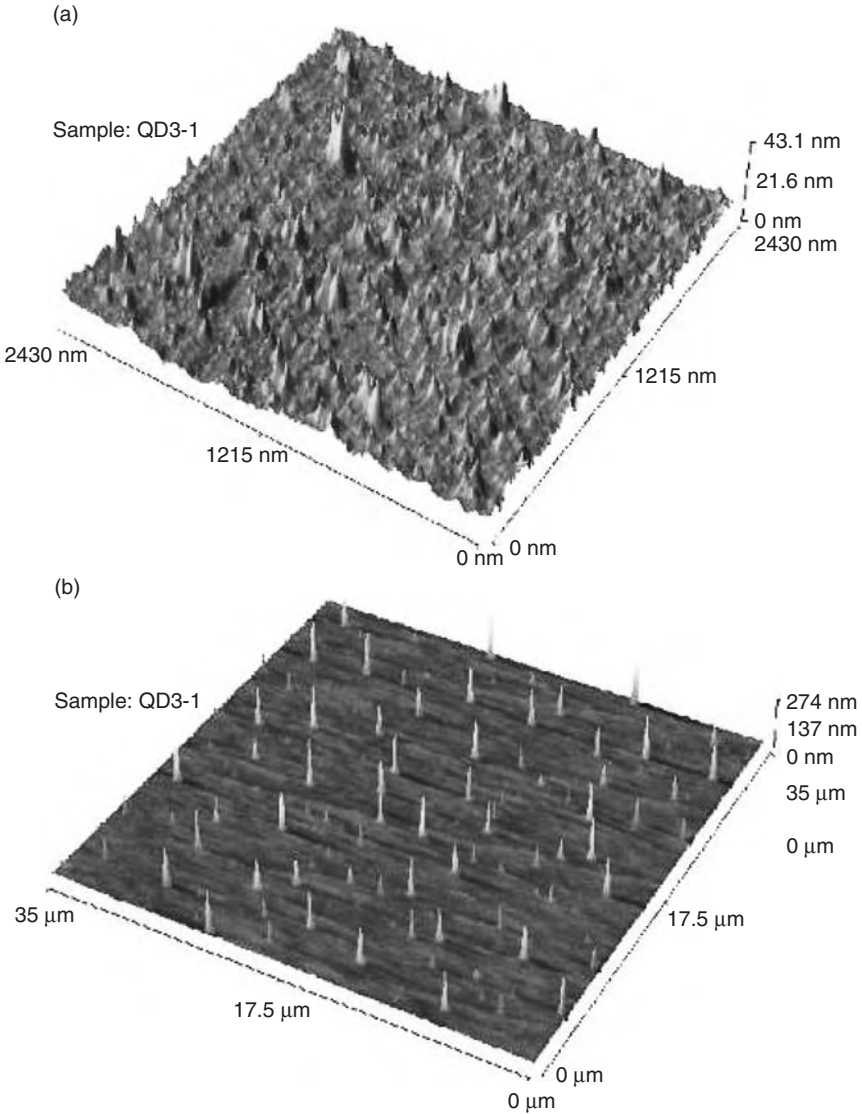


**Figure 8.12** AFM image of InSb QDs grown on a GaAs(100) substrate: (a) grown at 330 °C with 16 °C supercooling; (b) the same region at low magnification showing the large dots. (The image areas are: (a) 2380 nm × 2380 nm; (b) 35 μm × 35 μm, respectively. Note that height and length scales differ). Reproduced from [59] by permission of IOP Publishing Ltd

on GaAs(100) at  $\sim 400^\circ\text{C}$  by MBE [60–62]. An AFM image of the same region at low magnification is shown in Figure 8.12(b). Large ‘needle-shaped’ InSb QDs are clearly distinguishable; they are 50 nm in height and 300 nm in diameter with a lower density of  $2 \times 10^7 \text{ cm}^{-2}$ . Although grown from the liquid phase, these large InSb QDs are again quite similar to those grown by MBE at similar substrate temperatures. Closer examination reveals that the height and diameter of the large QDs grown by LPE are about twice as large as those grown by MBE, while the density is one order of magnitude lower [60, 61]. As mentioned above, the coexistence of both small and large QDs is consistent with thermodynamic considerations of formation energy, which typically results in bimodal states at low growth temperature [61, 63–65].

Figure 8.13(a) shows an AFM image of unencapsulated InSb QDs on InAs(100) grown at  $465^\circ\text{C}$  with  $10^\circ\text{C}$  supercooling and using a 1 ms melt–substrate contact time. There are two kinds of QDs visible on the surface. The small QDs are 4 nm in height and 20 nm in diameter with a high area density of  $4 \times 10^{10} \text{ cm}^{-2}$ . The large QDs are 12 nm in height and 60 nm in diameter, but with a much lower density of  $8 \times 10^8 \text{ cm}^{-2}$ . The large QDs are about three times smaller than those grown by MBE, but the density is about three times higher [60, 61]. During the early stages of epitaxial layer growth onto lattice-mismatched substrates, a wetting layer is usually formed and the deformation energy increases with increasing thickness. Self-assembled QDs are then obtained above some critical thickness to reduce the deformation energy. The larger the lattice mismatch between the substrate and epitaxial layer, the smaller the size of the resulting dots. The deformation energy is not only affected by the lattice mismatch but also by the atomic interactions, substrate temperature, etc. As the layer thickness increases further, larger islands can form, again to minimise the deformation energy. This behaviour is essentially known as bimodal growth. High-density small dots should be self-assembled and dislocation-free, whereas the larger dots may contain defects, which help to consume the residual strain. By way of comparison, we note that in the Si-Ge system, the growth rate is determined by diffusion of Si-Ge atoms from the Bi melt across the boundary layer [62]. This is a much slower process than the interface segregation in the InSb/InAs or GaAs system investigated here. Consequently, the growth rate is relatively small, which enables the evolution of QD growth to be readily investigated. Unfortunately this is not possible in this III-V system.

In contrast to the QDs shown in Figure 8.13(a), the InSb QDs shown in Figure 8.13(b) are more coalesced together. These QDs were grown at  $320^\circ\text{C}$  with  $26^\circ\text{C}$  supercooling and with a longer contact time of 60 s. The QDs are 5 nm in height and 80 nm in diameter with a density of  $1 \times 10^{10} \text{ cm}^{-2}$ . Clearly, the above AFM results confirm that the rapid slider LPE technique can be used to prepare high density and uniformly distributed InSb QDs from the liquid phase, which are comparable with those produced by MBE, despite the higher mass transport. Figure 8.14 shows the dependence of average height and density of the InSb QDs grown on InAs using different amounts of melt supercooling. The average height (taken over the whole AFM image) mainly represents the height of the small QDs due to the lower density and surface coverage of the large QDs. The average height was observed to increase by about a factor of two as the supercooling increased from  $10$  to  $20^\circ\text{C}$ , principally due to the growth of the smaller QDs. However, the average height decreased as the supercooling was increased further from  $20$  to  $30^\circ\text{C}$  because the small QDs then become partly coalesced and spread out to cover the surface rather than increase in height. Therefore, in order to grow InSb QDs on InAs from the liquid phase with a maximum (average) height but without significant coalescence, it would appear

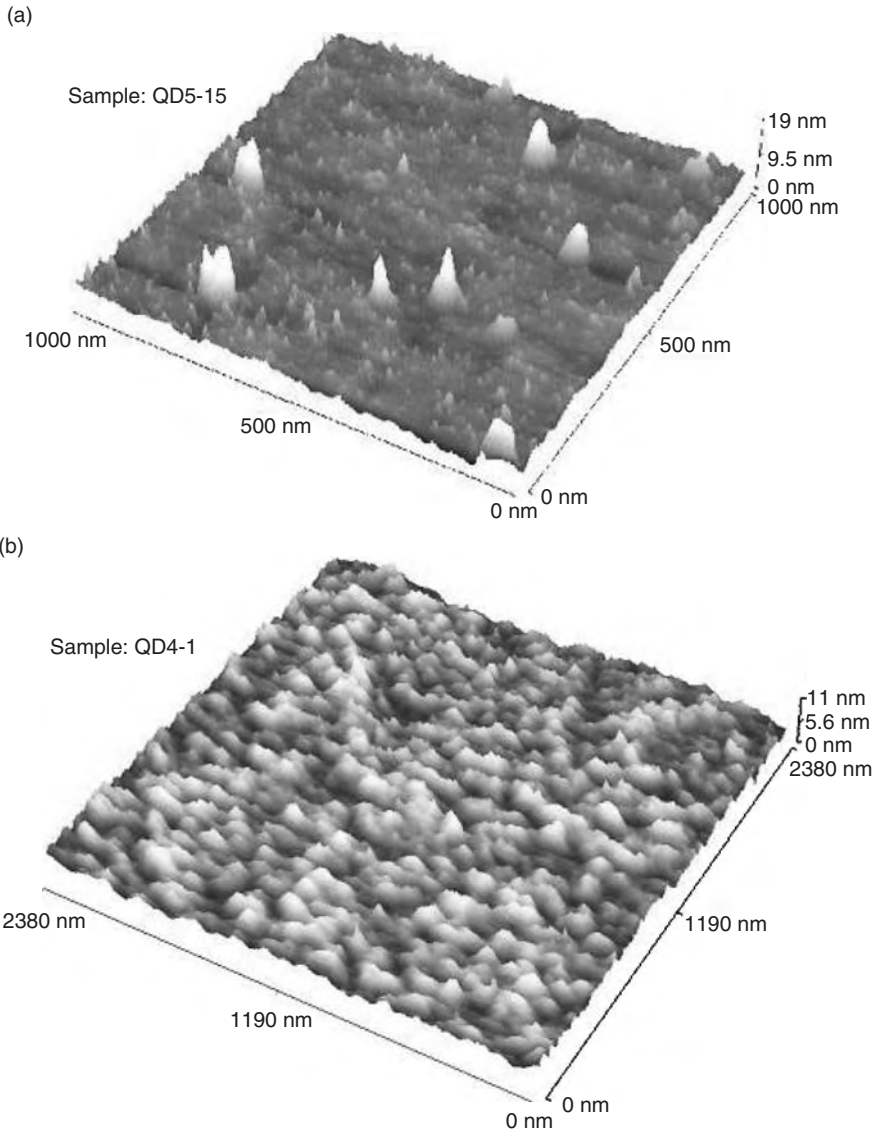


**Figure 8.13** AFM images of InSb QDs grown by LPE on an InAs(100) substrate: (a) grown at 465 °C with 10 °C supercooling and 1 ms melt–substrate contact time. The image area is 1000 nm × 1000 nm, and exhibits both small and large QDs; (b) grown at 320 °C with 26 °C supercooling and 60 s contact time. Reproduced from [59] by permission of IOP Publishing Ltd

that the optimum supercooling should be 20 °C for a given melt-substrate contact time. By extrapolating the average height to zero, the critical minimum supercooling necessary to obtain QD formation in this system is obtained at a value of 6 °C. The density of the large QDs increases slowly but continuously with increasing supercooling, which suggests that high supercooling is favourable for the formation of large QDs. The density of the small QDs on the other hand reaches a maximum and decreases slightly at high supercooling.

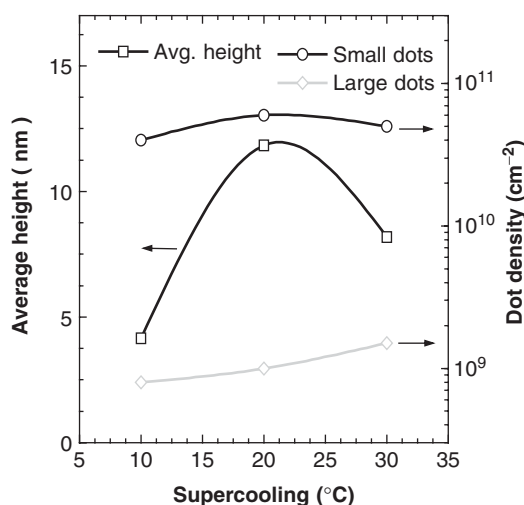


**Figure 8.14** Average height and density of small and large InSb QDs grown on InAs and their dependence on supercooling. The samples were grown using 1 ms contact time. Reproduced from [59] by permission of IOP Publishing Ltd

The densities of both the small and large QDs are changed only relatively little with respect to the supercooling which leads us to suppose that the density of InSb QDs is dominated by nucleation and strain consistent with self-assembled QD formation.

## 8.8.2 Investigation of InAsSb QDs

Although it is possible to grow InSb QD on InAs, subsequent encapsulation with InAs was difficult to achieve due to the higher melt temperature required for InAs epitaxial overgrowth of sufficiently high quality, which has the effect of etching the underlying InSb dots. Consequently, InAsSb QD were grown instead which could be produced at higher temperature, compatible with the requirement for subsequent InAs encapsulation. InAs<sub>1-x</sub>Sb<sub>x</sub> quantum dots with  $x \sim 0.2$  were grown on n-type (S doped  $1 \times 10^{18} \text{ cm}^{-3}$ ) InAs (100) substrates. The InAs buffer and encapsulation layers were grown from an In-rich melt, whereas the InAs<sub>1-x</sub>Sb<sub>x</sub> was grown from a pseudo-binary melt [66]. AFM was used to investigate the resulting morphology and to obtain the fundamental parameters of the InAs<sub>1-x</sub>Sb<sub>x</sub> QDs at different positions (along the passing direction of the melt) across the substrate.

Figure 8.15 shows three AFM images taken from regions P3, P5 and P7, respectively, at different positions along the sample as shown in the inset [67]. Even though the contact time is very short (1 ms), with 25 °C supercooling there is still local depletion of As from the InAs<sub>1-x</sub>Sb<sub>x</sub> melt at the growth interface, resulting in a variation in solid composition across the sample along the passing direction of the melt (i.e. Sb increases P3–P7). This means one is conveniently able to examine the resulting morphology and PL properties corresponding to different InAs<sub>1-x</sub>Sb<sub>x</sub> compositions having different amounts of lattice mismatch to the InAs substrate. AFM and PL measurements on an InAs epitaxial control layer grown using the same techniques revealed a flat surface without any dots and PL



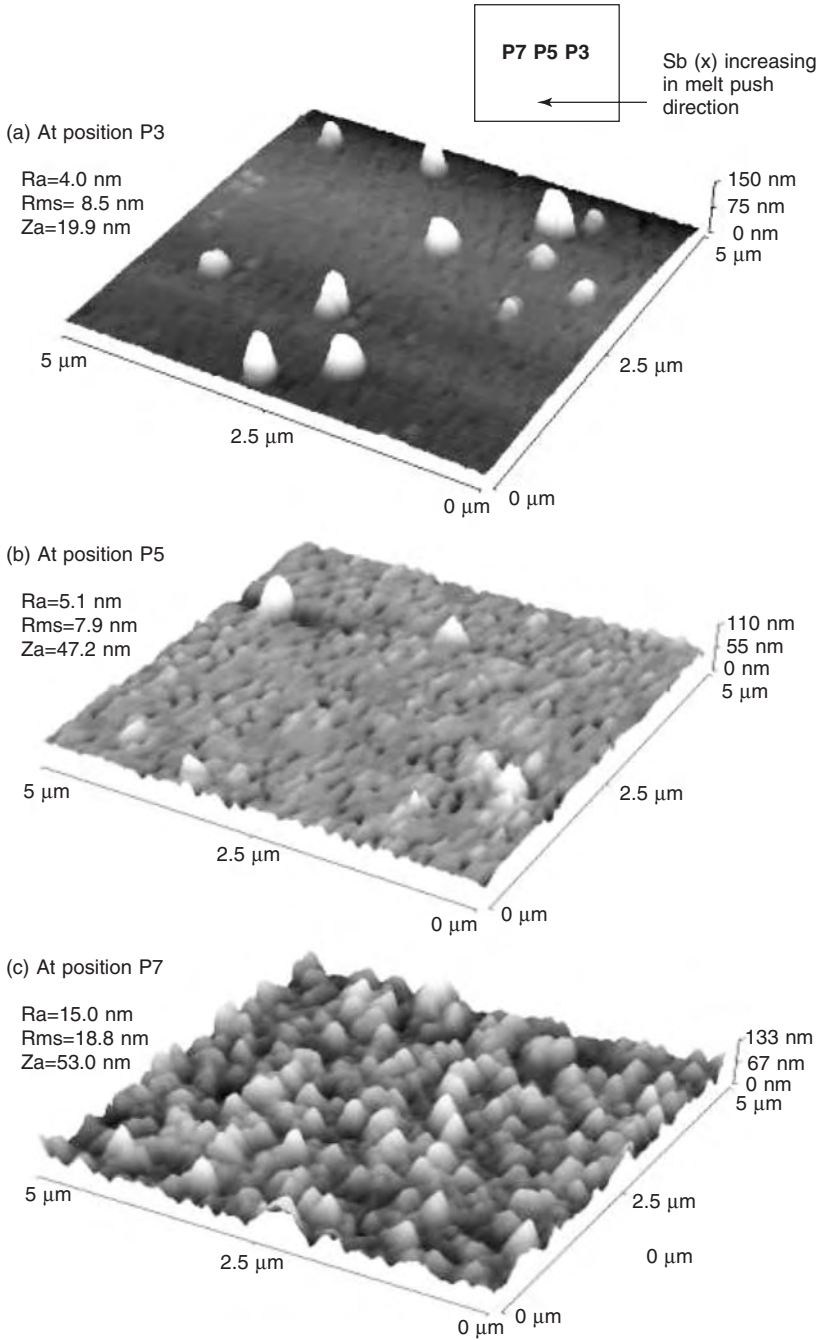


**Figure 8.15** AFM images obtained from unencapsulated  $\text{InAs}_{1-x}\text{Sb}_x$  QDs with increasing Sb composition grown by LPE and corresponding to the passing direction of the melt across the substrate. Approximate compositions are: (a)  $x = 0.20$ ; (b)  $x = 0.25$ ; (c)  $x = 0.30$ . Reproduced from [67] by permission of the American Institute of Physics

characteristic of near band edge recombination, and only weak emission associated with defects. One may observe the onset of three-dimensional growth of isolated QDs from a coalesced (quantum well) layer as a function of strain. Consequently, the  $\text{InAs}_{1-x}\text{Sb}_x$  in region P3 [Figure 8.15(a)] has a relatively small Sb content ( $x = 0.2$ ) and associated strain. The AFM image of P3 shows quite a smooth continuous  $\text{InAs}_{1-x}\text{Sb}_x$  layer. Some islands about 300 nm in diameter and 100 nm in height are visible. This means that a strained epilayer covers most of the area in the vicinity of P3, but some large dots have nucleated to help consume the local strain energy. The image from region P5 [Figure 8.15(b)] ( $x = 0.25$ ) shows a relatively uniform self-assembled layer of coalesced QDs with a few larger islands. The coalesced QDs are about 150 nm in diameter and 50 nm in height, with an area density of  $\sim 5 \times 10^9 \text{ cm}^{-2}$ . Region P7 [Figure 8.15(c)] has the highest Sb composition ( $x = 0.3$ ) of the three and the AFM image shows isolated QDs, some of which have coalesced together. The area density of the isolated dots shown here is  $\sim 2 \times 10^9 \text{ cm}^{-2}$ .

## 8.9 MID-INFRARED LUMINESCENCE OF ENCAPSULATED $\text{InAsSb}$ QDs

As mentioned above, InAs and its alloys are promising materials for the fabrication of mid-infrared (2–5  $\mu\text{m}$ ) optoelectronic devices for use in gas sensors and many other applications [68]. There is increasing interest in accessing this spectral region using a variety of materials engineering approaches and techniques. In recent years, InSb, GaSb, AlSb and InAs QDs have been grown on GaSb and GaAs substrates by MBE and MOVPE. For example, self-assembled InSb QDs have been grown at 400 °C by MBE on GaAs and AlGaSb substrates [61, 62], and at 460–500 °C by MOVPE on GaSb [69]. However, the resulting PL emission from these QDs was observed in the near infrared [59–62, 69–71]. By comparison there have been very few, if any, reports of InSb or  $\text{InAs}_{1-x}\text{Sb}_x$  QDs exhibiting emission in the spectral range  $> 2 \mu\text{m}$ .

A schematic diagram of the type II  $\text{InAs}_{1-x}\text{Sb}_x/\text{InAs}$  QD system is shown in Figure 8.16. The PL of InAs is normally dominated by transitions between shallow donors  $E_S$ , deep donors  $E_D$  and deep acceptors ( $E_{A1}$  and  $E_{A2}$ ). At low temperature, the PL of undoped and n-type InAs generally shows two peaks A and B. However, additional peaks C and D corresponding to the transitions from  $E_D$  to  $E_V$  and from  $E_S$  to  $E_{A2}$ , are observed in p-type material [72]. The system affords deep hole confinement ( $E_V \sim 100 \text{ meV}$ ) in the QD based on band offset considerations. Figure 8.17 shows the 5 K PL spectra measured from the QD encapsulated sample at several different positions P1–P9 along the wafer, again corresponding to increasing Sb composition [where P3, P5 and P7 relate approximately to the corresponding AFM images in Figure 8.15(a)–(c)]. The PL spectra at P1 and P2 show two peaks A and B located at 418 and 406 meV, associated with band–band transitions and donor–acceptor transitions in InAs, respectively. These originate from the capping and buffer layers. But, in the PL at P3, another peak (F) located at 378 meV is observed, which correlates with the  $\text{InAs}_{1-x}\text{Sb}_x$  ‘quantum well’ layer [shown in the AFM image in Figure 8.15(a)]. At P2 the ‘quantum well’ layer is thinner than at P3 and peak F shifts to higher energy and enhances peak B compared with the PL observed at P1. In the spectra observed from positions P3 to P7, peak F shifts from 378 meV to 316 meV, and decreases in intensity as the 289 meV peak G increases in

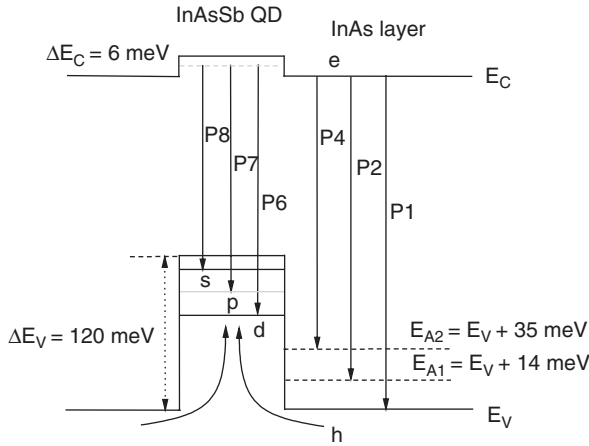


**Figure 8.16** Schematic diagram showing the type II  $\text{InAs}_{1-x}\text{Sb}_x/\text{InAs}$  encapsulated QD energy band diagram. Reprinted from *Physica E*, **15**, Krier and Huang, Mid-infrared electroluminescence from InAsSb quantum dot light emitting diodes grown by liquid phase epitaxy, 159, Copyright (2002), with permission from Elsevier

intensity. This suggests that moving across the sample with increasing Sb composition ( $x$ ) and hence strain, the emission is initially representative of a strained quantum well layer and gradually becomes characteristic of self-assembled coalesced QDs. Then finally at some critical composition ( $x \sim 0.25$ ) PL is observed mainly from isolated QDs of fixed size at P7. The two dips in the broad peak G at around 290 meV ( $4.3 \mu\text{m}$ ) are due to  $\text{CO}_2$  absorption in the unpurged laboratory atmosphere. Moving further along from position P7 to P9, peak G decreases in intensity, while the defect related peak D and its phonon replica peak E, as well as peak B increase in intensity. This is consistent with the overgrowth of the isolated QDs resulting in the production of more deep states in the InAs in the immediate vicinity outside of the dots, which enhances peaks B and D, as well as introducing recombination centres within the QD to quench peak G.

The peak F blue shifts by 6 meV as the laser excitation intensity increases which is consistent with a type II band alignment for the coalesced QDs. The blue shift of the isolated QDs (peak G) is found to be even larger than that of peak F with increasing excitation energy, as would be expected from the smaller density of states in the isolated QDs compared with the coalesced QDs. By comparison, the InAs related peaks exhibit only a small blue shift (1.2 meV), consistent with type I recombination. The peak energy of peak G is always about 35 meV lower than that of peak F, because the confinement in the three-dimensional isolated QDs is stronger than the two-dimensional confinement in the coalesced dots. The integrated intensity of peak G also increases almost linearly with excitation intensity, whereas the intensity of the InAs related peak shows a strong saturation. The temperature dependence of the integrated intensities of these PL peaks provides additional evidence of the strong quantum confinement inside the QDs. The PL intensity of the isolated QDs increases slightly from 5 to 80 K (peak G) before quenching at a temperature above 100 K with an activation energy of 89 meV. The quenching is associated with holes being thermally excited out of the QD confinement potential. The behaviour of peak F is similar. By comparison the integrated intensity of the InAs-related

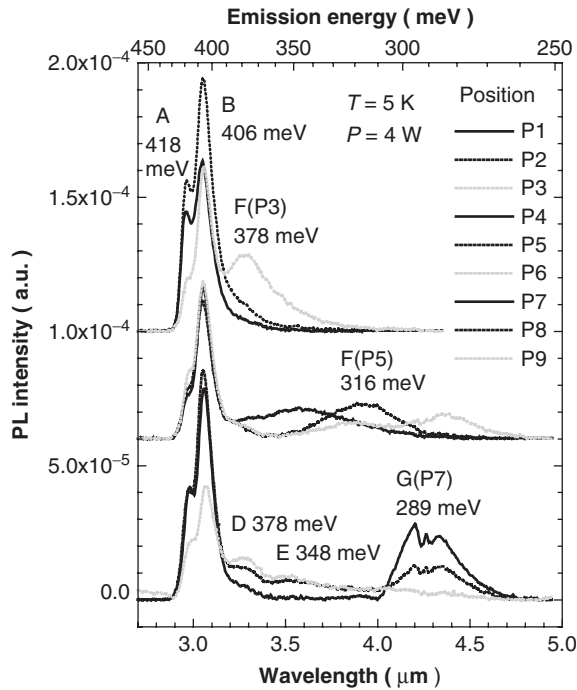


**Figure 8.17** Photoluminescence spectra measured at 4 K from the  $\text{InAs}_{1-x}\text{Sb}_x$  QDs with increasing Sb content from positions P1 to P9 along the sample. (Top curves: P1, P2, P3; middle curves: P4, P5, P6; lower curves: P7, P8, P9). Reproduced from [67] by permission of the American Institute of Physics

peak B quenched rapidly with increasing temperature above 5 K, with an activation energy of only 4.6 meV.

## 8.10 ELECTROLUMINESCENCE OF $\text{InAsSb}$ QD LEDs

By introducing a layer of  $\text{InAsSb}$  QD into the active region of an  $\text{InAs}$  homojunction p-i-n diode it is possible to investigate electroluminescence (EL). Figure 8.18 shows the 4 K EL spectrum obtained from one such QD LED using 250 mA injection current. The broad peak in the region near  $4 \mu\text{m}$  is due to QD-related transitions. The large FWHM is characteristic of the inhomogeneous broadening from the size distribution. By using Gaussian line shapes for fitting, three peaks (s, p, d) can be deconvoluted from the spectrum, which are attributed to recombination involving confined hole states in the QD. The remaining peaks ( $2.98$ ,  $3.08$  and  $3.24 \mu\text{m}$ ) can be assigned to characteristic recombination in the  $\text{InAs}$  encapsulation based on previously observed results in the literature. We note that the QD emission is wider in EL than in PL due to the higher carrier injection level, which suggests that more QD sublevels are populated. As the injection level is increased Pauli blocking causes a saturation of the carrier number in lower energy states inside the QD and the relaxation rate from higher states decreases leading to observable emission from the excited levels. Two additional peaks P3 ( $3.16 \mu\text{m}$ )

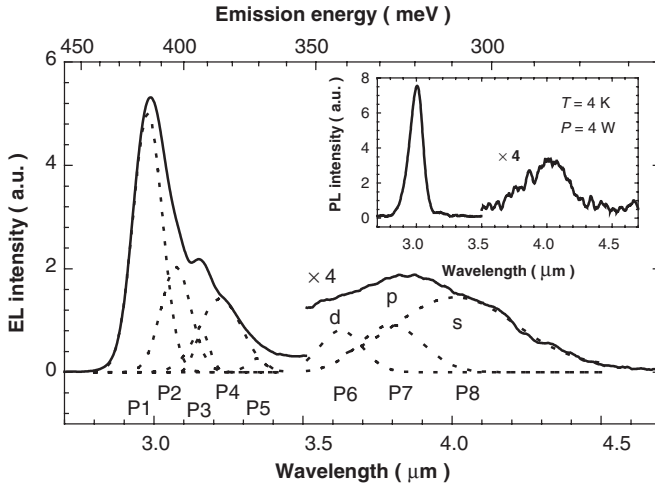


**Figure 8.18** Electroluminescence emission spectrum obtained from an InAsSb QD LED measured at 4 K using 250 mA injection current. Reprinted from *Physica E*, **15**, Krier and Huang, Mid-infrared electroluminescence from InAsSb quantum dot light emitting diodes grown by liquid phase epitaxy, 159, Copyright (2002), with permission from Elsevier

and P5 (3.33 μm) can also be deconvoluted, but these are much weaker and are difficult to identify with certainty. However, these two peaks are each shifted down in energy by ~10 meV from P2 and P4, respectively, and so may be associated either with a thin wetting layer or a strained InAs layer covering the InAsSb QD. Figure 8.19 shows the

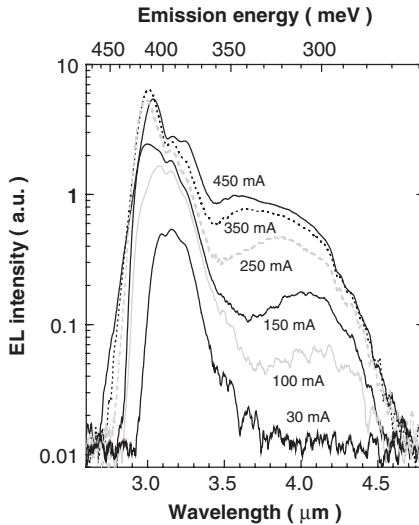


**Figure 8.19** The 4 K electroluminescence spectrum of the QD LED at various injection currents. Reprinted from *Physica E*, **15**, Krier and Huang, Mid-infrared electroluminescence from InAsSb quantum dot light emitting diodes grown by liquid phase epitaxy, 159, Copyright (2002), with permission from Elsevier

QD LED emission spectra and the dependence on injection current at 4 K. It is evident that at 30 mA there is essentially no QD emission and the injection has to be increased to 100 mA before any significant QD emission is observable. This is evidence of a phonon bottleneck where there are insufficient phonons available to scatter holes into the deep QD potential and the dots can become populated essentially by Auger scattering, which only becomes significant at high carrier densities.

## 8.11 SUMMARY

Despite the far-reaching success of MBE and MOVPE growth technologies it has been shown that it is possible to use a modified 'rapid slider' LPE growth technique to form quantum well and QD nanostructures. This is made possible essentially by employing a thin slit in the graphite boat melt chamber to enable short contact times between the melt and substrate for epitaxy from the liquid phase. Various researchers have demonstrated single and multiple quantum wells in a number of different III-V systems where the thickness of the resulting epitaxial structures is limited only by the thickness of the transition regions at the heterojunctions, which is typically less than 40 Å. High efficiency InGaAsP/InP quantum well lasers have been demonstrated with performance suitable for a wide variety of applications and excellent reliability. More recently, rapid slider technology has been used to investigate growth of QDs from the liquid phase. In(As)Sb quantum dots can be successfully grown onto InAs or GaAs substrates. AFM examination shows that in some cases the density and surface morphology of these Sb-based QDs are generally similar to those prepared by MBE and MOVPE techniques. The density, size and shape of the dots is dependent on growth temperature, supercooling and growth time interval, as well as the choice of substrate, in much the same manner as for the other methods. Although the degree of precision and control over the growth is by no means as high, the capability to grow InAs quantum wells and InAsSb QDs by LPE potentially opens up a promising route towards the practical realisation of inexpensive mid-infrared optoelectronic devices which are required for a wide variety of industrial and commercial gas sensor applications. For these applications at least, where component volumes are envisaged to be relatively small LPE represents a highly attractive route to manufacture and the possibilities of this traditional method are far from being exhausted.

## ACKNOWLEDGEMENTS

We wish to thank the UK Engineering and Physical Research Council (EPSRC) for supporting various aspects of the work described here through grants GR/M07373 and GR/L28364. We gratefully acknowledge the assistance of Dr G. McPherson and Dr R. Murray of Liverpool University for TEM. We also wish to thank Dr A. Hammiche of Lancaster University for preparation of the AFM images and Dr D. Nohavica, of the Institute of Radio Engineering and Electronics, Czech Academy of Sciences, Prague, for valuable discussions.

## REFERENCES

1. D.Z. Garbuzov, E.V. Zhuravkevich, A.I. Zhmakin, Y.N. Makarov and A.V. Ovchinnikov. On the peculiarities of short time ( $T_g < 10$ ms) solid solution LPE growth onto the moving substrate. *J. Cryst. Growth* **110**, 955 (1991)
2. D.Z. Garbuzov, E.V. Zhuravkevich, A.I. Zhmakin, Y.N. Makarov and A.V. Ovchinnikov. On the peculiarities of short time ( $T_g < 10$ ms) solid solution LPE growth onto the moving substrate. *Cryst. Prop. Prep.* **31**, 75 (1991)
3. E.A. Rezek, N. Holonyak, B.A. Vojak and H. Shichijo. Single and multiple thin layer ( $L_z \leq 400$ Å)  $\text{In}_{1-x}\text{Ga}_x\text{P}_{1-z}\text{As}_z$ -InP heterostructure light emitters and lasers ( $\lambda \approx 1.1 \mu\text{m}$ , 77 K). *J. Appl. Phys.* **49**, 69 (1978)
4. N. Holonyak, R.M. Kolbas, R.D. Dupurs and R.D. Dapkus. Quantum well heterostructure lasers. *IEEE J. Quantum Electron.* **QE-16**, 170 (1980)
5. E.A. Rezek, N. Holonyak, B.A. Vojak, G.E. Stillman, J.A. Rossi, D.L. Keune and J.D. Fairing. 5LPE  $\text{In}_{1-x}\text{Ga}_x\text{P}_{1-z}\text{As}_z$  ( $x \approx 0.12$ ,  $z \approx 0.26$ ) DH Laser with multiple thin layer (<500Å) active region. *Appl. Phys. Lett.* **31**, 288 (1977)
6. N. Holonyak, R. Chin, J.J. Coleman, D.L. Keune and W.O. Groves. Limitations of the direct-indirect transition on  $\text{In}_{1-x}\text{Ga}_x\text{P}_{1-z}\text{As}_z$  heterojunctions. *J. Appl. Phys.* **48**, 635 (1977)
7. E.A. Rezek, R. Chun, N. Holonyak, S.W. Kirchafer and R.M. Kolbas. Quantum well InP- $\text{In}_{1-x}\text{Ga}_x\text{P}_{1-z}\text{As}_z$  heterostructure lasers grown by liquid phase epitaxy. *J. Electron. Mater.* **9**, 1 (1980)
8. N.K. Dutta, S.G. Napholtz, R. Yen, T. Wessel, T.M. Shen and N.A. Olsen. Long wavelength InGaAsP ( $\lambda \approx 1.3 \mu\text{m}$ ) modified multiquantum well laser. *Appl. Phys. Lett.* **46**, 1036 (1985)
9. N.K. Dutta, S.G. Napholtz, R. Yen, R.L. Brown, T.M. Shen, N.A. Olsen and D.C. Craft. Fabrication and performance characteristics of InGaAsP multiquantum well double channel planar buried heterostructure lasers. *Appl. Phys. Lett.* **46**, 19 (1985)
10. E.A. Rezek, N. Holonyak and B.K. Fuller. Temperature dependence of threshold current for coupled multiple quantum well  $\text{In}_{1-x}\text{Ga}_x\text{P}_{1-z}\text{As}_z$ -InP heterostructure laser diodes. *J. Appl. Phys.* **51**, 2402 (1980)
11. F. Bantien, K. Kelting and E. Bauser. Liquid phase epitaxy of GaAs quantum well structures. *J. Cryst. Growth* **85**, 194 (1987)
12. U. Morlock *et al.* Morphology of GaAs quantum well interfaces grown by liquid phase epitaxy. *Phys. Rev. B* **44**, 8792 (1991)
13. W. Hornischer *et al.* Quantum wires prepared by liquid phase epitaxial overgrowth of dry-etched AlGaAs-GaAs heterostructures. *Appl. Phys. Lett.* **60**, 2998 (1992)
14. E. Lendvay Z. Labadi and A. Barna. Preparation of high quality abrupt GaAs/GaAlAs heterojunctions by advanced liquid phase epitaxy. *Cryst. Prop. Prep.* **32-34**, 582 (1991)
15. I.N. Arsent'ev, N.Yu. Antonishkis, D.S. Garbuzov, V.V. Krasovskii, A.B. Komisarov and V.B. Khaifin. Quantum-size effects in InGaAsP/GaAs heterostructures grown by liquid epitaxy and characterised by active regions of thicknesses from 40 to 300 Å. *Sov. Phys. Semicond.* **21**, 109 (1987)
16. Z.I. Alferov, N.Yu. Antonishkis, I.N. Arsent'ev, D.Z. Garbuzov and V.V. Krasovskii. Photoluminescence of InGaAsP/GaAs quantum well heterostructures formed by the laser epitaxy method. *Sov. Phys. Semicond.* **20**, 1342 (1986)
17. K. Kelting, K. Koehler and P. Zwicknagl. Luminescence of GaAlAs single quantum wells grown by liquid phase epitaxy. *Appl. Phys. Lett.* **48**, 157 (1986)
18. S. Becher, V. Gottschalch, G. Wagner, R. Schwabe and J.L. Staehli. Characterisation of lattice-matched single InGaAsP quantum wells grown by conventional liquid phase epitaxy. *Semicond. Sci. and Technol.* **9**, 1558 (1994).
19. V.N. Bessolov, S.G. Konnikov, M.V. Lebedev, E.B. Novikov, K.J. Pogrebitsky and B.V. Tsarenkav. Relaxation liquid phase epitaxy under conditions of inversed mass transfer and

- its possibilities in growing thin layers of III-V compounds. *Crystal Prop. Prep.* **32–34**, 562 (1991)
20. J.L. Benchimol, S. Slempek, D.C. N'Guyen, G. Le Roux, J.F. Bresse and J. Primot. InGaAsP superlattices grown by LPE. *J. Appl. Phys.* **59** (12), 4068 (1986)
  21. Y.-C. Lu, E. Bauser and H.-J. Queisser. Thin epitaxial gallium aluminum arsenide layers grown by multi-compartment liquid-phase epitaxy. *J. Cryst. Growth* **121** (4), 566 (1992)
  22. D. Nohavica, P. Gladkov, M.A. Laurenco, Z. Yang, K. Homewood and D. Ehrentraut. Meander type LPE-new approach to growth InP and GaInAsP layers. *Proc. 8th Int. Conf. on InP and Related Mater*, April 1996, Schwabisch Gmund, Germany, IEEE, New York, 560; *Crystal Res. Technol.* **31**, S305 (1996).
  23. A. Krier and X. L. Huang. Mid-infrared electroluminescence from InAsSb quantum dot light emitting diodes grown by liquid phase epitaxy. *Physica E* **15**, 159 (2002).
  24. D. Nohavica and J. Teminova. Controlled epitaxial growth of GaInAsP/InP from the liquid phase. *Crystal Prop. Prep.* **32–34**, 630 (1991)
  25. D. Nohavica and J. Oswald. Preparation of periodic structures by meander type LPE. *J. Cryst. Growth* **146**, 287 (1995)
  26. D. Nohavica, K.P Homewood, W.P. Gillin, M.A. Lourenco, Z Yang and J. Oswald. LPE growth and high temperature stability of elastically strained GaInAsP/InP layers. *Cryst. Res. Technol.* **31**, 305 (1996)
  27. P. Besomi, J. Degani, N.K. Dutta, W.R. Wagner and R.J. Nelson, High quality InGaAsP DH material grown by near equilibrium LPE technique. *J. Appl. Phys.* **56** (10), 2879 (1984)
  28. L. Reynolds, M.C. Tamargo, P.J. Anthony and J.L. Zilko. Analysis of the short time liquid phase epitaxial growth of  $\text{Al}_x\text{Ga}_{1-x}\text{As}$ . *J. Cryst. Growth* **57**, 109 (1982)
  29. M. G. Astles. *Liquid Phase Epitaxial Growth of III-V Compound Semiconductor Materials and their Device Applications*, Adam Hilger, Bristol (1990)
  30. G.A. Antypas and L.Y.L. Shen. Growth and characterization of InGaAsP lattice-matched to InP. *Inst. Phys. Conf. Ser.* **33b**, 96 (1976)
  31. S.Y. Leung and N.E. Schumaker. Simulation of slider induced convection in horizontal LPE slider system. *J. Cryst. Growth* **60**, 421 (1982)
  32. L.-J. Chen, K.-L. Hsueh, C.-C. Wan and J. Gong. Mass transfer rate measurement of short time LPE growth using an electrochemical method. *Appl. Electrochem.* **21**, 998 (1991)
  33. P.E. Brunemeier, J.J. Roth, N. Holonyak and G.E.J. Stillman. Inhomogeneity of LPE InGaAsP lattice matched on InP—effects of transient growth. *Appl. Phys.* **56** (6), 1707 (1984)
  34. M. Feng, L.W. Cook, M.M. Tashima, G.E. Stillman and R.J. Blattner. Auger profile study of the influence of lattice mismatch on the LPE InGaAsP–InP heterojunction interface. *Appl. Phys. Lett.* **34** (10), 697 (1979)
  35. L.W. Cook, M. Feng, M.M. Tashima, R.J. Blattner and G.E. Stillman. Interface grading in InGaAsP LPE heterostructures. *Appl. Phys. Lett.* **37** (2), 173 (1980)
  36. E.A. Rezek, B.A. Vojak, R. Chin and N. Holonyak Jr. Thin layer LPE of InGaAsP heterostructures in short intervals (<100ms), non-diffusion limited growth. *J. Electron. Mater.* **10** (1), 255 (1981)
  37. K.D. Moiseev, A.A. Sitnikova, N.N. Faleev and Yu P. Yakovlev. Type II broken gap InAs/GaInAsSb heterostructures with abrupt planar interface. *Semiconductors* **34** (12), 1381 (2000)
  38. N. Kuwano, T. Goto, K. Oki, S. Uchiyama and K. Iga. Electron microscopic observation of heterointerface in GAXIN1-XASYPI-Y INP grown by liquid phase epitaxy. *Jpn. J. Appl. Phys.* **27**, 1768 (1988)
  39. J.A. Chen, J.-H. Lee, S.-C. Lee and H.H. Lin. Abrupt heterointerfaces in AlGaAs/AlGaAs/AlGaAs QW structure grown by LPE. *J. Appl. Phys.* **65** (10), 4006 (1989)
  40. Y. Sasai, N. Hase and T. Kajiwara, A 1.3 micron InGaAsP/InP multiquantum laser grown by LPE. *J. Appl. Phys.* **24** (2), L137 (1985)
  41. B. Baoxue, G. Xin, Q. Yi, Z. Xingde and G. Dingsan. InGaAsP/GaAs SCH SQW laser arrays grown by LPE. *Op. Laser. Tech.* **32**, 335 (2000)



42. D. Nohavica, J. Teminova, D. Berkova, J. Zelinka, M. Zahradkova, J. Zavadil and V. Malina 1.07–1.67  $\mu\text{m}$  GaInAsP/InP DC PBH Injection Lasers, presented at Photonics 92, 8–11 September 1992, Olomouc, Czech Republic, Rozvid, 247 (in English) (1992)
43. N.K. Dutta, S.G. Napholtz, A.B. Picarilli and G. Przybylek. InGaAsP distributed feedback multiquantum well laser. *Appl. Phys. Lett.* **48** (21), 1419 (1986)
44. C.A. Green, N.K. Dutta and W. Watson, Linewidth enhancement factor in InGaAsP/InP multiple quantum well lasers. *Appl. Phys. Lett.*, **50** (20), 1409 (1987)
45. Y. Mao and A. Krier. 2.5 micron LED in InAs(0.36) Sb(0.36)P(0.44) for HF detection. *IEE Proc. Optoelectron.* **144** (5), 355 (1977)
46. H.R. Dizaji and R. Dhanasekaran. Investigation of concentration profiles and growth rate of InAs LPE by computer simulation technique. *Il Nuovo Cimento* **17D**, 601 (1995)
47. M.R. Wilson, A. Krier and Y. Mao. Phase equilibria in InAsSbP Quaternary alloys grown by LPE. *J. Electron. Mater.* **25**, 1439 (1996)
48. A. Krier and Z. Labadi, Modelling of InAs thin layer growth from the liquid phase. *IEE Proc. Optoelectron.* **147** (3), 222 (2000)
49. A. Krier, S.E. Krier and Z. Labadi. Photoluminescence from InAs quantum wells grown by liquid-phase epitaxy. *Appl. Phys. A* **71** (3), 249 (2000)
50. S. Adachi. Bandgaps and refractive indices of AlGaAsSb, GaInAsSb and InPAsSb—key properties for a variety of the 2–4 micron optoelectronic device applications. *J. Appl. Phys.* **61**, 4869 (1987)
51. C.G. Van der Walle and R.M. Martin. Band line-ups and deformation potentials in the model solid theory. *Phys Rev.* **39**, 1871 (1989)
52. I.N. Stranski and L. Krastanow. *Sitzungber. Akad. Wissenschaft. Wien* **146**, 797 (1937)
53. M. Sugawara, Self-assembled InGaAs/GaAs quantum dots. *Semicond. Semimetals* **60**, 332 (1999)
54. R. Leon, C. Lobo, A. Clark, R. Bozek, A. Wyszomolek, A. Kurpiewski and M. Kaminska. Different paths to tunability in III-V quantum dots. *J. Appl. Phys.* **84**, 248 (1998)
55. A. Krier. Physics and technology of mid-infrared light emitting diodes. *Phil. Trans. R. Soc. (Lond) A* **359**, 599 (2001)
56. R. Murray, D. Childs, S. Malik, P. Siverns, C. Roberts, J.M. Hartmann and P. Stavrinou. 1.3  $\mu\text{m}$  room temperature emission from InAs/GaAs self-assembled quantum dots. *Jpn. J. Appl. Phys., Part 1*, **38**, 528 (1999)
57. B.M. Kinder and E.M. Goldys. Microstructural evolution of GaSb self-assembled islands grown by metalorganic chemical vapor deposition. *Appl. Phys. Lett.* **73** (9) 1233 (1998)
58. N.T. Yeh, T.E. Nee, P.W. Shiao, M.N. Chang, J.I. Chyi and C.T. Lee. Photoluminescence characteristics of self-assembled In<sub>0.5</sub>Ga<sub>0.5</sub>As quantum dots on vicinal GaAs substrates. *Jpn. J. Appl. Phys., Part 1*, **38**, 550 (1999)
59. A. Krier, X.L. Huang and A. Hammiche. Liquid phase epitaxial growth and morphology of InSb quantum dots. *J. Phys. D: Appl. Phys.*, **34**, 874 (2000).
60. B.R. Bennett, R. Magno and B.V. Shanabrook. Molecular beam epitaxial growth of InSb, GaSb, and AlSb nanometer-scale dots on GaAs. *Appl. Phys. Lett.* **68**, 505 (1996).
61. M. Yano, Y. Seki, H. Ohkawa, K. Koike, S. Sasa and M. Inoue. Characteristics of self-assembled InSb dots grown on (100) AlGaSb by molecular beam epitaxy. *Jpn. J. Appl. Phys.* **37**, 2455 (1998)
62. B.R. Bennett, P.M. Thibado, M.E. Twigg, E.R. Glaser, R. Magno, B.V. Shanabrook and L.J. Whitman. Self-assembled InSb and GaSb quantum dots on GaAs(001). *J. Vac. Sci. Technol.*, **B14**, 2195 (1996)
63. J.A. Floro, E. Chason, M.B. Sinclair, L.B. Freund and G.A. Lucadamo. Dynamic self-organization of strained islands during SiGe epitaxial growth. *Appl. Phys. Lett.* **73**, 951 (1998)
64. C.S. Peng, Q. Huang, W.Q. Cheng, J.M. Zhou, Y.H. Zhang, T.T. Sheng and C.H. Tung. Improvement of Ge self-organized quantum dots by use of Sb surfactant. *Appl. Phys. Lett.* **72**, 2541 (1998)

65. F.M. Ross, J. Tersoff and R.M. Tromp. Coarsening of self-assembled Ge quantum dots on Si(001). *Phys. Rev. Lett.* **80**, 984 (1998)
66. G. B. Stringfellow and P. E. Greene. Calculation of ternary and quaternary III-V phase diagrams: InGaAs and InAsSb. *J. Phys. Chem. Solids* **30**, 1779 (1969)
67. A. Krier, X. L. Huang and A. Hammiche. Mid-infrared photoluminescence of InAsSb quantum dots grown by liquid phase epitaxy. *Appl. Phys. Lett.* **77**, 3791 (2000)
68. B. Matveev *et al.* InAsSbP/InAs LEDs for the 3.3–5.5  $\mu\text{m}$  spectral range. *IEE Proc. Optoelectron.* **145**, 254 (1998)
69. E. Alphandery, R. J. Nicholas, N. J. Mason, B. Zhang, P. Mock and G. R. Booker. Self-assembled InSb quantum dots grown on GaSb: a photoluminescence, magnetoluminescence, and atomic force microscopy study. *Appl. Phys. Lett.* **74**, 2041 (1999)
70. E. R. Glaser, B. R. Bennett, B. V. Shanabrook and R. Magno. Photoluminescence studies of self-assembled InSb, GaSb, and AlSb quantum dot heterostructures. *Appl. Phys. Lett.* **68**, 3614 (1996)
71. S. P. Guo, H. Ohno, A. D. Shen, Y. Ohno and F. Matsukura. Photoluminescence study of InAs quantum dots and quantum dashes grown on GaAs (211)B. *Jpn. J. Appl. Phys.* **37**, 1527 (1998)
72. H.H. Gao, A. Krier and V.V. Sherstnev. High quality InAs grown by LPE using gadolinium gettering. *Semicond. Sci. Technol.* **14**, 441 (1999)



# 9 Liquid Phase Epitaxy of $\text{Hg}_{1-x}\text{Cd}_x\text{Te}$ (MCT)

**P. CAPPER**

*SELEX Sensors and Airborne Systems Infrared Ltd, PO Box 217, Millbrook, Southampton SO15 0EG, UK*

---

9.1 Introduction	259
9.2 Growth	261
9.2.1 Introduction	261
9.2.2 Phase diagram and defect chemistry	262
9.2.3 LPE growth techniques	264
9.3 Material characteristics	269
9.3.1 Composition and thickness	271
9.3.2 Crystal quality and surface morphology	272
9.3.3 Impurity doping and electrical properties	273
9.3.4 Multiple-layer heterojunction structures	278
9.4 Device status	278
9.4.1 LPE growth on Si-based substrates	283
9.5 Summary and future developments	283
References	284

---

## 9.1 INTRODUCTION

This chapter describes the growth of the ternary  $\text{Hg}_{1-x}\text{Cd}_x\text{Te}$  (MCT) by liquid phase epitaxy (LPE). The chapter is an update of this author's previous summary [1] with recent additions in the areas of growth, layer annealing, doping, reactive ion etching (RIE) and device applications, where there has been notable progress in the last few years. Baker [2] and Reine [3] have given recent summaries of infrared (IR) detector types made in MCT and this chapter draws on these two sources for some material.

MCT is the most widely used material for high-performance IR detectors at present and, as a consequence, is the third most studied semiconductor after Si and GaAs. By changing the composition,  $x$ , the detector spectral response can be made to cover the range from 1 to beyond  $17\ \mu\text{m}$ . The advantages of this system arise from a number of features, notably: high optical absorption coefficient, low carrier generation rate, high electron mobility and readily available doping techniques. These advantages mean that very sensitive IR detectors can be produced at relatively high operating temperatures.

MCT continues to be developed as the material of choice for high-performance long-wavelength (8–12  $\mu\text{m}$ ) arrays and has an established market at the medium (3–5  $\mu\text{m}$ ) and short wavelength (1–2.5  $\mu\text{m}$ ) ranges.

While photoconductive IR arrays have mainly used bulk material [4] photovoltaic arrays mainly use epitaxial layers. Photovoltaic arrays have inherently low power consumption and can be easily connected to a silicon integrated circuit to produce a retina-like focal plane array. Such arrays are key for so-called second-generation thermal imaging cameras that break through the performance limits imposed by photoconductive arrays in first-generation cameras. Photovoltaic devices tend to fall into two categories: long linear arrays of long-wavelength (LW) (8–12  $\mu\text{m}$ ) diodes and matrix arrays of medium wavelength (MW) (3–5  $\mu\text{m}$ ) diodes and short-wavelength (SW) diodes (1.5–3  $\mu\text{m}$ ).

Long linear arrays are required for systems with just one dimension of scanning. Here MCT is the sensor material of choice because the stringent sensitivity requirements of these systems demands a high quantum efficiency and near background limited infrared photoconductor (BLIP)-limited performance detectors. Development work in the 1980s and 1990s in the USA and Europe has led to a family of detectors for long-waveband thermal imaging, such as the US SADA II system based on a  $480 \times 6$  format or the UK STAIRS 'C' system based on a  $768 \times 8$  array format (producing a high-definition  $1250 \times 768$  image). In the detector examples quoted there are six or eight rows of diodes and the signal from each row is delayed in time and added to provide an enhancement. This is called time-delay and integration (TDI).

Long linear arrays can also use the MW band but the flux levels are over an order less than the LW band and the performance is compromised by the short integration time in a scanned system. MW detectors therefore tend to use matrix arrays where the integration time can approach the frame time. The problem of point defects is considerably reduced in the medium waveband and large two-dimensional (2D) arrays are more practical. The emphasis for MW detectors is to develop wafer-scale processes to provide large, economical 2D arrays for staring thermal imaging cameras. The MW band thermal imaging market is concentrated on arrays using half-TV ( $320 \times 256$  or  $384 \times 288$ ) or full-TV formats ( $640 \times 480$  or  $640 \times 512$ ) and is divided between indium antimonide (InSb), MCT and platinum silicide. Broadly, manufacturing companies from USA and Israel tend to prefer InSb, and European and some US companies have specialized in MCT. Currently, IR cameras based on MCT arrays are in production and are producing remarkable sensitivities, over an order better than first-generation cameras.

Considerable progress has been made in the last two decades in the epitaxial growth of MCT. Bulk growth methods are still used for providing good-quality material for photoconductor arrays but for photovoltaic arrays there are problems associated with crystal grain boundaries, which are electrically active, and cause lines of defects. Also, there are limitations in the boule size, which makes bulk-grown material suitable for only small arrays.

Several epitaxial growth techniques are in use today. Manufacturers will select a technique that suits their device technology and the type of detectors they are trying to make. For instance, high-performance LW arrays will call for the best possible crystal quality, whereas, large-area MW arrays can probably accept poorer material but must have large, uniform wafers. It is the aim of most manufacturers to produce high-quality layers in large areas at low cost but this ideal has been elusive. At the present time the best structural quality material is grown using LPE onto lattice-matched substrates of CdZnTe, and

this has been used successfully in homojunction technologies where the photosensitive junction is diffused into a homogeneous monolith of material. There is a trend to move away from expensive CdZnTe substrates and both LPE and vapor phase epitaxy (VPE) are now used on a variety of alternative substrates.

LPE of MCT at present provides the lowest crystal defect levels, and very good short- and long-range uniformity. LPE layers are grown using an isothermal supersaturation or programmed cooling technique or some combination of these. A detailed knowledge of the solid–liquid–vapor phase relation is essential to control the growth particularly in view of the high Hg pressure. Challenges include: the compositional uniformity through the layer, the surface morphology, the incorporation of dopants and the specifications for thickness, wavelength, etc. A common component leading to high structural quality is the use of lattice-matched substrates of CdZnTe. These are grown by Bridgman and vertical gradient freeze (VGF) processes and can supply slices as large as  $6 \times 8$  cm. The CdZnTe substrates must be of the highest quality and often this is a significant cost driver for the process.

Two different technical approaches are used: growth from a Hg-rich solution and growth from a Te-rich solution. Advantages of the Hg-rich route include: excellent surface morphology, a low liquidus temperature, which makes cap layer growth more feasible and the ease of incorporation of dopants. Also, large melts can provide for very good compositional and thickness uniformity in large layers and give consistent growth characteristics over a long period of time. Growth from Te-rich solutions can use three techniques to bring the melt into contact with the substrate: dipping, tipping and sliding. Sliding boat uses small melt volumes and is very flexible for changing composition, thickness and doping. Tipping and dipping can be scaled up easily and can provide thick, uniform layers but the large melts limit flexibility.

Most manufacturers have taken their chosen growth system and tailored it to provide optimum material for their device technology. In particular the use of dopants and the deliberate introduction of compositional grades are very specific to the device structure. A crucial figure of merit, however, is the dislocation count that controls the number of defects in 2D arrays. Etch pit densities of  $3\text{--}7 \times 10^4 \text{ cm}^{-2}$  are typically seen in the Te-rich sliding boat process, reproducing the substructure of the CdZnTe substrate [5]. The etch pits are associated with threading dislocations that appear to be normal or near normal to the layer surface. The substrate defect level can be as low as mid- $10^3 \text{ cm}^{-2}$  in some horizontal Bridgman CdZnTe but this is not easy to reproduce. Device processing therefore must expect to cope with defect levels in the mid- $10^4 \text{ cm}^{-2}$  range for routine MCT epilayers and this will set the ultimate limit on the number of defects in MCT 2D arrays. Several groups have used the LPE process on low-cost substrates including: CdZnTe or CdTe on GaAs/Si wafers [6] or the PACE technology on sapphire [7].

## 9.2 GROWTH

### 9.2.1 Introduction

Historically, crystal growth of MCT has been a major problem mainly because a relatively high Hg pressure is present during growth, which makes it difficult to control the stoichiometry [ $y$  in  $(\text{Hg}_{1-x}\text{Cd}_x)_y\text{Te}_{1-y}$ ] and composition ( $x$ ) of the grown material. Low-temperature growth processes, such as molecular beam epitaxy (MBE) and metal-organic

vapor phase epitaxy (MOVPE), and high-temperature processes, including bulk growth and LPE, all suffer from this problem. Proper Hg vapor pressure must be furnished and controlled during growth. LPE technology has advanced to the point where material can now be routinely grown for high-performance photoconductive (PC), photovoltaic (PV), and laser detector devices in the entire 2–18  $\mu\text{m}$  spectral region.

Two different technical approaches have been pursued, with virtually equal success: growth from Te solutions and growth from Hg solutions. The pioneering work on the Te corner of the phase diagram of the Hg-Cd-Te system [8] and the associated LPE growth experiment [9] provided the necessary groundwork that led to several variations of open-tube LPE from Te solutions [10]. Santa Barbara Research Center (SBRC) pioneered the phase diagram study of the Hg corner of the Hg-Cd-Te system [11]. This knowledge was used to design equipment and experiments before a reproducible Hg-solution technology was developed [12]. One major advantage of the Hg-solution technology is its capability to produce layers of excellent surface morphology due to the ease of melt decanting. Two additional unique characteristics have now been widely recognized as essential for the fabrication of high-performance double-layer heterojunction (DLHJ) detectors by LPE: low liquidus temperature ( $<400^\circ\text{C}$ ), which makes the cap-layer growth step feasible, and ease of incorporating both p-type and n-type, temperature-stable impurity dopants, such as As, Sb and In, during growth.

Early layers were grown on very small CdTe substrates,  $<1\text{ cm}^2$ , but lattice matching was soon realized to be very important and  $\text{Cd}_{0.96}\text{Zn}_{0.04}\text{Te}$  was then used [13]. Because of the high cost of bulk substrates, fragility, and poor thermal matching between the silicon processor and MCT/CdZnTe, alternative substrates such as CdTe/GaAs [14], CdTe/GaAs/Si and CdTe/sapphire have also been used [7]. CdTe/sapphire substrates are in production for near infrared (NIR) and mid infrared backside illuminated devices [15]. MCT layers grown on alternative substrates, however, tend to have higher dislocation densities and as a result, the predominant substrate material used is still CdZnTe grown by vertical or horizontal Bridgman techniques [16, 17].

While layers grown from Hg-rich solutions are easily doped with group VB elements with high solubility [18], layers grown from Te-rich solutions are not [19]. Group VB dopants have low solubility and are not 100% active electrically. Group IIIB elements, indium in particular, are easily incorporated from both solutions. Indium doping from Te-rich melts, however, has the one advantage that the segregation coefficient is near unity (i.e. 1–4 depending on  $x$  value—unpublished results from the author's laboratory).

A number of LPE techniques have been used to grow both thin and thick films. The principal LPE techniques used are tipping, dipping and sliding boat techniques. Schematic diagrams of these three processes are shown in Figure 9.1. The tipping and dipping techniques have been implemented by using both Te- and Hg-rich solutions, whereas only Te-rich solutions have been used with the sliding boat.

## 9.2.2 Phase diagram and defect chemistry

The major difficulty in the growth of homogeneous alloy crystals from dilute or stoichiometric melts results from the differences in the equilibrium compositions of the liquid and solid phases, which leads to segregation during solidification and compositional variations. Knowledge of the solid–liquid phase relation is essential for proper use of solution

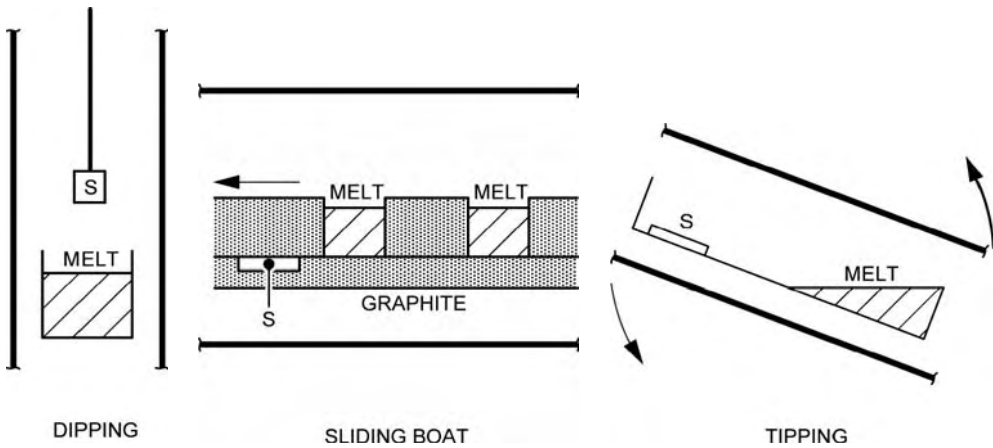


**Figure 9.1** Schematic diagram of the three principal LPE growth techniques. Reprinted from *Narrow-gap II-VI Compounds for Optoelectronic and Electromagnetic Applications*, 1997, p. 32, P. Capper *et al.*, Figure 2.1. Copyright (1997) with kind permission of Springer Science and Business Media

and bulk growth processes. In addition, the solid–vapor and liquid–vapor phase relations are of practical importance, especially in view of the high Hg pressure in the growth process [20] and the effect of the vapor of constituent components upon post-growth annealing and the consequent electrical properties [1].

Extensive experimental phase diagram and thermodynamic data have been critically reviewed, along with the results calculated by the associated solution model [21]. The associated solution model has been developed successfully to describe and predict the phase diagram of the entire Hg–Cd–Te system. A significant portion of the thermodynamic data for this system consists of the partial pressures of Hg, Cd, and Te for both the metal-saturated and the Te-saturated solid solution, and quantities derived from these. All these partial pressures, especially the predominant Hg vapor pressures, are crucial for defect chemistry analysis.

Astles [10] has reviewed the experimental data of Te-rich LPE growth at 460–550 °C. As an example, to compare growth parameters for Te solutions with those for Hg solutions, consider the growth of LWIR MCT ( $x = 0.2$ ) at 500 °C from both Te and Hg solutions. The  $x_{\text{Cd}}$  for Te-rich solutions is  $8.3 \times 10^{-3}$  while  $x_{\text{Cd}}$  for Hg-rich solutions is  $2.6 \times 10^{-4}$ . This is one of the difficulties encountered in LPE growth from Hg-rich solutions. Use of large melts, however, overcomes the Cd-depletion problem.

The net hole concentration of bulk  $\text{Hg}_{0.8}\text{Cd}_{0.2}\text{Te}$  equilibrated under Te-saturated condition ( $P_{\text{Hg}} = 0.13 \text{ atm}$ ) at 500 °C is  $10^{18} \text{ cm}^{-3}$ , while that of Hg-saturated  $\text{Hg}_{0.8}\text{Cd}_{0.2}\text{Te}$  ( $P_{\text{Hg}} = 7.3 \text{ atm}$ ) is  $8 \times 10^{16} \text{ cm}^{-3}$ . The net hole concentration at 77 K of SBRC's undoped MCT ( $x \sim 0.2$ ) layers grown from the Hg-rich solution at 515 °C, is  $\sim 1\text{--}2 \times 10^{17} \text{ cm}^{-3}$ , while that of undoped layers grown from Te-rich solution at 450–500 °C is significantly higher ( $2 \times 10^{17}\text{--}2 \times 10^{18} \text{ cm}^{-3}$ ) [10, 22]. It has been accepted that excess Te is accommodated in the MCT lattice through the formation of metal vacancies acting as doubly ionized acceptors. It is expected, therefore, that internal microprecipitation as a result of the retrograde solubility of Te in MCT should occur more readily in Te-saturated



material than in Hg-saturated material [23, 24]. It is also possible that electrically neutral native defects are significant in Te-saturated material, as indicated by self-diffusion measurements [21, 25]. The measurements have been interpreted as showing Hg-vacancy concentrations 20 to 100 times larger than inferred from Hall measurements [21].

## 9.2.3 LPE growth techniques

### 9.2.3.1 Introduction

It has been difficult to prepare homogeneous, high-quality epitaxial layers even from Te-rich solutions, mainly because of the relatively high vapor pressure of Hg ( $\sim 0.1$  atm) at typical growth temperatures ( $\sim 500$  °C). The initial growth solution composition can be drastically changed during the growth cycle due to Hg being absorbed into or evaporated from the growth solution [26]. Unless provision is made during the growth process to keep the growth solution composition constant, MCT epilayers of uniform composition cannot be grown reproducibly. Several approaches have been adopted to overcome this problem: reducing Hg loss from the melt by applying a high argon or hydrogen overpressure [27]; by confining the melt in a tight-fitting slider containing extra HgTe [28]; use of a sealed, closed-tube tilting technique [29] and active control of the Hg vapor pressure over the growth solution by means of a two-temperature-zone system [30, 31] (one zone controls the solution temperature while the other controls the Hg pressure over the solution). For a particular growth temperature and solution composition, the three-phase diagram can be used to choose a partial pressure of Hg such that the composition of the growth solution remains constant with time [26].

LPE growth from Hg-rich solutions was first attempted with unsatisfactory results by Bowers *et al.* [32]. Despite the very high Hg vapor pressure ( $>10$  atm) and the extremely low solubility of Cd in the Hg solution ( $<10^{-3}$  mol%), the ‘infinite melt’ vertical LPE (VLPE) growth from Hg solution was selected by SBRC for MCT growth. Other researchers also realized that this approach had some advantages over Te-melt LPE. Chandra *et al.* [33] deposited thin doped layers at relatively low temperatures. They used the method to form heterojunctions on base-layers grown from Te-rich solutions for photovoltaic focal plane arrays (PV FPAs).

Growth of MCT from Te-rich solutions was first used in the 1970s to grow layers as the required equipment was fairly simple and easy to implement. The quality was poor due to microstructure, dislocations and low substrate purity, mainly copper contamination [34, 35]. Copper contamination is largely responsible for the anomalous transport properties of MCT [35]. This has been the subject of much study but the source is now understood and solutions implemented [36].

The difficulties with substrates and the details of the MCT phase diagram were not well known in the early phases of the technology development and this gave problems in run-to-run composition reproducibility, and composition gradient control. It was not until Brebrick *et al.* [37] completed their phase diagram studies that accurate control of the composition was established. Composition uniformity and reproducibility was also complicated by the lack of good temperature control [38]. LPE growth from Te- and Hg-rich melts is usually carried out in quartz crucibles when using the dipping or tipping techniques, mainly because quartz is available in very high purity, the melt does not

interact with the quartz and it can be easily formed. IR detectors require purity levels  $\leq 10^{15} \text{ cm}^{-3}$  and quartz makes this achievable. Growth from the sliding boat, however, has been carried out in high-purity graphite boats also with great success [5, 31, 39, 40].

### 9.2.3.2 Hg-rich growth

The design and operation of a system for MCT growth from Hg-rich melts is dominated by consideration of the high vapor pressure of Hg, which comprises  $\geq 90\%$  of the growth solution. A secondary but related factor is the requirement to minimize melt composition variation during and between growths due to solvent or solute loss. These factors led to the evolution of a vertical high-pressure furnace design with a cooled reflux region. A simplified vertical liquid phase epitaxy (VLPE) system design is shown schematically in Figure 9.2 [11].

The furnace should provide a controllable, uniform and stable thermal source for the melt vessel capable of maintaining at least  $550^\circ\text{C}$  continuously. The cylindrical melt vessel consists of a high-strength stainless steel chamber lined with quartz. Such systems

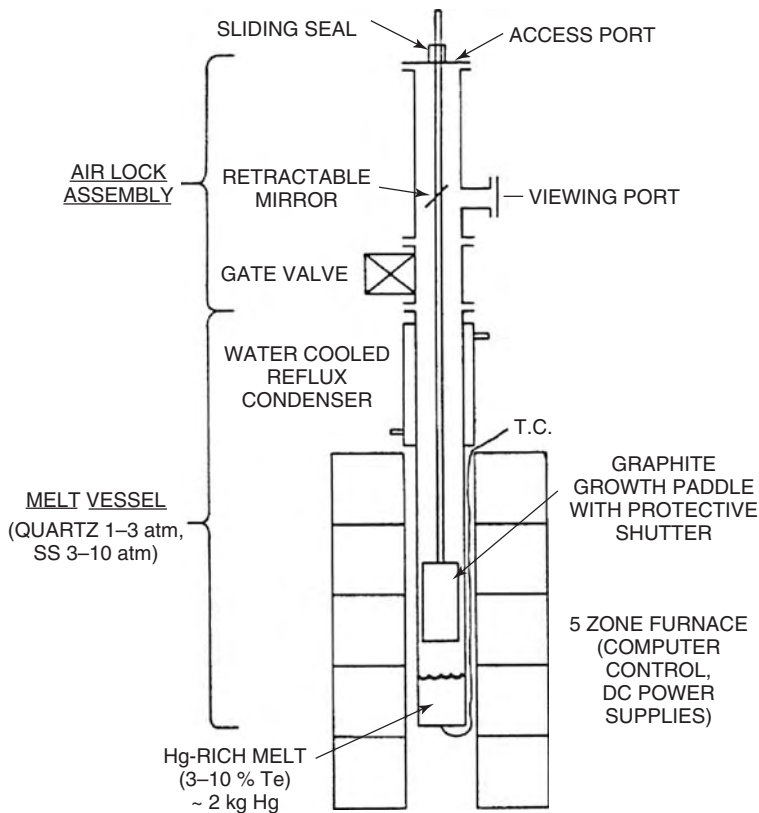


**Figure 9.2** Schematic diagram of a simplified Hg-melt VLPE system. Reprinted from *Narrow-gap II-VI Compounds for Optoelectronic and Electromagnetic Applications*, 1997, p. 36, P. Capper *et al.*, Figure 2.3. Copyright (1997) with kind permission of Springer Science and Business Media

are capable of containing about 10–20 kg of melt at 550 °C for several years with no degradation in melt integrity or purity.

To keep the Hg-rich melt from boiling or oxidizing at temperatures above 360 °C the system must be pressurized and leak-free. Typical pressures range up to 200 psi and the pressurization gas may be high-purity H<sub>2</sub> or a less-explosive reducing-gas mixture containing H<sub>2</sub>. The melts are always kept saturated and are maintained near to the growth temperature and pressure between successive runs. The prepared substrates are introduced into the melt through a transfer chamber or air lock. Prior to growth, the transfer chamber is evacuated and filled to pressure at which time the gate valve can be opened. A high-purity graphite paddle with externally actuated shutters holds the substrates. The paddle assembly can be lowered into the melt and rotated to stir the melt.

In general, the high-purity melt components are introduced into the clean melt vessel at room temperature. The system is sealed, evacuated and pressurized. The temperature of the furnace is raised above the predicted melting point and held constant until all the solute dissolves. The use of large melts results in a near-constant saturation temperature from run-to-run and ensures excellent reproducibility of layer characteristics. The amount of material removed from the melt during each growth run is relatively insignificant.

Optimum layer smoothness occurs on lattice-matched CdZnTe substrates oriented close to the <111> plane. Both sides of the substrate are mechanically and then chemically polished to optimum parallelism and planarity. A typical growth procedure begins by lowering the paddle plus substrates into the melt and allowing thermal equilibrium to be reached while stirring. After reaching equilibrium, a programmed ramp reduces the melt temperature to the required level at which point the shutters are opened and the substrates are exposed to the melt. The growth rate and layer thickness are determined mainly by the exposure temperature relative to the saturation point and the total growth range. The composition of the layer and its variation are determined mainly by the melt composition and its thermal uniformity. Upon completion, the paddle is withdrawn into the transfer chamber and the isolation valve is closed.

Large melts allow the production of layers up to 30 cm<sup>2</sup> with excellent compositional and thickness uniformity and allow dopant impurities to be accurately weighed for incorporation into layers and to maintain stable electrical characteristics over a long period of time. Four layers (30 cm<sup>2</sup> each) with a total area of 120 cm<sup>2</sup> can be grown in a single run [12]. Norton *et al.* [41] have also scaled up for the growth of cap layers from Hg-rich solutions, each reactor capable of growth on four 24 cm<sup>2</sup> base layers per run.

### 9.2.3.3 Te-rich growth

MCT growth from Te-rich solution solves a number of problems encountered with bulk crystal growth techniques. The most important being the reduction of the Hg vapor pressure over the liquid by almost two orders of magnitude at the growth temperature. Large-area layers can be grown with thicknesses up to ~ 150 μm reproducibly. Since the early 1980s the CdZnTe substrate and corresponding LPE layer size have increased considerably, from 2 cm<sup>2</sup> in 1983 to over 80 cm<sup>2</sup> in 1995. Growth from Te-rich solutions is widely used in three embodiments, dipping, tipping and sliding-boat technologies. While the tipping process may be used for low-cost approaches, it is not as widely used in production as the sliding boat and the dipping techniques. A comparison of the three techniques is shown in Table 9.1.

**Table 9.1** Comparison of the three LPE growth techniques. Reprinted from *Narrow-gap II-VI Compounds for Optoelectronic and Electromagnetic Applications*, 1997, p. 39, P. Capper *et al.*, Table 2.1. Copyright (1997) with kind permission of Springer Science and Business Media

Technique	Advantages	Disadvantages
Sliding boat	thickness control large area double layers	thick layers difficult to grow substrate thickness/planarity control high cost
Tipping	thickness control lowest investment for experimental investigation closed system/good $P_{\text{Hg}}$ control	high cost scale up
Dipping	thick layer growth high throughput low cost large/flexible area	thin layer thickness control double layers

Dipping LPE reactors were initially very simple, utilizing small transparent gold-coated furnaces with melts of  $\sim 200$  g allowing growth on  $\sim 5$  cm<sup>2</sup> substrates [42]. As LPE moved from R&D to production reactors became larger and more sophisticated. Current reactors are capable of growing in excess of 60 cm<sup>2</sup> per growth run and are kept at temperature for long periods (>6 months). Melts, on the other hand, last a very long time (>5 years). Westphal *et al.* [38] described a sensor-based reactor capable of growing MCT thick layers at relatively high production volumes and excellent reproducibility (Figure 9.3). The temperature can be controlled within a maximum range of  $\pm 0.005$  °C at a temperature of  $\sim 480$  °C. The melts weigh about 4 kg with a liquidus temperature of  $\sim 480$  °C for a solid MCT composition  $x = 0.225$ . The mercury reservoir is essential and accurate mercury vapor pressure control ensures constant liquidus and thus constant liquid composition.

Sliding-boat LPE is the most widely used technique for compound semiconductor LPE. It normally consists of a graphite boat with a recess in the base for holding the substrate wafer and a movable block with wells that contain the LPE solution and that allows the solution to be brought into contact with the substrate and then wiped off after growth. Advantages of the technique are the efficient use of solution and the ease of growing multi-layers. Disadvantages are the need for careful machining of the boat components in order to get efficient removal of the solution after growth and the need for precisely sized substrate wafers to fit into the recess in the boat.

Layers grown from Te-rich solutions are usually grown by isothermal supersaturation or programmed cooling techniques or a combination of both. The details of the mass transport of Hg-Cd-Te solutions during LPE growth have been presented by Shaw [43]. He predicted that isothermal growth of thin layers from supersaturated solutions would yield layers with uniform composition but the growth rate would change during growth.

Colombo *et al.* [30] used a melt-tracking technique to control the composition of the solid. The technique utilizes the phase diagram to calculate the Hg partial pressure and melt additions required to maintain the composition of the growing layers constant. Table 9.2 shows a comparison of reactors with and without sensors.

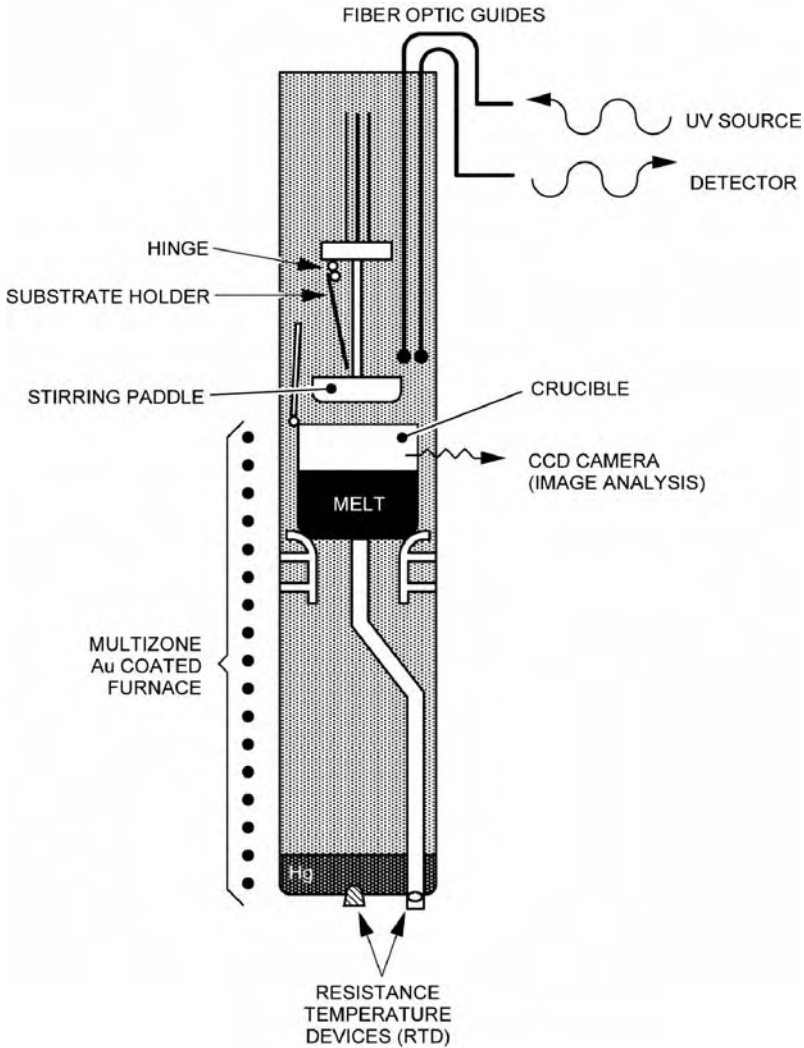


**Figure 9.3** Schematic diagram of a dipping LPE reactor showing the Te-rich melt, the mercury reservoir and position of the sensors [38]. Reprinted from *Narrow-gap II-VI Compounds for Opto-electronic and Electromagnetic Applications*, 1997, p. 40, P. Capper *et al.*, Figure 2.5. Copyright (1997) with kind permission of Springer Science and Business Media

The sliding-boat growth process has several variants [10] but essentially, a polished substrate is placed in the well of a graphite slider and the Te-rich solution is placed in a well in the body of the graphite boat above the substrate and displaced horizontally from it (Figure 9.4). Normally, a separate well contains the HgTe charge to provide the Hg vapor pressure needed during growth and during cool-down to control the stoichiometry. The boat is loaded into a single-ended silica tube that can be flushed with nitrogen/argon prior to the introduction of Pd-diffused  $H_2$  for the growth phase. The furnace surrounding the work tube is slid over the boat and the temperature is increased to 10–20 °C above

**Table 9.2** Comparison of LPE layer properties between a reactor with and without sensors. Reprinted from *Narrow-gap II-VI Compounds for Optoelectronic and Electromagnetic Applications*, 1997, p. 43, P. Capper *et al.*, Table 2.2. Copyright (1997) with kind permission of Springer Science and Business Media

Property	Without sensors	With sensors
Temperature control (°C)	±0.1	±0.005
Pressure control (torr)	±10	±1
Composition control	±0.2265 ± 0.0033 (1111 films)	±0.225 ± 0.0013 (1500 films)
Thickness (μm)	105 ± 26 (±25 %)	111 ± 22 (±25 %)

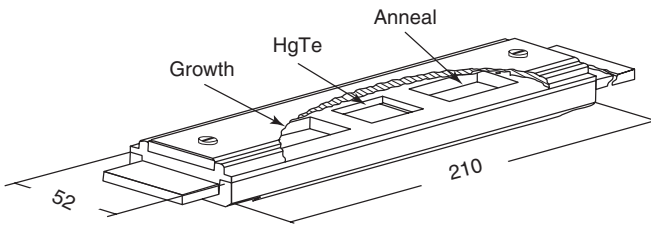


**Figure 9.4** Schematic of Te-rich sliding-boat arrangement, dimensions in mm [44]. Reproduced from P. Capper *et al.*, in *Growth and Processing of Electronic Materials*, editor N. McN Alford (1998) (ISBN 1-86125-072-X published by IOM Communications, London) p. 38, Fig. 1, by permission of Marcy Publishing

the relevant liquidus. A slow temperature ramp ( $2\text{--}3\text{ }^{\circ}\text{C h}^{-1}$ ) is initiated and when the temperature is close to the liquidus of the melt the substrate is slid under the melt and growth commences. After sufficient time has elapsed to grow the required thickness of MCT (typical growth rates are  $9\text{--}10\text{ }\mu\text{m h}^{-1}$ ) the substrate is withdrawn and the temperature is decreased to an annealing temperature before being reduced rapidly to room temperature [5]. Thicknesses of  $25\text{--}30\text{ }\mu\text{m}$  are normally produced for loophole diode applications, see [2]. Capper *et al.* [44] showed wavelength uniformity over a  $2 \times 3$  cm LPE layer (see Figure 9.5 for more recent similar examples on  $2 \times 4$  cm LW and MW layers). In that same paper the importance of Zn distribution in substrates (for lattice-matching purposes) was stressed. This aspect was discussed in more detail by Gower *et al.* [45] who presented Zn maps produced by NIR and X-ray diffraction (XRD) techniques (Figure 9.6) where good agreement was seen.

Destefanis *et al.* [46] have described their current Te-slider process onto  $20\text{-cm}^3$ -sized areas, where array sizes are now up to  $640 \times 512$  ( $20\text{ }\mu\text{m}$  pitch),  $1500 \times 2$  ( $30\text{ }\mu\text{m}$  pitch) long linears and  $1000 \times 1000$  ( $15\text{ }\mu\text{m}$  pitch) MW arrays. Recently, Denisov *et al.* [47] carried out a numerical study of convection in the Te-slider arrangement. They predicted the occurrence of convection cells and linked these to  $x$  nonuniformity.

### 9.3 MATERIAL CHARACTERISTICS

LPE technology has demonstrated excellent control of critical material properties (cut-off wavelength, thickness, surface morphology, crystal quality, defect density, wafer size,

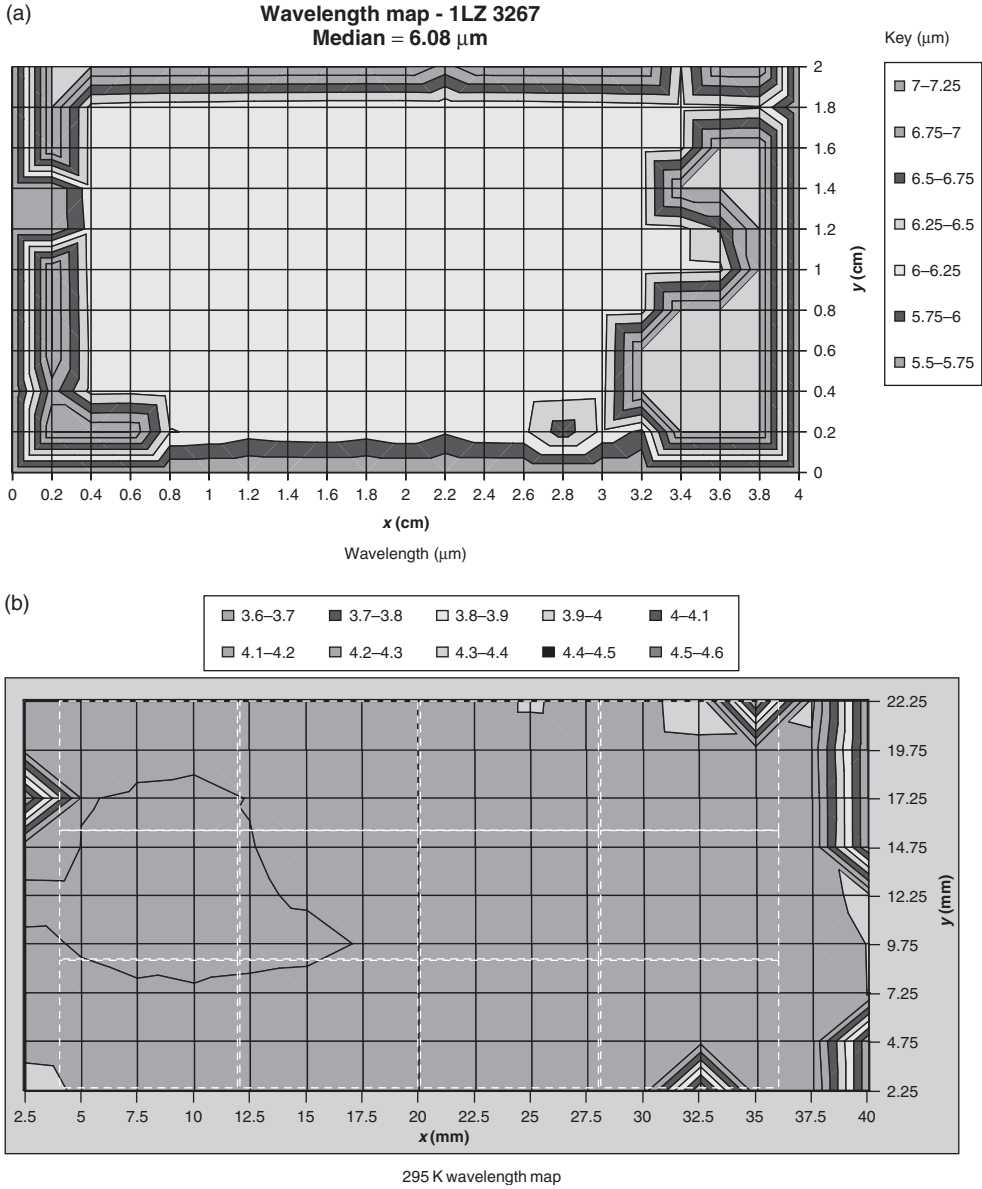


**Figure 9.5** Wavelength uniformity plots of (a) LW and (b) MW  $2 \times 4$  cm LPE layers from Te-rich sliding-boat growth. Courtesy of SELEX

electrical properties, and junction quality) in terms of run-to-run reproducibility and across-wafer uniformity. Test structure analysis reveals excellent focal plane array performance parameters, including leakage current, quantum efficiency, capacitance, spectral response, operating temperature, uniformity, operability, optical cross-talk, array format, and pixel size [2, 3]. Data on material properties realized by both Hg- and Te-rich technologies are described below.

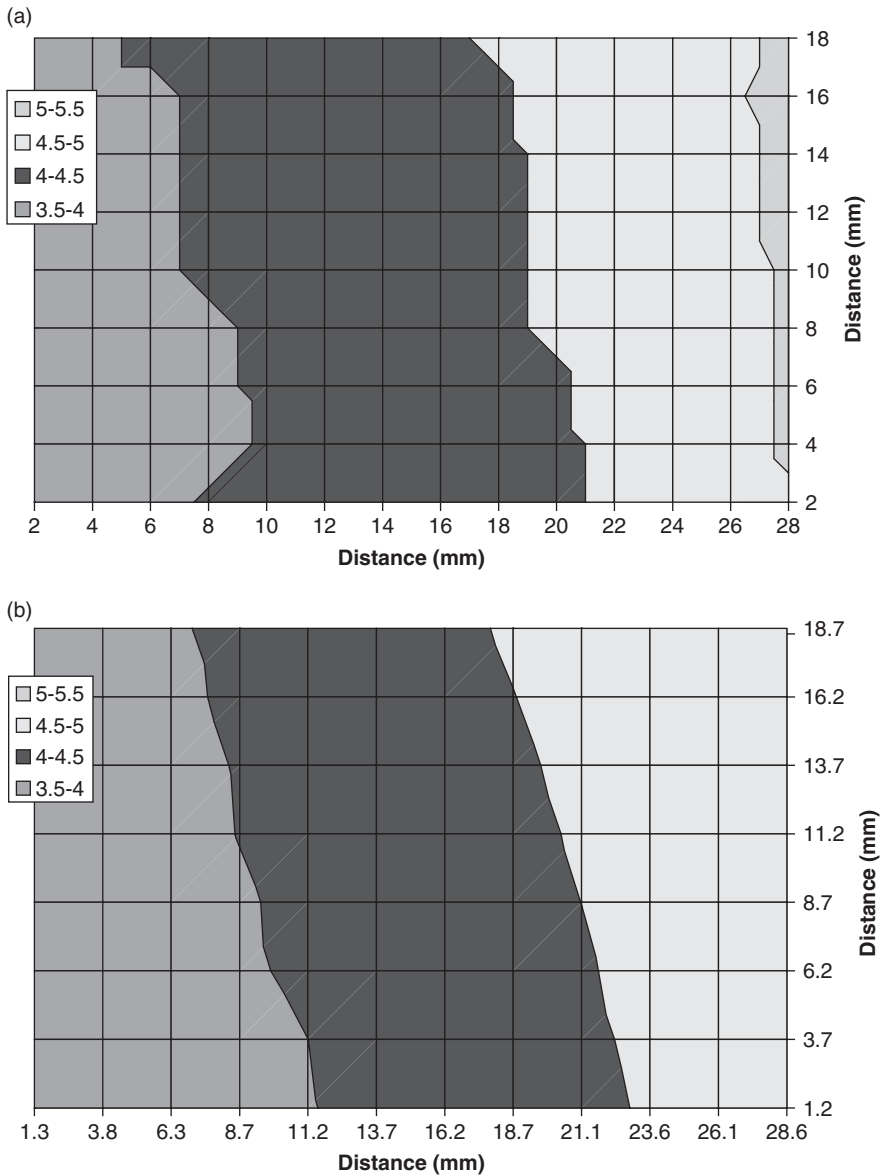


**Figure 9.6** Zn maps of  $2 \times 3$  cm CdZnTe substrates using (a) NIR and (b) XRD techniques. Courtesy of SELEX

### 9.3.1 Composition and thickness

Good composition uniformity, both laterally and in depth, is essential to obtain the required uniform device performance. Growth parameters that need to be optimized in Hg-rich LPE to obtain good composition uniformity include the degree of supercooling and mixing of the melt, the geometrical configuration of the growth system, the melt size, and the phase



diagram. The standard deviation of the cut-off wavelength, measured and calculated for 12 spots by Fourier transform infrared (FTIR) transmission measurements at 80 K across a  $30 \text{ cm}^2$  LWIR layer, is  $0.047 \mu\text{m}$ . The standard deviation of the layer thickness is  $<0.27 \mu\text{m}$ . Both the cut-off wavelength of the layer and the layer thickness are measured by FTIR [48].

Growth of low composition gradient, thick LPE layers from small Te-rich melts has been demonstrated [49] and in large melts by isothermal supersaturation where the composition gradient was as low as  $1.5 \times 10^{-5} \mu\text{m}^{-1}$ . Layers grown by programmed cooling, however, showed composition gradients ranging from 0.7 to  $2 \times 10^{-4} \mu\text{m}^{-1}$  at a growth temperature of  $\sim 480^\circ\text{C}$  [49]. Composition control and uniformity of layers grown by dipping Te-rich LPE is one of the strengths of this process. The layer composition is measured using FTIR, as above [49]. The cut-off wavelength reproducibility is  $10.05 \pm 0.18 \mu\text{m}$  (or  $\pm 8.5 \times 10^{-5}$  moles of cadmium). Dipping Te-rich LPE is used mainly to grow thick films, about  $100 \mu\text{m}$ , hence thickness control is not one of its advantages. Thickness control is about  $\pm 15\%$  and  $\pm 20\%$  for layers  $<20 \mu\text{m}$  thick due to the relatively large amount of solidified material even at small values of undercooling.

For Te-rich sliding boat LPE layers of  $\sim 30 \mu\text{m}$  thickness can show wavelength uniformity at room temperature of  $6.5 \pm 0.05 \mu\text{m}$  over 90% of the area of  $20 \times 30 \text{ mm}$  layers [5] and equivalent values over MW layers [44, 50].

### 9.3.2 Crystal quality and surface morphology

Substrate growth technology has been continuously improved and CdZnTe substrates of excellent characteristics, including large size ( $>50 \text{ cm}^2$ ), high crystal quality (full width at half maximum, FWHM  $<30$  arcsec), low dislocation density ( $<3 \times 10^5 \text{ cm}^{-2}$ ), and high purity, are now produced in support of LPE production [35, 51, 52]. The latter group [52] has shown how to produce Te-precipitate-free material from  $\sim 12\text{-cm}$  diameter crystals via annealing slices in a Cd atmosphere. They also demonstrate that switching from a quartz to a pyrolytic boron nitride growth crucible reduces etch pit densities to  $<1 \times 10^4 \text{ cm}^{-2}$  reproducibly. Good crystal quality and excellent surface morphology of LPE materials have been routinely achieved with these substrates. The FWHM of X-ray double-crystal rocking curves of typical LPE layers is  $\sim 40$  arcsec. X-ray topography shows uniform contrast with a typical cross-hatch pattern due to misfit dislocations generated near the interface. The threading dislocation density of the LPE layer as measured by the etch pit density (EPD) technique coincides with that of the CdZnTe substrate.

The ease of decanting the Hg-rich melt after layer growth results in smooth and specular surface morphology if a precisely oriented, lattice-matched CdZnTe substrate is used. There are two additional factors contributing to the excellent surface morphology: (1) excellent thermal stability of the large Hg-melt growth system; (2) low etching or dissolution of the substrate as a result of the low solubility of CdTe or Cd in the Hg solution. Good morphology is essential to meet the stringent operability requirements of large high-density arrays. Epitaxial growth essentially reproduces the substructure of the substrate especially in the case of homoepitaxy [53]. Zhu *et al.* [54] showed how surface morphology was improved in a Te-dipping system by increasing the temperature by  $4^\circ\text{C}$  just prior to wipe-off.

The dislocation density of LPE MCT and its effects on device characteristics has received much attention [55, 56]. The dislocation density is dominated mainly by the

dislocations of the underlying substrate as demonstrated by Yoshikawa [57]. Yoshikawa further reported that the dislocation density of MCT on CdZnTe did not depend greatly on the degree of lattice mismatch for ZnTe mol % ranging from  $\sim 2.5$  to 4.25. Colombo *et al.* [58] found this to be true but also found that for ZnTe  $>4.25\%$  there was a dramatic increase in dislocation density. Further, the dislocation density of MCT layers grown simultaneously under identical growth conditions varied as a function of depth. Figge-meier *et al.* [59] show the effect of EPD in their Te-dipper layers where LW diode yields increased as dislocation density decreased. For layers grown on substrates with ZnTe  $\sim 3\text{--}4\%$  the dislocations are limited to the interface region and the dislocation density is close to that of the substrate.

For LPE material grown in a sliding-boat system, Baker *et al.* [5] showed this same variation of dislocation density with depth (typical values are  $3\text{--}7 \times 10^4 \text{ cm}^{-2}$ ) and the effect of dislocation density on diodes is discussed in Baker [2].

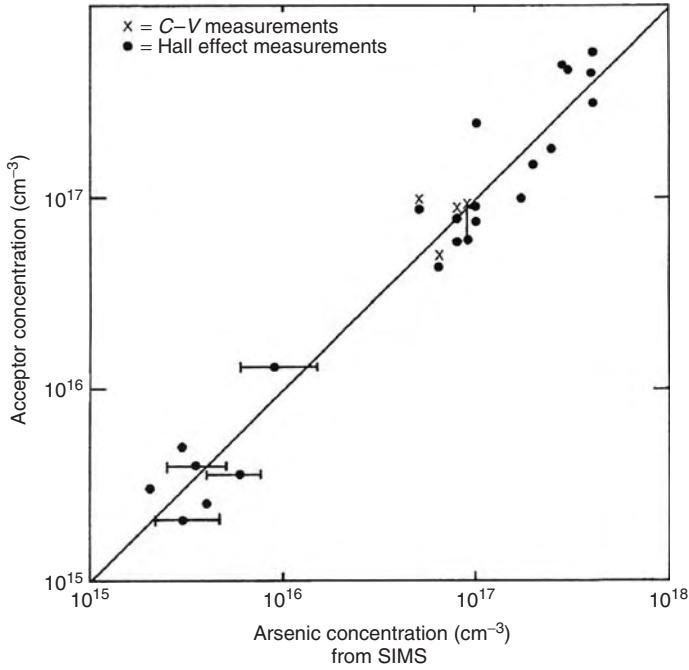
### 9.3.3 Impurity doping and electrical properties

Impurity doping is one of the key elements in the development of complex semiconductor devices. In order to produce heterostructure detectors with MCT epitaxial layers, it is essential that suitable impurity dopants be incorporated during growth to form well-behaved and stable p-n junctions. An ideal impurity dopant should have low vapor pressure, low diffusivity, and small impurity ionization energy. Since the initial experiments in doping layers grown from Hg solution [60], many studies (for reviews see Capper [22, 61]) have established the group V and the group III dopants, As, Sb for p-type, and In for n-type, as the dopants of choice for MCT. It was evident that Hg-rich melts could readily be doped to produce n- and p-type temperature-stable layers. Compared with impurity doping in layers grown from Te-rich solutions (for reviews see Capper [22, 61]), it was evident that Hg is a preferred solvent. Solubilities of most of the useful dopants are significantly higher than in Te-rich solutions, most notably for group V dopants, which are among the most difficult to be incorporated into MCT.

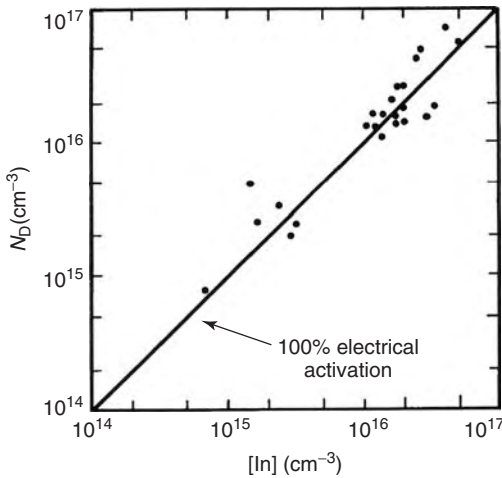
Determination of dopant concentration in the solid involves the use of Hall effect measurements as well as corroboration with secondary ion mass spectrometry (SIMS) concentration profiles. The correspondence in the concentration of a dopant measured by SIMS and Hall effect or capacitance–voltage ( $C\text{--}V$ ) methods is an indication of activity of that dopant. Measurements on the same sample by the two techniques are required to unequivocally substantiate the electrical activity of impurity dopants.

Figure 9.7 is a plot of the acceptor concentration measured by the Hall effect and  $C\text{--}V$  methods versus the As concentration measured by SIMS for Hg-rich LPE. It is clear that the measurements correlate and that As is 100% active over three orders magnitude ( $10^{15}\text{--}10^{18} \text{ cm}^{-3}$ ). Indium is also found to be 100% active over at least two orders of magnitude ( $10^{15}\text{--}10^{17} \text{ cm}^{-3}$ ), as shown in Figure 9.8 [62]. If the desired dopant concentration is lower than the native defect concentration dictated by the growth conditions, the layer must be annealed at low temperatures ( $<300^\circ\text{C}$ ) under saturated Hg vapor to remove the native defects (Hg vacancies).

The doping characteristic of an LPE growth process is best described by the distribution coefficient ( $k$ ) of an impurity dopant, defined as the ratio of the impurity concentration incorporated into the solid to that dissolved in the melt. Values of  $k$  vary with growth



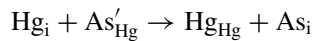
**Figure 9.7** Comparison of As concentration (SIMS) and acceptor concentration (Hall effect and C–V measurements) in intentionally doped MCT epitaxial layers grown from Hg-rich solution. Reprinted from *Narrow-gap II-VI Compounds for Optoelectronic and Electromagnetic Applications*, 1997, p. 49, P. Capper *et al.*, Figure 2.13. Copyright (1997) with kind permission of Springer Science and Business Media



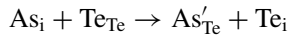
**Figure 9.8** Comparison of In concentration (SIMS) and donor concentration (Hall effect measurement) in intentionally doped MCT epitaxial layers grown from Hg-rich solution. Reprinted from *Narrow-gap II-VI Compounds for Optoelectronic and Electromagnetic Applications*, 1997, p. 50, P. Capper *et al.*, Figure 2.14. Copyright (1997) with kind permission of Springer Science and Business Media

conditions, e.g. the composition of the melt. In the case of In,  $k$  has been measured as 100–10 for Hg-rich LPE. For As, values range from 10 to 0.1. In all cases,  $k$  decreases with increasing Te content in the melt. Values of  $k$  are also a function of nonstoichiometry. In the case of group V dopants,  $k$  values in MCT grown from Hg-rich melts at about 500 °C and from pseudobinary melts at 830 °C [63] are  $\geq 100$  times those from Te-rich melts at 500 °C [64].

There has been a great deal of work in recent years in the area of As doping in Te-rich LPE [65–68]. Schaake [65] gives a quantitative analysis of this process, in which it is assumed that  $As'_{Hg}$  and  $As'_{Te}$  are the only As species present at equilibrium. A high-temperature (400 °C) Hg anneal creates an inward net flux of Hg interstitials,  $Hg_i$ , which initiate the reaction sequence:



followed by:



where  $As_i$  and  $Te_i$  are the As and Te interstitial species, respectively. Involvement of the Te vacancy was excluded in favor of  $Hg_i$  and  $Te_i$  because of separate evidence for self-diffusion by both self-interstitials. Schaake [65] assumed that the transfer rate was limited by the out-diffusion of  $Te_i$  and obtained numerical solutions to the diffusion equation for the local build up of  $As'_{Te}$ ,  $\partial c_{Te}(x, t)/\partial t$ , where  $c_{Te}(x, t)$  is the  $As'_{Te}$  concentration at depth  $x$  below the surface at time  $t$ . This model of site transfer was tested further by Chandra *et al.* [66] who showed that As could be 50–100 % active even under Te-saturated conditions. This same group [69] have studied As doping at low levels ( $10^{15} \text{ cm}^{-3}$ ) using the same site-transfer anneal procedure and showed some preliminary results of  $I-V$  curves at 120–280 K, i.e. in HOT (higher operating temperature) devices.

It is expected, however, that MCT grown under both Hg- and Te-saturated conditions can be readily doped with group I and group III elements, which substitute on the metal sublattice. The concentration of available Hg vacancies is relatively high for MCT grown under Hg- as well as Te-saturated growth conditions at temperatures above 350 °C. Ease of incorporating group I and group III dopants into MCT irrespective of nonstoichiometry has been confirmed experimentally [22, 61].

The excess carrier lifetime is one of the most important material characteristics of MCT since it governs the device performance and frequency response. The objective is to routinely produce material with lifetime that is limited by Auger processes, or by the radiative process in the case of the wider bandgap medium-wavelength infrared (MWIR) and short-wavelength infrared (SWIR) material. It has been reported that intentionally impurity-doped LPE MCT material grown from Hg-rich melt can be obtained with relatively high minority-carrier lifetime [70]. A clear inverse linear dependence of the lifetime, measured by the photoconductive decay technique at 77 K, on the doping concentration was observed for both LWIR and MWIR As-doped MCT layers from Hg-rich solutions. The 77 K lifetimes for As-doped MWIR ( $x = 0.3$ ) MCT layers are significantly higher than those for undoped bulk MCT [71] and, furthermore, are within a factor of two of theoretical values of the radiative lifetime for MCT. Lifetimes in In-doped MWIR MCT were also found to exhibit an inverse linear dependence on the doping concentration [70], with  $N_D \tau$  products similar to  $N_A \tau$  products observed for the As-doped material (where

$N_D$  is the donor concentration.  $N_A$  is the acceptor concentration and  $\tau$  is the lifetime). Lifetimes of LWIR In-doped LPE material are limited by the Auger-recombination process typically at doping levels above  $1 \times 10^{15} \text{ cm}^{-3}$ .

Electrical properties of impurity-doped, large-size, Hg-rich melts are very stable over time. Several such melts have maintained virtually constant electrical properties (doping concentration, carrier mobility, etc.) for a period of 6 years. Electrical properties of impurity-doped LPE layers are also very uniform across the layer. Standard deviation of carrier concentration and mobility measured for nine selected Hall samples across a typical  $15 \text{ cm}^2$  LWIR In-doped MCT layer is less than 5 % [12].

Unintentionally doped n-type MCT grown by Te-rich LPE was initially very difficult to produce because of a high background acceptor concentration (copper). Indium is normally used as a donor dopant. The motivation for donor doping was to reduce the anomalous behavior of the transport properties at low temperatures [29]. Chen and co-workers [72, 73] have shown that once the background acceptor effects have been overcome at mid- $10^{14} \text{ cm}^{-3}$  levels by indium the transport properties of MCT are well behaved down to 20 K. Pelliciani *et al.* [40], on the other hand, achieved classical transport properties without indium, presumably by using higher-purity substrates and/or improved handling techniques to increase process cleanliness, as has the present author's group [44]. Considerable effort in determining which elements are electrically active in MCT [44] has led to new chemical analysis techniques, such as laser scan mass spectrometry (LSMS) [74] but the sensitivity of these techniques is still not sufficient to measure impurities down to the  $1 \times 10^{14} \text{ cm}^{-3}$  level. Nevertheless, Table 9.3 shows results of an LSMS analysis of a layer grown on an in-house produced substrate. This is a technique specifically developed to produce a survey of impurities in thin epitaxial layers. A Nd:YAG laser is rastered over the surface where it ablates material and produces a high yield of positive ions suitable for mass spectrometry. It has several important advantages over other mass spectrometry techniques, particularly with regard to MCT analyses, such as having relative ion sensitivities near unity, making calibration unnecessary. There is also a marked reduction in multiply charged ion species, thus reducing spectral interferences. Impurity levels, including O, in the center of the layer are extremely low, as are those in the CdZnTe substrate, with the exceptions of C and O. There is also no evidence of interface concentration enhanced peaks that have been observed by other groups. This layer yielded a mid- $10^{14} \text{ cm}^{-3}$  n-type background level after Hg annealing at  $200^\circ \text{C}$ .

**Table 9.3** LSMS impurity survey in LPE layer grown on in-house CdZnTe substrate ( $\times 10^{15} \text{ cm}^{-3}$ )

Element	Distance from surface ( $\mu\text{m}$ )						
	0–1	1–5	5–9	9–17	17–21	21–25 <sup>a</sup>	25–27
C	1500	1000	3000	150	30	100	150
O	>300	15	5	1	1	1	10
Na	30	1.5	0.2	0.1	0.1	0.1	0.1
Si	600	1	1	1	<1	<1	<1
K	1.5	1	0.2	<0.03	<0.03	0.2	0.2

From *Adv. Mater. Opt. Electron.*, F. Grainger *et al.* 1995. © John Wiley & Sons Limited. Reproduced with permission. <sup>a</sup> Layer/substrate interface region.

In Te-rich LPE MCT indium is 100 % active, it can be uniformly distributed within the LPE layer and is easily reproduced. The segregation coefficient of indium during Te-rich LPE growth at  $\sim 480^\circ\text{C}$  is  $\sim 1-4$ . Colombo *et al.* [30] reported the carrier concentration at 77 K over 100 growth runs indicating only a small melt depletion as a result of melt dilution. Overall, indium is a well-established dopant, particularly for DLHJ devices where the photon collection volume is n-type MCT. Indium has the additional advantage of controlling the minority carrier lifetime and thus the minority carrier diffusion length. The diffusion length is an important parameter for controlling FPA characteristics such as cross-talk when the collection volume is not bound as is the case for DLHJ. Chen *et al.* [73] have studied the minority carrier lifetime of MCT:In in the range  $\sim 10^{14}-10^{16}\text{ cm}^{-3}$ . The hole lifetime for n-type MCT is Auger-limited down to about mid  $10^{14}\text{ cm}^{-3}$ . Below  $5 \times 10^{14}\text{ cm}^{-3}$  background impurities and native defects are believed to dominate.

Group IB doping has also been investigated with various degrees of success [75]. Recently, Shih *et al.* [76] investigated doping with In ( $2 \times 10^{14}\text{ cm}^{-3}$ ) for the n-type side and gold ( $7 \times 10^{15}\text{ cm}^{-3}$ ) for the p-type side. These group I elements, in general, have been avoided as they tend to have high diffusion coefficients, are thought to be unstable in device structures, and have been reported to have low segregation coefficients. However, Shih *et al.* [76] report on VLW ( $13.2\ \mu\text{m}$  at 77 K) diodes, where the Au-doped material shows better thermal stability (and theoretical lifetime values) than equivalent Cu-doped layers. This group have since reported on low As doping to replace the more mobile group I elements, with equivalent diode results being found [77]. A later paper also showed equivalent lifetime values in this As-doped material [78].

For vacancy-controlled as-grown p-type LPE from the sliding-boat system, Baker *et al.* [5] reported that uniformity of vacancy concentration is critical for loop-hole junction depth control. This control has been demonstrated, via post-growth, *in situ* annealing, between  $0.1$  and  $2 \times 10^{17}\text{ cm}^{-3}$  to within  $\pm 5\%$  of the mean over  $20 \times 30\text{ mm}$  layers. Conversion to  $< 5 \times 10^{14}\text{ cm}^{-3}$  n-type after 66 h at  $200^\circ\text{C}$  in Hg vapor is usually found in these layers. Several studies have been carried out in recent years on the properties of undoped LPE layers. Capper *et al.* [79] presented a summary of p to n conversion, developed the original Schaake *et al.* model [80] and explained earlier results of Jones *et al.* [81] and Dutton *et al.* [82]. A discussion was also presented on the relative effects of Hg vacancies and Hg interstitials as possible Shockley-Read traps (following the suggestion of Vydyanath [83]). Annealing schedules (e.g.  $250^\circ\text{C}$  MCT +  $150^\circ\text{C}$  Hg) were proposed to minimize the concentrations of these two defects and subsequent unpublished work in the author's lab suggested that there may be a slight beneficial affect on lifetime using such anneals. Shaw and Capper [84] extended the p to n conversion discussion to include the skin/core boundary of Bogoboyashchii *et al.* [85] and drew together work on conversion by annealing, ion beam milling, reactive ion etching and anodic oxidation. Chandra *et al.* [67] have carried out a detailed study of annealing Te-rich LPE layers with  $x = 0.18-0.51$ . The diffusion rate (rate of conversion) decreased as  $x$  increased (agreeing with the findings of McAllister *et al.* [86]), with a marked change in slope at  $x \sim 0.3$ .

There has also been a great deal of work on the effects of reactive ion etching (RIE), both from the materials perspective and the device-processing point of view. Agnihotri *et al.* [87] provide a good summary of this area, where it is thought that Hg interstitials on the sample surface diffuse in and fill Hg vacancies. A kick-out mechanism is also proposed, as is an effect of hydrogen from the plasma on the type-conversion process.

The proposals that H may passivate Hg vacancies, may act as an acceptor and may interact with In donors were first put forward by Hughes *et al.* [88] and these ideas have been built upon by several groups since that time. Kim *et al.* [89] found that for  $x \sim 0.21$  diode performance increased by a factor of 30 after H<sub>2</sub> treatment (thought to be due to passivation of Hg vacancies). White *et al.* [90] discuss the same features of H neutralizing acceptors in  $x \sim 0.3$  material. Nguyen *et al.* [91] used quantitative mobility spectrum analysis (QMSA) [92] to study in detail the electrical properties of both undoped and Au-doped LPE layers after RIE.

Lee *et al.* [93] have reported on an automated noncontact lifetime measuring system, using millimeter wave reflections, at 80 K in double layers grown by Te-rich (for In doping) and Hg-rich (for As cap formation) LPE. Tobin *et al.* [94] used XRD as a non-contact method to measure thickness and composition profiles in such double layers, with the results confirmed with FTIR and SIMS.

### 9.3.4 Multiple-layer heterojunction structures

The first heterojunction detectors were formed by Hg-rich LPE [95]. The structure was a single-layer heterojunction (SLHJ) consisting of an n-type layer grown on p-type bulk MCT slices that were polished down to 20  $\mu\text{m}$  thickness. Further work advanced the technology and basic understanding of MCT heterojunctions [96]. For DLHJ, a second LPE (cap) layer is grown over the first (base) layer. The key is to grow the cap layer doped with slow-diffusing impurities. For n-on-p DLHJ structures, the dopant of choice for the n-type cap layer is In, while for p-on-n DLHJ structures the p-type cap layer uses As or Sb.

SIMS measurements on both n-on-p and p-on-n DLHJ structures have established that the p-n junctions are abrupt ( $<0.1 \mu\text{m}$ ), while the heterojunctions were centered on the electrical junctions and graded over a 0.6–1.3  $\mu\text{m}$ -wide region [96]. The MCT HJ is formed by Hg-rich LPE growth of a cap layer of In-doped n-type wide-bandgap  $\text{Hg}_{0.7}\text{Cd}_{0.3}\text{Te}$  onto a As-doped p-type narrow-bandgap  $\text{Hg}_{0.77}\text{Cd}_{0.23}\text{Te}$  base layer. The HJ is graded due to interdiffusion between Hg and Cd during growth, which is usually carried out at 400–420 °C. A different approach was developed to form an n-on-p DLHJ structure by LPE [97]. The undoped narrow-bandgap base layer is capped by a top layer doped with both In at high- $10^{16}$  level and Cu at low- $10^{16}$  level. The base layer is grown in a horizontal tipping/sliding system from a Te-rich melt, while the cap layer is grown from Hg solution. Since In diffuses slowly and Cu diffuses rapidly, In remains in the cap layer while Cu diffuses throughout both the cap and base layers during growth.

## 9.4 DEVICE STATUS

Table 9.4 summarizes the various MCT photodiode designs and processes used by the major FPA manufacturers today for both back-illuminated bump-interconnected FPAs (BAE North America, RIRCOE, Rockwell/Boeing and Sofradir), and front-illuminated loophole FPAs (DRS, SELEX).

The largest MCT FPAs yet produced are the staring SW 1024  $\times$  1024 and 2048  $\times$  2048 units developed by Rockwell for astronomy applications [98]. These backside-illuminated

**Table 9.4** Summary of the various MCT PV detector technologies used for 2D hybrid focal plane arrays. Reprinted from *Infrared Detectors and Emitters: Materials and Devices*, 2001, p. 321, P. Capper and C. T. Elliott (eds), Table 1. Copyright (2001) with kind permission of Springer Science and Business Media

Photodiode configuration	Junction-formation method	Company
P-on-n mesa	Two-layer LPE on CdZnTe Base: Te-solution slider, indium-doped Cap: Hg-solution dipper, arsenic-doped	BAE North America
P-on-n mesa	Two-layer LPE on CdZnTe or Si Base: Hg-solution dipper, indium doped Cap: Hg-solution dipper, arsenic-doped	Raytheon Infrared Center of Excellence (RIRCoE, formerly SBRC) and Hughes Research Laboratories (HRL)
P-on-n planar buried-junction heterostructure	Arsenic implant into indium-doped N-n	Rockwell/Boeing
$n^+ - n^- - p$ planar homojunction	Boron implant into Hg-vacancy p-type, grown by Hg-solution tipper on $\sim 7.6$ cm diameter sapphire with MOVPE CdTe buffer; ZnS passivation	
$n^+ - on - p$ planar	Ion implant into acceptor-doped p-type LPE film grown by Te-solution slider	Sofradir (Societe Francaise de Detecteurs Infrarouge)
n-on-p VIP	Ion implantation forms n-on-p diode in p-type MCT layer, grown by Te-solution LPE on CdZnTe and epoxied to silicon ROIC wafer; over the edge contact	DRS Infrared Technologies (formerly Texas Instruments)
n-p loophole	Ion beam milling forms n-type islands in p-type Hg-vacancy-doped layer grown by Te-solution LPE on CdZnTe, and epoxied onto silicon ROIC wafer; cylindrical lateral collection diodes	SELEX Sensors and Airborne Systems Infrared Ltd (formerly BAE SYSTEMS Infrared Ltd)

Upper case P and N denote wider-gap layers, e.g. P-on-n denotes a wider-gap p-type layer grown onto a narrow-gap n-type absorber layer. Adapted from [3].



FPA's have a unit cell size of  $18 \times 18 \mu\text{m}^2$  and cut-off wavelengths near  $2.5 \mu\text{m}$ , and operate at temperatures around 77 K. The MCT array size for the  $2048 \times 2048$  FPA is  $3.7 \times 3.7 \text{ cm}^2$ . The detector array architecture is the planar ion-implanted ZnS-passivated n-on-p photodiode, fabricated from p-type single-layer MCT films grown by LPE onto  $\sim 7.6$  cm diameter sapphire substrates, which incorporate an MOVPE-deposited CdTe buffer layer. Avalanche gain had been demonstrated previously in SW MCT photodiodes. Shin *et al.* [99] reported avalanche gains of 15 in planar boron-implanted n-on-p homojunctions, fabricated in LPE MCT films, with cut-off wavelength of  $1.25 \mu\text{m}$  at 300 K. Hwang *et al.* [100] grew  $x \sim 0.75$  layers ( $\lambda = 1\text{--}1.7 \mu\text{m}$ ) by Te-rich slider at  $440^\circ\text{C}$  for fiber-optic communications and avalanche photodiodes. They used meltback at the end of growth, prior to wipeoff, to improve surface morphology. Terterian *et al.* [101] described the growth of  $x \sim 0.5$  layers ( $\lambda = 2.5 \mu\text{m}$ ) LPE As-on-In double layers for both planar- and mesa-type devices.

The VLW spectral region, defined roughly as those wavelengths beyond  $12 \mu\text{m}$  (just beyond the edge of the  $8\text{--}12 \mu\text{m}$  atmospheric window) and extending to around  $25 \mu\text{m}$ , is critical for a number of applications such as spaceborne remote sensing. Here the unique advantages of MCT detector technology—variable band gap, high quantum efficiency and high operating temperature—make it the best choice for spaceborne applications.

The process flow of the via-hole device using LPE material is illustrated in Figure 9.9 [5, 102]. The process has two simple masking stages. The first defines a photoresist film with a matrix of holes of, say,  $5 \mu\text{m}$  diameter. Using ion beam milling, the MCT is eroded away in the holes until the contact pads are exposed. The holes are then backfilled with a conductor, to form the bridge between the walls of the hole and the underlying metal pad. The junction is formed around the hole during the ion beam milling process. The second masking stage enables the p-side contact to be applied around the array. Figure 9.9 shows a photomicrograph of one corner of the hybrid illustrating the membrane-like nature of the MCT on the silicon. The device structure inherently produces low crosstalk in small pixels.

The planar device structure is the simplest device structure currently used. It is consistent with a number of junction-forming processes, e.g. ion implantation, diffusion and ion milling. The matrix of junctions is mass connected to an underlying silicon multiplexer using indium bumps. The strength of the process is the simplicity and the compatibility with epitaxially grown materials. A process based on high-quality LPE material and ion-implanted junctions is conducive to good-quality detectors and volume production [103]. In the simplest form, the process needs three masking stages, for the junction and pixel contact, and one for the contact to the p-side. The device is backside illuminated, i.e. it is illuminated through the substrate, and so this must be of high optical quality. Careful control of the junction geometry is needed to avoid crosstalk due to the diffusion of minority carriers into adjacent pixels especially in the case of small pixel sizes. The thermal expansion mismatch between the MCT/CdZnTe substrate combination and the silicon multiplexer is another important consideration in this device structure and can restrict the practical size of the array unless the CdZnTe substrate is thinned.

DLHJ devices have been developed mainly in the USA for LW detectors with low thermal leakage currents [or high zero-bias dynamic resistance—junction area ( $R_0A_j$ ) values]. A number of elegant device structures have been reported with  $R_0A_j$  values an order higher than that of via-hole or planar diodes. The back-illuminated mesa  $P^+n$  heterojunction, illustrated in Figure 9.10, is a widely used device and has been reported from both

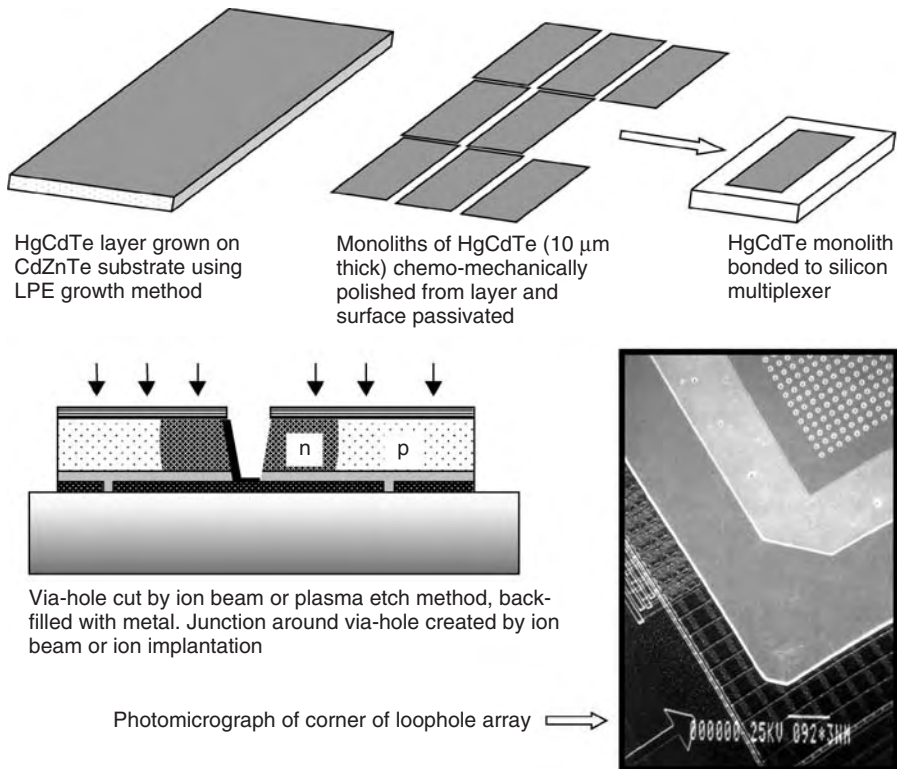


**Figure 9.9** Processing of MCT arrays using LPE material and loophole technology [2]. Reprinted from II-VI narrow bandgap semiconductors: optoelectronics in *Handbook of Electronic and Optoelectronic Materials*, 2007, 1. Baker, Figure 13. Copyright (2007) with kind permission of Springer Science and Business Media

LPE and MBE material. This structure makes good use of the n-type absorber to give high fill factor. Devices have been made using a vertical dipper LPE process from a Hg-rich solution [104] and using a horizontal slider LPE process from a Te-rich solution [41, 93, 105]. The p-type layer is doped with arsenic to around  $1\text{--}4 \times 10^{17} \text{ cm}^{-3}$  and is grown by the vertical dipper LPE process from a Hg-rich solution.

Another approach, known as PACE, has also been used [7]. The process uses a 75-mm diameter substrate of highly polished sapphire, which remains with the device throughout. The thermal expansion problem is overcome by using a carrier substrate of sapphire so the silicon multiplexer is sandwiched in the middle. The process starts with a buffer layer of CdTe deposited using a MOVPE process to 8.5  $\mu\text{m}$  thickness followed by a 10- $\mu\text{m}$  thick p-type MCT layer grown by LPE. The n-p diodes are formed by ion implantation. This process has been used to fabricate  $1024 \times 1024$  arrays with 3.2  $\mu\text{m}$  cut-off [106] and  $2048 \times 2048$  SW arrays of 16  $\text{cm}^2$  in area [107].

Important applications in the SW (1–2.5  $\mu\text{m}$ ) waveband include: thermal imaging (using nightglow), spectroscopy and active imaging using lasers. Other materials can be used for SW detectors but products such as InGaAs tend to have high noise beyond 1.7  $\mu\text{m}$  due to defects arising from the lattice mismatch with the InP substrate. Most MCT

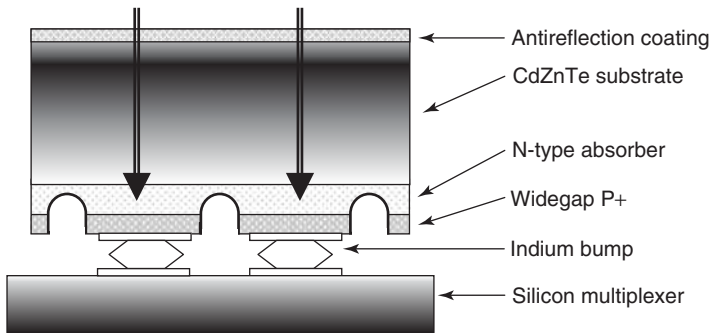


**Figure 9.10** Schematic of a DLHJ [2]. Reprinted from II-VI narrow bandgap semiconductors: optoelectronics in *Handbook of Electronic and Optoelectronic Materials*, 2007, 1. Baker, Figure 15. Copyright (2007) with kind permission of Springer Science and Business Media

technologies can be extended to SW with little change to the processing. Carrier lifetimes should be dominated by radiative recombination but in fact Shockley–Read centers and technological-related limits probably apply in practice. SW detectors can produce good-quality diodes in the presence of fairly high levels of misfit dislocations and so can be made using some of the newer technologies. For imaging and spectroscopy applications typical operating temperatures are around 200 K and thermo-electric coolers are often offered as standard products.

In most SW applications the photon flux is low and it is difficult to achieve reasonable signal-to-noise performance. However, it is relatively easy to enhance the signal by providing some avalanche gain in the device. Electron avalanching in MW MCT via-hole diodes has been described [108, 109]. The electron and hole ionization rates are very different in MCT and this allows almost pure exponential, noise-free avalanche gain at fairly moderate voltages. So avalanche gain can readily be achieved for wavelengths above about 2.5  $\mu\text{m}$  when the absorber region is p-type and electrons are the minority carriers. Typically, a gain of 10 is observed for around 5 V at a cut-off of 5  $\mu\text{m}$ . An alternative structure uses SW material (1.6  $\mu\text{m}$ ) and a resonant enhancement of the hole impact ionization rate when the bandgap equals the spin-orbit split-off energy [110]. Gains of 30–40 have been seen with voltages of 85–90 V.

SW laser-gated imaging systems using avalanche gain in MCT are now being reported for use in long-range identification applications [111]. Here the combination of sophisticated readout integrated circuits and high-quality Te-slider LPE MCT device processing is producing  $320 \times 256$  arrays with a sensitivity down to 10 photons rms.

Tobin *et al.* [112] reported  $R_0A_j$  data for a VLW LPE P-on-n MCT diagnostic array at 60 K, with a cut-off wavelength of 16.3  $\mu\text{m}$ . Krueger *et al.* [113] reported back-illuminated 350  $\mu\text{m}$  diameter LPE P-on-n MCT photodiodes with cut-off wavelengths as long as 17.5  $\mu\text{m}$  at 70 K, with nonantireflection coated quantum efficiencies of 61–73 %. The  $R_0A$  products of 0.7  $\text{ohm cm}^2$  at 70 K are within a factor of two of the one-dimensional n-side thin-base diffusion current limit.

It is also notable that LPE from Hg-rich solution has been designed to grow a four-layer MW/LW bias-selectable dual-band  $n^+ \text{-p}^+ \text{-n}$  structure [114], and data have been reported for a more producible three-layer  $n \text{-p}^+ \text{-n}$  bias-selectable structure [115, 116], with growth temperatures of 400–450  $^\circ\text{C}$ . Numerical modeling of LPE film growth has

allowed band-gap engineering of the compositional gradients due to alloy interdiffusion at the higher LPE growth temperatures [116].

### 9.4.1 LPE growth on Si-based substrates

Si-based substrates are being developed as a replacement for bulk CdZnTe substrates. This effort is directed at improvements in substrate size, strength, cost, and reliability of hybrid FPAs. These alternative substrates, which consist of epitaxial layers of CdZnTe or CdTe on GaAs/Si wafers [117, 118] or directly on Si wafers [119], are particularly advantageous for the production of large arrays. High-quality epitaxial MCT has been successfully grown on the Si-based substrates by the Hg-melt LPE technology for the fabrication of p-on-n DLHJ detectors [119, 120]. The first high-performance  $128 \times 128$  MWIR and LWIR arrays have been demonstrated [120]. MWIR arrays as large as  $512 \times 512$  and  $1024 \times 1024$  have also been produced [121].

P-on-n DLHJ detectors fabricated on Si-based substrates show performance comparable with that of detectors fabricated on bulk CdZnTe substrates at high temperatures but not at low temperatures. To determine the mechanisms that limit the performance at low temperatures, the  $R_0A_j$  product was measured as a function of temperature. The results show that an increased dislocation density, associated with heteroepitaxial thin-layer substrates, has a much stronger effect on device performance at lower temperatures, where the  $R_0A_j$  product is not diffusion-limited but rather generation-recombination or tunneling-limited [117, 120, 122]. This is illustrated by the comparison of  $R_0A_j$  versus temperature for MWIR detectors co-fabricated on thin-layer and bulk CdZnTe substrates as shown in Johnson *et al.* [117]. These results are consistent with a recent study of the effect of dislocations on the electrical and optical properties of LWIR PV detectors [56].

$480 \times 640$ ,  $256 \times 256$ , and  $480 \times 4$  LWIR arrays of MCT grown by Hg-melt LPE on Si-based substrates have been demonstrated [118, 121, 122]. LWIR imagery has been demonstrated for a  $480 \times 640$  staring array with  $20 \mu\text{m}$  pixels fabricated on a Si-based substrate [121]. The first LWIR  $256 \times 256$  FPA using a CdZnTe/Si substrate showed the following 78 K performance: average  $D^* = 2.6 \times 10^{11} \text{ cm Hz}^{0.5} \text{ W}^{-1}$ , average responsivity  $= 1.0 \times 10^{12} \text{ mV photon}^{-1} \text{ cm}^{-2} \text{ s}^{-1}$ , average NEDT  $= 56 \text{ mK}$ , mean  $R_0A_0$  product  $= 613 \Omega \text{ cm}^2$ , quantum efficiency  $= 64 \%$  without antireflection coating, cut-off wavelength  $= 9.4 \mu\text{m}$ . A further reduction in the dislocation density for MCT grown on Si-based substrates is needed to improve the LWIR detector performance margin at 78 K and to improve detector performance at lower temperatures [122]. The growth of epitaxial MCT on CdZnTe/GaAs/Si and CdTe/Si substrates by Te-rich slider LPE has also been reported with reasonable detector performance at 78 K [123].

## 9.5 SUMMARY AND FUTURE DEVELOPMENTS

LPE from both Te-rich and Hg-rich solutions is one of the most successful technologies for the preparation of epitaxial MCT of excellent material characteristics. LPE materials are being grown routinely for PV and photoconductive detectors with state-of-the-art performance in the entire 2–18  $\mu\text{m}$  spectral region. The DLHJ is the key element to further improvement in PV MCT detector performance. The high throughput and high yield have

enabled production of high-performance second-generation FPAs at affordable cost. Photodiode structures with excellent performance, including p-on-n as well as n-on-p DLHJs, have been manufactured. The trend for developing multiple-layer heterojunction structures, including DLHJ and triple-layer heterojunction as well as heteroepitaxial growth, is toward application of vapor-phase epitaxial techniques. LPE will, however, continue to play a major role in the development of such structures because of its simplicity and maturity.

Knowledge of fundamental material properties for the Hg-Cd-Te system has been established and utilized for better understanding and control of the growth process. Four key areas are phase diagram, defect chemistry, impurity doping and heterojunction formation. Such knowledge provides a basis for evaluating material characteristics that are dictated by thermodynamic equilibrium conditions. Native defects are ubiquitous in MCT and are often found to deteriorate material characteristics. Further work is needed to elucidate the origin and nature of various native defects and the complex interaction between native defects and impurity dopants. Dislocations, precipitates and certain impurities are detrimental to detector performance, especially at low temperatures. Significant progress has been made in reducing these extended defects and undesirable impurities. Further work is still needed to unequivocally identify the key defects for their effective reduction, especially for low-temperature, low-background applications. Both Hg- and Te-rich LPE can produce material of excellent compositional uniformity and crystalline quality. While donor doping is under control acceptor doping is still not well understood in Te-rich growth. Acceptor doping using group V elements has been explored but it is very difficult to achieve success. The same is not true for group IB dopants, which may still provide an opportunity that has not been completely explored. Acceptor doping with group V elements in Hg-rich LPE leads to improved lifetime, stable electrical properties and the successful fabrication of DLHJ devices.

## REFERENCES

- [1] P. Capper (2001) in *Infrared Detectors and Emitters: Materials and Devices*, P. Capper and C.T. Elliott (eds), Kluwer Academic, Boston, Chapter 10
- [2] I.M. Baker (2007) in *Handbook of Electronic and Optoelectronic Materials*, S. Kasap and P. Capper (eds), Springer, Heidelberg, 855
- [3] M.B. Reine (2001) in *Infrared Detectors and Emitters: Materials and Devices*, P. Capper and C.T. Elliott (eds), Kluwer Academic, Boston, Chapter 12
- [4] P. Capper (2006) in *Handbook of Electronic and Optoelectronic Materials*, S. Kasap and P. Capper (eds), Springer, Heidelberg, 313
- [5] I.B. Baker, G.J. Crimes, J.E. Parsons and E.S. O'Keefe (1994) *Proc. SPIE*, **2269**, 636.
- [6] S.M. Johnson, J.A. Vigil, J.B. James, *et al.* (1993) *J. Electron. Mater.* **22**, 835.
- [7] G. Bostrup, K.L. Hess, J. Ellsworth, D. Cooper and R. Haines, (2001), *J. Electron. Mater.* **30**, 560.
- [8] T.C. Harman (1980) *J. Electron. Mater.* **9**, 945.
- [9] T.C. Harman (1979) *J. Electron. Mater.* **8**, 191.
- [10] M.G. Astles (1994) in *Properties of Narrow Gap Cadmium-based Compounds*, Emis Data-review series, No. 10, P. Capper (ed.), IEE, London, 13.
- [11] P. Herning (1984) *J. Electron. Mater.* **13**, 1.
- [12] T. Tung, L.V. DeArmond, R.F. Herald, *et al.* (1992) *Proc. SPIE* **1735**, 109.
- [13] S.L. Bell and S.J. Sen (1985) *Vac. Sci. Technol. A* **3**, 112.

- [14] J.L. Schmit (1986) *J. Vac. Sci. Technol. A* **4**, 2141.
- [15] L.O. Bubulac, D. Lo, W. Tennant, *et al.* (1986) *J. Vac. Sci. Technol. A* **4**, 2169.
- [16] P.-K. Liao, H.F. Schaake, J.H. Tregilgas, *et al.* (1994) *US Workshop on the Physics and Chemistry of Mercury Cadmium Telluride and Other Materials Ext. Abstr.* 11–13.
- [17] S. Sen, W.H. Konkel, S.J. Tighe, *et al.* (1988) *J. Cryst. Growth* **86**, 111.
- [18] T. Tung (1988) *J. Cryst. Growth*, **86**, 161.
- [19] M.C. Chen and J.A. Dodge (1986) *Solid State Commun.* **56**, 449.
- [20] J. Steininger (1976) *J. Electron. Mater.* **5**, 299.
- [21] T.-C. Yu and R.F. Brebrick (1994) *Properties of Narrow Gap Cadmium-based Compounds*, Emis Datareview series, No. 10 P. Capper (ed.), IEE, London, 55.
- [22] P. Capper (1994) *Properties of Narrow Gap Cadmium-based Compounds*, Emis Datareview series, No. 10, P. Capper (ed.), IEE, London, 151.
- [23] A.J. Strauss and R.F. Brebrick (1970) *J. Phys. Chem. Solids*, **31**, 2293.
- [24] J.H. Tregilgas (1994) *Properties of Narrow Gap Cadmium-based Compounds*, Emis Datareview series, No. 10, P. Capper (ed.), IEE, London, 185.
- [25] H.H. Woodbury (1966) *Phys. Rev. Lett.* **17**, 1093.
- [26] T.C. Harman (1981) *J. Electron. Mater.* **10**, 1069.
- [27] D.D. Edwall, E.R. Gertner and W.E. Tennant (1984) *J. Appl. Phys.* **55**, 1453.
- [28] J.C. Tranchart, B. Latorre, C. Foucher and Y. Le Gouge, (1985) *J. Cryst. Growth*, **72**, 468.
- [29] M. Yoshikawa, S. Ueda, K. Maruyama and H. Takigawa (1985) *J. Vac. Sci. Technol. A* **3**, 153.
- [30] L. Colombo, G.H. Westphal, P.K. Liao, *et al.* (1992) *Proc. SPIE* **1683**, 33.
- [31] J.C. Brice, P. Capper, B.C. Easton, *et al.* (1987) *Semicond. Sci. Technol.* **2**, 710.
- [32] J.E. Bowers, J.L. Schmit, C.J. Speersneider and R.B. Maciolek (1980) *IEEE Trans. Electron Devices* **ED-27**, 24.
- [33] D. Chandra, M.W. Goodwin, M.C. Chen and L.K. Magel (1995) *J. Electron. Mater.* **24**, 599.
- [34] J.H. Tregilgas, J. Dodge, L. Colombo and P.-K. Liao (1995) *MCT Workshop Ext. Abstr.*
- [35] J.P. Tower, S.P. Tobin, M. Kestigian, *et al.* (1995) *J. Electron. Mater.* **24**, 497.
- [36] J.P. Tower, S.P. Tobin, P.W. Norton, A.B. Boolong, A. Socha, J.H. Tregilgas, C.K. Ard and H.F. Arlinghaus (1996) *J. Electron. Mater.* **25**, 1183.
- [37] R.F. Brebrick, C-H. Su and P-K. Liao (1983) *Semicond. Semimet.* **19**, 171.
- [38] G.H. Westphal, L. Colombo and J. Anderson (1994) *Proc. SPIE* **2228**, 342.
- [39] K. Yasumura, T. Murakami, M. Suita, *et al.* (1992) *J. Cryst. Growth* **117**, 20.
- [40] B. Pelliciani, J.P. Chamonal, G.L. Destefanis and L.D. Cioccio (1987) *Proc. SPIE* **865**, 22.
- [41] P.W. Norton, P. LoVecchio, G.N. Pultz, *et al.* (1994) *Proc. SPIE* **2228**, 73.
- [42] C.F. Wan, D.F. Weirauch and R. Korenstein (1986) *J. Electron. Mater.* **15**, 151.
- [43] D.W. Shaw (1983) *J. Cryst. Growth*, **62**, 247.
- [44] P. Capper, J. Gower, C.D. Maxey, E.S. O'Keefe, J.H. Harris, L. Bartlett and S. Dean (1998) *Growth and Processing of Electronic Materials*, IOM Communications Ltd, London.
- [45] J. Gower, C.D. Maxey, P. Capper, E.S. O'Keefe and T. Skauli (1999) *J. Mater. Sci. Mater. Electron.* **10**, 589.
- [46] G. Destefanis, A. Astier, J. Baylet, P. Castelein, J.P. Chamonal, E. DeBorniol, O. Grandand, F. Marion, J.L. Martin, A. Million, P. Rambaud, F. Rothan and J.P. Zanatta (2003) *J. Electron. Mater.* **32**, 592.
- [47] I.A. Denisov, V.M. Lakeenkov, O.S. Mazhorova and Yu.P. Popov (2002) *J. Cryst. Growth*, **245**, 21.
- [48] S.P. Price and P.R. Boyd (1993) *Semicond. Sci. Technol.* **8**, 842.
- [49] L. Colombo and G.H. Westphal (1994) *Proc. SPIE* **2228**, 66–72.
- [50] P. Capper, E.S. O'Keefe, C.D. Maxey, *et al.* (1997) *J. Cryst. Growth* **161**, 104.
- [51] S. Sen, S.M. Johnson, J.A. Kiele, *et al.* (1991) *Mater. Res. Soc. Symp. Proc.* **161**, 3.
- [52] R. Hirano and H. Kurita (2005) in *Bulk Crystal Growth of Electronic, Optical and Optoelectronic Materials*, P. Capper (ed.), John Wiley & Sons, Ltd, Chichester, 241.
- [53] M.G. Astles, N. Gordon, D. Bradley, *et al.* (1984) *J. Electron. Mater.* **13**, 167.

- [54] J. Zhu, J. Chu, B. Li, X. Chen J. Cao and J. Cheng (1996) *Phys. Status Solidi A* **157**, 83.
- [55] R.S. List (1993) *J. Electron. Mater.* **22**, 1017.
- [56] S.M. Johnson, D.R. Rhigier, J.P. Rosbeck, *et al.* (1992) *J. Vac. Sci. Technol. B* **10**, 1499.
- [57] M. Yoshikawa (1988) *J. Appl. Phys.* **63**, 1533.
- [58] L. Colombo, G.H. Westphal, P.-K. Liao and H.F. Schaake (1994) *US Workshop on the Physics and Chemistry of Mercury Cadmium Telluride and Other Materials Ext. Abstr.* 97.
- [59] H. Figgemeier, M. Bruder, K.-M. Mahlein, R. Wollrab and J. Ziegler (2003) *J. Electron. Mater.* **32**, 588.
- [60] M.H. Kalisher (1984) *J. Cryst. Growth* **70**, 365.
- [61] P. Capper (1991) *J. Vac. Sci. Technol. B*, **9**, 1667.
- [62] L.E. Lapidus, R.L. Whitney and C.A. Crosson (1985) *Mater. Res. Soc. Symp. Proc.* **48**, 365.
- [63] P. Capper (1982) *J. Cryst. Growth* **57**, 280.
- [64] H.R. Vydyanath, J.A. Ellsworth and C.M. Devaney (1987) *J. Electron. Mater.* **16**, 13.
- [65] H.F. Schaake (2000) *J. Appl. Phys.* **88**, 1765; H.F. Schaake (2001) *J. Electron. Mater.* **30**, 789.
- [66] D. Chandra, H.F. Schaake, M.A. Kinch, F. Aqariden, C.F. Wan, D.F. Weirauch and H.D. Shih (2002) *J. Electron. Mater.* **31**, 715.
- [67] D. Chandra, H.F. Schaake and M.A. Kinch (2003) *J. Electron. Mater.* **32**, 810.
- [68] P. Capper and D. Shaw (2006) *Proc. SPIE.* **6294**, 6294OM.
- [69] D. Chandra, D.F. Weirauch, H.F. Schaake, M.A. Kinch, F. Aqariden, C.F. Wan and H.D. Shih (2005) *J. Electron. Mater.* **34**, 963.
- [70] W.A. Radford, R.E. Kvaas and S.M. Johnson (1986) *Proc. IRIS Specialty Group on Infrared Materials*, Menlo Park, CA.
- [71] D.L. Polla, R.L. Aggarwal, D.A. Nelson, *et al.* (1983) *Appl. Phys. Lett.* **43**, 941.
- [72] M.C. Chen and L. Colombo (1993) *J. Appl. Phys.* **73**, 2916.
- [73] M.C. Chen, L. Colombo, J.A. Dodge and J.H. Tregilgas (1995) *J. Electron. Mater.* **24**, 539.
- [74] F. Grainger, I. Gale, P. Capper, C.D. Maxey, P. Mackett, E.S. O'Keefe and J. Gosney (1995) *Adv. Mater. Opt. Electron.* **5**, 71.
- [75] D.D. Edwall, E.R. Gertner and W. Tennant (1985) *J. Electron. Mater.* **14**, 245.
- [76] H.D. Shih, M.A. Kinch, F. Aqariden, P.K. Liao and H.F. Schaake (2003) *Appl. Phys. Lett.* **82**, 4157.
- [77] M.A. Kinch, D. Chandra, H.F. Schaake, H.D. Shih and F. Aqariden (2004) *J. Electron. Mater.* **34**, 880.
- [78] M.A. Kinch, F. Aqariden, D. Chandra, P.-K. Liao, H.F. Schaake and H.D. Shih (2005) *J. Electron. Mater.* **33**, 590.
- [79] P. Capper, C.D. Maxey, C.L. Jones, J.E. Gower, E.S. O'Keefe and D. Shaw (1999) *J. Electron. Mater.* **28**, 637.
- [80] H.F. Schaake, J.H. Tregilgas, M.A. Kinch and B.E. Gnade (1985) *J. Vac. Sci. Technol.* **A3**, 143.
- [81] C.L. Jones, M.J.T. Quelch, P. Capper and J.J.G. Gosney (1982) *J. Appl. Phys.* **53**, 9080.
- [82] D.T. Dutton, E. O'Keefe, P. Capper, C.L. Jones, S. Mugford and C. Ard (1993) *Semicond. Sci. Technol.* **8**, S266.
- [83] H.R. Vydyanath (1996) *J. Cryst. Growth* **161**, 64.
- [84] D. Shaw and P. Capper (2000) *J. Mater. Sci. Mater. Electron.* **11**, 169.
- [85] V.V. Bogoboyashii, A.I. Elizarov, V.I. Ivanov-Omskii, V.R. Petrenko and V.A. Petryakov (1985) *Sov. Phys. Semicond.* **19**, 505.
- [86] A. McAllister, E. O'Keefe, P. Capper, F.A. Capocci, S. Barton and D.T. Dutton (1996) *J. Electron. Mater.* **25**, 1014.
- [87] O.P. Agnihorti, H.C. Lee and K. Yang (2002) *Semicond. Sci. Technol.* **17**, R11.
- [88] W.C. Hughes M.L. Swanson and J.C. Austin (1993) *J. Electron. Mater.* **22**, 1011.
- [89] Y.-H. Kim, T.-S. Kim, D.A. Redfern, C. Musca, M. C. Lee and C.K. Kim (2000) *J. Electron. Mater.* **29**, 859.

- [90] J. White, R. Pall, J.M. Dell, C.A. Musca, J. Antoszewski, L. Faraone and P. Burke (2001) *J. Electron. Mater.* **30**, 762.
- [91] T. Nguyen, J. Antoszewski, C. Musca, D.A. Redfern, J.M. Dell and L. Faraone (2002) *J. Electron. Mater.* **31**, 652.
- [92] J.R. Meyer, C.A. Hoffman, F.J. Bartoli, J. Antoszewski, L. Faraone, S.P. Tobin, P.W. Norton, C.K. Ard, D.J. Reese, L. Colombo and P.K. Liao (1996) *J. Electron. Mater.* **25**, 1157.
- [93] D. Lee, R. Briggs, T. Norton, D. Parker, F. Smith, S.P. Tobin, J. Welsch, F. Case, J. McCurdy and P. Mitra (1998) *J. Electron. Mater.* **27**, 709.
- [94] S.P. Tobin, M.A. Hutchins and P.W. Norton (2000) *J. Electron. Mater.* **29**, 781.
- [95] K.J. Riley and A.H. Lockwood (1980) *Proc. SPIE* **217**, 206.
- [96] K. Kosai and W.A. Radford (1990) *J. Vac. Sci. Technol. A* **8**, 1254.
- [97] C.C. Wang (1991) *J. Vac. Sci. Technol. B* **9**, 1740.
- [98] Y. Bai, J.T. Monroy, J.D. Blackwell, M.C. Ferris, L.J. Kozlowski and K. Vural (2000) *Proc. SPIE* **4028**, 174.
- [99] S.H. Shin, J.G. Pasko, H.D. Law and D.T. Cheung (1982) *Appl. Phys. Lett.* **40**, 965.
- [100] D.L. Hwang, Y.S. Tsai, H.L. Hwang and C.Y. Sun (1988) *J. Cryst. Growth* **96**, 673.
- [101] S. Terterian, M. Chu, S. Mesropian, H.K. Gurgonian, M. Ngo and C.C. Wang (2002) *J. Electron. Mater.* **31**, 720.
- [102] I.M. Baker, G.J. Crimes, C.K. Ard, *et al.* (1990) *4th Int. Conf. on Advanced Infrared Detectors and Systems*, IEE Conf. Pub. No. 321, 78.
- [103] P. Tribulet, J-P. Chatard, P. Costa and S. Paltrier (2001) *J. Electron. Mater.* **30**, 574.
- [104] T. Tung, M.H. Kalisher, M.H. Stevens, *et al.* (1987) *Mater. Res. Soc. Symp. Proc.* **90**, 321.
- [105] G.N. Pulz, P.W. Norton, E.E. Krueger and M.B. Reine (1991) *J. Vac. Sci. Technol. B* **9**, 1724.
- [106] L.J. Kozlowski (1996) *Proc. SPIE* **2745**, 2.
- [107] K. Vural, L.J. Kozlowski, D.E. Cooper, *et al.* (1999) *Proc. SPIE* **3698**, 24.
- [108] J.D. Beck, C.-F. Wan, M.A. Kinch and J.E. Robinson (2001) *Proc. SPIE* **4454**, 188.
- [109] M.A. Kinch, J.D. Beck, C.-F. Wan, F. Ma and J. Campbell (2004) *J. Electron. Mater.* **33**, 630.
- [110] T.J. deLyon, J.E. Jenson, M.D. Gordwitz, *et al.* (1999) *J. Electron. Mater.* **28**, 705.
- [111] I.M. Baker, S.S. Duncan and J.W. Copley (2004) *Proc. SPIE* **5406**, 133.
- [112] S.P. Tobin, M.H. Weiler, M.A. Hutchins, T. Parodos and P.W. Norton (1999) *J. Electron. Mater.* **28**, 596.
- [113] E.E. Krueger, D. Lee, C. Miller, *et al.* (1997) *Proc. SPIE* **3122**, 355.
- [114] K. Kosai and G.R. Chapman (1995) Dual-band Infrared Radiation Detector Optimized for Fabrication in Compositionally Graded MCT, US Patent 5 457 331.
- [115] J.A. Wilson, E.A. Patten, G.R. Chapman, *et al.* (1994) *Proc. SPIE* **2274**, 117.
- [116] K. Kosai (1995) *J. Electron. Mater.* **24**, 635.
- [117] S.M. Johnson, M. Kalisher, W. Ahlgren, *et al.* (1990) *Appl. Phys. Lett.* **56**, 946.
- [118] S.M. Johnson, J.A. Vigil, J.B. James, *et al.* (1993) *J. Electron. Mater.* **22**, 835.
- [119] T.J. deLyon, J.A. Roth, O.K. Wu, *et al.* (1993) *Appl. Phys. Lett.* **63**, 818.
- [120] S.M. Johnson, J.B. James, W.L. Ahlgren, *et al.* (1991) *Mater. Res. Soc. Symp. Proc.* **216**, 141.
- [121] P.R. Norton (1994) *Proc. SPIE* **2274**, 82.
- [122] S.M. Johnson, T. deLyon, C. Cockrum, *et al.* (1995) *J. Electron. Mater.* **24**, 467.
- [123] F.T. Smith, P. Norton, P. LoVecchio, *et al.* (1995) *J. Electron. Mater.* **24**, 1287.





# 10 Liquid Phase Epitaxy of Widegap II-VIs

J. F. WANG AND M. ISSHIKI

*Institute of Multidisciplinary Research for Advanced Materials, Tohoku University, 2-1-1 Katahira, Aoba-Ku, Sendai 980-8577, Japan*

---

10.1 Introduction	289
10.2 Basic properties	289
10.3 LPE technique	291
10.4 Review of some experimental results	292
10.4.1 Growth from Zn, Zn-Ga and halide solvents	293
10.4.2 Growth from Te and Se solvents	296
10.4.3 Growth from Sn solvent	299
10.4.4 Growth from Bi solvent	301
10.5 Conclusion	302
References	302

---

## 10.1 INTRODUCTION

The liquid phase epitaxy (LPE) method is well known and widely applied as an effective technique in fabricating light emitting diodes (LEDs), laser diodes (LDs) and other devices in several binary, ternary and quaternary III-V group compounds. On the other hand, widegap II-VI compounds are expected to be one of the most vital materials for high-performance optoelectronic devices such as LEDs and LDs operating in the blue or ultraviolet spectral range. Additionally, the high ionicity of these compounds makes them good candidates for high electro-optical and electromechanical coupling. Investigation on LPE of widegap II-VI compounds was begun in the 1970s.

## 10.2 BASIC PROPERTIES

Widegap II-VI compound semiconductors have higher melting points, volatilization and ionicity than III-V compounds and elemental semiconductors. Therefore, before introducing the film growth by LPE technique, it is necessary to review their physical and chemical properties. Table 10.1 shows some fundamental properties of widegap II-VI compound semiconductors [1–14].

**Table 10.1** Properties of some widebandgap II-VI compound semiconductors

Property	ZnS	ZnO	ZnSe	ZnTe	CdS	CdSe
Melting point (K)	2038 (WZ, 150 atm)	2248	1797	1513	2023 (WZ, 100 atm)	1623
$E_g$ at 300 K (eV)(ZB*/WZ*)	3.68/3.91	—/3.37	2.7	2.26	2.50/2.50	—/1.75
$dE_g/dT$ ( $\times 10^{-4}$ eV K <sup>-1</sup> )	4.6/8.5	—/9.5	4.0/—	5.5/—	—/5.2	—/4.6
ZB/WZ						
Structure	ZB/WZ	WZ	ZB/WZ	ZB	WZ	WZ
Bond length ( $\mu$ m)	2.342 (WZ)	1.977 (WZ)	2.454 (ZB)	2.636 (ZB)	2.530 (ZB)	2.630 (ZB)
Lattice constant (ZB) $a_0$ at 300 K (nm)	0.541	—	0.567	0.610	0.582	0.608
ZB nearest-neighbor distance at 300 K(nm)	0.234	—	0.246	0.264	0.252	0.263
ZB density at 300 K (g cm <sup>-3</sup> )	4.11	—	5.26	5.65	4.87	5.655
Lattice constant (WZ) at 300 K (nm)						
$a_0 = b_0$	0.3811	0.32495	0.398	0.427	0.4135	0.430
$c_0$	0.6234	0.52069	0.653	0.699	0.6749	0.702
$c_0/a_0$	1.636	1.602	1.641	1.637	1.632	1.633
WZ density at 300 K (g cm <sup>-3</sup> )	3.98	5.606	—	—	4.82	5.81
Symmetry ZB/WZ	C6me/F43m	—/C 6me	—/F 43 m	—/F 43 m	C6 me/F 43m	C6 me/F4 3m
$\chi$ (eV)			4.09	3.53	4.79	4.95
Phase stable at 300 K	ZB & WZ	WZ	ZB	ZB	ZB & WZ	ZB & WZ
Solid–solid phase transition temperature (K)	1293	—	1698	—	—	403
$\Delta H_{LS}$ (kJ mol <sup>-1</sup> )	44	62	52	56	58	45
$C_p$ (cal mol <sup>-1</sup> K <sup>-1</sup> )	11.0	9.6	12.4	11.9	13.2	11.8
Ionicity (%)	62	62	63	61	69	70
Equilibrium pressure at c.m.p (atm)	3.7	—	1.0	1.9	3.8	1.0
Minimum pressure at mp (atm)	2.8	7.82	0.53	0.64	2.2	0.4–0.5
Specific heat capacity (J g <sup>-1</sup> K <sup>-1</sup> )	0.469	—	0.339	0.16	0.47	0.49
Thermal conductivity (W cm <sup>-1</sup> K <sup>-1</sup> )	0.27	0.6	0.19	0.18	0.2	0.09
Linear expansion coefficient ( $\times 10^{-6}$ K <sup>-1</sup> ) ZB/WZ	—/6.9	2.9/7.2	7.6/—	8.0/—	3.0/4.5	3.0/7.3
Poisson ratio	0.27		0.28			
$\epsilon_0/\epsilon_\infty$	8.6/5.2	8.65/4.0	9.2/5.8	9.3/6.9	8.6/5.3	9.5/6.2
Refractive index ZB/WZ	2.368/2.378	—/2.029	2.5/—	2.72/—	—/2.529	2.5/—
Absorption coefficient (including two surfaces) ( $\lambda = 10.6 \mu$ m)(cm <sup>-1</sup> )	$\leq 0.15$	—	$1-2 \times 10^{-3}$	—	$\leq 0.007$	$\leq 0.0015$
Electron effective mass ( $m^*/m_0$ )	—0.40	—0.27	0.21	0.2	0.21	0.13
Hole effective mass $m^*_{dos}/m_0$	—	—	0.6	Circa 0.2	0.8	0.45
Electron hall mobility (300) K for $n = \text{lowish}$ (cm <sup>2</sup> /V <sup>-1</sup> s <sup>-1</sup> )	165	125	500	340	340	650
Hole hall mobility at 300 K for $p = \text{lowish}$ (cm <sup>2</sup> /V <sup>-1</sup> s <sup>-1</sup> )	5	—	30	100	340	—
Exciton binding energy (meV)	36	60	21	10	30.5	15
Average phonon energy (meV) ZB/WZ	16.1/17.1	—	15.1/—	10.8/—	—/13.9	18.9/25.4
Elastic constant ( $10^{10}$ N m <sup>-2</sup> )						
$C_{11}$	$1.01 \pm 0.05$	—	$8.10 \pm 0.52$	$0.72 \pm 0.01$	—	—
$C_{12}$	$0.64 \pm 0.05$	—	$4.88 \pm 0.49$	$0.48 \pm 0.002$	—	—
$C_{44}$	$0.42 \pm 0.04$	—	$4.41 \pm 0.13$	$0.31 \pm 0.002$	—	—
Knoop hardness(N cm <sup>-2</sup> )	0.18	0.5	0.15	0.13	—	—
Young's modulus	10.8 Mpsi	—	10.2 Mpsi	—	45 Gpa	$5 \times 10^{11}$ dyne cm <sup>-2</sup>

$E_g$ , energy gap;  $\chi$ , electron affinity;  $\Delta H_{LS}$ , heat of crystallization;  $C_p$ , heat capacity;  $\epsilon_0/\epsilon_\infty$ , dielectric constant

### 10.3 LPE TECHNIQUE

Before the 1970s, the films of widegap II-VI compound semiconductors were mainly grown from solid phase [15] and vapor phase epitaxy (VPE) [16–20]. With the success of LPE in growing high quality epilayers of III-V compounds for device application, it began to be applied for growing widegap II-VI compounds [21–24]. For the sake of comparison, some epitaxial growth methods have been summarized in Table 10.2.

There are two methods to contact the substrate with the solution. One is the dipping method and a schematic diagram is shown in Figure 10.1. The other is the slide-boat method and its schematic diagram is presented in Figure 10.2. Both of the LPE growths occur at near-thermodynamic equilibrium conditions.

There are two ways to control the supersaturation of the solution in the LPE process. One way is equilibrium cooling. After contact between the saturated solution and the substrate, the temperature is slowly lowered and the solution becomes supersaturated, which enables a slow epitaxial growth on the substrate. Another way is step cooling. The saturated solution is cooled down a few degrees to obtain a supersaturated solution. The substrate is inserted into the supersaturated solution, and epitaxial growth occurs due to the supersaturation, but the growth rate gradually decreases and the growth finally stops. For both techniques, if the substrate is contacted in sequence with several different melt sources, multi-layer structures can be grown.

**Table 10.2** Comparison of several epitaxial growth techniques

LPE	Low growth rate
Thermodynamic equilibrium growth	Need safety precautions
Easy-to-use materials	MOCVD
Low temperature growth	Gaseous reaction for deposition
High purity	Precise composition
Multiple layers	Patterned/localized growth
Thickness control not very precise	Potentially easier large area multiple wafer scale-up
Poor surface/interface morphology	
HWE	Low temperature growth
Easy-to-use materials	High vapor pressure materials growth allowed
Low cost	About 1 monolayer $s^{-1}$ deposition rate
Thermodynamic equilibrium	Expensive equipment
Hard to growth thick layer	Need safety precautions
Thickness control not very precise	MBE and MOMBE
VPE	Physical vapor deposition
Easy to operate	Ultra-high vacuum environment
Economic	About 1 monolayer $s^{-1}$ deposition rate
Thinner layers	<i>In situ</i> growth front monitoring
High growth rates	Precise composition
Easier composition control	Low growth rate
High temperature (800–1000 °C)	Sophisticated equipment
ALE	Limit for high vapor pressure materials growth (MBE)
Gaseous reaction for deposition	
Low temperature growth	
Precise composition	

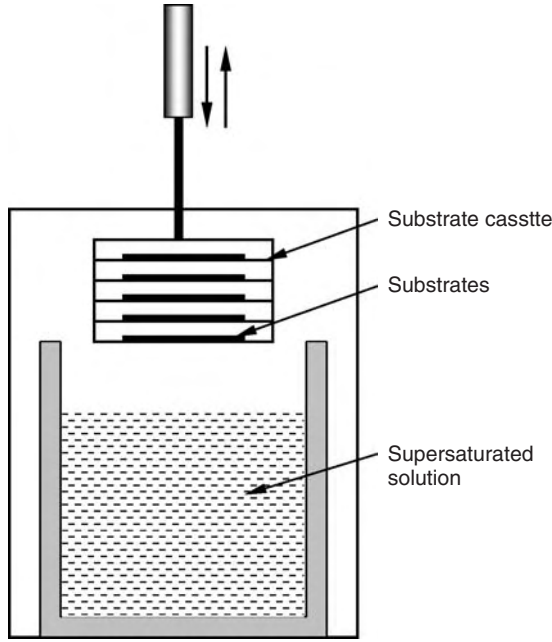


Figure 10.1 Schematic diagram of the dipping method

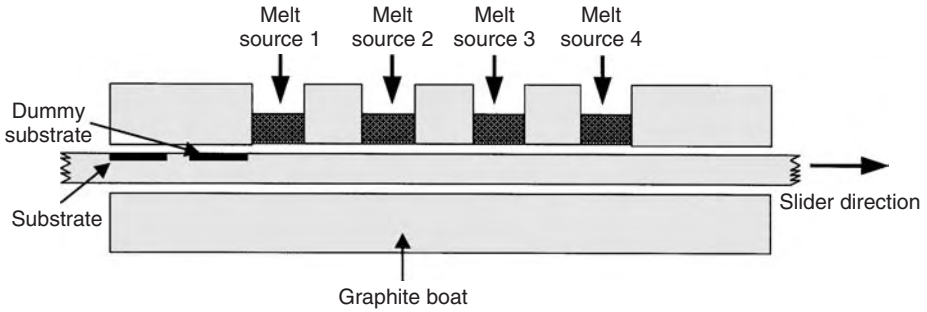


Figure 10.2 Schematic diagram of a typical slide-boat method

By LPE, homo- and heterostructures can be successfully and inexpensively grown. As the growth is carried out under thermal equilibrium, an epilayer with very low native defect density can be obtained. From the above description, it could be said that temperature control is the key in LPE growth.

### 10.4 REVIEW OF SOME EXPERIMENTAL RESULTS

As widegap compound semiconductors have high melting points and vapor pressures, the selection of solvent is very important in LPE growth. The development process of LPE for widegap II-VI compound semiconductors is a process of searching for suitable solvents.

### 10.4.1 Growth from Zn, Zn-Ga and halide solvents

Since wide gap II-VI compounds have higher ionicity, higher melting points and higher vapor pressures, it is very easy to deviate stoichiometry when the bulk or film crystal is grown. For example, ZnSe crystals contain zinc vacancy ( $V_{Zn}$ ) with high concentration. These vacancies easily associate with the donor (D) impurities to form a so-called self-activated center ( $V_{Zn}-D$ ). This results in a high-resistivity and a weak band-edge emission. It was reported that the intensity of blue emission could be enhanced by doping Ga into ZnSe crystals [25, 26]. LPE growth is expected to overcome this problem by selecting the solvent. Since Ga has a very low melting point, it is very suitable as a solvent in LPE growth. In the late 1970s Fujita *et al.* [27] reported LPE growth of ZnSe. LPE growth was carried out by a tilting method using a graphite boat in a vacuum quartz ampoule under the pressure of  $10^{-6}$  Torr (Figure 10.3). ZnS<sub>x</sub>Se<sub>1-x</sub> single crystal grown by iodine transport method was used as the substrate. The solvents are 6N grade Zn-Ga alloy with Ga mole fraction of 0–76%. Undoped ZnSe crystal pre-heated at 950 °C for 48 h was used as a solute. Growth temperature was varied from 850 to 1050 °C; cooling rate was 0.27–1 °C min<sup>-1</sup> cooling interval was 200–350 °C; the holding duration for dissolving the ZnSe in the solvent was 3 h. Undoped or Ga doped ZnSe single crystal layers with thicknesses between 3 μm and 13 μm were grown on ZnS<sub>x</sub>Se<sub>1-x</sub> substrates from Zn or Zn-Ga solvents. Smooth and uniform epitaxial layers with high crystal perfection were obtained on the (111)- and (100)-oriented substrates. All the epitaxial layers showed *n*-type conductivity and low resistivity. A remarkable enhancement of the blue emission in the photoluminescence (PL) spectra was observed at room temperature for the epitaxial layers grown from Zn-Ga solvents. The results show that LPE method is effective in controlling  $V_{Zn}$  concentration in ZnSe epilayer by using a suitable solvent.

At the beginning of the 1980s, Ido and Miyasato [28] grew ZnSe films using the LPE technique in a closed tube from a Ga solvent. They compared the surfaces of substrate that were thermally etched in Ga and Ga+Zn solutions. In the case of Ga solution, the surface had many etch pits with island-shape. On the other hand, the substrates were scarcely changed when Zn was added into Ga solution. Therefore, mixing Ga+Zn was used for growing ZnSe epilayers. The undoped, semi-insulating ZnSe (111) and undoped ZnSe<sub>0.4</sub>S<sub>0.6</sub> single crystals were used for substrates. The ZnSe crystals as the source were cut from the same boule as the substrates. The growth ampoule containing ZnSe

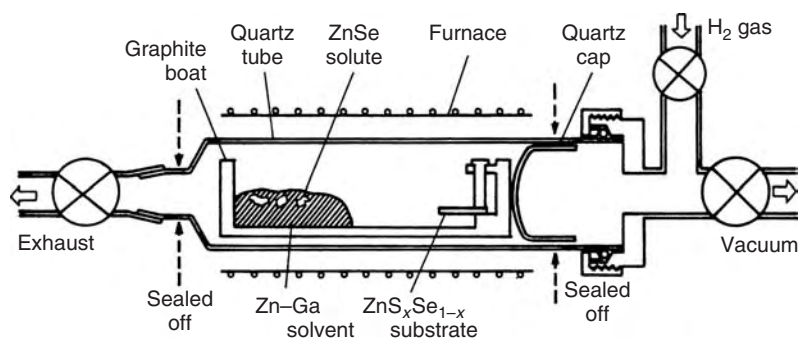


**Figure 10.3** Experimental arrangement of the growth ampoule for LPE. Reprinted from *J. Cryst. Growth*, 45, Fujita *et al.*, 281, Copyright (1978), with permission from Elsevier

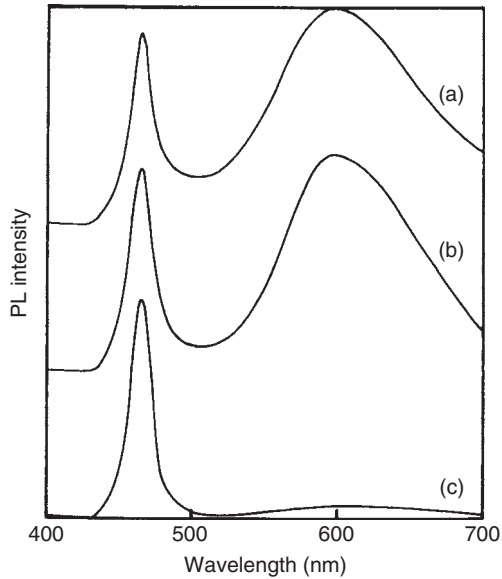


**Figure 10.4** PL spectra measured at room temperature on ZnSe LPE layers with excitation by a  $N_2$  laser. (a) Gradual temperature lowering method; (b) temperature difference method (TDM) at  $T_{\text{sub}} = 900^\circ\text{C}$  and  $\Delta T = 15^\circ\text{C}$ ; (c) TDM at  $T_{\text{sub}} = 1000^\circ\text{C}$  and  $\Delta T = 10^\circ\text{C}$ . Reprinted from *J. Cryst. Growth*, **59**, Ido and Miyasato, 178, Copyright (1982), with permission from Elsevier

source, ZnSe substrate, Zn grains and Ga was sealed after the ampoule was evacuated to  $10^{-6}$  Torr. The substrate temperature and the temperature difference between substrate and source were varied from 850 to  $1000^\circ\text{C}$  and from 10 to  $40^\circ\text{C}$ , respectively. After 5 h growth, the ampoule was quenched rapidly to room temperature. The PL spectra at room temperature are shown in Figure 10.4. The epilayer grown at 1273 K showed a strong blue emission even at room temperature. On the other hand, the layer grown at a lower substrate temperature or that grown by the gradual temperature lowering method showed orange color luminescence at room temperature, which was thought to be related to the Zn vacancy.

The differences of above PL spectra were thought to be a result from the difference of Zn vapor pressure during growth. Furthermore, the growth rate also influenced the properties of epilayers. However, authors thought the difference of the vapor pressure of Zn is more important than the growth rate. Therefore, blue emission at room temperature from ZnSe epitaxial layer was obtained by controlling Zn vapor pressure during the crystal growth.

From the above experimental results, auto-doping of Ga is inevitable when Ga is used as a solvent. This makes it difficult to study the effect of impurities on the properties of ZnSe. For this reason, Sano *et al.* [29] tried to grow homo-ZnSe epilayers from Zn solvent and studied the electrical and optical properties of the ZnSe layers doped with various impurities, although the saturation solubility of ZnSe in the Zn solvent is low at the growth temperature usually used in LPE. The results showed that the group-VII elements (Cl, Br, I) were much more suitable for preparing a low resistivity *n*-type ZnSe than the group III elements (Al, Ga, In). It has also been proven that the Hall mobility and

the intensity ratio of the deep and edge emissions in the PL spectrum depended on the Se pressure applied during the annealing of the ZnSe source crystal. The deep emission in the PL spectrum was suppressed by using a ZnSe source material annealed under Se pressure of 8 atm prior to growth. The maximum Hall mobility was  $380 \text{ cm}^2 \text{ V}^{-1} \text{ s}^{-1}$  at a carrier density of  $1.6 \times 10^{17} \text{ cm}^{-3}$ . They thought that LPE is suitable to grow a high-purity ZnSe epilayer from Zn solvent for a blue LED.

In general, ZnSe epilayer is grown by LPE from a metal solution such as Zn [29] and Zn+Ga solvents [28], and the growth is usually carried out at  $1000^\circ\text{C}$ . From the viewpoint of thermal defect theory, it is well known that the higher the growth temperature, the higher the native defects such as Zn vacancies, Se interstitials, and incorporated acceptor impurities or residual impurities. To avoid these problems caused by high temperature growth, the growth should be done at a temperature as low as possible. Halide solvents were used in LPE growth due to their advantages that the solubility of II-VI compounds in them is higher than that in metal solvents at the same temperature, they do not react with conventional graphite container materials, and they are easily dissolved in water, alcohol and other solvents.

Simashkevich and Tsiuyan [30] grew CdSe, ZnTe and ZnSe epilayers on ZnTe and ZnSe substrates from halide solvents. The LPE growth was carried out in an open system with an argon atmosphere. In order to prevent the evaporation of the solvents,  $\text{B}_2\text{O}_3$  was used for encapsulant. In the case of CdSe layers, the starting temperature of growth was  $580^\circ\text{C}$ , the cooling rate was  $1^\circ\text{C min}^{-1}$  and the cooling span was  $50\text{--}60^\circ\text{C}$ . Under these growth conditions, a CdSe layer with a thickness of  $25 \mu\text{m}$  was grown. In the CdSe/ZnTe heterostructure, ZnTe crystal has a cubic structure and CdSe has two kinds of crystal structures, namely cubic and hexagonal. When both crystals have cubic structure, the lattice mismatch is 0.3%. For this reason, the growth conditions for cubic CdSe were examined. The experimental results showed that the CdSe layers have both cubic and hexagonal modifications when pure  $\text{CdCl}_2$  was used. When  $\text{CdI}_2$  was mixed with  $\text{CdCl}_2$ , the CdSe layer with cubic structure was easily grown.

It was verified by X-ray microanalysis that CdSe-ZnTe solid solutions exist on the interface between substrate and epilayer. When the solvent consists of 90%  $\text{CdCl}_2$  and 10%  $\text{CdI}_2$ , the solid solution is as thick as  $6 \mu\text{m}$ . The formation of CdSe-ZnTe solid solutions at the interface shows that the solvent has high viscosity. Addition of KCl up to 7% into the solvent overcame this problem.

On the other hand, ZnTe layers were also grown from the solvent containing  $\text{CdCl}_2$  and  $\text{CdI}_2$ . X-ray microanalysis showed that the solid solution of ZnTe-CdTe existed throughout the epilayer, and its composition was changed. When epilayer thickness increased, the content of ZnTe also increased. When the epilayer thickness was  $10 \mu\text{m}$ , the epilayer had a composition of  $\text{Zn}_{0.7}\text{Cd}_{0.3}\text{Te}$ . In addition, ZnSe epilayer was also grown from  $\text{ZnCl}_2$  on ZnTe substrate, but details were not reported.

Ido [31] examined the dependence of ZnSe solubility in  $\text{ZnCl}_2$  on temperature in the range of  $500\text{--}700^\circ\text{C}$ . At  $700^\circ\text{C}$ , the solubility of ZnSe in  $\text{ZnCl}_2$  solution was larger than that in metal solutions such as Zn and Ga at  $1000\text{--}1100^\circ\text{C}$  [32, 33]. In this study [31], ZnSe epilayers were grown on (111),  $(\bar{1}\bar{1}\bar{1})$  and (110) ZnSe substrates in a closed tube in the range of  $550\text{--}700^\circ\text{C}$ . The growth started at  $700^\circ\text{C}$  and ended at  $550^\circ\text{C}$ . The cooling rate was  $1\text{--}5^\circ\text{C min}^{-1}$ . The epilayers were  $40\text{--}60 \mu\text{m}$  in thickness and the surfaces were smooth. The X-ray diffraction showed that the epilayers were single crystals. The resistivity and the Hall mobility of as-grown layers were  $10^4\text{--}10^6 \Omega \text{ cm}$  and about  $80 \text{ cm}^2$



$V^{-1} s^{-1}$  at room temperature, respectively. The PL spectra showed both a sharp blue edge emission and a broad red emission in all epilayers. The blue emission was identified to be related to intrinsic emission, and the broad red emission to the self-activated center.

Although CdSe, ZnTe and ZnSe epilayers could be grown from halide solutions by LPE at a temperature below 600 °C, the results are unsatisfactory. The main problem is the formation of solid solution at the interface, even throughout the epilayer.

### 10.4.2 Growth from Te and Se solvents

Since ZnSe, ZnTe and ZnS have suitable solubilities in liquid Te and Se, their epilayers were also grown by the LPE technique from Te [21] and Se [34, 35] or Te-Se solvents [36].

Washiyama *et al.* [37] measured the solubility of ZnS, ZnSe and CdS in liquid Te. The results are shown in Figure 10.5(a). Furthermore, Nakamura *et al.* [36] measured the solubility of other II-VI compounds, as shown in Figure 10.5(b). According to this figure, Nakamura and Aoki [21] successfully grew ZnS, ZnSe and ZnSSe layers on ZnS substrates by LPE from Te solvent with an open-tube slide-boat system (Figure 10.6). ZnS substrates with different orientations were cut from an ingot grown by the high-pressure Bridgman technique. The solvent material was 6N-grade Te. The ZnS as a solute was a sintered ingot prepared from 5N-grade powder. A suitable starting temperature was 850 °C for ZnS and 700–800 °C for ZnSe, and the cooling rate was 5 °C min<sup>-1</sup> for ZnS and 2–4 °C min<sup>-1</sup> for ZnSe growth. The surface of ZnS epilayers grown on ZnS with {111}A and {111}B with about 1 μm thickness was smooth, but the surfaces of ZnS layers grown on {110} and {100} ZnS were rough. Measurement by X-ray microanalyser showed that these epilayers contained Te with a concentration of about 0.1 at. %. The PL spectra at 77 K and room temperature showed strong whitish-blue emission. In the case of ZnSe layers, the thickness was 15–30 μm. Although the surfaces were smooth, Te concentration in ZnSe epilayer was higher than that of ZnS. PL spectra at 77 K showed efficient green and weak red emissions.

The phase diagram is very important for LPE growth. Aoki *et al.* [38] and Nakamura *et al.* [36] presented the ternary phase diagram of Zn-Se-Te (Figure 10.7). Based on this diagram, Nakamura *et al.* [36] grew ZnSe layers on ZnTe {111}B substrates using closed-tube tipping LPE from a Te-Se solution at 800 °C. The ZnSe epilayers grown had good surface morphology and serious melt-back of the substrates was not found. They estimated the concentration of Te in the epilayer and results showed a value of less than 1 at. %. Furthermore, a solar cell fabricated from the *n*-ZnSe/*p*-ZnTe heterojunction showed high open-circuit voltage of 0.9 V. This result suggests that the ZnSe epilayer is effective also as a window material for the solar cell.

The above results showed that epilayers grown from Te or Te + Se solvent contained a small amount of Te, and the epilayers were actually ZnSe<sub>1-x</sub>Te<sub>x</sub>. Nakamura *et al.* [23] summarized the molar solubilities of ZnSe in various kinds of solvents as shown in Figure 10.8 [33, 37–40]. They tried to grow ZnSe epilayers from solvents of As<sub>0.4</sub>Se<sub>0.6</sub> [38] and Sb<sub>0.4</sub>Se<sub>0.6</sub> [23]. Owing to the high vapor pressure of As<sub>0.4</sub>Se<sub>0.6</sub>, it is very difficult to apply this solvent to open-tube LPE growth. In the case of Sb<sub>0.4</sub>Se<sub>0.6</sub> solvent, the LPE growth of ZnSe epilayers was successfully carried out by the open-tube slide-boat method. The growth conditions were: growth temperature over 800 °C

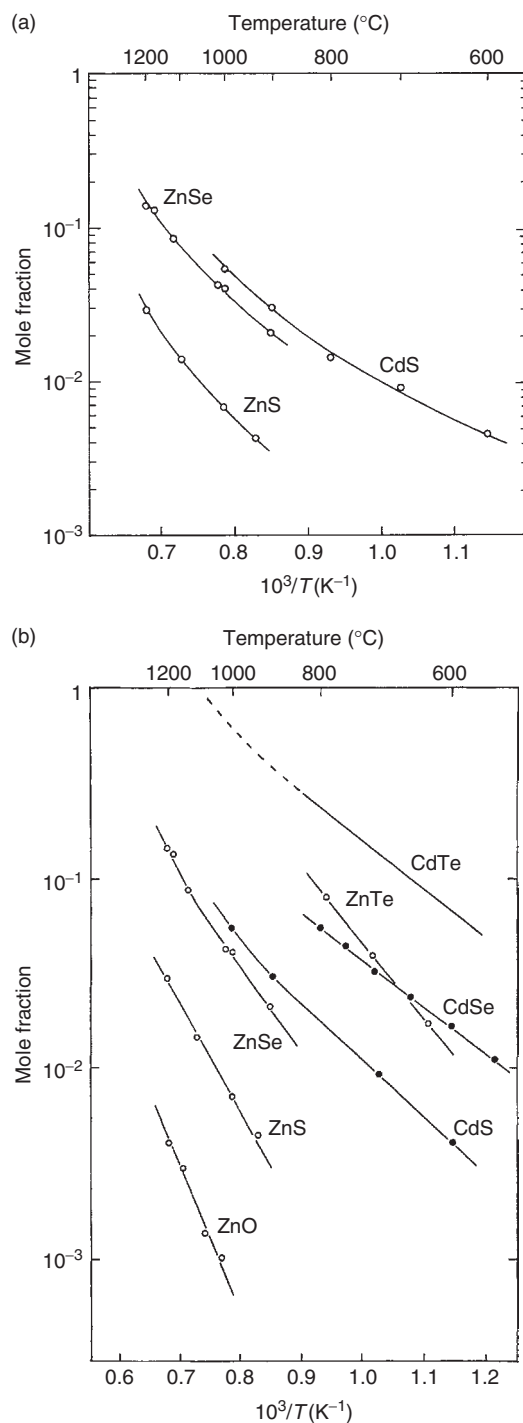


**Figure 10.5** Solubilities of various II-VI compounds in liquid Te. (a) Reproduced from [37] by permission of the Institute of Pure and Applied Physics. (b) Reproduced from [36] by permission of the Institute of Pure and Applied Physics

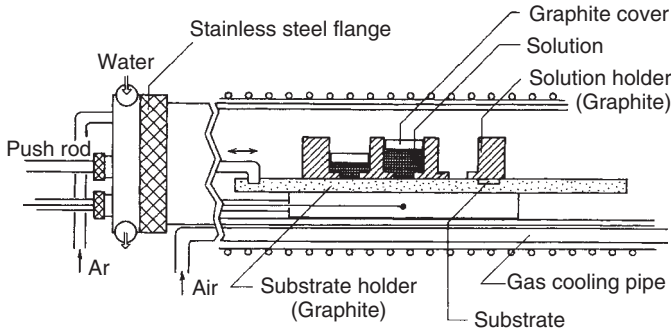


**Figure 10.6** Main part of the growth apparatus for LPE of ZnS, ZnSe and ZnS<sub>1-x</sub>Se<sub>x</sub>. Reproduced from [21] by permission of the Institute of Pure and Applied Physics

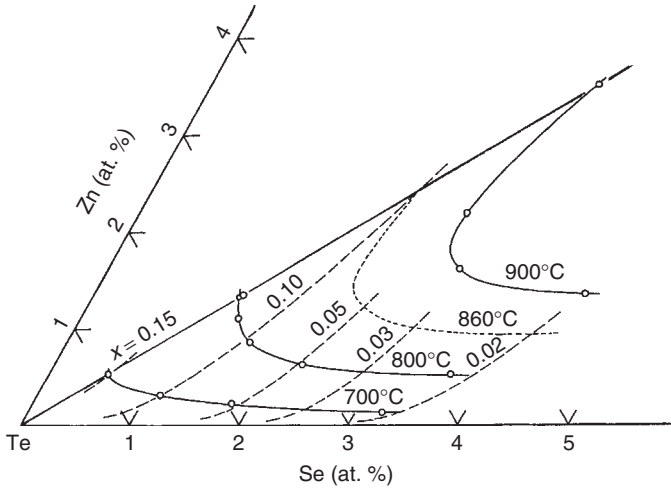


**Figure 10.7** Te corner of the Zn-Se-Te ternary phase diagram. Solid lines show liquidus isotherms and broken lines show solidus curves. Reproduced from [36] by permission of the Institute of Pure and Applied Physics

and cooling rate lower than 1 °C min<sup>-1</sup>. PL spectra of epilayer with thickness more than 30 μm were similar to that of the bulk crystal grown from Sb-Se solution. Nakamura *et al.* considered this technique a promising method to obtain high purity epilayers of ZnSe.

The deviation from stoichiometry in II-VI compounds is a severe problem. Since the temperature difference method under controlled Zn vapor pressure (TDM-CVP) has been proved to be effective in growing films of III-V compounds [41], Sakurai *et al.* [34, 35] grew ZnSe epilayers by TDM-CVP from a Se solvent. Figure 10.9 shows the schematic figure of the epitaxial growth system and the temperature distribution of the furnace. LPE growth was carried out in a quartz ampoule with dimensions of 8 mm in inner diameter and 50–80 mm in length. The ampoule can be divided into three zones: Zn partial pressure zone, Se solvent zone containing polycrystal ZnSe source crystal, and growth zone containing substrate. To grow *p*-type ZnSe layers, Na<sub>2</sub> Se, Na<sub>2</sub>S and LiN<sub>3</sub> were added as

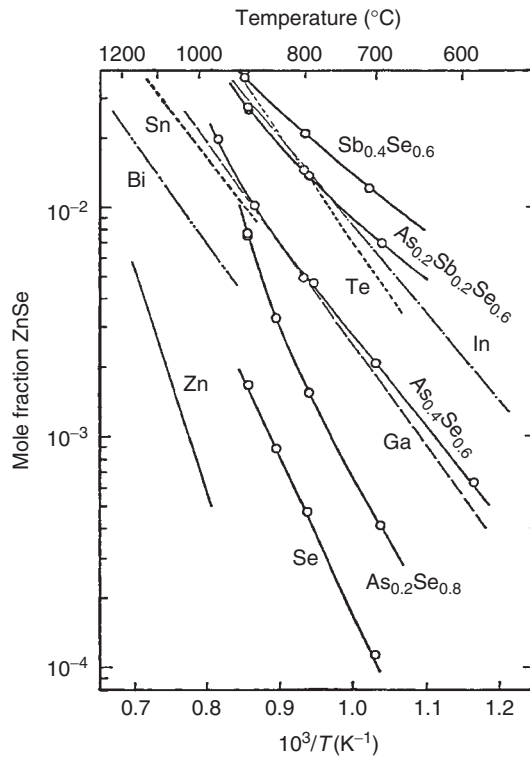


**Figure 10.8** Molar solubilities of ZnSe in various kinds of solvents. Reproduced from [23] by permission of the Institute of Pure and Applied Physics

dopants into Se solvent. The growth ampoule was sealed in vacuum below  $2 \times 10^{-6}$  Torr. The growth was performed at 950 and 1060 °C. In the case of growing at 950 and 1060 °C, Zn partial pressure was controlled at 3.0 and 8.2 atm, respectively. The temperature gradient between substrate and source zone was  $1-5$  °C  $\text{cm}^{-1}$ . At these growth conditions, the growth rate was  $2-10$   $\mu\text{m h}^{-1}$ . The electrical measurements showed that the ZnSe epilayers doped with  $\text{Na}_2\text{Se}$ ,  $\text{Na}_2\text{S}$  and  $\text{LiN}_3$  showed  $p$ -type conductive features. The highest hole concentration was  $1 \times 10^{18} \text{ cm}^{-3}$  in  $\text{Na}_2\text{Se}$ -doped ZnSe layer. Furthermore, the  $p-n$  junction diodes were fabricated by Ga diffusion into the  $\text{Na}_2\text{S}$ -doped  $p$ -type ZnSe epilayer. The fabricated LED emitted blue light at 471 nm at room temperature.

### 10.4.3 Growth from Sn solvent

In LPE growth, unintentional doping from the solvent is inevitable. Therefore, the high-purity solvent is necessary. Since high purity Sn is commercially available, and Sn has the lowest vapor pressure as well as a suitable solubility for ZnSe, Sn was used as a solvent in LPE growth [22, 42–44]. Werkhoven *et al.* [22] grew ZnSe layers on ZnSe substrates from Sn solvent using a conventional slider boat of high-purity graphite. Appropriate amounts of Zn and Se were added to ensure saturation of the melt at the starting temperature of growth. Growth temperature was varied from 900 to 830 °C and the cooling

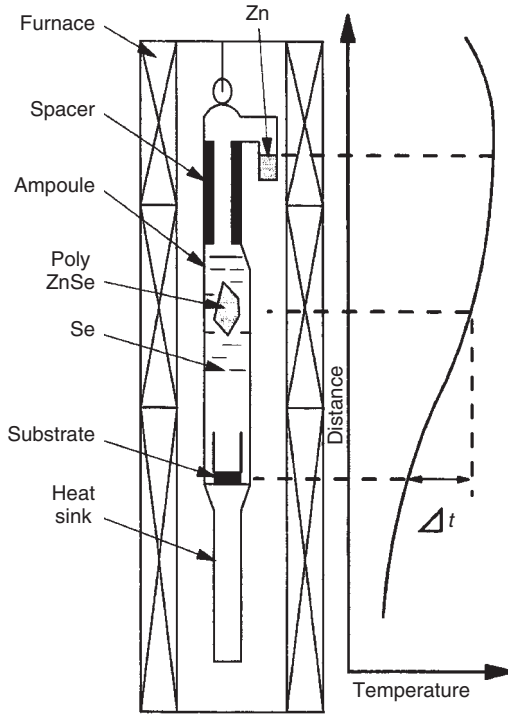


**Figure 10.9** Schematic drawing of the epitaxial growth system and the temperature distribution of the furnace. Reprinted from *J. Cryst. Growth*, **172**, Sakurai *et al.*, 75, Copyright (1997), with permission from Elsevier

rate was  $0.5\text{ }^{\circ}\text{C min}^{-1}$ . Epitaxial layers with thickness from 5 to  $10\text{ }\mu\text{m}$  were grown. PL spectra of these samples were employed to study the origin and nature of background compensating impurities in undoped ZnSe layers. The width of bound exciton lines in PL spectra was used to define the quality of the material, and the energy of the lines was used to identify these low-level impurities. The sharpest spectrum was obtained in layers grown on a buffer layer, indicating the importance of impurity outdiffusion from the substrate into the growing layer. Furthermore, they estimated that the total concentration of electrically active impurities ( $N_A + N_D$ ) was  $< 10^{17}\text{ cm}^{-3}$  from the sharpness of the bound exciton emission lines and mass spectroscopy. This showed that the control of substrate autodoping by selection of the buffer layer resulted in a reproducible growth of the material. These results suggested that the *n*-type conductivity of ZnSe is actually due to extrinsic impurities rather than native defects and the *p*-type ZnSe may be achieved by appropriate doping.

Heurtel *et al.* [42] calculated the ternary equilibrium phase diagram of Zn-Sn-Se for a liquid with composition from  $X_{\text{Zn}} = X_{\text{Se}} = 10^{-2}$  to  $5 \times 10^{-2}$  and estimated the solubility of ZnSe in Sn. Figure 10.10 shows the part of the liquidus line corresponding to  $X_{\text{Zn}} = X_{\text{Se}}$ . Furthermore, authors designed an apparatus to measure solubility and to make LPE growth. The measured results were consistent with the theoretical calculation. Electrical and PL measurements of the grown ZnSe epilayers on ZnSe substrates from a Sn solvent showed that pure ZnSe epilayer could be obtained by this method.

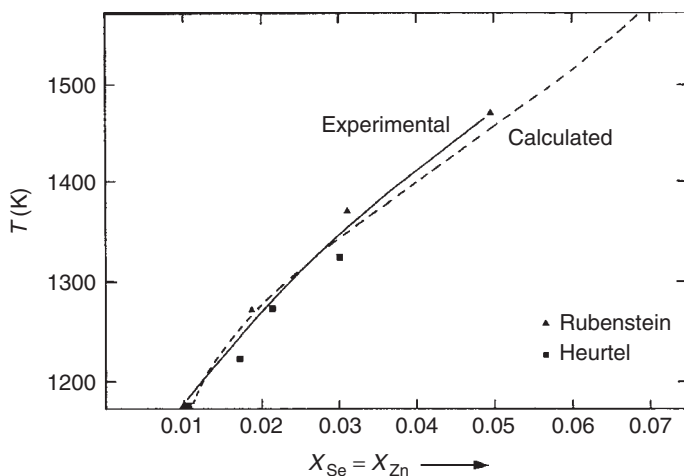


**Figure 10.10** Solubility of ZnSe in Sn. Reprinted from *J. Cryst. Growth*, **59**, Heurtel *et al.*, 167, Copyright (1982), with permission from Elsevier

In order to study deep centers in ZnSe, Ido and Okada [44] prepared ZnSe layers on ZnSe (111) substrates in a closed tube from an Sn solution by the temperature difference method. Ga and P were used as dopants. The traps in ZnSe epitaxial layers grown on (111) ZnSe substrates were investigated by photocapacitance and deep level transient spectroscopy (DLTS) methods. The photocapacitance study revealed a electron trap at 0.14 eV and two hole traps at 0.57 and 0.10 eV, which were identified as a self-activated center and Na or Li acceptors, respectively. The DLTS study elucidated a 0.32 eV trap in a P-doped sample and a 0.30 eV trap in an undoped sample, which seems to be due to Se vacancy. Traps were found also at 0.15, 0.29 and 0.52 eV in a Ga-doped sample. The DLTS spectra of the first two traps changed remarkably under light irradiation.

#### 10.4.4 Growth from Bi solvent

Several papers were published on ZnSe layers grown by LPE from Bi system solvent [45–49]. These works mainly focused on studying the behavior of some acceptor impurities. Kosai *et al.* [46] grew ZnSe epilayers doped with Li, Na, N and P from Bi solvent on ZnSe  $\langle 111 \rangle$  substrates in a horizontal slider reactor which was used for GaAlAs laser structures. The growth temperature interval was in the range of 950–800 °C at a cooling rate of about 0.5 °C min<sup>-1</sup>. These epilayers were proved to be *p*-type by estimating the position of the Fermi levels through photocapacitance and photoconductivity measurement. This result showed that the shallow acceptors, Li, Na, N and P, had been effectively incorporated in ZnSe. Furthermore, in order to identify unintentional donor impurities in ZnSe and to understand their roles in the compensation, Kosai [49] studied deep donor impurities occurring in variously doped *n*-type ZnSe layer grown by LPE from Bi solution. Electron traps were observed with activation energies of 0.17, ~ 0.3, 0.64 and 1.4 eV below the conduction band. These data are very helpful in understanding intrinsic defects as well as extrinsic defects in ZnSe.

Beside the solvents mentioned above, the solvents of In [33, 40], Pb [50], LiF [51], etc. were also used for preparing epilayers of ZnSe, ZnTe, etc.

## 10.5 CONCLUSION

The epilayers of some widegap compounds, such as ZnSe, ZnTe and CdSe, have been grown by the LPE method. Some valuable results have been obtained. Low resistivity *p*-type ZnSe epilayers with carrier concentration of  $10^{18} \text{ cm}^{-3}$  were grown and LED was fabricated. These results are comparable with advanced metal-organic chemical vapor deposition (MOCVD) or the molecular beam epitaxy (MBE) technique.

Although some successful examples have been shown, there is a viewpoint that the LPE technique is not a very suitable method for epitaxial growth of widegap II-VI compounds. The number of published papers has gradually reduced in recent years. This is mainly due to some difficulties, such as high melting point and volatilization. These difficulties cannot be overcome by the LPE technique.

## REFERENCES

- [1] Harmann, H., Mach, R. and Sell, B. (1982) in *Current Topics in Materials Science*, Vol. 9 (ed. Kaldis, E.), North-Holland, Amsterdam, p. 1.
- [2] Rudolph, P., Schäfer, N. and Fukuda, T. (1995) *Mater. Sci. Engin.*, **R15**, 85.
- [3] Shetty, R., Balasubramanian, R. and Wilcox, W.R. (1990) *J. Cryst. Growth*, **100**, 51.
- [4] Böer, K.W. (1990) in *Survey of Semiconductor Physics, Vol. 1: Electrons and Other Particles in Bulk Semiconductors* (ed. Whitaker, J.C.), Van Nostrand, New York.
- [5] Wolf, C.M., Holonyak, N. and Stillman, G.E. (eds) (1989) in *Physical Properties of Semiconductors*, Prentice Hall, Englewood Cliffs, NJ, p. 242.
- [6] Smart, L. and Moore, E. (eds) (1998) in *Solid State Chemistry*, 2nd Edn, Chapman & Hall, p. 12.
- [7] Weast, R.C. (ed.) (1972–1973) *Handbook of Chemistry and Physics*, 53rd Edn, CRC Press, Boca Raton.
- [8] Singh, J. (1993) *Physics of Semiconductors and their Heterostructures*, McGraw-Hill, New York.
- [9] Yamamoto, N., Horinaka, H. and Miyauchi, T. (1997) *Jpn. J. Appl. Phys.*, **18**, 225.
- [10] Neumann, H. (1980) *Kristall Technik*, **15**, 849.
- [11] Camassel, J., Auvergne, D. and Mathieu, H. (1974) *J. Phys. Colloq.*, **35**, C3-67.
- [12] Shan, W., Song, J.J., Luo, H. and Furdyna, J.K. (1994) *Phys. Rev. B*, **50**, 8012.
- [13] Dmitrenko, K.A., Shevel, S.G., Taranenko, L.V. and Marintchenko, A.V. (1986) *Phys. Status Solidi B*, **134**, 605.
- [14] Logothetidis, S., Cardona, M., Lautenschlager, P. and Garriga, M. (1986) *Phys. Rev. B*, **34**, 2458.
- [15] Lau, S.S. and van der Weg, W.F. (1978) in *Thin Films—Interdiffusion and Reactions* (eds Poate, J.M., Tu, K.N. and Mayer, J.W.), John Wiley & Sons, Inc., New York, p. 433.
- [16] Lopez-Otero, A. (1978) *Thin Solid Films*, **49**, 1.
- [17] Manasevit, H.M. and Simpson, W.I. (1971) *J. Electrochem. Soc.*, **118**, 644.
- [18] Chang, L.L. and Ludeke, R. (1975) in *Epitaxial Growth, Part A* (ed. Matthews, J.W.), Academic Press, San Diego, p. 37.
- [19] Veuhoff, E., Pletschen, W., Balk, P. and Luth, H. (1981) *J. Cryst. Growth*, **55**, 30.
- [20] Suntola, T. (1989) *Mater. Sci. Rep.*, **4**, 261.

- [21] Nakamura, H. and Aoki, M. (1981) *Jpn. J. Appl. Phys.*, **20**, 11.
- [22] Werkhoven, C., Fitzpatrick, B.J., Herko, S.P., Bhargava, R.N. and Dean, P.J. (1981) *Appl. Phys. Lett.*, **38**, 540.
- [23] Nakamura, H., Kojima, S., Wasgiyama, M. and Aoki, M. (1984) *Jpn. J. Appl. Phys.*, **23**, L617.
- [24] Skobeeva, V.M., Serdyuk, V.V., Semenyuk, L.N. and Malishin, N.V. (1986) *J. Appl. Spectrosc.*, **44**, 164.
- [25] Bouley J.C., Blanconnier, P., Harman, A., Ged, Ph., Henoc, P. and Noblanc, J.P. (1975) *J. Appl. Phys.*, **46**, 3549.
- [26] Yamaguchi, M., Yamamoto, A. and Kondo, M. (1977) *J. Appl. Phys.*, **48**, 5237.
- [27] Fujita, S., Mimoto, H. and Noguchi, T. (1978) *J. Cryst. Growth*, **45**, 281.
- [28] Ido, T. and Miyasato, K. (1982) *J. Cryst. Growth*, **59**, 178.
- [29] Sano, M., Yamashita, Y. and Okuno, Y. (1993) *J. Appl. Phys.*, **74**, 6133.
- [30] Simashkevich, A.V. and Tsiyuanu, R.L. (1976) *J. Cryst. Growth*, **35**, 269.
- [31] Ido, T. (1981) *J. Cryst. Growth*, **51**, 304.
- [32] Rubenstein, M. (1968) *J. Cryst. Growth*, **3/4**, 309.
- [33] Wagner, P. and Lorentz, M.R. (1966) *J. Phys. Chem. Solids*, **27**, 1749.
- [34] Sakurai, F., Fujishiro, H., Suto, K. and Nishizawa, J. (1991) *J. Cryst. Growth*, **112**, 153.
- [35] Sakurai, F., Motozawa, M., Suto, K. and Nishizawa, J. (1997) *J. Cryst. Growth*, **172**, 75.
- [36] Nakamura, H., Sun, L.Y., Asano, A., Nakamura, Y., Washiyama, M. and Aoki, M. (1983) *Jpn. J. Appl. Phys.*, **22**, 499.
- [37] Washiyama, M., Sato, K. and Aoki, M. (1979) *Jpn. J. Appl. Phys.*, **18**, 869.
- [38] Aoki, M., Washiyama, M., Nakamura, H. and Sakamoto, K. (1982) *Jpn. J. Appl. Phys.*, **21** (Suppl. 1), 11.
- [39] Rubenstein, M. (1966) *J. Electrochem. Soc.*, **11**, 623.
- [40] Kikuma, I. and Furukoshi, M. (1980) *J. Cryst. Growth*, **50**, 654.
- [41] Nishizawa, J., Okuno, Y. and Tadano, H. (1975) *J. Cryst. Growth*, **31**, 215.
- [42] Heurtel, A., Marbeuf, A., Tews, H. and Marfaing, Y. (1982) *J. Cryst. Growth*, **59**, 167.
- [43] McGee III, T.F. and Werkhoven, C. (1982) *J. Cryst. Growth*, **59**, 649.
- [44] Ido, T. and Okada, M. (1985) *J. Cryst. Growth*, **72**, 170.
- [45] Van Der Does De Bye, J. A. W., Vink, A.T., Bosman, A.J. and Peters, R.C. (1970) *J. Lumin.*, **3**, 185.
- [46] Kosai, K., Fitzpatrick, B.J., Grimmeiss, H.G., Bhargava, R.N. and Neumark, G.F. (1979) *Appl. Phys. Lett.*, **35**, 194.
- [47] Bhargava, R.N., Seymour, R.J., Fitzpatrick, B.J. and Herko, S.P. (1979) *Phys. Rev. B*, **20**, 2407.
- [48] Fitzpatrick, B.J., Werkhoven, C., McGee, T.F., Harnack, P., Herko, S.P., Bhargava, R.N. and Dean, P.J. (1981) *IEEE Trans. Electron Devices*, **28**, 440.
- [49] Kosai, K. (1981) *J. Appl. Phys.*, **53**, 1018.
- [50] R. Widmer, R., Bortfeld, D.P. and Kleinknecht, H.P. (1970) *J. Cryst. Growth*, **6**, 237.
- [51] Krasnov, A.N. (1995) *J. Cryst. Growth*, **148**, 432.





# 11 Liquid Phase Epitaxy of Garnets

**TAKETOSHI HIBIYA**

*Tokyo Metropolitan University, 6-6, Asahigaoka, Hino 191-0065, Tokyo, Japan*

**PETER GÖRNERT**

*Innovent eV, Pruessingstr. 27 B, D-07745 Jena, Germany*

---

11.1 Introduction	305
11.2 LPE growth	309
11.3 Phase diagram and chemistry	311
11.3.1 Phase diagram	311
11.3.2 Chemical thermodynamics of LPE	314
11.3.3 Effect of oxygen partial pressure on magnetic properties	317
11.4 Growth mechanism and morphology	317
11.4.1 Mass transport and growth rate	317
11.4.2 Control of morphology	321
11.5 Bi-substituted garnet films	323
11.6 Properties of magnetic garnet films	325
11.6.1 Misfit strain	325
11.6.2 Faraday rotation	328
11.6.3 Optical absorption	328
11.6.4 Magnetic anisotropy	333
11.7 Applications of garnet films	334
11.8 Conclusions	337
Acknowledgements	337
References	337

---

## 11.1 INTRODUCTION

The electronic and optoelectronic application of magnetic garnets was initiated in the 1950s in the field of microwave communication technology, due to its very narrow resonance absorption width  $\Delta H$ . Typical compositions were  $Y_3Fe_5O_{12}$  and  $Ca_{2x}Bi_{3-2x}Fe_{5-x}V_xO_{12}$ , with polycrystalline materials employed, as well as spherical single crystals. Triggered by the invention of bubble memory devices [1], epitaxial technologies, in particular

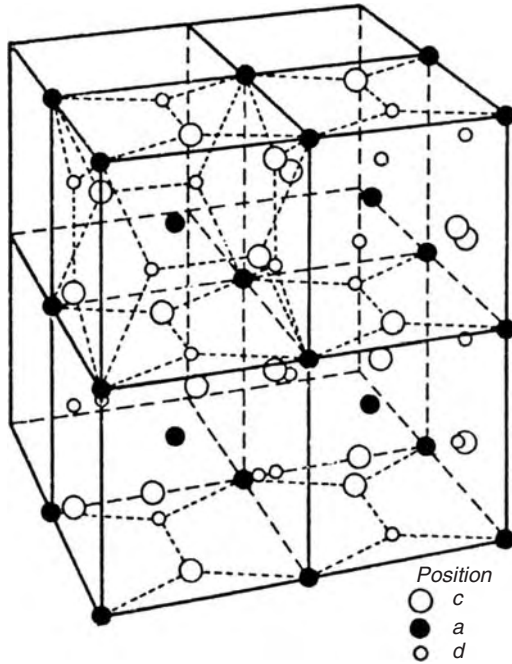


**Figure 11.1** Garnet crystal (only cations are shown; the oxygen ion is eliminated for convenience). Reprinted from *Bell Labs Technical Journal*, S. Geller, H.J. Williams, G.P. Espinosa and R.C. Sherwood, 365, Copyright (1964), with permission from John Wiley & Sons, Ltd

liquid phase epitaxy (LPE), of garnet materials have been successfully developed on a wide scale [2]. By applying the LPE technique, material design can be facilitated more easily than with other techniques. The garnet crystals have considerable freedom for designing functions, due to the three cation sublattice sites, i.e. 24c (dodecahedral), 16a (octahedral) and 24d (tetrahedral) sites, as shown in Figure 11.1, where only cations are shown for convenience. Depending on the ionic radius, many kinds of cations can enter the garnet crystal lattice, as shown in Table 11.1. The crystal lattice of a family of natural and synthetic garnets represents the body-centered cubic (bcc) of oxygen ions and the space group is  $O_h^{10}$  (Schoenflies) or Ia3d (international) [3]. These characteristics of garnet materials allow many electronic and optoelectronic applications. For magnetic garnets, they are microwave devices, bubble domain memory [1], magnetostatic wave devices [4, 5], an optical isolator [6] and a magnetic sensor [7]. For nonmagnetic garnets, such as  $Y_3Al_5O_{12}$  and  $Gd_3Ga_5O_{12}$  garnets, applications were laser hosts, cathode luminescence devices and

**Table 11.1** Metallic ions incorporated in garnet crystals

C (sublattice 24 c)	$Y^{3+}$ , rare-earth ions, such as $La^{3+}$ , $Gd^{3+}$ , $Sm^{3+}$ , $Lu^{3+}$ , ... $Ca^{2+}$ , $Bi^{3+}$ , $Pb^{2+}$ , ...
A (sublattice 16 a)	$Fe^{3+}$ , $Ga^{3+}$ , $Al^{3+}$ , $Mn^{3+}$ , ...
D (sublattice 24 d)	$Fe^{3+}$ , $Ga^{3+}$ , $Al^{3+}$ , $Ge^{4+}$ , $Si^{4+}$ , $V^{5+}$ , ...

substrates of an epitaxial layer of magnetic garnets. Although various preparation methods for garnet films have been attempted, i.e. LPE, radio frequency (rf) sputtering [8], vapor phase epitaxy [9], hydrothermal growth [10], LPE techniques have significant advantages compared with other techniques.

Liquid phase epitaxial growth has been most successful in supplying chips for bubble domain memories. LPE magnetic garnet single crystal films were prepared from the  $\text{PbO-B}_2\text{O}_3$  fluxed melts using a rotating nonmagnetic garnet substrate, such as GGG ( $\text{Gd}_3\text{Ga}_5\text{O}_{12}$ ) of diameter up to 3 in. (75 mm). This technique assures a high growth rate, homogeneous distribution of the film thickness and magnetic properties, and no defects [11, 12]. Increasing the wafer diameter required a clear understanding of the heat and mass transport phenomena in the LPE crucible and large diameter substrate garnet crystals. However, research and development on LPE growth has been mainly carried out with the aim of designing and developing new garnet films with superior magnetic properties for use in bubble domain devices; combining rare-earth ions which substitute into the 24c-site and nonmagnetic ions into the 16a- and 24d-sites [13]. Growth temperature, a degree of undercooling and the substrate rotation rate are also important in controlling the magnetic properties, because they are closely related to the distribution coefficient of cations, which enter three sublattice sites independently: namely 24c, 16a and 24d sites. Growth induced magnetic anisotropy, one of the most important magnetic properties for bubble memory applications, is also sensitive to the aforementioned growth condition. For the bubble memory application of LPE garnet films, growth direction was mainly  $\langle 111 \rangle$ . Although the  $\{111\}$  is not a natural surface of garnet crystals,  $\{111\}$  growth is preferentially employed, because an easy magnetisation axis perpendicular to the films surface is required for the magnetic bubble application. This requirement is satisfied by an appropriate combination of rare-earth ions; growth-induced uniaxial magnetic anisotropy perpendicular to the surface was obtained by selecting the growth direction as  $\langle 111 \rangle$ , although the garnet system is cubic and isotropic [14, 15]. This magnetic anisotropy cannot be obtained for a garnet film prepared using a chemical vapor deposition (CVD) technique, because the CVD garnet film is prepared at a higher temperature. Growth-induced magnetic anisotropy includes the feature of a nonequilibrium phenomenon and cannot be obtained at such a high temperature as  $1225^\circ\text{C}$  [9]. This is a significant advantage of the LPE technique. Using the latter, a very flat surface was obtained from the perspective of the magnetic bubble application, because the required film thickness was in the order of micrometers, although  $\{111\}$  is a non-natural surface (singular surface).

Given the diminishing development of bubble memory devices, the LPE technique has been applied to magneto-optic applications since the early 1980s, corresponding to the development of fiberoptic communications of wavelength of  $1.3\text{--}1.5\ \mu\text{m}$  [16]. There were also attempts to apply the LPE growth technique to cathode luminescence devices [17]. Figure 11.2 shows a laser diode for a light source of fiberoptic communications, which is equipped with an optical isolator. Critical specifications from a material design perspective for the optical isolator application are relatively uncomplicated compared with those for bubble memory applications; namely the Faraday rotation, its temperature coefficient, saturation magnetization, uniaxial magnetic anisotropy, whose easy magnetization axis is perpendicular to the surface, optical absorption at a specific wavelength and liberation form of optical birefringence. In particular, uniaxial magnetic anisotropy is indispensable for optical isolator applications, where light impinges perpendicular to the surface (Figure 11.3). In order to reduce the production cost of isolator chips, an LPE wafer with

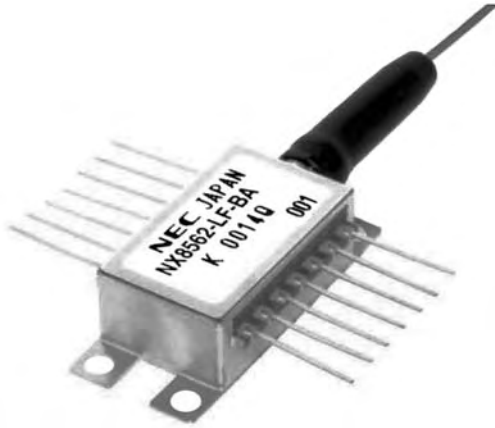


**Figure 11.2** Distributed feedback laser diode module for dense wavelength division multiplexing equipped with an optical isolator (wavelength 1.55  $\mu\text{m}$ ). Courtesy of NEC Compound Semiconductor Devices

a larger diameter is required. Currently, LPE wafers 100 mm in diameter are available (Figure 11.4).

From the perspective of crystal growth, the objective involved how to prepare LPE films more than 300  $\mu\text{m}$  thick, satisfying the aforementioned specification. In the case of {111} growth, growth-induced uniaxial magnetic anisotropy can be obtained by selecting an appropriate combination of rare-earth ions; this was an established technique and considerable knowledge has been amassed through designing bubble memory garnets. However, {111} growth results in numerous problems to be solved, when thick films, of thickness exceeding 100  $\mu\text{m}$ , are required for magneto-optic applications.

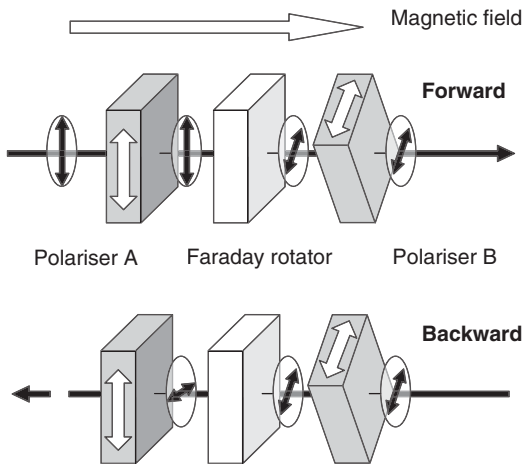


**Figure 11.3** Optical isolator using an LPE garnet chip for a Faraday rotator. Linear polarised light rotates 45°, passing through LPE garnet film. The rotation direction depends on the direction of the magnetic field

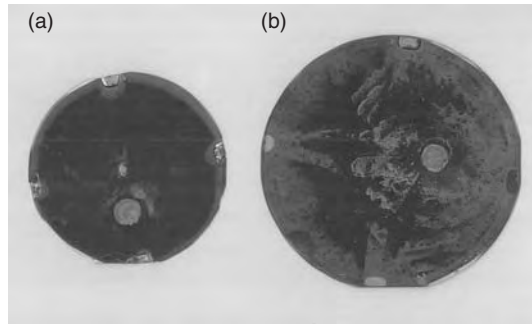


**Figure 11.4**  $(\text{YbTbBi})_3\text{Fe}_5\text{O}_{12}$  garnet LPE wafers 75 mm in diameter and  $540\ \mu\text{m}$  in thickness (a) and 100 mm in diameter and  $540\ \mu\text{m}$  in thickness (b). Stain at the surface is caused by a residue of flux melt after growth. For Bi-substituted garnet films, flux remains on the wafer surface after high speed rotating of the wafer for flux removal due to wetting. Courtesy of Sumitomo Metal Mining

The fundamentals, as well as the preparation, characterisation, and application of magnetic garnets, were comprehensively reviewed for the first time by Winkler [18]. The basic concept of crystal growth from high temperature fluxed melts is outlined by Elwell and Scheel [19]. LPE technologies are reviewed by Görnert and Sinn [20], Görnert [21] from the perspective of growth kinetics, Fratello and Wolfe [22] the magneto-optical applications, Tolksdorf and Klages [23] the growth of Bi-substituted garnets and Hibiya [24] the morphology control for thick films. In this chapter, the LPE growth of magnetic garnets is reviewed from the perspective of thermodynamics, crystal growth mechanism, material design and application.

## 11.2 LPE GROWTH

Liquid phase epitaxial garnet layers are grown on nonmagnetic garnet substrates, using a horizontal dipping technique. Figure 11.5 shows a typical dipping apparatus. This consists of a vertical three-zone furnace, a platinum crucible, a scavenging duct to extract fumes, mechanisms to handle substrate crystals and electronics for control [25]. The temperature distribution within the furnace is measured and controlled by thermocouples and a proportional integral derivative (pid) system, while fluxed melts are contained by a crucible made of platinum or a platinum alloy. Details of the chemical components of fluxed melts are explained in the next section and the temperature of the liquids range from  $800$  to  $1000\ ^\circ\text{C}$ ; with LPE garnet layers grown using  $5$ – $10\ \text{K}$  of undercooling. Nonmagnetic  $\text{Gd}_3\text{Ga}_5\text{O}_{12}$  (GGG) and substituted GGG, e.g. Ca, Zr, Mg-doped GGG wafers are used for substrate crystals and the diameter of a substrate is 75 mm. Nowadays, substrates 100 mm in diameter are used for the production of LPE garnet films for use in optical isolators. Single or multiple substrates are sustained by a jig made of platinum or platinum alloy, as shown in Figure 11.6. The GGG and substituted GGG wafers are prepared using the Czochralski method (crystal pulling) and sliced and polished (Figure 11.7). Liquid phase epitaxial garnet films grow on the substrates by dipping substrates into the slightly undercooled flux melts. By rotating substrates at a rotation speed of  $50$ – $100\ \text{rpm}$ , garnet films

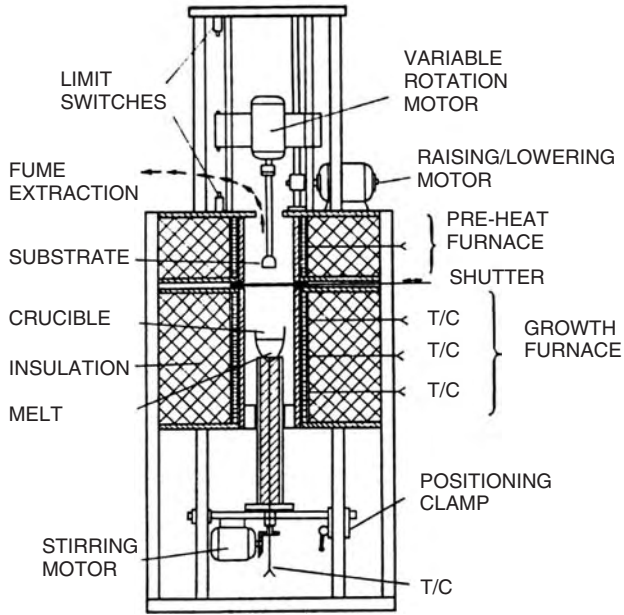


**Figure 11.5** LPE growth furnaces [25]. Reprinted from *Radio Electron. Engin.*, **45**, E.A.D. White and J.D.C. Wood, Bubble materials—composition, growth and evaluation, 711, Copyright (1975), with permission from the Institution of Engineering & Technology

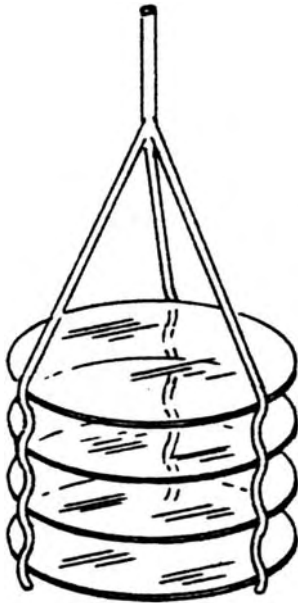


**Figure 11.6** Substrate holder [25]. Reprinted from *Radio Electron. Engin.*, **45**, E.A.D. White and J.D.C. Wood, Bubble materials—composition, growth and evaluation, 711, Copyright (1975), with permission from the Institution of Engineering & Technology

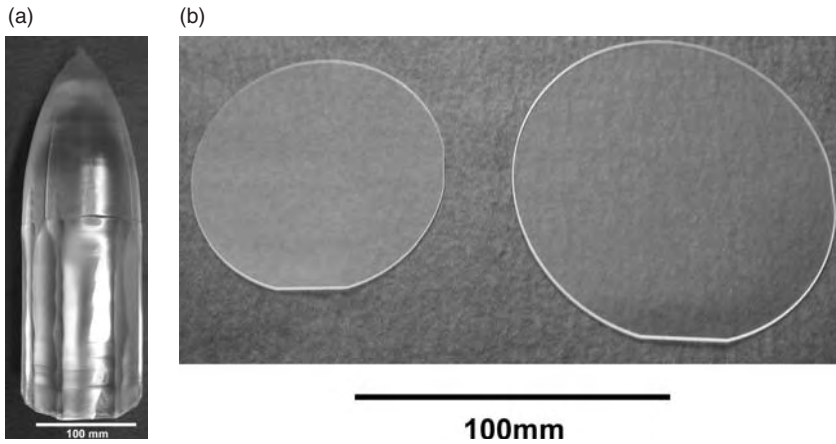


**Figure 11.7** Ca, Zr, Mg-doped  $Gd_3Ga_5O_{12}$  bulk crystals 100 mm in diameter (a) and substrate wafers 75 mm and 100 mm in diameter (b). Courtesy of Sumitomo Metal Mining

of uniform thickness are obtained. After the growth of LPE films, substrates are withdrawn from the melt and residual fluxed melts are removed by rotating the wafers at high speed. For Bi-substituted garnet films, however, the residual melt tends to adhere to the melt surface due to wetting, even after high-speed rotation [26]. The surfaces of the Bi-substituted garnet films are stained with this residual fluxed melt, as shown in Figure 11.4. Since fluxed melt contains  $PbO$  and  $Bi_2O_3$ , with relatively high vapor pressure at LPE temperature, fumes from these substances must be extracted through a scavenging duct, gathered and treated appropriately.

## 11.3 PHASE DIAGRAM AND CHEMISTRY

### 11.3.1 Phase diagram

To grow garnet single crystals or single crystalline films, knowledge of phase equilibria between the crystals and environment phases is indispensable. The phase relationship between  $Fe_2O_3$  and  $YFeO_3$  has been reported by van Hook [27];  $Y_3Fe_5O_{12}$  can be formed through a peritectic reaction between  $YFeO_3$ , which is a primary phase, and a melt, which contains more  $Fe_2O_3$  than the  $Y_3Fe_5O_{12}$  composition. Based on this phase diagram, high quality  $Y_3Fe_5O_{12}$  single crystals were grown between the peritectic ( $1555^\circ C$ ) and eutectic ( $1469^\circ C$ ) temperatures, either by a top-seeded solution growth [28] or a travelling-solvent-floating-zone method [29]. Single crystal growth of  $Y_3Fe_5O_{12}$  has been attempted for the first time from a  $PbO$  fluxed melt by Nielsen and Dearborn [30], i.e. a flux method. Through the flux growth of  $Y_3Fe_5O_{12}$  single crystals, they prepared a phase diagram for the  $PbO \cdot B_2O_3 \cdot Y_2O_3 \cdot Fe_2O_3$  system. Later, Jonker reported precise phase diagrams for the pseudo-ternary  $PbO \cdot B_2O_3 \cdot Y_2O_3 \cdot Fe_2O_3$  system, as shown in Figure 11.8 [31]. The solubility of rare earth oxides can be enhanced by a factor of about ten if mixtures of  $PbO \cdot PbF_2$  are used as solvents [32]. An improvement in quality and size was obtained by the addition of a small amount of  $B_2O_3$  in  $PbO$  [33] and in  $PbO \cdot PbF_2$  [34].  $PbF_2$  has



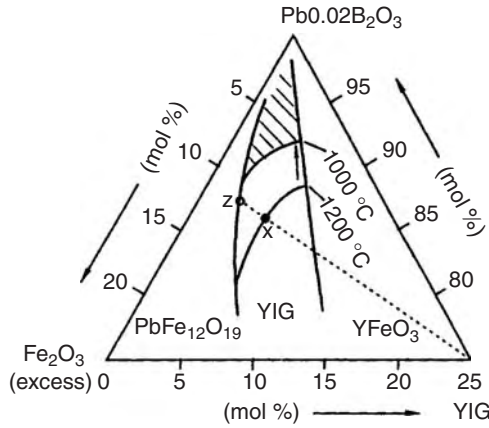


**Figure 11.8** Phase diagram for pseudo-ternary  $\text{PbO-B}_2\text{O}_3\text{-Y}_2\text{O}_3\text{-Fe}_2\text{O}_3$  system [31]. Reprinted from *J. Cryst. Growth*, **28**, H. D. Jonker, Investigation of the phase diagram of the system  $\text{PbO-B}_2\text{O}_3\text{-Fe}_2\text{O}_3\text{-Y}_2\text{O}_3$  for the growth of single crystals of  $\text{Y}_3\text{Fe}_5\text{O}_{12}$ , 231, Copyright (1975), with permission from Elsevier

significant volatility and cannot be used in open crucibles. Therefore, the current garnet films are grown using solvents of  $\text{PbO-B}_2\text{O}_3\text{-(Fe}_2\text{O}_3)$  or  $\text{PbO-Bi}_2\text{O}_3\text{-B}_2\text{O}_3\text{-(Fe}_2\text{O}_3)$  for Bi substituted magneto-optical garnets. For the LPE growth of Bi-substituted garnet cases, Bi ions play a role, both as solvent and constituent.

The systems have sometimes been described as pseudo-binary of solvent and garnet constituents for convenience, as shown in Figure 11.9 [35, 36], where abscissa shows a garnet concentration, or the parameter  $R_4$ , which represents the ratio of constituent

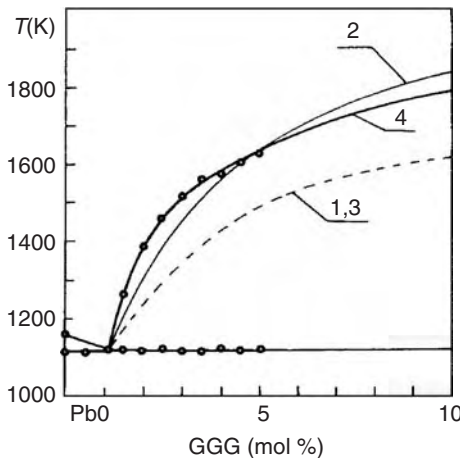


**Figure 11.9** Pseudo-binary phase diagram for the garnet-solvent system: (1) ideal solution model; (2) quasi-regular solution model; (3) bare ion model; (4) bare complex ion model [36]. Reprinted from *J. Cryst. Growth*, **89**, M. Nevriiva and K. Fischer, Modelling of equilibrium solid-liquid curves in the pseudobinary  $\text{PbO-Gd}_3\text{Ga}_5\text{O}_{12}$  system, 571, Copyright (1988), with permission from Elsevier

**Table 11.2** Parameter  $R$  describing compositions for LPE growth of garnets [35]

$$\begin{aligned}
 R_1 &= [\text{Fe}_2\text{O}_3]/\Sigma[\text{Ln}_2\text{O}_3] \\
 R_2 &= [\text{Ga}_2\text{O}_3]/([\text{Fe}_2\text{O}_3] + [\text{Ga}_2\text{O}_3]) \\
 R_2 &= [\text{GeO}_2]/([\text{FeO}_{1.5}] + [\text{GeO}_2]) \\
 R_3 &= [\text{PbO}]/[\text{B}_2\text{O}_3] \\
 R_4 &= (\Sigma[\text{Ln}_2\text{O}_3] + [\text{Fe}_2\text{O}_3] + [\text{Ga}_2\text{O}_3])/(\Sigma[\text{Ln}_2\text{O}_3] + [\text{Fe}_2\text{O}_3] + [\text{Ga}_2\text{O}_3] + [\text{PbO}] + [\text{B}_2\text{O}_3]) \\
 R_4 &= (\Sigma[\text{Ln}_2\text{O}_3] + [\text{Fe}_2\text{O}_3] + [\text{CaO}] + [\text{GeO}_2])/(\Sigma[\text{Ln}_2\text{O}_3] + [\text{Fe}_2\text{O}_3] + [\text{Ga}_2\text{O}_3] \\
 &\quad + [\text{CaO}] + [\text{GeO}_2] + [\text{PbO}] + [\text{B}_2\text{O}_3]) \\
 R_5 &= [\text{CaO}]/([\text{CaO}] + [\text{GeO}_2])
 \end{aligned}$$

concentration to total melt. Other parameters are defined as shown in Table 11.2. Melt compositions can be designed using these parameters.

Metastable behavior in the system, including garnet and perovskite phases, is sometimes confusing and troublesome. During the LPE growth of magnetic garnet ( $\text{Gd}_{0.2}\text{Y}_{2.8}\text{Fe}_5\text{O}_{12}$  Gd:YIG), thick garnet films ( $> 100 \mu\text{m}$ ), once grown on the GGG substrate, were found to be dissolved, while small crystallites of perovskite (yttrium orthoferrite:  $\text{YFeO}_3$ ) were found to be adhered to the LPE crystal films, even though thin garnet films were reproducibly grown, as shown in Figure 11.10 [37]. This suggests that the melt can be supersaturated, for both the garnet and perovskite phases, and that garnet can grow more easily than perovskite, because of the existence of a substrate; whereas for perovskite to appear, the nucleation process is required. Once the perovskite phase has appeared, the unstable garnet phase disappears (Figure 11.11).

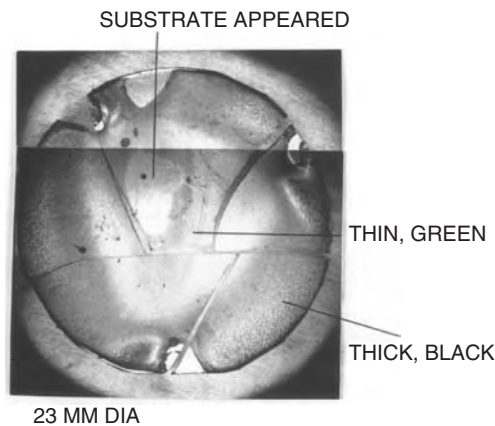


**Figure 11.10** Photograph showing dissolution of the thick garnet layer, which has once grown, and crystallites of orthoferrite appeared [37]. The amount of dissolved YIG layer thickness depends on the distance from the center of the LPE layer. At the center, the thick garnet layer was dissolved completely and the GGG substrate appeared. A thin green layer was observed near the center, whilst a thick YIG LPE layer (black) remained at the edge of the LPE crystal. Reprinted from *J. Cryst. Growth*, **64**, T. Hibiya, Growth and dissolution of liquid phase epitaxial garnet films in orthoferrite primary phase melt, 499, Copyright (1984), with permission from Elsevier

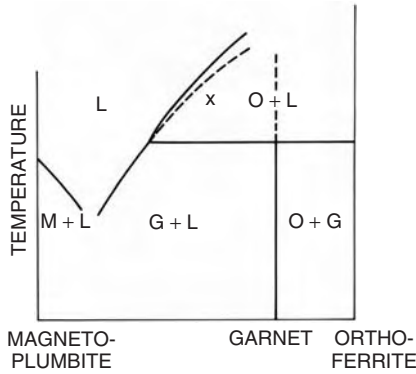
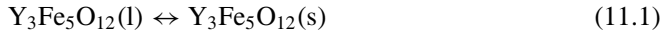


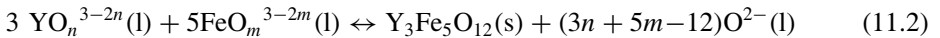
**Figure 11.11** Metastable behavior of the garnet phase. The composition denoted by x can be supersaturated, for both the garnet and orthoferrite phases [37]. Reprinted from *J. Cryst. Growth*, **64**, T. Hibiya, Growth and dissolution of liquid phase epitaxial garnet films in orthoferrite primary phase melt, 499, Copyright (1984), with permission from Elsevier

**11.3.2 Chemical thermodynamics of LPE**

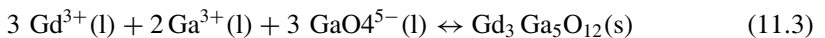
The base to understand the growth kinetics of any crystal in solution is the knowledge of the liquidus curve. Liquidus curves are mostly defined in terms of pseudo-binary systems, consisting of solvent, e.g.  $PbO-B_2O_3-(Fe_2O_3)$  and solute, e.g.  $Y_3Fe_5O_{12}$ . Therefore, the phase transition liquidus (l)–solid (s) is described in terms of a so-called single-molecule model:



where concentrations are defined in terms of a  $Y_3Fe_5O_{12}$  molecule. Physico-chemical studies of different flux melts showed, however, that the garnets decompose in cation-oxygen complexes:



where solubility products are defined in terms of such species, which were comprehensively surveyed earlier [20, 21]. In order to check these results, Nevriiva and Fischer investigated the fairly simple pseudo-binary system  $PbO-Gd_3Ga_5O_{12}$  (GGG) (Figure 11.9) [36]. GGG is congruently melting and no other phase exists in this system. The authors discussed the ideal and quasi-regular solution model according to phase transition [Equation (11.1)], where  $Y_3Fe_5O_{12}$  has to be replaced by  $Gd_3Ga_5O_{12}$ . As eight-particle systems, they considered a bare ion model, where Y in Equation (11.2) is replaced by Gd, Fe by Ga and  $n = m = 0$ , and a bare-complex model:



The complex ions  $GaO_4^{5-}(l)$  are thought to be incorporated into tetrahedral,  $Ga^{3+}(l)$  into octahedral, and  $Gd^{3+}(l)$  into dodecahedral sites. Curve 4 in Figure 11.9

reveals that model 3 [Equation (11.3)] provides the best explanation for the differential thermal analysis (DTA) results of GGG. This is in agreement with the conclusions of physico-chemical investigations with YIG, such as electrical conductivity, viscosity, electromotive force and cryoscopy [38, 39]. According to Equation (11.3), solubility products are defined for GGG as  $L_{GGG} = [\text{Gd}^{3+}]^3 [\text{Gd}^{3+}]^2 [\text{GaO}_4^{5-}]^3$  and correspondingly  $L_{YIG} = [\text{Y}^{3+}]^3 [\text{Fe}^{3+}]^2 [\text{FeO}_4^{5-}]^3$  for YIG. In fact, considerable experimental data are plotted in terms of different types of solubility products. De Gasperis and Marcelli [40] used the activities  $a[\text{YO}_n]$  and  $a[\text{FeO}_m]$  of yttrium-oxygen and iron-oxygen complexes and defined  $L_{YIG} = a[\text{YO}_n]^3 a[\text{FeO}_m]^5$  using Equation (11.2). Figure 11.12 shows the corresponding data for YIG [40] and GGG [41]. The solubility product  $L$  is written as follows:

$$\ln L = \ln L_0 - \Delta H/RT \quad \text{with} \quad \ln L_0 = \Delta S/R \quad (11.4)$$

where the heats of the solution are  $\Delta H = 301 \text{ kJ mol}^{-1}$  (YIG) and  $\Delta H = 306 \text{ kJ mol}^{-1}$  (GGG), and entropy change of solution  $\Delta S = 109 \text{ J mol}^{-1} \text{ K}^{-1}$  (YIG) and  $\Delta S = 96 \text{ J mol}^{-1} \text{ K}^{-1}$  (GGG).

Furthermore, it has been found that the concentration of free oxygen ions in oxidic flux melts play a key role in understanding both the actual species and the primary crystallisation fields [38]. A concentration cell has been developed to measure the electromotive force of low viscous melts in order to estimate the free oxygen concentration  $[\text{O}^{2-}]_{\text{rel}} = [\text{O}^{2-}]/[\text{O}^{2-}]_{\text{PbO}}$  related to PbO [42]. Figure 11.13 illustrates the change in the relative oxygen ion concentration  $[\text{O}^{2-}]_{\text{rel}}$  of PbO after the stepwise addition of  $\text{B}_2\text{O}_3$ ,  $\text{Fe}_2\text{O}_3$ ,  $\text{Y}_2\text{O}_3$  forming a flux melt for the LPE of YIG at  $920^\circ\text{C}$  [43]. Figure 11.14 shows the primary crystallisation fields of  $\text{YFeO}_3$ , YIG and  $\text{PbFe}_{12}\text{O}_{19}$  in the solvent  $(1-x)\text{PbO} \cdot x(0.5 \text{ PbF}_2 \cdot 0.5 \text{ B}_2\text{O}_3)$  with the corresponding oxygen ion concentration  $[\text{O}^{2-}]_{\text{rel}}$  for different mole fractions of solute YIG [38].

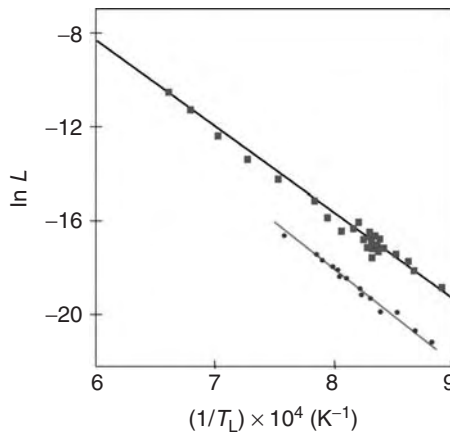


**Figure 11.12** Solubility of  $\ln L$  of YIG (●) [40] and GGG (■) [41] as a function of the reciprocal liquidus temperature  $1/T_L$  [21]. Reprinted from *Prog. Cryst. Growth Charact.*, **20**, P. Gönert, Kinetics and mechanisms of flux crystal growth, 263, Copyright (1990), with permission from Elsevier

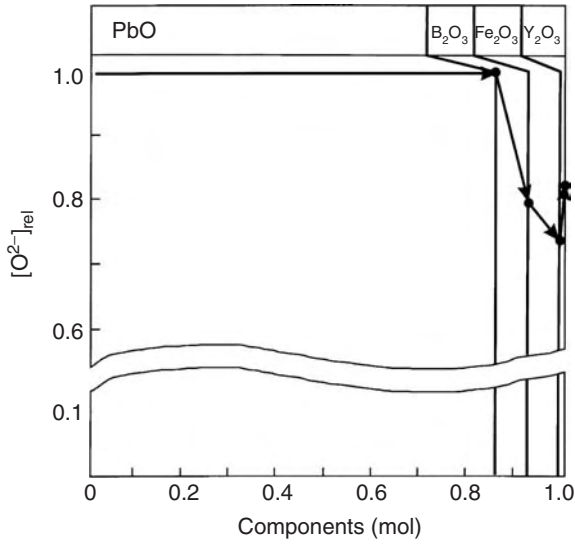


**Figure 11.13** Change of the relative ion concentration  $[O^{2-}]_{rel}$  of PbO after the stepwise addition of  $B_2O_3$ ,  $Fe_2O_3$ ,  $Y_2O_3$ , forming a flux melt for the LPE of YIG at  $920^\circ C$ . Reproduced from [43] by permission of Wiley-VCH

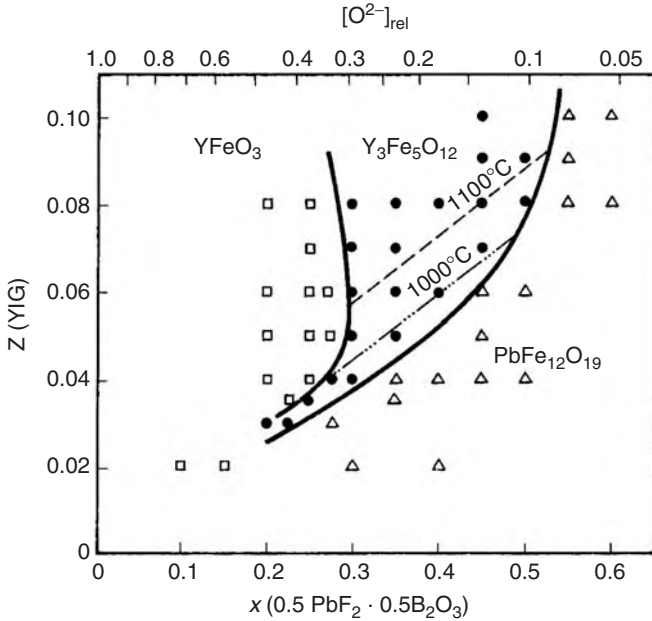


**Figure 11.14** Primary crystallisation fields of  $YFeO_3$ , YIG and  $PbFe_{12}O_{19}$  in the solvent  $(1-x)PbO \cdot x(0.5PbF_2 \cdot 0.5B_2O_3)$  with corresponding oxygen ion concentration  $[O^{2-}]_{rel}$  and different mole fractions of solute  $z(YIG)$ . Reproduced from [38] by permission of Wiley-VCH

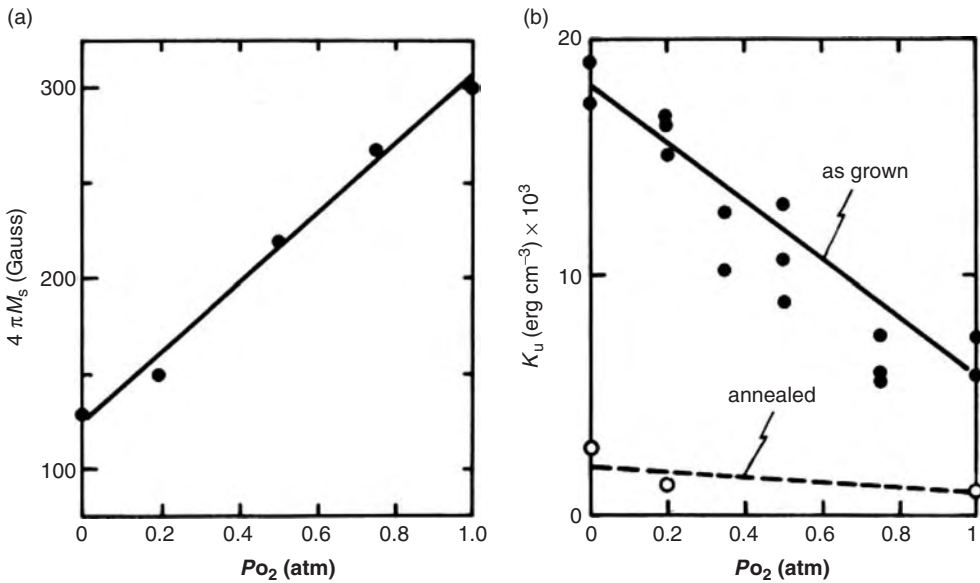


**Figure 11.15** Saturation magnetisation  $4\pi M_s$  (a) and uniaxial magnetic anisotropy energy  $K_u$  (b) as a function of the oxygen partial pressure ( $P_{O_2}$ ) of the ambient atmosphere during the LPE growth [44]. Reprinted with permission from *AIP Conf. Proc.*, No. 34, T. Hibiya, H. Makino and Y. Hidaka, Growth atmosphere effects on Ca, Ge-substituted garnet LPE film bubbles properties, 163, Copyright (1976), American Institute of Physics

### 11.3.3 Effect of oxygen partial pressure on magnetic properties

Other important oxygen-related phenomena are the effects of oxygen partial pressure on the LPE growth of garnets [44]. When  $(Y\text{SmLuCa})_3(\text{FeGe})_5\text{O}_{12}$  LPE garnet films were grown under various oxygen partial pressures, the properties of LPE films showed a marked dependence on the oxygen partial pressure of an ambient atmosphere, as shown in Figure 11.15; lattice constant, saturation magnetisation increased and Curie temperature and uniaxial magnetic anisotropy energy decreased with an increase in oxygen partial pressure. These effects are mainly attributable to the substitution of  $\text{Pt}^{4+}$  for  $\text{Fe}^{3+}$  at the 16a-site;  $\text{Pt}^{4+}$  is dissolved from a crucible wall and its amount depends on the oxygen partial pressure of the ambient LPE growth atmosphere. As for the decrease in uniaxial magnetic anisotropy energy with an increase in oxygen partial pressure, it is unclear whether or not  $\text{Pt}^{4+}$  substitution decreases anisotropy energy. The growth atmosphere effect is noticeable for Ca, Ge-substituted garnets, which contain divalent and tetravalent cations, but is not the case for garnets, which consist of only trivalent cations [45, 46].

## 11.4 GROWTH MECHANISM AND MORPHOLOGY

### 11.4.1 Mass transport and growth rate

The growth species characterised by Equations (11.1)–(11.3) are transported and incorporated into the crystal phase via bulk transport and interfacial processes. Convection

and diffusion occur in the bulk melt; surface diffusion and so-called desolvation processes at the interface [47], where desolvation stands for all chemical and steric reactions of growth species at the interface. Because of a lack of information on these sophisticated elementary processes in the bulk liquid and at the interface, explanation using Equations (11.2) or (11.3) does not function well. Instead, the single-molecule model [Equation (11.1)] is normally applied, which is a suitable approximation to describe the growth rate  $v$  from diluted solutions [48]:

$$v = \frac{\Delta H_1 c_L \Delta T}{c_s R_g T_L T_e} \left( \frac{\delta}{D} + \frac{1}{k} \right)^{-1} \quad (11.5)$$

where  $c$  represents the concentrations of garnet molecules,  $c_L$  of the bulk liquid and  $c_s$  of the solid state,  $\Delta H_1$  is the solution enthalpy, which is about  $100 \text{ kJ mol}^{-1}$  in terms of the single-molecule model [49],  $\Delta T = T_L - T_e$  is the undercooling, defined as the difference between the liquidus temperature  $T_L$  and the equilibrium temperature  $T_e$ ,  $R_g$  is the gas constant,  $\delta$  the thickness of the so-called diffusion boundary layer,  $D$  the diffusion coefficient and  $k$  the kinetic coefficient of garnet species. Since LPE growth is generally carried out by the dipping of horizontally rotating substrates, we may use the thickness  $\delta$ :

$$\delta = 1.6 D^{1/3} \nu^{1/6} \omega^{-1/2} \quad (11.6)$$

of the diffusion boundary layer [50] of a rotating disk; with  $\nu$  kinematic viscosity,  $\omega (\text{rad s}^{-1}) = 2\pi r/60$  (rotations  $\text{min}^{-1}$ ) angular frequency and  $r$  rotation rate. A typical value is  $\delta = 100 \mu\text{m}$  for  $r = 100 \text{ rpm}$ . According to mass conservation, the kinetic coefficient  $k$  is defined as:

$$D \left. \frac{\partial c}{\partial z} \right|_{z=0} = k(c_i - c_e) \quad (11.7)$$

with the interfacial concentration gradient  $(\partial c/\partial z)_{z=0}$  and the interfacial supersaturation  $(c_i - c_e)$ , where  $c_i$  stands for the interfacial concentration.

To characterise the growth rate  $v$  as a function of the integral undercooling  $\Delta T = T_L - T_e$ , which can be larger than  $100 \text{ K}$  for some hours without spontaneous nucleation, we have to distinguish principally between atomically rough and atomically smooth faces, expressed phenomenologically by different kinetic coefficients  $k$  in Equation (11.5). A representative example of the dependence of growth rate  $v$  of YIG films on atomically rough  $\{111\}$   $\text{Gd}_3\text{Ga}_5\text{O}_{12}$  (GGG) faces on the growth temperature  $T_e$  is shown in Figure 11.16, where the corresponding compositions are given in Table 11.3 [20]. Figure 11.16 presents the well known linear relation between the growth rate and undercooling near the thermodynamic equilibrium. The saturation-like behavior of the growth rate in Figure 11.16 (curves 1 and 2) can be explained in terms of viscosity increase and changes in some other parameters at lower temperatures, which has been comprehensively discussed by Sure [51]. Increasing the content of  $\text{B}_2\text{O}_3$  and decreasing that of  $\text{Y}_2\text{O}_3$  reduces the liquidus temperature  $T_L$ , which is defined in the limit  $v \rightarrow 0$ . Obviously the negative slope of growth rate against temperature  $(dv/dT_e)_{v \rightarrow 0}$  increases with increasing  $\text{Y}_2\text{O}_3$  content and liquidus temperature  $T_L$ . The same conclusions are valid for the Bi containing flux melts, although the growth temperatures are quite different.

**Table 11.3** Composition of flux melts 1–6 for the growth of  $Y_3Fe_5O_{12}$  films [21]

Flux melt no.	Mass ratio			
	$R_1$		$R_3$	$R_4$
1	20.1		6.5	0.130
2	20.2	18.3	20.1	11.3
3	16.8	18.3		8.5
4				11.3
5			6.5	0.172
6			11.7	0.165

Definition of parameter  $R$  is the same as that in Table 11.2. Reprinted from *Prog. Crystal Growth Charact.*, **20**, P. Görnert, Kinetics and mechanisms of flux, 263, Copyright (1990), with permission from Elsevier

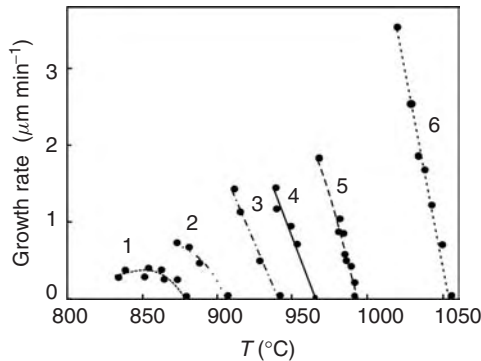


**Figure 11.16** Growth rate of YIG films on atomically rough {111} GGG substrates as a function of the temperature of flux melts 1–6, defined in Table 11.3. Rotation rate  $r = 100$  rpm [21]. Reprinted from *Prog. Cryst. Growth Charact.*, **20**, P. Görnert, Kinetics and mechanisms of flux crystal growth, 263, Copyright (1990), with permission from Elsevier

For practical applications, the LPE on atomically rough faces—such as {111} and to some degree {100}—is preferred because of the excellent homogeneity of the film thickness obtained using horizontally rotating substrates. The growth rate on atomically smooth (or singular) garnet faces, such as {110} and {211}, is primarily lower, depends nonlinearly on the undercooling, and is strongly dependent on the crystallographic orientation—at least at low undercooling as illustrated in Figure 11.17(a) [48]. It should be stressed that the growth rate on crystallographically perfect singular faces, such as {110} or {112}, is extremely low under small undercooled conditions, as shown in Figure 11.17(b). At the higher undercooled conditions, such as over 20 K, however, the growth rate  $v$  of the {110} and {112} face becomes larger due to two-dimensional nucleation, which is termed kinetic roughening. In addition, growth hillocks due to spiral growth can appear,



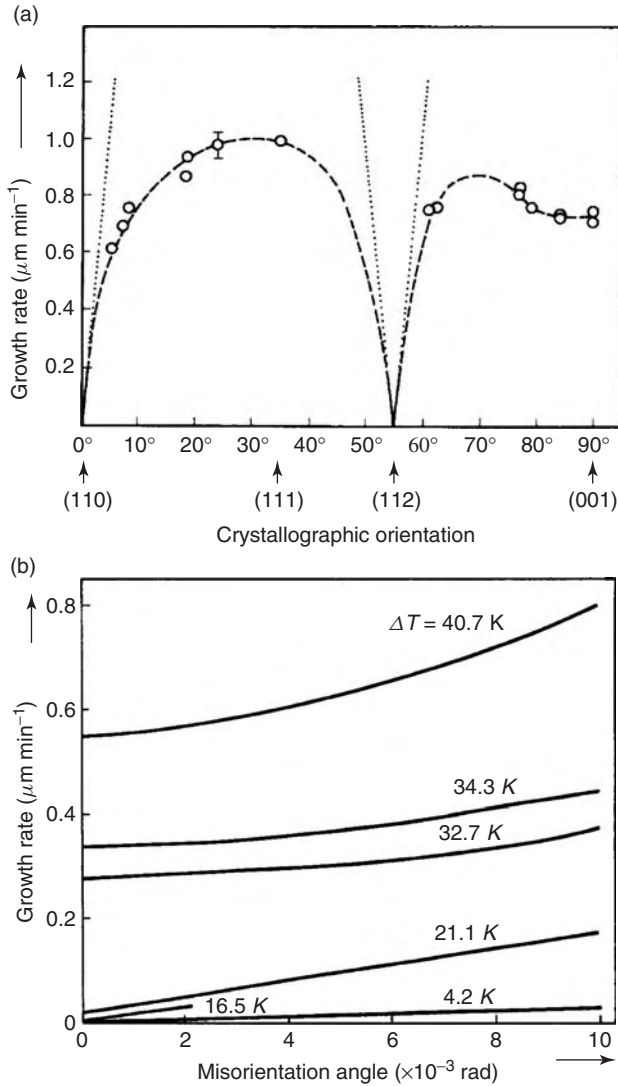


**Figure 11.17** (a) Dependence of growth rate on crystallographic direction for  $(\text{YSm})_3(\text{FeGa})_5\text{O}_{12}$  film [48]. Reprinted from *J. Cryst. Growth*, **52**, P. Görnert, Bulk transport and interfacial growth processes of garnets, 88, Copyright (1981), with permission from Elsevier. (b) Growth rate of  $(\text{YSm})_3(\text{FeGa})_5\text{O}_{12}$  films versus misorientation angle with regard to  $\langle 110 \rangle$  for different undercoolings  $\Delta T$  [49]. Reprinted from *Current Topics in Materials Science*, **11**, P. Görnert and F. Voigt, Ch. 1, Copyright (1984), with permission from Elsevier

as shown in Figure 11.18 [52]. The vicinal faces near the singular orientations consist of terraces, which are more or less separated, and the growth occurs via a step mechanism. Here the growth rate is described by the simple geometric relation  $v = v_{\text{st}} \sin \alpha$ , where  $v_{\text{st}}$  is the step velocity and  $\alpha$  the vicinal angle. Therefore, the film thickness is prone to in praxis inhomogeneities. Through careful analysis of the surface processes under low

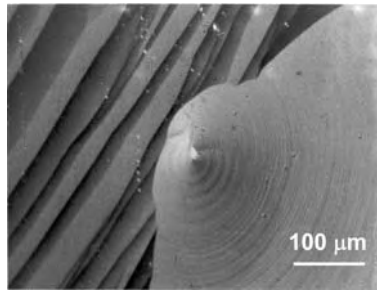


**Figure 11.18** Hillocks and macrosteps observed for a thick {110}  $\text{Gd}_{2.71}\text{Bi}_{0.29}\text{Fe}_5\text{O}_{12}$  film [52]. Reprinted from *NEC Res. Dev.*, No. 80, T. Hibiya, T. Ishikawa, Y. Morishige, J. Nakashima and Y. Ohta, 1, Copyright (1986), with permission from NEC

undercooled conditions, the kinetic coefficients of faces  $k$  and steps  $k_{\text{st}}$ , as well as the anisotropy of the step motion of vicinal faces, have been clarified [49]. Typical values of  $k_{\text{st}}$  for garnets are in the order of  $10^{-2} \text{ cm s}^{-1}$ .

#### 11.4.2 Control of morphology

Magneto-optic applications for optical isolators require homogeneous, thick LPE garnet films ( $> 300 \mu\text{m}$ ), while a thickness of a few micrometers is sufficient for magneto-optic sensors or bubble memory devices. A ‘mirror’ surface, which assures smooth magnetic domain motion, can be obtained for thin films that are only a few micrometers thick, regardless of growth orientation. In the early stage of development of {111} thick garnet films, a degradation in crystal quality, such as flux inclusion, was found, when a ‘swirl’ pattern appeared at the crystal surface (Figure 11.19) [52]. This is due to morphological change with increasing film thickness. Evolution of surface morphology of {111} thick films was found with increasing film thickness, as shown in Figure 11.20(a)–(c): ‘mirror’ to ‘striation’ and ‘swirl’. The above observed morphological evolution is described as follows. Even for films a few micrometers thick, the LPE film surface shows irregularity, which reflects the growth striation of the GGG substrates and this can be detected

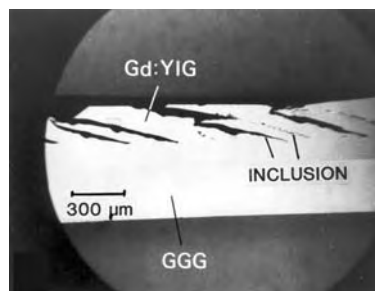


**Figure 11.19** Cross-section of thick {111} film that shows ‘swirl’ pattern morphology. Flux inclusion takes place as a result of the appearance of the ‘swirl’ pattern [53]. Reprinted from *J. Cryst. Growth*, **62**, T. Hibiya, Surface morphologies and quality of thick liquid phase epitaxial garnet films for magneto-optic devices, 87, Copyright (1983), with permission from Elsevier

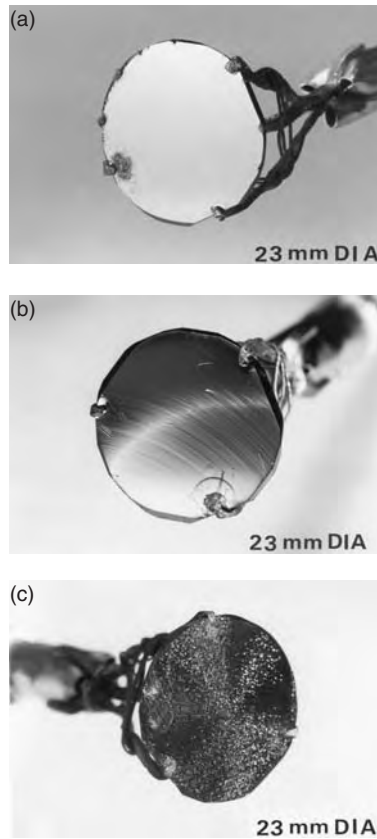


**Figure 11.20** Morphologies of thick {111} LPE garnet films: (a) ‘mirror’; (b) ‘striation’; and (c) ‘swirl’. For ‘striation’, the growth striation of the GGG substrate cut from 75 mm diameter wafer was taken over to 23 mm diameter LPE films. ‘Swirl’ shows {110} and {211} facets [53]. Reprinted from *J. Cryst. Growth*, **62**, T. Hibiya, Surface morphologies and quality of thick liquid phase epitaxial garnet films for magneto-optic devices, 87, Copyright (1983), with permission from Elsevier

when the LPE film surface is observed using a Nomarski interference microscope. The irregularity is due to the fact that {111} is not a natural face and that strain along the growth striation of the GGG substrate modifies the growth rate. The height of irregularity increases with increasing film thickness (Figure 11.20). Irregularity can be recognised at a glance as ‘striation’, when the height of irregularity becomes 0.1–1.0  $\mu\text{m}$ . This irregularity interferes with the melt flow along the LPE film surface and causes extraordinary growth downstream of the flow, due to the hydrodynamic effect, and results in the formation of an eave, which consists of {110} and {211} facets, as shown in Figure 11.19. The surface morphology pattern depends not only on the film thickness but also on the growth temperature. An increase in  $\text{B}_2\text{O}_3$  concentration caused the surface morphology to become mild [54]. LPE films over 300  $\mu\text{m}$  thick can be obtained without the appearance of {110} and {211} facets, i.e. no flux inclusion. This suggests that an increase in  $\text{B}_2\text{O}_3$  concentration prohibits the growth mechanism change, from a continuous one at the rough

surface to lateral growth at the singular surface. Growth kinetics for thick garnet layers were discussed, i.e. effective diffusion constant and kinetic coefficient, as were transport resistance and interfacial resistance [55].

## 11.5 BI-SUBSTITUTED GARNET FILMS

For the magneto-optic application of LPE garnet films, garnets with high Faraday rotation are required. Since Bi-substitution was found to enhance the Faraday rotation for  $\text{Bi}_{3-2x}\text{Ca}_{2x}\text{Fe}_{5-x}\text{V}_x\text{O}_{12}$  garnets [56], the effect of Bi-substitution on the Faraday rotation was investigated for rare-earth iron garnet and its epitaxial film [57–59]. Bi-substituted rare earth ion garnets are promising materials for magneto-optical devices. The Bi ion contributes, not only to enhance the Faraday rotation but also to increase growth-induced magnetic anisotropy. The magnetic and magneto-optical properties of Bi-substituted garnets have been studied intensively by the Philips group [60], Fratello (USA) group [61] and Japanese group [6]. Hansen and Krumme reviewed precisely [60]. Since there is a limit to the  $\text{Bi}^{3+}$  substitution level for rare earth ions in the 24c sites, depending on the radius of rare-earth ions [62], optimisation of the garnet compositions, melt compositions and LPE process is indispensable. Figure 11.21 shows that the Bi content of  $(\text{YBi})_3(\text{FeGaAl})_5\text{O}_{12}$  films increases with increasing undercooling and also with decreasing liquidus temperature [5]. Klages and Tolksdorf [63], Chani and Balbashov [64] and Fratello *et al.* [65] have systematically investigated how to control the  $\text{Bi}^{3+}$  substitution level. Even though there is a limit to the amount of Bi-substitution under thermal equilibrium conditions, up to 2.2 excess  $\text{Bi}^{3+}$  can enter the 24c site per garnet formula unit [66] when an LPE technique is employed due to the metastable behavior of LPE

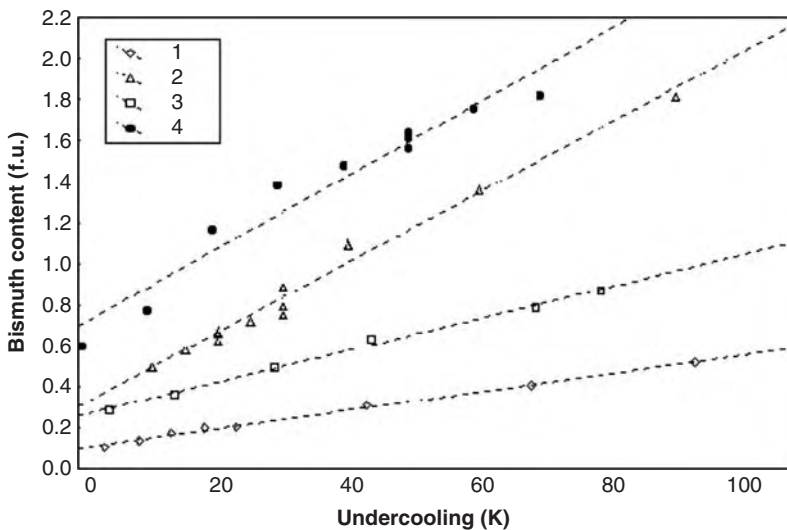


**Figure 11.21** Bismuth content of garnet layers as a function of the undercooling of the fluxed melt for the LPE growth of  $(\text{YBi})_3(\text{FeGa})_5\text{O}_{12}$  (nos 1, 2 and 4) and  $(\text{YBi})_3(\text{FeAlGa})_5\text{O}_{12}$  (no. 3) with various liquidus temperatures. Liquidus temperatures are 904, 791, 845 and 751°C, respectively, for melts 1–4 [5]. Reproduced from [5] by permission of Wiley-VCH

growth. Since Bi-substituted garnets are prepared on nonmagnetic garnet substrate crystals, thermal expansion mismatch, as well as the lattice mismatch between LPE layers and substrates, should be taken into account, to avoid the formation of cracks in LPE layers, due to thermal stress during the cooling process from growth to room temperature. This is due to the relatively large thermal expansion coefficient of Bi-substituted garnets compared with conventional garnets. Avoiding crack formation is a very important argument from the perspective of production of LPE garnet layers for commercial use, as reported by Fratello *et al.* [67, 68].

In order to apply a Bi-substituted garnet layer for an optical isolator for use in fiberoptic communications, particularly for common carriers at a 1.3  $\mu\text{m}$  wavelength, a 300  $\mu\text{m}$  thick Bi-substituted gadolinium iron garnet LPE film is proposed [6]. The characteristics of this film are summarised in Tables 11.4 and 11.5. Table 11.4 shows that the Faraday rotation of  $-1530 \text{ deg cm}^{-1}$  assures an optical isolator, of thickness 300  $\mu\text{m}$ . As shown in Table 11.5 and Figure 11.22, since an easy magnetization axis is along the  $\langle 111 \rangle$ , i.e. normal to the LPE surface; the external field for saturation is as small as 16  $\text{kA m}^{-1}$ .

**Table 11.4** Magneto-optical properties of the 300  $\mu\text{m}$  thick LPE  $(\text{GdBi})_3(\text{FeAlGa})_5\text{O}_{12}$  film [6]

Wavelength ( $\mu\text{m}$ )	1.3	0.8
Faraday rotation ( $\text{deg cm}^{-1}$ )	-1530	-7500
Optical absorption ( $\text{cm}^{-1}$ )	1.3	75
Figure of merit ( $\text{deg dB}^{-1}$ )	270	23
Extinction ratio (dB)	37	37

Reprinted from *IEEE Trans. Magn.*, **MAG-22**, T. Hibiya, T. Ishikawa and Y. Ohta, Growth and characterization of 300- $\mu\text{m}$  thick bi-substituted gadolinium iron garnet films for an optical isolator, 11, Copyright (1986), IEEE

**Table 11.5** Magnetic properties of  $\{111\}$   $(\text{GdBi})_3(\text{FeAlGa})_5\text{O}_{12}$  film [6]

Saturation magnetisation, $4\pi M_s$ (mT)	22.8
Uniaxial anisotropy energy, $K_u$ ( $\text{J m}^{-3}$ )	928
Uniaxial anisotropy field, $H_K$ ( $\text{kA m}^{-1}$ )	81.3
Field for saturation, $H_s$ ( $\text{kA m}^{-1}$ )	$\sim 16$

Reprinted from *IEEE Trans. Magn.*, **MAG-22**, T. Hibiya, T. Ishikawa and Y. Ohta, Growth and characterization of 300- $\mu\text{m}$  thick bi-substituted gadolinium iron garnet films for an optical isolator, 11, Copyright (1986), IEEE

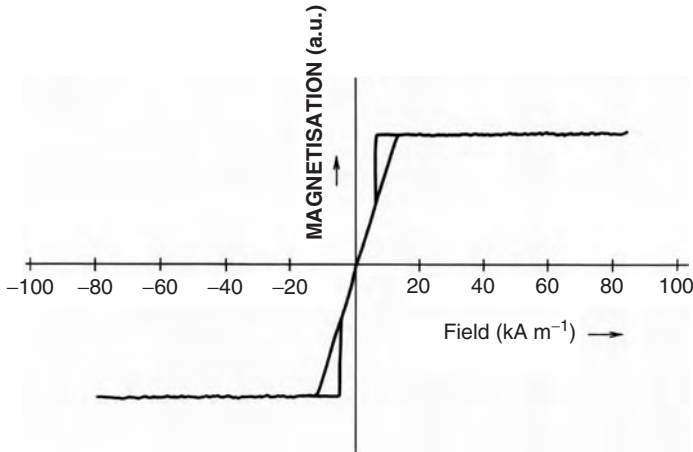


**Figure 11.22** Magnetisation–magnetic field loop for thick LPE  $(\text{GdBi})_3(\text{FeAlGa})_5\text{O}_{12}$  film. An external field is applied normally to the surface [6]. Reprinted from *IEEE Trans. Magn.*, **MAG-22**, T. Hibiya, T. Ishikawa and Y. Ohta, Growth and characterization of 300-mm thick bi-substituted gadolinium iron garnet films for an optical isolator, 11, Copyright (1986), IEEE

## 11.6 PROPERTIES OF MAGNETIC GARNET FILMS

The properties of garnet films are optimised with respect to each specific application. Therefore, the material design is a compromise of many different properties. Some important properties of magneto-optical application are discussed in this section, i.e. the misfit strain between film and substrate, Faraday rotation and optical absorption.

### 11.6.1 Misfit strain

A garnet layer is strained, due to a misfit of both the lattice constant and the thermal expansion coefficient between the LPE film and the substrate; which is described as follows [69]:

$$\varepsilon_x = (1 - \eta)(a_s - a_f)/a_f + \eta \cdot \Delta\alpha \cdot \Delta T \quad (11.8)$$

Here,  $a_s$  and  $a_f$  are the lattice constants of substrate and film under strain-free conditions.  $\varepsilon_x$  is the strain in the LPE film parallel to the surface,  $\Delta\alpha$  and  $\Delta T$  are the difference in thermal expansion coefficient between the film and substrate and the temperature difference between the growth and room temperatures, respectively.  $\eta$  is the partial relief of misfit strain at the LPE growth temperature;  $\eta = 0$  means that the strain parallel to the film at growth temperature is caused by elastic deformation, whereas  $\eta = 1$  means that the LPE film shows no more elastic strain but releases strain by introducing misfit dislocation. A garnet structure is featured with difficulty of dislocation formation. Thus, garnet crystals can be deformed elastically to a certain limit, beyond which they

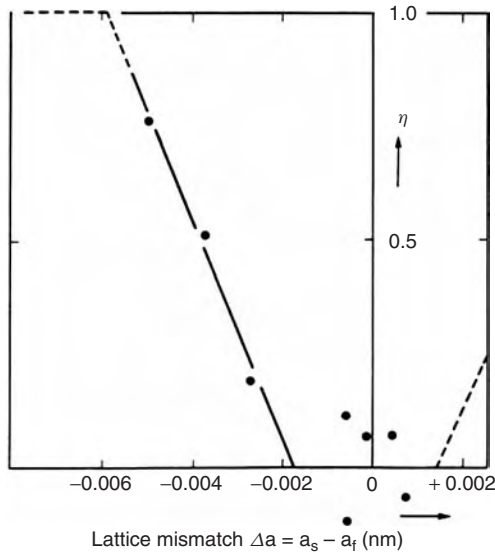


**Figure 11.23** Partial strain relief observed for  $(YEu)_3(FeGa)_5O_{12}$  films at the LPE growth temperature [70]. Reprinted from *NEC Res. Dev.*, No. 34, H. Makino, T. Hibiya and K. Matsumi, Misfit strain in LPE (Y, Eu) $_3$ (FeGa) $_5$ O $_{12}$  garnet films, 51, Copyright (1974), with permission from NEC

start to release strain. For an LPE garnet used in magneto-optical application, the misfit strain of the LPE films must be discussed, not only from the perspective of optical and magnetic properties, but also from that of mechanical properties, i.e. morphological instability caused by dislocation formation, crack formation, birefringence and stress-induced magnetic anisotropy.

An X-ray double crystal diffractometer is useful to investigate the very small lattice constant difference between LPE films and a substrate. Figure 11.23 shows partial strain relief  $\eta$  at the LPE growth temperature [70]. In the region of lattice constant difference at room temperature  $-0.017 \text{ nm} < \Delta a < 0.015 \text{ nm}$ , where  $\Delta a$  is defined as  $a_s - a_f$ , strain relief did not take place. However, outside this region, strain relief was evident. Since strain relief is caused by a dislocation formation and its climb to the epitaxial layer surface, etch pits can be observed by etching, using phosphoric acid. Under such conditions, the surface of the LPE film is no more mirror-like but shows surface irregularity, because dislocation enhances local growth. At the first stage, the surface was wavy and then  $\{110\}$  surface appeared, when the slope of the surface of a wavy structure reaches the same angle as that between  $\{111\}$  and  $\{110\}$ , as shown in Figure 11.24 [5]. In the region of  $\Delta a < 0.0005 \text{ nm}$ , a crack was formed, even though strain relief did not take place at the growth temperature; due to the significant tensile strain. In order to avoid the aforementioned misfit problems for Bi-substituted garnet LPE films, the use of lattice matched Ca, Mg, Zr-substituted  $\{111\}$  GGG (GGCMZ) substrates is recommended [71]. Homogeneous GGCMZ substrates can be prepared with lattice constants  $1.2382 \text{ nm} < a_s < 1.2511 \text{ nm}$ . For LPE garnet films more than  $300 \mu\text{m}$  in thickness and  $100 \text{ mm}$  in diameter, cracking due to misfit and thermal stresses is a serious problem; and causes the production yield of isolator chips to deteriorate. In order to avoid this problem, the lattice constant along the thickness changes [72].

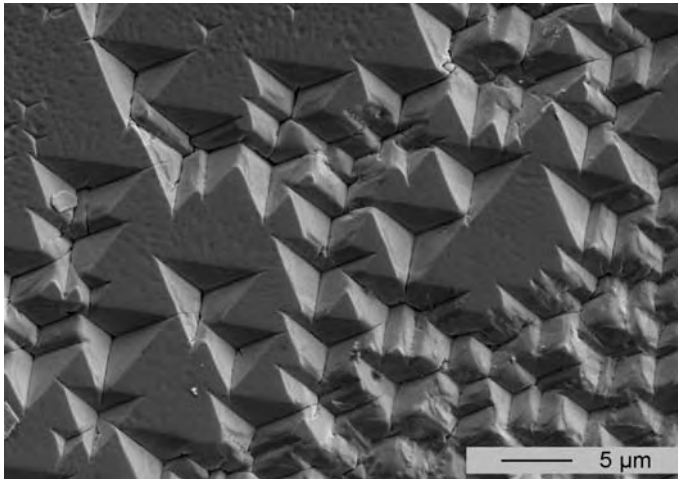


**Figure 11.24** {110} faces on a (111) surface as a result of morphologically unstable growth, due to the formation of misfit dislocation. Reproduced from [5] by permission of Wiley-VCH

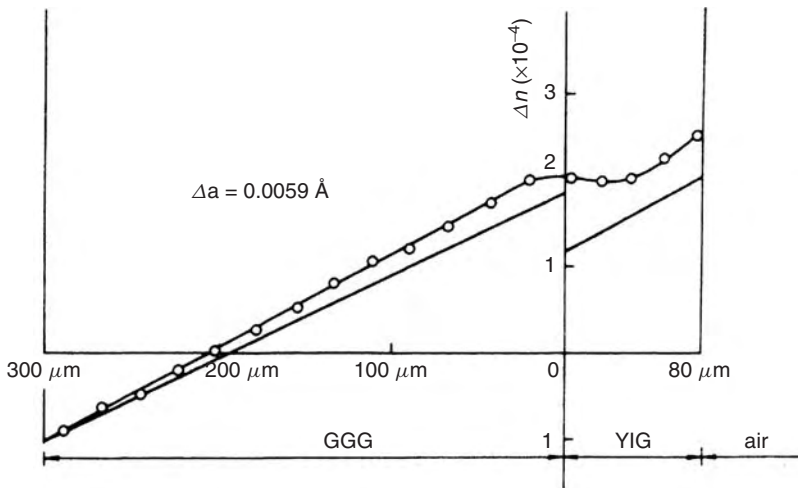


**Figure 11.25** Distribution of stress birefringence through 80  $\mu\text{m}$  thick  $(\text{Ygd})_3\text{Fe}_5\text{O}_{12}$  film and 300  $\mu\text{m}$  thick GGG substrate. Open circles show the measured values, whereas solid lines show the calculated values [16]. Reprinted from *IEEE Lightwave Technol.*, **LT-1**, T. Aoyama, T. Hibiya and Y. Ohta, A new Faraday rotator using a thick Gd:YIG film grown by liquid phase epitaxy and its application to an optical isolator and optical switch, 280, Copyright (1983), IEEE

Misfit strain also causes stress birefringence within a garnet crystal, although garnets belong to a cubic system (isotropic). Even a minute amount of misfit strain renders garnet optically anisotropic, i.e. stress birefringence caused by a photoelastic effect. Figure 11.25 shows the distribution of stress birefringence through 80  $\mu\text{m}$  thick  $\text{Y}_3\text{Fe}_5\text{O}_{12}$  film and 300  $\mu\text{m}$  thick GGG substrate, where a laser beam with a wavelength of 1.3  $\mu\text{m}$  impinges from the edge of a thick film parallel to the film surface [16]. Open circles show the



measured values using Vabinet's optical compensator, whereas the solid line shows the calculated values. It should be noted that, if an LPE layer is suffering from misfit strain, isolation deteriorated due to the existence of the stress birefringence for an optical isolator, where a light beam impinges parallel to the surface.

### 11.6.2 Faraday rotation

Faraday rotation  $\theta_F(\omega)$  originates from an imaginary part of the nondiagonal component of the dielectric tensor  $\varepsilon''_{xy}$ , which depends on magnetization  $M$ , as follows [73]:

$$\theta_F(\omega) = -(\omega/2c) \cdot (\varepsilon''_{xy}/n) \quad (11.9)$$

Here  $\omega$  and  $c$  are the angular frequency and velocity of the light in vacuum, respectively.  $n$  is the refractive index. On the other hand, the Faraday rotation per film thickness has been described, conventionally and phenomenologically, by Crossley and Cooper [74] as follows:

$$\begin{aligned} \theta_F(\omega) = & \frac{2\pi n}{c} [\underbrace{\gamma_{\text{Fe}}(M_{\text{Fe}}^{\text{tetrah.}} - M_{\text{Fe}}^{\text{octah.}})}_{\text{gyromagnetic}} - \underbrace{\gamma_{\text{RE}} M_{\text{RE}}}_{\text{gyroelectric}}] \\ & + B(\omega)M_{\text{Fe}}^{\text{tetrah.}} - A(\omega)M_{\text{Fe}}^{\text{octah.}} - C(\omega)M_{\text{RE}} \end{aligned} \quad (11.10)$$

where the gyromagnetic part may be neglected in the visible range.  $\gamma$  is the gyromagnetic ratio of Fe and RE (rare-earth) ions;  $M$  represents the sublattice magnetisations of tetrahedral, octahedral and dodecahedral (RE) sites, while  $B$ ,  $A$  and  $C$  correspond superficially to the Verdet coefficients for paramagnetic materials; noting that the concept of the Verdet coefficient is valid only for paramagnetic materials. Faraday rotation in  $\text{Y}_3\text{Fe}_5\text{O}_{12}$  is mainly determined by the spin-orbit coupling coefficient of the 3d electron  $\zeta_{3d}$ , which is much larger than that of the 2p electron  $\zeta_{2p}$ . On the other hand, Faraday rotation in  $\text{Bi}^{3+}$  substituted  $\text{Y}_3\text{Fe}_5\text{O}_{12}$  is determined by  $\zeta_{2p}$ , which is increased from the original  $\zeta_{2p}$  by the hybridization of 6p bismuth orbitals. Thus, for  $\text{Bi}^{3+}$  substituted  $\text{Y}_3\text{Fe}_5\text{O}_{12}$ ,  $\zeta_{2p}$  is modified as  $\zeta_{*2p} \sim \zeta_{2p} + \gamma^2\zeta_{6p}$ , where  $\gamma$  is the covalency factor and  $\zeta_{6p}$ , is the spin-orbit coupling coefficient of 6p electrons in bismuth ( $\zeta_{6p} = 17000 \text{ cm}^{-1}$ ).

Figure 11.26 shows an example of enhancement of the Faraday rotation by substituting for rare earth ions by  $\text{Bi}^{3+}$  [75]. From the perspective of the application of garnet films to an optical isolator, the temperature coefficient is critical to keep high isolation in the wide temperature range. In order to satisfy this requirement, a mixture of Bi-substituted garnets, whose temperature coefficient shows opposite signs, is employed. As shown in Figure 11.27, the use of Tb or Dy is effective to realise an optical isolator whose isolation is almost temperature independent [76].

### 11.6.3 Optical absorption

For the magneto-optical application of LPE garnet films, optical absorption must be minimised, because a high figure of merit, i.e. the ratio of the Faraday rotation to absorption coefficient ( $\text{deg dB}^{-1}$ ), is required. Although garnets are transparent at wavelengths

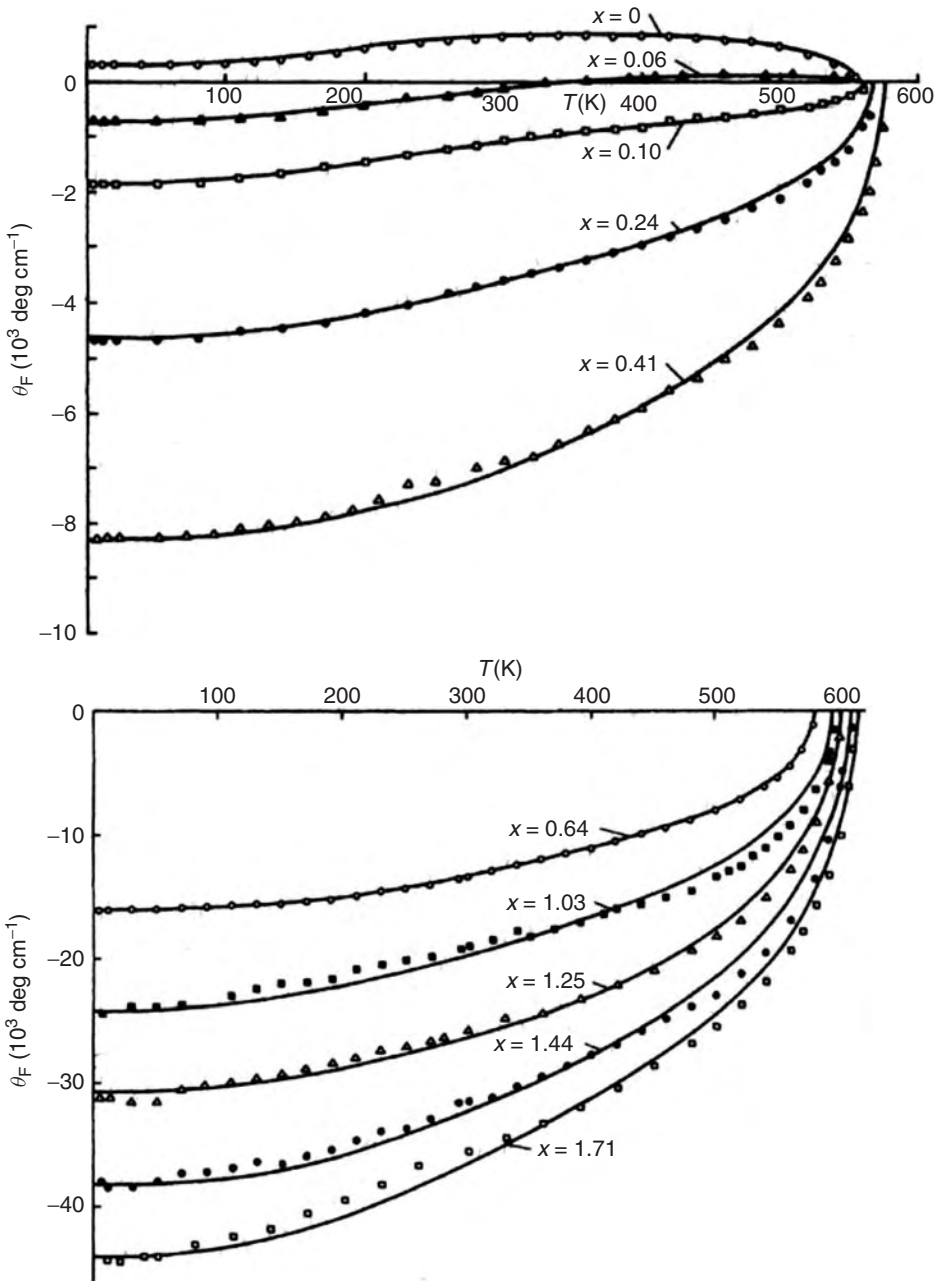


**Figure 11.26** Faraday rotation of  $\text{Y}_{3-x}\text{Bi}_x\text{Fe}_5\text{O}_{12}$  LPE films at a wavelength of 633 nm as a function of temperature. Plots are experimental data and the solid lines show calculations after the Crossley equation [75]. Reprinted Figure 11 with permission from *Phys. Rev. B*, 27, P. Hansen, K. Witter and W. Tolksdorf, Magnetic and magneto-optic properties of lead- and bismuth-substituted yttrium iron garnet films, 6608. Copyright (1983) by the American Physical Society

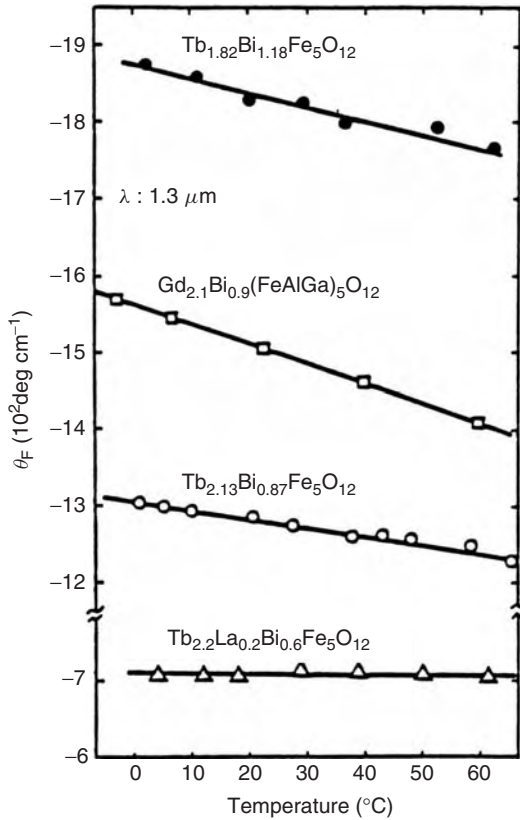


**Figure 11.27** Temperature dependence of Faraday rotation at a wavelength of  $1.3 \mu\text{m}$  for  $\text{Tb}_{1.82}\text{Bi}_{1.18}\text{Fe}_5\text{O}_{12}$ ,  $\text{Gd}_{2.1}\text{Bi}_{0.9}(\text{FeAlGa})_5\text{O}_{12}$ ,  $\text{Tb}_{2.13}\text{Bi}_{0.87}\text{Fe}_5\text{O}_{12}$  and  $\text{Tb}_{2.2}\text{La}_{0.2}\text{Bi}_{0.6}\text{Fe}_5\text{O}_{12}$  films [76]. Reprinted from *J. Mag. Soc. Jpn.*, **11**, Y. Honda, T. Ishikawa and T. Hibiya, Temperature dependence of Faraday rotation for bi-substituted Tb iron garnet films, 361, Copyright (1987), with permission from The Magnetics Society of Japan

of over  $1.1 \mu\text{m}$ , a tail of absorption near  $0.9 \mu\text{m}$  affects that over  $1.1 \mu\text{m}$ , as shown in Figure 11.28 [77]. Specific absorptions also exist, depending on rare earth species (Figure 11.29) [77]. Gd, Yb, Dy, Tb and Y are potential candidates for hosting rare earth ions from the perspective of material design. Besides these intrinsic absorptions, the fluctuation in the valence of  $\text{Fe}^{3+}$  to  $\text{Fe}^{2+}$  or  $\text{Fe}^{4+}$  causes additional absorption [22], which is due to an LPE process and controllable by optimising melt compositions and LPE growth conditions. Figure 11.30 shows the optical absorption of LPE Gd:YIG films at a wavelength of  $1.3 \mu\text{m}$  as a function of growth temperature, where  $T_L$  denotes the liquidus temperature of the melts [78]. This suggests that optical absorption depends on the degree of supercooling of the melt and that the minimum optical absorption of the LPE garnet films, i.e. absorption extrapolated to the liquidus temperature (the equilibrium condition), depends on the melt compositions. Figure 11.30 also suggests that there exists a window of the liquidus temperature of the melts, from which LPE garnet films with low optical absorption can be obtained ranging from  $900$  to  $1000^\circ\text{C}$ . As shown in Figure 11.31, the reason for the increase in optical absorption is the incorporation of impurity ions,

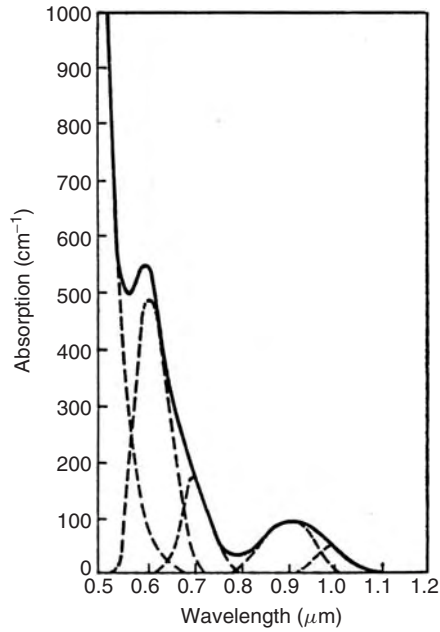


**Figure 11.28** Absorption spectrum for  $Y_3Fe_5O_{12}$  [77]. Reprinted with permission from *J. Appl. Phys.*, **38**, D. L. Wood and J. P. Remeika, Effect of impurities on the optical properties of yttrium iron garnet, 1038, Copyright (1967), American Institute of Physics

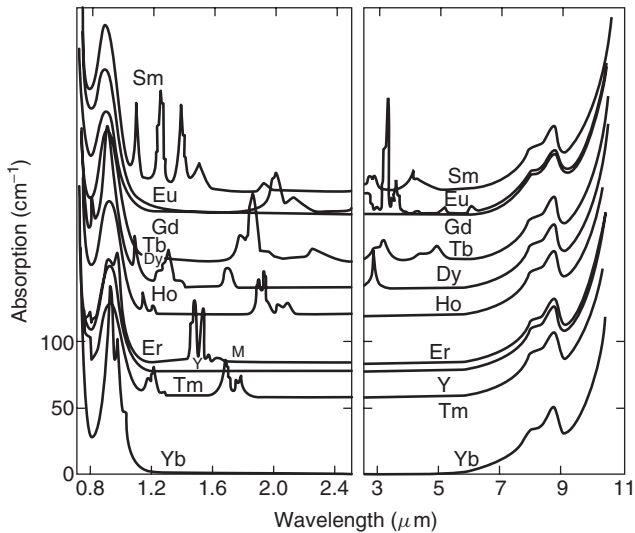


**Figure 11.29** Effect of host rare-earth ion species on optical absorption in the near-infrared region [77]. Reprinted with permission from *J. Appl. Phys.*, **38**, D. L. Wood and J. P. Remeika, Effect of impurities on the optical properties of yttrium iron garnet, 1038, Copyright (1967), American Institute of Physics

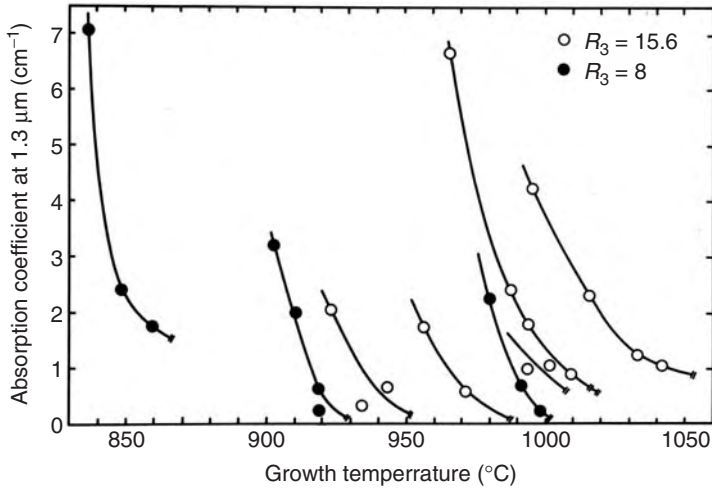


**Figure 11.30** Optical absorption of LPE Gd:YIG films at a wavelength of 1.3 μm as a function of growth temperature [78]. Reprinted with permission from *J. Appl. Phys.*, **54**, T. Hibiya and J. Nakashima, Optical absorption of liquid phase epitaxial garnet films at 1.3-μm wavelength for magneto-optic application, 7110, Copyright (1983), American Institute of Physics

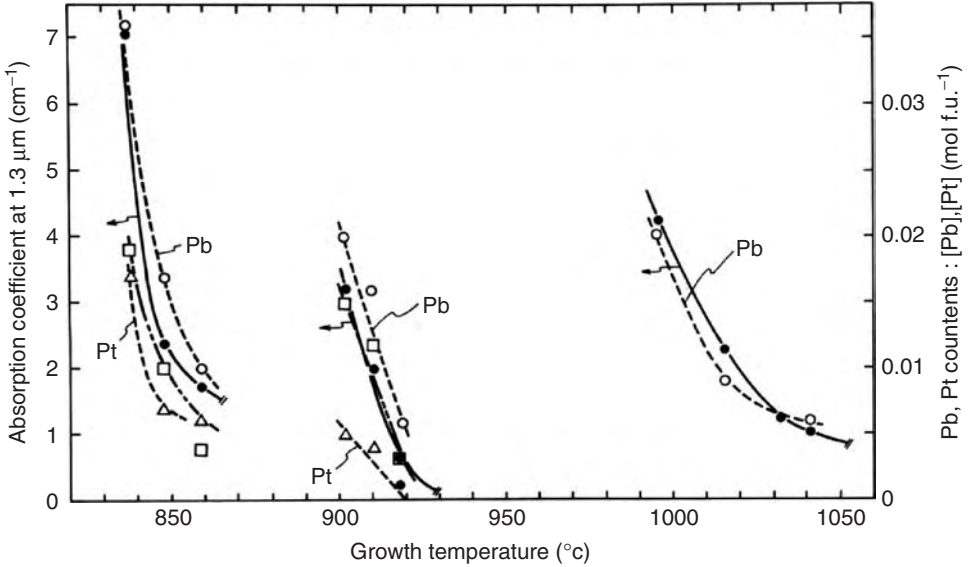


**Figure 11.31** Optical absorption coefficient, Pb contents, Pt contents and the difference between Pb and Pt contents as a function of growth temperature: (●) absorption coefficient; (○) Pb contents; (△) Pt contents; (□) difference between Pb and Pt contents [78]. Reprinted with permission from *J. Appl. Phys.*, **54**, T. Hibiya and J. Nakashima, Optical absorption of liquid phase epitaxial garnet films at 1.3-μm wavelength for magneto-optic application, 7110, Copyright (1983), American Institute of Physics

whose valence is different from 3+, such as  $\text{Pb}^{2+}$ ,  $\text{Pb}^{4+}$  and  $\text{Pt}^{4+}$ . Since the Pb contents are higher than that of Pt, the valence condition of part of the Pb ion is suggested at 4+ [78]. Incorporation of these ions causes the valence of  $\text{Fe}^{3+}$  to change to 2+ or 4+, if charged neutrality cannot be attained by the impurities themselves. For a series of LPE garnet films grown from melts, of liquidus temperature  $930^\circ\text{C}$ , neutrality is expected to be well attained, because LPE garnet films show low absorption, even though Pb and Pt are detectable from the LPE films.

#### 11.6.4 Magnetic anisotropy

The magnetic anisotropy plays a key role, when garnet films are used for practical applications. Besides magnetocrystalline anisotropy  $K_1$ , which arises from the symmetry of garnet crystals, uniaxial magnetic anisotropy appears for {111} films; they are growth-induced anisotropy  $K_u^g$ , stress-induced anisotropy  $K_u^s$  and shape anisotropy  $K_u^{\text{shape}}$ , which is due to a demagnetisation field. The most important one is growth-induced magnetic anisotropy, which has been the object of considerable study through the development of bubble memory garnets [1]. Growth-induced magnetic anisotropy, which is a metastable phenomenon, appears during the growth process through the ordering of rare-earth ions. For {111} growth, an easy magnetisation axis lies along the  $\langle 111 \rangle$  axis for  $K_u^g > 0$ . The ordering of rare-earth and Bi ions causes significant growth-induced anisotropy. Hansen and Krumme reviewed the growth-induced anisotropy of Bi-substituted garnets in detail [60]. This has also been systematically done by Fratello *et al.* [61]. Figure 11.32 shows a stripe domain pattern, due to growth-induced uniaxial magnetic anisotropy perpendicular to the surface, observed by the Kerr effect for  $300\ \mu\text{m}$  thick  $(\text{GdBi})_3(\text{FeAlGa})_5\text{O}_{12}$  film [6]. A hysteresis

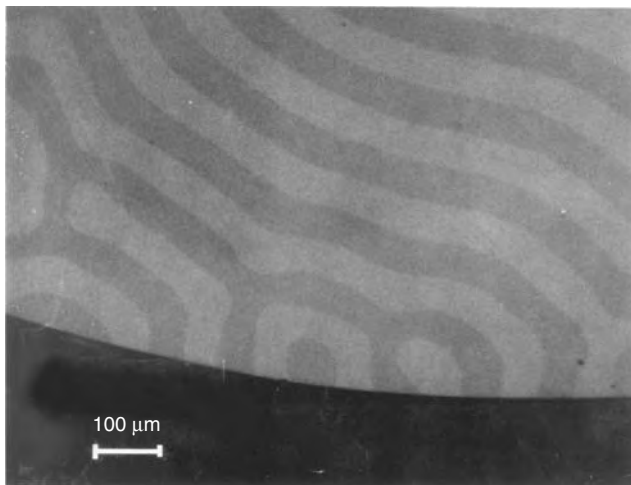


**Figure 11.32** Stripe domain pattern due to growth-induced uniaxial magnetic anisotropy perpendicular to the surface observed by the Kerr effect for  $300\ \mu\text{m}$  thick  $(\text{GdBi})_3(\text{FeAlGa})_5\text{O}_{12}$  film [6]. Reprinted from *IEEE Trans. Magn.*, **MAG-22**, T. Hibiya, T. Ishikawa and Y. Ohta, Growth and characterization of 300-mm thick bi-substituted gadolinium iron garnet films for an optical isolator, 11, Copyright (1986), IEEE

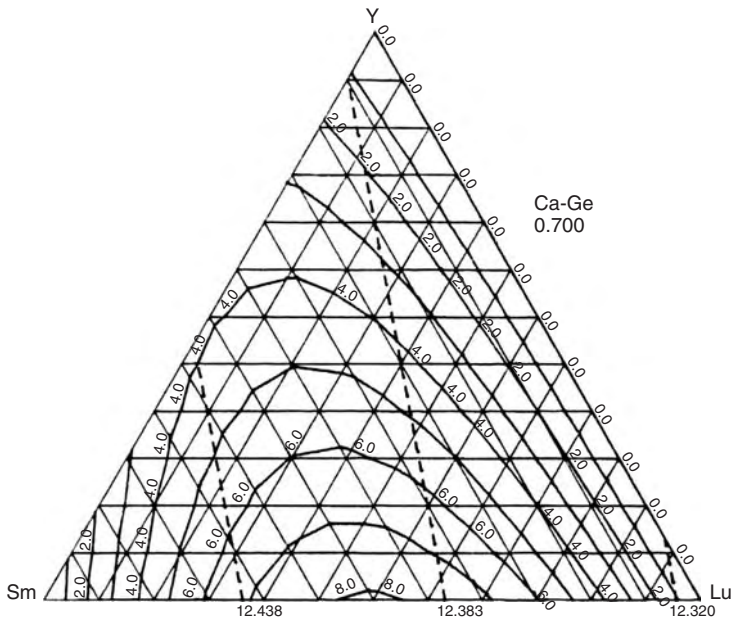


**Figure 11.33** Numerically obtained growth-induced anisotropy energy  $K_u^g$  for  $(Y\text{SmLu})_{2.3}\text{Ca}_{0.7}\text{Fe}_{4.3}\text{Ge}_{0.7}\text{O}_{12}$  garnet films. Dashed lines show the garnet compositions, whose lattice constants match those of  $\text{Gd}_3\text{Ga}_5\text{O}_{12}$  and  $\text{Sm}_3\text{Ga}_5\text{O}_{12}$  substrate crystals [79]. Reprinted from *Mater. Res. Bull.*, **16**, T. Hibiya and H. Makino, Empirical values for growth-induced anisotropy energy coefficient for designing garnet films, 847, Copyright (1981), with permission from Elsevier

curve for this material is shown in Figure 11.22. [6]. In order to support the material design for {111}, LPE garnet films for use in bubble memory devices and growth-induced anisotropy energy  $K_u^g$  can be estimated numerically, based on experimentally observed data, e.g. for Ca, Ge-substituted garnets, as shown in Figure 11.33 [79]. Because dashed lines show the compositions of garnets, whose lattice constants match those of  $\text{Gd}_3\text{Ga}_5\text{O}_{12}$  and  $\text{Sm}_3\text{Ga}_5\text{O}_{12}$  substrate crystals, it is easy to design material compositions.

For the {110}  $(Y\text{Bi})_3(\text{FeGa})_5\text{O}_{12}$ ,  $(Y\text{TmBi})_3(\text{FeGa})_5\text{O}_{12}$ ,  $(\text{GdBi})_3\text{Fe}_5\text{O}_{12}$  and  $(\text{GdBi})_3(\text{FeAlGa})_5\text{O}_{12}$  films, growth-induced orthorhombic magnetic anisotropy can be obtained; with an easy magnetisation axis along the  $\langle 110 \rangle$  [80, 81]. For garnet films with orthorhombic magnetic anisotropy, high-speed wall velocity is available; and high-speed read-out heads for magnetic media can be applied to these materials. Although for {111} growth, growth-induced magnetic anisotropy is systematically investigated [14, 60, 61], there is less study for orthorhombic magnetic anisotropy for {110} films.

## 11.7 APPLICATIONS OF GARNET FILMS

Magnetic garnets are important for current telecommunication systems and sensors. The most important application of LPE garnet films is as an optical isolator for use in fiberoptic communication systems. More than 1 million chips of  $1\text{ mm}^2$  area were produced in 2005, although production plummeted after the collapse of the information technology (IT)

bubbles. Thick LPE Bi-substituted garnet films with perpendicular magnetisation are now used in practice, with more than 90% of chips produced in Japan [82]. For microwave applications, such as filters and oscillators, small and high quality Ga substituted YIG spheres, of diameter 0.3 mm, are used. YIG stripes, with a thickness of about 100  $\mu\text{m}$ , were studied for the excitation and propagation of magnetostatic modes for electronically controlled delay lines [5].

LPE garnet films with in-plane magnetisation have been studied for waveguide devices in the infrared region [83]. For magneto-optic (MO) sensors in the visible (VIS) range, both in-plane and perpendicular magnetised films are applied [7]. Let us show a result of the recent study on VIS-MO sensor films. The principal set-up of a MO system and the construction of a sensor film are shown in Figure 11.34. Although this system contains a film with in-plane anisotropy, a film with perpendicular anisotropy could be used in the same way. The components of this MO system are an intense source of linearly polarised light, the magneto-optical garnet film placed in the magnetic field to be imaged and a detection unit for probing the polarisation state, which is in general elliptical form due to Faraday rotation. The commonly applied transmitting mode of the operation mode may be converted into a reflection mode by equipping the garnet film with a reflection layer (e.g. aluminum, cf. Figure 11.34). In this case the sensor is placed in front of the surface of a magnetic material or device to project its stray field distribution. The light beam traverses the garnet layer twice, thus doubling the rotation angle. The high sensitivity and excellent homogeneity of MO garnet films allow the following technical applications for sensors:

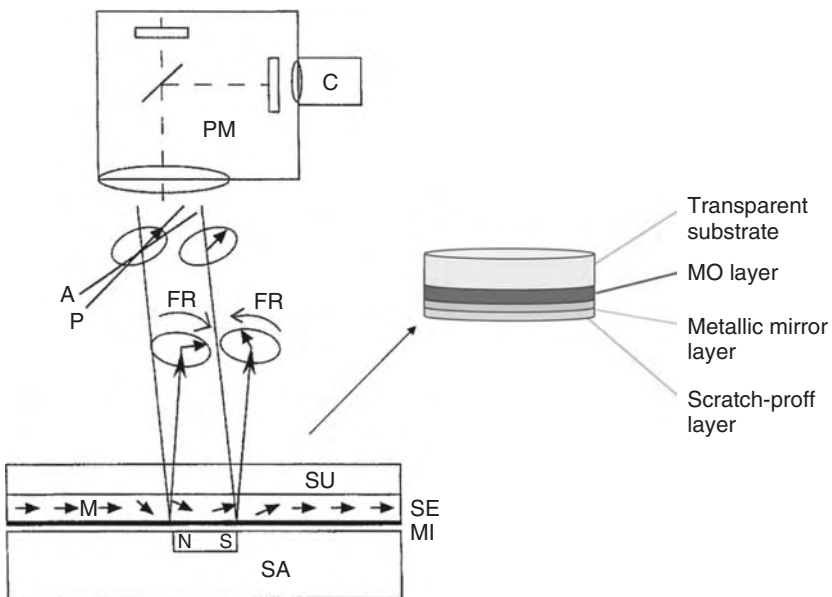


**Figure 11.34** Set-up of a magneto-optic (MO) system containing a sensor with an in-plane anisotropy. C, camera; PM, polarisation microscope; A, analyser; P, polariser; FR, Faraday rotation; SU, substrate; SE, sensor; M, magnetisation; MI, mirror; SA, sample; NS, magnetic poles (N and S). Reproduced from [5] by permission of Wiley-VCH



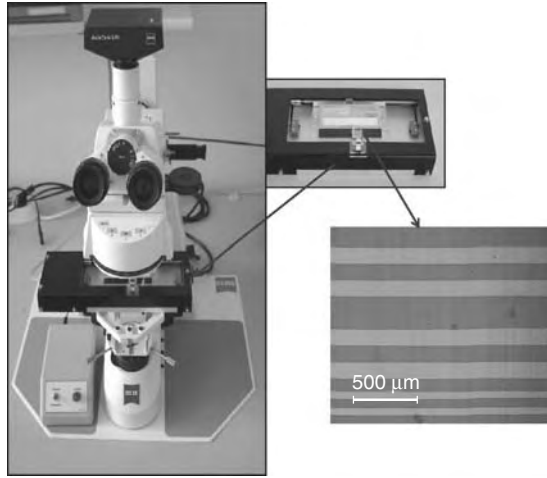


**Figure 11.35** Visualisation and reconstruction of magnetic recorded digital information on a data carrier

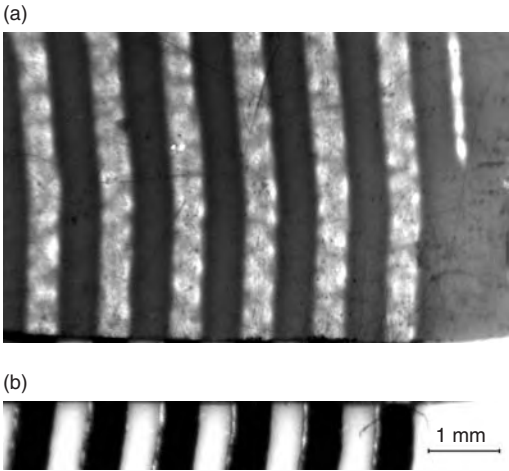


**Figure 11.36** Part of a magnetic spiral encoder structure: magneto-optical (a) and optical (b) image. Reproduced from [5] by permission of Wiley-VCH

- (i) Magnetic field imaging, where the contrast is created by different local magnetic fields in the direction of light propagation.
- (ii) Nondestructive evaluation (NDE) of materials with a high spatial resolution.

Currently, MO sensors are manufactured predominantly for forensic applications to visualise and reconstruct magnetically recorded digital and analog information on data carriers (credit cards, floppy disks, audio and video tapes) to check e.g. manipulations of the recording by subsequent overwriting. A commercial system for forensic applications

developed by Innovent Jena is shown in Figure 11.35. This and other equipment contain different sensor units, which are manufactured according to customer demands.

Furthermore, MO sensors are applied to characterise magnetic materials, such as screen printed magnetic encoders as shown in Figure 11.36. This figure illustrates the magnetic homogeneity of a polymeric bond Ba hexaferrite powder. Of course, similar investigation can be carried out to investigate the magnetic homogeneity of different magnetic materials with a lateral resolution limited by Abbe's fundamental theory. Spiral encoders, as presented in Figure 11.36, allow the absolute rotation angle to be measured within the range  $0\text{--}360^\circ$  with accuracy to within less than  $0.5^\circ$ . The magnetic signal is detected with commercial anisotropic magneto-resistive (AMR) sensors.

## 11.8 CONCLUSIONS

The LPE of garnets is a simple, reproducible, and inexpensive technique to grow high quality films with diameters of up to 10 cm (4 in.) for commercial application and research purposes. The relevant parts of phase diagrams are known. Intensive studies of the nature of growth species clearly indicate a dissociation of garnet molecules during dissolution in  $\text{PbO-B}_2\text{O}_3$  based flux melts. However, the growth kinetics are described in terms of a single-molecule model because of a lack of information concerning diffusion coefficient, diffusion boundary layer thickness, and the kinetic coefficient of the individual cation-oxygen complexes. Morphology control is essential to prepare high quality thick LPE garnet films for use in optical isolators. Although  $\{111\}$  is not a natural face of garnet systems, a smooth surface can be obtained from the practical perspective. By the use of  $\{111\}$  growth, uniaxial magnetic anisotropy can be obtained, which is required for an optical isolator. The incorporation of Bi ions into dodecahedral sites enhances the magneto-optic Faraday rotation and growth-induced anisotropy. Control of stress, induced by both lattice mismatch and the cooling process, is the key to obtaining crack-free thick LPE films. Optical absorption in the visible and near-infrared range is due to  $\text{Fe}^{3+}$  ions and the valence change of  $\text{Fe}^{3+}$  to  $\text{Fe}^{2+}$  or  $\text{Fe}^{4+}$ . VIS-MO sensor films with a high spatial resolution are applied for magnetic field imaging and nondestructive material evaluation. Currently, such sensors are manufactured predominantly for forensic applications.

## ACKNOWLEDGEMENTS

The author (T.H.) thanks Prof. Shinagawa of Toho University for discussion on the Faraday rotation mechanism and Drs Nomi and Iino for supplying photographs of LPE garnets and substrate crystals. The author (P.G.) thanks his colleagues Dr Habil. R. Hergt and Dr K. Fischer (IPHT Jena) and Dr-Ing H. Richert, PD Dr Habil. D. Berkov, Dr T. Aichele, Dr C. Dubs, Dipl.-Chem. A. Lorenz and Dipl.-Ing. M. Lindner (Innovent Jena) for their fruitful cooperation.

## REFERENCES

- [1] A. H. Bobeck and E. Della Torre, *Magnetic Bubbles*, North-Holland, Amsterdam, 1975.
- [2] R.C. Linares, R.B. McGraw and J.B. Schroeder, *J. Appl. Phys.*, **36**, 2884 (1965).

- [3] S. Geller, H., J. Williams, G. P. Espinoza and R. C. Sherwood, *Bell System Tech. J.*, **43**, 565 (1964).
- [4] M. A. Tsankov, M. Chen and C. E. Patton, *J. Appl. Phys.*, **79**, 1595 (1996).
- [5] T. Aichele, A. Lorenz, R. Hergt and P. Görnert, *Cryst. Res. Technol.*, **38**, 575 (2003).
- [6] T. Hibiya, T. Ishikawa and Y. Ohta, *IEEE Trans. Magn.*, **MAG-22**, 11 (1986).
- [7] N. Imaizumi, T. Fukuhara, Y. Kuwano and K. Shiroki, *Mater. Res. Soc. Symp. Proc.*, **834**, 123 (2005).
- [8] E. Sawatzky and E. Kay, *J. Appl. Phys.*, **40**, 1460 (1969).
- [9] J.E. Mee, G.R. Pulliam, J.L. Archer and P.J. Besser, *IEEE Trans. Magn.*, **MAG-5**, 717 (1969).
- [10] E.D. Kolb and R.A. Laudise, *J. Appl. Phys.*, **42**, 1552 (1971).
- [11] R R. C. Linares, *J. Cryst. Growth*, **3/4**, 443 (1968).
- [12] H. J. Levinstein, S. Licht, R.W. Landorf and S. L. Blank, *Appl. Phys. Lett.*, **19**, 486 (1971).
- [13] H. Makino and T. Hibiya, *J. Appl. Phys.*, **50**, 7815 (1979).
- [14] A. H. Boeck, E. G. Spencer, D. H. Smith and L. G. Van Uitert, *IEEE Trans. Magn.*, **MAG-7**, 461 (1971).
- [15] W. Tolksdorf and F. Welz, in *Topics in Crystal Growth*, Vol. 1, ed. C. J. Rooijmans, Springer, Berlin, 1978.
- [16] T. Aoyama, T. Hibiya and Y. Ohta, *IEEE J. Lightwave Technol.*, **LT-1**, 280 (1983).
- [17] J. M. Robertson and M. W. van Tol, *Thin Solid Films*, **114**, 221 (1984).
- [18] G. Winkler, *Magnetic Garnets*, Vieweg Verlag, Braunschweig/Wiesbaden, 1981.
- [19] D. Elwell and H.J. Scheel, *Crystal Growth from High Temperature Solutions*, Academic Press, London, 1975.
- [20] P. Görnert and E. Sinn, in *Crystal Growth of Electronic Materials*, ed. E. Kaldis, North-Holland, Amsterdam, 1985, Ch. I.3.
- [21] P. Görnert, *Prog. Crystal Growth Charact.*, **20**, 263 (1990).
- [22] V.J. Fratello and R. Wolfe, in *Handbook of Thin Film Devices Vol. 4*, ed. M.H. Francombe, Academic Press, London, 2000, Ch. 3, 93.
- [23] W. Tolksdorf and C.-P. Klages, *Thin Solid Films*, **114**, 33 (1984).
- [24] T. Hibiya, *Current Top. Cryst. Growth Res.*, **3**, 199 (1997).
- [25] E. A. D. White and J. D. C. Wood, *Radio Electron. Engin.*, **45**, 711 (1975).
- [26] T. Hibiya and O. Okada, *J. Cryst. Growth*, **67**, 566 (1984).
- [27] H.J. van Hook, *J. Am. Ceram. Soc.*, **44**, 208 (1961).
- [28] M. Kestigian, *J. Am. Ceram. Soc.*, **50**, 165 (1967).
- [29] S. Kimura and I. Shindo, *J. Cryst. Growth*, **41**, 192 (1977).
- [30] J.W. Nielsen and E.F. Dearborn, *Phys. Chem. Solids*, **5**, 202 (1958).
- [31] H. D. Jonker, *J. Cryst. Growth*, **28**, 231 (1975).
- [32] J.W. Nielsen, *J. Appl. Phys. Suppl.*, **31**, 518 (1960).
- [33] A.G. Titova, *Fiz. Tverd. Tela*, **1**, 1971 (1959).
- [34] L.G. Van Uitert, W.H. Grodkiewicz and E.F. Dearborn, *J. Am. Ceram. Soc.*, **48**, 105 (1965).
- [35] S. L. Blank and J. W. Nielsen, *J. Cryst. Growth*, **17**, 302 (1972).
- [36] M. Nevriya and K. Fischer, *J. Cryst. Growth*, **89**, 571 (1988).
- [37] T. Hibiya, *J. Cryst. Growth*, **64**, 499 (1984).
- [38] K. Fischer and E. Sinn, *Cryst. Res. Technol.*, **21**, 711 (1986).
- [39] K. Fischer, D. Linzen, E. Sinn and S. Bornmann, *J. Cryst. Growth*, **52**, 729 (1981).
- [40] P. De Gasperis and R. Marcelli, *Mater. Res. Bull.*, **22**, 235 (1987).
- [41] E.A. Giess, M.M. Faktor, R. Ghez and C.F. Guerci, *J. Cryst. Growth*, **56**, 576 (1982).
- [42] D. Linzen, E. Sinn, K. Fischer, Th. Klupsch and S. Bornmann, *Cryst. Res. Technol.*, **18**, 165 (1983).
- [43] E. Sinn, D. Linzen and K. Fischer, *Cryst. Res. Technol.*, **20**, 965 (1985).
- [44] T. Hibiya, H. Makino and Y. Hidaka, *AIP Conf. Proc.*, **No. 34**, 163 (1976).
- [45] T. Hibiya and H. Makino, *Proc. 3rd Int. Conf. Ferrites*, 467 (1980).

- [46] V. J. Fratello, S. E. G. Slusky, V. V. S. Rana, C. D. Brandle and J. E. Ballantine, *J. Appl. Phys.*, **59**, 564 (1986).
- [47] K. Th. Wilke and J. Bohm, *Kristallzüchtung*, Deutscher Verlag der Wissenschaften, Berlin, 1988.
- [48] P. Görnert, *J. Cryst. Growth*, **52**, 88 (1981).
- [49] P. Görnert and F. Voigt, in *Current Topics in Materials Science*, Vol. 11, ed. E. Kaldis, North-Holland, Amsterdam, 1984, Ch. 1.
- [50] J.A. Burton, R.C. Prim and W.P. Slichter, *J. Chem. Phys.*, **21**, 1987 (1953).
- [51] St. Sure, *Herstellung magnetischer Granatfilme durch Flüssigphasen-Epitaxie für Anwendungen in der integrierten Optik*, Verlag Shaker, Aachen, 1995.
- [52] T. Hibiya, T. Ishikawa, Y. Morishige, J. Nakashima and Y. Ohta, *NEC Res. Dev.*, No.80, 1 (1986).
- [53] T. Hibiya, *J. Cryst. Growth*, **62**, 87 (1983).
- [54] T. Hibiya, *J. Cryst. Growth*, **64**, 400 (1983).
- [55] P. Görnert, R. Hergt, E. Sinn, M. Wendt, B. Keszei and J. Vandlik, *J. Cryst. Growth*, **87**, 331 (1988).
- [56] C. F. Buhner, *J. Appl. Phys.*, **40**, 4500 (1969).
- [57] R. V. Pisarev, E. V. Berdenikova and R. A. Petrov, *Sov Phys. Solid State*, **12**, 1218 (1970).
- [58] J. M. Robertson, S. Wittekoek and T. J. A. Popma, *Appl. Phys.*, **2**, 219 (1973).
- [59] H. Takeuchi, S. Itoh, I. Mikami and S. Taniguchi, *J. Appl. Phys.*, **44**, 4789 (1973).
- [60] P. Hansen and J.-P. Krumme, *Thin Solid Films*, **114**, 69 (1984).
- [61] V. J. Fratello, S. E. G. Slusky, C. D. Brandle and M. P. Norelli, *J. Appl. Phys.*, **60**, 2488 (1986).
- [62] K. Shinagawa and S. Taniguchi, *Jpn. J. Appl. Phys.*, **13**, 1663 (1974).
- [63] C.-P. Klages and W. Tolksdorf, *J. Cryst. Growth*, **64**, 275 (1983).
- [64] V. I. Chani and A. Balbashov, *J. Cryst. Growth*, **66**, 616 (1984).
- [65] V. J. Fratello, S. J. Licht and M. P. Norelli, *J. Cryst. Growth*, **97**, 657 (1989).
- [66] P. Hansen, W. Tolksdorf and K. Witter, *IEEE Trans. Mag.*, **MAG-20**, 1099 (1984).
- [67] V. J. Fratello, H. M. O'Bryan and C.D. Brandle, *J. Cryst. Growth*, **166**, 774 (1996).
- [68] V. J. Fratello, S. J. Licht, C. D. Brandle, H. M. O'Bryan and F. A. Baiocchi, *J. Cryst. Growth*, **142**, 93 (1994).
- [69] R. J. Besser, J. E. Mee, P. E. Elkins and D. M. Heinz, *Mater. Res. Bull.*, **6**, 1111 (1971).
- [70] H. Makino, T. Hibiya and K. Matsumi, *NEC Res. Dev.*, No. 34, 51 (1974).
- [71] D. Mateika and E. Völkel, *J. Cryst. Growth*, **102**, 994 (1990).
- [72] T. Iino, International Workshop on Crystal Growth Technology, Beatenberg, Switzerland, September 11–17, 2005.
- [73] K. Shinagawa, in *Magneto-Optics*, eds S. Sugano and N. Kojima, Springer Series in Solid-State Sciences, Springer, Berlin, 1984, 137.
- [74] W.A. Crossley, R.W. Cooper, J.L. Page and R.P. van Staple, *Phys. Rev.*, **181**, 896 (1969).
- [75] P. Hansen, K. Witter and W. Tolksdorf, *Phys. Rev. B*, **27**, 6608 (1983).
- [76] Y. Honda, T. Ishikawa and T. Hibiya, *J. Mag. Soc. Jpn.*, **11**, 361 (1987).
- [77] D. L. Wood and J. P. Remeika, *J. Appl. Phys.*, **38**, 1038 (1967).
- [78] T. Hibiya and J. Nakashima, *J. Appl. Phys.*, **54**, 7110 (1983).
- [79] T. Hibiya and H. Makino, *Mater. Res. Bull.*, **16**, 847 (1981).
- [80] T. Hibiya, H. Makino and S. Konishi, *J. Appl. Phys.*, **52**, 7347 (1981).
- [81] T. Hibiya, H. Honda, H. Makino and Y. Honda, *J. Magn. Magn. Mater.*, **53**, 98 (1985).
- [82] Fuji Chimera Research Institute Inc., *Opt-Electronics Industry—Handbook for Future Trends*, 2004.
- [83] H. Dötsch, Herstellung und Charakterisierung magnetischer Granatschichten, Abschlußbericht Teilprojekt A2, Modulatoren und Laser in ranat-Wellenleitern Teilprojekt D11, Universität Osnabrück, 2000.



# 12 Liquid Phase Epitaxy: A Survey of Capabilities, Recent Developments and Specialized Applications

**MICHAEL G. MAUK**

*School of Engineering and Applied Science, University of Pennsylvania, Philadelphia, PA 19101, USA*

---

12.1	Introduction	342
12.2	Comparison of epitaxy techniques and some advantages of LPE	343
12.3	Previous reviews of LPE	355
12.4	Modeling of LPE processes	355
12.5	Survey of new developments and specialized applications of LPE	356
12.5.1	Five- and six-component III-V semiconductor alloys by LPE	357
12.5.2	LPE layers with atomically smooth surfaces	358
12.5.3	Quantum wells, superlattices and nanostructures by LPE	358
12.5.4	Growth of thick ternary and quaternary alloy layers for 'virtual' substrates with adjustable lattice parameters	360
12.5.5	Selective epitaxy and ELO	363
12.5.6	Melt epitaxy	366
12.5.7	Rare earth doping and other doping effects in LPE	366
12.5.8	Fundamental studies of crystal growth, melt convection and liquid-metal transport properties	367
12.5.9	Novel melt compositions for LPE	369
12.5.10	Liquid phase electroepitaxy	370
12.5.11	LPE of thallium-, manganese-, and bismuth-containing III-V alloys	373
12.5.12	Control of segregation in LPE-grown alloys	374
12.5.13	LPE heteroepitaxy	376
12.5.14	SiC and III-V nitride LPE	381

12.5.15	Some other materials grown by LPE or solution growth	383
12.5.16	LPE for shaped crystal growth	389
12.6	Conclusions and outlook	391
	References	392

---

## 12.1 INTRODUCTION

Liquid phase epitaxy (LPE) is a method and technology for depositing oriented, crystalline films or layers of material onto a crystalline substrate from a solution (multicomponent ‘melt’). Epitaxial film/layer thicknesses can range from less than a micrometer to several hundred micrometers. For LPE of the common semiconductors, such as GaAs, the liquid phase is typically a molten metal solution. Thus, for example, an AlGaAs epitaxial film is grown on a GaAs substrate wafer from a Ga-rich Ga-Al melt saturated with (~1 at. %) arsenic. Other solvents including fused oxides and molten salts have been employed for LPE growth of nonsemiconductor materials such as garnets. Growth temperatures for LPE range from several hundred degrees to close to 2000 K, depending on the epitaxial material, melt, and substrate. For semiconductor device applications, the substrates are cut from single-crystal semiconductor wafers, but there is interest in applying LPE-like processes, e.g. metallic solution growth, for deposition of semiconductors on other types of substrates including glass, ceramics, and metals for making solar cells, light emitting diodes (LEDs), and large-area detectors. Also, selective epitaxy on patterned, partially masked substrates, or structured substrates with nonplanar surface topologies, can be used to grow discrete crystals, in contrast to the continuous, planar films as are routinely produced in conventional epitaxy processes. Selective growth of epitaxial mesas and faceted crystals can be used to reduce crystalline defects and thermal stress effects, and also to provide electrical isolation and optical elements such as reflective surfaces and lens-like structures. Many of the features achieved by selective LPE and related techniques of epitaxial lateral overgrowth cannot be easily realized with other methods of epitaxy.

LPE is a mature technology and has been used in the production of III-V compound semiconductor optoelectronic devices for some 40 years. LPE has also been applied to silicon, germanium, SiC, and II-VI and IV-VI compound semiconductors, as well as magnetic garnets, superconductors, ferroelectrics, and other optical materials. Many semiconductor devices including LEDs, laser diodes, infrared detectors, heterojunction bipolar transistors and heteroface solar cells were pioneered with LPE (Kuphal, 1991). Further, in many cases LPE can produce epitaxial semiconductor layers of superior material quality with respect to minority carrier lifetime and luminescence efficiency. Nevertheless, LPE has fallen in disfavor in recent years, especially for device applications requiring large-area uniformity, critical layer thickness and composition control, and smooth and abrupt surfaces and interfaces. For making superlattices, quantum wells, strained layer structures, and heterostructures with large lattice mismatch or heterostructures comprised of materials with substantial chemical dissimilarity (e.g. GaAs-on-silicon), LPE is often dismissed out of hand in favor of other epitaxy technologies such as molecular beam epitaxy (MBE) or metal-organic chemical vapor deposition (MOCVD). One might conclude that despite the long and venerable history of LPE, progress has stagnated with few prospects for new

applications. Kroemer (Kroemer, 2000) in his Nobel Prize address noted that the seminal demonstration of the double-heterostructure laser in 1970 was achieved by LPE; he nevertheless characterized LPE as ‘a beautifully simple technology, but with severe limitations.’ In particular, LPE suffers under widely held perceptions of poor run-to-run reproducibility; areal inhomogeneities and variations in doping, layer thickness and alloy composition; intrinsic limitations in growing thin (<50 nm) layers, and practical difficulties in scale-up for large-area substrates and high-throughput operation. Wood and Brown (Wood and Brown, 1998) have chronicled Sony Corporation’s transition from LPE to MOCVD for development and mass production of laser diodes used in CD players, and which serves as an illustrative study of the shortcomings of LPE for certain commercial applications. A more recent case relates to development of AlGaAsSb/InGaAsSb heterojunction phototransistors, where Swaminathan *et al.* (Swaminathan *et al.*, 2006) concluded that although LPE provided initial prototypes demonstrating feasibility and produced devices with excellent performance characteristics, MOCVD offers better control over alloy composition, doping, interface abruptness, and epilayer thicknesses, which should prove crucial in future detector array applications. Further, there are many heterojunction structures that cannot readily be made by LPE due to high lattice mismatch and nonequilibrium dissolution (meltback) effects. Nevertheless, and as the accompanying chapters describe in more detail, on-going efforts and recent developments in LPE continue to widen its scope of applications and circumvent some of its traditional limitations. New modes of liquid phase epitaxial growth can provide novel device structures that would be difficult to make by other epitaxy techniques. The limitations and deficiencies of conventional LPE as mentioned above are addressed by new techniques and approaches based on novel melt chemistries, alternative methods of inducing growth (e.g. through imposed temperature gradients, electric currents, mixing and forced convection, Peltier cooling, and solvent evaporation), hybrid processes that combine LPE with other methods of epitaxy, and LPE on structured and/or masked substrates. Further, unique attributes that distinguish LPE from competing semiconductor epitaxy technologies such as MBE and MOCVD enable LPE to serve important niches in semiconductor device technology.

## 12.2 COMPARISON OF EPITAXY TECHNIQUES AND SOME ADVANTAGES OF LPE

The selection of a particular epitaxy technique for a specified materials system and device application can be guided by practical considerations such as capital investment and operating costs, throughput, safety, reproducibility, required skill, and performance with respect to thickness and doping control (Astles, 1990). A more fundamental comparison of epitaxy methods on the basis of thermodynamics, interface kinetics, surface energetics, mass transfer, as well as a recognition of the dominant or operative modes of nucleation, growth and defect formation, is also useful. Table 12.1 contrasts several epitaxy methods with regard to operational parameters; order-of-magnitude costs, routinely achievable epilayer specifications with respect to control of composition, layer thickness, and doping; manufacturing issues; and other salient features [see for example Wood (Wood, 1982) for more detailed comparisons of various epitaxy technologies relevant to field-effect transistor applications]. The data in Table 12.1 (as well as Tables 12.2 and 12.3) are for



**Table 12.1** Comparison of semiconductor epitaxy technologies (data mostly for GaAs)

	LPE	CSVT	Cl-CVD	MOCVD	MBE
Invention	<i>early 1960s</i> (RCA) (Nelson, 1963)	<i>early 1960s</i> (RCA) (Robinson, 1963; Nicoll, 1963)	<i>early 1960s</i> (Plessey) (Effer, 1963) <sup>a</sup>	<i>late 1960s</i> (Rockwell) (Manasevit and Simpson, 1968, 1969; Manasevit, 1983)	<i>late 1960s</i> (AT&T Bell Labs) (Arthur and Lepore, 1969; Cho, 1971a,b)
Capital cost (\$)	25–100 K	15–20 K	50–200 K	300 K–1 M	300 K–1 M
Versatility	high	modest	modest	high	modest
Adaptability	high	high	good	limited	limited
Operation	simple	simple	simple	complex	moderate
Operator skill	high	moderate	moderate	low for automated systems	high
Man-hours per run	4	2	1–4	1–4	1–4
Runs per day	2	5	2	2	2–3
Annual operating costs	low	low	low	high	moderate
Safety/environmental hazards/problems	slight (hydrogen)	slight	moderate	highly toxic precursors (e.g. AsH <sub>3</sub> )	slight
Pressure	atmospheric	atmospheric	10–760 Torr	10–760 Torr	<10 <sup>-9</sup> Torr
Max. growth rate (μm min <sup>-1</sup> )	1–10	1–3	1–2	0.1–1.0	0.01–0.1
Max. substrate diameter (mm)	75	75	>100	>100	>100
Thickness control (± nm)	100	100	100	<10	<1 or 1 %
Sharpness of layer transitions (MLs)	4–18	4–18	>10	1–3	1
Material utilization/ yield (%)	1–5 (slideboat) 100 (inf.melt)	1–5 (slideboat) 100 (inf. melt)	1–25	5–20	10–30
Background impurities (cm <sup>-3</sup> )	10 <sup>12</sup> –10 <sup>13</sup>	10 <sup>16</sup>	10 <sup>14</sup>	10 <sup>15</sup>	10 <sup>14</sup>
Areal alloy compositional uniformity (%)	±10	±10	±5–10	±2–5	±1
Dopant selection	wide	limited	limited	limited	modest
Substrate impurity outdiffusion	fair	poor	poor	good	good
Run-to-run (%)	±10	±5	5	2–5	2–5
Reproducibility of layer thickness					
Areal uniformity of layer thickness (across 2 cm) (%)	5–10	5–10	5	2–5	<2
In situ metallization?	no	no	no	no	yes
Aluminum-containing III-V alloys?	yes	no	no	yes	yes

**Table 12.1** (continued)

	LPE	CSVT	Cl-CVD	MOCVD	MBE
Direct monitoring of growth process	no	no	ambient sampling	ellipsometry, RGA	in situ real-time LEED, RHEED

LPE, liquid phase epitaxy; CSVT, close-spaced vapor transport; Cl-CVD, chloride chemical vapor deposition; MOCVD, metal organic chemical vapor deposition; MBE, molecular beam epitaxy; ML, monolayer; RGA, residual gas analyzer; LEED, low energy electron diffraction; RHEED, reflection high energy electron diffraction.

<sup>a</sup>Silicon CVD methods predate the development of CVD for compound semiconductors.

#### References

- J.R. Arthur and J.J. LePore (1969) GaAs, GaP, and GaAs<sub>x</sub>P<sub>1-x</sub> epitaxial films grown by molecular beam deposition. *J. Vacuum Sci. Technol.* **6**, 545–548.
- M.G. Astles (1990) *Liquid-phase Epitaxy and Phase Diagrams for Compound Semiconductor Materials and their Device Applications*. Adam Hilger, Bristol.
- A.Y. Cho (1971a) GaAs epitaxy by a molecular beam method: observations of surface structure on the (001) face. *J. Appl. Phys.* **42**, 2074–2081.
- A.Y. Cho (1971b) Film deposition by molecular-beam techniques. *J. Vacuum Sci. Technol.* **8**, S31–S38.
- D. Effer (1963) Epitaxial growth of doped and pure GaAs in an open flow system. *J. Electrochem. Soc.* **112**, 1020–1024.
- J.D. Grange and D.K. Wickenden (1985) Comparison and critique of the epitaxial growth technologies in *The Technology and Physics of Molecular Beam Epitaxy*, E.H.C. Parker, ed. Plenum, New York, Ch. 17.
- J.J. Hsieh (1980) Liquid phase epitaxy in *Handbook of Semiconductors*, Vol. **3**, T.S. Moss and S.P. Keller, eds. North-Holland, Amsterdam, 415–497.
- E. Kuphal (1991) Liquid phase epitaxy. *Appl. Phys. A* **52**, 380–409.
- C. Li, Z. Du, D. Luo and W. Zhang (2000) Epitaxial techniques for compound semiconductor growth: from LPE to MOVPE. *Rare Metals* **19**, 81–86.
- H.M. Manasevit (1983) Epitaxial composite and method of making. US Patent 4 368 098.
- H.M. Manasevit and W.I. Simpson (1968) The use of metal-organics in the preparation of semiconductor materials-1 in *Abstracts from 133rd Meeting of the Electrochemical Society, Boston*. Electrochemical Society, New York, 13.
- H.M. Manasevit and W.I. Simpson (1969) Use of metal-organics in the preparation of semiconductor materials on insulating substrates. *J. Electrochem. Soc.* **116**, 1725–1732.
- R.L. Moon (1980) Liquid phase epitaxy in *Crystal Growth*, 2nd Edn., B.R. Pamplin, ed. Pergamon, Oxford, 421–460.
- R.L. Moon (1997) MOVPE: is there any other technology for optoelectronics?. *J. Cryst. Growth* **170**, 1–10.
- H. Nelson (1963) Epitaxial growth from the liquid state and its application to the fabrication of tunnel and laser diodes. *RCA Rev.* **24**, 603–615.
- F.H. Nicoll (1963) The use of close spacing in chemical transport systems for growing epitaxial layers of semiconductors. *J. Electrochem. Soc.* **110**, 1165–1167.
- P.H. Robinson (1963) Transport of gallium arsenide by close-spaced technique. *RCA Rev.* **24**, 574–584.
- W. Thulke (1991) Can liquid phase epitaxy still be useful for optoelectronic devices? *Mater. Sci. Eng. B* **9**, 61–67.
- H. Watanabe, T. Mizutani and A. Usui (1990) Fundamentals of epitaxial growth and atomic layer epitaxy in *Very High Speed Integrated Circuits: Heterostructures*, T. Ikoma, ed. Academic Press, Boston, 1–52.
- C.E.C. Wood (1982) Molecular beam epitaxy for microwave field effect transistors in *GaAs FET Principles and Technology*, J.V. DiLorenzo and D.D. Khandelwal, eds. Artech, Boston, 111.

illustrative purposes and rough comparisons only, and should not be construed as definitive characterizations of a particular epitaxy technique. The data are mostly for GaAs (and AlGaAs) epitaxy, as all of the prominent methods of epitaxy have been applied and

**Table 12.2** Typical parameters and fundamental characteristics of main epitaxy techniques (as applied to GaAs and related materials)<sup>a</sup>

	Epitaxy methods					
	LPE (Ga)	LPE(Bi)	CSVT	Cl-CVD	MOCVD	MBE
Typical growth temp. <i>T</i> (°C)	650–850	650–850	700–850	600–750	550–750	500–700
Free energy change ('thermodynamic driving force') $\Delta G$ (kcal mol <sup>-1</sup> )	0–2	0–2	0–5	2–4	25–35	12–26
Rate-limiting species	As	As and/or Ga	Ga (Ga <sub>2</sub> O)	Ga (GaCl <sub>3</sub> )	Ga (TMG)	Ga
$C_i$ (cm <sup>-3</sup> )	10 <sup>21</sup>	10 <sup>20</sup>	10 <sup>16</sup>	7 × 10 <sup>15</sup>	10 <sup>11</sup> –10 <sup>16</sup>	10 <sup>10</sup>
$J_i$ (cm <sup>-2</sup> s <sup>-1</sup> )	10 <sup>25</sup>	10 <sup>24</sup>	10 <sup>16</sup>	10 <sup>16</sup>	6 × 10 <sup>14</sup>	6 × 10 <sup>14</sup>
$J_e$ (cm <sup>-2</sup> s <sup>-1</sup> )	≅ $J_e$	≅ $J_e$	≅ $J_e$	≅ $J_e$	0	0
$J_{net} = J_i - J_e$ (cm <sup>-2</sup> s <sup>-1</sup> )	10 <sup>16</sup>	10 <sup>15</sup>	10 <sup>16</sup>	10 <sup>15</sup>	6 × 10 <sup>14</sup>	6 × 10 <sup>14</sup>
$\lambda = (J_i - J_e)/(J_i + J_e)$	~4 × 10 <sup>-8</sup>	~10 <sup>-8</sup>	~4 × 10 <sup>-4</sup>	~4 × 10 <sup>-4</sup>	~1	~1
V/III ratio	0.01–0.05	0.01–5	0.5–2	0.5–5	5–100	5–20
Approx. surface energies $\gamma$ (erg/cm <sup>2</sup> )	600	400	900	900	900	1000
Process controlled mainly by	temp.	temp.	temp.	flow rates	flow rates	fluxes
Growth rate limited mainly by	bulk liquid diffusion	bulk liquid diffusion	bulk liq. diffusion	reaction kinetics	reaction kinetics	surface diffusion
Typical surface diffusion $L_s$ length ( $\mu$ m)	5–50	?	5–10	?	1–5	1–5

$C_i$ , concentration of rate-limiting species;  $J_i$ , impinging flux of rate-limiting species on substrate;  $J_e$ , exiting flux of rate-limiting species desorbed from substrate;  $J_{net}$ , net flux providing growth rate; TMG, trimethylgallium Ga(CH<sub>3</sub>)<sub>3</sub>.

<sup>a</sup>For references see Table 12.3.

extensively developed for GaAs-based materials, thus enabling a fairer comparison of the different epitaxy techniques. The data are culled from various published reports over a 20 year period, and so in some cases may not represent the true state-of-the-art. For some aspects of epitaxy, the information for a systematic comparison between different techniques is lacking. Likewise, it is generally true that epitaxy techniques can be modified and adapted to perform over and above their usual performance specifications. For instance, although the growth of quantum wells and superlattices with conventional LPE is often deemed unpractical, there are numerous clever apparatuses involving slideboats with rapid slidebar action and centrifugal/rapid rotation LPE systems that can grow structures with layer thickness control approaching that of MBE or MOCVD. Similarly, although traditional MOCVD of III-V employs highly toxic precursors, there are alternative precursors and growth chemistries, as well as methods for *in situ* generation of precursors,

**Table 12.3** Rational basis for selecting an epitaxial growth method

objective	controlling characteristic/requirement	LPE (Ga-rich melt)	LPE (Bi-rich melt)	CSVT	CI-CVD	MOCVD	MBE
Heteroepitaxy (>1% lattice mismatch)	$\Delta G \ll 0$	poor	poor	limited	fair	good	good
Selective epitaxy	$\Delta G \approx 0$ ; high $L_s$	excellent	excellent	good	possible	difficult	no
Defect control	$\Delta G \approx 0$ ; low growth $T$ ; control chemical potentials for optimum V/III ratio	good	good	unknown	acceptable	acceptable	acceptable
High growth rates	Large $J_i - J_e$ ; $D_S N_S / J_S > 1$	yes	fair	yes	moderate	no	no
Thickness control	$J_i \approx 0$	poor	better	modest	good	excellent	excellent
Composition control	$\Delta G \ll 0$ ; low $J_i, J_e$	limited	limited	limited	good	excellent	excellent
Metastable alloys	$\Delta G \ll 0$	no	no	no	no	yes	yes
Faceting, shaped growth	favorable surface energies; $\Delta G \approx 0$	typical	typical	no	no	no	no
Anisotropic, high-aspect lateral overgrowth	$\Delta G \ll 0$ ; high $L_s$ ; anisotropic $\gamma$	excellent	excellent	modest	modest	very modest	generally small

*References*

- M.G. Astles (1990) *Liquid-phase Epitaxy and Phase Diagrams for Compound Semiconductor Materials and their Device Applications*. Adam Hilger, Bristol.
- J.D. Grange and D.K. Wickenden (1985) Comparison and critique of the epitaxial growth technologies in *The Technology and Physics of Molecular Beam Epitaxy*, E.H.C. Parker, ed. Plenum, New York, Ch. 17.
- D.T.J. Hurlle (1999) A comprehensive thermodynamic analysis of native point defect and dopant solubilities in gallium arsenide. *J. Appl. Phys.* **85**, 6957–7022.
- T. Isu, M. Hata, Y. Morishita, Y. Nomura and Y. Katayama (1991) Surface diffusion length during MBE and MOMBE measured from distribution of growth rates. *J. Cryst. Growth* **115**, 423–427.
- M. Kasu, H. Saito and T. Fukui (1991) Step density dependence of growth rate on vicinal surface of MOCVD. *J. Cryst. Growth* **115**, 406–410.
- E. Kuphal (1991) Liquid phase epitaxy. *Appl. Phys. A* **52**, 380–409.
- M. Lopez and Y. Nomura (1995) Surface diffusion length of Ga atoms in molecular-beam epitaxy on GaAs(100)-(110) facet structures. *J. Cryst. Growth* **150**, 68–72.
- T. Nishinaga (2005) Understanding of crystal growth mechanisms through experimental studies of semiconductor epitaxy. *J. Cryst. Growth* **275**, 19–28.
- T. Nishinaga, T. Shitara, K. Mochizuki and K.I. Choi (1990) Surface diffusion and related phenomena in MBE growth of III-V compounds. *J. Cryst. Growth* **99**, 482–490.

**Table 12.3** (continued)

- 
- T. Nishinaga and T. Suzuki (1991) The role of step kinetics in MBE of compound semiconductors. *J. Cryst. Growth* **115**, 398–405.
- T. Nishinaga and T. Suzuki (1993) Towards understanding the growth mechanism of III-V semiconductors on an atomic scale. *J. Cryst. Growth* **128**, 37–43.
- G.B. Stringfellow (1989) *Organometallic Vapor Phase Epitaxy: Theory and Practice*. Academic Press, New York.
- G.B. Stringfellow (1991) Fundamental aspects of vapor growth and epitaxy. *J. Cryst. Growth* **115**, 1–11.
- M. Tanaka, T. Suzuki and T. Nishinaga (1991) Surface diffusion of Al and Ga atoms on GaAs (001) and (111)B vicinal surfaces in molecular beam epitaxy. *J. Cryst. Growth* **111**, 168–172.
- H. Watanabe, T. Mizutani and A. Usui (1990) Fundamentals of epitaxial growth and atomic layer epitaxy in *Very High Speed Integrated Circuits: Heterostructures*, T. Ikoma, ed. Academic Press, Boston, 1–52.
- C.E.C. Wood (1982) Molecular beam epitaxy for microwave field effect transistors in *GaAs FET Principles and Technology*, J.V. DiLorenzo and D.D. Khandelwal, eds. Artech, Boston, 111.

that greatly reduce the potential safety hazards of MOCVD. Further, enhancing the performance of a particular epitaxy technology with regard to one set of specifications is often achieved at the expense of other performance benchmarks. For example, systems designed for low-temperature growth may pay a penalty in growth rates and throughput. To complicate matters further, there are hybrid approaches to device technology that utilize different methods of epitaxy in various stages of device fabrication (e.g. CVD followed by LPE or vice versa), or use methods that combine features of traditionally distinct epitaxy techniques, such as, for example, metal-organic MBE or vapor–liquid–solid (VLS) processes.

Table 12.2 provides a more fundamental comparison of epitaxy techniques, based on thermodynamics, kinetics and surface energetics. Two types of GaAs LPE are considered. In the original and usual implementation, GaAs is grown from a gallium-rich melt saturated with arsenic. A later developed variation of GaAs LPE uses a bismuth-rich solvent in which case both gallium and arsenic are relatively dilute, and the ratio of Ga to As (and their respective chemical potentials) can be varied (Ratuszek *et al.*, 1987; Helak *et al.*, 1991). Bismuth is a ‘neutral’ solvent for GaAs LPE as it has a low concentration (~0.01 %) in GaAs and appears to be largely electrically ‘inactive’ (Yakusheva *et al.*, 1989). Table 12.2 also includes the close-spaced vapor transport (CSV) technique (Nicoll, 1963; Robinson, 1963; Perrier *et al.*, 1988), a near-equilibrium vapor phase epitaxy (VPE) method where a GaAs source is placed in close proximity (< 1–5 mm) to a GaAs substrate and wherein the GaAs source is maintained at a slightly higher temperature. Oxidizing agents (such as water vapor) create volatile Ga- and As-containing species which diffuse to the substrate and combine to form GaAs. On the basis of thermodynamics, particularly the relatively small free energy changes driving the growth process, and growth rates in the range of 0.1–1  $\mu\text{m min}^{-1}$ , CSV is the VPE method that is most similar to LPE, and therefore provides an interesting point of reference for comparison with LPE, along with more conventional CVD processes. Two other VPE techniques, chloride CVD using  $\text{GaCl}_3$  as a precursor for Ga and MOCVD using trimethylgallium and arsine as precursors, are also included for comparison, as well as MBE. Altogether, these methods are representative of the commercially important alternatives to conventional LPE and span the wide range of parameters, characteristic features and physical phenomena that are encompassed by epitaxial growth processes.

As indicated in Table 12.2, LPE can be distinguished from the other techniques on the basis of several criteria. Most prominently, LPE differs from most other epitaxy methods with regard to the thermodynamic driving force, as manifested by the degree of supercooling used to initiate and sustain growth, or analogously, the degree of supersaturation, or associated free energy change of the chemical reactions responsible for crystal growth. The near-equilibrium growth conditions of conventional LPE have definite benefits in some respects as discussed below, but also prevent or hinder the growth of metastable or strained epitaxial structures. Thus, it is generally difficult to grow heterostructures with high lattice mismatch or large miscibility gaps by LPE. As a consequence, 'lattice-pulling' or 'lattice latching' effects ensure close lattice matching of LPE-grown alloys to the binary substrates, which may be an advantage or disadvantage depending on the application. In many instances substrate-induced stabilization can permit the LPE growth of alloys with miscibility gaps (Quillec *et al.*, 1983). For example, thermodynamic analysis indicates the bulk InGaAsP alloy should not be stable at growth temperatures used for LPE, due to a miscibility gap, yet its lattice-matched growth on an InP substrate stabilizes the alloy, avoiding decomposition of the epilayer into separate phases. Although LPE is normally performed close to thermodynamic equilibrium with small supercoolings ( $\Delta T \sim 1-10$  °C) or slow cooling rates ( $0.1-1$  °C min<sup>-1</sup>), higher cooling rates ( $\sim 10$  °C min<sup>-1</sup>) (Hanke *et al.*, 2005) or quenching ( $10^2-10^3$  °C s<sup>-1</sup>) (Abramov *et al.*, 1991, 1994, 1996, 1997, 1999) can produce highly nonequilibrium conditions that drastically alter the growth characteristics of LPE and can be used to overcome strain energy impediments to growth.

LPE also differs from most other epitaxy techniques with regard to the rate-limiting species that controls growth rates (As versus Ga), the concentration  $C_i$  of rate-limiting species at the growth interface, the fluxes of the rate-limiting species incident or impinging on the growing crystal surface ( $J_i$ ) and leading to adsorption of adatoms, and the flux of rate-limiting species exiting (i.e. desorption) from the growing crystal ( $J_e$ ) (Watanabe *et al.*, 1990). For some methods of epitaxy, the relation between fluxes and crystal growth rates is more commonly described in terms of sticking coefficients for the species compromising the epitaxial layer.

As mentioned LPE operates with considerable smaller free energy differences than MOCVD or MBE, i.e. with a small thermodynamic driving force. In conventional GaAs LPE, the rate-limiting species is arsenic and the V/III ratio of fluxes is less than 1, in contradistinction to most vapor phase methods which exhibit a high V/III ratio, as growth occurs under excess arsenic conditions. As will be discussed, this can have considerable consequences with respect to the formation of point defects related to nonstoichiometry. Also, the concentration  $C_i$  of rate-limiting species and the incident flux  $J_i$  at the growth interface is much higher with LPE, and further, there is a 'two-way' traffic of rate limiting species with LPE in that the  $J_i \approx J_e$ . Thus, in LPE the net growth rate is the result of a difference between two relatively large and almost equal but opposing fluxes, typical of the dynamic nature of near-equilibrium processes. In contrast, in MOCVD or MBE, the growth rate is due almost entirely to a much smaller flux of the rate-limiting species (usually a group III atom or precursor) incident on the surface; the flux of desorbed atoms of the rate-limiting species is comparatively small, if not negligible. Another consequence of the differences in V/III ratio among the various epitaxy methods is the degree of sublattice ordering in III-V ternary and quaternary alloys. For example, in LPE-grown InGaAs, the indium and gallium atoms are randomly arranged on the group III sublattice,

while in MOCVD-grown InGaP the indium and gallium atoms often show CuPt-B type ordering (Prutskij *et al.*, 2003, 2005). This sublattice ordering results in a reduction in bandgap (50–100 meV), as readily detected by comparing photoluminescence spectra of LPE- and MOCVD-grown material, as well as valence band splitting. Sublattice ordering in III-V alloys appears to be restricted to materials grown with high V/III ratio (MOCVD, MBE, chloride VPE), and there is no report of CuPt-B ordering in III-V alloys grown by LPE (Suzuki, 2002).

Other differences in epitaxy methods can be cited. The surface energies of the crystal in contact with a melt interface as in LPE are about half that of a crystal in vacuum or a vapor ambient as in MBE or CVD. The surface diffusion length  $L_S$  represents the average or characteristic distance an adatom (an atom adsorbed on the growing crystal surface) of the rate-limiting species migrates before either desorbing or being incorporated into the growing crystal at a step or kink on the crystal surface. The adatom surface diffusion length  $L_S$  is related to the adatom residence or dwell time  $\tau$ , adatom surface diffusivity  $D_S$  and adatom surface mobility  $\mu_S$  by  $L_S = (D_S \cdot \tau)^{1/2}$ , where  $D_S$  is proportional to the adatom surface mobility. Surface diffusion length data are limited, as measurements are difficult and depend on growth conditions and the exact crystallographic orientation of the substrate which affects the step density and adsorption binding energy. Surface diffusion lengths in epitaxy are often inferred from indirect evidence, but test structures using structured and/or masked substrates can provide revealing experimental data (Nishinaga, 2005). For the most part, surface diffusion lengths seem to be  $\sim 10$  times larger in LPE than in VPE or MBE. Actually, it appears that while surface diffusion is the rate-limiting process in MBE and CVD, in LPE the rate-limiting step is bulk (in the melt) diffusion of solute directly to the growth step (Nishinaga and Suzuki, 1993), and this too constitutes another major distinction between LPE and other epitaxy techniques. These considerations are generalizations, and there may well be common or contrived situations that provide exceptions to these observations. For example, the addition of surfactant components to the epitaxy system can substantially alter the surface energies and surface diffusion lengths. Surfactants (e.g. bismuth and antimony) have been utilized in GaAs and silicon MBE and CVD to alter surface energetics and surface diffusion of adatoms, as well as the mode of growth (two-dimensional versus three-dimensional) (Copel *et al.*, 1990; Kern and Muller, 1995; Kandel and Kaxiras, 2000; Wixom *et al.*, 2004). Surface energies, and specifically the crystallographic orientation dependence of surface energies, play a large role in the habit of grown crystals. In metallic solution growth of silicon and III-V compounds, impurities added to melts can alter the surface energetics and crystal morphology (Faust *et al.*, 1968; Faust, 1969). As a more specific example, Zhang *et al.* (Zhang *et al.*, 2005) observed that the addition of Te impurities in selective LPE of GaSb stabilized certain crystal facets, substantially altering the morphology of the GaSb crystals.

The relatively high surface mobility of adatoms characteristic of LPE results in pronounced microscopic lateral growth rates (Bauser and Strunk, 1984; Kuphal, 1991), and significant growth rate anisotropy (Chand *et al.*, 1983). This is manifested in techniques used to planarize surfaces that are intentionally structured with grooves, mesas or notches. A surface etched with 4  $\mu\text{m}$  deep grooves in a (100) GaAs substrate can be completely planarized by an LPE step (Kuphal, 1991), a process commonly used in making buried heterostructure lasers (Botez *et al.*, 1976; Botez, 1984; Watanabe *et al.*, 1985). [It is

almost impossible to produce such structures using any of the other common epitaxial growth techniques' (Keuch and Tischler, 1996).] Conversely, the anisotropic growth characteristics of LPE can also produce highly faceted crystal shapes, especially on partially masked substrates (Oyama *et al.*, 2005). See Sections 12.5.5 and 2.5.16.

For many semiconductors, LPE yields material of the highest quality with respect to carrier mobility, minority carrier recombination lifetime, and luminescence efficiency. The distinction between high minority lifetime and luminescence efficiency is worth mentioning, since although closely related they do not necessarily track each other. Luminescence efficiency or internal quantum efficiency is the fraction of injected minority carriers that recombine radiatively and contribute to light emission. This figure of merit is important for LEDs and laser applications, and for solar cells and photodetectors that rely on photon recycling effects (Miller *et al.*, 1994). The radiative minority carrier lifetime ( $\tau_{\text{rad}}$ ) and the nonradiative minority carrier lifetime ( $\tau_{\text{nr}}$ ), the latter accounting for recombination due to bulk and surface defects, impurities, and Auger recombination, both contribute to the effective minority carrier lifetime  $\tau_{\text{eff}}$ :

$$\frac{1}{\tau_{\text{eff}}} = \frac{1}{\tau_{\text{rad}}} + \frac{1}{\tau_{\text{nr}}} \quad \text{or} \quad \tau_{\text{eff}} = \frac{\tau_{\text{rad}} \cdot \tau_{\text{nr}}}{\tau_{\text{rad}} + \tau_{\text{nr}}}$$

To achieve a high effective minority carrier lifetime  $\tau_{\text{eff}}$ , as useful for solar cells and bipolar transistors, *both*  $\tau_{\text{rad}}$  and  $\tau_{\text{nr}}$  must be large. For a high internal quantum efficiency  $\eta_i$ , as needed for LEDs,  $\tau_{\text{nr}} \gg \tau_r$ , which does not necessitate high values of either lifetime, only that nonradiative recombination lifetime is much greater than the radiative recombination lifetime, since:

$$\eta_i = \frac{\tau_{\text{rad}}}{\tau_{\text{rad}} + \tau_{\text{nr}}}$$

The radiative and nonradiative recombination depend on doping, impurity, and defect concentrations, injection levels, and proximity of surfaces (Bergh and Dean, 1976). Thus, definitive statements about the merits of one epitaxy technique over another with regard to material quality cannot easily be made. Several systematic comparisons of semiconductor transport and minority carrier recombination characteristics for epitaxial material produced by various methods have been reported, but unfortunately, many of these studies are somewhat dated. Pearsall *et al.* (Pearsall *et al.*, 1981) concluded that the electron and hole mobilities in  $\text{In}_{0.53}\text{As}_{0.47}\text{As}$  epilayers lattice matched to InP, grown by LPE, MOCVD and CVD, are in general quite similar. Colomb *et al.* (Colomb *et al.*, 1992) noted that electron mobilities in LPE-grown GaAs were higher than those of carbon-doped MOCVD-grown GaAs. Ahrenkel and Dunlavy (Ahrenkel and Dunlavy, 1989) observed that the minority carrier lifetimes in  $\text{Al}_{0.4}\text{Ga}_{0.6}\text{As}$  were appreciably larger in LPE material than in MOCVD material. Butcher *et al.* (Butcher *et al.*, 1995) grew thick ( $>200 \mu\text{m}$ ) GaAs layers in an LPE system with a fused silica boat and where silicon doping of the layer was moderated by careful control of oxygen levels in the hydrogen ambient. Room-temperature minority carrier diffusion lengths of between  $200 \mu\text{m}$  and  $800 \mu\text{m}$  were measured in *n*-type material with a carrier concentration  $10^{13}$ – $10^{14} \text{cm}^{-3}$ . These diffusion length values are much higher than usually observed with for GaAs. Fisher and Krier (Fisher and Krier, 1997) compared the photoluminescence of InAs grown by LPE, MOCVD and MBE and reported that the strongest emission is obtained from LPE material, and that LPE-grown samples did



not exhibit the excitonic recombination seen with MOCVD and MBE material. Moiseev *et al.* (Moiseev *et al.*, 2002) achieved the first-ever observation of room temperature mid-infrared photoluminescence in GaInAsSb quaternaries made by LPE. This III-V quaternary alloy is of interest for mid-infrared detectors, LEDs, lasers and thermovoltaic devices, and for which all three major epitaxy methods (LPE, MOCVD and MBE) are used. Some recent work on GaAs BIB (blocked impurity band) far-infrared detectors, in which the reduction of background doping is crucial to device operation, serves to demonstrate the potential of LPE for producing material with low levels of impurities (Haller and Beeman, 2002; Reichertz *et al.*, 2004, 2005, 2006; Cardoza *et al.*, 2005). LPE-grown GaAs with net donor levels  $|N_D - N_A| \leq 10^{12} \text{ cm}^{-3}$ , where  $N_D$  is the donor concentration and  $N_A$  is the acceptor concentration, was achieved. Similar efforts have been directed toward LPE-grown Ge blocked impurity band (BIB) detectors (Goyal *et al.*, 2002).

The high quality of LPE-grown GaAs (and related III-V materials) may be attributed to several factors (Stringfellow, 1989). The Ga-rich melt yields GaAs with a Ga-rich stoichiometry (in contrast to CVD and MBE), and thus Ga vacancies and As antisite defects (As atoms on the Ga sites) are virtually absent. The As antisite defect has been implicated in deep bandgap recombination states that degrade luminescence efficiency [see Hurlle (Hurlle, 1999) for more elaboration on this complicated phenomenon]. Also, the high purity of metal solvents and the preferential segregation of impurities to the liquid phase results in material with low background concentrations of impurities. For AlGaAs LPE, the aluminum melt component forms an insoluble oxide on the melt surface, thus reducing oxygen contamination of the AlGaAs epilayer. The near-equilibrium growth conditions of LPE result in an insufficient thermodynamic driving force for nucleating defects such as dislocations and stacking faults. Among epitaxy techniques, LPE is unique in that the structural quality of the epilayer can exceed that of the substrate on which it is seeded. In particular, LPE exhibits a tendency to 'anneal out' dislocations originating in the substrate. Thus, the epitaxial layer has a lower density of dislocations than that of the underlying substrate (Saul, 1971).

LPE melt compositions can be modified to appreciably change growth characteristics and electrical properties of the epilayer. As already mentioned, GaAs is commonly grown from Ga-rich solutions according to the Ga-As binary phase diagram. GaAs can also be grown from multicomponent, arsenic-saturated melts containing, for example, gallium, lead, bismuth, and tin. GaAs LPE with a bismuth-rich solvent, i.e. a Bi-Ga melt saturated with arsenic wherein the Ga:As ratio can be independently adjusted, adds an additional degree of freedom to the growth process (Shmartsev, 1991; Yakusheva and Pogadaev, 1992). With respect to at least several characteristics, GaAs LPE from Bi-rich melts can be made to mimic those of vapor phase methods (Saravanan *et al.*, 1997). For example, GaAs can be grown under conditions where Ga is diluted with bismuth, thus modifying the relative chemical potentials of As and Ga, changing the V/III ratio to As-rich conditions, and making Ga, instead of As, the rate-limiting species. The use of multicomponent melts to alter growth characteristics (nucleation and growth modes, growth rates, rates, faceting, surface energetics) or epilayer properties (point defects, doping characteristics) is an under-exploited area of LPE technology. Another avenue for manipulating material properties in LPE is through control of the vapor pressure of components in the melt and epilayer (Nishizawa and Okuno, 1975; Nishizawa *et al.*, 1975).

The thermodynamic and kinetic characteristics of epitaxy methods as presented in Table 12.2 determine the ability of an epitaxy technique to perform certain tasks.

Table 12.3 lists some typical specific objectives for epitaxial growth processes including: heteroepitaxy with large lattice mismatch or strain; selective epitaxy on patterned, masked substrates; control and avoidance of certain types of defects; achievement of high growth rates; layer thickness and/or composition control; realization of abrupt or sharp interfaces; the growth of metastable compounds and alloys; faceting of crystals for shaped crystal growth; and anisotropic growth characteristics in order to achieve high aspect ratios in epitaxial lateral overgrowth. The feasibility or difficulty in achieving a specific objective (Table 12.3, column 1) is often controlled or dominated by a particular growth characteristic (Table 12.3, column 2), such as the departure from thermodynamic equilibrium ( $\Delta G$ ), magnitude of fluxes,  $J_i$ , or surface diffusion lengths  $L_s$ . For instance, a low thermodynamic driving force, as exhibited by LPE or CSVT, facilitates better control of nucleation which is necessary for selective modes of growth on patterned, masked substrates. The low thermodynamic driving force may also help avoid the nucleation of nonequilibrium defects such as stacking faults and dislocations. On the other hand, high thermodynamic driving forces, as exhibited by MOCVD and MBE, are useful for heteroepitaxial growth where there is an energetic barrier due to strain or lattice mismatch that inhibits nucleation of the epitaxial layer. As already mentioned, in LPE, the composition of the epilayer is determined by phase equilibria considerations, whereas in MBE and CVD, the composition of the epilayer is controlled by the fluxes or precursors impinging the substrate, the relative values are not determined by thermodynamic considerations. Thus, there is more freedom for composition control with MBE or MOCVD, including the growth of metastable alloys.

Tables 12.2 and 12.3 suggest a rational basis for selection of an epitaxy process, namely, by recognizing the required characteristics or features needed to achieve a specified objective, along with the relevant corresponding characteristics exhibited by the various epitaxy methods. On this basis, a case can be made that for certain tasks LPE is the best choice due to inherent features and advantages relative to other competing methods of epitaxy. Further, the foregoing discussion points to what features of LPE are responsible for its limitations and suggests what, if any, modifications in conventional LPE techniques might widen its application or improve its performance.

To underscore some of the relative or unique advantages of LPE for the growth of semiconductor devices, a few of the more important features of LPE may be summarized as:

1. High LPE growth rates. Growth rates in the range of  $0.1\text{--}1\ \mu\text{m min}^{-1}$  can be achieved with LPE. This is 10–100 times faster than MBE or MOCVD, and thus thick device structures for epitaxial (e.g. thick ‘transparent’ AlGaAs) substrates and compositionally graded transition layers, as useful in virtual epitaxial substrates with tunable lattice constants and bandgaps, are feasible with LPE.
2. Flexibility. An LPE system can be readily adapted for the growth of a wide assortment of materials, usually simply by changing the melt and program ‘recipes’.
3. The wide range of dopants available with LPE. Virtually any element added to the melt will be incorporated into the epitaxial layer to some degree. The segregation of an impurity can be readily determined experimentally for controlled doping. This can be contrasted with other methods of epitaxy where precursors must be developed with compatible pyrolysis kinetics, or where dopants with favorable sticking coefficients

must be identified. Most of the entire periodic table can be utilized as dopants in LPE, and thus, LPE is an excellent tool for fundamental doping studies.

4. The preferential segregation of deleterious impurities to the liquid phase which results in low background impurities in the epitaxial layer. LPE can produce semiconductor material of extremely high purity.
5. The low defect densities due to near-equilibrium growth conditions and/or favorable chemical potentials of crystal components in the liquid phase, along with reductions in threading dislocations originating in the substrate or underlying layers.
6. The absence of highly toxic precursors or by-products.
7. Low capital equipment and operating costs.
8. The feasibility of selective epitaxy and epitaxial lateral overgrowth (ELO) with high aspect ratios.
9. The ability to produce shaped or faceted crystals for novel device structures.

To close the discussion comparing LPE with competing epitaxy methods, another aspect of crystal growth that serves to contrast LPE with other epitaxy technologies is illustrated by Figure 12.1. Crystal growth processes in general, and epitaxy methods in particular, are controlled by various process parameters such as temperature, pressure, precursor or solute concentrations, and are sensitive to other parameters such as substrate orientation and surface cleanliness. Not surprisingly, there are optimum ranges—or at least minimum requirements—for all of these parameters to ensure successful epitaxial growth and achieve sufficient material quality. In reality, the parameter space for epitaxy is multidimensional and there are uncontrolled variables that impact growth as well. Generally CVD has more experimental parameters than LPE, but the operating range for these parameters is fairly broad. With phase diagram in hand, it is straightforward to formulate an LPE process for an untried material, but it is fair to say that the ‘window’ for LPE growth is much narrower than other epitaxy technologies as suggested by Figure 12.1. Thus, LPE is less forgiving of process variations than other methods and more susceptible to process fluctuations and the effects of uncontrolled variables, both of which can lead to failed growth or poor material quality. In some cases, such as the LPE growth of InGaAsSb quaternary alloys, the growth temperature must be controlled to within 1 °C in order to produce an epitaxial layer. As another example, LPE appears to be much more sensitive

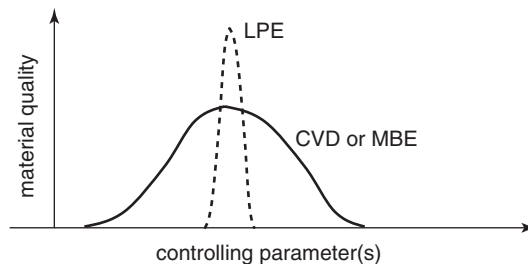


**Figure 12.1** Schematic of ‘process window’ and sensitivity of material quality to controlling parameters and variables

to the crystallographic (mis)orientation of the substrate than other epitaxy techniques. On the other hand, and on the positive side, when the LPE process *is* operated within its optimum parameter window, the material quality is often superior to that produced by other epitaxy techniques. Thus, the price for high material quality associated with LPE is more stringent demands on process control and greater susceptibility to process variations. Ultimately, this feature may be attributed in large part to the near-equilibrium nature of LPE that distinguishes it from CVD and LPE. Practitioners of epitaxy may regard this view as overly simplistic, but it offers some explanation to both the historic role of LPE in prototyping new semiconductor materials and device concepts, and to its ultimate disfavor for large-scale, high-throughput production of many commercial semiconductor devices, especially those with tight tolerances for composition, doping, and layer thicknesses.

### 12.3 PREVIOUS REVIEWS OF LPE

Besides complementing other chapters of this book, the present chapter is intended to supplement some of the previous reviews of LPE that have appeared in various articles, book chapters and monographs (Dawson, 1972; Giess and Ghez, 1975; Bergh and Dean, 1976; Kressell and Butler, 1977; Casey and Panish, 1978; Hollan *et al.*, 1980; Hsieh, 1980; Moon, 1980; Ufimtsev and Akchurin, 1983; Nakajima, 1985 (focused on InGaAsP LPE but applicable to LPE of other III-V semiconductors); Yamazaki *et al.*, 1984 (focused on InGaAs/InP avalanche photodiodes); Greene, 1987; Anderson, 1989; Astles, 1990; Kuphal, 1991; Swaminathan and Macrander, 1991; Small *et al.*, 1994; Bauser, 1996; Iga and Kinoshita, 1996; Konuma, 2002). In addition, numerous books (Brice, 1965, 1973, 1985; Laudise, 1970; Hartman, 1973; Elwell and Schell, 1975; Rosenberger, 1979; Pamplin, 1980; Chernov, 1984; Tiller, 1991, 1992; Hurle, 1994; Herman, *et al.* 2004; Dost and Lent, 2006) provide discussions of LPE and related solution growth methods from a wider perspective of crystal growth and epitaxy processes in general. Zschauer and Vogel (Zschauer and Vogel, 1971) describe a melt-solid Schottky barrier model to explain the growth rate and crystal orientation dependence of doping in GaAs LPE. Hurle (Hurle, 1999) has made an in-depth review and discussion of native point defects and doping solubilities in LPE-grown III-V materials. Treatments of nucleation and growth mechanisms in LPE (Hsieh, 1974; Kozlov *et al.*, 1975; Mattes, 1975; Bauser and Strunk, 1982, 1984; Bauser, 1985a, 1994; Konuma, 2002), surface morphology (Saul and Roccasecca, 1973; Toyoda *et al.*, 1979) and morphological stability, i.e. formation of surface ripples and waves (Bauser, 1978; Nishinaga *et al.*, 1978), and physical processes in LPE (Small and Crossley, 1974) focus on more specific aspects.

### 12.4 MODELING OF LPE PROCESSES

Modeling and simulation of LPE is useful for better understanding of the processes and mechanisms of epitaxial growth, assessing the importance of process parameters and variables on the growth characteristics, and design of the slideboat or other crucible apparatus. Especially important is the role of melt convection and solute distribution on the epilayer surface and areal uniformity with respect to thickness, composition, and impurity concentrations. In addition to modeling and simulation of the growth process, there is a considerable amount of literature on phase equilibria models pertinent to LPE. The

application of *regular* or *quasi-regular* solution models to LPE is treated in Panish (Panish, 1973), Casey and Panish (Casey and Panish, 1978), Stringfellow (Stringfellow, 1984), Tmar *et al.* (Tmar *et al.*, 1984) and Anderson (Anderson, 1989). *Associated* and *associated regular* solution models for melts that contain antimony or bismuth (which show anomalous behavior according to simple regular solution models) have been developed by Jordan (Jordan, 1976), Brebrick *et al.* (Brebrick *et al.*, 1983), and Schmid and Chang (Schmid and Chang, 1985). Another approach to modeling multicomponent phase equilibria for LPE is based on an analysis of excess thermodynamic functions and linear combination of chemical potentials (EF-LCP) (Baranov *et al.*, 1991; Kunitzva *et al.*, 1998). Strain energy effects due to lattice mismatch can be readily included in phase equilibria calculations (Baranov *et al.*, 1984; Larche and Cahn, 1987; Ohtani *et al.*, 2001). Dependence of phase equilibria on the crystallographic orientation of the substrate, as observed in many LPE-grown III-V alloys such as InGaAs (Pearsall *et al.*, 1979), is treated by Srinivasa and Bhattacharya (Srinivasa and Bhattacharya, 1985). For LPE of alloy semiconductors, the phase equilibria models can be used for prediction of miscibility gaps (Ishida *et al.*, 1989). Wei *et al.* (Wei *et al.*, 1995) described an artificial neural network approach to predicting phase equilibria in III-V quaternary alloys grown by LPE. Relevant solution phase equilibria models and data routinely appear in several journals including *CALPHAD*, *J. Phase Equilibria and Diffusion*, and *Bulletin of Alloy Phase Diagrams*.

LPE kinetics is analyzed by Crossley and Small (Crossley and Small, 1971), Hsieh (Hsieh, 1974), Bryskiewicz (Bryskiewicz 1978) and Krier and Labadi (Krier and Labadi, 2000). Diffusion-limited LPE growth of ternary alloys (e.g. LPE of InGaAs on InP) is treated by Ijuin and Gonda (Ijuin and Gonda, 1976), Joullié (Joullié, 1977), Traeger *et al.* (Traeger *et al.*, 1988), Kimura *et al.* (Kimura *et al.*, 1996a), Rezagholipour Dizaji and Dhanasekaran (Rezagholipour Dizaji and Dhanasekaran, 1996a,b), and Asomoza *et al.* (Asomoza *et al.*, 2001). Charykov *et al.* (Charykov *et al.*, 2002) present a general theory of multi-phase melt crystallization that includes solvent evaporation. Convection in LPE systems is analyzed by Kimura *et al.* (Kimura *et al.*, 1991, 1994) and Coşkun *et al.* (Coşkun *et al.*, 2002). Kimura *et al.* (Kimura *et al.*, 1994, 1996a) developed a time-dependent, two-dimensional model of LPE including convective and diffusive transport and interface kinetics. Other models of LPE including convection phenomena have been published (Qin *et al.*, 1996; Denisov *et al.*, 2004). Simulation of the growth rate and layer thickness for LPE under slider-induced convection is given by Leung and Schumaker (Leung and Schumaker, 1982), Chen and Wan (Chen and Wan, 1992) and Chao and Wang (Chao and Wang, 1993). Global numerical simulations including the temperature profile of the furnace for MCT (mercury cadmium telluride) LPE are reported by Lin *et al.* (Lin *et al.*, 2005). Several models of LPE combining three-dimensional mass and heat transport and a microscopic (Burton–Cabrera–Frank) model of crystal growth are developed by Eck and Emmerich (Eck and Emmerich, 2004). Inatomi and Kuribayashi (Inatomi and Kuribayashi, 2002) describe an analysis of morphological stability for GaP LPE in a static magnetic field.

## 12.5 SURVEY OF NEW DEVELOPMENTS AND SPECIALIZED APPLICATIONS OF LPE

The following sections survey some recent developments and subjects of focused efforts in LPE, as well as areas where LPE has unique capabilities or relative advantages over

competing methods of epitaxy. Also reviewed are novel adaptations or modifications of the LPE technique to address or circumvent limitations of conventional LPE technology, including specific innovations that may have not received wide attention for possibly broader application to LPE. The citations are included to provide the reader with literature sources for more detailed descriptions or other applications of the techniques discussed: the citations are not meant to suggest priority or due credit to the true inventors or discoverers of the particular topic at hand.

### 12.5.1 Five- and six-component III-V semiconductor alloys by LPE

In contrast to the fixed bandgaps and lattice constants of binary semiconductors, ternary III-V alloys, such as  $\text{Al}_x\text{Ga}_{1-x}\text{As}$ ,  $\text{In}_x\text{Ga}_{1-x}\text{P}$  and  $\text{InAs}_x\text{Sb}_{1-x}$ , permit adjustment of the bandgap and lattice constant. However, with the exception of  $\text{Al}_x\text{Ga}_{1-x}\text{As}$ , the lattice constant of the epilayer is generally mismatched to its binary substrate except for a single composition and corresponding bandgap. Quaternary alloys, such as  $\text{In}_x\text{Ga}_{1-x}\text{As}_y\text{Sb}_{1-y}$  or  $\text{Al}_x\text{Ga}_y\text{In}_{1-x-y}\text{P}$ , have an additional degree of freedom, and thus afford independent tuning of lattice constant and bandgap over a limited range. Nevertheless, constraints imposed by lattice matching to a binary substrate, as well as by possible miscibility gaps, still generally preclude many compositions (and bandgaps) for the epilayer. The use of (ternary) alloy substrates (see Section 12.5.4) provides a range of continuously variable lattice constants which can prove useful in maintaining lattice matching for the epitaxial layer(s) over a range of compositions and bandgaps.

Semiconductor alloys with *five* or more components would offer additional degrees of freedom, potentially avoiding miscibility gaps and yielding a wider selection of lattice constants, and further, would permit at least some adjustment of electron affinities, heterojunction offsets, and band discontinuities (Rubtsov *et al.*, 1997). There is generally no obstacle to growing III-V alloys with five or more components by LPE, thus giving device designers with a larger selection of materials parameters for heterostructures. The same cannot always be said of MOCVD and MBE, as growth temperature ranges for optimal pyrolysis of precursors and/or adatom adsorption may not be compatible for all the constituents of an epitaxial alloy with many components. In principle, a six-component melt can be used for LPE of a III-V alloy of general composition  $\text{Al}_x\text{Ga}_y\text{In}_{1-x-y}\text{P}_u\text{As}_v\text{Sb}_{1-u-v}$ , but the required phase equilibria data for formulating the melt and specifying growth temperatures are generally lacking. Addition of 'neutral' melt components that are incorporated to a small degree in the solid-phase alloy, such as bismuth, tin, germanium and lead (Kunitsvna *et al.*, 1998), may also be useful for modifying segregation coefficients in order to achieve target epilayer compositions. Extension of quaternary phase equilibria models for five, six, or a higher number of components is straightforward. The regular solution model used to estimate liquid- and solid-phase chemical potentials can be extended to systems with higher numbers of components (Charykov *et al.*, 1997; Xu *et al.*, 1997; Vasil'ev *et al.*, 1999). Bismuth and antimony, which show *associated* regular solution behavior due to formation of complexes (Jordan, 1976; Brebrick *et al.*, 1983), may complicate liquid-phase models. Also, while it is generally assumed all components show complete miscibility in the liquid phase, this may not be the case with complex melts containing numerous components. The modeling of the solid phase is more subtle, as it is partly dependent on the details of sublattice ordering (Onda *et al.*, 1986; Ichimura and Sasaki,

1988). Nevertheless, approximate models can be used to initiate and guide experimental studies. One consolation is that as more constituents are added to the melt, the melt becomes more dilute in every component and the activities  $a_i$  of components  $i$  approach Henry's law behavior, i.e.  $a_i = K_i(T) \cdot X_i$ , thus simplifying the phase equilibria calculations and improving their accuracy. Realization of five-component III-V alloys by LPE has been reported, and include AlGaInAsSb (Mishurnyi *et al.*, 1998a, b), AlGaInPAs (Xu *et al.*, 1998), GaInAsPSb (Kuznetsov *et al.*, 2006; Vasil'ev *et al.*, 2000). Charykov *et al.* (Charykov *et al.*, 1997) and Xu *et al.* (Xu *et al.*, 1997) model the phase equilibria for LPE of five-component alloys such as InGaAsSbP. Lunin *et al.* (Lunin *et al.*, 2002) determine the conditions for temperature-gradient epitaxial growth of  $\text{Al}_x\text{Ga}_y\text{In}_{1-x-y}\text{Sb}_{1-x}\text{Bi}_z/\text{InSb}$  heterostructures.

### 12.5.2 LPE layers with atomically smooth surfaces

Chernov and Scheel (Chernov and Scheel, 1995) argue that due to the low supersaturations characteristic of LPE, LPE layers closely lattice-matched to the substrate will grow by a Frank–van der Merwe ('layer-by-layer') mechanism that results in singular surfaces with terraces (i.e. step spacings) on the order of  $10\ \mu\text{m}$ . Such quasi-atomically flat surfaces should be of interest for high-performance optoelectronic devices, as well as superconductors, substrates for superlattices, crystallographic reference planes and surface catalysis. This potential advantage of LPE may be surprising since a perceived drawback of LPE is the difficulty in achieving smooth, uniform surfaces due to the presence of macrosteps, surface ripples, and meniscus lines. These features are probably due to extrinsic effects related to poor temperature control, inadequate substrate preparation and cleaning, and melt convection effects, rather than inherent features of the LPE process. Scheel (Scheel, 1980) contends that with more careful optimization and control of growth conditions, LPE should actually be superior to other epitaxy technologies with regard to production of atomically smooth, structurally perfect epitaxial layers. Other reports corroborate this contention. Morlock *et al.* (Morlock *et al.*, 1988) and Weishart *et al.* (Weishart *et al.*, 1994) demonstrated 'ultralow densities' of monomolecular steps on growth faces of GaAs mesas grown by selective LPE. Kumar *et al.* (Kumar *et al.*, 2004) developed a LPE process for atomically flat GaSb epilayers having a root mean square roughness of less than 1 nm over a  $5 \times 5\ \mu\text{m}^2$  area. These results were obtained in a dipping-type LPE system using an etchback-regrowth technique with a long (2–4 h) isothermal growth initially supercooled by 2–4 °C. Monomolecular steps with spacings as high as 400  $\mu\text{m}$  were indicated. Maruyama *et al.* (Maruyama *et al.* 2004, 2005) reported similar results for LPE growth of Ge mesas on masked Ge substrates. This feature of LPE has not as yet been extensively pursued for device applications.

### 12.5.3 Quantum wells, superlattices and nanostructures by LPE

LPE is generally deemed poorly suited for the production of quantum well and superlattice structures because it is difficult to achieve controllable, low growth rates for reproducibly forming thin (<100 nm), uniform epitaxial layers. The problem is exacerbated in heterostructures where strain energy of lattice mismatch impedes nucleation

and two-dimensional (step flow) growth, and because disequilibrium between the substrate and melt leads to substrate dissolution and/or formation of a compositionally graded or intermediary-composition transition layer (Ghez and Small, 1981). Nevertheless, there are many reports of quantum wells and superlattices grown by LPE, as well as nanostructures such as quantum dots, and these are briefly reviewed here. Still, it is generally true the application of LPE for making these structures is limited compared with MOCVD, MBE or atomic layer epitaxy (ALE).

Woodall (Woodall, 1972) described an isothermal solution mixing LPE technique for making AlGaAs superlattices with 20 periods of 100 nm thick epilayers. Two saturated melts with differing compositions are isothermally mixed in the presence of a GaAs substrate using a rotating crucible apparatus. Thompson and Kirkby (Thompson and Kirkby, 1974) reported a six-layer AlGaAs injection laser structure made by LPE with layer thicknesses of <40 nm for GaAs and <80 nm for AlGaAs. Rotating and centrifugal-based LPE systems have been proposed for brief contact of the melt with the substrate in order to achieve thin (<50 nm) epilayers and superlattices (Kass *et al.*, 1985; Lendvay *et al.*, 1985). Rezek *et al.* (Rezek *et al.*, 1977) demonstrated LPE-grown InGaAsP double heterostructure lasers with multiple thin layer (<50 nm) active regions. Zwicknagl *et al.* (Zwicknagl *et al.*, 1984) achieved *p-n-p-n* doped GaAs superlattices with periods as small as 50 nm using LPE. Aitieva *et al.* (Aitieva *et al.*, 1986) have studied the growth stages and evolution of epitaxial growth in the LPE of ultrathin GaAs layers on AlGaAs. Bantien *et al.* (Bantien *et al.*, 1987) reported LPE-grown AlGaAs/GaAs quantum wells with smooth interfaces as evidenced by photoluminescence (PL) emission widths of 2.5 meV. Kelting *et al.* (Kelting *et al.*, 1986) realized AlGaAs/GaAs single quantum wells by LPE with well thicknesses of 2.4–7 nm. Further reports of quantum confinement structures made by LPE include Lendvay *et al.* (Lendvay *et al.*, 1985) (GaAs-AlGaAs superlattices made with a rotating crucible LPE system), Golubev *et al.* (Golubev *et al.*, 1988) (LPE-grown AlGaAs/GaAs and InGaAs/InP heterostructures with two-dimensional electron gas confinement), Morlock *et al.* (Morlock *et al.*, 1991) (quantum wells with thicknesses of two to six monolayers and interfacial roughness standard deviations of 0.2 to 0.4 monolayers), Nohavica and Oswald (Nohavica and Oswald, 1995) (GaInAsP/InP quantum wells by LPE from a narrow slot into a 'meander form'), Krier *et al.* (Krier *et al.*, 1998) (2.5-nm thick InAs quantum wells by LPE using a rapid slider), and Chandvankar *et al.* (Chandvankar *et al.*, 1998) (feasibility of AlGaAs-GaAs-GaSb-AlGaSb strained-layer quantum confinement structures by LPE), Leshko *et al.* (Leshko *et al.*, 1998) (LPE-grown InGaAsP/InP multi-quantum well (3 × 60 nm) heterostructure lasers), Baoxue *et al.* (Baoxue *et al.*, 1998) (LPE growth of 10–50 nm thick InGaAsP layers) and Chandvankar *et al.* (Chandvankar *et al.*, 2004) (low-temperature LPE growth of AlGaAs strained, separately confined heterostructure lasers with 50–160 nm thick active layers and addition of P or Sb to introduce tensile or compressive strain to tune emission). Andreev *et al.*, (Andreev *et al.* 1996) used low growth temperature (400–600 °C) and a *piston* boat technique to make AlGaAs heterostructures with ultrathin (2–100 nm) layers. The above mentioned methods generally rely on either low growth temperatures to reduce growth rates, or short contact times, in order to produce very thin epilayers. Alternatively, *relaxational* LPE as described by Bessolov *et al.* (Bessolov *et al.*, 1988, 1990, 1993) and Demin (Demin, 1995) uses a second growth substrate in contact with the melt to induce reverse mass transport and relax melt supersaturation. This method can produce very thin (3.5 nm-thick GaAs) epilayers, and is purported to be applicable over a wider range of growth



temperatures, materials and contact times. Various LPE techniques for growing ultrathin layers are reviewed by Mishurnyi *et al.* (Mishurnyi *et al.*, 2006), as well as in Chapter 7.

Quantum dots can be realized in lattice-mismatched systems by taking advantage of the tendency for three-dimensional island growth due to strain energy effects. For example, Krier *et al.* (Krier *et al.*, 2001) reported the liquid phase epitaxial growth of InSb quantum dots ( $10^{10} \text{ cm}^{-2}$ , 5–15 nm height and 0.1–0.3 aspect ratios) on InAs and GaAs substrates. The same group (Krier *et al.*, 1999) has grown InAsSbP quantum dots on GaAs substrates using a rapid slider LPE technique. Hanke *et al.* (Hanke *et al.*, 2004) described LPE-grown Stranski–Krastanow islands (in the shape of truncated pyramids with dimensions on the order of 100 nm) of SiGe on silicon substrates from bismuth-silicon-germanium melts at 973 K. Sun *et al.* (Sun *et al.*, 2005) adapted LPE growth conditions to vary partial oxidation, melt undersaturation, and temperature-dependent Frank–van der Mere growth mode to achieve self-assembled island formation of AlGaAs. Meixner *et al.* (Meixner *et al.*, 2001) observed the formation of self-assembled nanoscale island chains of SiGe crystals grown on silicon by LPE. Wakayama *et al.* (Wakayama *et al.*, 1997) made self-assembled nanocomposites of silicon-gold using an LPE process starting with Au particles condensed from a gas phase on a silicon substrate.

### 12.5.4 Growth of thick ternary and quaternary alloy layers for ‘virtual’ substrates with adjustable lattice parameters

Commercially available substrates are generally limited to elemental (Si or Ge) or binary compound (e.g. GaAs, InP, SiC) semiconductor wafers sliced from melt-grown bulk crystals. For compound semiconductors, the wafers are cut from boules or ingots of the binary compounds solidified from near-stoichiometric melts, although vapor-phase growth of self-supporting substrates such as GaN and SiC is also feasible. Bulk crystal growth of compound semiconductors is mostly restricted to the congruently melting binary compounds (e.g. GaAs and GaSb) due to the severe segregation and stress effects inherent in the growth of ternary and alloy semiconductors. Commercial substrates are thus limited to a small, discrete set of lattice constants. As mentioned above, this imposes many limitations on epitaxial device technology due to lattice matching constraints and miscibility gaps. Also, for some semiconductor materials systems no lattice-matched semi-insulating substrate is available, which precludes simple electrical isolation of devices formed in the epitaxial layer(s). Further, for some applications such as high-brightness LEDs, a lattice-matched, wide-bandgap (transparent) substrate is desirable, but not available.

Customized substrates comprised of ternary and quaternary alloys with adjustable lattice constants and bandgaps would open up many new avenues for semiconductor device technology (Bryskiewicz and Laferrière, 1993). An alternative to the growth of boules or ingots is the use of LPE to grow thick ( $>50 \mu\text{m}$ ) ternary and quaternary alloys. Thick ( $>50 \mu\text{m}$ ), low-defect epitaxial layers of ternary and quaternary alloys, termed ‘virtual substrates’ by Mao and Krier (Mao and Krier, 1997), would effectively satisfy many of the applications anticipated for wafers cut from ternary and quaternary ingots.

The basic idea of epitaxial virtual substrates is to grow a thick, compositionally graded ternary or quaternary alloy layer on a binary compound substrate, or a composite structure comprised of multiple epitaxial ternary or quaternary layers with an abrupt, but small, change in lattice constant between adjacent layers. If the composition change is gradual,

for example, the alloy is compositionally graded over a thickness of about  $100\ \mu\text{m}$ , or if the lattice change at each growth interface is sufficiently small ( $<0.5\%$ ), defect generation can be suppressed (Abrahams *et al.*, 1969). Post-growth, the original seeding substrate can be removed by etching, and/or the epitaxial substrate can be bonded to a surrogate superstrate with desired optical or electrical properties. In this way, insulating substrates can be realized.

LPE-grown AlGaAs layers have been used as transparent substrates for commercial ultrabright red LEDs for many years (Ishigura *et al.*, 1983; Cook *et al.*, 1988; Steranka *et al.*, 1988). A  $200\text{--}250\ \mu\text{m}$  thick  $\text{Al}_z\text{Ga}_{1-z}\text{As}$  ( $z = 0.4\text{--}0.6$ ) is grown on a GaAs substrate by LPE. A double heterostructure AlGaAs LED structure is then grown by LPE on the thick AlGaAs layer, and the GaAs substrate is removed by selective etching. The comparatively fast growth rates of LPE make the growth of such thick epilayers feasible. In this case, the lattice matching conditions are not an issue as AlGaAs is closely lattice-matched to a GaAs seeding substrate. The achievement of epitaxial substrates with lattice constants different from binary compound substrates is of wider technological interest.

Gong *et al.* (Gong *et al.*, 1992) described the LPE growth of multigraded GaInAs layers on GaSb substrates by LPE to extend the cut-off wavelength from  $2.5\ \mu\text{m}$  (for a device based on lattice-matched layer of GaInSb to GaSb) to  $4.71\ \mu\text{m}$ . Similar approaches for InAsSb have been reported by Andrews *et al.* (Andrews *et al.*, 1976) and Gong *et al.* (Gong *et al.*, 1995). Mao and Krier (Mao and Krier, 1997) developed LPE methods to grow  $10\text{--}60\ \mu\text{m}$  thick compositionally graded ternary (InGaAs and InAsSb) and quaternary (InAsSbP) layers to provide ‘virtual substrates’ for subsequent device epitaxy. Modest lattice constant changes ( $0.2\%$ ) were achieved. For LPE of  $50\ \mu\text{m}$  thick  $\text{In}_{0.95}\text{Ga}_{0.05}\text{As}$  epilayers, very fast cooling rates ( $80\ ^\circ\text{C}\ \text{min}^{-1}$ ) could yield higher ( $0.3\%$ ) lattice constant changes, while still maintaining smooth, mirror-like surface morphology. Mikhailova *et al.* (Mikhailova *et al.*, 1997) utilized  $80\ \mu\text{m}$  thick, compositionally graded InAsSbP LPE layers on InAs substrates into which  $p\text{-}n$  junction photodiodes were formed. A sufficiently gradual compositional grading over a thickness of about  $80\ \mu\text{m}$  yields a low-defect quaternary composition with a bandgap ( $\sim 0.3\ \text{eV}$ ) that is otherwise unattainable with lattice-matched epitaxial layers (Figure 12.2). Removal of the InAs substrate would reduce parasitic absorption losses and enhance heat sinking of the device. Aidaraliev *et al.* (Aidaraliev *et al.*, 1998) reported a similar approach to make InAsSb(P) LEDs for room-temperature emission in the  $5\text{--}6\ \mu\text{m}$  wavelength range.

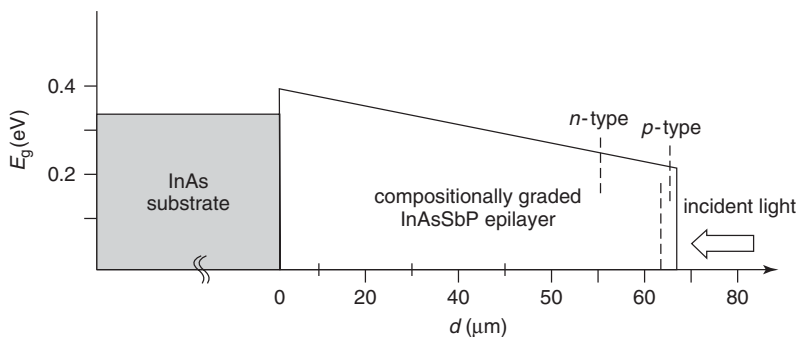


**Figure 12.2** Schematic cross-section bandgap profile of compositionally graded InAsSbP layer made by LPE. (After Mikhailova *et al.*, 1997)

By using a compositionally graded InAsSbP transition layer and growth temperatures (630–680 °C) where the InAs substrate exhibits high plasticity, dislocations were preferentially generated in the substrate rather than the epitaxial layer or mostly confined to the substrate epilayer interface, ultimately yielding  $p$ - $n$  junctions with  $<10^4 \text{ cm}^{-2}$  dislocations. Thick ( $>100 \mu\text{m}$ ) multilayer composites of InAsSb, InGaSb, AlGaAsSb, InGaAsSb and InAsSbP have been grown by LPE with abrupt compositional step gradings between adjacent layers (Mauk *et al.*, 2001, 2003). LPE can be readily adapted to the growth of such thick layers due to the relatively fast growth rates ( $>1\text{--}10 \mu\text{m min}^{-1}$ ). In particular, InAsSb and InAsSbP virtual substrates consisting of a stack of two or three thick, step-graded epitaxial layers were grown by LPE on InAs substrates. A virtual substrate comprised of three  $\sim 100\mu\text{m}$  thick layers of InAsSb on an InAs substrate and with the top layer having a composition of  $\text{InAs}_{0.8}\text{Sb}_{0.2}$  represents an approximately 1.5 % shift in lattice constant relative to the InAs substrate. Each layer of the composite was grown in a separate LPE step at 650 °C for 120 min, demonstrating that epitaxial layers could be used as ‘substrates’ for subsequent epitaxy steps. This capability of multiple LPE steps to make a single substrate greatly simplifies the growth process needed to make virtual substrate structures of arbitrary thickness and composition.

Liquid phase epitaxial regrowth refers to the growth of additional LPE layers after preceding LPE layers have been exposed to air at room temperature. This situation arises when an epitaxial layer is grown on a substrate using the normal LPE process, the furnace is cooled, the sample is removed from the furnace, possibly subjected to cleaning and processing steps such as masking and photolithography, and reloaded back into an LPE system for another high-temperature epitaxy step. For many materials systems, particularly those with aluminum, e.g. AlGaAs, such regrowth is impeded by oxidation of the epitaxial layer which prevents good wetting by the melt during subsequent LPE steps. Berkovitz *et al.* (Berkovitz *et al.*, 1993) have developed an LPE regrowth process for AlGaAs whereby the first-grown LPE layer is treated with a  $\text{Na}_2\text{S}$  solution. This surface treatment appears to remove oxides and passivate the surface, preventing excessive oxidation and permitting growth of a second LPE layer. Similar sulfide treatments have been reported for LPE of quaternary alloys on GaSb substrates (L’vova *et al.*, 1998; Andreev *et al.*, 1999; Papis *et al.*, 2000).

Steady-state, temperature-gradient LPE—although not as commonly used as transient cooling methods using step or ramp cooling—is nevertheless well established for the growth of III-V binaries and alloys (Long *et al.*, 1974). A solid source and substrate are separated by a layer of melt, as shown in Figure 12.3. The advantage of this mode of

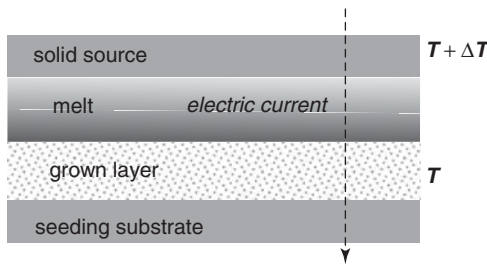


**Figure 12.3** Imposed temperature gradient or electro-migration for sustained, steady-state growth of thick epitaxial layers

growth is that the melt is continually replenished, thus permitting the growth of thick layers. Growth can also be driven by electro-migration or Peltier effects due to an electric current imposed across the melt. Electroepitaxy is further discussed in Section 12.5.10. The growth of thick ( $> 3 \text{ mm}$ ) AlGaSb layers on GaSb substrates using liquid phase electroepitaxy (LPEE) was reported by Bishopink and Benz (Bishopink and Benz, 1993). The advantages of using electroepitaxy with a nominally isothermal process are related to faster or more sustained growth and possibly amelioration of aluminum segregation effects. Bryskiewicz and Laferrière (Bryskiewicz and Laferrière, 1993) analyzed LPEE for the growth of alloy substrates with respect to generation, propagation, and multiplication of defects due to composition variations and lattice constant variations, and the effect of convection in the melt on growth interface stability and structural perfection of the alloy layer.

The growth of thick epitaxial alloy structures, such as GaInP, by a so-called 'yo-yo' solute feeding method, in which the source material and substrate are cycled between different temperatures provides another means for making virtual substrates by LPE (Watabe *et al.*, 1993). For example,  $100 \text{ }\mu\text{m}$  thick  $\text{In}_{0.3}\text{Ga}_{0.7}\text{P}$  layers were grown by the yo-yo method.

The usefulness of epitaxial substrates centers mostly on applications providing ternary and quaternary semiconductors. This, in turn, is closely linked to the ability to control segregation in LPE growth of alloys, a subject further discussed in Section 12.5.12.

### 12.5.5 Selective epitaxy and ELO

The near-equilibrium growth conditions of LPE are conducive to selective modes of crystal growth. In selective epitaxy (Kim, 1972; Bellavance and Campbell, 1977; Kim and Kwon, 1986) a substrate is coated with a masking layer of oxide (e.g.  $\text{SiO}_2$ ), nitride (e.g.  $\text{Si}_3\text{N}_4$ ) or other type of metallurgical barrier (e.g. TiN) or a refractory metal such as tungsten or molybdenum (Figures 12.4 and 12.5). The mask is patterned with openings to expose the underlying substrate. The exposed areas of substrate serve as selective seeding areas in the LPE process promoting preferential nucleation in the mask openings ('windows'). Epitaxial growth is restricted to the window regions of the mask; there is virtually no deposition on the mask itself. This is because the low thermodynamic driving force in LPE, i.e. the relatively small supersaturation of the liquid phase, is insufficient to induce nucleation on the mask since this type of heterogeneous nucleation has a higher energy barrier compared with lattice-matched, oriented nucleation on the exposed areas of the substrate. LPE is not unique in this regard as similar selective epitaxy can be achieved with some types of CVD. However, the ability to limit epitaxy to selective growth on masked substrates is practically inherent in the LPE process and requires no special optimization of growth conditions. Selective epitaxy is useful for reducing stress and defects associated with lattice mismatch and thermal expansion mismatch between the substrate and epitaxial layers, e.g. as occurs in GaAs or InP epitaxy on silicon substrates (Fitzgerald *et al.*, 1988; Ohashi, 1992). Ishihara *et al.* (Ishihara *et al.*, 1977) showed improved wetting of the substrate in selective GaAs LPE by coating the oxide-masked GaAs substrate with a  $50 \text{ nm}$  thick layer of sacrificial nickel. Enhanced wetting and improved reproducibility was also shown in InP LPE of the patterned, oxide-masked substrate by predeposition of a thin indium film (Naritsuka and Nishinaga, 1999).

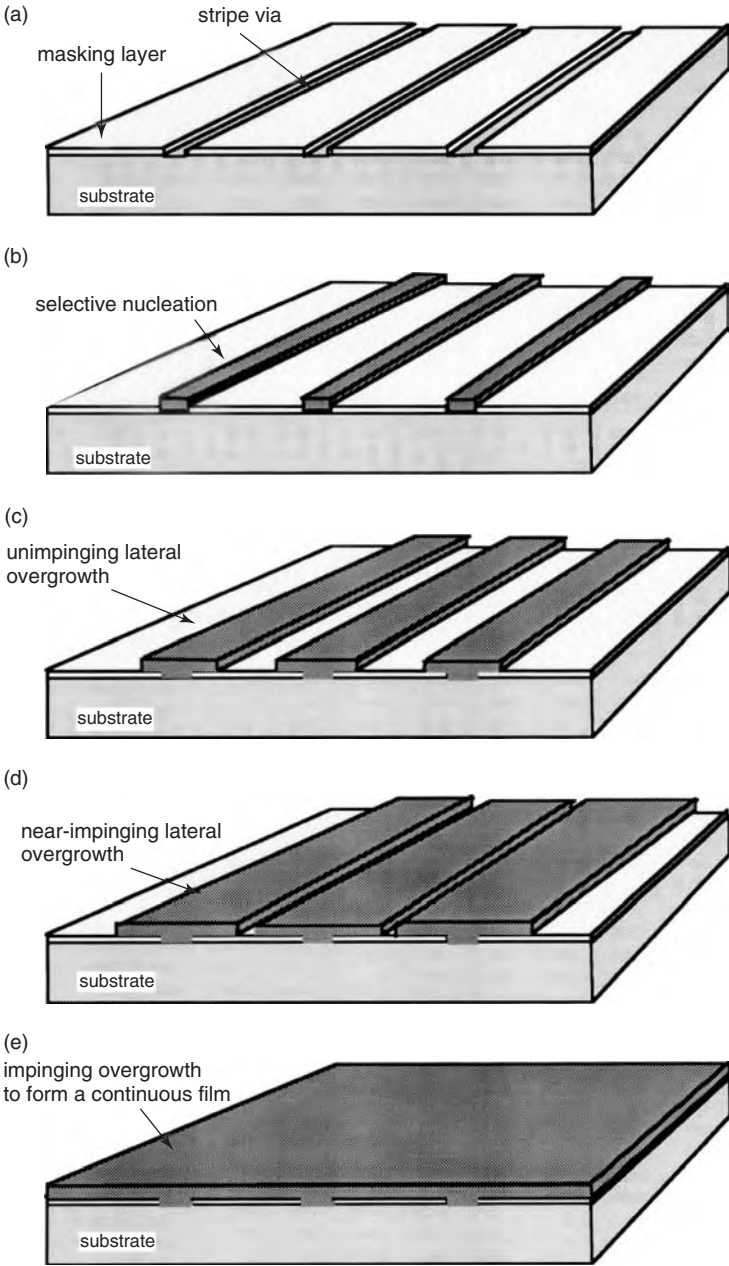


**Figure 12.4** Epitaxial lateral overgrowth: (a) prior to growth, a substrate is masked and patterned with stripe openings; (b) during the LPE step, stripe openings provide sites for preferential nucleation and selective epitaxy; (c) early stages of overgrowth; crystals spread laterally over the masked regions of the substrate; (d) during later growth stages, a substantial amount of the selectively nucleated crystals cover the mask; (e) ultimately, the crystals may impinge to form a continuous film. The aspect ratio is defined as the lateral width of the selectively grown crystal to the thickness of the crystal

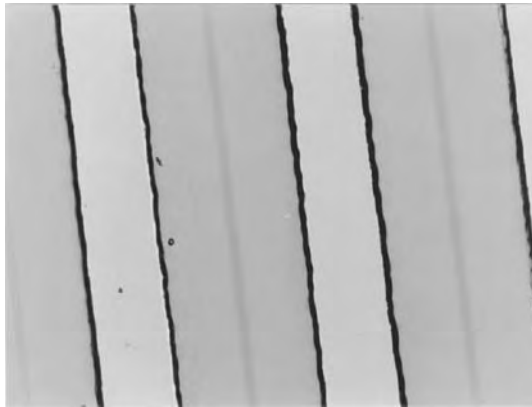


**Figure 12.5** Top-view photomicrograph of  $\text{Al}_{0.5}\text{Ga}_{0.5}\text{As}$  grown on a tungsten-masked (111)GaAs substrate by LPE. Stripe openings are  $10\ \mu\text{m}$  wide (visible through the semi-transparent AlGaAs layers) and spaced  $400\ \mu\text{m}$  apart

In ELO, the mask openings, usually in the form of narrow stripes several micrometers to tens of micrometers in width are spaced tens to hundreds of micrometers apart. Here the objective is to maximize the extent of lateral overgrowth atop the mask. The growth is optimized with respect to substrate crystallographic orientation (or misorientation) mask composition and thickness, via geometry and alignment, melt composition, and the time–temperature program of LPE such that the crystals seeded in the stripe openings subsequently overgrow the mask layer, with the result that a large portion of the epitaxial layer is formed directly over the mask. ELO by LPE has been developed for silicon (Suzuki and Nishinaga, 1989, 1990; Suzuki *et al.*, 1990; Kinoshita *et al.*, 1991; Bergmann, 1991; Zingg *et al.*, 1992; Köhler *et al.*, 1995; Silier *et al.*, 1996; Weber *et al.*, 1998; Jozwik and Olchowik, 2006) (see also Chapter 5), GeSi alloys (Hansson *et al.*, 1991), GaAs (Nishinaga *et al.*, 1988; Zhang and Nishinaga, 1990a), GaP (Zhang and Nishinaga, 1990b), InP (Naritsuka and Nishinaga, 1995; Kochiya *et al.*, 2003), InGaP (Nakayam *et al.*, 2002) and InGaAs (Balakrishnan *et al.*, 2000, 2002). A related technique, called microchannel epitaxy, for control of defects in LPE has been described in detail by Nishinga (Nishinga, 2004). High-aspect ratio lateral growth with epitaxial layers ( $\sim 5\ \mu\text{m}$  thick) extending hundreds of micrometers from the seeding region over the mask layer can be routinely achieved with LPE. These aspect ratios are at least ten times higher than those observed with other epitaxy methods, and high-aspect ratio ELO should be regarded as unique to LPE. Accordingly, ELO can simulate semiconductor-on-insulator structures that are useful for dielectric isolation. ELO can also provide defect filtering (Bryskiewicz, 1995), in that areas of the epitaxial layer grown over the mask exhibit dramatic reductions in defect densities compared with epitaxial layers grown on unmasked substrates (Kato *et al.*, 1991; Nakayama *et al.*, 2002). LPE ELO has been especially advantageous in hybrid epitaxy methods (Section 12.5.13.2) whereby LPE lateral overgrowth is initiated on exposed seeding areas of partially masked III-V buffer layers formed on silicon by MBE or CVD (Ujiie and Nishinaga, 1989; Sakawa and Nishinaga, 1991; Uen and Nishinaga, 1995; Chang *et al.*, 1997, 1998; Naritsuka *et al.*, 1997; Kaneko *et al.*, 2002; Nakayama *et al.*, 2002; Zytkeiwicz, 2002). ELO utilizing reflective mask layers, such as tungsten or deposited stacks of oxides and polysilicon to

form an interference reflector, can also be used to make device structures with buried mirrors for LEDs, detectors and solar cells (Mauk *et al.*, 1996). Dobosz *et al.* (Dobosz *et al.*, 2005) reported the use of ZrN as a mask for LPE ELO. Repeated applications of ELO have been suggested for three-dimensional semiconductor structures (Morrison and Duad, 1985; Bauser and Strunk, 1994).

### 12.5.6 Melt epitaxy

A new technique called *melt epitaxy* is being developed by Shizouka University and Hamamatsu Photonics (and more recently by collaborating groups in China) for making low-bandgap III-V antimonides with applications to long-wavelength detectors (Gao *et al.*, 1999, 2000, 2002). Melt epitaxy can be viewed as a variant of LPE. A modified slideboat is used to aliquot a thin layer of melt (with three or more components) that rapidly solidifies to form a 300  $\mu\text{m}$  thick slab of a ternary solid on a compound semiconductor substrate that acts as a seed crystal, as in conventional LPE. Here, the distinction between melt growth and solution growth is not sharp, as this technique may be more properly described as a solidification or casting technique rather than solution growth. Nevertheless, there is considerable technological overlap with traditional LPE techniques, particularly with respect to the use of metallic melts, a graphite slideboat and a horizontal tube furnace. In several reports of melt epitaxy, thick InGaSb layers with an optical transmission/absorption cut-off wavelength of 7–8  $\mu\text{m}$  were grown on GaAs substrates. Similarly, thick InAsSb layers with an optical transmission/absorption cut-off wavelength of 8–12  $\mu\text{m}$  were grown on InAs substrates. For InAs<sub>0.04</sub>Sb<sub>0.96</sub> on GaAs substrates (cut-off wavelength = 12  $\mu\text{m}$ ) low background doping ( $n = 8 \times 10^{15} \text{ cm}^{-3}$ , 300 K) and high electron mobilities (21 500  $\text{cm}^2 \text{ V}^{-1} \text{ s}^{-1}$ , 300 K) were achieved (Gao *et al.*, 2005). It is not entirely clear why this technique adequately avoids segregation and stress effects, but rapid cooling and growth rates in combination with the comparatively lower temperatures probably play a significant role. Perhaps more surprising is the ability to grow III-V nitrides by melt epitaxy. Gao *et al.* (Gao *et al.*, 2003) formulated melts containing antimony, indium, polycrystalline InAs and InN powder (10  $\mu\text{m}$  particles) to grow InNAsSb single crystals with nitrogen concentrations of 13–19 %, cut-off wavelengths of 11–13  $\mu\text{m}$  and 77 K electron carrier concentration and mobility of  $10^{16} \text{ cm}^{-3}$  and 55 800  $\text{cm}^2 \text{ V}^{-1} \text{ s}^{-1}$ . If the material produced by melt epitaxy proves suitable for high-performance photodetectors, the melt epitaxy technique applied to low-bandgap III-V antimonides could challenge the predominance of MCT in the 8–12  $\mu\text{m}$  wavelength range.

### 12.5.7 Rare earth doping and other doping effects in LPE

As already mentioned, an advantage of LPE is the feasibility of using a wide selection of dopants. Fundamental doping studies including the use of rare earth elements (Er, Gd, Ho, Nd, Pr) and device applications using rare earth doped semiconductors, can be readily implemented with LPE. There is considerable experimental work on rare earth doping of liquid-phase epitaxial GaAs (Shi *et al.*, 1993), InP (Prochazkova *et al.*, 1996, 1999), InAs (H. Gao *et al.*, 1999), AlGaAs (Raczynska *et al.*, 1989), InAsSb (Krier *et al.*, 2000), InGaAsP (Procházková *et al.*, 1996, 1999), InGaAs (Ho *et al.*, 1994), and

InGaAsP (Dolginov *et al.*, 1994; Gong *et al.*, 1997). The rare earths effect impurity gettering, significantly reducing background doping and  $p$ - $n$  junction saturation currents, and increasing carrier mobilities and minority carrier lifetimes. Rare earth doping can dramatically improve detector performance, in some cases as much as doubling the quantum efficiency of photodiodes. For instance, Krier *et al.* (Krier *et al.*, 2000) reported that rare earth doping of InAsSb LEDs made by LPE increased the luminescence by 10–100 times. Gong *et al.* (Gong *et al.*, 1997) showed that rare earth doping (gadolinium) in LPE-grown InAsPSb/InAs photodetectors could enhance the quantum efficiency (spectral response) by almost a factor of 2.

In addition to electrical doping, the use of isoelectronic impurities for improvement in material quality and surface smoothness is also a readily applied option with LPE. For instance, Chen and Wie (Chen and Wie, 1989) doped GaAs LPE layers with In and Sb—in which case the epilayer might be regarded instead as a dilute ternary alloy rather than a doped binary—and demonstrated lower dislocation densities and smoother surface morphologies. Similar results had been reported with regard to dislocation reduction in ‘quasi-ternary’ GaAs and InP LPE layers (Beneking *et al.*, 1986). Ganina *et al.* (Ganina *et al.*, 1982) showed that formation of dislocations in LPE-grown GaAs depended on doping levels (Sb and In). Kamiya *et al.* (Kamiya *et al.*, 1996) demonstrated controlled lattice compensation for reducing lattice-mismatch-induced stress in LPE-grown GaAs by simultaneous Te and Si doping.

Rare earth doping is also used to enhance or modify luminescence properties of silicon layers grown by LPE (Binetti *et al.*, 1998). Purification effects in LPE are not limited to the rare earths, Kondo *et al.* (Kondo *et al.*, 1987) reported that cobalt added to In-P melts gettered impurities by their incorporation into cobalt phosphide precipitates, resulting in high-purity InP epilayers with very high electron mobilities. Transitional metal doping of LPE-grown III-V semiconductors, including Cr in GaAs (Otsubo and Miki 1974) and Fe in InP (Ohtsuka *et al.*, 1990) has been used to render epilayers semi-insulating. The feasibility of achieving semi-insulating LPE materials of ternary and quaternary alloys (e.g. InGaAsSb) or of lower-bandgap binaries (GaSb or InAs) is not certain, but would be very useful in mid-infrared optoelectronics.

### 12.5.8 Fundamental studies of crystal growth, melt convection and liquid-metal transport properties

The LPE technique provides means for studying basic phenomena of crystal growth and defect formation, segregation and doping phenomena, as well as melt convection and mass transfer, and liquid-metal transport properties and transport phenomena. The horizontal slideboat technique affords a convenient if imperfect way to study steady-state (equilibrium) and transient (kinetics) phenomena related to the crystal-molten metal interface at high temperatures, as the metallic solution can be quickly decanted from the solid phase (substrate or growing crystal). For instance, Mishurnyi *et al.* (Mishurnyi *et al.*, 1999) used a graphite slideboat to measure the kinetics of solute evaporation and melt saturation, as well as infer the solid–liquid interface temperature in indium melts in contact InP wafers. Iyer *et al.* (Iyer *et al.*, 1984) used a current-controlled LPE apparatus (see Section 12.5.10) to determine the electromigration mobility and temperature-dependent diffusivity of arsenic in molten indium. The work of Bauser (Bauser 1978, 1985a, 1994),



Bauser and Strunk (1981, 1982, 1984), Bergmann (Bergmann 1991), Konuma (Konuma, 2002) and Nishinaga (Nishinaga, 2005) investigating epitaxial growth modes and atomic mechanisms (e.g. two-dimensional crystallization and step-flow, three-dimensional nucleation, dislocation-controlled growth) are illustrative examples of fundamental crystal growth studies using the LPE technique.

*In situ*, real-time observation of the growth interface is generally not compatible with the LPE process, and this is a decided disadvantage of LPE compared with MBE or CVD where electron diffraction, scanning electron and other vacuum surface analysis techniques can be performed during the growth process. Nevertheless, *in situ* imaging of the LPE growth interface and the observation macrostep formation using an infrared microscopic interferometer has been reported (Inatomi and Kuribayashi, 1993). Ludington and Immorlica (Ludington and Immorlica, 1979) deposited sputtered tungsten thermocouple structures directly on the graphite horizontal slideboat to measure vertical temperature gradients in LPE growth systems. In work that may find application to *in situ*, real-time LPE measurement, Ujihara *et al.*, (Ujihara *et al.*, 2002) used an infrared camera and X-ray fluorescence for the simultaneous measurement of solute and temperature in crystallization from Ga-Zn solutions. For the most part, however, the crystal growth phenomena associated with LPE have to be inferred from post-growth examination of samples. An instructive example is a study of the size, shape, faceting and ordering of  $\text{Si}_{1-x}\text{Ge}_x$  islands grown on (100) Si by LPE, including compositional dependence  $x$  of the SiGe alloy, and examined by post-growth scanning electron microscopy (Hanke *et al.*, 2005). LPE with patterned, masked substrates using various test structure patterns, in combination with substrates with critically oriented surfaces, provide excellent diagnostic tools for post-growth analysis of crystal growth defect formation, faceting phenomena, and elucidation of nucleation and growth modes and mechanisms.

The kinetics of LPEE can be used to determine electromigration mobilities, diffusivities, effective charges, resistivities in liquid metal solutions (Golubev *et al.*, 1995) and thermoelectric effects in liquid metal-semiconductor junctions. Impurity segregation effects are important in the stability of solidification, and LPE provides an opportunity to study impurity segregation in temperature ranges and liquid phase compositions markedly different from those for solidification from nearly pure melts. LPE film morphologies and thicknesses are sensitive to melt convection, and the slideboat technique provides a good test of theoretical models for the combined effects of convection, diffusion, and kinetics. Kimura *et al.* (Kimura *et al.*, 1991, 1994, 1996a,b) have reported experimental and numerical studies of solutal convection (including gravity effects) and diffusion and interface kinetics on substrate dissolution and film growth using silicon LPE from indium melts as a case study. These studies included positioning of the substrate on the bottom or top of the melt. Coşkun *et al.* (Coşkun *et al.*, 2002) described a numerical simulation based on a Chebyshev–Tau spectral-method of natural convection due to concentration gradients in a system similar to those studied by Kimura *et al.* Albrecht *et al.*, (Albrecht *et al.*, 1996) used transmission electron microscopy (TEM) and atomic force microscopy (AFM) of LPE grown Si-Ge alloys on Si substrates to study local variations of chemical potential during growth. They concluded that sinusoidal surface undulations are formed to relax mismatch strain, resulting in spatially varying differences in Gibbs free energy. As growth and dissolution rates (and thus epilayer thickness) profiles are due to local supersaturation, surface profiles of the epilayer indicate the local varying chemical potential across the sample.

Hurle (Hurle, 1999) has reviewed in detail the use of GaAs, AlGaAs and InP LPE from various melts (Ga, In, Bi, Sn) over a range of temperatures to analyze native point defects and doping phenomena in III-V semiconductors. Most VPE processes occur far from equilibrium and therefore do not reflect fundamental characteristics of doping, but rather process-specific doping kinetics. Therefore, it is difficult to unravel the role of native point defects, carrier concentration, compensation, dopant solubility, diffusion, surface band bending, and so forth on the doping process. On the other hand, while the solidification of compound semiconductors from stoichiometric melts is a near-equilibrium process, it encompasses a very limited range of group III and group V thermodynamic activities and growth temperatures. In contrast, LPE provides a means to study defect formation and doping incorporation over a wide range of temperatures and activities of the III-V components. As a specific example, Hurle uses experimental data on the dopant solubility in GaAs grown by LPE from Ga-Bi solutions (with varying Ga:Bi ratios to vary the arsenic and gallium activity) to determine the concentration of charged native point defects and its effect on dopant incorporation. LPE serves as a highly useful, and perhaps unique, tool for thermodynamic analysis of point defects and doping in semiconductors.

### 12.5.9 Novel melt compositions for LPE

The LPE growth of III-V compounds normally is based on crystallization of the III-V compound from melts rich in the group III component and dilute in the group V element. For instance, GaAs is grown from a Ga melt saturated with As in which the As atomic fraction is on the order of 1%. Some compounds such as InSb can be grown from either group III-rich melts or group V-rich melts, but it would be difficult to grow GaAs or InP from As- or P-rich melts, due to the high vapor pressure of the group V elements. As mentioned in Section 12.5.8, the growth of III-V semiconductors from group III-rich versus group V-rich melts impacts the material quality with respect to non-stoichiometric defects such as vacancies and antisites. MOCVD and MBE typically used group V-rich growth conditions, i.e. overpressures of As or As precursors or high V/III ratios for the precursors. In contrast, LPE-grown III-V layers typically exhibit different types of defects due to the group III-rich growth conditions. The low V/III ratio in LPE suppresses formation of As antisites and group V vacancies. The antisites are implicated in an electron level 2 (EL2) defect that reduces luminescence efficiency and this is considered one of the main reasons LPE material makes excellent LEDs and laser diodes. The V/III ratios also determine the behavior of dopants, especially the isoelectronic dopants that can substitute on either the group III sublattice or group VI sublattice. Bismuth melts for III-V LPE are also of interest because bismuth has a low surface tension and modifies the wetting and crystal faceting or surface energies of the epitaxy. Further, melts which reduce the solubility of a rate-limiting component may facilitate better growth rate control in the interest of achieving thin layers. For example, the growth rates of GaAs from bismuth-rich melts are two to four times slower than those from gallium-rich melts, for corresponding growth temperatures and cooling rates. Neutral melt components, i.e. elements which are incorporated to only a very small degree into the epitaxial layer and/or are electrically inactive (i.e. do not function as donors or acceptors), have been utilized to tailor the properties of LPE melts. For LPE of III-V materials, Pb (Andreev *et al.*, 1999) and Bi have proven useful. Gladkov *et al.* (Gladkov 2006) indicated several

advantages in InAs LPE with Bi (instead of In) melts including more controllable growth rates ( $40 \text{ nm min}^{-1}$ ), lower background doping (probably due to reduced concentration of silicon in bismuth melts) and more controlled  $n$ -type doping. Kunitsvna *et al.* (Kunitsvna *et al.*, 1998) reported that the native structural defects in GaSb due to Ga substituting for Sb could be reduced by two orders of magnitude by varying the Sb/Ga ratio in an LPE melt with Pb as a 'neutral solvent', and that this approach also appears applicable to other semiconductors such as GaInAsSb. Astles *et al.* (Astles *et al.*, 1985) reported the use of Bi and In solvents for LPE of CdTe, permitting growth temperatures as low as  $250^\circ\text{C}$ , and producing CdTe epilayers with long minority carrier diffusion lengths and high luminescence efficiency.

Assessments of nonmetallic melts for LPE of semiconductors have been very limited. No doubt an overriding concern with novel melt chemistries relates to the purity and consequent electrical and optical properties of the LPE-grown material that would result from using a melt with atypical melt constituents. Nevertheless, applications for epitaxial layers are varied, and their property specifications are not always as stringent or demanding with respect to impurities as with semiconductor optoelectronic devices such as lasers and detectors. Thus, there may well be instances where LPE with unconventional melt chemistries could be considered. One hindrance is the lack of the requisite phase diagrams. Scheel (Scheel, 1993) notes that while phase diagrams for practically all of the binary systems are known, only about 1% of the phase diagrams of the possible three-element systems and 0.1% of possible four-element systems are known. Buehler and Bachmann (Buehler and Bachmann, 1976) investigated the solubilities of InP and CdS in molten Cd, Sn, In, Bi, and Pb for potential solar cell applications of these materials using LPE. These binary or pseudo-binary systems followed a simple solution model such that:

$$\ln X = -\frac{\Delta H^S}{RT} + C$$

where  $X$  is the mole fraction of InP or CdS in the molten metal, when  $X < 2\%$ ,  $T$  is the absolute temperature,  $R$  is the gas constant,  $\Delta H^S$  is the enthalpy of solution, and  $C$  is a constant.

Tanaka and Sukegawa (Tanaka and Sukegawa, 2001) grew ZnSe from zinc chloride solvent ( $600\text{--}700^\circ\text{C}$ ) using successive LPE growth steps. The LPE growth of CdTe from molten  $\text{CdCl}_2$  (Kitagawa *et al.*, 1981), and the growth of GaN from Na fluxes (Aoki *et al.*, 2002), are two further examples indicating that LPE of compound semiconductors can be performed with melts besides the traditionally used metal solvents from columns III (Al, Ga, In), IV (Ge, Sn, Pb) or V (Bi, Sb) of the periodic table.

### 12.5.10 Liquid phase electroepitaxy

Liquid-phase electro-epitaxy (LPEE), sometimes called *current-controlled liquid phase epitaxy*, is a modification of conventional LPE wherein an electric current is imposed through the melt and across the growth interface (substrate–melt contact area) to effect crystal growth (Kumagawa *et al.*, 1973; Daniele, 1975; Jastrzebski *et al.*, 1976, 1978; Jastrzebski and Gatos, 1977; Lawrence and Eastman, 1977, 1978; Imamura *et al.*, 1978; Lagowski *et al.*, 1980; Yang *et al.*, 1982; Nikishin, 1983; Iyer *et al.*, 1984; Bryskiewicz 1986; Mouleeswaran and Dhanasekaran, 2004). There has been considerable work on LPEE in Eastern Europe; see Golubev *et al.* (Golubev *et al.*, 1995) and Shmartsev

(Shmartsev, 1991a,b) for an extensive bibliography of this LPEE work. The application of an electric current to induce some combination of Peltier cooling at the growth interface (and thus supercooling to drive the growth process) and/or solute electromigration to supplement diffusion in the melt, provides a mode of epitaxial growth that is distinct from LPE based on transient cooling of the melt, as is typically used in conventional LPE. A direct current on the order of  $1\text{--}100\text{ A cm}^{-2}$  is established across the growth interface. The current induces a Peltier cooling of the growth interface owing to the differences in thermoelectric properties of the semiconductor substrate and molten metal growth solution. This Peltier cooling supercools the melt in the vicinity of the substrate, and the resulting supersaturation provides a transient growth episode, much as in step-cooling a melt by reducing the temperature of an equilibrated melt before contact with the substrate. The Peltier cooling is typically  $1\text{--}5^\circ\text{C}$  in magnitude, and the extent of supercooling depends on the thermal resistance of the substrate and its ability to sustain a temperature gradient. This is because an opposing Peltier *heating* on the backside of the substrate accompanies the Peltier *cooling* on the side of the substrate in contact with the melt. For this reason, a thicker substrate with relatively low thermal conductivity (e.g. due to low doping) exhibits better Peltier cooling than a thin substrate. Conventional LPE slideboats can be adapted for LPEE, the main new features include the use of an insulating slideboat material, such as fused silica, or boron nitride, in place of electrically conducting graphite in order to confine the applied current through the melt. Many of the references cited here include diagrams and descriptions of the LPEE slideboat.

In addition to Peltier cooling, the current through the melt can induce electromigration. For instance, in a Ga-As melt, an electric current can cause As solute to migrate to the growth interface where it creates a local supersaturation. Electromigration phenomena have been demonstrated in molten metals, independent of LPE applications, but the solute electromigration is difficult to predict and is generally insufficient for economic separation processes to purify metals. Electromigration is explained in terms of differential migrations of solute and solvent due to momentum transfer from scattering of conduction electrons associated with the imposed current. Similar solid-state electromigration phenomena have been intensively studied as a failure mechanism in integrated circuit metallizations. Electromigration data (effective charges and mobilities, and directions of solute transport with respect to applied current) for liquid metals are compiled in Pratt and Sellors (Pratt and Sellors, 1973). Several workers have reported LPEE using alternating currents, which is somewhat surprising in view of the generally accepted mechanism of LPEE due to solute electromigration and/or Peltier cooling at the substrate. Takenaka *et al.* (Takenaka *et al.*, 1991a) reported that alternating currents enhance solute diffusion and nucleation. Takenaka *et al.* (Takenaka *et al.*, 1991) explain InP LPEE with low-frequency ( $\sim 50\text{ Hz}$ ) alternating currents as due to the Lorentz force on solute ( $P$ ) from a combination of electromigration induced by an applied ac current through the melt and the steady-state magnetic field in the melt produced by the current in the furnace heater coil(s). Demin *et al.* (Demin *et al.*, 1990) offered data supporting a model for frequency-dependent alternating current LPEE ( $1\text{--}4000\text{ Hz}$ ) of GaAs including first-order kinetics for growth and dissolution, solute concentration and mobility, thermal conduction and diffusivities of the substrate and melt. Modulation of doping in LPEE by current control is discussed by Lagowski *et al.* (Lagowski *et al.*, 1980). Several analyses (Nishinaga *et al.*, 1978; Okamoto *et al.*, 1982; Wollkind and Wang, 1988) have indicated that electroepitaxy effects stabilize the growth interface permitting higher growth rates, in some cases as high as  $25\text{ }\mu\text{m min}^{-1}$ .

LPEE has been applied to selective electroepitaxy of GaAs on SiO<sub>2</sub>-masked, GaAs-coated (made by MOCVD) silicon substrates (Sakai *et al.*, 1991; Sakai and Ohashi, 1992, 1994). Khenner and Braun (Khenner and Braun, 2005) presented numerical simulations of LPEE selective area growth showing the effect of electromigration and mask conductivity, and wetting contact angles on the relative rates of vertical and lateral growth.

It appears that LPEE has not found wide use as a method of LPE. The technique is tedious in its application, especially with respect to assuring a uniform current density across the growth interface. The contact resistances of the circuit used to impose a current across the LPE melt, including the various interfaces between substrates, electrodes and melts must be kept very low in order to avoid extraneous Joule heating which would counter the Peltier induced cooling or electromigration-induced supersaturation. Further, variations in contact resistance can lead to 'hot spots' which produce current filaments, leading to localized heating and consequent reduced resistance in the semiconductor at the current filament causing instabilities. Nevertheless, with careful substrate mounting and contact designs, many workers have successfully modified LPE slideboats and have achieved reproducible implementations of LPEE with good control. The issue then becomes whether any advantages of LPEE warrant the added complexity compared with conventional LPE. Several such advantages have been explored. LPEE can be operated with a steady-state temperature profile and using a solid source material to replenish the melt with solute, thus permitting the growth of thick epitaxial layers at constant temperature (see Section 12.5.4). LPEE growth of GaAs bulk crystals (Golubev *et al.*, 1991) and various ternary alloys such as AlGaSb (Bischopink and Benz, 1993) and InGaAs (Bryskiewicz, 1997) is feasible. Bryskiewicz and Laferrière (Bryskiewicz and Laferrière, 1993) present some theoretical considerations for LPEE of alloy substrates with regard to generation, propagation, and multiplication of dislocations due to compositional variations, melt convection and growth interface stability, lateral overgrowth on partially masked substrate seeds to block dislocations, and use of magnetic field to control convection in order to achieve large-diameter, high-quality substrates. Gevorkyan (Gevorkyan, 2003) has proposed an interesting variation of conventional LPEE using liquid sources where one or more reservoirs of saturated binary melts are connected by channels to a growth melt (Figure 12.6). The supplies of solutes are controlled by electromigration due to separate currents as shown. Modeling indicates this technique can provide controlled compositional grading from a binary alloy composition to a target ternary alloy composition, followed by growth of a thick layer of a ternary alloy of constant composition.

Two other applications of applied currents and electrodes in LPE provide enhanced function or better process control. Il'inskaya *et al.* (Il'inskaya *et al.*, 1987) used current-controlled 'deoxidation' to remove surface oxides from oxidized AlGaAs using a localized current, and thus permit selective epitaxy of a subsequent layer on deoxidized regions of the AlGaAs. Epitaxial layer thickness control was also demonstrated on grooved substrates. Such localized applications of currents for inducing epitaxial growth or removing surface oxides to promote preferential epitaxial may provide a means of selective epitaxy without intervening masking and patterning steps. Chang *et al.* (Chang *et al.*, 1983) described *in situ* electrochemical monitoring and control of dissolved oxygen in gallium melts used for LPE of GaAs. The electrochemical method employed an yttria stabilized zirconia (YSZ) electrolyte to measure dissolved oxygen and also deoxidize the gallium melt and thus modify oxygen-related, electrically active impurities in the GaAs epitaxial layer.

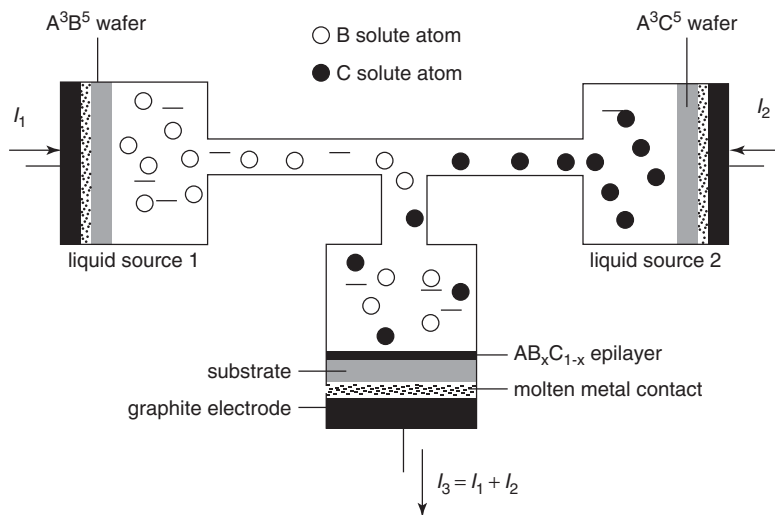


**Figure 12.6** LPEE with liquid sources. Applied currents  $I_1$ ,  $I_2$  and total substrate current  $I_3$ . (After Gevorkyan, 2003)

### 12.5.11 LPE of thallium-, manganese-, and bismuth-containing III-V alloys

Several groups have reported success with LPE growth of novel III-V alloys such as  $\text{In}_{1-x}\text{Tl}_x\text{Sb}$ ,  $\text{In}_{1-x}\text{Tl}_x\text{AsSb}$ ,  $\text{InSb}_{1-x}\text{Bi}_x$  and  $\text{Ga}_{1-x}\text{Mn}_x\text{As}$ . The  $x$  fractions in LPE-grown alloys have ranged from 0.0005 to 0.15. Evidently, the large size of the substituted Tl, Mn or Bi atom creates excessive strain, limiting its miscibility in the III-V host lattice. In this regard, a near-equilibrium growth technique such as LPE would be at a disadvantage for preparing these alloys, although as detailed below, some significant progress has been reported. Interest in  $\text{InTlAsSb}$  and  $\text{InBiSb}$  is primarily for making low-bandgap III-V detectors that would compete with detectors made in MCT. More complex melt chemistries, as discussed in Section 12.5.9, might widen the composition ranges of such alloys.

Gao and Yamaguchi (Gao and Yamaguchi, 1999) reported the growth of  $\text{InSb}_{1-x}\text{Bi}_x$  ( $0.01 < x < 0.14$ ) epilayers from In-Bi-Sn-Sb melts on (100) InSb substrates. Room temperature electron mobilities of  $3 \times 10^4 \text{ cm}^2 \text{ V}^{-1} \text{ s}^{-1}$  and carrier densities of  $6 \times 10^{18} \text{ cm}^{-3}$  were measured. Raczynska *et al.* (Raczynska *et al.*, 1999) described the LPE growth of InSbBi epilayers on (111) substrates. For nominally undoped epilayers, the conductivity type of the InSbBi epilayer depended on the pre-growth melt annealing ('bake-out'). Short bake-outs (5–20 h) yielded  $p$ -type epilayers ( $5 \times 10^{15} \text{ cm}^{-3}$ ), while with longer bake-outs (40–100 h), the samples were  $n$ -type ( $5 \times 10^{15} \text{ cm}^{-3}$ ). With regard to tin doping, in In-rich melts tin acted as an acceptor, while in Bi-rich melts tin acted as a donor.

Ackchurin *et al.* (Ackchurin *et al.*, 1997) realized  $\text{InAs}_{1-x-y}\text{Sb}_x\text{Bi}_y$  ( $x = 0.88\text{--}0.97$ ,  $y = 0.0016\text{--}0.0036$ ) heterostructures on InSb (111) by LPE, showing an epilayer optical absorption edge  $> 8 \mu\text{m}$  at 77 K, thus indicating attainment of bandgaps in the 0.07–0.15 eV (77 K) range are possible. Dixit *et al.* (Dixit *et al.*, 2002, 2003) and Bera *et al.* (Bera *et al.*, 2002, 2003) successfully developed the growth of  $\text{InBi}_x\text{Sb}_{1-x}$

( $x = 0.04$ ) and  $\text{InBi}_x\text{As}_y\text{Sb}_{1-x-y}$  ( $x = 0.025, y = 0.105$ ) on semi-insulating GaAs substrates using a slideboat LPE process with a growth temperature of around  $400^\circ\text{C}$ . The room temperature bandgap of  $\text{InBi}_{0.025}\text{As}_{0.105}\text{Sb}_{0.870}$  was found to be in the range of  $0.113\text{--}0.120\text{ eV}$  with a room temperature carrier concentration of  $8 \times 10^{16}\text{ cm}^{-3}$  and carrier mobility of  $3.1 \times 10^4\text{ cm}^2\text{ V}^{-1}\text{ s}^{-1}$ . Ruiz-Becerril *et al.* (Ruiz-Becerril *et al.*, 2002) reported difficulties in growing  $\text{InTlSb}$  by LPE, observing negligible TI incorporation. Lunin *et al.* (Lunin *et al.*, 2002) address the feasibility of LPE growth of  $\text{Al}_x\text{Ga}_y\text{In}_{1-x-y}\text{Sb}_{1-x}\text{Bi}_z/\text{InSb}$  heterostructures.

Magnetic semiconductors can be realized with a significant fraction of rare earth or transition metal ions substituted on lattice sites, as for example,  $\text{In}_{1-x}\text{Mn}_x\text{As}$  and  $\text{Ga}_{1-x}\text{Mn}_x\text{As}$ , where Mn is substituted for In or Ga in InAs and GaAs, respectively. These materials have potential application for spin transistors. Kim *et al.* (Kim *et al.*, 2002a, b) grew  $\text{Ga}_{1-x}\text{Mn}_x\text{As}$  epilayers by LPE on GaAs substrates. The Mn composition ranged from 1 to 7%. The GaMnAs layers were grown at  $595^\circ\text{C}$  from 1:1 Ga:Bi solvents saturated with arsenic and a manganese atomic fraction in the liquid phase ranging from 0.03 to 0.15. Surface morphology was observed to degrade with increasing Mn concentration. The addition of bismuth to the melt increased growth rates.

### 12.5.12 Control of segregation in LPE-grown alloys

A longstanding problem in LPE is related to growth of Al-containing III-V alloys that are of interest to optoelectronics and especially visible LEDs. With the notable exception of AlGaAs, many Al-containing III-V alloys, such as AlInP and AlGaInP, are notoriously difficult to grow by LPE. This is perhaps ironic since, historically, one of the original and most compelling motivations to develop LPE was related to its ability to grow AlGaAs structures; AlGaAs was less susceptible to oxidation effects in LPE than CVD. As Stringfellow (Stringfellow, 1988) noted, ‘many of the desirable properties of AlInGaP have been recognized for a number of years, yet this alloy remained in a rather primitive state due to near impossibility of growing the AlGaInP alloys either by LPE or chloride VPE.’ More generally, prior to the development of MOCVD and the use of organometallic precursors for Al, the high affinity of Al compounds for oxygen made vapor phase growth of Al-containing III-V materials impractical. For LPE of AlGaInP, the difficulty was related to controlled incorporation of Al into the solidifying III-V epilayer. Specifically, phase equilibria calculations indicate that the growth of AlGaInP from Al-In-Ga-P melts (or the growth of AlInP from Al-In-P melts) requires a melt composition that is dilute in aluminum ( $X_{\text{Al}} \approx 10^{-4}$ ) and rich in indium. However, the high segregation coefficient of Al in indium melts ( $k_{\text{Al}} \approx 10^4\text{--}10^5$ ) means that the melt is rapidly depleted of aluminum, and the Al fraction in the epilayer changes drastically.

Inadequate control of segregation to achieve target composition profiles of ternary and quaternary layers is a severe drawback of LPE. Since to a first order, the composition of the LPE layer is determined by phase equilibria considerations, this problem would be appear to be a fundamental limitation of LPE. Nevertheless, there is some work addressing this aspect of LPE, as well as related work that may find application to better control of LPE segregation effects and epitaxial layer compositions.

Shibano *et al.* (Shibano *et al.*, 1993) and Takahashi *et al.* (Takahashi *et al.*, 1994) achieved LPE-grown AlInGaP with high Al content using short growth times from a

nonequilibrium solution with a high aluminum fraction, and by growing the AlGaInP on an Al<sub>0.9</sub>Ga<sub>0.1</sub>As buffer layer. AlGaInP electroluminescence emission wavelengths of 645 nm were measured. Although this is outside the 590–630 nm range of commercial ultrabright AlGaInP LEDs, it suggests that improvements in the aluminum segregation phenomena for Al-/In-containing III-V alloys are possible. Kato *et al.* (Kato *et al.*, 1996) reported that AlGaInP alloys, with Al atomic fractions up to 0.2, could be grown on GaAs by depositing Al on the GaAs substrate and contacting the Al-coated substrate with a supercooled ( $\Delta T = 12^\circ\text{C}$ ) In-Ga-P melt at  $788^\circ\text{C}$ .

In general, the compositional grading observed in LPE is due to two effects: depletion of components from the melt as discussed above, and variation in the temperature-dependent segregation as the melt is cooled (Rado and Crawley, 1972). A large segregation coefficient (e.g.  $k > 10$ ) exacerbates melt depletion effects. More complex melt compositions that include ‘neutral’ components such as bismuth, tin, lead, and other components that are not incorporated to a significant degree into the epitaxial layer, but which may modify the segregation coefficients of epilayer components, can be considered. The segregation coefficient for a species  $i$  is a function of its activity in the liquid phase:

$$k_i \equiv \frac{X_i^S}{X_i^L} = \frac{\gamma_i^L}{\gamma_i^S} \cdot \exp \left[ \frac{\Delta G_i^{\text{FUS}}(T)}{RT} \right]$$

where  $\Delta G_i^{\text{FUS}}(T)$  is the free energy of fusion for the pure component,  $\gamma_i^L$  is the activity of the component in the liquid phase, and  $\gamma_i^S$  is the activity of the component in the alloy. In the regular solution model, the liquid phase segregation coefficient is given by, for example, for component 1 in a four-component melt, as (Panish, 1973):

$$\begin{aligned} RT \ln \gamma_1^L = & \Omega_{12}x_2^2 + \Omega_{13}x_3^2 + \Omega_{14}x_4^2 + (\Omega_{12} + \Omega_{13} - \Omega_{23})x_2x_3 \\ & + (\Omega_{12} + \Omega_{14} - \Omega_{24})x_2x_4 + (\Omega_{13} + \Omega_{14} - \Omega_{34})x_3x_4 \end{aligned}$$

where  $x_i$  are the liquid phase atomic fractions and  $\Omega_{ij}$  are the binary interaction parameters. Thus, it is conceivable that melt compositions and additions to the melt can be tailored to increase/decrease the liquid phase activity coefficients for particular components, and thereby increase/decrease their segregation coefficients. In particular, ‘neutral solvents’ such as Pb and Bi in III-V LPE can be explored for effects on segregation (Grebnyuk *et al.*, 1990). Also, Sangwal and Pa czyński (Sangwal and Pa czyński, 2000) indicate a supersaturation dependence of segregation coefficients in solution growth, which may also be operative in LPE. The temperature effects on segregation can be ameliorated by using a steady-state method of growth with a solid source and driven by an imposed temperature difference or by electric current induced electromigration or Peltier effects. Whether in general the segregation coefficient of a species can be modified by as much as a factor of 10 or 100 by optimizing melt composition is not certain.

The segregation of components may be modified by application of electric currents across the growth interface. Lagowski *et al.* (Lagowski *et al.*, 1980) derived expressions for the variation of (dopant) segregation in LPEE terms of LPEE growth parameters. Presumably, the segregation of alloy components (e.g. Al) in addition to dopants, could be similarly altered by application of an electric current. Further, the use of an AlGaAs (or AlGaP) solid source in contact with the melt during growth, rather than using a GaAs (or GaP) source, or relying on an As-saturated, Al-containing melt, might be used to



replenish the melt with Al, and thus reduce compositionally grading due to depletion of Al from the melt. Similar approaches have been used with solution growth of bulk GaInSb crystals where a polycrystalline GaInSb is used for continuous solute feeding of the growth solution (Tanaka *et al.*, 1998). For the case of Al segregation in Al-containing III-V alloys, estimates of the degree to which the segregation can be altered by electroepitaxy effects or tailoring melt composition indicate modest utility of these approaches, although melt compositions that might dramatically impact aluminum segregation have not been fully explored. Abramov *et al.* (Abramov *et al.*, 1997) demonstrated that the aluminum segregation in AlGaAs LPE could be substantially modified by using ultrafast cooling rates ( $10^2$ – $10^3$  °C s<sup>-1</sup>), and that aluminum composition gradients in the epilayer could be reversed from what is observed in LPE with slow cooling.

Another option is to grow thin layers of the alloy semiconductor in successive LPE steps. In the case of aluminum III-V alloys, a stack of thin layer of high-Al content alloy could be grown from separate melts, followed by post-growth annealing to level the composition profile. Finally, certain growth techniques to control segregation developed for bulk crystal growth of ternary alloys may be adaptable to LPE. For example, double crucible, floating crucible or solute feeding methods (Mataré, 1963; Watanabe *et al.*, 1993; Ono *et al.*, 1994; Koh and Fukuda, 1996; Nakajima and Kusunoki, 1996; Tanaka *et al.*, 1998; Kinoshita *et al.*, 2000; Kozhemyakin, 2000; Mitric *et al.*, 2004; Yildiz *et al.*, 2005) where controlled solute delivery to the growth interface by diffusion through one or more capillaries connecting two melts of distinct compositions, could be implemented for LPE.

### 12.5.13 LPE heteroepitaxy

In general, the application of LPE for the growth of heterostructures with relatively large lattice mismatch has proved difficult. Typically, LPE has been limited to growth of epitaxial layers with less than 1% relative lattice mismatch between the epitaxial layer and substrate, but as discussed below, there are many exceptions. It is often difficult or problematic to induce a thermodynamic driving force for growth from the liquid phase that is sufficient to overcome the energetic barrier associated with nucleating a lattice-mismatched epilayer on a substrate. The required high supersaturations may lead to homogeneous nucleation in the bulk of the melt. Even if homogeneous nucleation can be avoided, high supersaturations promote three-dimensional discrete nucleation, and the coalescence of discrete nuclei to form a continuous layer results in defects. Also, for many heterostructure pairs there is a significant disequilibrium between the melt and the exposed solid phase (i.e. the substrate or epilayer grown in a previous step), such that appreciable dissolution of the underlying substrate or epilayer occurs upon contact with the melt. As a specific example, to grow InGaP on GaAs, a GaAs substrate is brought in contact with a melt containing In, Ga and P. This melt can never be in equilibrium with a GaAs substrate, and there will be a tendency to meltback the substrate in order to saturate the melt with arsenic, and the regrowth will be InGaAsP. Limitations with regard to the growth of heterostructures constitute one of the major disadvantages of the LPE technique relative to MBE and MOCVD.

Thus, LPE of heterostructures raises a host of issues, many related to phenomena that curtail the applicability of LPE for producing a number of heterostructure types, or

else limit the abruptness of the interfaces. Almost inevitable, the interface between the melt and substrate (or previously grown layer) exhibits thermodynamic instability, and this results in potential dissolution (etch-back) of the substrate, which in turn alters the melt composition in the vicinity of the substrate. Fortunately, there are many systems where dissolution can be avoided or minimized including AlGaAs on GaAs, GaAs on InGaP and InGaAs on InP (Hsieh, 1980). Often, increasing the supersaturation can suppress substrate meltback. Kuphal (Kuphal, 1989) reduced meltback in GaInAsP/InP LPE heteroepitaxy using a grating surface, a tin-based melt, and low growth temperature. Kim *et al.* (Kim *et al.*, 1995) showed addition of Se to the melt could prevent substrate meltback in GaAs on InP LPE. The complex phenomena that occur during LPE heteroepitaxy, such as dissolution of the substrate, solid-phase diffusion of substrate components and liquid-phase diffusion of melt components, formation of transition layers, achievement of local equilibrium and lattice mismatch effects, have been treated by numerous workers (Aleksandrov, 1975; Batryev *et al.*, 1979; Small and Ghez, 1979, 1980, 1984; Small *et al.*, 1980; Bolkhovityanov, 1981, 1982, 1989, 1991; Ghez and Small, 1981; Benchimol and Quillec, 1982; Bolkhovityanov and Chikicher, 1983; Bolkhovityanov *et al.*, 1986a,b, 1988, 1989; Kuznetsov *et al.*, 1988; Olchowik *et al.*, 1994, 1995, 1996; Kimura *et al.*, 1996; Asomoza *et al.*, 2002).

### 12.5.13.1 III-V heterostructures by LPE

Despite the above generalizations, there are numerous reports for using LPE to grow lattice-mismatched heterostructures, as well as heterostructures between semiconductors with widely differing compositions (Table 12.4). Gottschalch *et al.* (Gottschalch *et al.*, 1978) noted that the growth of GaP on GaAs by LPE from Ga melts is difficult due to dissolution of the GaAs substrate in saturated Ga-P solutions. Instead, they were able to grow GaP on GaAs using Ge or Sn as the solvent, and for which GaAs has a lower solubility. More recent LPE work suggests that melt chemistries and optimized temperature schedules can be formulated to reduce substrate dissolution and facilitate heteroepitaxial growth in systems with relatively large lattice mismatch. A few examples are illustrative. Udon *et al.* (Udon *et al.*, 1996) optimized supersaturations in GaAs-on-GaP LPE to reduce twinning defects. Kim and Lee (Kim and Lee, 1994); Kim *et al.* (Kim *et al.*, 1995) grew high-quality GaAs on InP by LPE using a two-step growth process that included an initial Se-doped GaAs buffer layer. The selenium doping prevented or reduced substrate meltback. Maronchuck *et al.* (Maronchuck *et al.*, 2004) used a 'pulse cooling' technique wherein a pre-cooled substrate is contacted with melt for a short time (0.1 to several seconds). The substrate temperature is about 25 °C lower than the melt temperature at contact. Using this technique, they were able to grow GaSb and GaSb-rich alloys on InAs substrates and avoid dissolution of the substrate. Most reports provided little in the way of materials characterization, so it is not clear to what degree material quality is compromised by using atypical melt chemistries and growth regimens. Repeated application of LPE, where an initial LPE step is performed, the sample removed from the LPE system, subjected to various processing steps, and returned to the LPE system for additional epitaxial regrowth is also feasible, and may facilitate LPE production of certain heterostructures. Elaborate load-locks and/or glove boxes are often employed in LPE systems to avoid excessive oxidation or other contamination of the substrate (Iga and Kinoshita, 1996).

**Table 12.4** LPE of Some III-V heterostructures

Epilayer	Substrate	Approx. lattice mismatch (%)	Melt	Growth Temp (°C)	Ref.
AlGaAs	GaP	4	Al-Ga-As	850–900	Woodall <i>et al.</i> , 1972
Al <sub>0.48</sub> In <sub>0.52</sub> As	InP	0	Al-In-As	700–800	Nakajima <i>et al.</i> , 1982
AlGaAs	InGaP/GaAs	0	Al-Ga-As	780	Wu <i>et al.</i> , 1991
AlGaInP	GaAs	0	Al-Ga-In-P	800	Kazumura <i>et al.</i> , 1983
AlGaSb	InAs	0.6	Al-Ga-Sb		Pramatarova and Tret'yakov, 1982
AlGaAsSb	GaSb	<0.5	Al-Ga-As-Sb	590–594	Piskorski <i>et al.</i> , 2004
GaAs	InP	5	Ga-As (Se)	750	Kim and Lee, 1994; Kim <i>et al.</i> , 1995
GaAs	GaP	4	Ga-As	700–800	Udono <i>et al.</i> , 1996
GaAsSb	GaAs	0.3	Ga-Sb-As	850	Wosinski <i>et al.</i> , 1995
GaP	GaAs	4	Bi, Pb, Sn	900–1000	Gottschalch <i>et al.</i> , 1978
GaSb	InAs	0.6	Ga-Sb	450	Maronchuk <i>et al.</i> , 2004
InAs	GaAs	7	In-As		Butter <i>et al.</i> , 1974
InAsSb	InAs	1.8	In-Sb-As	300–400	Popov <i>et al.</i> , 1998
InAsSb	GaAs	7–9	In-Sb-As	430–550	Dixit <i>et al.</i> , 2004; Peng <i>et al.</i> , 2006
InGaAs	InP	0	In-Ga-As	680–750	Yamazaki <i>et al.</i> , 1984
In <sub>0.8</sub> Ga <sub>0.2</sub> P	GaAs	2.3	In-Ga-P	780	Uematsu <i>et al.</i> , 2005
In <sub>0.8</sub> Ga <sub>0.2</sub> P	InP	1.4	In-Ga-P	600	Kaneko <i>et al.</i> , 2002
InGaAsP	GaAs	0.5–1	In-Ga-As-P	785	Tanaka <i>et al.</i> , 1986
InGaAsSb	GaSb	<1	In-Ga-As-Sb	600	Joullie <i>et al.</i> , 1986; Tournie <i>et al.</i> , 1991
InGaAsSb	InP, InAs	<1	In-Ga-As-Sb	500	Gong <i>et al.</i> , 1989
InAsSbP	InAs	<0.5	In-Sb-P-As	560–600	Tournie <i>et al.</i> , 1991; Mani <i>et al.</i> , 1992
InSb	GaAs	14	In-Sb	400–420	Dixit <i>et al.</i> , 2002

### References

- E. Butter, B. Jacobs and J. Stary (1974) LPE growth of InAs on GaAs substrates. *Phys. Status Solidi A* **26**, k105–k107.
- V.K. Dixit, B.V. Rodrigues, H.L. Bhat, R. Venkataraghavan, K.S. Chandrasekaran and B.M. Arora (2002) Growth of InSb epitaxial layers on GaAs (001) substrates by LPE and their characteristics. *J. Cryst. Growth* **235**, 154–160.
- V.K. Dixit, B. Bansal, V. Venkataraman, H.L. Bhat, K.S. Chandrasekharan and N.M. Arora (2004) Studies of high resolution x-ray diffraction, optical and transport properties of InAs<sub>x</sub>Sb<sub>1-x</sub>/GaAs ( $x \leq 0.06$ ) heterostructures grown using liquid phase epitaxy. *J. Appl. Phys.* **96**, 4989–4997.
- X.Y. Gong, F.-S. Gao, Z.-G. Wang and W.-Q. Han (1989) LPE characterization of Ga<sub>x</sub>In<sub>1-x</sub>As<sub>1-y</sub>Sb<sub>y</sub>/InP and Ga<sub>x</sub>In<sub>1-x</sub>As<sub>1-y</sub>Sb<sub>y</sub>/InAs. *Sci. China, Ser. A* **32**, 1146–1152.
- V. Gottschalch, E. Butter, K. Jacobs and P. Kramer (1978) Liquid phase epitaxial deposition of GaP on GaAs. *J. Cryst. Growth* **44**, 157–162.
- A. Joullie, F. Jia Hua, F. Karouta and H. Mani (1986) LPE growth of GaInAsSb/GaSb system: The importance of the sign of the lattice mismatch. *J. Cryst. Growth* **75**, 309–318.

**Table 12.4** (continued)

- M. Kaneko, S. Nakayama, K. Kashiwa, S. Aizawa and N.S. Takahashi (2002) Lattice mismatched LPE growth of InGaP on patterned InP substrate. *Cryst. Res. Technol.* **37**, 177–182.
- M. Kazumura, I. Ohta and I. Teramoto (1983) Feasibility of the LPE growth of  $\text{Al}_x\text{Ga}_y\text{In}_{1-x-y}\text{P}$  on a GaAs substrate. *Jpn. J. Appl. Phys.* **22**, 654–657.
- D.-K. Kim and B.-T. Lee (1994) Heteroepitaxial growth of GaAs on (100) GaAs and InP by selective liquid phase epitaxy. *Jpn. J. Appl. Phys., Part 1* **33**, 5870–5874.
- D.-K. Kim *et al.* (1995) Liquid phase epitaxial growth of high quality GaAs on InP using Se-doped GaAs buffer layer and grating-patterned substrates. *J. Appl. Phys.* **66**, 2531–2533.
- H. Mani, E. Tournie, J.L. Lazzari, C. Alibert, A. Joullie and B. Lambert (1992) Liquid phase epitaxy and characterization of  $\text{InAs}_{1-x-y}\text{Sb}_x\text{P}_y$  on (100) InAs. *J. Cryst. Growth* **121**, 463–472.
- I.Y. Maronchuk, V.V. Kurak, E.V. Andronova and Y.A. Baganov (2004) Obtaining GaSb/InAs heterostructures by liquid phase epitaxy. *Semicond. Sci. Technol.* **19**, 747–751.
- K. Nakajima, T. Tanahashi and K. Akita (1982) Liquid phase epitaxial growth of lattice-matched  $\text{Al}_{0.48}\text{In}_{0.52}\text{As}$  on InP. *Appl. Phys. Lett.* **41**, 194–196.
- C. Peng, N. Chen, F. Gao, X. Zhang, C. Chen, J. Wu and Y. Yu (2006) Liquid-phase-epitaxy-grown  $\text{InAs}_x\text{Sb}_{1-x}/\text{GaAs}$  for room-temperature 8–12  $\mu\text{m}$  infrared detectors. *Appl. Phys. Lett.* **88**, 242108-1–242108-3.
- M. Piskorski *et al.* (2004) LPE growth and characterization of GaInAsSb and GaAlAsSb quaternary layers on (100) GaSb substrates. *Thin Solid Films* **459**, 2–6.
- A.S. Popov, A.M. Koinova and S.L. Tzeneva (1998) The In-As-Sb phase diagram and LPE growth of InAsSb layers on InAs at extremely low temperatures. *J. Cryst. Growth* **186**, 338–343.
- L.D. Pramatarova and D.N. Tret'yakov (1982) Growth of heterostructures based on InAs- $\text{Al}_x\text{Ga}_{1-x}\text{Sb}$ . *Cryst. Res. Technol.* **17**, 1463–1467.
- S. Tanaka, K. Hiramatsu, Y. Habu, N. Sawaki and I. Akasaki (1986) The initial stage of LPE growth of InGaAsP on GaAs in the region of the miscibility gap. *J. Cryst. Growth* **79**, 978–983.
- E. Tournie, J.L. Lazzari, H. Mani, F. Pitard, C. Alibert and A. Joullie (1991) Growth by liquid phase epitaxy and characterization of GaInAsSb and InAsSbP alloys for mid-infrared applications (2–3  $\mu\text{m}$ ). *Proc. SPIE* **1361**, 641–656.
- H. Uono, A. Motogaito, M. Kimura, A. Tanaka and T. Sukegawa (1996) Suppression of twins in GaAs layers grown in a GaP(111)B substrate by liquid phase epitaxy. *J. Cryst. Growth* **169**, 181–184.
- S. Uematsu, M. Nomoto, S. Nakayama and N.S. Takahashi (2005) Large area lateral overgrowth of mismatched InGaP on GaAs(111)B substrates. *Cryst. Res. Technol.* **40**, 1113–1117.
- J.M. Woodall, R.M. Potemski, S.E. Blum and R. Lynch (1972)  $\text{Ga}_{1-x}\text{Al}_x\text{As}$  LED structures grown on GaP substrates. *Appl. Phys. Lett.* **20**, 375–377.
- T. Wosinski, A. Makosa, T. Figielski and J. Raczyska (1995) Deep levels caused by misfit dislocations in GaAsSb/GaAs heterostructures. *Appl. Phys. Lett.* **67**, 1131–1133.
- M.-C. Wu, S.-C. Lu, C.-Y. Lee and Y.-C. Yang (1991) Interface abruptness and LED performance of the AlGaAs/InGaP single heterostructure grown on liquid-phase epitaxy. *J. Cryst. Growth* **112**, 803–807.
- S. Yamazaki, K. Nakajima and Y. Kishi (1984) Liquid phase epitaxial growth for (111)A InP/InGaAs heterostructure avalanche photodiodes. *Fujitsu Sci. Tech. J.* **20**, 329–383.

Using a combination of chemical etching, heat-cleaning, melt-back and substrate soaking in HCl to remove surface oxides, Takeda *et al.* (Takeda *et al.*, 1984) were able to achieve LPE growth of AlGaSb on GaSb substrates at temperatures as low as 250 °C. Surface passivations, such as the sulfide treatments mentioned in Section 12.5.4, or other processing and etching steps, should be helpful in this regard. Systematic studies of surface

effects and improved methods of substrate preparation are warranted. Along these lines, Zhou (Zhou, 1987) observed the effects of localized regions of concentrated stress on substrate surfaces in inhibiting LPE growth. Olvera-Hernández *et al.* (Olvera-Hernández *et al.*, 2004) noted that the substrate conductivity and doping type influenced LPE growth rates, and this was attributed to electric field at the substrate–melt interface that modifies the initial crystallization kinetics. Saitoh *et al.* (Saitoh *et al.*, 2000) concluded that exposure to air resulted in the GaP–GaP interface LPE regrowth with an excess ion density (probably due to silicon, iron, oxygen surface contaminants) that could be reduced by HCl/H<sub>2</sub>O etching, optimizing growth rates, and control of phosphorus vapor pressure in the growth ambient. Gas bubble formation in the melt may also contribute to irregular growth features in LPE (Nguyen Thanh Nghi, 1988).

### 12.5.13.2 III-V heteroepitaxy on silicon and hybrid epitaxy

The LPE growth of GaAs directly on silicon is feasible but requires some special considerations. High supersaturations are needed to overcome the 4% lattice mismatch between silicon and GaAs, which often results in three-dimensional nucleation and high defect levels. More troublesome is dissolution of the silicon substrate in the melt, which creates rough interfaces and results in high-silicon doping of the LPE layer. Nevertheless, there are several reports of LPE growth of GaAs, GaP or Ge directly on silicon using high supercoolings (Donnelly and Milnes, 1966; Nakano, 1967; Kurata and Hirai 1968; Rosztochy and Stein, 1972; Beneking *et al.*, 1977; Presnov *et al.*, 1978; Zolper and Barnett, 1989; Brovkin *et al.*, 1988; Saidov and Saidov, 1991; Zavadski *et al.*, 1991; Dorogan *et al.*, 1992; Valery *et al.*, 1992).

To overcome these problems, hybrid epitaxy methods have been developed that combine an initial CVD or MBE step with a subsequent LPE step (Sakai *et al.*, 1988; van der Ziel *et al.* 1988; Nakamura *et al.*, 1989; Yazawa *et al.*, 1990; Cotter *et al.*, 1992; Baldus *et al.*, 1994; Schnabel *et al.*, 1995). A GaAs-on-silicon ‘buffer’ layer is first grown by CVD or MBE. A GaAs (or AlGaAs) LPE layer is then grown on the GaAs-on-silicon buffer layer. The rationale for such hybrid epitaxy methods is that the GaAs-on-silicon buffer layer serves to bridge the lattice mismatch between GaAs and silicon and protect the underlying silicon substrate from dissolution in the LPE step. The buffer layer is highly defective, but the LPE layer grown on the buffer layer will exhibit a significant reduction in defects. For example, Saravanan *et al.* (Saravanan *et al.*, 1998) reported ‘drastic reduction’ in dislocation densities in GaAs-on-silicon using a hybrid LPE/MOCVD technique compared with MOCVD alone. Similar hybrid LPE/CVD processes have also been reported for GaAs on spinel (Ladany and Wang, 1972), GaP on silicon (Igarashi, 1977), InGaAsP on InP (Asahi *et al.*, 1983), and mercury cadmium telluride (Sand *et al.*, 1985).

Similar hybrid epitaxy techniques have been developed for InP-on-silicon (Collins *et al.*, 1990; Naritsuka *et al.*, 2000), and the method can be advantageously combined with selective epitaxy and epitaxial lateral overgrowth techniques for further defect reduction (see Section 12.5.5). These latter methods serve to reduce defects associated with lattice mismatch as well as those due to thermal stress effects caused by the difference in thermal expansion coefficients of the silicon substrate and III-V epitaxial layers. Chang *et al.* (Chang *et al.*, 1998) showed a combination of hybrid LPE/MBE approach with ELO could produce 43µm wide areas of dislocation-free GaAs-on-silicon epilayers. Chen *et al.*

(Chen *et al.*, 2004) described a ‘parasitic LPE/MBE’ process that occurs in MBE of InAs on GaP due to an initial dissolution and recrystallization from a liquid phase that forms on the growth surface.

### 12.5.13.3 Heterostructures formed by chemical conversion

One method of circumventing heteroepitaxy limitations and unfavorable segregation coefficients is based on the post-growth chemical conversion of the epitaxially grown material into an alloy. Such chemical conversions can be implemented in LPE systems and can considerably widen the applications of LPE-grown material.

Sukegawa *et al.* (Sukegawa *et al.*, 1993; Uono *et al.*, 1993) reported a new LPE technique for conversion of GaAs to GaAsP by annealing a GaAs-on-GaP epilayer in a Ga-As-P melt. Their technique was based on three observations: (1) a GaAs layer can be grown on a GaP substrate by LPE despite the large (4%) lattice mismatch; (2) a substrate (or underlying layer) having a melting point lower than that of the grown alloy epilayer tends to erode (dissolution in the melt), which can change its composition; and (3) growth of an epitaxial alloy with a melting point lower than that of the substrate (or underlying layer) tends to be stable. To grow GaAsP alloys over a wide composition range, a 4  $\mu\text{m}$  thick GaAs epilayer is first grown on a (111)B GaP substrate from a Ga-As-P melt at 795 °C. The GaAs epilayer is then contacted with a Ga-As-P melt at 795 °C for 1 h, which converts the GaAs layer into a GaAs<sub>1-x</sub>P<sub>x</sub> solid alloy. The alloy composition can be controlled by adjusting the composition of the Ga-As-P melt. Additional epitaxial layers of GaAsP can be grown on the GaAsP layer formed by conversion. Kimura *et al.* (Kimura *et al.*, 1996c) present a computational model of the GaAsP conversion process. Motogaito *et al.* (Motogaito *et al.*, 1997) described a similar process wherein an InP layer grown on a GaP substrate is converted to GaInP by isothermal contact with a saturated InGaP solution. Ruiz *et al.* (Ruiz *et al.*, 2004) report a process for forming Al<sub>x</sub>Ga<sub>1-x</sub>Sb films over GaSb substrates. Al films were evaporated on GaSb substrates. AlGaSb layers were formed by annealing for specified times and temperatures, on both of which the composition and thickness of the AlGaSb depends.

### 12.5.14 SiC and III-V nitride LPE

Difficulties in reproducibly growing bulk crystals and epitaxial layers of silicon carbide and gallium nitride with low defect densities and controlled doping have impeded device applications of these wide-bandgap semiconductors for several decades. Currently, SiC is predominantly grown by CVD processes with mixtures of hydrocarbons, silanes or silane derivatives as precursors for carbon and silicon. GaN and related III-V nitrides and alloys are mainly grown by MOCVD (with organometallic precursors for the group III elements and ammonia for the group V element) on sapphire or SiC substrates. Problems and limitations related to *p*-type doping of the III-V nitrides have been solved with MOCVD, thus enabling blue LEDs, lasers, and wide-bandgap bipolar transistors for high-temperature and high-frequency applications. Nevertheless, these wide-bandgap materials still commonly exhibit performance-limiting defects such as micropipes in SiC (Muller *et al.*, 2004) and various point and extended defects in the III-V nitrides (Pearton *et al.*,

1999). Thus, application of LPE and other solution growth methods for production of low-defect SiC and III-V nitrides merits consideration, as it is well established from work with other III-V compound semiconductors that several defect-generating mechanisms commonly observed with other methods of epitaxy and bulk crystal growth either are nonoperative or are less severe with LPE.

LPE of SiC from silicon melts (saturated with carbon) was used to make some of the first commercial SiC blue LEDs (Brander and Sutton, 1969; von Munch *et al.*, 1976; von Munch, 1977; Suzuki *et al.*, 1976; Matsunami *et al.*, 1977; von Munch and Kurzinger, 1978). This process is technically challenging due to the high temperatures ( $\sim 2000^\circ\text{C}$ ) necessitated by the use of molten silicon as a solvent (Holmann and Mueller, 1999). Moreover, the SiC growth rates are slow. Also problematic are the relatively high levels of background impurities, and difficulties with a molten silicon melt, which is highly reactive. Subsequently, interest in SiC blue LEDs diminished with the advent of GaN-based blue LEDs. Nevertheless, there are still many applications for high-quality SiC material, including as a substrate for III-V nitride epitaxy, and for high-temperature electronics and sensors. LPE growth of SiC using metal solvents offers a means to reduce to growth temperatures, permitting use of conventional LPE systems with a graphite slideboat and furnace set-up (with a fused silica tube and a standard resistively heated horizontal tube furnace) similar to that used for III-V and silicon LPE. Again, the principal difficulty is the sparing solubility of carbon in metallic melts at temperatures below the melting point of silicon. Early work in this area included the growth of SiC from iron-containing melts (Halden, 1960), chromium-rich Cr-Si-C melts (Wolff *et al.*, 1969; Pellegrini *et al.*, 1972) and titanium-containing melts (Pellegrini and Feldman, 1974). Transition metals tend to form silicides and carbides in preference to SiC. Dmitriev *et al.* (Dmitriev *et al.*, 1992) reported the LPE growth of SiC from Ga-Al and Sn-Al melts in the temperature range of  $1200\text{--}1400^\circ\text{C}$  and also discussed the growth of SiC from Ge melts. Safaraliev *et al.* (Safaraliev *et al.*, 1984) described the current-induced crystallization of SiC from gallium-ytterbium melts. Dmitriev (Dmitriev, 1993) compiled solubility data of carbon in molten lead, tin, germanium, gallium, aluminum and silicon for application to SiC LPE, and Dmitriev and Cherenkov (Dmitriev and Cherenkov, 1993) reported LPE growth of SiC-AlN solid solution LPE layers with *p-n* junctions. Selective SiC LPE on masked substrates has also been demonstrated (Dmitriev *et al.*, 1992; Nikolaev *et al.*, 1996). Yakimova *et al.* (Yakimova *et al.*, 1996) studied the effect of growth parameters on the quality of LPE SiC grown from silicon-scandium solvents. Mauk *et al.* (Mauk *et al.*, 2001b) explored a number of metal solvents including Ga, Sn, Ga/Sn, Ni, Cu, and Zn-Al for low-temperature ( $900\text{--}1200^\circ\text{C}$ ) LPE of SiC. In the case of melts containing Zn, the (isothermal) growth mechanism is attributed to supersaturation induced by solvent evaporation. Tanaka *et al.* (Tanaka *et al.*, 2002, 2004a,b; Tanaka and Katsuno, 2006) developed low-temperature ( $\sim 1000^\circ\text{C}$ ) LPE of SiC using a Si-saturated Al-Sn melt replenished with carbon by exposure to  $\text{C}_3\text{H}_8$  gas. Experimental evidence for the utility of LPE in reducing defects in SiC epitaxy has been reported by Filip *et al.* (Filip *et al.*, 2004, 2005). LPE of SiC from 1:1 Si:Ge melts at  $1650^\circ\text{C}$  was shown to reduce micropipe (hollow-core dislocations) density by about 80%.

LPE of GaN and other III-V nitrides has also been developed. Jones and Rose (Jones and Rose, 1984) presented liquidus calculations for III-V nitrides (AlN, GaN and InN). The solubility of nitrogen in gallium is low (Thurmond and Logan, 1972) but can be

increased by using an overpressure of nitrogen (Madar *et al.*, 1975; Karpinski *et al.*, 1984). GaN can also be formed by reacting molten Ga with ammonia gas (Johnson *et al.*, 1932; Zetterstrom, 1970; Ejder, 1974; Elwell *et al.*, 1984). Logan and Thurmond (Logan and Thurmond, 1972) described the growth of GaN from Ga-Bi solvents using an imposed temperature-gradient across the melt to drive the growth process. The low solubility of nitrogen in molten metals was circumvented by replenishing the melt with nitrogen by a pyrolysis reaction of ammonia catalyzed by the surface of the molten metal. Klemenz and Scheel (Klemenz and Scheel, 2000) developed LPE of GaN on sapphire, LiGaO<sub>2</sub>, LiAlO<sub>2</sub> and GaN substrates. Novikov *et al.* (Novikov *et al.*, 1997) demonstrated controlled selective meltback etching of GaN epilayers using LPEE techniques. Several groups have reported GaN LPE techniques with molten sodium (Yamane *et al.*, 1998; Aoki *et al.*, 2002) and calcium (Kawamura *et al.*, 2003) as the solvent, representing a significant departure from conventional LPE techniques that normally use group II (Zn, Cu, Au), III (Al, In, Ga), IV (Sn, Pb) or V (Sb, Bi) metals. Kawamura *et al.* (Kawamura *et al.*, 2006) reported a 'drastic decrease' in dislocations during LPE of GaN. Kamei *et al.* (Kamei *et al.*, 2006) developed an LPE technique for AlN on 6H-SiC substrates using Cu-Al-Ti solutions under a nitrogen atmosphere and growth temperatures of 1600–1800 °C. For >30 μm thick AlN epilayers, dislocation densities as low as 10<sup>5</sup> cm<sup>-2</sup> were observed. A detailed treatment of the crystal growth of AlN, GaN, and InN from metallic solutions, including thermodynamics, transport, crystallographic aspects can be found in Krukowski *et al.* (Krukowski *et al.*, 2005) (See Chapter 6 for more on SiC LPE and Chapter 7 for more on GaN LPE.)

Alloys of III-V compounds with dilute nitrogen as group V substituent are of interest for reducing the bandgap of the parent III-V compound (Bi and Tu, 1997; Nishikawa *et al.*, 2003). Gao *et al.* (Gao *et al.*, 2003) used melt epitaxy to produce InNAsSb single crystals (see Section 12.5.5). Dhar *et al.* (Dhar *et al.*, 2004, 2005) reported the LPE growth of GaAsN from a Ga melt at 750 °C using a polycrystalline GaN (~2 wt%) as the source of nitrogen. The GaAsN had a nitrogen content of about 0.7% and an interstitial nitrogen defect related electron trap (with ionization energy of 0.65 eV) was observed. Addition of the rare earth erbium to the melt reduced the nitrogen content of the GaAsN. Mondal *et al.* (Mondal *et al.*, 2006) developed a similar process for LPE growth of GaSbN. Nitrogen incorporation in the GaSbN epilayer of up to 1.7% was determined with a bandgap reduction (relative to GaSb) of 0.37 eV.

### 12.5.15 Some other materials grown by LPE or solution growth

The foregoing has focused mainly on III-V semiconductors. LPE has also figured prominently in the development of mercury cadmium telluride (MCT)-based devices for infrared detection. LPE of MCT is reviewed in Chapter 9. Many other II-VI compounds and alloys have also been grown by LPE. Most II-VI compounds can be grown from group II-rich melts saturated with the group VI component, in processes completely analogous to III-V LPE. Alternatively, other metal solvents, such as tin or bismuth, can be employed. For example, ZnS, ZnSe, ZnTe, CdS, CdSe and CdTe can be grown from solution using bismuth (Rubenstein, 1966) or tin (Rubenstein, 1968) as a solvent. Generally, wide-bandgap II-VI compounds are difficult to dope both *p*- and *n*-type, thus thwarting the realization of *p-n* homojunctions for application to LEDs, laser diodes, solar cells and photodiodes. As



already discussed in other contexts, there is considerable latitude in modifying LPE processes to change point defect densities, luminescence characteristics, and impurity doping behavior. For example, Sano *et al.* (Sano *et al.*, 1993) reported LPE growth of ZnSe using a temperature-gradient method with a Zn-rich melt and controlled Se overpressure during post-growth annealing to achieve high luminescence and improved Hall mobilities. In the late 1990s, progress on nonequilibrium nitrogen *p*-type doping of ZnSe and related alloys improved the prospects of II-VI blue-emitting LEDs and lasers, but this renewed interest was overshadowed by the ground breaking work on GaN-based LEDs. (LPE work on II-VI materials relevant to blue LEDs is reviewed in the accompanying chapter on LEDs.) Interest in wide-bandgap II-VI semiconductors for application to blue LEDs has persisted (see Chapter 13), if for no other reason than to avoid infringing patents for GaN technology. The wide selection of dopants possible with LPE, as well as the capability tailoring melt compositions to control the relative activities of the group II and group VI components, in combination with controlling the partial pressures in the ambient vapor phase, can be exploited to address doping issues with these semiconductors. For instance, Sakurai *et al.* (Sakurai *et al.*, 1997) reported the liquid phase epitaxial growth of *p*-type ZnSe from a Se-rich melt using Na doping and a Zn overpressure of 3 atm. Thus, LPE shows promise for solving some of the previously intractable doping problems that have impeded progress in wide-bandgap II-VI semiconductor technology. Nevertheless, an important consideration is whether such doping limitations in general are the result of fundamental thermodynamic limitations, in which case, nonequilibrium processes are needed to produce metastable doping, and therefore LPE as a near-equilibrium growth process would have limited use. The viability of ZnSe-based optoelectronics is largely based on the realization of *p*-type ZnSe by nitrogen doping resulting from treatment with nitrogen-containing plasmas. Isoelectronic nitrogen doping of LPE-grown GaP and GaAsP for green-emitting LEDs is a well-established technology (Bergh and Dean, 1976). The usual method of nitrogen doping in LPE is to inject ammonia into the hydrogen ambient during LPE growth, which presumably results in atomic nitrogen dissolved in the melt and incorporation of nitrogen into the epitaxial layer. Alternative means of nitrogen incorporation are also possible. As mentioned in the previous section, Dhar *et al.* (Dhar *et al.*, 2004) report the use of polycrystalline GaN mixed in with the melt as a source for nitrogen for the LPE growth of GaAsN. This suggests that it might be feasible to incorporate nitrogen doping into LPE processes for doping wide-bandgap II-VI materials.

As an indication of the versatility and scope of solution (or melt) growth techniques in general, and LPE in particular, Table 12.5 provides a survey of some less-common materials grown from metallic or metal-containing liquid phases, as well as other melts and solvent systems. In some cases, a conventional LPE process was used to grow a film of the desired material on a substrate, but other cases involving unseeded precipitation or bulk crystal growth from dilute solutions or stoichiometric melts of the solidified material are also included, because presumably these systems could be adapted to an LPE technology for film growth as well. Along similar lines, Klemenz and Scheel (Klemenz and Scheel, 1997) have reviewed some of the previous work on growing high-temperature superconductors (YBCO, NdBCO and  $\text{Bi}_2\text{Sr}_2\text{CaCu}_2\text{O}_y$ ) by LPE. The use of fused oxides and molten salts portends consideration of different solvent types for LPE. Some recent developments in ionic liquids (molten salts with melting points below 100 °C) (Ohno, 2005) may offer the potential for very low-temperature liquid phase growth of semiconductors (Endres, 2004).

**Table 12.5** LPE or solution growth of various materials

Epilayer or solution-grown crystal	Substrate <sup>a</sup>	Solvent or melt	Approx. growth temp. (°C)	Ref.
BaB <sub>2</sub> O <sub>4</sub>	BaB <sub>2</sub> O <sub>4</sub>	Na <sub>2</sub> O flux	800–900	Liu <i>et al.</i> , 2004
Bi <sub>2</sub> Sr <sub>2</sub> CaCu <sub>2</sub> O <sub>x</sub>	MgO	KCl flux	850	Yasui <i>et al.</i> , 1992, Yamaguchi <i>et al.</i> , 1993
BiFeO <sub>3</sub>	SrRuO <sub>3</sub> /SrTiO <sub>3</sub>	Bi <sub>2</sub> O <sub>3</sub> -Fe <sub>2</sub> O <sub>3</sub>	700–800	Li <i>et al.</i> , 2006
CdGeAs <sub>2</sub>	—	Bi	400–600	Feigelson <i>et al.</i> , 1975
CdGeP <sub>2</sub>	—	Bi	700	Miotowski <i>et al.</i> , 1980
CdSe	ZnTe	Te	560	Onome <i>et al.</i> , 1989
CdSe	ZnTe, ZnSe	CdCl <sub>2</sub> , CdI <sub>2</sub> , or ZnCl <sub>2</sub>	600	Simashkevich and Tsiulanyu, 1976
CdSnP <sub>2</sub>	InP	Sn-Cd-P	500–600	Shay <i>et al.</i> , 1974
CdSiP <sub>2</sub>	—	Sn	1200	Buehler and Wernick, 1971
CuInS <sub>2</sub>	ZnSe	In-Cu-S	700	Takenoshita and Nakau, 1982a
CuInSe <sub>2</sub>	Mo-coated SiO <sub>2</sub>	In-Cu-Se	650	Ernst <i>et al.</i> , 2005
CuGa <sub>1-x</sub> In <sub>x</sub> S <sub>2</sub>	ZnSe	In	650	Takenoshita and Nakau, 1981
CuAlS <sub>2</sub> , CuAl <sub>1-x</sub> Ga <sub>x</sub> S <sub>2</sub>	—	In-Cu-Al-S	700–800	Yamamoto <i>et al.</i> , 1975
(CuNiPb)Fe <sub>2</sub> O <sub>4</sub> , CuFe <sub>2</sub> AlO <sub>4</sub>	MgO	PbO-B <sub>2</sub> O <sub>3</sub>	800–900	van der Straten and Mestselaar, 1980
CuSi <sub>2</sub> P <sub>3</sub>	—	Sn		Omar, 1998
GaS	—	Ga	1000–1200	Hársy, 1968
GaSe	—	Ga-Se	1000	Anis, 1981
Ga <sub>2</sub> Se <sub>3</sub>	—	Ga	1000–1200	Hársy, 1968
(Ge <sub>2</sub> ) <sub>1-x</sub> (ZnSe) <sub>x</sub>	Ge, GaAS	Sn	600–900	Saidov <i>et al.</i> , 2000
InS	—	In	1000–1200	Hársy, 1968
LiNbTaO <sub>3</sub>	LiNbO <sub>3</sub>	V <sub>2</sub> O <sub>5</sub>	1220	Kondo <i>et al.</i> , 1979
LiNbTaO <sub>3</sub>	LiNbO <sub>3</sub>	LiNbTaO- LiVO <sub>3</sub>	885–990	Kaigawa <i>et al.</i> , 1998
LiYF <sub>4</sub>	LiYF <sub>4</sub>	LiF + Y, Nd, Gd	800–900	Rogin and Hulliger, 1997
LuLaSmGaFe	Gd <sub>3</sub> Ga <sub>15</sub> O <sub>12</sub> garnet	PbO-V <sub>2</sub> O <sub>5</sub> flux	950	Berkstresser and Blank, 1981
(LuNdBi) <sub>3</sub> (FeAl) <sub>5</sub> O <sub>12</sub>	Gd <sub>3</sub> Ga <sub>15</sub> O <sub>12</sub> garnet	PbO-B <sub>2</sub> O <sub>3</sub> flux	750	Yokoi <i>et al.</i> , 1999
MgZnO	ZnO	MgCl <sub>2</sub> /ZnCl <sub>2</sub> / K <sub>2</sub> CO <sub>3</sub>	650	Sato <i>et al.</i> , 2006
MnCdHgTe	CZT	Mn-Cd-Hg-Te		Bazhenov <i>et al.</i> , 1992

(continued overleaf)

**Table 12.5** (continued)

Epilayer or solution-grown crystal	Substrate <sup>a</sup>	Solvent or melt	Approx. growth temp. (°C)	Ref.
Na <sub>2</sub> CaGe <sub>6</sub> O <sub>4</sub>	Nd <sub>3</sub> Ga <sub>5</sub> SiO <sub>14</sub>	K <sub>2</sub> O-V <sub>2</sub> O <sub>5</sub> flux	1000	Chani <i>et al.</i> , 1999
Na <sub>1-y</sub> K <sub>y</sub> Ta <sub>1-x</sub> Nb <sub>x</sub> O <sub>3</sub>	KaTaO <sub>3</sub>	KF/NaF/KTN flux	950	Sitar <i>et al.</i> , 1994
NdBa <sub>2</sub> Cu <sub>3</sub> O <sub>y</sub>	MgO	BaO <sub>2</sub> -CuO	1000	Takagi <i>et al.</i> , 1998
PbSnSe	PbSe/BaF <sub>2</sub> /CaF <sub>2</sub> /Si	Pb-Sn	500–620	Sachar <i>et al.</i> , 1998; Li <i>et al.</i> , 2000
PbTe	PbTe	Pb	560	Ito <i>et al.</i> , 1996
Pb <sub>0.8</sub> Sn <sub>0.2</sub> Te	Pb <sub>0.8</sub> Sn <sub>0.2</sub> Te	Pb-Sn-Te	520	Eger <i>et al.</i> , 1981
REBa <sub>2</sub> Cu <sub>3</sub> O <sub>7</sub> (RE = Y, Yb)	LiAlO <sub>3</sub>	BaO-CuO	900–1100	Qi and MacManus-Driscoll, 2001
SnO <sub>2</sub>	SnO <sub>2</sub>	Cu <sub>2</sub> O flux	1300	Kawamura <i>et al.</i> , 2002
SrFe <sub>8</sub> Al <sub>4</sub> O <sub>19</sub>	SrGa <sub>12</sub> O <sub>19</sub>	Bi <sub>2</sub> O <sub>3</sub>	1400–1500	Haberey <i>et al.</i> , 1980, 1983
Y <sub>3</sub> Fe <sub>5</sub> O <sub>12</sub>	Y <sub>3</sub> Al <sub>5</sub> O <sub>12</sub> , Cd <sub>3</sub> Ga <sub>5</sub> O <sub>12</sub> , Y <sub>3</sub> Ga <sub>5</sub> O <sub>12</sub>	BaO-B <sub>2</sub> O <sub>3</sub>	1050	Linares <i>et al.</i> , 1965
Y <sub>3</sub> Fe <sub>5</sub> O <sub>12</sub>	Gd <sub>3</sub> Ga <sub>5</sub> O <sub>12</sub>	MoO <sub>3</sub> -Li <sub>2</sub> O flux	1060–1160	Takagi <i>et al.</i> , 2002
Zn <sub>3</sub> As <sub>2</sub>	(CdZn) <sub>3</sub> As <sub>2</sub>	Bi	300–500	Matsuo <i>et al.</i> , 1978
ZnSe	—	PbCl <sub>2</sub>	1000	Triboulet <i>et al.</i> , 1999
ZnO	—	Sn	950	Spring-Thorpe and Pamplin, 1968
ZnSiP <sub>2</sub> , CdSiP <sub>2</sub> , ZnGeP <sub>2</sub> , CdGeP <sub>2</sub>	—	Sn	1300	Buehler and Wernick, 1971
ZnSnP <sub>2</sub>	GaAs	Zn+Sn+SnP <sub>3</sub>	500–700	Davis and Wolfe, 1983
ZnSnAs <sub>2</sub>	ZnSe	Sn	600	Takenoshita and Nakau, 1986
ZnTe	ZnSe	molten ZnCl <sub>2</sub>	600	Dobrynina <i>et al.</i> , 1986
ZnSe	ZnTe, ZnSe	CdCl <sub>2</sub> , CdI <sub>2</sub> , or ZnCl <sub>2</sub>	600	Simashkevich and Tsiulanyu, 1976
ZnSe	ZnSe	molten ZnCl <sub>2</sub>	600–700	Tanaka and Sukegawa, 2001

<sup>a</sup>Where no substrate is indicated, the method reported was a solution growth technique of bulk crystals instead of epitaxial films.

#### References

M.K. Anis (1981) The growth of single crystals of GaSe. *J. Cryst. Growth* **55**, 465–469.

**Table 12.5** (continued)

- N.L. Bazhenov, S.I. Gasanov, V.I. Ivanov-Omskii, K.E. Mironov and V.F. Movile (1992) High performance p-n junctions in LPE  $\text{Mn}_x\text{Cd}_y\text{Hg}_{1-x-y}$  Te layers. *Infrared Phys.* **33**, 169–173.
- G.W. Berkstresser and S.L. Blank (1981) LPE of LuLaSmGaFe garnet from a  $\text{PbO-V}_2\text{O}_5$  flux. *J. Appl. Phys.* **52**, 2332–2334.
- E. Buehler and J.H. Wernick (1971) Concerning growth of single crystals of II-IV-V diamond-like compounds  $\text{ZnSiP}_2$ ,  $\text{CdSiP}_2$ ,  $\text{ZnGeP}_2$  and  $\text{CdSnP}_2$  and standard enthalpies of formation for  $\text{ZnSiP}_2$  and  $\text{CdSiP}_2$ . *J. Cryst. Growth* **8**, 324–332.
- V.I. Chani, H. Takeda and T. Fukuda (1999) Liquid phase epitaxy of films with langasite structure. *Mater. Sci. Eng.* **B 60**, 212–216.
- G.A. Davis and C.M. Wolfe (1983) Liquid phase epitaxial growth of  $\text{ZnSnP}_2$  on GaAs. *J. Electrochem. Soc.* **130**, 1408–1412.
- E.S. Dobrynina, V.I. Petrov, A.V. Simashkevich and R.L. Sobolevkaja (1986) Properties of ZnTe grown from salt solvents. *J. Cryst. Growth* **76**, 83–87.
- D. Eger, A. Zemel, S. Rotter, N. Tamari, M. Oron and A. Zussman (1981) Junction migration in PbTe-PbSnTe heterostructures. *J. Appl. Phys.* **52**, 490–495.
- F. Ernst, J. Cowen, L. Lucas, P. Pirouz, A. Hepp and S. Bailey (2005) Liquid-phase deposition of single-phase alpha copper-indium-diselenide. *Mater. Sci. Eng.* **116**, 311–319.
- R.S. Feigelson, R.K. Route and H.W. Swarts (1975) Solution growth of  $\text{CdGeAs}_2$ . *J. Cryst. Growth* **28**, 138.
- F. Haberey, R. Leckebusch, M. Rosenberg and K. Sahl (1980) LPE-grown hexagonal strontium aluminoferrite films. *IEEE Trans. Magn.* **MAG-16**, 681–683.
- F. Haberey, R. Leckebusch, M. Rosenberg and K. Sahl (1983) Flux growth of  $\text{SrGa}_{12}\text{O}_{19}$  single crystals. *J. Cryst. Growth* **61**, 284–288.
- M. Hársy (1968) Synthesis and growth of ZnS, ZnSe, ZnTe, GaS,  $\text{Ga}_2\text{Se}_3$  and InS crystals in Ga and In melts. *Mater. Res. Bull.* **3**, 483–488.
- O. Ito, K. Suto and J.-I. Nishizawa (1996) Growth and electrical properties of PbTe epitaxial layers grown by temperature difference method under controlled vapor pressure liquid phase epitaxy. *J. Cryst. Growth* **163**, 353–358.
- K. Kaigawa, T. Kawaguchi, M. Imaeda, H. Saiki and T. Fukuda (1998) Crystal structure of LPE-grown  $\text{LiNb}_{1-x}\text{Ta}_x\text{O}_3$  epitaxial films. *J. Cryst. Growth* **191**, 119–124.
- F. Kawamura, T. Tsukasa, U. Futoshi and Y. Itaru (2002) AFM observation of the  $\text{SnO}_2$  bunching in high-temperature LPE growth. *J. Cryst. Growth* **244**, 173–177.
- S. Kondo, K. Sugii, S. Miyazawa and S. Uehara (1979) LPE growth of  $\text{Li}(\text{Nb,Ta})\text{O}_3$  solid-solution thin film waveguides on  $\text{LiTaO}_3$  substrates. *J. Cryst. Growth* **46**, 314–322.
- C.P. Li, P.J. McCann and X.M. Fang (2000) Strain relaxation in PbSnSe and PbSe/PbSnSe layers grown by liquid-phase epitaxy on (100) oriented silicon. *J. Cryst. Growth* **208**, 423–430.
- M. Li, A. Kursumovic, X. Qi and J.L. McManus-Driscoll (2006) Rapid epitaxial growth on magneto electric thick  $\text{BiFeO}_3$  films by hybrid liquid-phase epitaxy. *J. Cryst. Growth* **293**, 128–135.
- R.C. Linares, R.B. McGraw and J.B. Schroeder (1965) Growth and properties of yttrium iron garnet single-crystal films. *J. Appl. Phys.* **36**, 2884–2886.
- J. Liu, C. Xia, X. He, G. Zhou and J. Xu (2004) Residual stress in beta barium borate ( $\beta\text{-BaB}_2\text{O}_4$ ) thin films grown by liquid phase epitaxy. *J. Cryst. Growth* **267**, 161–165.
- I. Matsuo, M. Iwami and K. Kawabe (1978) Solubility of  $\text{Zn}_3\text{As}_2$  in Bi and LPE growth of  $\text{Zn}_3\text{As}_2$  on  $(\text{Cd}_x\text{Zn}_{1-x})_3\text{As}_2$  substrates from Bi solution. *Jpn. J. Appl. Phys.* **17**, 439–440.
- I. Miotkowski, S. Miotkowski and A. Horak (1980) Solution growth of  $\text{CdGeP}_2$  crystals and layers. *J. Cryst. Growth* **50**, 567–570.

**Table 12.5** (continued)

- M.S. Omar (1998) Tin solution growth and the analysis of single crystals of  $\text{Cu}_2\text{SiP}_2$  semiconductor. *J. Synth. Cryst.* **27**, 191–194. (in Chinese).
- S. Onome, T. Yamada, M. Sano and M. Aoki (1989) Relationship between surface treatment of ZnTe substrates and morphology of CdSe epitaxial layers in liquid phase epitaxy. *Jpn. J. Appl. Phys.* **28**, 1648–1653.
- X. Qi and J.L. MacManus-Driscoll (2001) Liquid phase epitaxy processing for high temperature superconductor tapes. *Curr. Opin. Solid State Mater. Sci.* **5**, 291–300.
- P. Rogin and J. Hulliger (1997)  $\text{LiYF}_4$  liquid-phase epitaxy using an inverted slider geometry. *J. Cryst. Growth* **179**, 551–558.
- H.K. Sachar, I. Chao, X.M. Fang and P.J. McCann (1998) Growth and characterization of PbSe and  $\text{Pb}_{1-x}\text{Sn}_x\text{Se}$  layers on Si(100). *MRS Symp. Proc.* **487**, 651–656.
- M.S. Saidov, A.S. Saidov, A.Sh. Razzakov (2000) Liquid phase epitaxy, photoluminescence and photoelectrical properties of variband  $(\text{Ge}_2)_{1-x}(\text{ZnSe})_x$  layers. *SPIE Proc.* **3975**, 1424–1427.
- H. Sato, D. Ehrentraut and T. Fukuda (2006) Growth of  $\text{Mg}_x\text{Zn}_{1-x}\text{O}/\text{ZnO}$  heterostructures by liquid phase epitaxy. *Jpn. J. Appl. Phys., Part 1* **45**, 190–193.
- J.L. Shay, K.J. Bachmann and E. Buehler (1974) Preparation and properties of CdSnP<sub>2</sub>/InP heterojunctions grown by LPE from Sn solution. *J. Appl. Phys.* **45**, 1302–1310.
- A.V. Simashkevich and R.L. Tsiulyanu (1976) Liquid-phase epitaxy of CdSe, ZnSe, and ZnTe layers. *J. Cryst. Growth* **35**, 269–272.
- Z. Sitar, R. Gutmann, H. Pierhofer and P. Gunter (1994) Liquid phase epitaxy of  $\text{Na}_{1-y}\text{K}_y\text{Ta}_{1-x}\text{Nb}_x\text{O}_3$  for pyroelectric applications. *MRS Symp. Proc.* **361**, 589–594.
- A.J. Spring-Thorpe and B.R. Pamplin (1968) Growth of some single crystal II-IV-V<sub>2</sub> semiconducting compounds. *J. Cryst. Growth* **3**, 313–316.
- A. Takagi, J.G. Wen, I. Hirabayashi and U. Mizutani (1998) Growth mode dependence of microstructures and superconducting and superconducting properties of  $\text{Nd}_{1+x}\text{Ba}_{2-x}\text{Cu}_3\text{O}_y$  thick films prepared by liquid-phase epitaxy. *J. Cryst. Growth* **193**, 71–79.
- T. Takagi, M. Fujino and T. Fujii (2002)  $\text{MoO}_3\text{-Li}_2\text{O}$  flux LPE growth of YIG films and its characterization. *J. Cryst. Growth* **237–239**, 725–729.
- H. Takenoshita and T. Nakau (1981) p-CuGa<sub>1-x</sub>In<sub>x</sub>S<sub>2</sub>/n-ZnSe by LPE method from in solution. *Jpn. J. Appl. Phys.* **20**, 1873–1878.
- H. Takenoshita and T. Nakau (1982a) Heteroepitaxy of CuInSe<sub>2</sub> on ZnSe by LPE method from in solution. *Jpn. J. Appl. Phys.* **21**, 18–22.
- H. Takenoshita and T. Nakau (1982b) LPE growth of ZnSnAs<sub>2</sub> on a ZnSe substrate from tin solution. *Jpn. J. Appl. Phys., Part 2*, **21**, 212–214.
- A. Tanaka and T. Sukegawa (2001) ZnSe growth from zinc chloride solvent by successive liquid phase epitaxy. *J. Cryst. Growth* **229**, 87–91.
- R. Triboulet, J.M. N'tep, M. Barbe, P. Lemasson, I. Mora-Sero and V. Munoz (1999) Some fundamentals of the vapor and solution growth of ZnSe and ZnO. *J. Cryst. Growth* **198–199**, 968–974.
- P.J.M. van der Straten and R. Metselaar (1980) LPE growth of Mn-Ni and Al-substituted copper ferrite films. *J. Appl. Phys.* **51**, 3236–3240.
- T. Yamaguchi, F. Ueda and M. Imamura (1993) Growth of superconductive  $\text{Bi}_2\text{Sr}_2\text{CaCu}_2\text{O}_x$  film by liquid phase epitaxy. *Jpn. J. Appl. Phys.* **32**, 1634–1635.
- N. Yamamoto, H. Kubo and T. Miyauchi (1975) The solution growth of CuAlS<sub>2</sub> and  $\text{CuAl}_{1-x}\text{Ga}_x\text{S}_2$  in In solution. *Jpn. J. Appl. Phys.* **14**, 299–300.
- K. Yasui, T. Ido, H. Terada and S. Muto (1992) LPE growth of  $\text{Bi}_2\text{Sr}_2\text{CaCu}_2\text{O}_y$  from KCl solution. *J. Cryst. Growth* **125**, 653–655.
- H. Yokoi, T. Mizumoto and T. Takano (1999) Selective-area growth of magnetic garnet crystals by liquid-phase epitaxy and its application to waveguide devices. *Jpn. J. Appl. Phys., Part 1* **38**, 4847–4851.

### 12.5.16 LPE for shaped crystal growth

Due to the near-equilibrium growth conditions typical of LPE and other characteristics of LPE that lead to anisotropic growth features under certain, but easily attained conditions, LPE selective growth on masked or structured substrates can be used to produce faceted or shaped structures for various semiconductor device and optics applications. This may be contrasted with the morphology of other epitaxy methods, wherein deposition generally yields a conformal film blanketing the substrate, regardless of any masking, patterning, or relief structure. There are numerous utilizations of selective growth or melt-back in LPE to make semiconductor structures with various optical features (King and Spring-Thorpe, 1975; Hahm *et al.*, 1991). Kim and Kwon (Kim and Kwon, 1987) made monolithic GaAs waveguides by selective LPE; facets of the selectively grown crystal served as critically oriented mirrors. Tapered GaAs-based optical waveguides with controllable profiles were made by selective LPE (Kim *et al.*, 1986). Cho *et al.* (Cho *et al.*, 1993) described a meltback-etching and regrowth process using AlGaAs/GaAs LPE on masked GaAs substrates that produced hemispherical microlens structures for LEDs (see Chapter 13). By controlling the mask opening area, composition of the melt and melt etching time, a precise control of the etch shape was possible.

Trah (Trah, 1990) and Konuma (Konuma, 2002) catalog some of the prismatic and corrugated shapes that can be realized in Si and SiGe LPE on masked substrates patterned with openings for selective epitaxy and ELO. Most of these features can be achieved in III-V compound LPE as well. Such faceted structures are of interest for solar cells, LEDs, thermophotovoltaic devices and detectors in that nonplanar surfaces and interfaces can enhance optical coupling and light-trapping effects, and also reduce defects and relieve stress. Hollow truncated InGaAs and GaSb pyramid structures have been grown by LPE (Balakrishnan *et al.*, 2002; Zhang *et al.*, 2005). AlGaAs pyramids with base dimensions of  $10\ \mu\text{m}$  or less have been grown by LPE as microtips for scanning near-field optical microscopy (Hu Lizhong *et al.*, 2002, 2004; Zhang Hongzhi *et al.*, 2006). A few additional examples display the capabilities of LPE processes in producing intricate structures. Figure 12.7 shows a faceted crystal of AlGaAs grown by selective LPE on a tungsten-masked GaAs substrate. Mauk and Curran (Mauk and Curran, 2001) observed a bridging formation in silicon LPEE on stripe-patterned, tungsten-masked (111) silicon

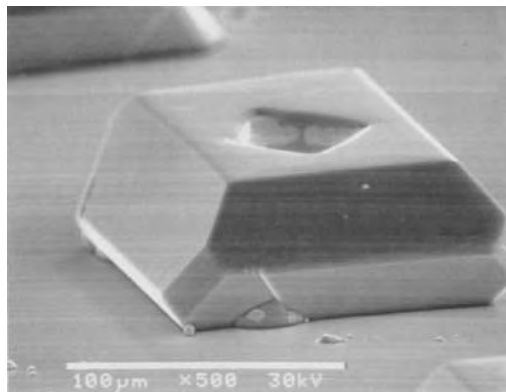


**Figure 12.7** Selectively grown LPE AlGaAs on GaAs substrates

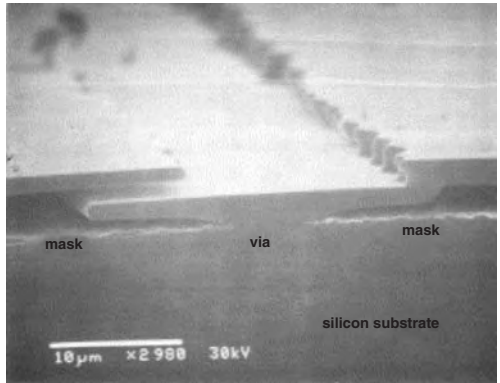


**Figure 12.8** LPEE lateral overgrowth of silicon on stripe-patterned, tungsten-masked (111) silicon substrates. From Mauk and Curran (2001)

substrates (Figure 12.8). The arching of the epitaxial layer over the masked areas of the substrate is attributed, in part, to the unfavorable energetics of the silicon epilayer ‘wetting’ the tungsten mask. Weber *et al.* (Weber *et al.*, 1998) demonstrated a rectangular mesh silicon structure grown by LPE on patterned, oxidized silicon substrates (Figure 12.9). It has long been noted that impurities can drastically alter growth morphology including

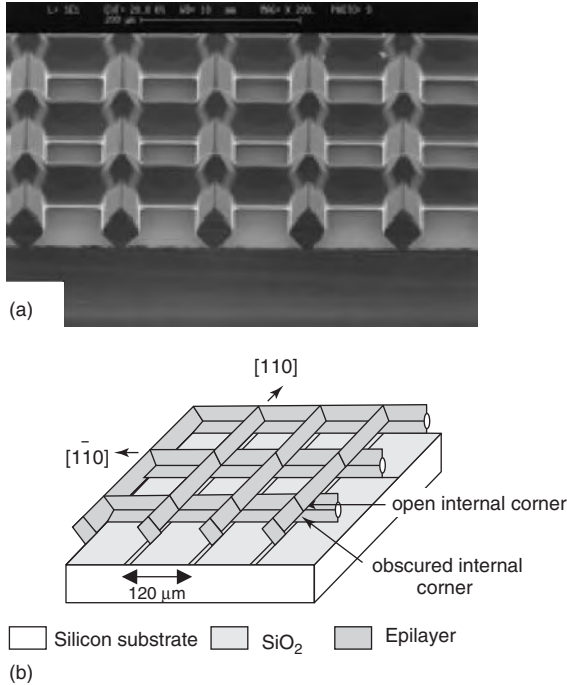


**Figure 12.9** Selective LPE of silicon mesh on grid-patterned, oxidized silicon substrate. (a) Photomicrograph, and (b) schematic showing crystallographic planes. Reprinted with permission from K.J. Weber, K. Catchpole and A.W. Blakers, Epitaxial lateral growth of Si . . . , *J. Cryst. Growth*, 186, 3, 369–374, Copyright (1998) Elsevier

the dominant faceting exhibited by semiconductor crystals grown from liquid metal solutions (Faust *et al.*, 1968). Adsorbed impurities and melt components, as well as strain, can alter surface energies of various crystal planes, stabilize certain facets and change nucleation kinetics, resulting in drastically different crystal morphologies (Hansson *et al.*, 1993). With regard to shaped LPE growth, Zhang *et al.* (Zhang *et al.*, 2005) reported the influence of tellurium impurities in modifying (in some cases drastically) the morphology of LPE GaSb on patterned substrates.

Thus, a unique feature of LPE is the ability to build complicated semiconductor structures and avoid elaborate post-growth processing steps (masking, lithography, selective and anisotropic etching). Instead, pre-growth preparation of the substrate leads to complicated or novel structures that would otherwise be impossible or difficult to achieve using other epitaxy techniques.

## 12.6 CONCLUSIONS AND OUTLOOK

While it is unlikely LPE will compete directly with MBE or MOCVD for production of ‘mainstream’ microelectronics devices, lasers, space solar cells and detector arrays, the foregoing suggests that some of the unique features of LPE can be exploited for many specialized semiconductor device and optics applications.

The simplicity of the LPE process—and its basis on phase equilibria rather than complex precursor chemistry, growth kinetics and mass transfer—provides a good platform for exploring new semiconductor materials, and developing and prototyping novel semiconductor device structures. The achievement of LPE layers with atomically flat surfaces over dimensions of 10  $\mu\text{m}$  is perhaps not widely appreciated. As discussed here, LPE can be advocated for at least several important near-term commercial applications. For example, the growth of customized, ‘virtual substrates’ with tunable lattice constants comprised of thick LPE-grown semiconductor alloy layers, perhaps utilizing ELO to reduce defect densities, and optionally enhanced by electroepitaxy phenomena induced by applied currents, as well as temperature-gradient induced effects, and modifications of solute distribution via a double-crucible apparatus adapted for LPE to control solute and dopant segregation, would profitably exploit the many inherent and unique features of LPE. Such customized LPE substrates would be more costly than current commodity substrate wafers made by Czochralski, float zone, Bridgman, or vertical gradient freeze bulk crystal growth techniques, and currently limited to elemental or binary semiconductors. However, in view of the prices commanded for SiC and GaN substrates in recent years, it is clear that for at least some applications, the semiconductor industry is willing to pay a high premium for substrates that enable improved material quality and/or new devices. In the future, LPE may thus compete more against these other liquid phase (bulk) crystal growth methods, rather than vacuum and vapor phase thin-film epitaxy technologies.

LPE still figures prominently in low-bandgap III-V optoelectronics for mid-infrared applications. In many cases, the best reported results for LEDs and detectors are for devices made by LPE. For these LPE-grown materials (InAsSb, InAsSbP, InGaAsSb, and related alloys), the low defect densities and impurity levels, the latter achieved often with impurity gettering by rare earths, are decisive. Some of the limiting features of LPE may yet be circumvented by novel melt chemistries and new methods of inducing growth, including imposed temperature gradients and/or electric currents, solvent evaporation,



solute feeding by mixing or capillary flow, and pre-cooling or pre-heating of the substrate prior to contact with the melt. The ability of LPE to produce a wide range of shaped or faceted crystals is virtually unique among the epitaxy methods and this feature could be exploited in LED designs to increase optical coupling (Schubert, 2006). The diversity of complex materials that can be grown by LPE or solution growth, as evidenced by Table 12.5, suggest the candidate materials for and capabilities of LPE are far from exhausted. MBE or MOCVD of some of these multicomponent materials would be very challenging.

## REFERENCES

- A.V. Abramov, N.G. Deryagin, A.V. Dolganov, M.N. Mizerov, O.V. Seliverstov, D.N. Tretyakov and N.N. Faleev (1991) Superhigh cooling rates in LPE. *Cryst. Prop. Prep.* **32–34**, 397–402.
- A.V. Abramov, N.G. Deryagin and D.N. Tretyakov (1994) Growth of GaAs and  $(\text{Ge}_2)_x(\text{GaAs})_{1-x}$  on Si using ultrafast cooling of the growth solution. *Semiconduct. Sci. Technol.* **9**, 1815–1822.
- A.V. Abramov, N.G. Deryagin and D.N. Tretyakov (1996) Supercritical supersaturations and ultrafast cooling of the growth solution in liquid phase epitaxy of semiconductors. *Semiconduct. Sci. Technol.* **11**, 607–619.
- A. Abramov, B.Ya. Ber, A.G. Deryagin, N.G. Deryagin, V.I. Kuchinskii, A.V. Merkulov, D.N. Tretyakov and N.N. Faleev (1997) Parameters of AlGaAs epitaxial layers grown by ultrafast cooling of the growth solution. *Inst. Phys. Conf. Ser.* **155**, 247–250.
- A.V. Abramov, N.G. Deryagin, and D.N. Tretyakov and N.N. Faleev (1999) Application of superfast ( $10^2$ – $10^3$  °C/s) cooling of solution-melt in the liquid phase epitaxy of semiconductors. *Semiconductors* **33**, 1030–1033.
- M.S. Abrahams, L.R. Weisberg, C.J. Buiocchi and J. Blanc (1969) Dislocation morphology in graded heterojunctions:  $\text{GaAs}_{1-x}\text{P}_x$ . *J. Mater. Sci.* **4**, 223–235.
- R.K. Ahrenkeil and D.J. Dunlavy (1989) Minority carrier lifetime in  $\text{Al}_x\text{Ga}_{1-x}\text{As}$ . *J. Vacuum Sci. Technol. A* **7**, 822–826.
- M. Aidaraliev, N.V. Zotova, S.A. Karandashev, B.A. Matveev, M.A. Remennyi, N.M. Stus' and G.N. Talalakin (1998) Long-wavelength uncooled sources of  $\lambda = 5$ – $6$   $\mu\text{m}$  radiation using graded-index InAsSb(P) layers grown by liquid-phase epitaxy. *Tech. Phys. Lett.* **24**, 243–245.
- G.T. Aitiyeva, V.N. Bessolov, A.T. Denisova, S.E. Klimenko, S.A. Kukushkin, M.V. Lebedev and B.V. Tsarenkov (1986) Liquid phase epitaxial growth of ultrathin GaAs layers on a GaAlAs substrate. *Sov. Phys. Tech. Phys.* **31**, 552–554.
- M. Albrecht, S. Christiansen, J. Michler, H.P. Strunk, P.O. Hansson and E. Bauser (1996) Local varying chemical potential and growth surface profile: a case study on solution grown Si(Ge)/Si. *J. Cryst. Growth* **167**, 24–31.
- R. Kh. Akchurin, V.A. Zhegalin, T.V. Sakharova and S.V. Seregin (1997) Epitaxial structures based on narrow band-gap  $\text{InAs}_{1-x}\text{Sb}_x\text{Bi}_y$  solid solutions. *Proc. SPIE* **3182**, 369–374.
- L.N. Aleksandrov (1975) Formation and properties of transition layers in epitaxial films. *J. Cryst. Growth* **31**, 103–112.
- Zh.I. Alferov, V.M. Andreev, B.V. Egorov, S.G. Konnikov and V.M. Lantratov (1978) Fabrication of AlAs-GaAs heterostructures by selective liquid-phase epitaxy. *Sov. Phys. Tech. Phys.* **23**, 209–214.
- T.J. Anderson (1989) Liquid phase epitaxy and phase diagrams for compound semiconductors in *Microelectronics Processing: Chemical Engineering Aspects*, D.H. Hess and K.F. Jensen, eds. American Chemical Society, Washington, DC.
- I.A. Andreev, T.V. L'vova, M.P. Mikhailova, E.V. Kunitsyna, V.A. Solv'ev and Yu.P. Yakolev (1998) Using sulfide treatment to improve the performance of GaSb/GaInAsSb/GaAlAsSb photo-diode heterostructures for spectral range 1.7–2.5  $\mu\text{m}$ . *ASDAM'98 Conference Proceedings Second*

*International Conference on Advanced Semiconductor Devices and Microsystems*. IEEE, New York, 155–158.

- I.A. Andreev, E.V. Kunitsyna and Yu.V. Solov'ev (1999) Use of lead as a neutral solvent for obtaining solid  $\text{Ga}_{1-x}\text{InAs}_y\text{Sb}_{1-y}$  solutions. *Tech. Phys. Lett.* **25**, 792–793.
- V.M. Andreev, V.P. Khvostikov, E.V. Paleeva, V.D. Romyantsev and S.V. Sorokina (1996) Low temperature LPE of AlGaAs nanostructures in 23rd *International Conference on the Physics of Semiconductors*, Vol. 2, M. Scheffler and R. Zimmerman, eds. World Scientific, Singapore, 1055–1058.
- A.M. Andrews, D.T. Cheung, E.R. Gertner and J.T. Longo (1976) Liquid-phase epitaxial growth of stepwise-graded  $\text{InAs}_{1-x}\text{Sb}_x\text{-InAs}$  heterostructures. *J. Vacuum Sci. Technol.* **13**, 961–963.
- A.F.M. Anwar and R.T. Webster (1998) Energy bandgap of  $\text{Al}_x\text{Ga}_{1-x}\text{As}_{1-y}\text{Sb}_y$  and conduction band discontinuity of  $\text{Al}_x\text{Ga}_{1-x}\text{As}_{1-y}\text{Sb}_y$  and  $\text{Al}_x\text{Ga}_{1-x}\text{As}_{1-y}\text{Sb}_y/\text{InGaAs}$  heterostructures. *Solid State Electron.* **42**, 2101–2104.
- M. Aoki, H. Yamane, M. Shimada, S. Sarayama and F.J. DiSalvo (2002) GaN single crystal growth using high purity Na as flux. *J. Cryst. Growth* **242**, 70–76.
- Y. Arima and T. Irisawa (1991) Influence of surface diffusion on the structure of growing crystal surface. *J. Cryst. Growth* **115**, 428–432.
- A. Asahi, Y. Kawamura, Y. Noguchi, T. Matsuuoka and H. Nagai (1983) Hybrid LPE/MBE-grown InGaAsP/InP DFB lasers. *Electron. Lett.* **19**, 507–509.
- R. Asomoza, V.A. Elyukhin, J. Martinez-Juarez and R. Peña-Sierra (2001) Crystallization of the  $\text{A}_x^{\text{III}}\text{B}_{1-x}^{\text{III}}\text{C}^{\text{V}}$  alloys from the supercooled liquid solutions. *J. Cryst. Growth* **231**, 458–465.
- R. Asomoza, V.A. Elyukhin, R. Pena-Sierra and B.L. Rivera Flores (2002) Initial stage of liquid phase heteroepitaxy of III-V alloys. *J. Cryst. Growth* **243**, 381–388.
- M.G. Astles (1990) *Liquid-phase Epitaxy and Phase Diagrams for Compound Semiconductor Materials and their Device Applications*. Adam Hilger, Bristol.
- M. Astles, G. Blackmore, N. Gordon and D.R. Wight (1985) The use of alternative solvents for the low-temperature LPE growth of CdTe films. *J. Cryst. Growth* **72**, 61–71.
- K. Balakrishnan, S. Iida, T. Koyama, M. Kumagawa and Y. Hayakawa (2000) Study on LPE growth of InGaAs bridge layers on GaAs {111} substrates. *Bull. Res. Inst. Electron. Shizouka Univ.* **35**, 1–7.
- K. Balakrishnan, S. Iida, M. Kumagawa and Y. Hayakawa (2002) Influence of indium on the morphology of LPE growth  $\text{In}_x\text{Ga}_{1-x}\text{As}$  ( $x = 0-0.06$ ) epilayers on patterned bridge layers on patterned GaAs(100) substrates. *J. Mater. Sci. Lett.* **21**, 1355–1358.
- A. Baldus, A. Bett, O.V. Sulima and W. Wettling (1994) Hybrid molecular beam epitaxy/low-temperature liquid phase epitaxy growth of GaAs (AlGaAs) layers on silicon. *J. Cryst. Growth* **141**, 315–323.
- F. Bantien, K. Kelting and E. Bauser (1987) Liquid phase epitaxy of GaAs quantum well structures. *J. Cryst. Growth* **85**, 194–196.
- Bo Baoxue, Zhu Baoren, Zhang Baoshun and Zhang Xingde (1998) LPE growth of ultra-thin InGaAsP layer. *Proc. SPIE* **3175**, 433–435.
- Bo Baoxue, Gao Xing, Qu Yi, Zhang Xingde and Gao Dingsan (2000) InGaAsP/GaAs SCH SQW laser arrays grown by LPE. *Optics Laser Technol.* **32**, 335–338.
- A.N. Baranov, S.G. Konnikov, T.B. Popova, V.E. Umansky and Yu.P. Yakovle (1984) Liquid phase epitaxy of  $\text{Ga}_{1-x}\text{Al}_x\text{Sb}_{1-y}\text{As}_y/\text{GaSb}$  and the effect of strain on phase equilibria. *J. Cryst. Growth* **66**, 547–552.
- A.N. Baranov, N.A. Charykov, A.M. Litvak, V.V. Shertsnev and Y.P. Yakovlev (1991) Application of EF-LCP method to the calculation of epitaxial crystal growth processes in A3B5 semiconductor systems: In-Ga-As-Sb, In-As-Sb-P, al-Ga-As-Sb. *Cryst. Prop. Prep.* **32–34**, 387–391.
- N.I. Batryev, V.B. Ufimetshev and M.V. Chukichev (1979) Formation of an intermediate layer during epitaxial growth of a solid-solution  $\text{In}_{1-x}\text{Ga}_x\text{P}$  on a gallium arsenide wafer. *Sov. Phys. Crystallogr.* **24**, 192–195.

- E. Bauser (1978) Development of depressions and voids during LPE growth of GaAs. *Appl. Phys.* **15**, 243–252.
- E. Bauser (1985a) LPE-grown surfaces and growth mechanisms in *Crystal Growth of Electronic Materials*, E. Kaldis, ed. Elsevier, Amsterdam, Ch. 4.
- E. Bauser (1985b) The preparation of modulated semiconductor structures by liquid phase epitaxy in *Proceedings of the NATO Advanced Research Workshop on Thin Film Growth Techniques for Low-dimensional Structures*, J.T. DeVreese and F.M. Peters, eds. Plenum, New York, 171–195.
- E. Bauser (1994) Atomic mechanisms in semiconductor epitaxy in *Handbook of Crystal Growth*, Vol. 3, D.T.J. Hurle, ed. Ch. 20.
- E. Bauser (1997) Liquid-phase epitaxy in 23rd *International Conference on the Physics of Semiconductors*, Berlin, July 1996, Vol. 2, M. Scheffler and R. Zimmermann, eds. World Scientific, Singapore, 1043–1050.
- E. Bauser and K.W. Benz (1982) LPE of GaAs and related compounds: substrate orientation and surface morphology. *Microelectron. J.* **13**, 10–14.
- E. Bauser and H. Strunk (1981) Analysis of dislocations creating monomolecular growth steps. *J. Cryst. Growth* **51**, 362–366.
- E. Bauser and H. Strunk (1982) Dislocations as growth step sources in solution growth and their influence on interface structures. *Thin Solid Films* **93**, 185–194.
- E. Bauser and H.P. Strunk (1984) Microscopic growth mechanisms of semiconductors: experiments and models. *J. Cryst. Growth* **69**, 561–580.
- E. Bauser and H.P. Strunk (1994) Liquid phase epitaxial process for producing three-dimensional semiconductor structures by liquid phase epitaxy. US Patent 5326716.
- D.W. Bellavance and J.C. Campbell (1977) Selective liquid phase epitaxy for integrated optical circuits in *Proceedings of the 6th International Symposium on Gallium Arsenide and Related Compounds*. Institute of Physics, London, 81–87.
- J.L. Benchimol and M. Quillec (1982) Self-supersaturation in liquid phase epitaxy of InGaAs on InP: a simplified technique. *J. Physique* **43**, (Suppl. 12) C5–C9.
- H. Beneking, H. Roehle, P. Mischel and G. Schul (1977) Growth and properties of GaP liquid phase epitaxial layers on Si substrates. *Inst. Phys. Conf.* **331**, 51–57.
- H. Beneking, P. Narozny, N. Emeis and K.H. Goetz (1986) Reduction in dislocations in GaAs and InP epitaxial layers by quasi ternary growth and its effect on device performance. *J. Electron. Mater.* **15**, 247–250.
- P. Bera, V.K. Dixit, K.S. Keerthi and H.L. Bhat (2002) Growth of  $\text{InBi}_x\text{Sb}_{(1-x)}$  films grown on GaAs(001) substrates using liquid phase epitaxy and their characterization. *J. Cryst. Growth* **241**, 321–326.
- P. Bera, V.K. Dixit, K.S. Keerthi, H.L. Bhat and M.S. Hegde (2003) Structural and compositional analysis of  $\text{InBi}_x\text{As}_y\text{Sb}_{(1-x-y)}$  films grown on GaAs(001) substrates by liquid phase epitaxy. *Appl. Surf. Sci.* **220**, 321–326.
- A.A. Bergh and P.J. Dean (1976) *Light-emitting Diodes*. Clarendon Press, Oxford.
- R. Bergmann (1991) Model for defect-free epitaxial lateral overgrowth of Si over  $\text{SiO}_2$  by liquid phase epitaxy. *J. Cryst. Growth* **110**, 823–834.
- V.L. Berkovitz, V.M. Lantratov, T.V. L'vova, G.A. Shakiashvili, V.P. Ulin and D. Paget (1993) Liquid-phase epitaxial regrowth on sulfide-passivated GaAlAs. *Appl. Phys. Lett.* **63**, 970–972.
- V.N. Bessolov, S.A. Kukushkin, M.V. Lebedev and B.V. Tsarenkov (1988) Relaxation liquid phase epitaxy based on reversal of the mass transport and its potential for making ultrathin layers of III-V materials. *Sov. Phys. Tech. Phys.* **33**, 902–905.
- V.N. Bessolov, S.G. Konnikov, M.V. Lebedev, K.Yu. Pogrebetskii and B.V. Tsarenkov (1990) Experimental confirmation of the model of relaxation liquid phase with reversal of mass transport for making ultrathin III-V films. *Sov. Phys. Tech. Phys.* **35**, 99–101.
- V.S. Bessolov, S.G. Konnikov, S.A. Kukushkin, M.V. Lebedev, E.B. Novikov, K.Yu. Pogrebetskii and B.V. Tsarenkov (1993) Relaxational liquid phase epitaxy with reverse mass transport and

- its potential for preparing thin films of  $A^3B^5$  semiconductors in *Growth of Crystals*, Vol. 19, E.I. Givagizov and S.A. Grinberg, eds. Consultants Bureau, New York.
- W.G. Bi and C.W. Tu (1997) Bowing parameter of the band-gap energy of  $GaN_xAs_{1-x}$ . *Appl. Phys. Lett.* **70**, 1608–1610.
- S. Binetti, A. Cavallini, A. Dellafiore, B. Fraboni, E. Grilli, M. Guzzi, S. Pizzini and S. Sanguinetti (1998) Erbium-doped silicon epilayers grown by liquid phase epitaxy. *J. Luminesc.* **80**, 347–351.
- G. Bischofink and K.W. Benz (1993) Growth of  $Al_xGa_{1-x}Sb$  and  $GaSb$  bulk crystal with liquid phase electro-epitaxy (LPEE). *J. Cryst. Growth* **128**, 466–469.
- Yu.B. Bolkhovityanov (1981) The peculiarities of isothermal contact of liquid and solid phase during the LPE of  $A^3B^5$  compounds. *J. Cryst. Growth* **55**, 591–598.
- Yu.B. Bolkhovityanov (1982) The contact phenomena between the liquid phase and the substrate during LPE of  $A^3B^5$  compounds. *J. Cryst. Growth* **57**, 84–90.
- Yu.B. Bolkhovityanov (1989) The transition layers in  $AlGaAs/GaAs$  and  $InGaAsP/GaAs$  heterostructures grown by LPE. *Cryst. Res. and Technol.* **24**, 1103–1111.
- Yu.B. Bolkhovityanov (1991) Growth instabilities in LPE processes: the initial steps of heteroepitaxy. *Cryst. Prop. Prep.* **31**, 37–53.
- Yu.B. Bolkhovityanov and S.I. Chikichev (1983) Instability of ‘slow’ solid-liquid interface relaxation before the hetero-LPE of III-V compounds. *Cryst. Res. Technol.* **18**, 847–857.
- Yu.B. Bolkhovityanov, R.I. Bolkhovityanova, Yu.D. Vaulin and B.Z. Ol’shanetskii (1986a) Growth mechanism of the separating  $AlGaAs$  layer on a  $GaAs$  surface in isothermal contact with liquid  $AlGaAs$ . *Sov. Phys. Tech. Phys.* **31**, 364–365.
- Yu.B. Bolkhovityanov, R.I. Bolkhovityanova, Yu.D. Vaulin, T.A. Gavrilova, B.Z. Olshanetsky and S.I. Stenin (1986b) The formation of  $AlGaAs$  layers by regrowth on the surface of  $GaAs$  during its contact with the undersaturated liquid-containing  $Al$ . *J. Cryst. Growth* **78**, 335–341.
- Yu.B. Bolkhovityanov, R.I. Bolkhovityanova, Yu.D. Vaulin and T.A. Gavrilova (1988) Mechanism of formation of transition layer in  $AlGaAs/GaAs$  heterostructure. *Sov. Phys. Crystallogr.* **33**, 426–429.
- Yu.B. Bolkhovityanov, I.M. Logvinskii and N.S. Rudaya (1989) A difference between initial growth stage of  $AlGaAs/GaAs$  and  $GaAs/AlGaAs$  heterostructures produced by contact replacement solutions. *Cryst. Res. Technol.* **24**, 1103–1111.
- D. Botez (1984) Liquid phase epitaxy over channeled substrates. *J. Cryst. Growth* **70**, 150–154.
- D. Botez, W.T. Tsang and S. Wang (1976) Growth characteristics of  $GaAs-Ga_{1-x}Al_xAs$  structures fabricated by liquid phase epitaxy over preferentially etched channels. *Appl. Phys. Lett.* **28**, 234–237.
- R.W. Brander and R.P. Sutton (1969) Solution grown  $SiC$  p-n junctions. *Br. J. Appl. Phys.* **2**, 309–318.
- R.F. Brebrick, C.-H. Su and P.-K. Liao (1983) Associated solution model for  $Ga-In-Sb$  and  $Hg-Cd-Te$  in *Semiconductors and Semimetals*, Vol. 19. Academic Press, San Diego, Ch. 3.
- J.C. Brice (1965) *The Growth of Crystals from the Melt*. North Holland, Amsterdam.
- J.C. Brice (1973) *The Growth of Crystals from Liquids*. North Holland, Amsterdam.
- J.C. Brice (1986) *Crystal Growth Processes*. Blackie/John Wiley & Sons, Ltd, New York.
- V.N. Brovkin and A.I. Kazakov and V.A. Presnov (1988) Liquid phase epitaxy of  $GaAs$  on  $Si$  substrates. *Cryst. Res. Technol.* **21**, 1331–1336.
- T. Bryskiewicz (1978) Investigation of the mechanism and kinetics of growth of LPE  $GaAs$ . *J. Cryst. Growth* **43**, 101–114.
- T. Bryskiewicz (1986) Liquid phase electroepitaxy of semiconductor compounds. *Prog. Crystal Growth Charact.* **12**, 29–43.
- T. Bryskiewicz (1995) In quest of unrestricted growth of bulk crystals by liquid phase electroepitaxy. *J. Cryst. Growth* **153**, 19–24.
- T. Bryskiewicz (1997) Structural defects in thick  $InGaAs$  layers grown by LPEE on partially masked  $GaAs$  substrates. *Mater. Res. Soc. Symp. Proc.* **448**, 231–240.

- T. Bryskiewicz and A. Laferrière (1993) Growth of alloy substrates by liquid phase electroepitaxy: theoretical considerations. *J. Cryst. Growth* **129**, 429–442.
- E. Buehler and K.J. Bachmann (1976) Solubilities of InP and CdS in Cd, Sn, In, Bi, and Pb. *J. Cryst. Growth* **35**, 60–64.
- K.S.A. Butcher, L. Mo, D. Alexiev and T.L. Tansley (1995) Growth of high purity liquid phase epitaxial GaAs in a silica growth system. *J. Cryst. Growth* **156**, 361–367.
- B.L. Cardozo, L.A. Reichertz, J.W. Beeman and E.E. Haller (2005) Characterization of liquid phase epitaxial GaAs for blocked-impurity far-infrared detectors. *Infrared Phys. Technol.* **46**, 400–407.
- H.C. Casey Jr and M.B. Panish (1978) *Heterostructure Lasers, Part B: Materials and Operating Characteristics*. Academic Press, New York, Ch. 6.
- N. Chand, A.V. Sybru and P.A. Houston (1983) LPE growth effects of InP, In<sub>0.53</sub>Ga<sub>0.47</sub>As and InGaAsP on structured InP substrates. *J. Cryst. Growth* **61**, 53–60.
- S.S. Chandvankar, V.P. Khostikov, B.M. Arora and K.S. Chandrasekaran (1998) Can one make strained quantum structures by liquid phase epitaxy: a case study of GaSb on GaAs. *Phys. Semiconduct. Devices*, Part 1 **1**, 293–296.
- S.S. Chandvankar, A.P. Shah, A. Bhattacharya, K.S. Chandrasekaran and B.M. Aora (2004) Synthesis of AlGaAs-based strained separately confined heterostructure laser diodes by low temperature liquid-phase epitaxy. *J. Cryst. Growth* **260**, 348–359.
- S.C. Chang, G.Y. Meng and D.A. Stevenson (1983) In situ electrochemical monitoring and control of oxygen in liquid phase epitaxial growth of GaAs. *J. Cryst. Growth* **62**, 465–474.
- Y.S. Chang, S. Naritsuka and T. Nishinaga (1997) Effect of growth temperature on epitaxial lateral overgrowth of GaAs on silicon substrate. *J. Cryst. Growth* **174**, 630–634.
- Y.S. Chang, S. Naritsuka and T. Nishinaga (1998) Optimization of growth conditions for wide dislocation-free GaAs on Si substrates by microchannel epitaxy. *J. Cryst. Growth* **192**, 18–22.
- F.-L. Chao and W.-S. Wang (1993) Analysis of cavity geometric effect of liquid phase epitaxy process. *IEEE/CHTM Int. Electron. Manufact. Symp.* 103–106.
- N.A. Charykov, A.M. Litvak, M.P. Mikhailova, K.D. Moiseev and Yu. P. Yavolev (1997) Solid solution In<sub>x</sub>Ga<sub>1-x</sub>As<sub>y</sub>Sb<sub>2</sub>P<sub>1-y-z</sub>: a new material for infrared optoelectronics. I. Thermodynamic analysis of the conditions for obtaining solid solutions, isoperiodic to InAs and GaSb substrates by liquid-phase epitaxy. *Semiconductors* **31**, 344–349.
- N.A. Charykov, V.V. Sherstnev and A. Krier (2002) General theory of multiphase melt crystallization. *J. Cryst. Growth* **234**, 762–772.
- A. Chen, A. Yulius, J.M. Woodall and C.C. Broadbridge (2004) A hybrid epitaxy method for InAs on GaP. *Appl. Phys. Lett.* **85**, 3447–3449.
- J.F. Chen and C.R. Wie (1988) Structural and electrical contact properties of LPE grown GaAs doped with indium. *J. Electron. Mater.* **17**, 501–507.
- J.F. Chen and C.R. Wie (1989) Effects of In and Sb doping in LPE growth thermodynamics and in GaAs layer qualities. *J. Electron. Mater.* **18**, 209–214.
- L.-J. Chen and C.-C. Wan (1992) Simulation of the growth rate and layer thickness for liquid phase epitaxy (LPE) under slider-induced convection. *J. Cryst. Growth* **121**, 322–334.
- A.A. Chernov (1984) *Modern Crystallography III: Crystal Growth*, Springer Series in Solid State Sciences. Springer Verlag, Berlin.
- A. Chernov and H.J. Scheel (1995), Extremely flat surfaces by liquid phase epitaxy. *J. Cryst. Growth* **149**, 187–195.
- G.-S. Cho, S.-H. Hahmn and Y.-Se Kwon (1993) Meltback etching and regrowth of GaAs/AlGaAs in liquid phase epitaxy for fabrication of microlens. *J. Electron. Mater.* **22**, 353–359.
- S.R. Collins, A.M. Barnett, M.H. Hannon and J.J. Joannides (1990) Selective liquid phase epitaxial growth of InP on silicon *2nd International Conference on Indium Phosphide and Related Materials*. IEEE, New York, 199–202.
- C.M. Colomb, S.A. Stockman, S. Varadarajan and G.E. Stillman (1992) Minority carrier transport in carbon doped gallium arsenide. *Appl. Phys. Lett.* **60**, 65–67.

- L.W. Cook, M.D. Camras, S.L. Rudaz and F.M. Steranka (1988) High efficiency 650 nm aluminum gallium arsenide light emitting diodes in *Gallium Arsenide and Related Compounds, Proceedings of the 14th International Symp.* IOP, Bristol, 777–780.
- M. Copel, M.C. Reuter, M. Horn von Hoegen and R.M. Tromp (1990) Influence of surfactants in Ge and Si epitaxy on Si(001). *Phys. Rev. B* **42**, 11682–11689.
- A.U. Coşkun, Y. Yener and F. Armç (2002) Simulation of dissolution of silicon in an indium solution by spectral methods. *Model. Simulat. Mater. Sci. Engin.* **10**, 539–550.
- J.E. Cotter, M.G. Mauk, L.D. Garrett, J.B. Berryhill, K.D. Hobart and A.M. Barnett (1992) Monolithic integration of AlGaAs/GaAs surface-emitting LEDs with silicon- or GaAs-based bipolar transistor drivers. *Proc. SPIE* **1582**, 71–82.
- I. Crossley and M.B. Small (1971) Computer simulation of liquid phase epitaxy of GaAs in Ga solution. *J. Cryst. Growth* **11**, 157–165.
- J.J. Daniele (1975) Peltier-induced LPE and composition stabilization of GaAlAs. *Appl. Phys. Lett.* **27**, 373–375.
- L.R. Dawson (1972) Liquid phase epitaxy in *Solid State Chemistry*, H. Reiss, ed. Pergamon, Oxford, 7.
- S. Dhar, N. Halder, J. Kumar and B.M. Arora (2004) Observation of 0.7 eV electron trap in dilute GaAsN layers grown by liquid phase epitaxy. *Appl. Phys. Lett.* **85**, 964–966.
- S. Dhar, N. Halder, A. Mondal, Bhavtosh Bansal and B.M. Arora (2005) Detailed studies on the origin of the nitrogen-related electron traps in dilute GaAsN layers grown by liquid phase epitaxy. *Semiconduct. Sci. Technol.* **20**, 1168–1172.
- V.N. Demin (1995) Possibility of applying relaxation liquid-phase epitaxy for growing ultrathin III-V homoepitaxial films. *Tech. Phys.* **40**, 512–513.
- V.N. Demin, O.V. Naroahnyaya and F.A. Kuznetsov (1990) Liquid phase electroepitaxy of gallium arsenide in an ac electric field. *Sovi. Phys. Tech. Phys.* **35**, 620–622.
- I.A. Denisov, O.S. Mazhorova, Yu.P. Popov and N.A. Smirnova (2004) Numerical modeling for convection in growth/dissolution of solid solution CdxHg1-xTe by liquid-phase epitaxy. *J. Cryst. Growth* **269**, 284–291.
- V.K. Dixit, K.S. Keerthi, H.L. Bhat, P. Bera and M.S. Hedge (2002a) Growth of InBi<sub>x</sub>Sb<sub>(1-x)</sub> films grown on GaAs(001) substrates by liquid phase epitaxy and their characterization. *J. Cryst. Growth* **241**, 171–176.
- V.K. Dixit, K.S. Keerthi, P. Bera and H.L. Bhat (2003) Structural and compositional analysis of InBi<sub>x</sub>As<sub>y</sub>Sb<sub>(1-x-y)</sub> films grown on GaAs(001) substrates by liquid phase epitaxy. *Appl. Surf. Sci.* **220**, 321–326.
- V.A. Dmitriev (1993) Silicon carbide and SiC-AlN solid solution p-n structures grown by liquid-phase epitaxy. *Physica B* **185**, 440–452.
- V.A. Dmitriev and A. Chernkov (1993) Growth of SiC and SiC-AlN solid solution by container-free liquid phase epitaxy. *J. Cryst. Growth* **128**, 343–348.
- V.A. Dmitriev, L.B. Elfimov, N.D. Il'inkaya and S.V. Rendakova (1992), Liquid-Phase Epitaxy of Silicon Carbide at Temperatures of 1100–1200 °C in *Amorphous and Crystalline SiC III*, Springer Physics Proceedings, Vol. 56, G.L. Harris, M.G. Spencer and C.Y. Yang, eds. Springer Verlag, Berlin, 307–311.
- D. Dobosz, K. Golaszewska, Z.R. Zytkeiwicz, E. Kaminska, A. Piotrowska, T.T. Piotrowski, A. Barcz, and R. Jakiela (2005) Properties of ZrN films as substrate masks liquid phase epitaxial lateral overgrowth of compound semiconductors. *Crystal Res. and Technol.* **40**, 492–497.
- L.M. Dolginov, I.V. Tunitskaya, A.Y. Polyakov, L.V. Druzhinina, G.V. Vinogradova, N.B. Smirnov, A.V. Govorkov, O.M. Borodina, E.A. Kozhukhova, A.A. Balmashnov and A.G. Milnes (1994) The effect of Gd doping on carrier concentration in InGaAsSb layers grown by liquid phase epitaxy. *Thin Solid Films* **251**, 147–150.
- J.P. Donnelly and A.G. Milnes (1966) The epitaxial growth of Ge on Si by solution growth techniques. *J. Electrochem. Soc.* **113**, 297–298.

- V.V. Dorogan, V.A. Kosyak, V.G. Trofim and S.K. Railyan (1992) Distinctive features of GaAs deposition from ultrafine liquid phase in a temperature gradient. *Inorg. Mater.* **28**, 549–551.
- S. Dost and B. Lent (2006) *Single Crystal Growth of Semiconductors from Metallic Solutions*. Elsevier, Amsterdam.
- R.D. Dupuis (2000) III-V semiconductor heterojunction devices grown by metalorganic chemical vapor deposition. *IEEE J. Quantum Electron.* **6**, 1040–1050.
- Ch. Eck and H. Emmerich (2004) Models for liquid phase epitaxy, Preprint 146 SPP **1095**, *Analysis, Modeling and Simulation of Multiscale Problems*, Friedrich-Alexander Universität, Erlangen Nurnberg (<http://www1.am.uni-erlangen.de/~eck/publications.html>).
- F. Endres (2004) Ionic liquids: promising solvents for the electrodeposition of nanoscale metals and semiconductors. *Meeting Abstracts, 2004 Joint International Meeting- 206th Meeting of the Electrochemical Society*. Electrochemical Society Inc., Pennington, NJ.
- E. Ejder (1974) Growth and morphology of GaN. *J. Cryst. Growth* **22** 44–46.
- D. Elwell and H.J. Scheel (1975) *Crystal Growth from High-temperature Solutions*. Academic Press, London.
- D. Elwell, R.S. Fiegelson, M.M. Simkins and W.A. Tiller (1984) Crystal growth of GaN by the reaction between gallium and ammonia. *J. Cryst. Growth* **66**, 45–54.
- J.W. Faust Jr (1969) The influence of solvent and impurities on the habit and morphology of semiconductor crystals. *Acta Crystallogr., Sect. A* **25**, S236.
- J.W. Faust, Jr., H.F. John, and G. Pritchard (1968) Influence of solvent and impurities on habit and morphology of semiconductor crystals. *J. Cryst. Growth* **3**, 321–326.
- O. Filip, B. Epelbaum, M. Bickermann and A. Winnacker (2004) Micropipe healing in SiC wafers by liquid phase epitaxy in Si-Ge melts. *J. Cryst. Growth* **271**, 142–150.
- O. Filip, B. Epelbaum, M. Bickermann and A. Winnacker (2005) LPE of silicon carbide using diluted Si-Ge flux. *Mater. Sci. Forum* **483–485**, 133–136.
- M. Fisher and A. Krier (1997) Photoluminescence of epitaxial InAs produced by different growth methods. *Infrared Phys. Technol.* **38**, 405–413.
- E.A. Fitzgerald, P.D. Kirchner, R. Proano, G.D. Pettit, J.M. Woodall and D.G. Ast (1998) Elimination of interface defects in mismatched epilayers by a reduction in growth area. *Appl. Phys. Lett.* **52**, 1496–1498.
- T. Fukui and T. Kobayashi (1979) Effect of impurities on the surface morphology of LPE-grown InGaAsP and InP. *Jpne. J. Appl. Phys.* **18**, 2307–2308.
- N.V. Ganina, M.G. Mil'vidskii, A.N. Shershakov and T.G. Yugova (1982) Influence of doping with isovalent impurities on defect formation in homoepitaxial GaAs layers. *Sov. Phys. Crystallogr.* **27**, 617–618.
- H.H. Gao, A. Krier and V.V. Sherstnev (1999) High quality InAs grown by liquid phase epitaxy using gadolinium gettering. *Semiconduct. Sci. Technol.* **14**, 441–445.
- Y.Z. Gao and T. Yamaguchi (1999) Liquid phase epitaxial growth and properties of InSbBi films grown from In, Bi and Sn solutions. *Cryst. Res. Technol.* **34**, 285–292.
- Y.Z. Gao, X.Y. Gong, H. Kan, M. Aoyama and T. Yamaguchi (1999) InAs<sub>1-y</sub>Sb<sub>y</sub> single crystals with cutoff wavelength of 8–12 μm grown by new method. *Jpne. J. Appl. Phys.* **38**, 1939–1940.
- Y.Z. Gao, H. Kan, M. Aoyama and T. Yamaguchi (2000) Germanium and zinc-doped p-type InAsSb single crystals with cutoff wavelength of 12.5 μm grown. *Jpn. J. Appl. Phys.* **1**, 2520–2522.
- Y.Z. Gao, H. Kan, X.Y. Gong, F.S. Gao and T. Yamaguchi (2002) Improved purity of long-wavelength InAsSb epilayers grown by melt epitaxy in fused silica boats. *J. Cryst. Growth* **234**, 85–90.
- Y.Z. Gao, T. Yamaguchi, X.Y. Gong, H. Kan, M. Aoyama and N. Dai (2003) InNAsSb single crystals with cutoff wavelength of 11–13.5 μm grown by melt epitaxy. *Jpn. J. Appl. Phys.* **1** 4203–4206.
- Y.Z. Gao, X.Y. Gong, Y.H. Chen and T. Yamaguchi (2005) High quality InAsSb/GaAs single crystals with a cutoff wavelength of 12 μm grown by melt epitaxy. *Proc. SPIE* **6029**, 60291-1–60291-6.

- E.A. Geiss and R. Ghez (1975) Liquid-phase epitaxy in *Epitaxial Growth, Part A*, J.W. Matthews, ed. Academic Press, New York, 183–213.
- V.A. Gevorkyan (2003) A new liquid-source version of liquid phase electroepitaxy. *J. Cryst. Growth* **249**, 149–158.
- R. Ghez and M.B. Small (1981) Growth and dissolution of ternary alloys of III-V compounds in liquid phase epitaxy and the formation of heterostructures. *J. Cryst. Growth* **52**, 699–709.
- P. Gladkov, D. Nohavica, Z. Sourek, A.P. Litvinchuk and M.N. Iliev (2006) Growth and characterization of InAs layers obtained by liquid phase epitaxy from Bi solvents. *Semicond. Sci. Technol.* **21**, 544–549.
- L.V. Golubev, A.M. Kreschuk, S.V. Novikov, T.A. Polyanskaya, I.G. Savel'ev and I.I. Saidashev (1988), Fabrication of heterostructures with a two-dimensional electron gas by conventional liquid phase epitaxy. *Sov. Phys. Semiconduct.* **22**, 1234–1237.
- L.V. Golubev, A.V. Egorov, S.V. Novikov and Yu.V. Shmartsev (1991) Liquid phase electroepitaxy of GaAs bulk crystals. *Cryst. Prop. Prep.* **36–38**, 417–429.
- L.V. Golubev, A.V. Egorov, S.V. Novikov and Yu.V. Shmartsev (1995) Liquid phase electroepitaxy of III-V semiconductors. *J. Cryst. Growth* **146**, 277–282.
- X.Y. Gong, K. Okitsu, T. Yamaguchi and M. Kumagawa (1992) LPE Ga<sub>1-x</sub>In<sub>x</sub>Sb multigrading layers with cut-off wavelength up to 4.71 μm ( $x = 0.75$ ). *Jpn. J. Appl. Phys., Part 1* **31**, 1016–1017.
- X.Y. Gong, H. Kan, T. Makino, T. Yamaguchi, T. Nakatskasa, M. Kumagawa, N.L. Rowell, A. Wang and R. Rinfret (1995) High quality InAs<sub>1-y</sub>Sb<sub>y</sub>/InAs multilayers for mid-IR detectors. *Cryst. Res. Technol.* **30**, 603–612.
- X.Y. Gong, T. Yamaguchi, T. Makino, T. Iida, T. Kato, M. Aoyama and M. Kumagawa (1997). Room temperature InAs<sub>x</sub>P<sub>1-x-y</sub>Sb<sub>y</sub>/InAs photodetectors. *Jpn. J. Appl. Phys., Part 1* **36**, 2614–2616.
- S. Goyal, J. Bandrau, J.W. Beeman and E.E. Haller (2002) Germanium blocked impurity band detectors in *Proceedings of the Far-IR, Sub-mm and mm Detector Detector Technology Workshop*, J. Wolf, J. Farhoomand and C.R. McCreight, eds. NASA, Washington, DC, NASA/CP-211408, Manuscript No. 3–16.
- J. D. Grange and D.K. Wickenden (1985) Comparison and critique of the epitaxial growth techniques in *The Technology and Physics of Molecular Beam Epitaxy*, E.H.C. Parker, ed. Plenum, New York, Ch. 17.
- A.M. Grebenyuk, S.I. Krukovskii, A.M. Litvak, N.A. Charykov and Yu.P. Yakovlev (1990) Melt-solid phase equilibria during liquid phase epitaxy of III-V compounds from 'inert solvents' (in the example of the Pb-InAs-InSb and Bi-Ga-GaAs systems). *Sov. Tech. Phys. Lett.* **16**, 894–895.
- P.D. Greene (1987) Liquid phase epitaxy of III-V compounds in *Chemistry of the Semiconductor Industry*. Blackie, Glasgow, 157–174.
- S.-H. Hahm, G.-S., Cho and Y.-S. Kwon (1991) GaAs/AlGaAs lensed light emitting diode by the meltback and regrowth in liquid phase epitaxy. *Jpn. J. Appl. Phys., Part 2* **30**, L910–L913.
- F.A. Halden (1960) The growth of silicon carbide from solution in *Silicon Carbide: a High Temperature Semiconductor*, J.R. O'Connor and J. Smittens, eds. Pergamon, New York, 115–123.
- E.E. Haller and J.W. Beeman (2002) Far infrared photoconductors: Recent advances and future prospects in *Proceedings of the Far-IR, Sub-mm and mm Detector Detector Technology Workshop*, J. Wolf, J. Farhoomand and C.R. McCreight, eds. NASA, Washington, DC, NASA/CP-211408, Manuscript No. 2–06.
- M. Hanke, M. Schmidbauer, D. Grigoriev, H. Raidt, P. Schafer, R. Kohler, A.K. Gerlitzke and H. Wawra (2004) SiGe/Si(001) Stranski–Krastanow islands by liquid-phase epitaxy: diffuse x-ray scattering versus growth observations. *Phys. Rev. B* **69**, 75317-1–7.
- M. Hanke, T. Boeck, A.-K. Gerlitzke, F. Syowatka, F. Heyroth and R. Kohler (2005) Size, shape and ordering of SiGe(001) islands grown by liquid phase epitaxy under far-equilibrium growth conditions. *Appl. Phys. Lett.* **86**, 142101-1–3.



- P.O. Hansson, R. Bergmann and E. Bauser (1991) Heteroepitaxial lateral overgrowth of  $\text{Ge}_x\text{Si}_{1-x}$  over  $\text{SiO}_2/\text{Si}$  structures by liquid phase epitaxy. *J. Cryst. Growth* **114**, 573–580.
- P.O. Hansson, E. Bauser, M. Albrecht and H.P. Strunk (1993) Solvents influencing the morphology of epitaxial solution grown strained Ge/Si layers. *Solid State Phenom.* **32–33**, 403–408.
- P. Hartman, ed. (1973) *Crystal Growth: an Introduction*. North-Holland, Amsterdam.
- Z. Helak, R. Korbutowicz, M. Panek, R. Paskiewicz and M. Taczała (1991) Ga-As-Bi phase equilibrium study by LPE for thin solutions. *J. Cryst. Growth* **115**, 294–298.
- M.A. Herman, W. Richter and H. Sitter (2004) *Epitaxy: Physical Foundation and Technical Implementation*. Springer, Berlin.
- W.-J. Ho, M.-C. Wu and Y.M. Lin (1994) InGaAs pin photodiodes grown by liquid phase epitaxy using erbium gettering. *Electroni. Lett.* **30**, 83–84.
- L. Hollan, J.P. Hallais and J.C. Brice (1980) The preparation of gallium arsenide. *Curr. Top. Mater. Sci.* **5**, 1–217.
- D.H. Holmann and M.H. Mueller (1999) Prospects of the use of liquid phase techniques for the growth of bulk silicon carbide crystals. *Mater. Sci. Eng., B* **61–62**, 29–39.
- P.A. Houston (1980) The growth of buffered GaAs MESFET structures by LPE. *J. Electron. Mater.* **9**, 79–93.
- J.J. Hsieh (1974) Thickness and surface morphology of GaAs LPE layers grown by supercooling, step-cooling, equilibrium-cooling, and two-phase solution techniques. *J. Cryst. Growth* **27**, 49–61.
- J.J. Hsieh (1980) Liquid phase epitaxy in *Handbook on Semiconductors*, Vol. 3, T. S. Moss and S.P. Keller eds. North Holland, Amsterdam, 415–497.
- R.C. Hughes, T.E. Zipperian, L.R. Dawson, R.M. Biefeld, R.J. Walko and M.A. Dvorack (1991) Gallium phosphide junctions with low leakage for energy conversion and near ultraviolet detectors. *J. Appl. Phys.* **69**, 6500–6505.
- Hu Lizhong, Sun Jie, Meng Qingduan, Su Yingmei and Zhao Yu (2002)  $\text{Al}_{0.3}\text{Ga}_{0.7}\text{As}$  microtips grown by self-assembled LPE for integrated SNOM sensors. *J. Cryst. Growth* **240**, 98–103.
- Hu Lizhong, Zhang Hong Shi, Wang Zhijun, Sun Jie, Zhao Yu and Liang Xiuping (2004). GaAs pyramidal microtips grown by selective liquid-phase epitaxy. *J. Cryst. Growth* **271**, 46–49.
- D.T.J. Hurle, ed. (1994) *Handbook of Crystal Growth*. Elsevier, Amsterdam.
- D.T.J. Hurle (1999) A comprehensive thermodynamic analysis of native point defect and dopant solubilities in gallium arsenide. *J. Appl. Phys.* **85**, 6957–7022.
- M. Ichimura and A. Sasaki (1988) Atom arrangement in III-V quaternary semiconductors of (ABC)D type. *Jpn. J. Appl. Phys., Part 1* **27**, 642–648.
- K. Iga and S. Kinoshita (1996) *Process Technology for Semiconductor Lasers: Crystal Growth and Microprocesses*. Springer-Verlag, Berlin, Ch. 5.
- O. Igarashi (1977) Two-stage epitaxial growth of GaP on Si. *Jpn. J. Appl. Phys.* **16**, 1863–1864.
- H. Ijuin and S.-i. Gonda (1976) Computer simulations of liquid phase epitaxy of III-V ternary alloys. *J. Cryst. Growth* **33**, 215–222.
- N.D. Il'inskaya, S.D. Nishikin, M.A. Sinityn, D.V. Sinyavskii, L.P. Sorokina and B.S. Yavitch (1987) 'Current control of the thickness profile and "current deoxidation" of (AlGa)As layers grown in grooves'. *Sov. Phys. Tech. Phys.* **32**, 470–472.
- Y. Imamura, L. Jastrzebski and H.C. Gatos (1978) Surface morphology of GaAs layers grown by electroepitaxy and thermal LPE. *J. Electrochem. Soc.* **125**, 1560–1561.
- Y. Inatomi and K. Kuribayashi (1993) *In-situ* observation of morphological change on LPE grown surfaces in semiconductors. *J. Cryst. Growth* **128**, 557–561.
- Y. Inatomi and K. Kuribayashi (2002) Morphological stability of GaP(111)B in LPE under static magnetic field. *J. Cryst. Growth* **241**, 395–403.
- K. Ishida, T. Nomura, H. Tokunaga, H. Ohtani and T. Nishizawa (1989) Miscibility gaps in the GaP-InP, GaP-GaSb, InP-InSb and InAs-InSb systems. *J. Less-Common Met.* **155**, 193–206.
- O. Ishihara, M. Otsubo and S. Mitsui (1977) Selective epitaxial growth of GaAs from the liquid phase. *Jpn. J. Appl. Phys.* **16**, 2109–2113.

- S. Isozumi, C.J. Herman, A. Okamoto, J. Lagowski and H.C. Gatos (1981) New approach to liquid phase electroepitaxy (LPEE) of III-V compounds. *J. Electrochem. Soc.* **128**, 2220–2223.
- T. Isu, M. Hata, M. Morishita, Y. Nomura and Y. Katayama (1991) Surface diffusion length during MBE and MOMBE measured from distribution of growth rates. *J. Cryst. Growth* **115**, 423–427.
- S. Iyer, E.K. Stefanakos, A. Abul-Fadl and W.J. Collis (1984) Diffusion coefficient and differential mobility of As in In for LPE and current-controlled LPE. *J. Cryst. Growth* **67**, 337–342.
- L. Jastrzebski and H.C. Gatos (1977) Electrical characteristics of GaAs layers and p-n junctions grown by current-controlled LPE in *Proceedings of the Sixth International Symposium on Gallium Arsenide and Related Compounds*. Institute of Physics, London, 88–95.
- L. Jastrzebski, H.C. Gatos and A.F. Witt (1976) Electromigration in current-controlled LPE. *J. Electrochem. Soc.* **123**, 1121–1122.
- L. Jastrzebski, Y. Imamura and H.C. Gatos (1978) Thickness uniformity of GaAs layers grown by electroepitaxy. *J. Electrochem. Soc.* **125**, 1140–1146.
- W.C. Johnson, J.B. Parsons and M.C. Crew (1932) Nitrogen compounds of gallium III. Gallic nitride. *J. Phys. Chem.* **36**, 2651–2654.
- R.D. Jones and K. Rose (1984) Liquidus calculations of III-N semiconductors. *CALPHAD* **8**, 343–354.
- A.S. Jordan (1976) Calculation of phase equilibria in the Ga-Bi and Ga-P-Bi systems based on a theory of regular associated solutions. *Metall. Trans. B* **7**, 191–202.
- A. Joullié (1977) Computer simulation of solution growth of ternary III-V alloys. *J. Cryst. Growth* **38**, 45–54.
- I. Jozwik and J.M. Olchowik (2006) The epitaxial lateral overgrowth of silicon by two-step liquid phase epitaxy. *J. Cryst. Growth* **294**, 367–372.
- K. Kamei, S. Inoue, Y. Shirai, T. Tanaka, N. Okada and A. Yauchi (2006) LPE growth of AlN from Cu-Al-Ti solution under nitrogen atmosphere. *Phys. Status Solidi A* **203**, 1720–1723.
- T. Kamiya, M. Kimura, A. Tanaka and T. Sukegawa (1996) Lattice compensation in LPE-grown GaAs crystals by simultaneous Te and Si doping. *J. Cryst. Growth* **165**, 482–484.
- D. Kandel and E. Kaxiras (2000) The surfactant effect in semiconductor thin-film growth in *Solid State Physics*, Vol. 54, H. Ehrenreich and F. Spaepen, eds. Academic Press, New York, 219.
- M. Kaneko, S. Nakayama, K. Kashiwa, S. Aizawa and N.S. Takahashi (2002) Lattice mismatched LPE growth of InGaP on patterned InP substrate. *Crsyt. Res. Technol.* **37**, 177–182.
- J. Karpinski, J. Jun and S. Porowski (1984) Equilibrium pressure of N<sub>2</sub> over GaN and high pressure solution growth of GaN. *J. Cryst. Growth* **66**, 1–10.
- D. Kasemset, C.S. Hong, N.B. Patel, P.D. Dapkus, K. Mohammed and J.L. Merz (1983) MOCVD growth and characterization of high luminescence efficiency Al<sub>x</sub>Ga<sub>1-x</sub>As in *Gallium Arsenide and Related Compounds*. Institute of Physics, Bristol, 78–84.
- D. Kass, M. Warth, W. Appel, H.P. Strunk and E. Bauser (1985) Silicon multilayers grown by liquid phase epitaxy in *Proceedings of First International Symposium on Silicon Molecular Beam Epitaxy*. Electrochemical Society, Pennington, NJ, 250–258.
- M. Kasu, H. Saito and T. Fukui (1991) Step density dependence of growth rate on vicinal surface of MOCVD. *J. Cryst. Growth* **115**, 406–410.
- K. Kato, T. Kusunoki, C. Takenaka, T. Tanahashi and K. Nakajima (1991) Reduction of dislocations in InGaAs layer on GaAs using epitaxial lateral overgrowth. *J. Cryst. Growth* **115**, 174–179.
- K. Kato, H. Uekita, M. Ichimura, N. Kitamura, A. Usami and T. Wada (1992) Extremely-low temperatures LPE growth of Al<sub>x</sub>Ga<sub>1-x-y</sub>In<sub>y</sub>Sb. *Mater. Lett.* **13**, 93–95.
- T. Kato, T. Matsumoto, H. Ogura and T. Shida (1996) Solution growth of InGaAlP on Al-predoped GaAs (100) substrates. *J. Cryst. Growth* **158**, 425–429.
- F. Kawamura *et al.* (2003) Growth of transparent, large size GaN single crystals with low dislocations using Ca-Na flux system. *Jpn. J. Appl. Phys., Part 2* **42**, L729–731.
- F. Kawamura *et al.* (2006) Drastic decrease in dislocations during liquid phase epitaxy growth of GaN single crystals using Na flux methods without any artificial process. *Jpn. J. Appl. Phys., Part 1* **45**, 2528–2523.

- K. Kelting, K. Koehler and P. Zwicknagl (1986) Luminescence of  $\text{Ga}_{1-x}\text{Al}_x\text{As}/\text{GaAs}$  single quantum wells grown by liquid phase epitaxy. *Appl. Phys. Lett.* **48**, 157–159.
- R. Kern and P. Muller (1995) Three-dimensional towards two-dimensional coherent epitaxy initiated by surfactants. *J. Cryst. Growth* **146**, 193–197.
- T.F. Keuch and M.A. Tischler (1996) Epitaxial growth in *Materials Science and Technology: a Comprehensive Treatment*, Vol. 16, R.W. Cahn, P. Haasen and E.J. Kramer, eds. VCH, Weinheim, 107–172.
- M. Khenner and R.J. Braun (2005) Numerical simulation of liquid phase electro-epitaxial selective area growth. *J. Cryst. Growth* **279**, 213–228.
- D.K. Kim and B.-T. Lee (1994) Heteroepitaxial growth of GaAs on (100) GaAs and InP by selective liquid phase epitaxy. *Jpn. J. Appl. Phys., Part 1* **33**, 10 5870–5874.
- D.K. Kim *et al.* (1995) Liquid phase epitaxial growth of high quality GaAs on InP using Se-doped GaAs buffer layer and grating patterned substrates. *Appl. Phys. Lett.* **66**, 2531–2533.
- H.J. Kim (1972) Liquid phase epitaxial growth of silicon in selected areas. *J. Electrochem. Soc.* **119**, 1394–1398.
- H.-M. Kim, J.-H. Leem and T.-W. Kang (2002a) Correlation of surface morphologies with Mn composition of  $\text{Ga}_{1-x}\text{Mn}_x\text{As}$  epilayers grown by liquid phase epitaxy. *Mater. Lett.* **53**, 39–42.
- H.-M. Kim, J.-H. Leem and T.-W. Kang (2002b)  $\text{Ga}_{0.97}\text{Mn}_{0.03}\text{As}$  epitaxial layers grown from Ga-Mn-As-Bi solutions by liquid phase epitaxy. *Mater. Lett.* **53**, 43–46.
- S.B. Kim and Y.S. Kwon (1986) Selective liquid phase epitaxy of GaAs: Kinetics and morphology. *J. Korea Inst. Electron. Eng.* **23**, 820–832.
- S.B. Kim, K. S. Kwon and Y.S. Kwon (1986) New fabrication technique for integrated-optical taper with controllable profile by selective liquid-phase epitaxy of GaAs. *Electron. Lett.* **22**, 806–808.
- M. Kimura, A. Tanaka and T. Sukegawa (1991) Convection phenomenon during the dissolution of silicon in an indium solution. *J. Cryst. Growth* **109**, 181–185.
- M. Kimura, N. Djilali and S. Dost (1994) Convective transport and Interface kinetics in liquid phase epitaxy. *J. Cryst. Growth* **143**, 334–348.
- M. Kimura, Z. Qin and S. Dost (1996a) A solid-liquid diffusion model for growth and dissolution of ternary alloys by liquid phase epitaxy. *J. Cryst. Growth* **158**, 231–240.
- M. Kimura, N. Djilali, S. Dost, H. Kanai, A. Tanaka and T. Sukegawa (1996b) Liquid phase epitaxy of silicon: an experimental and numerical study. *J. Cryst. Growth* **167**, 516–524.
- M. Kimura, S. Dost, H. Udono, A. Tanaka, T. Sukegawa and Z. Qin (1996c) A numerical simulation for the conversion phenomenon of GaAs to GaAsP on a GaP substrate in an LPE system. *J. Cryst. Growth* **169**, 697–703.
- F.D. King and A.J. Spring-Thorpe (1975) The Integral lens and coupled LED. *J. Electron. Mater.* **4**, 243–253.
- K. Kinoshita, H. Kato, S. Matsumoto, and S.-I. Yoda (2000) Growth of homogeneous  $\text{In}_{1-x}\text{Ga}_x\text{Sb}$  crystals by the graded solute concentration method. *J. Cryst. Growth* **216**, 37–43.
- S. Kinoshita, Y. Suzuki, and T. Nishinaga (1991) Epitaxial lateral overgrowth of Si on non-planar substrate. *J. Cryst. Growth* **115**, 561–566.
- M. Kitagawa, J. Saraie and T. Tanaka (1981) Injection electroluminescence from CdTe p-n junctions prepared by LPE. *Appl. Phys. A* **26**, 151–156.
- C. Klemenz and H.J. Scheel (1997) Liquid phase epitaxy of high- $T_c$  superconductors. *J. Cryst. Growth* **129**, 421–428.
- C. Klemenz and H.J. Scheel (2000) Crystal growth and liquid-phase epitaxy of gallium nitride. *J. Cryst. Growth* **211**, 62–67.
- T. Kochiya, Y. Oyama, K. Suto and J.-i. Nishizawa (2003) Epitaxial lateral overgrowth of InP by liquid phase epitaxy on InP (001), (111)A,B and (110) surfaces. *Mater. Sci. Semiconduct. Process.* **6**, 465–468.
- H.J. Koh and T. Fukuda (1996)  $\text{Si}_{1-x}\text{Ge}_x$  mixed crystals grown by pull-down technique with multi-capillary channels. *Crystal Res. Technol.* **31**, 151–158.

- R. Köhler, B. Jenichen, H. Raidt, E. Bauser and N Nagel (1995) Vertical stress in liquid-phase epitaxy Si layers on SiO<sub>2</sub>/Si evaluated by x-ray double-crystal topography *J. Phys. D* **28**, A50-A55.
- S. Kondo, T. Amamo and H. Nagai (1987) High purity LPE growth of InP by Co addition to an In-P melt. *Jpn. J. Appl. Phys.* **26**, 1997–2001.
- M. Konuma (2002) Feature and mechanisms of layer growth in liquid phase epitaxy of semiconductor materials in *Chemical Physics of Thin Film Deposition Processes for Micro- and Nano-Technologies*, Y. Pauleau, ed., Kluwer Academic, Dordrecht, 43–68H.
- G.N. Kozhemyakin (2000) Indium inhomogeneity in In<sub>x</sub>Ga<sub>1-x</sub>Sb ternary crystals grown by floating crucible Czochralski method. *J. Cryst. Growth* **220**, 39–45.
- Yu.M. Kozlov, L.N. Aleksandrov, and A.G. Cherevko (1975) Film growth mechanism in liquid epitaxy in *Growth of Crystals*, Vol. **9**, N.N. Sheftal' and E.I. Givargizov, eds. Consultants Bureau, New York.
- H. Kressel and J.K. Butler (1977) *Semiconductor Lasers and Heterojunction LEDs*. Academic Press, New York.
- A. Krier and Z. Labadi (2000) Modeling InAs thin layer growth from the liquid phase *IEE Proc.-Optoelectron.* **147**, 222–224.
- A. Krier, Z. Labadi and J. Richardson (1998) Rapid slider growth of InAs quantum wells. *IEE Proc. Optoelectron.* **145**, 297–301.
- A. Krier, Z. Labadi and A. Hammiche (1999) InAsSbP quantum dots grown by liquid phase epitaxy. *J. Phys. D, Appl. Phys.* **32**, 2587–2589.
- A. Krier, H.H. Gao and V.V. Sherstnev (2000) Investigation of rare earth gettering for the fabrication of improved mid-infrared LEDs. *IEE Proc. Optoelectron.* **147**, 217–221.
- A. Krier, H.H. Gao, and V.V. Sherstnev (2000) Investigation of rare earth gettering for the fabrication of improved mid-infrared LEDs. *IEE Proc. Optoelectron.* **147**, 217–221.
- A. Krier, X.L. Huang and A. Hammiche (2001) Liquid phase epitaxial growth and morphology of InSb quantum dots. *J. Phys. D: Appl. Phys.* **34**, 874–878.
- H. Kroemer (2000) Nobel Lecture: quasidelectric fields and band offsets: teaching electrons new tricks. *Rev. of Mod. Phys.* **73**, 783–793.
- S. Krukowski, I. Grzegory, M. Bockowski, B. ucznik, T. Suski, G. Nowak, J. Borysiuk, M. Wróblewski, M. Leszczyński, P. Perlin and S. Porowski (2005) Growth of AlN, GaN and InN from Solution. *Int. J. Mater. Product Technol.* **22**, 226–261.
- M. Kumagawa, A.F. Witt, M. Lichtensteiger and H.C. Gatos (1973) Current-controlled growth and dopant modulation in liquid phase epitaxy. *J. Electrochem. Soc.* **100**, 583–584.
- A. Kumar, S. Sridaran and P.S. Dutta (2004) Atomically flat III-V antimonide epilayers grown using liquid phase epitaxy. *Int. J. High-Speed Electron.* **14**, 652–657.
- E.V. Kunitsvna, I.A. Andreev, N.A. Charykov, Yu.V. Solov'ev and Yu.P. Yaltovfev (1998) Liquid phase epitaxial growth of Ga<sub>1-x</sub>In<sub>x</sub>As<sub>y</sub>Sb<sub>1-y</sub> solid solution using Pb neutral solvent in *ASDAM '98 Conference Proceedings of the Second International Conference on Advances in Semiconductor Devices and Microsystems*. IEEE, New York, 55–8.
- E. Kuphal (1989) Nearly back-dissolution-free LPE growth from Sn solutions over gratings for DFB lasers. *Electron. Lett.* **25**, 1581–1583.
- E. Kuphal (1991) Liquid Phase Epitaxy. *Appl. Phys.* **A 52**, 380–409.
- K. Kurata and T. Hirai (1968) A study on making abrupt heterojunctions by solution growth. *J. Electrochem. Soc.* **115**, 870–874.
- V.V. Kuznetsov, P.P. Moskvina, and V.S. Sorokin (1988) Coherent phase diagram and interface relaxation processes during LPE of A<sup>III</sup>B<sup>V</sup> solid solutions. *J. Cryst. Growth* **88**, 241–262.
- V. Kuznetsov, E.R. Rubtsov and E.A. Kognovitskaya (2006) Epitaxial films of GaInPAsSb quinary solid solutions. *Mater. Sci. Poland* **24**, **4**, 1057–1966.
- I. Ladany and C.C. Wang (1972) Two-stage epitaxial growth of GaAs E1 diodes on spinel. *J. Appl. Phys.* **43**, 236–238.

- J. Lagowski, L. Jastrzebski and H.C. Gatos (1980) Liquid-phase electroepitaxy: Dopant segregation. *J. Appl. Phys.* **51**, 364–372.
- F.C. Larche and J.W. Cahn (1987) Stress effects on III-V solid-liquid equilibria. *J. Appl. Phys.* **62**, 1232–1239.
- R.A. Laudise (1970) *The Growth of Single Crystals*. Prentice-Hall, Englewood Cliffs, NJ.
- D.J. Lawrence and L.F. Eastman (1977) Electric current controlled liquid phase epitaxy of GaAs on  $N^+$  and semi-insulating substrates. *J. Electron. Mater.* **6**, 1–24.
- D.J. Lawrence and L.F. Eastman (1978) Use of current controlled GaAs l.p.e. for optimum doping profiles in i.s.a. diodes. *Electron. Lett.* **14**, 77–78.
- E. Lendvay, T. Gorog and V. Rakovics (1985) LPE growth of GaAs-GaAlAs superlattices. *J. Cryst. Growth* **72**, 616–620.
- A. Yu. Leshko, A.V. Lyutetskii, A.V. Murashova, N.A. Pikhtin, I.S. Tarasov, I.N. Arsent'ev, B. Ya. Ber, Yu. A. Kudryavtsev, Yu.V. Il'in and N.V. Fetisova (1998) Multiwell laser heterostructures fabricated by liquid phase epitaxy. *Tech. Phys. Lett.* **24**, 854–856.
- S.Y. Leung and N.E. Schumaker (1982) Simulation of slide-induced convection in horizontal LPE slider system. *J. Cryst. Growth* **60**, 421–433.
- C. Li, Z. Du, D. Luo and W. Zhang (2000) Epitaxial techniques for compound semiconductor growth: from LPE to MOVPE. *Rare Metals* **19**, 81–86.
- K. Lin, P. Dold, H. Figgemeier and K.W. Benz (2005) Numerical modeling and investigation of liquid phase epitaxy of  $Hg_{1-x}Cd_xTe$  infrared detectors. *Cryst. Res. Technol.* **40**, 832–838.
- H. Lizhong, S. Jie, M. Qingduan, S. Yingmei and Z. Yu (2002)  $Al_{0.3}Ga_{0.7}As$  microtips grown by self-assembled LPE for integrated SNOM sensors. *J. Cryst. Growth* **240**, 98–103.
- S.I. Long, J.M. Ballantyne and L.F. Eastman (1974) Steady-state LPE of GaAs. *J. Cryst. Growth* **26**, 13–20.
- R.A. Logan and C.D. Thurmond (1972) Heteroepitaxial thermal gradient solution growth of GaN. *J. Electrochem. Soc.* **119**, 1727–1735.
- B.W. Ludington and A.A. Immorlica, Jr (1979) Temperature-gradient measurement in liquid epitaxial growth systems. *J. Cryst. Growth* **47**, 619–622.
- L.S. Lunin, A.V. Blagin and A.A. Barannik (2002) Determination of the melt undercooling required for producing  $Al_xGa_yIn_{1-x-y}Sb_{1-x}Bi_z/InSb$  heterostructures. *Inorg. Mater.* **38**, 1202–1205.
- T.V. L'vova, I.A. Andreev, E.V. Kunitsyna, M.P. Mikhailova, V.P. Ulin and Y.P. Yakovlev (1998) Liquid phase epitaxial growth of GaSb-related compounds on sulphide treated (100) GaSb substrates. *IEE Proc. Optoelectron.* **145**, 303–306.
- R. Madar, G. Jacob, J. Hallais and R. Fruchart (1975) High-pressure solution growth of GaN. *J. Cryst. Growth* **31**, 197–203.
- Y. Mao and A. Krier (1997) LPE growth of mixed composition III-V 'virtual substrates' for mid-infrared optoelectronic devices. *Mater. Res. Soc. Symp.* **450**, 49–54.
- I. Y. Maronchuk, V.V. Kurak, E.V. Andronova and Y. A. Baganov (2004) Obtaining GaSb/InAs heterostructures by liquid phase epitaxy. *Semicond. Sci. Technol.* **19**, 747–751.
- T. Maruyama, K. Matsuda, N. Saikawa and S. Nartisuka (2004) LPE growth of atomically flat Ge on a mesa pattern. *Mater. Res. Soc. Symp. Proc.* **788**, 583–587.
- T. Maruyama, K. Matsuda and S. Naritsuka (2005) Multinuclear layer-by-layer growth of Ge(111) by LPE. *J. Cryst. Growth* **275**, e2155–e2160.
- H.F. Mataré (1963) General considerations concerning the double-crucible method to grow uniformly doped germanium crystals of high perfection. *Solid State Electron.* **6**, 163–167.
- H. Matsunami, M. Ikeda, S. Suzuki and T. Tanaka (1977) SiC Blue LED's by liquid-phase epitaxy. *IEEE Trans. Electron Devices* **ED-24**, 958–961.
- B.L. Mattes (1975) Liquid/solid interfaces during epitaxial nucleation and growth of III-V compounds. *CRC Crit. Rev. Solid State Sci.* **Nov.**, 457–473.
- B.L. Mattes and R.K. Route (1974) LPE growth of GaAs: formation of nuclei and surface terraces. *J. Cryst. Growth* **27**, 122–141.

- M.G. Mauk and J.P. Curran (2001) Electro-epitaxial lateral overgrowth of silicon from liquid-metal solutions. *J. Cryst. Growth* **225**, 348–353.
- M.G. Mauk, P.A. Burch, S.W. Johnson, T.A. Goodwin and A.M. Barnett (1996) Buried metal/dielectric/semiconductor reflectors for light trapping in epitaxial thin-film solar cells. *Proceedings of the 25th IEEE Photovoltaic Specialists Conference*. IEEE, New York, 147–150.
- M.G. Mauk, A.N. Tata and J.A. Cox (2001a) Solution growth of thick III-V antimonide epilayers (InAsSb, InGaSb, InGaAsSb, AlGaAsSb, and InAsSbP) for ‘virtual substrates’. *J. Cryst. Growth* **225**, 236–243.
- M.G. Mauk, B.W. Feyock, A. Sharma and R.G. Hunsperger (2001b) Experimental assessment of metal solvents for low-temperature liquid-phase epitaxy of silicon carbide. *J. Cryst. Growth* **225**, 322–329.
- M.G. Mauk, A.N. Tata, J.A. Cox, O.V. Sulima and S. Datta (2003) Ternary and quaternary alloy III-V antimonide (InAsSb and InAsSbP) ‘virtual’ substrates made by liquid phase epitaxy. *IEEE Proc. Optoelectron.* **150**, 395–398.
- M. Meixner, E. Schöll, M. Schmidbauer, H. Raidt and R. Köhler (2001) Formation of island chains in SiGe/Si heteroepitaxy by elastic anisotropy. *Phys. Rev. B* **64**, 245307-1-4.
- M.P. Mikhailova, S.V. Slobodchikov, N.D. Stoyanov, N.M. Stus’ and Yu.P. Yakovlev (1997) Non-cooled InAsSbP/InAs photodiodes for the spectral range 3–5  $\mu\text{m}$ . *Tech. Phys. Lett.* **22**, 672–673.
- K.L. Miller, H.Z. Fardi and R.E. Hayes (1994) Effect of multiple reflection propagation on photon recycling in GaAs/AlGaAs double heterostructures. *J. Appl. Phys.* **75**, 8158–8162.
- V.A. Mishurnyi, F. de Anda, A. Yu. Gorbachev, V.I. Vasil’ev, V.M. Smirnov and N.N. Faleev (1998a) AlGaAsSb and AlGaInAsSb growth from Sb-rich solutions. *Cryst. Res. Technol.* **33**, 457–464.
- V.A. Mishurnyi, F. de Anda, A. Yu. Gorbachev, V.I. Vasil’ev, V.M. Smirnov and N.N. Faleev (1998b) Multicomponent Sb-based solid solutions grown from Sb-rich liquid phases in *Proceedings of the 24th IEEE International Symposium on Compound Semiconductors*. IEEE, New York, 37–40.
- V.A. Mishurnyi, F. de Anda, I.C. Hernández de Castillo and A. Yu. Gorbachev (1999) Temperature determination by solubility measurements and a study of evaporation of volatile components in LPE. *Thin Solid Films* **340**, 24–27.
- V.A. Mishurnyi, F. de Anda, V.A. Elyukin and I.C. Hernandez (2006) Growth of quantum well heterostructures by liquid phase epitaxy. *Crit. Rev. Solid State Mater. Sci.* **31**, 1–13.
- A. Mitric, J. Vincent, R. Caillard, V. Beermudez, E. Dieguez and T. Duffar (2004)  $\text{Ga}_{(1-x)}\text{In}_x\text{Sb}$  bulk crystal growth for thermophotovoltaic application in *Thermophotovoltaic Generation of Electricity, Sixth Conference*, A. Gopinath, T.J. Coutts and J. Luther, eds. American Institute of Physics, Melville, New York, 377–386.
- K.D. Moiseev, M.P. Mikhailova, Yu.P. Yakovlev, T. Šimecek, E. Hulcius and J. Oswald (2002) Photoluminescence of  $\text{Ga}_{0.94}\text{In}_{0.06}\text{As}_{0.13}\text{Sb}_{0.87}$  solid solution lattice matched to InAs. *Opt. Mater.* **19**, 455–459.
- A. Mondal, T.S. Das, N. Halder, S. Dhar and J. Kumar (2006) Growth of dilute GaSbN layers by liquid-phase epitaxy. *J. Cryst. Growth* **297**, 4–6.
- R.L. Moon (1980) ‘Liquid phase epitaxy’ in *Crystal Growth*, 2nd Edn, B. Pamplin, ed. Pergamon, Oxford, 421–460.
- R.L. Moon (1997) MOVPE: is there any other technology for optoelectronics. *J. Cryst. Growth* **170**, 1–10.
- U. Morlock, M. Kelsch and E. Bauser (1988) Extremely flat layer surfaces in liquid phase epitaxy of GaAs and  $\text{Al}_x\text{Ga}_{1-x}\text{As}$ . *J. Cryst. Growth* **87**, 343–349.
- U. Morlock, J. Christen, D. Bimberg, E. Bauser, H.-J. Queisser and A. Ourmazd (1991) Morphology of GaAs-quantum-well interfaces grown by liquid-phase epitaxy. *Phys. Rev. B: Condens. Matter* **44**, 8792–8797.
- A.D. Morrison and T. Duad (1985) Low defect, high purity crystalline layers grown by selective deposition. US Patent 4 522 661.

- A. Motogaito, M. Kimura, S. Dost, H. Katsuno, A. Tanaka and T. Sukegawa (1997) Growth of alloy GaInP crystals by compositional conversion of InP layers grown on GaP substrates in an LPE system. *J. Cryst. Growth* **182**, 275–280.
- D. Mouleeswaran and R. Dhanasekaran (2004) Investigations on liquid phase electroepitaxial growth kinetics of GaAs. *Mater. Sci. Eng. B* **112**, 91–95.
- St.G. Muller *et al.*: (2004) Defects in SiC substrates and epitaxial layers affecting semiconductor device performance. *Eur. Phys. J: Appl. Phys.* **27**, 29–35.
- R. Muralidharan and S.C. Jain (1980) Improvements in the theory of growth of LPE of GaAs and the interpretation of recent experiments. *J. Cryst. Growth* **50**, 707–719.
- K. Nakajima (1985) The liquid-phase epitaxial growth of InGaAsP in *Semiconductors and Semimetals*, Vol. 22, Part A, R. K. Willarson and A. C. Beer, eds. Academic Press, San Diego, 1–94.
- K. Nakajima and T. Kusunoki (1996) Constant temperature LEC growth of InGaAs ternary bulk crystals using double crucible method. *J. Cryst. Growth* **169**, 217–222.
- K. Nakajima, T. Tanahashi and K. Akita (1982) Liquid phase epitaxial growth of lattice-matched  $\text{Al}_{0.48}\text{In}_{0.52}\text{As}$  on InP. *Appl. Phys. Lett.* **41**, 194–196.
- S. Nakamura, S. Sakai, S.S. Chang, R.V. Ramawamy, J.-H. Kim, G. Radhakrishnan, J.K. Liu and J. Katz (1989) Transient-mode liquid phase epitaxial growth of GaAs on GaAs-coated Si substrates prepared by migration-enhanced molecular beam epitaxy. *J. Cryst. Growth* **97**, 303–309.
- T. Nakano (1967) Preparation and properties of GaAs-Si heterojunctions by solution growth method. *Jpn. J. Appl. Phys.* **6**, 854–863.
- S. Nakayama, M. Kaneko, S. Aizawa, K. Kashiwa and N.S. Takahashi (2002) InGaP lattice-mismatched LPE growth on GaAs substrates by epitaxial lateral overgrowth technique. *J. Cryst. Growth* **236**, 132–136.
- S. Naritsuka and T. Nishinaga (1995) Epitaxial lateral overgrowth of InP by liquid phase epitaxy. *J. Cryst. Growth* **146**, 314–318.
- S. Naritsuka and T. Nishinaga (1999) Liquid-phase epitaxy (LPE) microchannel epitaxy of InP with high reproducibility achieved by predeposition of In thin layer. *J. Cryst. Growth* **203**, 459–463.
- S. Naritsuka, Y.S. Chang, K. Tachibana and T. Nishinaga (1997) Vertical cavity surface emitting laser fabricated on GaAs laterally grown on Si substrate in *Proceedings of the Twenty-Seventh State-of-the-Art Program on Compound Semiconductors (SOTAPOCS XXVII)*. Electrochemical Society, Pennington, N J, 86–90.
- S. Naritsuka, T. Nishinaga, M. Tachikawa and H. Mori (2000) Optimization of InP microchannel epitaxy on Si substrate achieved by addition of upper source. *J. Cryst. Growth* **211**, 359–399.
- Nguyen Thanh Nghi (1988) Heterogeneous gas bubble formation during GaP solution growth. *Cryst. Res. Technol.* **23**, 715–722.
- F.H. Nicoll (1963) The use of close spacing in chemical transport systems for growing epitaxial layers of semiconductors. *J. Electrochem. Soc.* **110**, 1165–1167.
- S.A. Nikishin (1983) Analysis of mass transport during electroliquid epitaxy of gallium arsenide. *Sov. Tech. Phys.* **28**, 334–338.
- A.E. Nikolaev, V.A. Ivantsov, S.V. Rendakova, M.N. Blashenkov and V.A. Dmitriev (1996) SiC liquid phase epitaxy on patterned substrates. *J. Cryst. Growth* **166**, 607–611.
- A. Nishikawa, R. Katayama, K. Onabe and Y. Shiraki (2003) MBE growth and photorefectance study of GaAsN alloy films grown on GaAs (001). *J. Cryst. Growth* **251**, 427–431.
- S.A. Nishikin and D.V. Sinyavskii (1990) Crystallization of gallium arsenide from a stirred melt solution for short ( $10^{-3}$ – $10^{-1}$  sec) times of contact with the substrate. *Sov. Phys. Crystallogr.* **35**, 578–581.
- T. Nishinaga (2004) Microchannel epitaxy—Physics of lateral and vertical growth and its applications. *Crystal Growth—from Fundamentals to Technology*, G. Müller, J.-J. Métois and P. Rudolph, eds. Elsevier, Amsterdam, 271–293.
- T. Nishinaga (2005) Understanding of crystal growth mechanisms through experimental studies of semiconductor epitaxy. *J. Cryst. Growth* **275**, 19–28.

- T. Nishinaga and T. Suzuki (1991) The role of step kinetics in MBE of compound semiconductors. *J. Cryst. Growth* **115**, 398–405.
- T. Nishinaga and T. Suzuki (1993) Towards understanding the growth mechanism of III-V semiconductors on an atomic scale. *J. Cryst. Growth* **128**, 37–43.
- T. Nishinaga, K. Pak and S. Uchiyama (1978) Studies of LPE ripple based on morphological stability theory. *J. Cryst. Growth* **43**, 85–92.
- T. Nishinaga, T. Nakano and S. Zhang (1988) Epitaxial lateral overgrowth of GaAs by LPE. *Jpn. J. Appl. Phys., Part 2* **27**, 964–947.
- T. Nishinaga, T. Shitara, K. Mochizuki and K.I. Choi (1990) Surface diffusion and related phenomena in MBE growth of III-V compounds. *J. Cryst. Growth* **99**, 482–490.
- J. Nishizawa and Y. Okuno (1975) Liquid phase epitaxy of GaP by a temperature difference method under controlled vapor pressure. *IEEE Trans. Electron Devices* **ED-22**, 716–721.
- J. Nishizawa, Y. Okuno and H. Tadano (1975) Nearly perfect crystal growth of III-V compounds by the temperature difference methods under controlled vapour pressure. *J. Cryst. Growth* **31**, 215–222.
- D. Nohavica and J. Oswald (1995) Preparation of periodic structures by meander type liquid phase epitaxy. *J. Cryst. Growth* **146**, 287–292.
- Y. Nomura, Y. Morishita, S. Goto, Y. Katayama and T. Isu (1994) Surface diffusion length of Ga adatoms on (111)B surfaces during molecular beam epitaxy. *Appl. Phys. Lett.* **64**, 1123–1125.
- S.V. Novikov, T.S. Cheng, Z. Mahmood, I. Harrison and C.T. Foxon (1997) Selective meltback etching of GaN layers in liquid phase electroepitaxial technique. *J. Cryst. Growth* **173**, 1–4.
- T. Ohashi (1992) Suppression of dislocation accumulation in GaAs film on Si substrate by combination of impurity doping and selective area growth. *J. Mater. Res.* **7**, 3032–3038.
- H. Ohno, ed. (2005) *Electrochemical Aspects of Ionic Liquids*. John Wiley & Sons, Ltd, Hoboken, NJ.
- H. Ohtani, K. Kobayashi and K. Ishida (2001) Thermodynamic study of phase equilibria in strained III-V alloy semiconductors. *J. Phase Equilib.* **22**, 276–286.
- K. Ohtsuka, T. Ohishi, Y. Abe, H. Sugimoto and T. Matsui (1990) High resistivity InP layer grown by low temperature liquid phase epitaxy. *J. Cryst. Growth* **106**, 467–470.
- A. Okamoto, J. Lagowski and H.C. Gatos (1982) Enhancement of interface stability in liquid phase electroepitaxy. *J. Appl. Phys.* **53**, 1706–1713.
- J.M. Olchowik (1994) Influence of the interface contact on supersaturation of Ga-In-P-As alloys. *Phys. Status Solidi A* **146**, K19–K22.
- J.M. Olchowik, W. Sadowski and D. Szymczuk (1994) Erosive dissolution of InP substrates during liquid phase epitaxy. *Phys. Status Solidi A* **148**, 469–474.
- J.M. Olchowik, W. Sadowski and D. Szymczuk (1995) Effect of interface energy on erosion of AIIIBV substrates during liquid phase epitaxy. *J. Cryst. Growth* **153**, 11–18.
- J.M. Olchowik, W. Sadowski and D. Szymczuk (1996) Study of generation of  $Ga_xIn_{1-x}P_yAs_{1-y}$  transition layers obtained by liquid phase epitaxy. *J. Cryst. Growth* **158**, 241–247.
- J. Olvera-Hernández, P. de Jesús, F. de Anda and M. Rojas-López (2004) Influence of substrate conductivity on layer thickness in LPE GaAs. *J. Cryst. Growth* **268**, 375–377.
- T. Onda, R. Ito and N. Ogasawara (1986) Thermodynamic theory of III-V semiconductor ternary solid solutions. *Jpn. J. Appl. Phys.* **25**, 82–89.
- N. Ono, M. Kida, Y. Arai, K. Abe and K. Sahira (1994) A new technique for controlling dopant concentration in the double-crucible method. *J. Cryst. Growth* **135**, 359–364.
- M. Otsubo and H. Miki (1974) Chromium-doped semi-insulating gallium arsenide crystals grown by liquid phase epitaxy. *Jpn. J. Appl. Phys.* **13**, 1655–1656.
- Y. Oyama, T. Kochiya, K. Suto and J.-I. Nishizawa (2005) Angular dependence of lateral growth rate and kink-step structure on InP surface during liquid phase epitaxial condition. *J. Cryst. Growth* **275**, e97–e101.
- B.R. Pamplin, ed. (1980) *Crystal Growth*. Pergamon, Oxford.



- M.B. Panish (1973) Phase equilibria in the system Al-Ga-As-Sn and electrical properties of Sn-doped liquid phase epitaxial  $\text{Al}_x\text{Ga}_{1-x}\text{As}$ . *J. Appl. Phys.* **44**, 2667–2675.
- E. Papis, *et al.* (2000) Sulfide treatment of GaSb surface: influence on the LPE growth of InGaAsSb/AlGaAsSb heterostructures. *Vacuum* **57**, 171–178.
- N. Paul and B. Voigtlander (2004) Removal of the surfactant in Bi/Ge/Si(111) surfactant mediated epitaxy. *Surface Sci.* **551**, 80–90.
- N. Paul, H. Asaoka and B. Voigtlander (2004) Removal of the surfactant in Bi/Ge/Si(111) surfactant mediated epitaxy. *Surface Sci.* **564**, 187–200.
- T.P. Pearsall, M. Quillec and M.A. Pollack (1979) The effect of substrate orientation on the liquid–solid distribution coefficients in the temperature range 600–700 °C. *Appl. Phys. Lett.* **35**, 342–344.
- T.P. Pearsall, G. Beuchet, J.P. Hirst, N. Visentin, M. Bonnet and A. Roizes (1981) Electron and hole mobilities in  $\text{Ga}_{0.47}\text{In}_{0.53}\text{As}$  (epitaxial layers) in *Gallium Arsenide and Related Compounds*. IOP, Bristol, 639–649.
- S.J. Pearton, J.C. Zolper, R.J. Shui and F. Ren (1999) GaN: processing, defects and devices. *J. Appl. Phys.* **86**, 1–78.
- P.W. Pellegrini, B.C. Giessen and J.M. Feldman (1972) A survey of the Cr-rich area of the Cr-Si-C phase diagram. *J. Electrochem. Soc.* **119**, 535–537.
- P.W. Pellegrini and J.M. Feldman (1974) Liquid phase epitaxial growth of SiC from transition-metal silicide solvents. *J. Cryst. Growth* **27**, 320–324.
- G. Perrier, R. Phillippe and J.P. Dodelet (1988) Growth of semiconductors by the close-spaced vapor transport technique: a review. *J. Mater. Res.* **3**, 1031–1042.
- J.N. Pratt and R.G.R. Sellors (1973) *Electrotransport in Metals and Alloys*. Trans Tech, Riehen, Switzerland.
- V.A. Presnov, A.I. Kazakov, V.N. Brovkin and V.S. Shobik (1978) Heteroepitaxy of gallium arsenide on silicon. *Sov. Phys. Crystallogr.* **23**, 121–122.
- O. Procházková, F. Šrobár, J. Novotný and J. Zavadil, (1996) Growth of InP and GaInAsP layers by liquid phase epitaxy using homium gettering and doping in *Heterostructure Epitaxy and Devices*, J. Novák and A. Schlachetzki, eds. Kluwer Academic, Dordrecht, 57–60.
- O. Procházková, J. Novotný, J. Zavadil and K. Žďánský (1999) Effect of rare earth addition on liquid phase epitaxial InP-based semiconductor layers. *Materials Science and Engineering* **B66**, 63–66.
- T.A. Prutskij, P. Diez-Arencibia, A. Mintairov, J. Merz and T. Kosel (2003) Some evidences of ordering in InGaP layers grown by liquid phase epitaxy. *Applied Surface Science* **212–213**, 230–234.
- T. Prutskij, C. Pelosi and R.A. Brito-Orta (2005) Comparative study of photoluminescence of InGaP layers grown on GaAs substrates by LPE and MOCVD techniques. *Microelectronics J.* **36**, 374–378.
- Z. Qin, M. Kimura and S. Dost (1996) Convection model for growth and dissolution of ternary alloys by liquid phase epitaxy. *J. Cryst. Growth* **167**, 74–86.
- M. Quillec, H. Launois and M.C. Joncour (1983) Liquid phase epitaxy of unstable alloys: Substrate-induced stabilization and connected effects. *J. Vacuum Sci. Technol. B* **1**, 238–242.
- J. Raczynska, K. Fronc, J.M. Langer, K. Lischka and A. Pesek (1989),  $\text{Ga}_{1-x}\text{Al}_x\text{As}$  purification during its liquid phase epitaxial growth in the presence of Yb. *Appl. Phys. Lett.* **54**, 700–702.
- J. Raczynska, A. Rogalski, J. Rutkowski and K. Fronc (1999) Liquid phase epitaxial growth and characterization of In(Sb,Bi). *Proc. SPIE* **3725**, 66–71.
- W.G. Rado and R.L. Crawley (1972) The variation of solid composition during the LPE growth of  $\text{Ga}_{1-x}\text{Al}_x\text{As}$ . *J. Electrochem. Soc.* **119**, 1779–1780.
- M. Ratuszek, M. Panek and M. Tlaczala (1987) Application of Bi for LPE of GaAs layers from Ga-As-Bi solutions in *Proceedings of MELECON '87: Mediterranean Electrotechnical Conference and 34th Congress on Electronics Joint Conference* IEEE, New York, 293–296.

- L.A. Reichertz, J.W. Beeman, B.L. Cardoza, N.M. Haegel, E.E. Haller, G. Jakob and R. Katterloher (2004) GaAs BIB photodetector development for far-infrared astronomy. *Proc. SPIE* **5543**, 231–238.
- L.A. Reichertz, B.L. Cardoza, J.W. Beeman, D.I. Larsen, S. Tschanz, G. Jakob, R. Katterloher, N.M. Haegel and E.E. Haller (2005) First results on GaAs blocked impurity band (BIB) structures for far-infrared detector arrays. *Proc. SPIE* **5883**, 1–8.
- L.A. Reichertz, J.W. Beeman, B.L. Cardoza, G. Jakob, R. Katterloher, N.M. Haegel and E.E. Haller (2006) Development of a GaAs based BIB detector for sub-mm wavelengths. *Proc. SPIE* **6275**, 62715S.
- H. Rezagholipour Dizaji and R. Dhanasekaran (1996a) Simulation studies of liquid phase epitaxial growth of  $\text{In}_{1-x}\text{Ga}_x\text{As}$ . *Mater. Sci. Eng. B* **39**, 117–122.
- H. Rezagholipour Dizaji and R. Dhanasekaran (1996b) Concentration profile and growth rate studies of  $\text{In}_{1-x}\text{Ga}_x\text{P}$  LPE by computer simulation. *J. Mater. Sci.: Mater. Electron.* **7**, 181–185.
- E.A. Rezek, N. Holynyak Jr, B.A. Vojak, G.E. Stillman, J.A. Rossi, D.L. Keune and J.D. Fanning (1977) LPE  $\text{In}_{1-x}\text{Ga}_x\text{P}_{1-z}\text{As}_z$  ( $x \sim 0.12$ ,  $z \sim 0.26$ ) DH Laser multiple thin-layer (<500 Å) active region. *Appl. Phys. Lett.* **31**, 288–290.
- P.H. Robinson (1963) Transport of gallium arsenide by close-spaced techniques. *RCA Rev.* **24**, 574–584.
- F. Rosenberger (1979) *Fundamentals of Crystal Growth*, Vol. 1. Springer, Berlin.
- F.E. Rosztochy and W.W. Stein (1972) The growth of Ge-GaAs and GaP-Si heterojunctions by liquid phase epitaxy. *J. Electrochem. Soc.* **119**, 119–121.
- M. Rubenstein (1966) Solubilities of some II-VI compounds in bismuth. *J. Electrochem. Soc.* **113**, 623–624.
- M. Rubenstein (1968) Solution growth of some II-VI compounds using tin as a solvent. *J. Cryst. Growth* **3**, 309–312.
- E.R. Rubtsov, V.S. Sorokin and V.V. Kuznetsov (1997) Prediction of the properties of heterostructures based on five-component  $\text{A}^{\text{III}}\text{B}^{\text{V}}$  solid solutions. *Russ. J. Phys. Chem.* **71**, 346–351.
- E.R. Rubtsov, V.V. Kuznetsov and O.A. Lebedev (1998) Phase equilibria in III-V quinary systems. *Inorg. Mater.* **34**, 422–426.
- C.M. Ruiz, N.P. Barradas, E. Alves, J.L. Plaza, V. Bermúdez and E. Diéguez (2004) Formation of  $\text{Al}_x\text{Ga}_{1-x}\text{Sb}$  film over GaSb substrates by Al diffusion. *Eur. Phys. J. Appl. Phys.* **27**, 423–426.
- I. Ruiz-Becerril, M. Hernández-Sustaita, F. de Anda, V.A. Mishurnyi, A.Yu Gorbachev and L. Narvaez (2002) Some experiments on the growth of InTlSb by LPE. *J. Cryst. Growth* **241**, 101–107.
- G.K. Safaraliev, B.A. Bilalov and A.Z. Efendiev (1984) Current-induced crystallization of silicon carbide from a liquid phase. *Sov. Phys. Tech. Phys.* **29**, 1181–1183.
- A.S. Saidov and M.S. Saidov (1991) Liquid phase epitaxy of  $(\text{Ge}_2)_{1-x}(\text{GaAs})_x$  and  $(\text{Si}_2)_{1-x}(\text{GaP})_x$  solid solutions. *Cryst. Prop. Prep.* **36–38**, 515–518.
- T. Saitoh, Y. Oyama, K. Suto, J.-I. Nishizawa and T. Kimura (2000) Excess on density at the GaP/GaP liquid-phase epitaxial regrowth surface. *J. Cryst. Growth* **209**, 666–674.
- S. Sakai and Y. Ohashi (1992) Selective growth of GaAs on GaAs-coated Si substrate by liquid phase electroepitaxy. *Mater. Res. Soc. Symp.* **237**, 565–570.
- S. Sakai and Y. Ohashi (1994) Selective lateral growth mechanism of GaAs by liquid-phase electroepitaxy. *Jpn. J. Appl. Phys., Part 1* **33**, 23–27.
- S. Sakai, R.J. Matyi and H. Shichijo (1988) Growth of GaAs on GaAs-coated Si by liquid phase epitaxy. *J. Appl. Phys.* **63**, 1075–1079.
- S. Sakai, Y. Ohashi and Y. Shintani (1991) Selective liquid-phase electroepitaxy of GaAs on GaAs-coated Si substrates. *J. Appl. Phys.* **70**, 4899–4902.
- S. Sakawa and T. Nishinaga (1991) Faceting of LPE GaAs grown on a misoriented Si(100) substrate. *J. Cryst. Growth* **115**, 145–149.

- F. Sakurai, M. Motozawa, K. Suto and J.-I. Nishizawa (1997) Liquid phase epitaxial p-type ZnSe growth from a Se solution and fabricated pn junctions with diffused n-type layers. *J. Cryst. Growth* **172**, 75–82.
- E. Sand, D. Levy and Y. Nemirovsky (1985) Combination of open-tube vapor and liquid phase epitaxy of  $\text{Hg}_{1-x}\text{Cd}_x\text{Te}$ . *Appl. Phys. Lett.* **46**, 501–503.
- K. Sangwal and T. Pa czyński (2000) On the supersaturation and impurity concentration dependence of segregation coefficient in crystals grown from solutions. *J. Cryst. Growth* **212**, 522–531.
- M. Sano, Y. Yamashita and Y. Okuno (1993) Growth and characterization of ZnSe epitaxial layers grown by solution growth method. *J. Appl. Phys.* **74**, 6133–6188.
- S. Saravanan, K. Jeganathan, K. Baskar, J. Kumar, C. Subramanian, T. Soga, T. Jimbo, B.M. Arora and M. Umeno (1997) High quality GaAs epitaxial layers grown from Ga-As-Bi solutions by liquid phase epitaxy. *Jpn. J. Appl. Phys.* **36**, 3385–3388.
- S. Saravanan, K. Jeganathan, K. Baskar, T. Jimbo, T. Soga and M. Umeno (1998) Crystal growth of high quality hybrid GaAs heteroepitaxial layers on Si substrate by metalorganic chemical vapor deposition and liquid phase epitaxy. *J. Cryst. Growth* **192**, 23–27.
- R.H. Saul (1971) Reduced dislocation densities in liquid phase epitaxy layers by intermittent growth. *J. Electrochem. Soc.* **118**, 793–796.
- R.H. Saul and D.D. Roccasecca (1973) Surface morphology of liquid-phase epitaxial layers. *J. Appl. Phys.* **44**, 1983–1988.
- H.J. Scheel (1980) Transition to faceting in multilayer liquid phase epitaxy of GaAs. *Appl. Phys. Lett.* **37**, 70–73.
- H.J. Scheel (1993) Historical introduction in *Handbook of Crystal Growth*, Vol. 1a, D.T.J. Hurle, ed. Elsevier, Amsterdam, Ch. 1.
- R. Schmid and Y.A. Chang (1985) A thermodynamic study of an associated solution model for liquid alloys. *CALPHAD* **9**, 363–382.
- R.F. Schnabel, M. Grundmann, R. Engelhardt, J. Oertel, A. Krost, D. Bimberg, R. Optiz, M. Schmidbauer and R. Köhler (1995) High quantum efficiency InP mesas grown by hybrid epitaxy on Si substrates. *J. Cryst. Growth* **156**, 337–342.
- E.F. Schubert (2006) *Light-emitting Diodes*, 2nd Edn. Cambridge University Press, Cambridge.
- R.C. Sharma, T.L. Ngai and Y. A. Chang (1987) Thermodynamic analysis and phase equilibria calculations for the In-Sb and Ga-Sb systems. *J. Electron. Mater.* **15**, 307–313.
- Y. Shi, Y. Li, S. Li, M. Ding, J. Zhou and Y. Yuan (1993) Study of rare earth doped GaAs by LPE. *Acta Electron. Sinica* **21**, 101–102.
- E. Shibano, S. Fujiwara, K. Kohno, N.S. Takahashi and S. Kurita (1993) Liquid phase epitaxy of AlGaInP on GaAs substrate using AlGaAs buffer layer. *Cryst. Res. Technol.* **28**, 469–477.
- I. Silier, A. Gutjahr, N. Nagel, P.O. Hansson, E. Czech, M. Konuma, E. Bauser, F. Banhart, R. Köhler, H. Raidt and B. Jenichen (1996) Solution growth of epitaxial semiconductor-on-insulator layers. *J. Cryst. Growth* **166**, 727–730.
- Yu.V. Shmartsev (1991a) Controlling the physical properties of epitaxial semiconductor films by isovalent impurity doping. *Cryst. Prop. Prep.* **31**, 156–174.
- Yu.V. Shmartsev (1991b) Liquid phase electroepitaxy. *Cryst. Prop. Prep.* **31**, 174–205.
- M.B. Small and I. Crossley (1974) The physical processes occurring during liquid-phase epitaxial growth. *J. Cryst. Growth* **27**, 45–38.
- M.B. Small and R. Ghez (1979) Growth and dissolution kinetics of III-V heterostructures formed by LPE. *J. Appl. Phys.* **50**, 5322–5330.
- M.B. Small and R. Ghez (1980) Growth and dissolution kinetics of III-V heterostructures formed by LPE. II. Comparison between thermodynamic and kinetic models. *J. Appl. Phys.* **51**, 1589–1592.
- M.B. Small and R. Ghez (1984) Reversal in the growth or dissolution of III-V heterostructures by liquid phase epitaxy. *J. Appl. Phys.* **55**, 926–930.
- M.B. Small, R. Ghez, R.M. Potemski and W. Reuter (1980) The dissolution kinetics of GaAs in undersaturated isothermal solutions in the Ga-Al-As system. *J. Electrochem. Soc.* **127**, 1177–1182.

- M.B. Small, E.A. Giess and R. Ghez (1994) Liquid phase epitaxy in *Handbook of Crystal Growth*, Vol. 3, D.T.J. Hurle, ed. Elsevier, Amsterdam, Ch. 6.
- S. Srinivasa and P.K. Bhattacharya (1985) Orientation-dependent phase equilibria in  $\text{In}_{1-x}\text{Ga}_x\text{As}$ : A model including surface energies. *J. Phys. Chem. Solids* **46**, 449–453.
- F.M. Steranka, D.C. DeFevere, M.D. Camras, C.-W. Tu, D.K. McElfresh, S.L. Rudaz, L.W. Cook and W.L. Snyder (1988) Red AlGaAs light-emitting diodes. *Hewlett-Packard J.* **Aug.**, 84–88.
- G.B. Stringfellow (1984a) III-V phase diagrams in *Advances in Electronic Materials*, B.W. Wessels, ed. American Society of Metals, Metals Park, OH, 11–40.
- G.B. Stringfellow (1984b) A critical appraisal of growth mechanisms in MOVPE. *J. Cryst. Growth* **68**, 111–122.
- G.B. Stringfellow (1989) *Organometallic Vapor Phase Epitaxy: Theory and Practice*. Academic Press, New York.
- G.B. Stringfellow (1991) Fundamental aspects of vapor growth and epitaxy. *J. Cryst. Growth* **115**, 1–11.
- G.B. Stringfellow (2004) Thermodynamics of modern epitaxial growth processes in *Crystal Growth—from Fundamentals to Technology*, G. Müller, J.J. Métois and R. Rudolph, eds. Elsevier, Amsterdam, 1–26.
- F. Sukarai, M. Motozawa, K. Suto and J.-I. Nishizawa (1997) Liquid phase epitaxial p-type ZnSe growth from a Se solution and fabrication of pn junctions with diffused n-type layers. *J. Cryst. Growth* **172**, 75–82.
- T. Sukegawa, H. Udono, M. Kimura, H. Katsuno and A. Tanaka (1993) Conversion from GaAs to GaAsP by annealing a GaAs layer on GaP in Ga-As-P solution. *Jpn. J. Appl. Phys., Part 2* **32**, L1164–L1166.
- J. Sun, P. Jin, Z.G. Wang, H.Z. Zhang and L.Z. Lu (2005) Changing planar thin film growth into self-assembled island formation by adjusting experimental conditions. *Thin Solid Films* **476**, 68–72.
- A. Suzuki, M. Ikeda, N. Nagao, H. Matsunami and T. Tanaka (1976) Liquid-phase epitaxial growth of 6H-SiC by the dipping technique for preparation of blue-light-emitting diodes. *J. Appl. Phys.* **47**, 4546–4550.
- T. Suzuki (2002) Basic aspects of atomic ordering in III-V semiconductor alloys in *Spontaneous Ordering in Semiconductor Alloys*, A. Mascarenhas, ed. Kluwer Academic, New York, Ch. 1.
- Y. Suzuki and T. Nishinaga (1989) Epitaxial lateral overgrowth of Si by LPE with Sn solution and its orientation dependence. *Jpn. J. Appl. Phys.* **28**, 440–445.
- Y. Suzuki and T. Nishinaga (1990) Si LPE lateral overgrowth from a ridge seed. *Jpn. J. Appl. Phys.* **29**, 2685–2689.
- Y. Suzuki, T. Nishinaga and T. Sanada (1990) The sources of atomic steps in epitaxial lateral overgrowth. *J. Cryst. Growth* **99**, 229–234.
- K. Swaminathan et al. (2006) Room-temperature AlGaAsSb/InGaAsSb heterojunction phototransistors. *Proc. SPIE* **6232**, 62320P-1–62320P-9.
- V. Swaminathan and A.T. Macrander (1991) *Materials Aspects of GaAs and InP based Structures*. Prentice-Hall, Englewood Cliffs, NJ.
- N. Takahashi, S. Fujiwara, K. Kaoru, E. Shibano and K. Shochiha (1994) AlGaInP/AlGaAs double heterostructure light emitting diodes grown by liquid phase epitaxy. *J. Cryst. Growth* **137**, 240–244.
- Y. Takeda, S. Noda, K. Nakashima and A. Sasaki (1984) Surface treatment of GaSb substrate and extremely low temperature LPE growth of AlGaSb. *J. Electron. Mater.* **13**, 855–866.
- C. Takenaka, T. Kusunoki and K. Nakajima (1991a) Solute transport mechanism during liquid phase epitaxial (LPE) growth with an applied current *J. Cryst. Growth* **108**, 519–524.
- C. Takenaka, T. Kusunoki and K. Nakajima (1991a) Effect of an electric current on the LPE growth of InP. *J. Cryst. Growth* **114**, 293–298.
- A. Tanaka and H. Katsuno (2006) Heavily p-type silicon carbide thick layer growth by low-temperature liquid phase epitaxy. *Jpn. J. Appl. Phys., Part 1*, **45**, 32–35.

- A. Tanaka and T. Sukegawa (2001) ZnSe growth from zinc chloride solvent by successive liquid phase epitaxy *J. Cryst. Growth* **229**, 87–91.
- A. Tanaka, T. Yoneyama, M. Kimura and T. Sukegawa (1998) Control of GaInSb alloy composition grown from ternary solution. *J. Cryst. Growth* **186**, 305–308.
- A. Tanaka, N. Shiozaki and H. Katsuno (2002) Synthesis and growth of 3-C SiC crystals from solution at 950 °C. *J. Cryst. Growth* **237–239** 1202–1205.
- A. Tanaka, T. Ataka, E. Ohkura and H. Katsuno (2004a) Epitaxial growth of SiC from Al-Si solution reacting with propane gas. *J. Cryst. Growth* **269**, 413–418.
- A. Tanaka, T. Ataka, E. Ohkura and H. Katsuno (2004b) Growth modes of silicon carbide in low-temperature liquid phase epitaxy. *Jpn. J. Appl. Phys.* **43**, 7670–7671.
- G.H.B. Thompson and P.A. Kirkby (1974) Liquid phase epitaxial growth of six-layer GaAs/(GaAl)As structures for injection lasers with 0.04  $\mu\text{m}$  thick centre layer. *J. Cryst. Growth* **27**, 70–85.
- W. Thulke (1991) Can liquid phase epitaxy still be useful for optoelectronic devices? *Mater. Sci. Eng., B* **9**, 61–67.
- C.D. Thurmond and R.A. Logan (1972) The equilibrium pressure of  $\text{N}_2$  over GaN. *J. Electrochem. Soc.* **119**, 622–626.
- W.A. Tiller (1991) *The Science of Crystallization: Microscopic Interfacial Phenomena*. Cambridge University Press, Cambridge.
- W.A. Tiller (1992) *The Science of Crystallization: Macroscopic Phenomena and Defect Generation*. Cambridge University Press, Cambridge.
- M. Tmar, A. Gabriel, C. Chartillon and I. Ansara (1984) Critical analysis and optimization of the thermodynamic properties and phase diagrams in the III-V compounds: the In-P and Ga-P systems. *J. Cryst. Growth* **68**, 557–580.
- N. Toyoda, M. Mihara and T. Hara (1979) Surface morphology of GaAs LPE layers: Effects of substrate misorientation and initial supercooling. *Jpn. J. Appl. Phys.* **18**, 2207–2213.
- G. Traeger, E. Kuphal and K.-H. Zschauer (1988) Diffusion-limited LPE growth of mixed crystals: Application to  $\text{In}_{1-x}\text{Ga}_x\text{As}$  on InP. *J. Crystal Growth* **88**, 205–214.
- H.-P. Trah (1990) Liquid phase epitaxy in the ternary system Si-Ge-Bi. *J. Cryst. Growth* **102**, 175–182.
- H. Uono, H. Katsuno, A. Tanaka and T. Sukegawa (1993) Conversion of GaAs layer grown on GaP substrate to GaAsP in LPE system. *Jpn. J. Appl. Phys. Suppl.* **32-3**, 735–736.
- W.Y. Uen and T. Nishinaga (1995) Liquid phase epitaxial lateral overgrowth of GaAs on 0.3°-misoriented epitaxial silicon substrates. *Mater. Chem. and Phys.* **42**, 231–236.
- V.B. Ufimtsev and R.Kh. Akcurin (1983) *Physical Basis of Liquid Phase Epitaxy*. Metallurgiya, Moscow (in Russian).
- T. Ujihara, K. Fujiwara, G. Sazaki, N. Usami and K. Nakajima (2002) Simultaneous in situ measurement of solute and temperature distributions in alloy solutions. *J. Cryst. Growth* **242**, 313–320.
- Y. Ujiie and T. Nishinaga (1989) Epitaxial lateral overgrowth of GaAs on a Si substrate. *Jpn. J. Appl. Phys.* **28**, L337–L339.
- V. Valery, V.A. Dorogan, V.A. Kosyak and V.G. Trofim (1992) Method of GaAs growth on single crystal Si substrate. *Mater. Res. Soc. Symp.* **263**, 199–202.
- J.P. van der Ziel, R.A. Logan and N. Chand (1988) Characteristics of GaAs/AlGaAs heterostructures grown by liquid-phase epitaxy on molecular-beam-coated GaAs on Si. *J. Appl. Phys.* **64**, 3201–3204.
- V.I. Vasil'ev, S.N. Losev, V.M. Smirnov, V.V. Kuznetsov, E.A. Kognoviskaya and E.R. Rubstov (1999) The study of Sb-rich regions in the phase diagrams of Ga-In-As-Sb, Ga-In-P-As-Sb and Al-Ga-In-As-Sb multicomponent systems in *Intermolecular Interactions in Matter*, K. Sangwal, E. Jartych and W. Polak, eds. Lublin, 96–100.
- V.I. Vasil'ev, V.I. Kuchinskii, I.P. Nikitina, D. Akhmedov, V.M. Smirnov and D.A. Vasukov (2000) Epitaxial growth of heterostructures based on InAsPSb and GaInAsSb isoperiodical with GaSb in

- Proceedings of the IEEE Twenty-Seventh International Symposium on Compound Semiconductors*. IEEE, New York, 233–238.
- W. von Munch (1977) Silicon carbide technology for blue emitting diodes. *J. Electron. Mater.* **6**, 449–463.
- W. von Munch and W. Kurzinger (1978) Silicon carbide blue-emitting diodes produced by liquid phase epitaxy. *Solid State Electron.* **21**, 1129–1132.
- W. von Munch, W. Kurzinger and I. Pfaffeneder (1976) Silicon carbide light emitting with epitaxial junctions. *Solid State Electron.* **19**, 871–874.
- Y. Wakanama and S. Tanaka (1997) Self-assembled nanocomposite structure of Si-Au system formed by liquid phase epitaxy. *J. Cryst. Growth* **181**, 304–307.
- S. Watabe, K. Tadatomo, T. Sukegawa and A. Tanaka (1993) Growth of GaInP thick layers by the modified yo-yo solute feeding technique. *J. Cryst. Growth* **128** 1–4, pt 1 479–482.
- A. Watanabe, T. Yamada, K. Imanaka, H. Horikawa, Y. Kawai and M. Sakuta (1985) AlGaAs/GaAs met-etched inner stripe laser diode with self-aligned structure. *Appl. Phys. Lett.* **46**, 1023–1025.
- A. Watanabe, A. Tanaka and T. Sukegawa (1993) GaSb solution growth by the solute feeding Czochralski method. *J. Cryst. Growth* **128**, 462–465.
- H. Watanabe, T. Mizutani and A. Usui (1990) Fundamentals of epitaxial growth and atomic layer epitaxy in *Very High Speed Integrated Circuits: Heterostructures*, T. Ikoma, ed. Academic Press, Boston, 1–52.
- K.J. Weber, K. Catchpole and A.W. Blakers (1998) Epitaxial lateral overgrowth of Si on (100)Si substrates by liquid phase epitaxy. *J. Cryst. Growth* **186**, 369–374.
- W. Wei, Y. Luming, W. Guangyu and P. Ruiwu (1995) Solid–liquid and solid–vapor equilibrium of Ga–In–As–Sb and artificial neural network prediction. *J. Appl. Phys.* **78**, 897–899.
- H. Weishart, E. Bauser, M. Konuma and H.-J. Quiesser (1994) Monomolecular steps of ultra-low density on (100) growth faces of liquid phase epitaxial GaAs. *J. Cryst. Growth* **137**, 335–346.
- R.R. Wixom, L.W. Rieth and G.B. Stringfellow (2004) Sb and Bi surfactant effects on homo-epitaxy of GaAs on (1001) patterned substrates. *J. Cryst. Growth* **265**, 367–374.
- G.A. Wolff, B.N. Das, C.B. Lamport and A.I. Mlavsky (1969) Principles of solution growth and traveling solvent growth of silicon carbide. *Mater. Res. Bull.* **4**, S67–S72.
- D.J. Wollkind and S. Wang (1988) A nonlinear stability analysis of a model equation for liquid phase electro-epitaxial growth of a dilute binary substance. *SIAM J. Appl. Math.* **48**, 52–78.
- C.E.C. Wood (1982) Molecular beam epitaxy for microwave field effect transistors in GaAs FET *Principles and Technology*, J.V. DiLorenzo and D.D. Khandelwal, eds. Artech, Boston, 111.
- S.C. Wood and G.S. Brown (1998) Commercializing nascent technology: the case of the laser diode at Sony. *J. Prod. Innovat. Manage.* **15**, 167–183.
- J.M. Woodall (1972) Solution grown Ga<sub>1-x</sub>Al<sub>x</sub>As superlattice structures. *J. Cryst. Growth* **12**, 32–38.
- Z. Xu, W. Xu, S. Lan, L. Li, C. Yang and H. Liu (1997) Solid–liquid equilibria for III-V quinary alloy semiconductors. *Solid State Commun.* **103**, 417–420.
- Z.L. Xu, W.J. Xu, L. Li, C.Q. Yang and H.D. Liu (1998) Liquid phase epitaxy growth of Al<sub>x</sub>Ga<sub>y</sub>In<sub>1-x-y</sub>P<sub>z</sub>As<sub>1-z</sub>/GaAs with direct bandgap up to 2.0 eV. *Appl. Phys. A* **66**, 565–567.
- H. Weishart, E. Bauser, M. Konuma and H.-J. Quiesser (1994) Monomolecular steps of ultra-low density on (100) growth faces of liquid phase epitaxial GaAs. *J. Cryst. Growth* **137**, 335–346.
- R. Yakimova, M. Tuominen, A.S. Bakin, J.-O. Fornell, A. Vehanen and E. Janzen (1996) Silicon carbide liquid phase epitaxy in the Si-Sc-C system, in *Silicon Carbide and Related Materials: Proceedings of the Sixth International Conference*, S. Nakashima, ed. Institute of physics, Philadelphia, 101–104.
- N.A. Yakusheva, K.S. Zhuravlev, S.I. Chikichev and O.A. Shegaj (1989) Liquid phase epitaxial growth of undoped gallium arsenide from bismuth and gallium melts. *Cryst. Res. Tech.* **24**, 235–246.
- N.A. Yakusheva and V.G. Pogadaev (1992) Amphoteric behavior of germanium during liquid phase epitaxy of GaAs from bismuth-gallium melts. *J. Cryst. Growth* **123**, 479–486.

- K. Yamaguchi and K. Okamoto (1993) Lateral supply mechanisms in selective metalorganic chemical vapor deposition. *Jpn. J. Appl. Phys.* **32**, 1523–1527.
- H. Yamane, M. Shimada, T. Sekiguchi and F.J. DiSalvo (1998) Morphology and characterization of GaN single crystals grown in a Na flux. *J. Cryst. Growth* **186**, 8–12.
- S. Yamazaki, K. Nakajima and Y. Kishi (1984) Liquid phase epitaxial growth for (111)A InP/GaInAs heterostructure avalanche photodiodes. *Fujitsu Sci. Tech. J.* **20**, 329–383.
- X.F. Yang, L. Huang and H.C. Gatos (1982) Selective epitaxial growth of GaAs by liquid phase electroepitaxy. *J. Electrochem. Soc.* **129**, 194–197.
- Y. Yazawa, T. Minemura and T. Unno (1990) High-quality GaAs/Si(100) grown by MBE-LPE hybrid method for reliable light-emitting diode in *Proceedings of the 2nd International Conference on Electronic Materials*. Materials Research Society, Pittsburgh, 319–324.
- Y. Yazawa, T. Minemura and T. Unno (1990) Photoluminescence of GaAs layers hybrid-grown on Si by MBE and LPE. *J. Cryst. Growth* **115**, 519–523.
- M. Yildiz, S. Dost and B. Lent (2005) Growth of bulk SiGe single crystals by liquid phase diffusion. *J. Cryst. Growth* **280**, 151–160.
- V.A. Zavadski, A.I. Kazakov, V.A. Mokritski and V.S. Shobik (1991) Peculiarities of epitaxial growth of GaAs and GaP on Si and Ge from the liquid phase. *Cryst. Prop. Prep.* **32–34**, 217–222.
- A. Zdyb, J.M. Olchowik and M. Mucha (2006) The dependence of GaAs and Si surface energy on crystal planes misorientation angle. *Mater. Sci. Poland* **24**, **4**, 1109–1114.
- R.B. Zetterstrom (1970) Synthesis and growth of single crystals of gallium nitride. *J. Mater. Sci.* **5**, 1102–1104.
- S. Zhang and T. Nishinaga (1990a) Epitaxial lateral overgrowths of GaAs on (001) GaAs substrates by LPE: growth behavior and mechanism. *J. Cryst. Growth* **99**, 292–296.
- S. Zhang and T. Nishinaga (1990b) LPE lateral overgrowth of GaP. *Jpn. J. Appl. Phys., Part 1* **29**, 545–550.
- G. Zhang, P. P. Jayavel, T. Koyoma, M. Kumagawa and Y. Hayakawa (2005) Influence of Te impurity on morphology of GaAsb epilayer grown GaSb (001) patterned substrate by liquid phase epitaxy. *J. Appl. Phys.* **97**, 023518-1–023581-5.
- Zhang Hongzhi, Hu Lizhong, Tian Yichun, Sun Xiaojuan, Liang Xiuping and Pan Shi (2006) Effects of different masks on GaAs microtips grown by selective liquid-phase epitaxy. *J. Cryst. Growth* **295**, 16–19.
- Zhou Bo-jun (1987) Observation of phenomena in liquid phase epitaxy-free regions. *Chine. Phys.* **7**, 225–228.
- R. P. Zingg, N. Nagel, R. Bergmann, E. Bauser, B. Höfflinger and H.J. Queisser (1992) First MOS transistors on insulator by silicon saturated liquid solution epitaxy. *IEEE Electron Device Lett.* **13**, 294–296.
- J.C. Zolper and A.M. Barnett (1989) Selective area solution growth of Ge and GaAs on Si. *J. Appl. Phys.* **66**, 210–214.
- K.-H. Zschau and A. Vogel (1971) Dependence of impurity incorporation on growth rate and crystal orientation during GaAs liquid-phase epitaxy in *Proceedings of the Third International Symposium on GaAs and Related Compounds*. Institute of Physics, London, 100–107.
- P. Zwicknagl, W. Rehm and E. Bauser (1984) Modulation of electronic properties in liquid phase epitaxially grown p-n-p-n GaAs multilayers. *J. Electron. Mater.* **13**, 545–558.
- Z.R. Zytkeiwicz (2002) Laterally overgrown structures as substrates for lattice mismatched epitaxy. *Thin Solid Films* **412**, 64–75.

# 13 Liquid Phase Epitaxy for Light Emitting Diodes

MICHAEL G. MAUK

*School of Engineering and Applied Science, University of Pennsylvania,  
Philadelphia, PA 19101, USA*

---

13.1 Introduction	415
13.2 Commercial LEDs	419
13.3 LPE for wide-bandgap (blue and UV) LEDs	420
13.3.1 Silicon carbide LEDs	420
13.3.2 Wide-bandgap II-VI compound LEDs	421
13.3.3 III-V nitride LEDs	422
13.4 LPE for mid-infrared LEDs	422
13.5 LPE for new LED design concepts	424
13.6 Outlook	426
References	430

---

## 13.1 INTRODUCTION

This chapter reviews the application of liquid phase epitaxy (LPE) to the production of semiconductor light emitting diodes (LEDs). LEDs are  $p$ - $n$  junction devices that when forward-biased with an applied voltage ( $\sim 1$  V) produce useful amounts of luminescence due to radiative recombination of electrically injected excess minority carriers (Figure 13.1). The luminescence emission wavelength  $\lambda_e$  corresponds approximately to the bandgap  $E_g$  of the semiconductor, i.e.  $\lambda_e(\text{nm}) \cong 1243/E_g$  (eV), and LEDs made in various semiconductor materials provide photon emission with a relatively narrow spectral width (roughly 50–100 nm) at wavelengths ranging from the UV ( $<300$  nm) to the mid-infrared ( $>5000$  nm). The  $p$ - $n$  junction areas of LEDs typically have lateral dimensions of 10  $\mu\text{m}$  to several millimeters (i.e.  $10^{-6}$ – $10^{-1}$   $\text{cm}^2$  in junction area) with applied current levels of 1 to several hundred milliamps, corresponding to current densities of several hundred to several thousand amps per square centimeter.

With a few exceptions (e.g. silicon carbide, SiC), commercial LEDs have traditionally been made in direct-bandgap inorganic compound semiconductor materials that can be effectively doped both  $p$ - and  $n$ -type. A favorable combination of high minority carrier injection efficiencies, high rates of minority carrier *radiative* recombination relative to nonradiative recombination, low electrical resistances, and low optical (re-)absorption



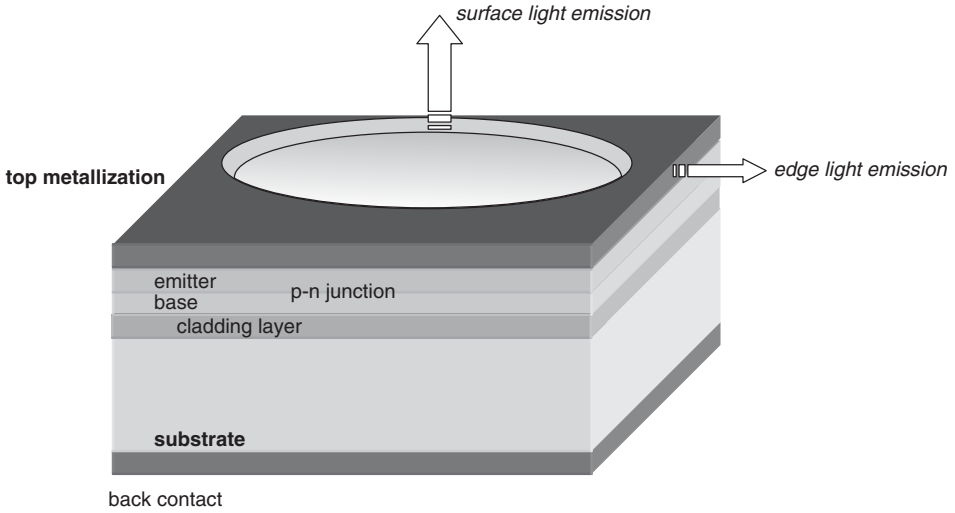


**Figure 13.1** Generic epitaxial LED structure comprising a *p-n* homojunction between the base and emitter layers (both of bandgap  $E_g$ ) or heterojunction (wherein the base layer has a bandgap of  $E_g$  and the emitter layer has a higher bandgap ( $E_g + \Delta E$ )). In both cases, light emission occurs mainly from recombination of minority carriers in the base. An optional wider bandgap cladding layer between the substrate and base can be included to confine injected minority carriers to the base layer and thus avoid losses associated with minority carrier recombination in the substrate. Depending on the details of the design, light exits primarily from the front surface or from the edges of the LED. Another LED design option comprises an undoped base layer sandwiched between wider bandgap emitter and cladding layers of opposite doping types

of the photons generated by recombination of minority carriers can be realized in *p-n* homojunction diodes formed in these materials, and thus practical room-temperature light emission with reasonable efficiencies can be achieved.

Common LED materials include the III-V compounds GaAs, InP, GaP, GaSb, InAs, AlAs, GaN, InN, AlN and their ternary and quaternary alloys; the II-VI semiconductors ZnSe, ZnS, and ZnTe and their alloys, and SiC. Virtually all of these materials can be grown by LPE. Some of the wide-bandgap II-VI semiconductors cannot be readily doped both *p*- and *n*-type, obviating a *p-n* homojunction and necessitating heterojunction designs. More generally, heterostructure LED designs with a *p-n* homojunction sandwiched between wide-bandgap cladding layers, or a *p-n* heterojunction between a wide-bandgap emitter and lower bandgap base, are often advantageous in reducing non-radiative recombination of minority carriers at surfaces, reducing self-absorption losses, and enhancing injection efficiency. Interest in the II-VI semiconductors and SiC originally stemmed from their use or potential use for blue-light-emitting LEDs. Due to the success of III-V nitrides, e.g. GaN and related alloys, for this application, work on these other wide-bandgap materials has greatly diminished. As a result of recent progress in the last decade, organic, polymer or nanostructured electroluminescent materials are displacing inorganic semiconductor LEDs in certain applications such as displays in cell phones, car dashboards, and other consumer electronics products. Nevertheless, it is likely that LEDs made in the familiar inorganic compound semiconductors will remain the dominant solid-state lighting technology for the foreseeable future due to their extensive technology

base and established manufacturing infrastructure, as well as their ruggedness, long operating lifetimes, and relatively high operating efficiencies. Moreover, even for mature LED technologies there is a realistic potential for continued improvements in performance and functionality, as well as further cost reductions. These attributes should be especially advantageous for outdoor lighting applications such as road signs, advertising, and streetlights, and in architectural lighting for homes, schools, offices and commercial buildings.

In conventional semiconductor LED technologies, quantum efficiencies—defined as the number of photons emitted per electron of applied current—can typically range from several per cent to over 20%. However, with excellent material quality and more sophisticated device designs, much higher quantum efficiencies (>50%) are feasible (Schnitzer *et al.*, 1993). Common applications of LEDs include indicator lights, displays, sources for optical fiber communication and infrared transmitters. As LED performance improves, LEDs are expected to challenge entrenched lighting technologies such as incandescents and fluorescents for indoor and outdoor lighting, as well as open up new applications in solid-state lighting, automotive displays, spectroscopy, medical devices, machine vision, artificial lighting for plants, and in industrial processing such as for curing adhesives. It is interesting to note that LEDs are probably the most ubiquitous discrete semiconductor device; yearly production is likely between 50 and 100 billion LED die or pixels, and increasing at about 20% annually.

Historically, LPE figured prominently in the development of LEDs. Starting from the early 1960s, many LED materials systems, such as gallium arsenide (GaAs), aluminum gallium arsenide ( $\text{Al}_x\text{Ga}_{1-x}\text{As}$ ), nitrogen-doped gallium phosphide (GaP:N), zinc- and oxygen-doped GaP (GaP:Zn,O), and other III-V compound semiconductors were first developed with LPE and many LED devices and design concepts were first demonstrated with LPE. LPE has provided some of the highest efficiency infrared and visible (red to green) LEDs, as well as photodiodes, solar cells and double heterostructure lasers. For several decades, LPE has served as the workhorse for production of LEDs used in a wide range of consumer and industrial products and military applications. Detailed descriptions of LPE technology applied to the manufacture of conventional LEDs are available (Bergh and Dean, 1976; Kressel and Butler, 1977; Williams and Hall, 1978; Gillissen, 1987). Loebner (Loebner, 1976) and Schubert (Schubert, 2006) have provided interesting histories of the LED and the role of LPE. More recent reviews of LEDs have appeared (Craford and Steranka, 1994; Žukauskas *et al.*, 2001, 2002; Gessman and Schubert 2004; Eisler *et al.*, 2005; Yam and Hassan, 2005).

For most of the III-V compound semiconductors, a strong case could be made that LPE-grown material provided superior performance with respect to luminescence efficiency and device performance. Further, there were numerous innovations in LPE growth techniques, such as multiple-substrate LPE boats, that enabled large-scale, economic production of epitaxial LED die. Nevertheless, the difficulty in scaling-up LPE processes for multilayer epitaxial device structures, both with respect to substrate diameter and number of substrates in a batch per epitaxy run, is a decided shortcoming of LPE, especially in comparison with chemical vapor deposition (CVD) processes. In the 1990s, a new chapter of LED technology was opened with the advent of high-brightness AlGaInP LEDs and III-V nitride LEDs. These materials systems were not conducive to LPE growth. For instance, aluminum segregation effects in indium-rich melts precluded the LPE growth of the AlGaInP alloys of interest for LEDs. Also, although LPE of GaN has been reported, metal-organic chemical vapor deposition (MOCVD) nevertheless has been the dominant

epitaxy technology for short-wavelength III-V nitride optoelectronics, including blue and UV LEDs. Thus, although LEDs are undergoing a renaissance for solid-state lighting, it is not entirely clear what the status and prospects of LPE are for LED technology. The situation has no doubt evolved somewhat from 1997 when Moon (Moon, 1997) observed that based on substrate usage, 60–70 % of optoelectronics was made by LPE, primarily for LEDs. At that time, according to Moon (Moon, 1997), LPE accounted for over 90 % of infrared LED production, over 40 % of laser diode manufacture, almost 80 % of visible LED production, and virtually all optocoupler production.

For several reasons, it can be argued that LEDs are the *ideal* device application for LPE. First, in general LPE produces material of high luminescence efficiency due to: (1) its near-equilibrium growth characteristics which yields material of low point defect density; (2) the favorable segregation of impurities to the liquid phase which reduces the background doping and residual impurities in the epilayer; and (3) the reduction of threading dislocations and other defects originating in the substrate. LPE is perhaps unique among epitaxy methods in that the crystallographic quality of the epitaxial layers is generally better than that of the substrate on which the epilayers are seeded. For Ga-containing III-V materials, LPE produces material with reduced arsenic antisites because, unlike MOCVD and molecular beam epitaxy (MBE), growth occurs under Ga-rich conditions which suppresses formation of Ga vacancies and As antisites (As atoms on the Ga sublattice). Arsenic antisites are implicated in the EL2 defect, a minority carrier recombination center that diminishes near-bandgap luminescence. Second, many LED device designs incorporate thick ( $\sim 10\ \mu\text{m}$ ) epitaxial layers which are feasible due to comparatively fast growth rates possible with LPE. LPE growth rates can be ten or more times faster than MOCVD or MBE. Third, LPE can still compete with other epitaxy methods on the basis of die cost. A square centimeter of epitaxial material yields sufficient die such that added cost of epilayer, whether by LPE or CVD, is consistent with total costs on the order of US\$ 0.10 per die. As a rough guide, about 10 % of final LED cost is due to substrate, and another 10 % is incurred by the epitaxy step. Consequently, there is no overriding cost consideration pointing to a single dominant epitaxy method to the exclusion of others for LED production. Thus, the choice of epitaxy method for a particular type of LED is better made on the basis of specific materials used, the device structure, and the required material quality. A strong case can be made for LPE for materials systems where LPE yields epitaxial layers with superior luminescence efficiency, or where very thick epitaxial layers are needed, such as for ‘transparent substrate’ designs that incorporate a thick ( $> 50\ \mu\text{m}$ ), self-supporting epitaxial layer. A secondary consideration in favor of LPE is its lack of highly toxic precursors or products, which lessens safety and environmental concerns. Finally, as a general rule many of the limitations associated with LPE technique with regard to layer thickness control, i.e. reproducibly achieving very thin layers with good doping control as needed for field effect transistors (FETs) and quantum well and superlattice devices, are not crucial issues for most types of LEDs. Therefore, the arguments made against LPE for production of solar cells, lasers and transistors are not pertinent for most LED applications. Nevertheless, as new materials and novel device concepts are developed for solid-state lighting, the role of LPE in future LED technology is not obvious. On the other hand, there are a host of LED structures that can be uniquely made by LPE, and which could establish niches for LPE technology if economic scale-up can be achieved. Finally, there is no reason an LED has to be made by only one type of epitaxy. For example, LPE could be utilized to grow thick substrates to achieve

transparency or a lattice constant not available with compound semiconductor wafers, as well as other specialized structures with favorable optical features. These LPE-grown epitaxial substrates and structures could then be used with MOCVD to grow the ‘active’ layers of the LED.

This chapter will review the status of LPE in LED production, its use in niche applications such as mid-infrared emitters, its prospects for competing with or contributing to wide-bandgap semiconductor LED technologies, and novel LED designs enabled by LPE. Some overlap with material covered in other chapters devoted to specific materials is inevitable, and LED applications and issues specific to LPE of LEDs are discussed rather than LPE processes themselves.

## 13.2 COMMERCIAL LEDs

LPE is still much used, and perhaps almost exclusively used, for the manufacture of several types of LEDs emitting in the infrared and red spectral regions. These include GaAs (940–950 nm), AlGaAs (650–660 nm), GaP:Zn-O (700 nm) and GaP:N (555–565 nm) LEDs. Nevertheless, nowadays there is little published in the way of research on these mature, mass-produced commodity devices. As mentioned, most of the commercial ultra-bright LEDs in AlGaInP (Vanderwater *et al.*, 1997; Streubel *et al.*, 2002), and the III-V nitrides (Nakamura *et al.*, 1991; Nakamura and Fasol, 1997), both of which have garnered considerable attention in the last decade, are made by MOCVD. The problems associated with high aluminum segregation in indium-rich melts encountered with LPE growth of AlGaInP have precluded broader application of LPE to the manufacture of AlGaInP LEDs. Takahashi *et al.* (Takahashi *et al.*, 1994) reported some progress in this area by growing AlGaInP on  $\text{Al}_{0.9}\text{Ga}_{0.1}\text{As}$  epitaxial layers instead of directly on GaAs substrates. This approach lessens the dissolution of the underlying layers on contact with the Al-Ga-In-P melt, and allowed the LPE growth of AlInGaP LEDs with an emission wavelength of 635–645 nm at room temperature operation. For LEDs with 650–660 nm wavelength emission, another good candidate materials system is based on InGaP ternary alloys lattice matched to GaAs substrates. Wu *et al.* (Wu *et al.*, 1991) developed LPE methods for  $\text{Al}_{0.7}\text{Ga}_{0.3}\text{As}/\text{In}_{0.5}\text{Ga}_{0.5}\text{P}/\text{GaAs}$  LEDs.

For conventional AlGaAs epitaxial LEDs grown on a GaAs substrate, there are considerable optical losses due to parasitic absorption in the GaAs substrate. To reduce substrate absorption losses, the epitaxial layers can be bonded to a superstrate and the substrate can be removed by controlled etching. Alternatively, Woodall *et al.* (Woodall *et al.*, 1972) used LPE to grow AlGaAs LEDs on undoped GaP substrates. In still another approach, these substrate absorption losses can be largely avoided by growing the AlGaAs LED structure on a thick  $\text{Al}_z\text{Ga}_{1-z}\text{As}$  ‘transparent’ substrate with a higher bandgap than the light-emitting  $\text{Al}_x\text{Ga}_{1-x}\text{As}$  layers, i.e.  $z > x$ . Such ternary alloy substrates are difficult to make by bulk crystal growth, and thus commercial substrate wafers are limited to elemental or binary compounds, e.g. Si, GaAs and GaP. A thick AlGaAs epitaxial layer can serve as a transparent substrate. For AlGaAs transparent substrate ultrabright LEDs, the epitaxial AlGaAs LED structure is formed on a thick ( $>50\ \mu\text{m}$ ) epilayer of  $\text{Al}_{0.5}\text{Ga}_{0.5}\text{As}$  grown on a GaAs substrate (Ishiguro *et al.*, 1983; Steranka *et al.*, 1988). The GaAs substrate is subsequently removed by etching, leaving a self-supporting AlGaAs LED structure which can be mounted in a package with a backside reflector to redirect photons

through the front surface of the LED. (In an AlGaAs LED made on a GaAs substrate, these photons are absorbed in the substrate.) Hsieh and Chang (Hsieh and Chang, 2003) investigated the use of LPE for forming thick current-spreading GaP window layers on MOCVD-grown AlGaInP double heterostructure LEDs. Adding indium to the Ga-P melt significantly enhanced the growth rate, permitting thick GaP window layers without perturbing the heterostructure doping profile. The inclusion of a GaP window approximately doubled the optical output power compared with an LED to no window layer.

### 13.3 LPE FOR WIDE-BANDGAP (BLUE AND UV) LEDs

There are three families of wide-bandgap semiconductors that are of main interest for short-wavelength (blue and UV) LEDs: (1) SiC; (2) the III-V nitrides including GaN, InN, AlN and their alloys; and (3) the II-VI compounds including ZnSe, ZnS, ZnTe and their alloys. LPE has been used to grow all of these materials with varying degrees of success. Commercial applications of LPE for these materials, and more specifically for LEDs made in these materials, are practically nil as blue LEDs made in the III-V nitrides grown by MOCVD have proved far superior to blue LEDs made in other materials. Nevertheless, a future role for other materials and epitaxy methods in blue LED technology should not be dismissed. For instance, LPE might find use for making high-quality, low-defect substrates for epitaxy of LEDs by other methods such as MOCVD. Some of the relevant LPE work is reviewed below.

#### 13.3.1 Silicon carbide LEDs

Liquid phase epitaxial growth of 6-H SiC on SiC substrates with molten silicon as the solvent has been used to grow *p-n* junction SiC blue LEDs (Suzuki *et al.*, 1976; von Munch and Kurzinger, 1978). For blue LEDs, Matsunami *et al.* (Matsunami *et al.*, 1977) described an LPE dipping technique with a silicon melt (with 2.5% aluminum as a *p*-type dopant) in the temperature range of 1500–1650 °C in an argon ambient. A 40 μm thick *p*-type SiC layer is first grown, and then 0.01 vol% nitrogen (an acceptor in SiC) is introduced into the ambient to compensate aluminum donors and dope the SiC *n*-type, thereby forming a *p-n* junction. For many years prior to the advent of the GaN LED and more efficient SiC blue LEDs made by physical vapor transport or CVD, LPE-grown SiC devices were perhaps the predominant blue LEDs. However, the performance was modest (quantum efficiencies of  $\sim 10^{-5}$ ), and demand for LPE-grown SiC LEDs was comparatively small relative to infrared, red, yellow and green LEDs made in the III-V semiconductors. LPE of SiC from molten silicon is difficult due to the high temperatures, the highly reactive nature of molten silicon, and the relatively slow growth rates. Other solvents for SiC LPE, such as Ga-Yb (Safaraliev *et al.*, 1984), Sn-Al-Ga, Ga-Al (Dmietriev, 1993), Sc (Yakimova *et al.*, 1995), Ga/Sn, Ni, Cu, and Zn-Al (Mauk *et al.*, 2001) and Al-Sn (Tanaka *et al.*, 2004), would permit lower growth temperatures (950–1200 °C) and/or higher growth rates. A more recent and specific application of LPE to SiC relates the reduction of micropipe defects in silicon carbide, which plague SiC material grown by physical vapor transport processes such as the modified Lely technique. Filip *et al.* (Filip *et al.*, 2004, 2005) described the LPE growth of SiC on 4-H SiC substrates from  $\text{Si}_x\text{Ge}_{1-x}$

( $x = 0.1, 0.2, 0.3$ ) melts at 1650 °C, saturated with carbon from the graphite crucible, with a growth rate of  $0.5 \mu\text{m h}^{-1}$ , yielding a micropipe reduction of about 80% in 10  $\mu\text{m}$  thick SiC epilayers. While this work is directed toward electronic power device applications that are sensitive to micropipes, the use of LPE to produce low-defect SiC epilayers could be of interest for SiC-based LEDs and SiC epitaxial substrates for GaN-based LEDs.

### 13.3.2 Wide-bandgap II-VI compound LEDs

ZnSe, and  $\text{ZnSe}_x\text{S}_{1-x}$  and  $\text{Zn}_{1-u-v}\text{Mg}_u\text{Be}_v\text{S}_x\text{Se}_{1-x}$  alloys, epitaxially grown on a ZnSe substrate, are also viable candidates for blue LEDs. There has been considerable effort devoted to these materials for blue LEDs and laser diodes, including a substantial amount of work using LPE (Ruda, 1992). The main limitations encountered with ZnSe and related alloys include the difficulty in doping them  $p$ -type, and the generation or accumulation of defects which degrade device performance and operating life, the latter of which is more crucial for lasers than LEDs due to the high current density employed with laser diodes. The notion that GaN technology has completely eliminated further consideration of ZnSe for blue LEDs, however, is not accurate. ZnSe-based blue LEDs have several potential advantages over GaN-based blue LEDs (*Compound Semiconductor*, 2002). First, a wider range of color temperatures (3500–8000 K for ZnSe versus 6000–8500 for GaN-based devices) provides ‘warm color lighting.’ Second, ZnSe conducting substrates permit front and back contacts, unlike GaN-on-sapphire devices where both contacts have to be made from the frontside. Third, the simultaneous bicolor (blue and yellow) emission possible with ZnSe LEDs can provide simpler approaches to white-light LEDs that otherwise require a yellow phosphor and more complicated packaging. Sumitomo Corporation is commercializing a ‘white’ ZnSe-based LED and reports operating lives of over 10 000 h (Nakamura, 2005).

For many years, it was considered practically impossible to dope ZnSe  $p$ -type for a number of fundamental reasons based on a combination of dopant solubility limits, native defect compensation, and doping self-compensation (Mandel, 1964; Dismukes, 1970; Laks and van de Walle, 1992, 1993; van de Walle *et al.*, 1992a,b, 1993, 1995; Chadi, 1994a,b). The numerous demonstrations of viable  $p$ - $n$  junction ZnSe LEDs shows that this conclusion was erroneous. Some of the early instances of practical  $p$ -type doping in ZnSe used nonequilibrium growth techniques, such as MOCVD and MBE, combined with nonequilibrium doping methods such as plasma nitrogen sources (Fan *et al.*, 1994). Thus, a relevant question is whether *near*-equilibrium growth process such as LPE could also produce  $p$ -type ZnSe material. More than a few reports indicate the affirmative. Bahrgava (Bahrgava, 1982) reviewed the liquid phase epitaxy of ZnSe and various efforts to incorporate acceptor impurities in ZnSe. Kosai *et al.* (Kosai *et al.*, 1979) reported the  $p$ -type doping of ZnSe by LPE using bismuth as a metallic solvent, yielding  $p$ -ZnSe epilayers with high resistivities ( $>10^5 \Omega \text{ cm}$ ) and low hole mobilities ( $<5 \text{ cm}^2 \text{ V}^{-1} \text{ s}^{-1}$ ), indicating a high level of compensation. Nishizawa *et al.* (Nishizawa *et al.*, 1992) showed that  $p$ -type ZnSe (with a net hole concentration up to  $3 \times 10^{17} \text{ cm}^{-3}$ ) could be grown at 950 °C from Se-rich melts with a 3 atm overpressure of zinc. Extending this process, Sakuri *et al.* (Sakuri *et al.*, 1997) described the LPE of  $p$ -type ZnSe using  $\text{Na}_2\text{S}$  or  $\text{LiN}_3$  as  $p$ -type dopants. Krasnov (Krasnov, 1995) reported the LPE growth of ZnSe using LiF as a dopant. With regard to doping studies, the wide selection of dopants available with LPE is an important advantage. Doping is also influenced by crystal stoichiometry ( $\text{Zn}_{1-\delta}\text{Se}$ ), and the

concentration of defects such as vacancies and antisites. In solution growth methods such as LPE, the solid-phase stoichiometry and concentration of point defects is determined in part by the relative chemical potentials in the liquid phase, e.g.  $\mu_{\text{Zn}}^{\text{L}}$  and  $\mu_{\text{Se}}^{\text{L}}$  in the case of ZnSe LPE and the overpressures of Zn and Se. The liquid phase chemical potentials of zinc and selenium can be adjusted by adding other components, e.g. bismuth, tin or gallium, to the melt. This provides some additional flexibility in controlling doping phenomena.

There are several other reports of LPE of ZnSe and related II-VI compounds of potential interest for LED applications. Rubinstein (Rubinstein, 1968) summarized the solubilities of some II-VI semiconductors (ZnS, ZnSe, ZnTe, CdS, CdSe, CdTe) in molten bismuth, cadmium, and tin. Fujita *et al.* (Fujita *et al.*, 1979) described the LPE growth of ZnSe-ZnTe heterojunctions. Fujita *et al.* (Fujita *et al.*, 1978) observed a ‘remarkable enhancement’ of blue luminescence in LPE ZnSe layers grown from Zn-Ga alloy melts which they attributed to a reduction in Zn vacancies. Nakamura and Aoki (Nakamura and Aoki, 1981) reported the growth of ‘highly luminescent’ layers of ZnS, ZnSe and ZnSe<sub>x</sub>S<sub>1-x</sub> alloys using tellurium as the metallic solvent. Heurtel *et al.* (Heurtel *et al.*, 1982) presented a thermodynamic calculation of the Zn-Se-Sn ternary phase diagram for the application of LPE to the special case of melt compositions with equal atomic fractions of Zn and Se. Fitzpatrick *et al.* (Fitzpatrick *et al.*, 1981) reported spectroscopic studies of background impurities in ZnSe grown by LPE. Werkhoeven *et al.* (Werkhoeven *et al.*, 1981) demonstrated high purity layers of ZnSe grown by LPE. Ido and Miyasato (Ido and Miyasato, 1982) described a temperature-difference technique for the growth of ZnSe from Ga solutions.

### 13.3.3 III-V nitride LEDs

GaN and related III-V nitrides are the pre-eminent material technology for blue LEDs. The application of LPE to GaN is challenging due to the high vapor pressure of nitrogen and its low solubility in molten Ga (Thurmond and Logan, 1972), although this could be ameliorated by using other solvents such as molten sodium that permit lower growth temperatures (Yamane *et al.*, 1998). GaN LPE is the subject of Chapter 7, so the discussion here is limited to a few potential LED applications. For instance, LPE might be employed for growth of low-defect layers, lateral overgrowth over patterned, masked substrates (see below) for buried mirror structures and defect filtering, for selective meltback of GaN layers (Novikov *et al.*, 1997), or for faceted growth to improve optical coupling as discussed in Section 13.5.

## 13.4 LPE FOR MID-INFRARED LEDs

This mid-infrared spectral range (2–6  $\mu\text{m}$  wavelength) is well served by LEDs and detectors made in LPE-grown III-V antimonides: InGaAsSb and InAsSbP, and their related alloys. The main application is molecular spectroscopy and gas sensing. It is relatively straightforward to modify melt compositions to grow semiconductors with bandgaps ranging from 0.25 to 0.6 eV, although miscibility gaps and lattice matching constraints limit the available bandgaps of some these materials systems. As LPE of these low-bandgap III-Vs are covered in more depth in companion chapters, a discussion of relevant LPE technology will be limited to a few representative LED applications, and in particular, to some

of the more prominent examples of LPE-grown mid-infrared LEDs that serve to underscore some of the achievements realized with LPE in this area. More extensive reviews of mid-infrared LEDs and their fabrication by LPE are given by Krier (Krier, 2001). As Krier (Krier, 2001) notes, there is a very extensive Russian literature on mid-infrared LEDs featuring efforts by the Ioffe Institute and other Russian and Eastern European workers. Fisher and Krier (Fisher and Krier, 1997) compared the photoluminescence efficiency of InAs grown by melt growth (i.e. bulk crystallization of InAs wafers), MOCVD and LPE, and found that LPE produced the material with highest luminescence efficiency. There does not appear to be any follow-up studies or more-recent systematic comparisons of different epitaxy methods and their utility for producing mid-infrared materials with high luminescence efficiency. However, a case can be made that LPE-grown material is superior in this respect due to the combination of low-point defect densities and low background doping, both of which are associated with mid-gap recombination centers that reduce near-bandgap luminescence. Low point defect densities result from near-equilibrium growth conditions, and possibly also from growth under group III-rich (i.e. Ga- or In-rich) conditions, as opposed to the group V-rich conditions encountered in MBE or MOCVD growth. With regard to impurities, in addition to the favorable impurity gettering inherent in growth from the liquid phase at low temperatures, rare-earth gettering can be employed in LPE to further reduce the background impurities or residual doping of LPE material (Gao *et al.*, 1999; Krier and Sherstnev, 2003). Still, the performance of mid-infrared emitters may be limited by nonradiative Auger recombination that competes with the near-band radiative recombination paths for injected minority carriers. Krier (Krier, 2001) notes two general approaches to improving the performance of mid-infrared LEDs: (1) rare-earth gettering to reduce residual impurities, as exploited exclusively in LPE; and (2) suppression of Auger recombination with type-II interface quantum well structures. The second expedient is difficult to realize with LPE. On the other hand, MBE and MOCVD have been used to make strained layer superlattices InAsSb and InAsP mid-infrared LEDs (Grietens *et al.*, 1997; Allerman *et al.*, 1998). The development of an LPE-based technique that could make device designs, e.g. quantum well, superlattice, or strained layer structures, that suppressed Auger recombination effects could lead to a significant improvement in mid-infrared LEDs.

Some other work in this area is worth noting. Gong *et al.* (Gong *et al.*, 2000) described InAs/InAs<sub>x</sub>P<sub>1-x-y</sub>Sb<sub>y</sub>/InAs<sub>x</sub>P<sub>1-x-y</sub>Sb<sub>y</sub> and InAs/InAs<sub>1-x</sub>Sb<sub>x</sub> compositionally graded layer multilayer LEDs made by LPE. At 300 K operation, an output power of 10 μW with peak emission of 4.8 μm was achieved. Gong *et al.* (Gong *et al.*, 2002) reported n<sup>+</sup>Ga<sub>0.1</sub>In<sub>0.9</sub>Sb/n-InSb/p<sup>+</sup>Ga<sub>0.1</sub>In<sub>0.9</sub>Sb heterostructure LEDs grown by LPE at growth temperatures between 350 °C and 360 °C. The LEDs exhibited a peak wavelength of 5.3 μm, and with drive currents of 300 mA, 200 μW of optical power was measured at an operating temperature of 77 K. These LEDs have potential applications for NO gas sensors. Moiseev *et al.* (Moiseev *et al.*, 2004) reported room-temperature photoluminescence of Ga<sub>0.96</sub>In<sub>0.04</sub>As<sub>0.11</sub>Sb<sub>0.89</sub> LPE-grown layers lattice-matched to InAs. Astakhova *et al.* (Astakhova *et al.*, 2004) made LEDs in GaInAsSb alloys grown from melts containing lead (Ga-In-As-Sb-Pb), which widens the range of compositions and growth temperatures compared with growth of GaInAsSb from Ga-In-As-Sb melts. External photon yields at room temperature were 1.6 % and 0.11 % for LEDs with emission wavelengths of 2.3 and 2.44 μm, respectively. Matveev *et al.* (Matveev *et al.*, 2002) discussed the operation of LPE-grown graded-bandgap InAsSbP LEDs,



including positive luminescence (forward-bias) and negative luminescence (reverse-bias) operation. Bonded LEDs made from this material operated at 20–85 °C with emission wavelengths ranging from 5 to 6  $\mu\text{m}$ .

### 13.5 LPE FOR NEW LED DESIGN CONCEPTS

The total efficiency  $\eta_{\text{total}}$  of an LED is the product of several efficiencies:

$$\eta_{\text{total}} = \eta_{\text{inj}} \cdot \eta_{\text{rad}} \cdot \eta_{\text{ext}}$$

where  $\eta_{\text{inj}}$  is the injection efficiency, the fraction of total current due to the injection of minority carriers into the luminescent ‘active’ region of the device. Less than perfect injection efficiency is due to perimeter or leakage currents or injection of minority carriers into the wide-bandgap emitter or cladding layers. The radiative efficiency,  $\eta_{\text{rad}}$ , is the fraction of injected minority carriers that recombine radiatively to generate a photon with near-bandgap energy. Losses in radiative efficiency are due to nonradiative minority carrier recombination at surfaces, defects, or otherwise due to mid-bandgap energy levels. The extraction efficiency,  $\eta_{\text{ext}}$ , represents the fraction of generated photons that are usefully coupled out of the device and contribute to the external luminescent emission. Losses in coupling efficiency are due to parasitic optical absorption in the substrate or metal contacts, or light escaping from surfaces or edges of the device that cannot be efficiently utilized for the particular application, such as sourcing an optical fiber or illuminating a display. Coupling efficiency losses are exacerbated by the multiple internal reflections due to the isotropic nature of radiative emission such that most emitted photons will be incident upon surfaces at angles exceeding the critical angle for total internal reflection.

For well-developed semiconductor materials, such as GaAs, AlGaAs and InGaP, the injection and radiative efficiencies can be very high, especially in heterostructures where the luminescent (base) layer is sandwiched between wide-bandgap emitter or cladding layers. Thus, there is little room for their further improvement with respect to injection and radiative efficiencies. The extraction or coupling efficiency, however, is relatively low ( $\sim 10\%$ ) in the rectangular LED die geometries such as shown in the Figure 13.1. It has been recognized for some time that shaped, sculpted or faceted LEDs could provide much improved extraction efficiencies. Conventionally, these shapes are produced from planar epitaxial structures using a combination of mechanical polishing and shaping, masking, photolithography, and selective etching. These processing steps are generally not cost-effective for most types of LEDs. On the other hand, the near-equilibrium growth conditions of LPE that facilitate selective epitaxy, selective meltback and regrowth, and epitaxial lateral overgrowth (ELO) on patterned, masked substrates, as well as conformal and faceted growth, can provide LED device geometries with high optical coupling efficiencies. Device structures with performance-enhancing optical features are achieved as a consequence of the growth phenomena characteristic of LPE, rather than through elaborate post-growth patterning, masking and etching. This could considerably lower fabrication costs, thus permitting the utilization of these features in inexpensive LED devices.

The following examples of LED and other optoelectronic devices produced by LPE will serve to illustrate the various device structures that can be achieved by selective LPE on masked substrates. Figure 13.2(a) shows selectively grown AlGaAs LED made

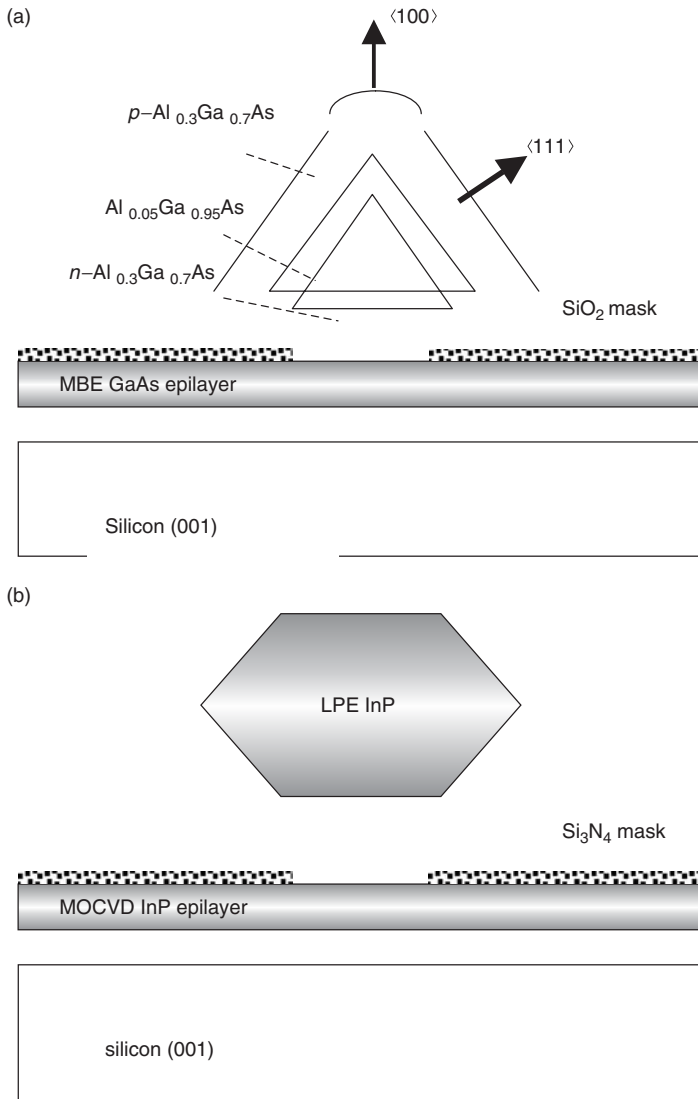


**Figure 13.2** Faceted structures made by LPE on masked substrates with mask opening for selective seeding. (a) Selective AlGaAs LEDs grown by LPE on stripe-patterned, oxide masked, MBE-grown GaAs-on-silicon epilayer. (After Sakai *et al.*, 1988). (b) Selective LPE of InP faceted crystals on masked, MOCVD-grown InP-on-silicon epilayer. (After Schnabel *et al.*, 1995)

by LPE on an oxide-masked GaAs-on-silicon epilayer grown by MBE. The mask is patterned with  $6\ \mu\text{m}$  wide stripe openings yielding an LED structure that can lead to higher extraction of light. Figure 13.2(b) shows a similar approach, but selectively grown InP on a stripe-patterned, nitride-masked InP-on-silicon layer made by MOCVD. The differences in morphology and facetting between Figure 13.2(a) and (b) are likely due to a combination of differences in growth temperature, melt supersaturation, substrate misorientation, effects of lattice mismatch (4% for GaAs on silicon, 9% for InP on

silicon), wetting properties of the mask layer for their respective melts, and differences in growth rate. Actually, the main objective of such approaches is to reduce the effects of lattice mismatch and thermal expansion mismatch on quality of the AlGaAs or InP material. These selective LPE processes for AlGaAs-on-silicon and InP-on-silicon are remarkably effective at producing optoelectronic device structures with high material quality, despite the high degree of lattice mismatch and thermal expansion mismatch (see Chapter 12). The unique faceted cross-sections, and their potential for improving the external coupling efficiencies of LEDs, are in some respects a gratuitous feature of these processes.

Along similar lines, although not developed for LEDs per se, selective LPE on masked substrates with circular trenched openings yields pyramidal structures, as shown in Figure 13.3. This particular selective LPE with trenched seeding regions produced ‘hollow’ pyramids thus demonstrating some of the truly unique structures possible with LPE. Solid pyramids (Trah, 1990), flat hexagons (Cotter *et al.*, 1992), and other highly faceted shapes (Zhang *et al.*, 2005) have been produced by selective LPE on patterned, masked substrates (with no trenching of the seeding region defined by openings in the mask coating the substrate).

Semiconductor structures with curved surfaces approximating conventional lenses can be made by LPE meltback and regrowth processes. Surface-emitting AlGaAs/GaAs LEDs with a buried window cylindrical lens (Figure 13.4) using a one-step LPE method were reported by Yoo *et al.* (Yoo *et al.*, 1988). The same group (Hahm *et al.*, 1991) developed a hemispheric AlGaAs microlens LED [Figure 13.5(a)] using a similar LPE meltback and regrowth technique, which showed significantly enhanced optical output with respect to similar LEDs with planar surfaces [Figure 13.5(b)].

ELO can be utilized to make LED structures with ‘buried mirrors’ to enhance performance. Mauk *et al.* (Mauk *et al.*, 1997) used LPE to grow AlGaAs double heterostructures over stripe-patterned, masked GaAs substrates such that a substantial part of the LED was formed over the reflective mask layer coating the substrate (Figure 13.6). Mask layers studied included oxides, nitrides, refractory metals, and multilayer stacks of e-beam deposited SiO<sub>2</sub> and polysilicon to form Bragg reflectors. A more than three-fold improvement in optical output could be attributed to the inclusion of the reflective mask between the substrate and epitaxial LED structure that functioned as a buried mirror to increase the external efficiency of the LED. As such, ELO can be developed for almost any semiconductor material that can be grown by LPE, and this approach should be widely applicable to many types of LEDs.

## 13.6 OUTLOOK

The future role of LPE in LED technology may be limited on account of the preference for MOCVD to make AlInGaP and III-V nitride materials for ultrabright, blue, and white LEDs. LPE could provide a supporting role for low-defect epitaxial substrates used for MOCVD growth of LED structures. More speculatively, commercial applications of the shaped LED structures that incorporate buried mirrors, faceted surfaces, or lens like structures, readily produced by selective LPE and selective meltback, could provide a versatile platform for LPE technology.

Mid-infrared LEDs made in the low-bandgap III-V antimonides could provide another niche market for LPE. It should be a simpler task to extend existing LPE technology

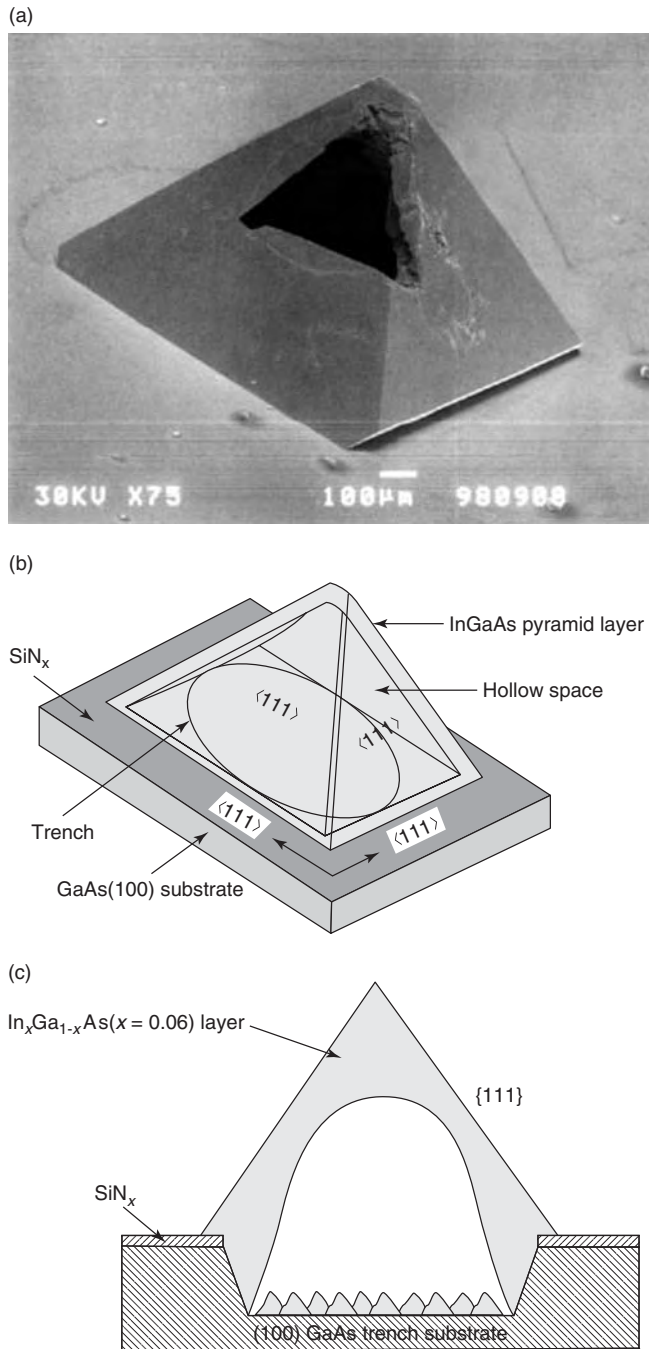


**Figure 13.3** Hollow pyramid structures produced by selective LPE in trrenched openings of a masked substrate (a) Photograph; (b) crystallographic planes; and (c) section indicating hollow interior. Reprinted from *Semiconduct. Sci. Technol.*, **17**, K. Balakrishnan *et al.*, 729, Copyright (2002), with permission from IOP publishing Ltd

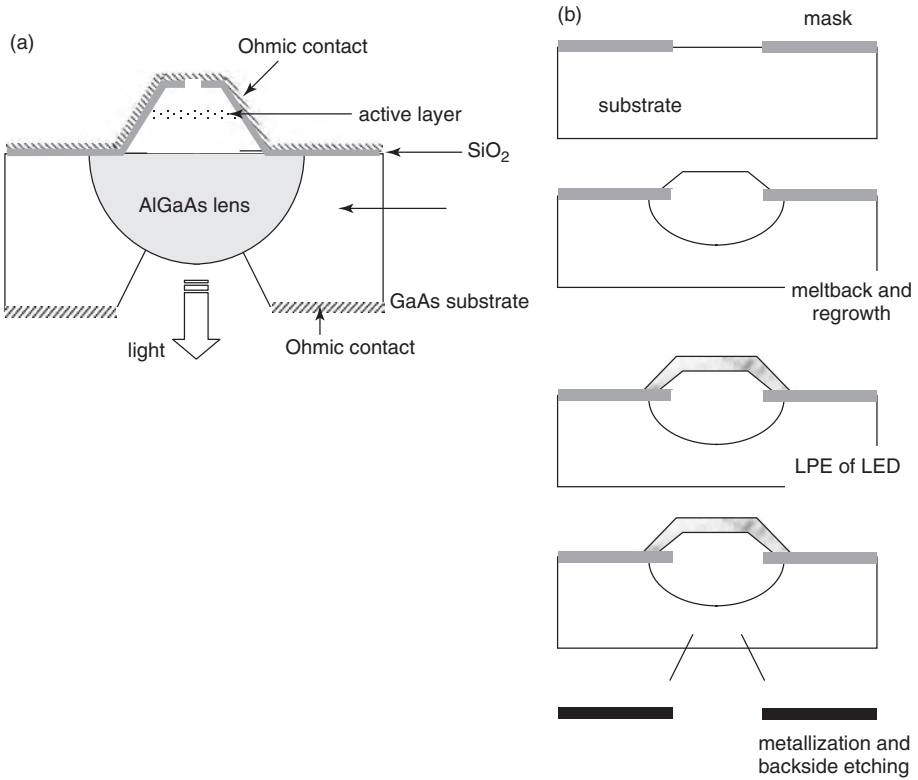


**Figure 13.4** (a) Surface-emitting AlGaAs/GaAs LED with buried-window cylindrical lens made by a one-step LPE process. (b) Fabrication process. Meltback, regrowth, and epitaxial growth of LED structure is performed in a single LPE process. (After Yoo *et al.*, 1988)

for the growth of novel quaternary and higher-component number alloys, than to develop MOCVD or MBE processes for these small-volume speciality applications. Further, it is plausible that superior material quality, especially with rare-earth gettering techniques, can be realized with LPE. The main limitation is that more sophisticated LED structures incorporating quantum wells, strained layers and superlattices cannot be easily made by LPE. These features may be crucial for reducing Auger recombination losses in some applications.

The economics of LPE for commercial LED production are favorable, more so than probably for any other device application. One LED equipment manufacturer offers a dipping-type LPE system designed for a three-layer epitaxial structure that can process one hundred 100 mm diameter substrate wafers per day. This would produce 7800 cm<sup>2</sup> of LED material per day, and assuming about 1 mm<sup>2</sup> of substrate is consumed for each LED die, daily production from one such LPE system would be roughly 780 000 LEDs. A rule of thumb allots about 10% of LED cost for epitaxy. For a manufacturing cost of US\$ 0.10 per LED die, this appears to provide sufficient rationale for such an LPE system with respect to capital investment and depreciation, operating costs (electrical consumption, maintenance, direct labor and overhead), and consumables (melt materials, hydrogen).

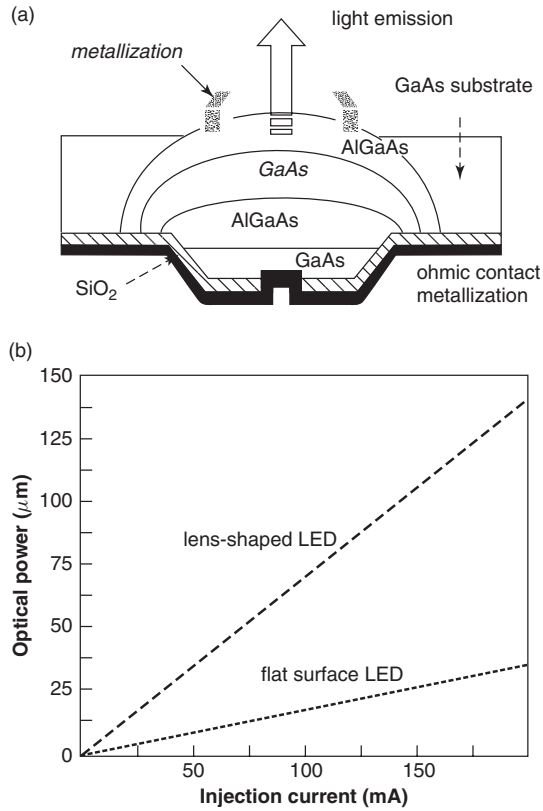


**Figure 13.5** (a) Cross-section of hemispherical microlens LED made by LPE meltback and regrowth. (b) Optical power comparison of microlens LED with conventional LED. (After Hahm *et al.*, 1991)

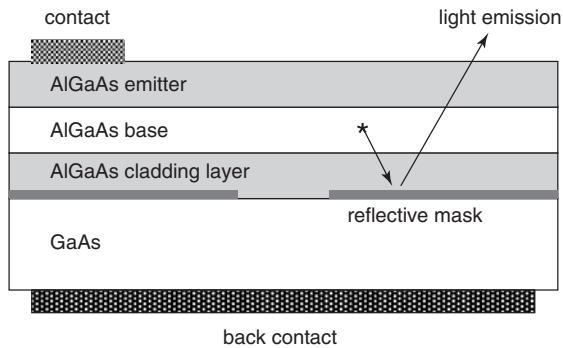


**Figure 13.6** AlGaAs double heterostructure formed by liquid-phase ELO on a substrate masked with a reflective coating. The coating is patterned with  $10\ \mu\text{m}$  wide stripe openings. Lateral overgrowth up to  $400\text{--}500\ \mu\text{m}$  in width can be achieved. The reflective coating between the GaAs substrate and AlGaAs device structure functions as a buried mirror, which prevents parasitic optical absorption of luminescence in the substrate, resulting in a higher optical output. (From Mauk *et al.*, 1997)

## REFERENCES

- A.A. Allerman, S.R. Kurtz, R.M. Biefeld, K.C. Baucom and J.H. Burkhart (1998) Development of InAsSb-based light emitting diodes for chemical sensing systems. *Proc. SPIE* **3279**, 126–133.
- A.P. Astakhova, E.A. Grebenshchikova, É.V. Ivanov, A.N. Imenkov, E.V. Kunitsyna, Ya.A. Parkhomenko and Yu.P. Yakovlev (2004) Infrared light-emitting diodes based on GaInAsSb solid solutions grown from lead-containing solution melts. *Semiconductors* **38**, 1419–1424.
- R.N. Bahrgava (1982) The role of impurities in refined ZnSe and other II-VI compounds. *J. Cryst. Growth* **59**, 15–26.
- K. Balakrishnan, S. Iida, M. Kumagawa and Y. Hayakawa (2002) Study of the formation mechanism of InGaAs pyramidal layers on GaAs(100) patterned substrates by LPE. *Semiconduct. Sci. Technol.* **17**, 729–734.
- A.A. Bergh and P.J. Dean (1976) *Light-emitting Diodes*. Clarendon Press, Oxford.
- (not attributed) *Compound Semiconductor* magazine (2002) Joint venture will produce ZnSe white LEDs. December.
- D.J. Chadi (1994a) Doping in ZnSe, ZnTe, MgSe, and MgTe wide-band-gap semiconductors. *Phys. Rev. Lett.* **72**, 534–537.
- D.J. Chadi (1994b) Acceptor and donor states of impurities in wide bandgap II-VI semiconductors. *J. Cryst. Growth* **138**, 295–300.
- J.E. Cotter, M.G. Mauk, L.D. Garrett, J.B. Berryhill, K.D. Hobart and A.M. Barnett (1992) Monolithic integration of AlGaAs/GaAs surface-emitting LEDs with silicon- or GaAs-based bipolar transistor driver circuits. *Proc. SPIE* **1582**, 71–82.
- M.G. Craford and F.M. Steranka (1994) Light-emitting Diodes, in *Encyclopedia of Physics*, Vol. 8, G. Trigg, ed. VCH Publishers, New York, Ch. 8.
- J.P. Dismukes, W.M. Yim, J.J. Tietjen and R.E. Novak (1970) Vapor deposition of semiconducting mononitrides of scandium, yttrium, and rare-earth elements. *RCA Rev.* **31**, 680–691.
- V.A. Dmietriev (1993) Silicon carbide and SiC–AlN solid-solution p-n structures grown by liquid-phase epitaxy. *Physica B* **185**, 440–452.
- D. Eisler, S. Illek and G. Bogner (2005) LED technology trends in *GaAs MANTech 2005: The International Conference on Compound Semiconductor Manufacturing Technology*. GaAs Mantech, St Louis MO, paper 6.1.
- Y. Fan, J. Han, L. He, R.L. Gunshor, M.S. Brandt, J. Walker, N.M. Johnson, and A. V. Nurmikko (1994) Observations on the limits to p-type doping in ZnSe. *Appl. Phys. Lett.* **65**, 1001–1003.
- O. Filip, B. Epelbaum, M. Bickermann and A. Winnacker (2004) Micropipe healing in SiC wafers by liquid-phase epitaxy in Si-Ge melts. *J. Cryst. Growth* **271**, 142–150.
- O. Filip, B. Epelbaum, M. Bickermann and A. Winnacker (2005) LPE of silicon carbide using diluted Si-Ge fluxes. *Mater. Sci. Forum* **483–485**, 133–136.
- M. Fisher and A. Krier (1997). Photoluminescence of epitaxial InAs produced by different growth methods. *Infrared Phys. Technol.* **38**, 405–413.
- B.J. Fitzpatrick, C.J. Werkhoeven, T.F. McGee, P.M. Harnack, S.P. Herko, R.N. Barghava and P.J. Dean (1981) Spectroscopic studies of ZnSe grown by liquid phase epitaxy. *IEEE Trans. Electron Devices* **ED-28**, 440–444.
- S. Fujita, H. Mimoto and T. Noguchi (1978) Liquid phase epitaxy of ZnSe from Zn-Ga solutions. *J. Cryst. Growth* **45**, 281–286.
- H.H. Gao, A. Krier and V.V. Shertsnev (1999) High quality InAs grown by liquid phase epitaxy using gadolinium gettering. *Semiconduct. Sci. Technol.* **14**, 441–445.
- Th. Gessmann and E.F. Schubert (2004) High efficiency AlGaInP light-emitting diodes for solid-state lighting applications. *J. Appl. Phys.* **95**, 2203–2216.
- K. Gillessen (1987) *Light-emitting Diodes: an Introduction*. Prentice Hall, Englewood Cliffs, NJ.
- X.Y. Gong, H. Kan, T. Makino, K. Watanabe, T. Iida, H. Suzuki, M. Aoyama, and T. Yamaguchi (2000) Light-emitting diodes fabricated from liquid phase epitaxial InAs/InAs<sub>x</sub>P<sub>1-x-y</sub>Sb<sub>y</sub>/InAs<sub>x</sub>P<sub>1-x-y</sub>Sb<sub>y</sub> and InAs/InAs<sub>1-x</sub>Sb<sub>x</sub> multi-layers. *Cryst. Res. Technol.* **35**, 549–555.

- X.Y. Gong, H. Kan, T. Makino, T. Iida, M. Aoyama, Y.Z. Gao and T. Yamaguchi (2002) Light-emitting diodes with a peak wavelength of 5.38  $\mu\text{m}$  from liquid-phase epitaxial  $\text{Ga}_{0.1}\text{In}_{0.9}\text{Sb}/\text{InSb}$  heterostructures. *Jpn. J. Appl. Phys. Part 1*, **41**, 3669–3670.
- B. Grietens, S. Nemeth, C. Van Hoof, P. Van Daele and G. Borghs (1997) Growth and characterization of mid-IR  $\text{InAs}_{0.9}\text{Sb}_{0.1}$ -InAs strained multiple quantum well light emitting diodes grown on InAs substrates. *LEE Proc. Optoelectron.* **144**, 295–298.
- S.-H. Hahm, G.-S. Cho and Y.-S. Kwon (1991) GaAs/AlGaAs lensed light emitting diode by the meltback and regrowth in liquid phase epitaxy. *Jpn. J. Appl. Phys. Part 2*, **30**, L910–L913.
- A. Heurtel, A. Marbeuf, H. Tews and Y. Marfaing (1982) Liquid phase epitaxy of ZnSe in Sn: calculation of the ternary phase diagram and electronic properties. *J. Cryst. Growth* **59**, 167–171.
- L.-Z. Hisieh and L.-Y. Chang (2003) The comparisons between GaP window layers of double-heterojunction light-emitting diodes using various dopants and source melts regrown by indium addition liquid phase epitaxy. *Jpn. J. Appl. Phys. Part 1* **42**, 5709–5713.
- T. Ido and K. Miyasato (1982) Liquid phase epitaxy of ZnSe by temperature difference method. *J. Cryst. Growth* **59**, 178–182.
- H. Ishiguro, K. Sawa, S. Nagao, H. Yamanaka and S. Koike (1983) High efficiency GaAlAs light-emitting diodes of 660 nm with a double heterostructure on a GaAlAs substrate. *Appl. Phys. Lett.* **43**, 1034–1036.
- K. Kosai, B.J. Fitzpatrick, H.G. Grimmeiss, R.N. Bhargava and G.F. Neumark (1979) Shallow acceptors and *p*-type ZnSe. *Appl. Phys. Lett.* **36**, 194–196.
- A.N. Krasnov (1995) Preparation of *p*-type ZnSe layers. *J. Cryst. Growth* **148**, 432.
- H. Kressel and J.K. Butler (1977) *Semiconductor Lasers and Heterojunction LEDs*. Academic Press, New York.
- A. Krier (2001) Physics and technology of mid-infrared light emitting diodes *Phil. Trans. R. Soc. London A* **359**, 599–619.
- A. Krier and V.V. Shertsnev (2003) The influence of melt purification and structure defects on mid-infrared light emitting diodes. *J. Phys. D Appl. Phys.* **36**, 1484–1488.
- D.B. Laks and C.G. Van De Walle (1992) Self-compensation and doping problems in ZnSe *Wide Band Gap Semiconductor Symposium*. (Materials Research Society, Pittsburgh, PA, 311–321.
- D.B. Laks and C.G. Van De Walle (1993) Doping limits in ZnSe. *Physica B* **185**, 118–127.
- E.E. Loebner (1976) Subhistories of the light emitting diode. *IEEE Trans. Electron Devices* **ED-23**, 675–699.
- G. Mandel (1964) Self compensation limited conductivity in binary semiconductors. L. Theory. *Phys. Rev.* **134**, A1073–A1079.
- H. Matsunami, M. Ikeda, A. Suzuki and T. Tanaka (1977) SiC blue LEDs by liquid-phase epitaxy. *IEEE Trans. Electron Devices* **ED-24**, 958–961.
- B.A. Matveev, N.V. Zotova, S.A. Karandashev, M.A. Remennyi, N.M. Stus, and G.N. Talalakin (2002) Towards longwave (5–6  $\mu\text{m}$ ) LED operation at 80 °C: injection or extraction. *IEE Proc. Optoelectron.* **149**, 33–35.
- M.G. Mauk, P.A. Burch, S.W. Johnson, Z.A. Shellenbarger, J.B. McNeely, T.A. Goodwin and B.W. Feyock (1997) Resonant cavity LEDs by Lateral epitaxy. *Proc. Spie* **3002**, 59–65.
- M.G. Mauk, B.W. Feyock, A. Sharma and R.G. Hunsperger (2001) Experimental assessment of metal solvents for liquid-phase epitaxy of silicon carbide. *J. Cryst. Growth* **225**, 322–329.
- K.D. Moiseev, A. Krier and Y.P. Yakovelev (2004) Room-temperature photoluminescence of  $\text{Ga}_{0.96}\text{In}_{0.04}\text{As}_{0.11}\text{Sb}_{0.89}$  lattice matched to InAs. *J. Electron. Mater.* **33**, 867–872.
- R.L. Moon (1997) MOVPE: is there any other technology for optoelectronics? *J. Cryst. Growth* **170**, 1–10.
- H. Nakamura and M. Aoki (1981) Liquid phase epitaxial growth of ZnS ZnSe and their mixed compounds using Te as a solvent. *Jpn. J. Appl. Phys.* **20**, 11–16.
- S. Nakamura, T. Mukai and M. Senoh (1991) High power GaN p-n junction blue light-emitting diodes. *Jpn. J. Appl. Phys. Part 2* **30**, L1998–L2001.



- S. Nakamura and G. Fasol (1997) *The Blue Laser Diode: GaN Based Light Emitters and Lasers*. Springer, New York.
- T. Nakamura (2005) Development of ZnSe-based white LEDs with longer lifetimes over 10,000 hrs. *Trans. Inst. Electr. Eng. Jpn, Part C* **125**, 195–199. (in Japanese).
- J.I. Nishizawa, K. Suto and Y. Oyama (1992) Stoichiometry control of compound semiconductors. *Mater. Res. Soc. Symp.* **242**, 179–190.
- S.V. Novikov, T.S. Cheng, Z. Mahmood, L. Harrison and C.T. Foxon (1997) Selective meltback etching of GaN layers in liquid-phase electroepitaxial technique. *J. Cryst. Growth* **173**, 1–4.
- M. Rubinstein (1968) Solution growth of some II-VI compounds using tin as a solvent. *J. Cryst. Growth* **3**, 309–312.
- H.E. Ruda, ed. (1992) *Widegap II-V Compounds for Opto-electronic Applications*. Chapman & Hall, New York.
- G.K. Safaraliev, B.A. Bilalov and A.Z. Efendiev (1984) Current-induced crystallization of silicon carbide from a liquid phase. *Sov. Phys. Tech. Phys.* **29**, 1181–1183.
- S. Sakai, S.S. Chang, R.J. Matyi and H. Shichijo (1988) Growth and characterization of LPE GaAs on GaAs-coated Si prepared by MBE. *Mater. Res. Soc. Symp.* **116**, 155–160.
- F. Sakuri, M. Motozawa, K. Suto and J.-I. Nishizawa (1997) Liquid phase epitaxial p-type ZnSe growth from a Se solution and fabricated pn junctions with diffused n-type layers. *J. Cryst. Growth* **172**, 75–82.
- R.F. Schnabel, M. Grundmann, R. Engelhardt, J. Oertel, A. Krost, D. Bimberg, R. Optitz, M. Schmidbauer and R. Köhler (1995) High quantum efficiency InP mesas grown by hybrid epitaxy on silicon substrates. *J. Cryst. Growth* **156**, 337–342.
- I. Schnitzer, E. Yablonoitch, C. Caneau and T.J. Gmitter (1993) Ultrahigh spontaneous emission quantum efficiency, 99.7% internally and 72% externally, from AlGaAs/GaAs/AlGaAs heterostructures. *Appl. Phys. Lett.* **62**, 131–133.
- E.F. Schubert 2006 *Light-emitting Diodes*, 2nd edn. Cambridge University Press, Cambridge.
- F.M. Steranka, D.C. DeFevre, M.D. Camras, C.-W. Tu, D.K. McElfresh, S.L. Rudaz, L.W. Cook and W.L. Synder (1988) Red AlGaAs light-emitting diodes. *Hewlett-Packard J.* **October**, 84–88.
- K. Streubel, N. Linder, R. Wirth and A. Jaeger (2002) High brightness AlGaInP light-emitting diodes. *IEEE J. Quantum Electron.* **8**, 321–332.
- A. Suzuki, M. Ikeda, N. Nagao, H. Matsunami and T. Tanaka (1976) Liquid phase epitaxial growth of 6H-SiC by the dipping technique for preparation of blue-light-emitting diodes. *J. Appl. Phys.* **47**, 4546–4550.
- N.S. Takahashi, S. Fujiwara, K. Kohno, E. Shibano and S. Kurita (1994) AlGaInP/AlGaAs double heterostructure light emitting diode grown by liquid phase epitaxy. *J. Cryst. Growth* **137**, 240–244.
- A. Tanaka, T. Ataka, E. Ohkura and H. Katsuno (2004) Growth modes of silicon carbide in low-temperature liquid phase epitaxy. *Jpn. J. Appl. Phys.* **43**, 7670–7671.
- C.D. Thurmond and R.A. Logan (1972) The equilibrium pressure of N<sub>2</sub> over GaN. *J. Electrochem. Soc.* **119**, 622–626.
- H.-P. Trah (1990) Liquid phase epitaxy in the ternary system Si-Ge-Bi. *J. Cryst. Growth* **102**, 175–182.
- C.G. van de Walle, D.B. Laks, G.F. Neumark and S.T. Pantiledes (1992a) Solubilities, defect reactions and doping limits in ZnSe. *J. Cryst. Growth* **117**, 704–709.
- G.C. van de Walle and D.B. Laks (1992b) Theory of defects, impurities, and doping in ZnSe. *J. Lumin.* **52**, 1–8.
- G.C. van de Walle, D.B. Laks, G.F. Neumark and S.T. Pantiledes (1993) First principle calculations of solubilities and doping limits: Li, Na, and N in ZnSe. *Phys. Rev. B: Condens. Matter* **47**, 9425–9435.
- G.C. van de Walle and D.B. Laks (1995) Nitrogen doping in ZnSe and ZnTe. *Solid State Commun.* **93**, 447–450.

- D.A. Vanderwater, I.-H. Tan, G.E. Höfler, D.C. Defever and F.A. Kish (1997) High-brightness AlGaInP light emitting diodes. *Proc. IEEE* **85**, 1752–1764.
- W. von Munch and W. Kurzinger (1978) Silicon carbide blue-emitting diodes produced by liquid-phase epitaxy. *Solid State Electron.* **21**, 1129–1132.
- C. Werkhoven, B.J. Fitzpatrick, S.P. Herko, R.N. Bhargava and P.J. Dean (1981) High purity ZnSe grown by liquid phase epitaxy. *Appl. Phys. Lett.* **38**, 540–542.
- E.W. Williams and R. Hall (1978) *Luminescence and the Light-emitting Diode*. Pergamon Press, Oxford.
- J.M. Woodall, R.M. Potemski and S.E. Blum (1972) Ga<sub>1-x</sub>Al<sub>x</sub>As LED structures grown on GaP substrates. *Appl. Phys. Lett.* **20**, 375–377.
- M.-C. Wu, S.-C. Lu, C.-Y. Lee and Y.-C. Yang (1991) Interface abruptness and LED performance of the AlGaAs/InGaP single heterostructure grown by liquid-phase epitaxy. *J. Cryst. Growth* **112**, 803–807.
- R. Yakimova, M. Tuominen, A.S. Bakin, J.-O. Fornell, A. Vehanen and E. Janzen (1995) Silicon carbide liquid phase epitaxy in the Si-Sc-C system. *Silicon Carbide and Related Materials*. IOP Publishing, Bristol, 101–104.
- F.K. Yam and Z. Hassan (2005) Innovative advances in LED technology. *Microelectronics J.* **36**, 129–137.
- H. Yamane, M. Shimada, T. Sekiguch and F.J. DiSalvo (1998) Morphology and characterization of GaN single crystals grown in a Na flux. *J. Cryst. Growth* **186**, 8–12.
- T.-K. Yoo, S.-H. Hahm and Y.-S. Kwon (1988) Surface-emitting AlGaAs/GaAs DH LED with buried-window cylindrical lens. *Jpn. J. Appl. Phys. Part 2* **27**, L2357–L2360.
- G. Zhang, P. Jayavel, T. Koyoma, M. Kumagawa and H. Hayakawa (2005) Influence of Te impurity on morphology of GaSb epilayer grown on GaSb (001) patterned substrate by liquid phase epitaxy. *J. Appl. Phys.* **97**, 023518-1–023518-5.
- A. Žukauskas, M.S. Shur and R. Gaska (2001) Light-emitting diodes: progress in solid-state lighting. *MRS Bull.* **October**, 764–769.
- A. Žukauskas, M.S. Shur and R. Gaska (2002) *Introduction to Solid State Lighting*. John Wiley & Sons, Ltd, New York.



# Index

Notes: Compounds are listed under their chemical formulae. Page numbers in *italic* refer to figures and tables.

- AlGaAs
  - heterostructures 378
  - LEDs 419, 426, 428
  - quantum well substrate 228
  - regrowth process 362
  - shaped crystal growth 389
  - as transparent substrate 361
- alloys
  - five- and six-component 357–8
  - solvents model 168–71, 370
  - see also* solvents
- AlN 203
- ambient gas 98–100
  - for GaN 214–15
- atomically smooth surfaces 358
  
- band gap and lattice matching 71
- binary solution
  - free energy and chemical potential 82–3
  - phase diagrams 46, 47, 49–51, 54–9
- boat design *see* sliding-boat systems
- bubble memory devices 305, 307
- bulk crystals 67
- buoyancy-driven convection 196
- buried window LED 426, 428, 429
  
- capillary growth process 23–5, 26, 228
- CdSe 295, 296
- CdZnTe substrate 262, 283
- centrifugal LPE 134–5, 228
- chemical potential 82–3
- chemical vapor deposition 344–5, 346, 347
  - silicon technology 112
- columnar growth 3, 8, 11
- commercial LPE systems 101–6
  
- composition latching phenomena 54
- container-free LPE 191–2
- controllers and heating 99–100
- costs 86
- crucibles
  - double 134
  - for GaN 213–14
  - materials 91
  - rotating 93
- crystal growth
  - shaped 389–91
  - studies 367–9
- cubic GaN 221
- current-controlled deoxidation 372
  
- differential thermal analysis 59
- dipping systems 60, 66, 87, 88, 263, 292
  - garnet 309, 310
  - HgCdTe 265, 268
  - Si 124–5
  - SiC 191
- dislocations, misfit *see* misfit
- distribution (segregation) coefficient 113, 171, 375
- doping
  - by rare-earth elements 35–7, 366–7
  - dopant depletion 134
  - and electrical properties of MCT 266, 273–8
  - III-V binary compounds 35–7
  - silicon and germanium 113–14, 116–17
  - thermodynamic model 171–6
- double-crucible technique 134
- double-layer heterojunction detectors 278–82, 283–4

- electrical properties
  - HgCdTe 273–8
  - LPE-grown silicon 140–1
- electro-epitaxy 129–31, 370–3, 390
- electroluminescence 251–3
- electromigration 130–1, 367–9
- epitaxial lateral overgrowth (ELO) 111, 364, 365–6, 390
  - GaN 204
  - LED structures 426, 429
- epitaxy
  - technologies reviewed/compared with LPE 343–5
  - see also* heteroepitaxy; homoepitaxy
- equilibrium cooling 67
- equilibrium phase diagrams 46–59
- equipment and instrumentation 60, 66–8, 85–108
  - ambient gas 98–9
  - characteristics of LPE systems 85–7
  - furnaces 90, 96–8
  - large-scale production systems 101–6
  - safety 101
  - slider-free technology 14, 96
  - temperature control and measurement 99–101
  - vertical dipping system 88
  - see also* sliding-boat systems
- faceting transition 8, 9, 10
- Faraday rotation 308, 328
  - Bi-substituted garnet 323
  - and optical absorption 329, 330
- fibreoptics 100, 307, 308, 324, 334
- focal plane arrays (FPAs) 278–83
- forced flow technique 133–4
- forming gas 98
- Frank–van der Merwe growth mode 3, 4, 7
  - GaN 207
  - phase diagrams 73–7
- furnaces and heating 90, 96–8
  - controllers 99–100
  - growth of garnets 310
  - silicon LPE 125
  - temperature measurement 100–1
- GaAs 204–5
  - comparison of epitaxy technologies 344–5, 346, 347–8
  - quality of LPE materials 352
  - quantum dot/well substrate 228, 243
  - substrate for LEDs 419–20
- GaN 203–25, 381–3
  - background and historical development 203–6
  - control of growth modes 207–9
  - crucibles 213–14
  - cubic 221
  - device applications 203–4, 205–6
  - growth atmosphere 214–15
  - growth methods 218–21
  - growth problems summarized 206, 221–2
  - phase diagrams and thermodynamics 209–11
  - solvents 211–13
  - substrates 215–18
- GaP 204–5
- garnets 305–39
  - applications 306–8, 334–7
  - Bi-substituted 323–5, 335
  - chemical thermodynamics 314–17
  - crystal structure and composition 305–6
  - Faraday rotation 308, 323, 328, 329, 330
  - growth methods 309–11
  - growth modes 10–11
  - growth rate and mass transport 317–21
  - magnetic anisotropy 333
  - misfit strain 325–8
  - morphology control 321–3
  - optical absorption 328–33
  - oxygen partial pressures and magnetic properties 317
  - phase diagrams 311–17
  - slider-free technology 14–15
  - wafers 309, 311
- gas analysers 100–1
- Gd<sub>3</sub>Ga<sub>5</sub>O<sub>12</sub> 306, 309
- germanium *see* silicon and germanium
- gravitation-induced convection 196–8
- group II–VI (wide-bandgap) systems 289–303, 383–9
  - basic properties 289–90, 292, 297, 299, 301
  - growth methods 291–2
    - from Bi solvent 301–2
    - from Sn solvent 299–301
    - from Te and Se solvents 296–9
    - from Zn, Zn–Ga and halide solvents 293–6
  - LEDs 416, 420, 421–2
  - phase diagram 296, 298
- group III–V systems 29–35
  - antimonide LEDs 416, 418, 422–4
  - binary compounds and rare-earths 35–7
  - compositional variation in layers 78

- five- and six-component alloys 357
- heterostructures 377–81
- layer thickness calculation 77–8
- materials and usage summarized 68–9
- nitrides 381–3
  - LEDs 416, 422
  - novel melt compositions 369–70
  - phase diagrams 46–66
  - Tl-, Mn-, and Bi-containing alloys 373–4
- growth, optimum, 2, 354–5
- growth atmosphere *see* ambient gas
- growth kinetics 77–8, 349, 367–9
- growth methods and techniques 124–5, 267, 291
  - capillary 23–5, 26, 228
  - centrifugal 134–5, 228
  - contact with metastable solid phase 129
  - dipping 60, 88, 124–5, 191, 263, 268, 292, 309
  - forced flow technique 133–4
  - hydrostatic pressure technique 132–3
  - isothermal and relaxational methods 133
  - liquid phase electro-epitaxy 129–31
  - LPE compared to other techniques 343–55
  - mercury melt VLPE system 265
  - microcapillary transport and double-crucible 134
  - modified travelling solvent 185, 186–91
  - rapid slider 228, 229
  - rotating substrate 219
  - single optimum principle 2
  - solvent evaporation 132
  - surface energy driven 135
  - temperature-gradient 127–8, 220, 362–3
  - temperature-induced melt convection 128–9
  - vapor phase saturation of the solution (VLS) 131–2, 192–3
    - see also* equipment and instrumentation;
- sliding-boat systems
- growth modes 3–15
  - phase diagrams of 73–7
- growth rate
  - maximum stable 5, 209
  - model for garnet 317–21
  - Nerst equation 5
  - rate-limiting species 349–50
  - solvent effect 183
- growth temperature 31–2
- heating *see* furnaces and heating
- heteroepitaxy 3, 376–7
  - growth 23–4, 74
  - III-V heterostructures 377–81
  - and lattice mismatch 6
  - and quantum wells 228
  - Si- and Ge-based alloys 141–2
- heterogeneous nucleation 122–3, 149–50
- heterojunction devices
  - MCT 278–83
  - Russian developments 21–2
- HgCdTe (MCT) 259–87
  - device applications of 259–60
  - growth methods 260–2, 263, 264–5, 267
    - mercury-rich growth 265–6
    - tellurium-rich growth 266–9
  - material characteristics 269–71
    - composition and thickness 271–2
    - crystal quality and surface morphology 272–3
    - impurity doping and electrical properties 273–8
  - multiple-layer heterojunction structures 278–83
    - photodiode designs summarized 279
  - phase diagrams and defect chemistry 262–4
  - substrates 262
    - silicon-based 283
- high-temperature semiconductor materials 205–6
- homoepitaxy 3, 11–12, 23–4
  - and quantum wells 228
- hybrid epitaxy 380–1
- hydrogen 98–9, 101
- hydrostatic pressure technique 132–3
- InAs 239–43, 251
  - photoluminescence 241–4
- InAsSb
  - electroluminescence 251–3
  - photoluminescence 249–51
  - virtual substrates 362
- InAsSbP LEDs 422–4
- infrared radiation
  - MCT detectors 259–60, 278–83
  - mid-infrared devices 243–51, 352, 422–4
  - waveguide devices 335
- InGaAs 36
- InGaAsP heterostructures 29–35, 228–9, 378
  - compositional homogeneity 236–7
  - device applications 237

- InGaAsP heterostructures (*continued*)  
 interface abruptness 235–6  
 isotherms 61–4  
 layer thickness 231–5
- InGaAsSb  
 LEDs 422–4  
 miscibility gap 65–6
- InN 203
- InP 36
- InSb quantum dots 243–7
- instrumentation *see* equipment and instrumentation
- interface abruptness 235–6
- interface energy 54–9
- interstep distances  
 and growth modes 7–8, 10, 12  
 supersaturation ratios from 6
- Ioffe Physicotechnical Institute 21
- isoelectronic impurities 367
- isothermal techniques 133
- isotherms for InGaAsP 61–4
- kinetics of growth 77–8
- kink growth 194
- kinked surface *see* rough surface
- lasers, quantum well 32, 68, 69, 203, 237–9  
 parameters 33
- lattice matching 67, 69–71
- lattice mismatch *see* misfit, lattice
- layer thickness *see* thickness of layer
- layer-by-layer growth mode *see* Frank–van der Merwe mode
- LEDs 11, 21, 36, 68, 415–33  
 commercial LEDs 419–20  
 common materials 416–17  
 efficiency 204–5, 417, 424  
 electroluminescence of InAsSb quantum dots 251–3  
 gallium nitride applications 203–4  
 generic structure 416  
 III-V antimonides (mid-infrared ) 422–4  
 new design concepts 424–9  
 overview 415–19  
 suitability of LPE materials 418–19  
 ultrabright red 361  
 wide-bandgap (blue and UV) 420  
 II-VI compounds 420, 421–2  
 III-V nitrides 422  
 silicon carbide 420–1
- liquid observation method 59
- liquid phase epitaxy (LPE)  
 advantages and disadvantages 85–7,  
 113–14, 227–8, 353–4  
 choice of parameters 354–5  
 commercial systems 101–6  
 other technologies reviewed/compared to LPE 343–55  
 overviews 1–19, 45–6, 110–15, 341–3  
 Russian work prior to 1990 21–43  
 summary of materials grown 385–6  
 survey of new developments/specialized applications 356–88
- liquidus  
 InGaAs isotherms 61–2  
 silicon-metal modeling 166–8  
 slopes for Si-metal binaries 120–1
- luminescence  
 efficiency 351  
*see also* electroluminescence;  
 photoluminescence
- macrostep-induced striations 8, 9
- magnetic anisotropy 333–4
- magnetic garnet *see* garnets
- magneto-optics 307–8, 335–7  
 Bi-substituted garnet 323–5  
 optical absorption 328–33
- maximum stable growth rate 5
- MCT *see* HgCdTe
- meander-type boats 231
- melt epitaxy 366
- meltback 114
- mercury melt VLPE system 265
- metal-organic vapor phase epitaxy 2, 22, 112  
 of GaN 204, 207–8  
 other technologies compared/reviewed 346–55
- metastable solid phase 129
- microcapillary transport 134
- micropipes 180, 195–6, 197  
 and GaN 208
- microwave detectors 260
- mid-infrared devices 243–51  
 LEDs 422–4
- minority carrier lifetime 351
- miscibility gap 64–6
- misfit, lattice  
 defined 6  
 GaN 204–5  
 and growth mode 6–7, 11, 13  
 misfit strain of garnets 325–8

- misfit-dislocation-free wafers 71–3
  - and phase diagrams 54
- modeling of LPE processes 355–6
  - see also* phase diagrams and modeling
- molecular beam epitaxy 2, 22, 112
  - compared to other epitaxy technologies 346–55
  - and gallium nitride 204, 207
- MQW laser 238
- multicomponent systems 357–8
- multilayer structures 33, 34
  - heterojunction MCT 278
  
- Nelson method 60, 66
- Nernst equation 5
- nitrides, III-V 381–3, 412, 416
- nucleation 3
  - heterogeneous 122–3
  - silicon from metal melts 119–24
  
- optimum growth
  - parameters 354–5
  - principle of 2
- oxidation
  - current-controlled deoxidation 372
  - GaN 214–15
  - silicon 175–8
  
- PACE detectors 281
- pedestal sliding-boat system 105, 106
- Peltier cooling/heating 371
- phase diagrams and modeling 45–108
  - alloy solvents 171
  - calculation of 49–59
  - chemical potential and free energy 83–4
  - described and illustrated 46–9
  - equilibria models 117–19
  - experimental determination 59–66
  - gallium nitride 209–11
  - garnet 311–17
  - growth kinetics 77–8, 356
  - growth mode 73–7
    - and growth technologies 66–8
  - HgCdTe 262–4
  - III-V materials and usage 68–9
  - interface and strain energies 54–9
  - for interface temperature determination 31–2
  - literature review 355–6
  - miscibility gap 64–6
  - misfit-dislocation-free wafers 71–3
  - SiC 181
    - silicon and germanium 115–19, 166–71
    - silicon-metal liquidus 166–71
    - widegap II-IV compounds 296, 298
  - photodetectors 36–7, 259–60, 278–83
    - InGaAs 36
  - photoluminescence
    - encapsulated InAsSb 249–51
    - InAs 241–4
    - ZnSe 294
  - photoresistors 36
  - piston sliding-boat 27–9, 31, 33–5, 95, 96
  - production LPE systems 101–6
  
- quantum dots 243–57, 360
  - electroluminescence 251–3
  - encapsulated InAsSb 247–9
    - mid-infrared luminescence 249–51
  - InSb on GaAs substrates 244–7
  - photoluminescence 241–4, 249–51
- quantum wells 69, 227–43, 253–7, 358–9
  - capillary growth process 23–5, 26
  - compositional homogeneity 236–7
  - devices with ultrathin LPE layers 237–9
  - growth and rapid slider methods 228–31
  - indium arsenide 239–43
  - InGaAsP in Russia prior to 1990 29–35
  - interface abruptness 235–6
  - low-temperature LPE 25–9, 30
    - thickness of rapid slider layers 231–5
    - use of rare-earth elements 35–7
- quaternary phase diagrams 46, 47, 48–9
  - calculation of 52–9
  
- ramp-cooling 67
- rapid slider methods 228–30
  - and layer thickness 231–5
- rare-earth elements 35–7, 366–7, 375–7
- Rayleigh number 196
- regrowth process 362
- relaxational techniques 133
- rotating boat 93
- rotating-crucible method 60, 66, 93
- rotating-melt system 96
- rotating-substrate method 219
- rough surface growth 3
  - garnet 10–15
  - SiC 193–5
- Russian work prior to 1990
  - quantum-well heterostructures 22–35
  - use of rare-earth elements 35–7



- safety 101
- salting out technique 133
- sapphire substrate 216, 218–19
- screw dislocations 7
- screw-island growth 3, 4
  - garnet 11
- seed-dissolution technique 59, 60–2
- segregation
  - coefficient 113, 171, 375
  - control of 374–6
- selective epitaxy 142–3, 363–6, 389–91
  - novel LEDs 424–9
- shaped crystal growth 389–91
- SiC 179–201, 381–2
  - characteristics 179–80
  - container-free LPE 191–2
  - device applications 198–9
  - dipping technique 191
  - growth methods 186–93
  - LEDs 420–1
  - LPE under reduced gravity 196–8
  - micropipe filling 195–6, 197
  - phase diagram 181
  - solvent choice and wetting 182–5
  - step-bunching 193–5
- silicon and germanium, silicon passivity 177–8
- silicon and germanium 109–79
  - background and historical perspective 111–15
  - binary phase diagrams 115–19
  - device applications (non-solar cell) 110, 150–1
  - dipping technique 124–5
  - doping 113–14, 116–17
    - thermodynamic model 171–6
  - electrical properties of LPE-grown silicon 140–1
  - furnace temperature and control 125
  - growth methods 124–35
  - heteroepitaxy on 380–1
  - impurities 171–6
  - low-temperature silicon LPE 137–8
  - non-silicon substrates 149–50
  - nucleation from molten metal solution 119–24
  - oxygen and water vapor 175–8
  - phase equilibria 115–19
    - modeling 166–71
  - purification of silicon for solar cells 113, 138–40
  - selective LPE and liquid phase ELO 142–4
  - silicon passivity 177–8
    - silicon- and germanium-based alloys 141–2, 168–71
    - Si–metal binary data 120
    - solar cells 110, 144–50
    - solvent selection 110, 113, 120, 135–8
  - single-layer heterojunction detectors 278–80
  - slider-free growth system 13–15
  - sliding-boat systems
    - crucible materials 91
    - design/development for multilayer heterostructures 25–9
    - horizontal 60, 87, 88, 89–92, 126, 263, 292
      - alternative designs 92–6
    - large-scale commercial systems 101–6
    - meander type 230–1
    - piston sliding-boats 27–9, 31, 33–5, 95, 96
    - problems with 14
    - rapid 228–30
    - tipping/rotating type 92, 93
  - solar cells 110, 144–50
  - solidus isotherms 62–4
  - solution growth methods *see* growth methods
  - solvent evaporation techniques 132
  - solvents
    - alloy solvents model 168–71, 370
    - for GaN 211–14
    - for garnets 311–17
    - III-V five- and six-component alloys 357–8
    - novel melt compositions 369–70
    - for silicon carbide 182–5
    - for silicon and germanium 110, 113, 120, 135–8
      - wetting and surface tension 184–5
      - for widegap II-IV compounds 293–302
  - spiral-island growth 3, 7
  - SQW laser *see* laser
  - steady-state growth methods 125–35
  - step-flow growth mode 3, 4, 8
  - step growth 194
  - step propagation 3
  - step bunching 3, 4, 8
    - SiC 193–5
  - step cooling 67
  - strain energy 54–9, 74, 75
  - Stranski–Krastinov growth mode 3, 4
    - gallium nitride 207, 208
    - phase diagrams 73–7
    - and quantum dots 243
  - substrates
    - for GaN 215–17
    - garnet 309, 311
    - heteroepitaxy 377–81

- for HgCdTe 262, 283
- for LEDs 419–20
- and materials grown 385–6
- and quantum wells 228
- requirements of 15–16
- for silicon 144–5, 149–50
- suppliers 217
- virtual 360–3
- supercooling
  - and nucleation 121–2
  - techniques 67–8
- superlattice structures 358–60
- supersaturation 5–6, 11, 12, 13, 67–8
  - and nucleation 121
  - silicon–metal melts 116, 119–24
- surface energy and diffusion 350
- surface nucleation 3
- surface tension 185
- surface-energy
  - LPE driven by 135
  - and phase diagrams 54–9
- technologies
  - LPE and other epitaxy techniques compared 343–55
  - see also* growth methods
- tellurium melt dipping reactor 286
- temperature
  - growth conditions 31–2
  - measurement and control 90, 99–101
- temperature-gradient solution growth 127–8, 220, 362–3
- temperature-induced melt convection 128–9
- ternary phase diagram 46, 47, 48
  - calculation of 51–2, 54–9
- thermal expansion 6, 72, 325
- thermocouple 100
- thermodynamics
  - binary solutions 82–3
  - epitaxy technologies compared 346
  - see also* phase diagrams and modeling
- thickness of layer
  - calculation for III-V system 77–8
  - factors affecting 23
- III-V *see* group III-V
- tipping boat 92, 93, 263
- travelling solvent method 185, 186–91
- tubes for processing 99
  - II-VI *see* group II-VI
- UV-emitting diodes 203, 204, 420–1
- vapor phase epitaxy
  - compared to LPE 2, 4–5
  - gallium nitride 204
- vapor–liquid–solid (VLS) method 131–2, 192–3
- via-hole device 280, 281
- virtual substrates 360–3
- Volmer–Weber growth mode 3, 4, 7–8
  - gallium nitride 207, 208
  - phase diagrams 74–7
- wetting 183–5
  - and gallium nitride 213–14
- wide-bandgap II-IV *see* group II-IV
- $Y_3Al_5O_{12}$  306
- $Y_3Fe_5O_{12}$  (YIG)
  - absorption spectrum 331, 332
  - chemical thermodynamics 314–17
  - growth rate 318–19
  - misfit strain 327–8
  - morphology 321
  - phase diagram and solution growth 311–14
- ZnS 296, 297, 298–9, 422
- ZnSe 293–6, 297, 298–302, 420, 421–2
  - photoluminescence spectra 294
- ZnTe 295, 296, 297, 422